GRANADA (SPAIN)
24-27 SEPTEMBER 2019

26TH ELGRA BIENNIAL SYMPOSIUM AND GENERAL ASSEMBLY

14TH INTERNATIONAL CONFERENCE ON TWO-PHASE SYSTEMS FOR SPACE AND GROUND APPLICATIONS

& ESA TOPICAL TEAMS MEETINGS

BOOK OF ABSTRACTS

OVERVIEW

Tuesday 24th			
Schedule			*Registration Desk*
9:00	13:00	**ELGRA Management Committee (per invitation)** **Chinese/European Two-Phase Heat Transfer meeting (per invitation)** **Student activity: The ten most beautiful experiments in Physics (per invitation)**	
		Califa room	
17:00	18:00	**Opening**	Registration
18:00	19:15	**Space agencies talks** Chair: R. González-Cinca	
19:30	21:00	*POSTER SESSION & WELCOME RECEPTION*	

Wednesday 25th					
Schedule		**Physical Sciences 1** *Reyes room*	**Physical Sciences 2** *Torre de los Picos room*	**Life Sciences / Education** *Room Mocarabes room I & II*	**ITTW** *Visir room*
8:30	8:45	**Diffusion in non-metallic mixtures** Chair: F. Croccolo	**Geophysical fluids flow** Chair: C. Egbers	**Plant Biology** Chair: J. Medina	**Keynote** Chair: M. Dreyer
8:45	9:00				
9:00	9:15				**Films, interfaces and contact line phenomena** Chairs: P. Stephan, J.L. Davalos Orozco
9:15	9:30				
9:30	9:45				
9:45	10:00				
10:00	10:15		Chair: T. Karapantsios		
10:15	10:30				
10:30	11:00	*COFFEE BREAK*			
11:00	11:15			**Education** Chair: P. Carvil	**Keynote** Chair: D. Del Col
11:15	11:30				
11:30	11:45				**Condensation** Chairs: S. Dehaeck, T. Karapantsios
11:45	12:00				
12:00	12:15	**Diffusion and Convection phenomena**	**Granular media**		
12:15	12:30	Chair: M. Bouali Saidi	Chair: E. Falcon	**Human Physiology and Medicine** Chair: M. Egli	
12:30	12:45				
12:45	13:00				
13:00	14:15	*LUNCH*			
14:15	14:30	**Marangoni convection** Chair: V. Shevtsova	**Thermophysical properties** Chair: M. Mohr		**Boiling and bubbles** Chairs: L. Tadrist, Z. Chen
14:30	14:45				
14:45	15:00				
15:00	15:15				
15:15	15:30				
15:30	16:00	*COFFEE BREAK*			
16:00	16:15			**Plant Biology group meeting**	
16:15	16:30				
16:30	16:45				
16:45	17:00				
17:15	21:00	*VISIT TO LA ALHAMBRA*			

OVERVIEW

Thursday 26th									
Schedule		Califa room Chairs: R.González-Cinca, P. di Marco	Schedule		Room Mocarabes I	Schedule		Room Visir
8:30	9:40	ELGRA Medalists						
9:40	10:15	ITTW Plenary talk						
10:15	10:45	*COFFEE BREAK*						
10:45	11:55	ELGRA-ASGSR						
11:55	12:55	ELGRA Presidents panel						
12:55	13:20	ELGRA goes Suborbital						
13:20	14:30	*LUNCH*						
14:30	14:50	Workshop "Seedling Growth"			TT meeting: Diffusion in non-metallic mixtures	14:30	14:45	Thermocapillary Flows
14:50	15:10	Chairs: J. Medina, J. Kiss				14:45	15:00	Chairs: D. Mangini, J. Wei
15:10	15:30		14:30	16:00		15:00	15:15	
15:30	15:50					15:15	15:30	
15:50	16:10					15:30	15:45	
						15:45	16:00	
16:00	16:30	*COFFEE BREAK*						
16:30	17:30	SELGRA Assembly	16:00	17:30	TT meeting; Space Grains	16:30	18:00	ITTW Scientific committee meeting
17:30	19:15	ELGRA General Assembly	17:30	19:00	TT meeting: Non-equilibrium phenomena in soft matter and complex fluids			
20:00	0:00	*GALA DINNER*						

Friday 27th				
Schedule		Physical Sciences /Technology *Reyes room*	Life Sciences *Mocarabes room I & II*	ITTW *Visir room*
8:30	8:45	**Vibrations in fluids**	**Cell Biology**	**Keynote**
8:45	9:00	Chair: J. Porter	Chair: A. Sundaresan	Chair: D. Zaitsev
9:00	9:15			**Drops**
9:15	9:30			Chairs: A. Robinson, C. Colin
9:30	9:45			
9:45	10:00			
10:00	10:15			
10:15	10:30			
10:30	11:00	*COFFEE BREAK*		
11:00	11:15		**Special session: What is the Perfect Ground-Based Facility for Microgravity Simulations in Life Science?**	
11:15	11:30			
11:30	11:45			**Experiments in micro-g**
11:45	12:00			Chairs: O. Kawanami, J. Kim
12:00	12:15	**Technology**		
12:15	12:30	Chair: C. Lockowandt		
12:30	12:45			
12:45	13:00			
13:00	13:15			
13:15	13:30			
13:30	14:45	*FAREWELL LUNCH*		
14:45	18:00			**ITTW meeting**

ELGRA-26

Conference Chair

Ricard González-Cinca
Universitat Politècnica de Catalunya-BarcelonaTech
Castelldefels (Barcelona), Spain

Conference Co-Chair

Christian Lockowandt
Swedish Space Corporation
Stockholm, Sweden

ELGRA-26 Scientific Committee:

Mounir Bouali Saidi, *Spain*
Miguel Cabrerizo, *Spain*
Philip Carvil, *UK*
Fabrizio Croccolo, *France*
Christoph Egbers, *Germany*
Marcel Egli, *Switzerland*
Eric Falcon, *France*
Hans-J. Fecht, *Germany*
Kurt Kemmerle, *Germany*
John Z. Kiss, *USA*
Carole Leguy, *Germany*
Monica Monici, *Italy*
David Pino, *Spain*
Valentina Shevtsova, *Belgium*
Nathaniel Szewczyk, *UK*
Vincent Yip, *UK*

ITTW-14

Conference Chair

Paolo di Marco
DESTEC, University of Pisa
Pisa, Italy

Conference Co-Chairs

Jungho Kim
University of Maryland,
MD, USA

Oleg A. Kabov
Kutateladze Institute of Thermo-physics SB RAS,
Novosibirsk, Russia

Haruhiko Ohta
Kyushu University
Fukuoka, Japan

Jian-Fu Zhao
Institute of Me-chanics,
Beijing, China

ITTW-14 Scientific Committee:

Vladimir S. Ajaev, *USA*
Sergey V. Alekseenko, *Russia*
Alidad Amirfazli, *Canada*
Hitoshi Asano, *Japan*
Zhenqian Chen, *China*
Avram Bar-Cohen, *USA*
Catherine Colin, *France*
Paolo di Marco, *Italy*
Davide Del Col, *Italy*
Michael Dreyer, *Germany*
Olga N. Goncharova, *Russia*
Osamu Kawanami, *Japan*
Zhenhui He, *China*
Oleg A. Kabov, *Russia*
Jungho Kim, *USA*
Qusheng Liu, *China*
Marco Marengo, *UK*
Dmitriy Markovich, *Russia*
Haruhiko Ohta, *Japan*
Eduard E. Son, *Russia*
Peter Stephan, *Germany*
Lounes Tadrist, *France*
John R. Thome, *Switzerland*
Balazs Toth, *The Netherlands*
Jian-Fu Zhao, IM, *China*
Jinjia Wei, *China*

INDEX

PLENARY TALKS

Plenary Talk 198

CNES program of physical science in microgravity

Christophe DELAROCHE[1]

[1]CNES, Toulouse, France
Christophe.delaroche@cnes.fr

Abstract
The CNES Physical science program covers all the current fields of research on fluids, combustion, complex fluids, material, biophysics… The objective is to help French laboratories to study the various physical phenomena through access to microgravity in order to determine the universal properties of the matter and its change of states out of gravity.
In France, with the CNES support, laboratories using microgravity are gathered in an association of researchers, the GdR MFA (Group of Researchers for physics in Microgravity, Fundamental and Applications) to exchange about science, simulation, instrument, diagnosis or cooperation.
CNES Science program funds the necessary complement to develop or adapt the scientific instruments to space experimentation. This funding contributes also to the data analysis and numerical modeling.
CNES offers scientists privileged access to two parabolic campaigns per year in the French Airbus Zero-G airplane. This access could be open to foreign scientists in the frame of international cooperation.
Numerical simulation, tests in the Zero-G airplane and then long term experiments in ISS or souding rocket is the regular way to take progressively advantage of the space facilities. This is made essentially through the ESA organization frame but also through direct cooperation with other space agencies, within or outside Europe.
A global overview of the program will be presented as well as last new subjects of research taken into account by the CNES program.
The orientations proposed to the CNES Seminar of Prospective at Le Havre 2019 will be exposed in advance.
A new organization in the Directory Innovation Application and Science that make place to exploration program will be also introduced.

Plenary Talk 199

ASGSR - Advocating Microgravity Research
An example: Microgravity Colloids
An International Research Program

William V. Meyer[1] and Anna-Lisa Paul[2]

[1]ASGSR (Governing Board Member) and USRA at NASA Glenn Research Center (GRC), Cleveland, OH, USA; William.V.Meyer@NASA.Gov , [2]ASGSR (Immediate Past President) and University of Florida, Gainesville, FL, USA; alp@ufl.edu

Introduction

We'll begin with an introduction to the American Society for Gravitational and Space Research – ASGSR, this ELGRAASGSR session talk will then provide examples of the kind of international collaborative work with which the speaker is associated and that ASGSR promotes though NASA's microgravity colloids program. This presentation will mention some of the pleasant surprises from the microgravity colloids research on the International Space Station (ISS). While that work is with P&G and Universities in the U.S., Europe, and South Korea, here we will highlight just a few and show some short and interesting movies that showcase some of the US and European science teams that are part of the Advanced Colloids Experiment (ACE). The intent is to strengthen the relationship between ELGRA and ASGSR.

ASGSR Overview

The Vision of ASGSR is to advance biological and physical science research in, of and for space by bringing together professional communities spanning gravitational biology, radiation biology, physical sciences, bioastronautics and astrobiology, and mentoring the future scientific and engineering leaders in these fields.

ASGSR advocates for areas of research in both Life Sciences and Physical Sciences. Many of these are pictured in the introductory slides of the presentation, Figures 1-4.

Figure 1. ISS Research – Life Sciences (1/2)

Figure 2. ISS Research – Life Sciences (2/2)

Figure 3. ISS Research – Physical Sciences (1/2)

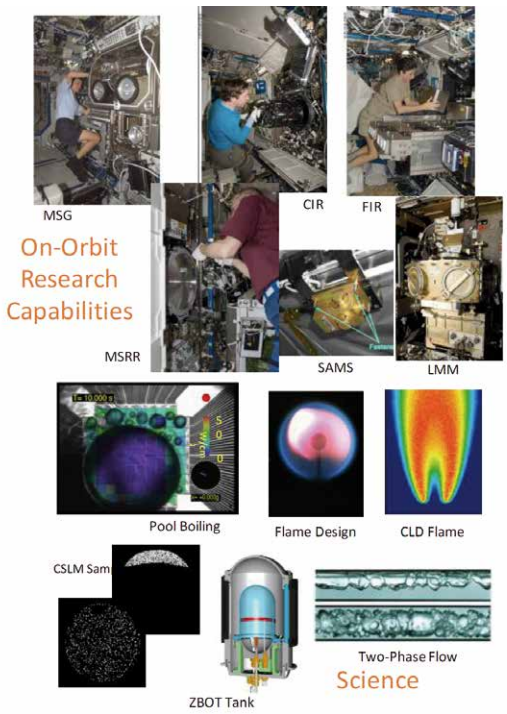

Figure 4. ISS Research – Physical Sciences (2/2)

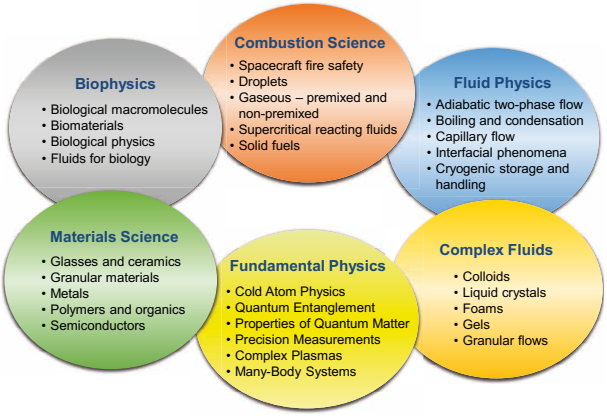

Figure 5. Space Life and Physical Sciences Research and Applications (SLPSRA) Gravity-Dependent Physical Sciences Research

Having been asked to give examaples from the field in which I work and have collaborations, I will focus on the microgravity colloids program experiments supported by SLPSRA (see Figure 5), CASIS and NSF, and with ESA support for our European colleagues (science teams).

Examples from the Microgravity Colloid Program

Some examples follow from the NASA-CASIS microgravity Colloids program showing the kind of microgravity research for which ASGSR advocates. They will showcase both US and European science teams. Specific examples of ASGSR promoting microgravity research in Complex Fluids include invited plenary talks in the field during the ASGSR Annual Meetings, which are attended by scientists and their funding agencies. Here are two recent examples of such plenary talks:

1. "Colloids, Granular and Soft Matter on Earth and In Space", Paul Chaikin, New York University, ASGSR, 33rd Annual Meeting, Symposium VII: 2017 Hot Topics - New Directions in Physical Sciences Research.

The NASA microgravity program has been instrumental in the development of the field of Soft Condensed Matter Physics over the past several decades (Zhu et al., 1997). Early space shuttle experiments changed our fundamental understanding of how liquids become crystals or glasses and how crystals grow. Further research showed the role of particle shape in how particles pack in both random and crystalline arrays. This discovery led the way to new building blocks and mechanisms for fabricating novel materials. The future will lead to active materials, that selfassemble, self-replicate and evolve. Such materials should prove useful in exploration and the methods used to study granular and soft materials may help answer questions relating to the history of celestial bodies and their surface particulates.

2. "Measurements on the ISS to Inspire and Enable the Creation of Transformative Products." - Matthew Lynch, Proctor & Gamble. ASGSR, 34th Annual Meeting, ENABLING TECHNOLOGIES, SYMPOSIUM #4: 2018 Hot Topics in Life and Physical Sciences, 2018 Meeting Video Webcast Archive: https://asgsr.org/index.php/2018-meeting-video-webcast-archive.

A few slides and some short and interesting movies that are interviews with US and European science teams leading ISS colloids research experiments follow. These interviews include: 1. Paul Chaikin [Stefano Sacanna, and Andrew Holllingsworth, Mena Youssef, and Issak Proano] (ACE-T7, NYU), Piet Swinkels [T. A. Nguyen, A. Manca, M. Potenza, G. Wegdam, P. Schall] (ACE-T2, University of Amsterdam and Università di Milano - ESA) Stefano Buzzaccaro [and Roberto Piazza] (ACE-T10, Politecnico di Milano - ESA).

Conclusions

The parallel goals and objectives of ASGSR and ELGRA make for an ideal partnership. The workshop that helped provide a roadmap for the existing NASA microgravity colloids program (Ref. 2) will be held again in the next year and it would be great to have you be part of that.

Acknowledgements

Our thanks to ELGRA for inviting us to participate in this meeting and for providing travel and accomodations for W. Meyer, and to Gale Allen for ASGSR material and discussions. W. Meyer also thanks USRA for supporting his time to attend this meeting and NASA for their review of the slides and movies.

References

Jixiang Zhu, Min Li, R. Rogers, W. Meyer, R. H. Ottewill, STS-73 Space Shuttle Crew, W. B. Russel & P. M. Chaikin, "Crystallization of hard-sphere colloids in microgravity (Letters to Nature)," Nature 387, 883-885 (June 26, 1997).

Report on the NASA Soft and Complex Condensed Matter Workshop, https://ntrs.nasa.gov/search.jsp?R=20030112858&hterms=chaikin&qs=N%3D0%26Ntk%3DAuthor-Name%26Ntt%3Dchaikin%26Ntx%3Dmode%2520matchall.

26th European Low Gravity Research Association Biennial Symposium and General Assembly
14th International Conference on "Two-Phase Systems for Space and Ground Applications"
European Space Agency Topical Teams meetings
Granada (Spain), September 24-27, 2019

Plenary Talk 200

Shapes and dynamics of confined liquid-vapor interfaces in two-phase systems in microgravity

V.S.Ajaev[1], J. A. Barrett[1]

[1]Southern Methodist University, Dallas, Texas, USA;
ajaev@smu.edu

Introduction

Many conventional two-phase heat transfer systems operating under normal gravity display entirely different behavior under microgravity conditions, as illustrated e.g. by the constrained vapor bubble (CVB) experiments (Kundan et al. 2014). CVB is a two-phase system constrained to a cuvette, heated from one end and cooled at the other. Under normal gravity, the set-up operates as an idealized heat pipe, with dry hot end and liquid condensation at the cold end. The capillary flow in the corners provides the liquid transport mechanism needed for continuous operation. However, in microgravity experiments onboard the International Space Station, the hot end was unexpectedly flooded with liquid. A typical image from the CVB experiment, shown in Fig. 1, illustrates the flooding of the hot end (left side of the picture) and the formation of two other interesting features: the pinch points at the interfaces in the corners and the central droplet. In additional to optical recordings, careful temperature measurements have been conducted in experiments. The main focus of our work is on mathematical modeling of confined vapor-liquid interfaces, as motivated by these CVB experiments.

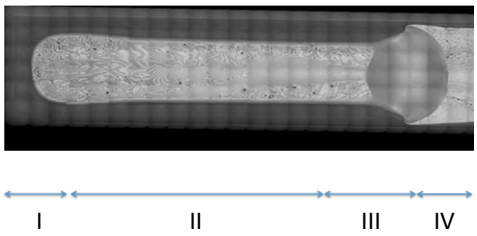

Figure 1: Experimental photo from CVB experiment showing flooding of the hot end (region I) and formation of a central droplet (part of regions III and IV). The corners of the cuvette as also filled with liquid, corresponding to the darker areas in the photo.

Models of droplets

We use lubrication-type models of small axisymmetric evaporating/condensing sessile droplets observed near the menisci in the CVB configuration (Gokhale et al. 2003). Our numerical model describes changes in interface shapes as a function of local substrate temperature, assumed uniform here. The numerical results are shown to describe experimental data well, as illustrated by a sample plot of droplet radius of curvature at its apex in Fig. 2. We used a wetting model based on two-component disjoining pressure, with parameters chosen to match the experimentally observed contact angles. The droplet model is then modified to investigate the non-symmertic central droplet seen in the experiments, e.g. in Fig. 1. Variation of the substrate temperature, based on the heat conduction model in the solid, and mass exchange with the liquid in the corners are incorporated into the model. The results allow us to describe the dynamics of the central droplet formation as the heater is turned on.

Corner flows

Studies of viscous flows in the corners of the cuvette are essential for understanding the overall heat and mass transfer in CVB. While wedge flow models are well developed (Markos et al. 2006), they are typically not capable of describing the complex coupling between the wedge flow and heat conduction in the substrate, resulting in substantial axial temperature gradient, as seen in the CVB system. We used finite-element method to investigate wedge flow using the model which incorporates the variation of the temperature seen in the CVB experiment, in the longitudinal direction. Both capillary pressure gradient and Marangoni forces are considered. By exploring the analogy with thin-film flows under conditions of normal gravity, we are able to explain the formation of the pinch points at the interface.

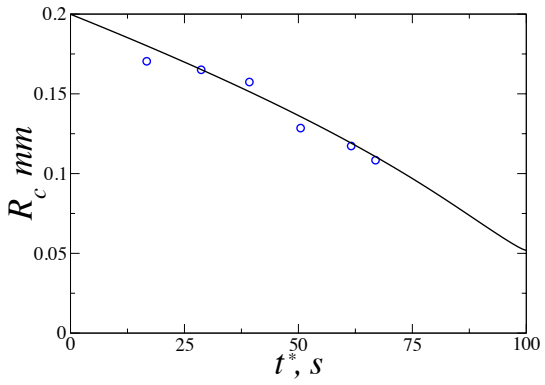

Figure 2: Comparison of the predictions of the radius of curvature at the top of a sessile evaporating droplet based on our numerical model (solid line) and experimental measurements (empty circles, data from Gokhale et al. 2003).

Conclusions

Novel mathematical models of confined liquid-vapor interfaces allow us to gain insight into the physics of the processes taking place under microgravity conditions in the CVB experimental system. The results on evaporation of droplets are shown to be in agreement with the experimental data. Mass transfer between the central droplet seen in the CVB experiment and the liquid in the corners is studied in the framework of non-axisymmetric droplet model.

Acknowledgements

This work was supported by NASA grant 80NSSC18K0332. We are grateful to Prof. J. Plawsky for numerous valuable discussions and for sharing the experimental data with us.

References

A. Kundan, J. L. Plawsky, P. C. Wayner Jr., Thermophysical characteristics of a wickless heat pipe in microgravity – Constrained vapor bubble experiment. *Int. J. of Heat and Mass Transfer* (2014) 781105-1113

S. J. Gokhale, J. L. Plawsky, P. C. Wayner Jr., Experimental investigation of contact angle, curvature, and contact line motion in dropwise condensation and evaporation, *J. Colloid Interface Sci.,* 259 (2003) 354-366

M. Markos, V. S. Ajaev, G. M. Homsy, Steady flow and evaporation of a volatile liquid in a wedge, *Phys. Fluids* 18 (2006) 092102

Plenary Talk 201

The German microgravity science program

T. Saltzmann[1], Thomas Driebe[1]

[1]German Aerospace Center – Space Administration, Bonn, Germany
Tobias.Saltzmann@dlr.de

As German Space Agency, the DLR Space Administration manages the German Space Program. This program integrates the German participation in the ESA programs, the activities in the National Program as well as the R&D activities of the DLR research institutes.
As one core element of the German space activities, Research under Space Conditions covers life and physical sciences utilizing space conditions such as weightlessness and space radiation. The tasks of this unit can be divided into three major elements:
(i) provision of microgravity platforms (e.g.: drop tower, parabola flights and sounding rockets),
(ii) development of flight hardware, and
(iii) preparation, execution, and analysis of microgravity experiments.

The Microgravity Sciences Program deals with gravity-dependent effects on physical and chemical processes. For life sciences, in addition to gravity-dependent effects, the influence of space radiation on living systems is being surveyed. Germany`s National Space Program aims at gaining scientific knowledge by addressing fundamental questions in physical as well as life sciences, fostering new technological developments and to reveal new application potentials by both fundamental as well as application-oriented research, especially utilizing the ISS.
In this talk, major German research topics and on-going facility developments in life as well as physical sciences for the ISS and other microgravity platforms are presented. Furthermore a review on last year's ISS Mission "HORIZONS" of German ESA astronaut Alexander Gerst will be given.

Plenary Talk 202

ESA's SciSpacE programme - Opportunities for Research and Applications

Sebastien Vincent-Bonnieu, on behalf of ESA's SciSpacE Team

Directorate of Human & Robotic Exploration, European Space Agency, Noordwijk, The Netherlands
email1@aff1, email2@aff2, email3@aff3

The SciSpacE programme (Science in Space Environment, previously known as ELIPS, the European Life and Physical Sciences programme) is progressing with a challenging and intense experimental programme. A variety of important new experiments is being prepared for implementation on-board the ISS and ground based facilities.

The European Columbus module is for the European Space Agency (ESA) the key research laboratory in space to exploit the unique potential of the International Space Station (ISS) in a broad range of utilisation areas. For ESA, life and physical sciences are the focal areas comprising human research, biology/astrobiology, radiation and materials science, fluids and fundamental physics. In addition, an increasing number of technology demonstrations are providing further knowledge necessary for Earth-related services and future human exploration in space. ESA has performed more than 220 experiments on the ISS since the launch of Columbus, within the scientific context of its SciSpacE programme. Selected highlights performed by ESA will be presented to show the latest accomplishments and future plans of the very active and broad European user community, including international scientific cooperation.

The Human Research Programme offers scientific activities on research platforms such as ground-based space analogs (e.g. bed rest studies, research on Antarctic stations, radiation facilities, isolation and confinement missions), as well as an ambitious research programme on-board the ISS. In addition to gaining fundamental knowledge on human health in space and making manned missions beyond Low Earth Orbit (LEO) a safe reality, the research carried out is also helping to deliver solutions to problems back on Earth, e.g. testing new medical techniques and biomedical instruments.

Space Biology research on-board the ISS advances our understanding of how biological systems are affected by altered gravity and other spaceflight factors, such as cosmic radiation. Research activities include experiments on cell biology, microbiology and plant biology which are conducted primarily in dedicated biology facilities such as KUBIK and Biolab in the Columbus module. In addition to advancing basic scientific knowledge, the results of these studies are relevant to understanding how biological processes relevant to human health are affected by spaceflight as well development of bioregenerative life support systems. In addition to traditional biology research, the exobiology programme aims to understand the origin and limits of life in the solar system, as well as how to identify signs of life such as biomarkers. The EXPOSE astrobiology experiments, on the external surface of the ISS, conducted and used for multiple experiments where various life forms (like bacteria, seeds, algae) and organic compounds (precursors of life or biomarkers) were exposed to the external space environment (vacuum, temperature extremes, radiation). Future biology and exobiology research will benefit from enhancement of the research capabilities on-board ISS.

The physical sciences research plan covers a broad range of topics such as fundamental physics, dynamics of complex fluids, thermal-diffusion, fluids dynamics and phase changes as well as melting and solidifications processes with a strong interdisciplinary dimension to most topics. In addition, the applied research focuses on the behaviour of complex fluids, two-phase heat transfer and the properties of materials for improving knowledge about physical behaviour and product processes on Earth and Space. Currently in operation on the ISS, the joint ESA-ROSCOSMOS experiment PK-4 studies the liquid phase and flow phenomena of cold dusty

plasmas. In the Atmospheric sciences, the ASIM payload monitors since 2018 the upper atmosphere of the Earth for gigantic electric discharges and Gamma-ray flashes powered by thunderstorms. Soon to come is a unique payload, ACES, equipped with high stability and accuracy atomic clocks. The clock signal generated on-board the ISS will be used to perform space-to-ground comparisons with the best atomic clocks available on Earth. ACES will perform accurate tests of Einstein's theory of General Relativity. Moreover, it will provide stable and accurate time for different applications, including differential geopotential measurements, time and frequency metrology, time transfer and synchronization experiments, atmosphere studies.

International science collaboration with other ISS partners and national agencies is continuously expanding and provides various significant mutual benefits. The increasing yield of unique scientific knowledge and simultaneous operational experience demonstrate the extraordinary exploitation value of the ISS as a permanent human outpost in Low Earth Orbit (LEO) for fundamental science, applications and technology demonstration, as well as for future human exploration.

Plenary Talk 203

Mission Space Research - Where Life Sciences meet Physical Sciences to Bring Humanity Together: A Perspective on Immune Function and Bone Loss in the Realms of Low Gravity.

Dr. Alamelu Sundaresan[1]
[1]Texas Southern University, Houston, United States
alamelu.sundaresan@tsu.edu

In space travel and long term space residence, crew, animals and cells are exposed to microgravity, radiation and other space stressors. In turn, these are potential hazards to the immune system and heavy bone loss.

The immune system is the body's defense against infectious organisms and other invaders. It is our immune system that keeps us healthy as we drift through a sea of pathogens. Healthy immune function depends on meticulous regulation of lymphocyte activation. Previous studies have shown unfavorable effects of μg on several physiological systems, including a significant reduction of the adaptive immune response and bone loss. Lymphocyte movement through interstitium is critically important for the immune response. Thus, the activation of lymphocytes depends on various factors such as cell-to-cell contact due to temporary contact, permanent aggregation or by the uptake of soluble factors such as interleukin 1. Microgravity induced loss of lymphocyte locomotory activity, along with diminished lymphocyte activation, can be counteracted by nutritional supplements such as nucleotides. Discoveries made in the course of space biomedical research on bone are already contributing to a better understanding of osteoporosis and the treatment of bone mass loss on Earth as well as in space. The single most important contribution that NASA research has made to the understanding of bone deterioration in osteoporosis is heightened awareness of the importance of gravity, activity, and biomechanics - that is, the mechanical basis of biological activity - in bone remodeling. A study conducted by Andreazzoli et al., proposes that the knowledge of cellular and molecular mechanisms of gravity and its influence on T cells is required for creating the provision of therapeutic and possible preventive targets to keep the bone and immune systems of astronauts fully functional during long-term space missions, in addition to aiding regular people with immune deficiencies. Therefore, studying both the long-term and short-term effects of microgravity on immune function and bone loss is of great significance, as it has an invalidation nature that affects how the regulators of both systems system are readily able to function. An experimental journey of experiments involving spanning the shuttle era to the ISS spanning these two systems involving biological and physical sciences is presented.

Acknowledgements
Grants from NASA, Amino Up Chemical (PI-Dr. Alamelu Sundaresan) and NSF TIP 1719318 (PI-Dr. Alamelu Sundaresan)

References

Vivek Mann, Daniela Grimm, Thomas J Corydon, Marcus Krüger, Markus Wehland, Stefan Riwaldt, Jayashree Sahana, Sascha Kopp, Johann Bauer, Janne E. Reseland, Manfred Infanger, Aina Mari Lian, Elvis Okoro and Alamelu Sundaresan 1. Changes in Human Foetal Osteoblasts Exposed to the Random Positioning Machine and Bone Construct Tissue Engineering. Int. J. Mol. Sci. 2019, 20(6), 1357; https://doi.org/10.3390/ijms20061357 (registering DOI)

Anil D Kulkarni, Marie-Francoise Doursout, Asmita Kulkarni, Alamelu Sundaresan, Takehito Miura, Koji Wakame and Hajime Fujii. Spaceflight: Immune Effects and Nutritional Countermeasure. Published: May 30th 2018.DOI: 10.5772/intechopen.74709

Sigrid Haugen, Jianying He, Alamelu Sundaresan, Astrid Kamilla Stunes, Kristin Matre Aasarød, Hanna Tiainen, Unni Syversen, Bjørn Skallerud, and Janne Elin Reseland, Adiponectin Reduces Bone Stiffness: Verified in a Three-Dimensional Artificial Human Bone Model In Vitro. Front Endocrinol (Lausanne). 2018; 9: 236.

Daniela Grimm, Marcel Egli, Marcus Krueger, Stefan Riwaldt, Thomas J Corydon, Sascha Kopp, Markus Wehland, Petra Wise, Manfred Infanger, Vivek Mann, Alamelu Sundaresan. Tissue engineering under microgravity conditions–use of stem cells and specialized cells. Stem cells and development 27 (12), 787-804

Vivek Mann, Elvis Okoro, Ayodotun Sodipe, Courtney Williams, Patricia Ngantcha and Alamelu Sundaresan. Lymphocyte Signaling and Function in Altered Physiological Environments. Published: December 17, 2018. DOI: 10.5772/intechopen.81171

Vivek Mann, Alamelu Sundaresan, Satish K Mehta, Brian Crucian, Marie F Doursout, Sundar Devakottai. Effects of microgravity and other space stressors in immunosuppression and viral reactivation with potential nervous system involvement. Neurology India 2019, 67 (Supplement): S198-S203

Vivek Mann, Alamelu Sundaresan, Maitreyi Chaganti, Cellular changes in the nervous system when exposed to gravitational variation. Neurology India 2019; 67:684-91


ORALS

Oral 001

From Ground-Based Microgravity Facilities To Suborbital Flights

Thorben Könemann[1]

[1]ZARM FAB mbH, Bremen, Germany;
thorben.koenemann@zarm.uni-bremen.de

Introduction

The Center of Applied Space Technology and Microgravity (ZARM) founded in 1985 is part of the Department of Production Engineering at the University of Bremen, Germany. ZARM is mainly concentrated on fundamental investigations of gravitational and space-related phenomena under conditions of weightlessness as well as questions and developments related to technologies for space. At ZARM, about 100 scientists, engineers, administrative staff, and many students from different disciplines are employed. Today, ZARM is one of the largest and well-known research center for space sciences and technologies in Europe.
With a height of 146 m, the Bremen Drop Tower is the predominant facility of ZARM and also the only drop tower of this kind in Europe. ZARM's ground-based laboratory offers the opportunity for daily short-term experiments under conditions of high-quality weightlessness at a level of 10(-6) g. Scientists may choose up to three times a day between a single drop experiment with 4.74 s in simple free fall [Dittus, H.] and an experiment in ZARM's worldwide unique catapult system with 9.3 s in microgravity [von Kampen, P., et al.].

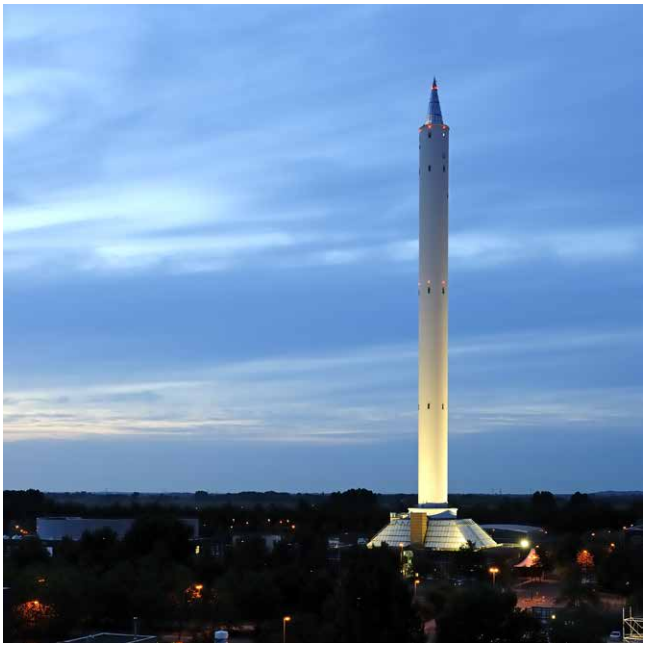

Figure 1: The Bremen Drop Tower of the Center of Applied Space Technology and Microgravity (ZARM) - University of Bremen.

Since the start of operation of the drop tower facility in 1990, over 8500 drops or catapult launches of more than 250 different experiment types from various research fields like fundamental physics, combustion, fluid dynamics, planetary formation / astrophysics, biology, chemistry, and material sciences have been accomplished so far. In addition, more and more technology tests have been performed under microgravity conditions at the Bremen Drop Tower, in order to prepare single space instruments or appropriate space missions in advance.

Abstract

In this paper, we demonstrate a simple approach to realize microgravity experiments on suborbital flights by preparing and qualifying the setups at ZARM's ground-based microgravity facilities. It means a full payload integration into the specific suborbital payload module to perform preliminary drop tower experiments under short-term microgravity conditions with the identical suborbital hardware, e.g. testing the overall setup, probing experiment parameters, obtaining first results in microgravity, etc..
A full qualification of the integrated flight module, doing additional shaker or thermal vacuum tests for instance, is also feasible with the help of services by ZARM Test Center. In this way, a comprehensive preparation and qualification of suborbital flight setups is possible at ZARM. Furthermore, we report about our experiences of such an approach during a suborbital flight with the New Shepard vehicle of Blue Origin in the USA in 2018, at which we were the first commercial customer to fly research payloads from Europe. Also, the status of experiment preparations utilizing the Bremen Drop Tower for the very first upcoming suborbital payload flight on the new European sounding rocket, MIURA 1, of PLD Space (Spain) is presented.
Finally, we give a status update on the GraviTower Bremen - Prototype (GTB-Pro), a novel ground- based microgravity facility [Gierse, A., et al.], which is in the final stage of assembling at ZARM. The GTB-Pro represents an actively driven drop tower system that is capable to perform over 100 short-term microgravity experiments per day. It offers a further alternative performing dedicated microgravity research or preparing experiments for suborbital flights or respectively for space missions.

Acknowledgements

ZARM gratefully acknowledges the support from the German Aerospace Center (DLR) Space Administration and the European Space Agency (ESA).

References

Dittus, H.: Drop Tower Bremen: a weightlessness laboratory on Earth. Endeavour, New Series 15(2), 72–78 (1991)

von Kampen, P., Kaczmarczik, U., Rath, H.J.: The new drop tower catapult system. Acta Astronaut. 59, 278-283 (2006)

Gierse, A., Kaczmarczik, U., Greif, A., Selig, H., von Kampen, P., Könemann, T., Lämmerzahl, C.: Microgravity Sci. Technol. 29:403-414 (2017)

26th European Low Gravity Research Association Biennial Symposium and General Assembly
14th International Conference on "Two-Phase Systems for Space and Ground Applications"
European Space Agency Topical Teams meetings
Granada (Spain), September 24-27, 2019

Oral 002

Thermocapillary stability of a thin film coating the inside of a cylinder with a thick wall with finite thermal conductivity

Luis A. Dávalos-Orozco

Universidad Nacional Autónoma de México, Instituto de Investigaciones en Materiales, Departamento de Polímeros
Ciudad Universitaria, Circuito Exterior S/N, C.P. 04510, Ciudad de México, México
ldavalos@unam.mx

The coating of cylinders by means of liquid films have been the subject of many research papers since many years ago. Review publications related with this research have been written by Weinstein and (Ruschak 2004) and (Quéré 1999). A more recent and general reviews have been written by (Dávalos-Orozco 2013,2016).

Flow down a cylinder was investigated by (Shlang and Sivashinsky 1982). They assumed a large relative radius of the cylinder and very strong surface tension of the fluid.

The coating of rotating cylinders was investigated analytically and numerically by (Dávalos-Orozco and Ruiz-Chavarría 1993) and (Ruiz-Chavarría and Dávalos-Orozco 1996, 1997). The cylinder was vertical and therefore the liquid film was subjected to gravity. They showed that for certain magnitudes of the parameters of the problem the first azimuthal mode m = 1 was able to be the most unstable one.

Thermocapillary effects have been the subject of many publications. In particular, (Dávalos-Orozco and You 2000) investigated numerically the linear stability of a liquid film coating a cylinder in the presence and in the absence of gravity. In both cases it was found that the azimuthal modes are excited by the thermal Marangoni effect, but that they can not be the most unstable. That is, in the linear problem only the axial mode prevails.

Viscoelastic effects in a film falling down a cylinder were investigated by (Moctezuma - Sánchez and Dávalos - Orozco 2008). Viscoelasticity was found to stimulate the azimuthal modes but it was not enough to let them become the most unstable. The axial mode m = 0 was the most unstable one. Thermocapillary and viscoelastic effects were considered by (Moctezuma - Sánchez and Dávalos - Orozco 2015) for thin films in the outside of the cylinder in the presence and in the absence of gravity. It was found that both effects excite the azimuthal modes but still the axial mode m = 0 was the most unstable one. It is interesting that in the absence of gravity and viscoelasticity it was found in this paper that for a wavenumber different from zero the maximum growth rates of the axial and azimuthal modes were the same. In other words, it is not possible to determine which mode will prevail from the point of view of linear stability. For this reason, calculations of the nonlinear sideband instability of the axial mode m = 0 against the first azimuthal mode m = 1 were done and the results were published in (Dávalos - Orozco 2017). There it was found the nonlinear range of the thermocapillary effects, surface tension and wavenumber where the axial mode becomes unstable against mode m = 1.

The nonlinear sideband instability was also calculated for a thin liquid film falling down a hot and thick walled cylinder with finite thermal conductivity. The evolution equation was calculated following (Frenkel 1993). The region where the axial mode is unstable against the first azimuthal mode was presented in (Dávalos - Orozco 2019).

Our goal here is to present preliminary results on the thermocapillary instability of a thin liquid film coating the inside of a thick walled cylinder of finite thermal conductivity. In this case it was also found that the maximum growth rates of the axial and azimuthal modes are the same. Therefore, the prevailing mode remains indeterminate.

Some results are presented in Fig. 1. There the growth rate is plotted against the wavenumber for a fixed Marangoni number Ma = 50, a nondimensional radius of magnitude 5 and three different crispation numbers. Here the increase of the growth rate with the crispation number Cr is monotonic. This is in contrast with thermocapillary convection outside the cylinder (Dávalos - Orozco 2017) where the variation of the growth rate with Cr presents a minimum. In the figures the selected crispation numbers are Cr = 0.01 (solid), Cr = 0.05 (dotted), Cr = 0.1 (dashed). The parameter d/Qc is varied. It is the ratio of d = ratio of wall thickness over that of the film and Qc = ratio of wall thermal conductivity over that of the film. Fig. 1a for d/Qc = 1 and Fig. 1b for d/Qc = 5. Notice how the growth rate decreases with the increase of d/Qc. The modes are indicated in the figures by means of the numbers m = 0 (axial), m = 1 (azimuthal) and m = 2 (azimuthal).

It is important to point out that the maxima of growth rate are the same for all modes when the corresponding wavenumber is different from zero, as found in previous work (Dávalos - Orozco 2017). Then it is not possible to know which mode will prevail. This indeterminacy will be solved in the nonlinear problem.

References

L. A. Dávalos-Orozco, "Stability of thin liquid films falling down isothermal and nonisothermal walls" *Interfacial Phenomena and Heat Transfer* **1** (2018) 93 – 138.

L. A. Dávalos-Orozco, "Thin liquid films falling down heated walls; a review of recent results" *Interfacial Phenomena and Heat Transfer* **4** (2016) 109 – 131.

L. A. Dávalos-Orozco, "Sideband thermocapillary instability of a thin film coating the outside of a thick walled cylinder with finite thermal conductivity in the absence of gravity" *Interfacial Phenomena and Heat Transfer* **5** (2017) 287-298.

L. A. Dávalos-Orozco, "Sideband thermocapillary instability of a thin film coating the outside of a thick walled cylinder with finite thermal conductivity in the absence of gravity"

Int. J. Non-Linear Mech. **109** (2019) 15 - 23.

L. A. Dávalos-Orozco and G. Ruiz-Chavarría, "Hydrodynamic instability of a fluid layer flowing down a rotating cylinder" *Phys. Fluids A* **5**, (1993) 2390 – 2404.

G. Ruiz-Chavarría and L. A. Dávalos-Orozco, "Stability of a liquid film flowing down a rotating cylinder subject to azimuthal disturbances", *J. Phys. II France*, **6** (1996) 1219 - 1227.

G. Ruiz-Chavarría and L. A. Dávalos-Orozco, "Azimuthal and streamwise disturbances in a fluid layer flowing down a rotating cylinder", *Phys. Fluids* **9**,(1997) 2899 – 2908.

A. L. Frenkel, "On evolution equations for thin films down solid surfaces", *Phys. Fluids A* **5** (1993) 2342 – 2347.

M. Moctezuma - Sánchez and L. A. Dávalos – Orozco, "Linear Three dimensional instability of viscoelastic fluid layers flowing down cylindrical walls" *Microgravity Sci. Technol.* **20** (2008) 161 – 164.

M. Moctezuma - Sánchez and L. A. Dávalos – Orozco, "Azimuthal instability modes in a viscoelastic liquid layer flowing down a heated cylinder" *Int. J. Heat Mass Transfer* **90** (2015) 15 - 25.

D. Quéré, "Fluid coating on a fiber", *Annu. Rev. Fluid Mech.* **31** (1999) 347 – 384.

T. Shlang and G. I. Sivashinsky, "Irregular flow of a liquid film down a vertical column", *J. Physique* **43** (1982) 459 – 466.

S. J. Weinstein and K. J. Ruschak, "Coating flows", Annu. *Rev. Fluid Mech.* **36**, (2004) 29 - 53.

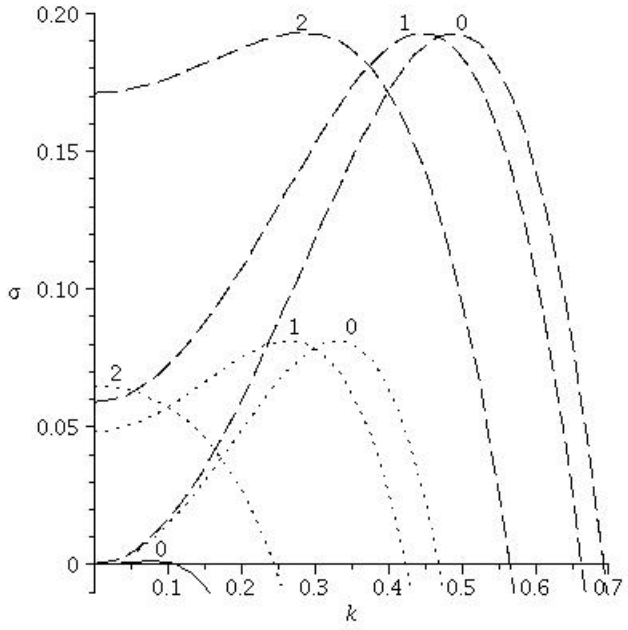

Fig. 1a

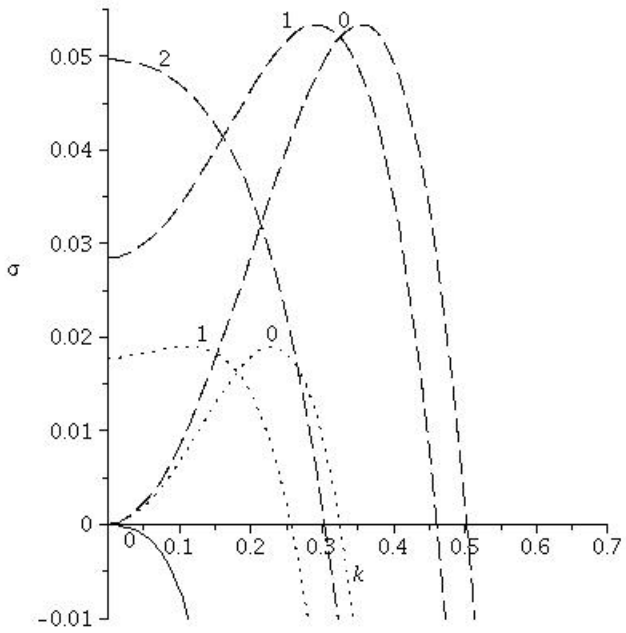

Fig. 1b

Figure 1: Growth rate against the wavenumber. Thin film coating the inside of a thick cylinder. Nondimensional radius = 5, Marangoni number = 50 and three different crispation numbers Cr = 0.01 (solid), Cr = 0.05 (dotted), Cr = 0.1 (dashed). Fig. 1a for d/Qc = 1 and Fig. 1b for d/Qc = 5.
Here, d = ratio of wall thickness over that of the film. Qc = ratio of wall thermal conductivity over that of the film. Notice the increase of the growth rate with Cr and the decrease observed with d/Qc.

26th European Low Gravity Research Association Biennial Symposium and General Assembly
14th International Conference on "Two-Phase Systems for Space and Ground Applications"
European Space Agency Topical Teams meetings
Granada (Spain), September 24-27, 2019

Oral 003

Molecular dynamics study of condensation on vertical and horizontal V-shaped surface with different gravity in nanoscale

Bo Xu1 and Zhenqian Chen2

Southeast University, School of Energy and Environment, Nanjing, 210096, China
email1: xubo@seu.edu.cn, email2: zqchen@seu.edu.cn

Introduction

Recent decades, many scholars' attention was attracted by phase change process with altered gravity to improve the heat transfer in space applications (Legros et al. 2018). In addition, as a main representative of phase change process, condensation was quite important and widely applied in space system. Molecular dynamics (MD) simulation is widely used to study the interactions including vapor condensation in microscale with the rapid development of computational capabilities. For example, Niu (2016) found that film-wise condensation (FWC) caused more efficient heat transfer than dropwise condensation (DWC) in macroscale because of a lower interfacial thermal resistance between condensed water and hydrophilic surface. Li (2009) observed a condensation phenomenon in free expansion plumes and developed a model of water cluster sizes, cluster-monomer collisions, and sticking probabilities necessary for the study of water homogeneous condensation in a plume expanding to low pressure, space conditions. Therefore, MD was quite suitable to study the mechanism and behavior of condensation with different gravity.

The model of water condensation containing 8340 water molecules and 85440 copper-type atoms was built in Fig. 1. The cold wall was in the size of 252.7 Å × 151.62 Å × 10.83 Å for direction of x × y × z. The length and bottom of V-shaped surface was 162.45 Å and 14.44 Å. The distance between cold wall and hot wall was 101.08 Å. The periodic boundary condition is applied in all three spatial dimensions of the simulation box. The interaction between copper-type surface and water molecules is also assumed to be 12-6 Lennard-Jones (LJ) particles (Alexiadis et al. 2008). The purple atoms represent hydrophobic and the green atoms represent hydrophilic. When applied microscale gravity (G) was smaller than 0.001 kcal/(mol·Å) (1 kcal/(mol·Å) = 2.33×10^{15} m/s^2), the condensation process and phenomena was similar to it without gravity. Therefore, The gravity changed from 0.001 kcal/(mol·Å) to 0.01 kcal/(mol·Å). The ratio (φ) of microscale gravity to normal macroscale gravity (g) was showed as followed:

$$\varphi = \frac{G}{g} = \frac{0.001\ \text{kcal/(mol}\cdot\text{Å)}}{9.8\ \text{m/s}^2} = 2.38\times10^{11}$$

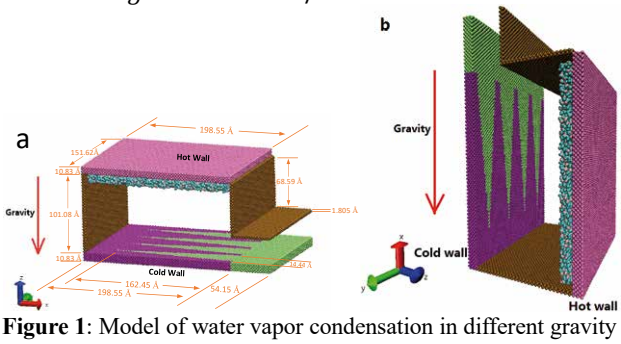

Figure 1: Model of water vapor condensation in different gravity (a. Horizontal surface; b. Vertical surface)

Horizontal surface

The condensation usually happened after 200ps, except in 0.01 kcal/(mol·Å). In this case, the condensation happened quickly after 100ps and nearly finished at 500ps. In addition, the condensation finished at 1000ps in 0.005 kcal/(mol·Å) and it was 1400ps for other conditions. Therefore, the condensation process was quicker with greater gravity. The final numbers of condensation water molecules was almost 3000 without gravity. It increased by 800 with gravity increased by 0.001 kcal/(mol·Å) when gravity was less than 0.002 kcal/(mol·Å). However, when gravity became to 0.003 kcal/(mol·Å), it increased by 3500, double of that without gravity. The final numbers of condensation water molecules couldn't increase indefinitely and get close to 8340 with larger gravity, because the all water molecules were determined.

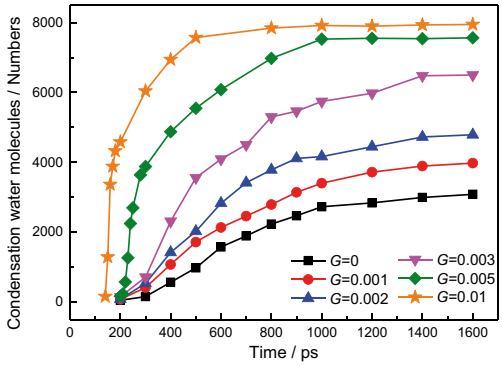

Figure 2: Numbers of condensation water molecules with different gravity on horizontal surface

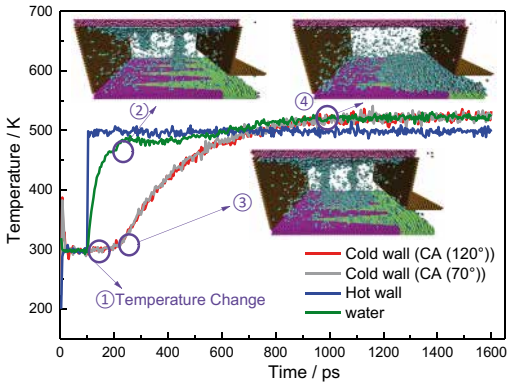

Figure 3: Temperature of condensation in G=0.005 kcal/(mol·Å)

The condensation process with large gravity was shown in Fig. 3. ① Temperature change suddenly. At this moment, the temperature of hot wall increased to 498K suddenly and two phase equilibrium will be broken. No water vapor molecule contacted cold wall. ② Partial water molecules separated from hot wall, but didn't contact cold wall. At this moment, the water molecules had already separated from hot wall like a "water column". It took time for "water column"

Granada (Spain), September 24-27, 2019

to drop down and "water column" still stayed in the air during this period. ③ Water molecules contacted cold wall. From this moment, the "water column" touched the cold wall and transferred heat to cold wall quickly, leading to the increase of cold wall temperature. It took 1000ps for cold wall to reach equilibrium to finish the condensation. ④ The final key state point was constant condensation phenomena. The temperature of water and cold wall were were larger than hot wall. It was because part of energy generated by gravity transferred to thermal energy of water and cold wall, and the other part transferred to kinetic energy of water.

Vertical surface

Condensation process on vertical surface with different gravity was shown in Fig. 4. The water molecules condensed on hydrophilic surface and grew up by coalescence with other molecules, which was not affected by gravity. When gravity was 0.0001 (kcal/(mol·Å)), several clusters formed on the top area of V-shaped surface and gradually grew up. Then the water clusters moved from top to the bottom of V-shaped surface with the increase of size and volume. Finally, the water clusters coalescence with each other to form the water nano-droplet at the bottom of V-shaped surface. When gravity increased to 0.0003 (kcal/(mol·Å)), water clusters also formed on the hydrophilic surface and grew up. Several water clusters moved to the bottom of V-shaped surface and coalesced with each other to form a large nano-droplet. As the gravity was large enough, the nano-droplet fell down with the effect of gravity. The nano-droplet drop phenomena was more obvious at gravity of 0.0005 (kcal/(mol·Å)). In this case, the water clusters formed at top of V-shaped surface and grew up by coalescence with other clusters. However, several relative large clusters fell down before they moved to bottom of V-shaped surface to form the nano-droplet. It was because the interaction force provided by V-shaped surface was smaller than the gravity.

Conclusions

The condensation process was much quicker with greater gravity, leading to the larger condensation rate at horizontal surface. For vertical surface, the water molecules could condense at top of V-shaped hydrophilic surface and moved to the bottom of V-shaped surface with the increasing size at low gravity, while the water molecules condense on hydrophilic surface and finally fell down at large gravity.

Acknowledgements

This work was supported by the international cooperation project of China Manned Space Program

References

Alexiadis A., Kassinos S. Molecular simulation of water in carbon nanotubes. Chem Rev, Vol. 108 pp. 5014-5034 (2008).

Legros J.C., Lutoshkina O., Piskunov M., Voytkov I. Water drops with graphite particles triggering the explosive liquid breakup, Exp Therm Fluid Sci, Vol. 96 pp. 154-161 (2018).

Li Z., Zhong J.Q., Levin D.A., Garrison B.J. Development of homogeneous water condensation models using molecular dynamics, AIAA J, Vol. 47 pp. 1241-1251(2009).

Niu D. and Tang G.H., Effect of surface wettability on water vapor condensation in nanoscale, Sci Rep-UK, Vol. 6 pp. 19192 (2016).

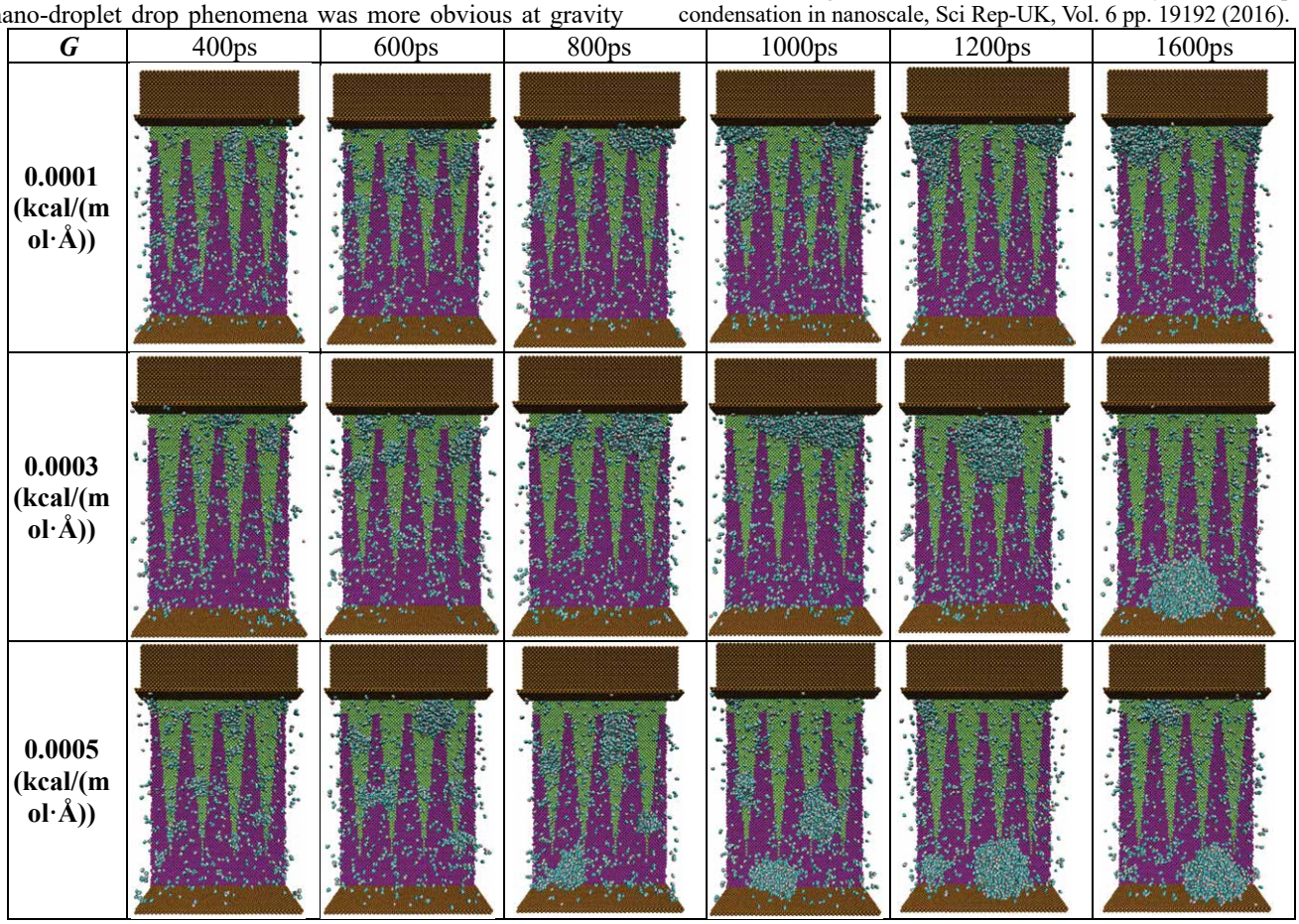

Figure 4: Condensation process on vertical surface with different gravity

26th European Low Gravity Research Association Biennial Symposium and General Assembly
14th International Conference on "Two-Phase Systems for Space and Ground Applications"
European Space Agency Topical Teams meetings
Granada (Spain), September 24-27, 2019

Oral 004

Numerical study of droplet transporting on chemically heterogeneous surfaces

Xin Wang, Zhenqian Chen

Southeast University, Nanjing, China
Xin_wang@seu.edu.cn, zqchen@seu.edu.cn

Introduction

Spontaneous movement of single droplet on chemically heterogeneous surfaces without any external force are widely existed in nature and industry. The surface structure with wetting gradient has been applied in engineering applications, such as microfluidic devices (Shastry et. al 2006, Lai et. al 2010, Chou et. al 2008), collecting fog (White et. al 2013, Seo et. al 2016) and condensation heat transfer enhancement (Huang et. al 2012). It has been demonstrated that the droplet dynamics on wetting gradient surfaces play an important role in condensation heat transfer enhancement. Hence, an in-depth understanding of the droplet dynamics on wetting gradient surfaces is of great value and significance.

Lattice Boltzmann (LB) method, as a mecroscopic model, has become an effective simulation tool in multiphase flow because of simplicity and natural parallelism. At present, LB models mainly include pseudopotential model, color model and free energy model. In this paper, the pseudopotential method is improved to simulate self-driving dynamics on composite wedge-shaped surfaces. Effects of solid friction and wetting gradients on dynamic behaviors are analyzed. Meanwhile, gravitational coefficients are also taken into consideration to investigate the droplet deformation and movement to understand the mechanism of spontaneous movement on composite wedge-shaped surfaces in depth. This work provides theoretical guidance for surface design to enhance condensation heat transfer.

Computational model

In this paper, the modified three-dimension with nineteen-velocity (D3Q19) Shan-Chen lattice Boltzmann model with BGK collision operator is described. According to Wei and Cheng (2018), a larger relaxation time is applied in early times while a smaller relaxation time is applied later due to the higher stability and low viscous droplets. The modified density distribution function can be given by:

$$f_\alpha(\mathbf{x}+\mathbf{e}_\alpha, \mathrm{t}+\delta_\mathrm{t}) - f_\alpha(\mathbf{x},\mathrm{t}) = \begin{cases} -\frac{1}{\tau_1}\left[f_\alpha(\mathbf{x},\mathrm{t}) - f_\alpha^{eq}(\mathbf{x},\mathrm{t})\right] + \Delta f_\alpha(\mathbf{x},\mathrm{t}) & \mathrm{t} \le 100 \\ -\frac{1}{\tau_2}\left[f_\alpha(\mathbf{x},\mathrm{t}) - f_\alpha^{eq}(\mathbf{x},\mathrm{t})\right] + \Delta f_\alpha(\mathbf{x},\mathrm{t}) & \mathrm{t} > 100 \end{cases} \quad (1)$$

where $f_\alpha(\mathbf{x},\mathrm{t})$ denotes the particle distribution function at the lattice $\mathbf{x}$ and time t. δ_t and δ_x are the time step and space step, respectively. τ_1 is an adjustable value to maintain the numerical stability when t≤100 and τ_2 is the real relaxation time related to the kinematic viscosity when t>100. According to Eq. (1), convection term is on the left and collision term is on the right. f_α^{eq} is the corresponding equilibrium distribution function, which is expressed as:

$$f_\alpha^{eq} = \omega_\alpha \rho \left[1 + \frac{\mathbf{e}_\alpha\cdot\mathbf{u}}{c_s^2} + \frac{(\mathbf{e}_\alpha\cdot\mathbf{u})^2}{2c_s^4} - \frac{\mathbf{u}^2}{2c_s^2}\right] \quad (2)$$

Here, exact difference method (EDM) is adopted to implement force term in the LB model, due to the better numerical stability and independent of relaxation time. The force term is given by:

$$\Delta f_\alpha(\mathbf{x},\mathrm{t}) = f_\alpha^{eq}[\rho(\mathbf{x},\mathrm{t}), \mathbf{u}+\Delta\mathbf{u}] - f_\alpha^{eq}[\rho(\mathbf{x},\mathrm{t}), \mathbf{u}] \quad (3)$$

where $\Delta\mathbf{u} = \mathbf{F}\delta_\mathrm{t}/\rho$ is the velocity change caused by the total force $\mathbf{F}$ during the time step δ_t. The total force $\mathbf{F}$ is consisted of fluid-fluid force $\mathbf{F_{int}}$, fluid-solid force $\mathbf{F_s}$ and gravitational force $\mathbf{F_g}$, which is given by:

$$\mathbf{F} = \mathbf{F}_\mathrm{int} + \mathbf{F}_\mathrm{s} + \mathbf{F}_\mathrm{g} \quad (4)$$

The macroscopic density and velocity are given by:

$$\rho = \textstyle\sum_\alpha f_\alpha(\mathbf{x},\mathrm{t}), \quad \rho\mathbf{u} = \textstyle\sum_\alpha \mathbf{e}_\alpha f_\alpha(\mathbf{x},\mathrm{t}) \quad (5)$$

$\psi(\mathbf{x})$ is the interaction potential function, calculated by:

$$\psi(\mathbf{x}) = \sqrt{2(\mathrm{p} - \rho c_s^2)/c_0 \mathrm{g}} \quad (6)$$

where c_0=6.0 and g=-1.0 in D3Q19 model. p denotes the pressure obtained from the actual equation of state. Here, P-R EOS is chosen to describe the liquid phase and vapor phase:

$$p = \frac{\rho RT}{1-b\rho} - \frac{a\rho^2\alpha(T)}{1+2b\rho-b^2\rho^2} \quad (7)$$

where R=1 is the gas constant, $\alpha(T) = \left[1 + 0.87324(1 - \sqrt{T/T_{cr}})\right]^2$. In this model, a=2/49 and b=2/21.

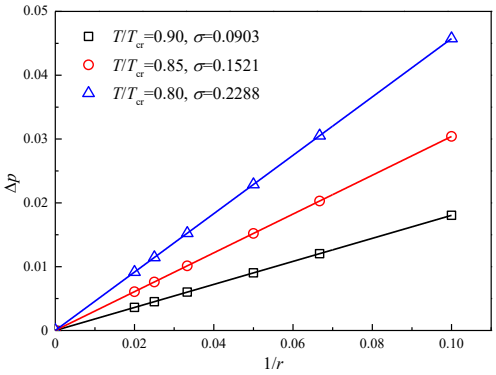

Figure 1: Comparison of LB results with the Lapalce's law

To verify the applicability of our model, Laplace's law is used. The pressure change inside and outside the droplet is linear with the derivative of the droplet radius, which can be written as:

$$\Delta p = p_\mathrm{in} - p_\mathrm{out} = \frac{2}{r}\cdot\sigma \quad (8)$$

where p_in and p_out are the pressure inside and outside the droplet, and σ is the droplet surface tension. As shown in Figure 1, Δp is in a linear relationship with 1/r.

Results and discussion

Figure 2 shows dynamic behaviors of single droplet movement on composite wedge-shaped surfaces from different views. Static contact angles of red region and blue region are 120.78º and 73.86º, respectively. The vertex angle of wedge-shaped surface is 45º. To be related with real physical properties, lattice units should be converted to real physical units. The length unit is determined by the dimensionless Ohnesorge number (*Oh*), calculated by:

$$\frac{[r]_{real}}{[r]_{lu}} = \frac{[\mu_l^2/(\rho_l\sigma_{lv})]_{real}}{[\mu_l^2/(\rho_l\sigma_{lv})]_{lu}} \quad (9)$$

The lattice time can be represented by inertial-capillary time:

$$t^* = t/\sqrt{\rho r_0^3/\sigma} \quad (10)$$

Initially, a droplet is static near the vertex angle. Here, t=5000 is defined as the initial moment of droplet movement (t^*=0). Due to the action of unbalanced capillary force, the droplet is pushed from the weaker wetting region to the stronger wetting region. As the time increases, the leading edge of droplet expands in the form of bulge along the x direction. It can be found from side views that the bulge is wetted advancing angle is significantly reduced. When the time is increased to 2.33, width of liquid head is larger compared with t^*=0.47. However, width of liquid head is smaller than the wedge track attributed to the limit of wedge track. Quickly, droplet footprint moves to the vertex at t^*=5.6, as can be seen from top views. Subsequently, receding angle is also greatly reduced. The bulge is found at the droplet footprint on account of the combined effects of viscosity and unbalanced capillary force. When t^*=10.27, the droplet completely moves beyond the wedge track. The shape with large head and small footprint can be seen, which is affected by the wedge shape. Finally, a droplet is static on the stronger wetting surface resisted by viscosity.

Conclusions

The model of droplet movement on chemically heterogeneous surfaces is built and investigated by improved 3D lattice Boltzmann method. The microscopic mechanism of droplet directional migration on wedge-shaped surfaces is analyzed. Effects of vertex angle and wetting gradient on the droplet dynamics are studied. Spontaneous movement of droplet between wedge-shaped tracks is driven by net surface tension. Vertex angle has an important influence on the azimuthal angles, thereby affecting net surface tension. A larger wetting gradient has a positive effect on the droplet movement.

Acknowledgements

This work was supported by ESA-CMSA International Cooperation of Space Experiment Project (Study on Condensation and Enhancement Methods under Microgravity).

References

Shastry, A. and Case, M.J. and Bohringer, K.F. Directing droplets using microstructured surfaces, *Langmuir* 22 (2006) 6161-6167.

Lai, Y.H. Yang, J.T. and Shieh, D.B. A microchip fabricated with a vapor-diffusion self-assembled-monolayer method to transport droplets across superhydrophobic to hydrophilic surfaces, *Lab Chip* 10 (2010) 499-504.

Chou, I.H. Benford, M. Beier, H.T. and Cote, G.L. Nanofluidic biosensing for beta-amyloid detection using surface enhanced Raman spectroscopy, *Nano Lett* 8 (2008) 1729-1735.

White, B. Sarkar, A. and Kietzig, A.M. Fog-harvesting inspired by the stenocara beetle-an analysis of drop collection and removal from biomimetic samples with wetting contrast, *Appl Surf Sci* 284 (2013) 826-836.

Huang, Z. Lu, Y. Qin, H. Yang, B. and Hu, X. Rapid Synthesis of Wettability Gradient on Copper for Improved Drop-Wise Condensation, *Adv Eng Mate* 14 (2012) 491-496.

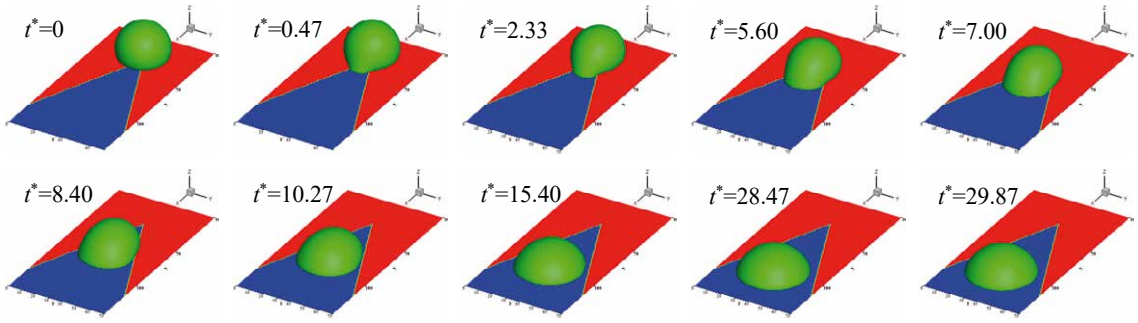

Figure 2: Dynamic behaviors of single droplet movement on composite wedge-shaped surfaces

26th European Low Gravity Research Association Biennial Symposium and General Assembly
14th International Conference on "Two-Phase Systems for Space and Ground Applications"
European Space Agency Topical Teams meetings
Granada (Spain), September 24-27, 2019

Oral 005

Thermocapillary structures formation, rupture and heat transfer enhancement in the falling liquid films

E. Chinnov

Kutateladze Institute of Thermophysics, Novosibirsk, 630090, Russia
chinnov@itp.nsc.ru

Introduction

It is known that two-dimensional waves in isothermal liquid films are unstable to three-dimensional perturbations. When two-dimensional waves decay into three-dimensional ones, the synchronous waves without phase displacement of waves in the transverse direction (Joo and Davis 1992). Park and Nosoko 2003 shown that the length of a wave unstable to transverse three-dimensional perturbations decreases with increasing Reynolds number.

To date, various mechanisms of rivulet formation in the heated liquid films have been discovered, and two thermocapillary regimes have been identified: A and B (Chinnov and Kabov 2003). The structures of two types A and B differ in the level of heat flux density, required for their formation, and size and nature of dependence of interrivulet distance on the heat flux density and Reynolds number.

Breakdown dynamics is studied in (Zaitsev et al 2007) using a fiber-optic sensor. The influence of substrate wettability on thermocapillary breakdown of a liquid film is considered in (Zaitsev et al 2015). In (Zaitsev et al 2016), the thermocapillary breakdown of a film is studied with a change in a wide range of Reynolds numbers and heater sizes.

This work is aimed at analysis and generalization of data on formation of various types of thermocapillary structures, heat transfer enhancement and breakdown of the heated liquid film flowing over a vertical surface with variation of Reynolds number from 0.1 to 150.

Results and discussion

Based on the analysis of experimental data on hydrodynamics of the flow of a heated liquid film, it has been established that the structures of type A are observed in the range of Reynolds numbers from 0.1 to 150. They appear on the liquid film surface when the threshold of heat flux density is reached. When structures of type A appear, high temperature gradients of up to 10-15 K/mm are registered in the upper part of the heater. The boundary condition close to T = const took place on the heater surface. Under the conditions of a developed wave flow, thermocapillary structures of type A were formed in the residual layer of liquid film after propagation of the three-dimensional wave front. The structures existed for a limited period of time and interacted with the front of the next wave transforming into rivulets that moved along the heater, changing their direction, Fig. 1.

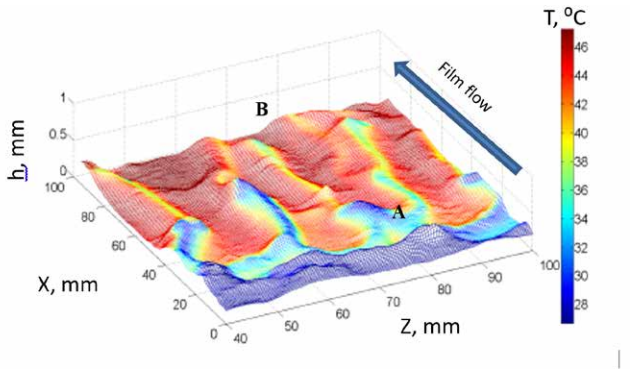

Figure 1: Three-dimensional distribution of thicknesses, temperatures over the water film surface, Re=50, q= 6 W/cm^2, heater of 150x100 mm.

In regime B, a rivulet flow was formed gradually with increasing heat flux and distance from the upper edge of the heater, Fig. 1. Structures of type B were registered in the range of Reynolds numbers from 0.1 to 500. Boundary condition q = const was implemented on the heater surface, and temperature gradients on the film surface did not exceed 1 K/mm.

Under the action of thermocapillary forces directed from the hotter to the colder areas, an increase in deformation of the film surface occurred. As a result, when the heat flux density became higher, the liquid film breakdown took place. When forming the structures of type A, the liquid film breakdown occurred in the upper part of the heater, where maximum deformations of the film surface were registered, and during formation of structures of type B, it occurred in the lower part of the heater.

Generalization of experimental data on the heat flux, corresponding to formation of structures of type A is fulfilled in the form of dependence between criterion Km_A^* and Re, Fig. 2.

$$Km_A^* = -q_A(\sigma_T/(c\rho^2 g^{2/3}\nu^{5/3}))L/l_\nu \quad (1)$$

where, g is acceleration of gravity, L is heater length, l_ν is scale of viscous-gravitational interaction equal to $(\nu^2/g)^{1/3}$, q_A is heat flux density, corresponding to formation of structures in regime A, ν is kinematic viscosity of liquid, σ_T is temperature derivative of surface tension coefficient equal to $\partial\sigma/\partial T$, ρ is liquid density.

The condition for structure formation in regime A on the liquid film surface is described by the following relation

$$Km_A^* = 113\mathrm{Re}^{1.08}. \quad (2)$$

Data on the liquid film breakdown during formation of A and B structures are presented in Fig. 1. If only structures B were formed on the liquid film surface, breakdown always occurred

in the lower part of the heater between the formed rivulets. With an increase in the heat flux density in the lower part of the heater, there was a sharp increase in liquid film deformation, which led to its breakdown. Data for the breakdown in regime B are summarized by dependence from (Chinnov and Sharina 2008)

$$Km_{crB}^* = 165Re. \quad (3)$$

During formation of structures in regime A on the liquid film surface, the heat flux densities corresponding to breakdown, increased significantly. The nature of liquid film breakdown changed, which is explained by a change in film deformation

$$Km_{crA}^* = 290Re. \quad (4)$$

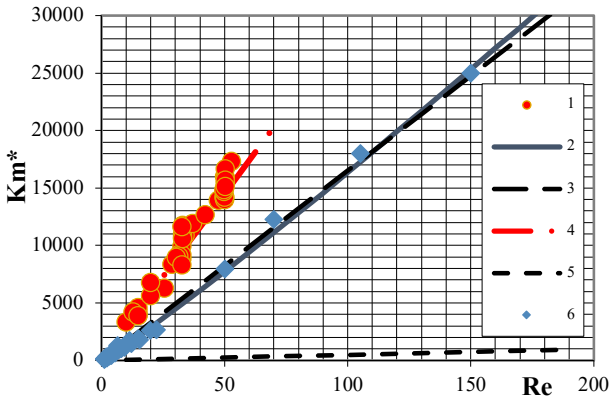

Figure 2: Generalization of experimental data on formation ofthermocapillary structures and liquid film breakdown. 1 – experimental data on water film breakdown after formation ofstructures A, 2 – dependence (2), 3 – dependence (3), 4 – dependence (4), 5 – line, above which structures B become perceptible, 6 – experimental data on formation of structures A on the water film surface.

Heat transfer enhancement during heat exposure was detected. Convective heat transfer coefficient increased with heat flux increasing. The area of the most intensive growth coincides with the value of the heat flux corresponding to the formation of type A thermocapillary structures. After the structures

formation in the upper part of the heater, the growth of the heat transfer coefficient with increasing heat flux does not stop, but becomes smoother. This result agrees with the data for the amplitudes of surface waves and rivulets deflection. It can be argued that data have been obtained that indicate a significant intensification of heat transfer with increasing wave amplitudes and rivulets deflection.

Conclusions

The data on formation of thermocapillary structures and breakdown of a heated liquid film flowing down a vertical surface have been analyzed and summarized. It is shown that the distances between rivulets of thermocapillary structures for these regimes do not depend on the Reynolds number. It has been established that formation of metastable thermocapillary structures of type A in the upper part of the heater affects the value of the critical heat flux corresponding to liquid film breakdown. It is shown that the critical heat flux increases with increasing film Reynolds number and at high Re numbers, it exceeds significantly the data on breakdown in the absence of thermocapillary structures of type A. The development of thermocapillary structures of type A at high heat flux initiated increasing of the waves and rivulets deflection amplitudes. It has been established that heat transfer enhances due to development of thermocapillary instability in the upper part of the heater, which leads to an increase in the amplitude of surface waves and rivulets deflection amplitudes.

Acknowledgements

This work was supported by the grant of Russian Science Foundation (Agreement No. 18-19-00407).

References

E.A. Chinnov, O.A Kabov, *Mechanics and Technical Physics* 44 (2003) 708–715.
E.A. Chinnov, I.A. Sharina, *Thermophysics and Aeromechanics*, 15 (2008) 113–121.
S. W. Joo, S.H. Davis, *J. Fluid Mech.* 242 (1992) 529-547.
C.D. Park, T. Nosoko, *AIChE Journal* 49 (2003) 2715-2727.
D.V. Zaitsev, D.A. Rodionov, O.A. Kabov, *Micrograv. sci. technol.,* 19 (2007) 100-103.
D.V. Zaitsev, D.P. Kirichenko, O.A. Kabov, *Technical Physics Letters,* 41 (2015) 551–553.
D.V. Zaitsev, A.A. Semenov, O.A. Kabov, *Thermophysics and Aeromechanics*, 23 (2016) 625-628.

26th European Low Gravity Research Association Biennial Symposium and General Assembly
14th International Conference on "Two-Phase Systems for Space and Ground Applications"
European Space Agency Topical Teams meetings
Granada (Spain), September 24-27, 2019

Oral 006

Vibrational instabilities at the interface separating two immiscible liquids in microgravity

P. Salgado Sánchez[1], V. Yasnou[2], Y. Gaponenko[2], A. Mialdun[2], J. Porter[1], V. Shevtsova[2]

[1]Escuela Técnica Superior de Ingeniería Aeronáutica y del Espacio, Universidad Politécnica de Madrid, Plaza de Cardenal Cisneros 3, 28040 Madrid, Spain,
[2] Microgravity Research Centre, CP-165/62, Université Libre de Bruxelles (ULB), av. F. D Roosvelt, 50, B-1050 Brussels, Belgium;

pablo.salgado@upm.es, vyasnou@ulb.ac.be, ygaponen@ulb.ac.be, amialdun@ulb.ac.be, jeff.porter@upm.es, vshev@ulb.ac.be

Introduction

A wide variety of interfacial phenomena occurs in vibrated fluid systems, depending on frequency, amplitude and forcing orientation. On earth, there is a clear qualitative difference between vertical and horizontal vibrations. Vertical vibrations can be understood as a modulation of effective gravity and may be stabilizing, as with the Rayleigh-Taylor instability (Wolf 1970), or destabilizing, as with the phenomenon of Faraday waves (Faraday 1831). Horizontal forcing, on the other hand, immediately excites harmonic waves near the container boundaries. When a critical amplitude is reached, it also excites subharmonic cross-waves (Garret, 1970). If the interface separates immiscible layers of different viscosity, vibrations can lead to frozen waves (Lyubimov, Cherepanov 1986; Talib et al. 2007), which are generally bounded by the restoring effects of gravity and interfacial tension.

Conversely, the absence of gravity means that flat density contours are no longer favoured and curved interfaces replace them, blurring the distinction between vertical and horizontal forcing. Nonetheless, such effective orientations may be identified locally in certain portions of a vibrated interface. The associated weightless behaviour, therefore, can be understood as a combination of typical phenomena observed on earth, and their interaction.

We consider the response to periodic forcing between 5 Hz and 50 Hz of an interface separating immiscible fluids under the microgravity conditions of a parabolic flight. Two pairs of liquids with viscosity ratios differing by one order of magnitude are investigated. By combining experiments with simulations, we describe a variety of dynamics including Faraday waves, harmonic waves, frozen waves, drop ejection (James et al. 2003), and their interaction. The effects of key parameters that control pattern selection are analysed, including vibrational forcing, viscosity, finite-size effects, and residual gravity. Complex behaviour, highlighted by the appearance of Faraday waves on the interface of a large columnar frozen wave structure is observed (Salgado Sánchez et al. 2019) analogous to the patterns seen in miscible fluid experiments (Shevtsova et al. 2016).

Experiments and simulations

The core of the experimental setup is a pair of cuboidal cells of interior dimension 15 mm x 7.5 mm x 5 mm [see Fig. 1 (left)], holding two different combinations of silicone oils (2 cSt and 20 cSt) with FC-40. The position of the interface, sampled at 80 Hz, was monitored directly through one of the sides of the cells; the different liquid transparencies provide different shading in the snapshots. The cells, along with the optical system, are attached to a linear motor that drives controlled linear oscillations at frequency f and amplitude A.

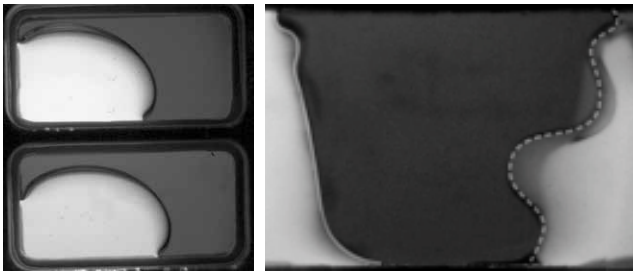

Figure 1: (left) Experiment cells. Behaviour of the interface in microgravity in the absence of vibrational forcing. (right) Snapshot showing subharmonic Faraday waves in one side of the frozen wave columnar structure for f = 22 Hz and A = 1.76 mm.

The experiments were performed in a parabolic flight campaign (Pletser at al. 2016) and, besides the fluid combinations considered, they were characterized by the applied forcing. We explored f and A intervals of 5-50 Hz and 1-5.3 mm with vibrations applied during 15 s, under isothermal conditions.

In order to simulate the dynamics of the immiscible interface, we developed a two-dimensional numerical model based on the level-set formulation (Salgado Sánchez et al. 2019). The essential features of the experimental fluid behaviour (except drop ejection) were reproduced over a wide parameter range. This response was characterized by the appearance of Faraday waves on the columnar interfaces of a frozen wave pattern [see Fig. 1 (right)]. This model was implemented in COMSOL Multiphysics 5.3, a commercial finite-element software.

Interfacial dynamics

Figure 2 describes the ways in which the interface between FC-40 and 2 cSt silicone oil is seen to respond to forced vibrations in microgravity in terms of the vibrational frequency f and amplitude A.

For interfacial modes associated with the fast timescale of the applied vibrations, experiment results can be separated into three different regimes: harmonic waves (yellow), subharmonic Faraday waves (light blue) and drop ejection (red), with thresholds in good qualitative agreement with numerical predictions (open markers). For comparison, we include theoretical predictions of the onsets for subharmonic Faraday waves under uniform vertical forcing (Kumar and Tuckerman, 1994), and for frozen waves (Luybimov and Cherepanov, 1986).

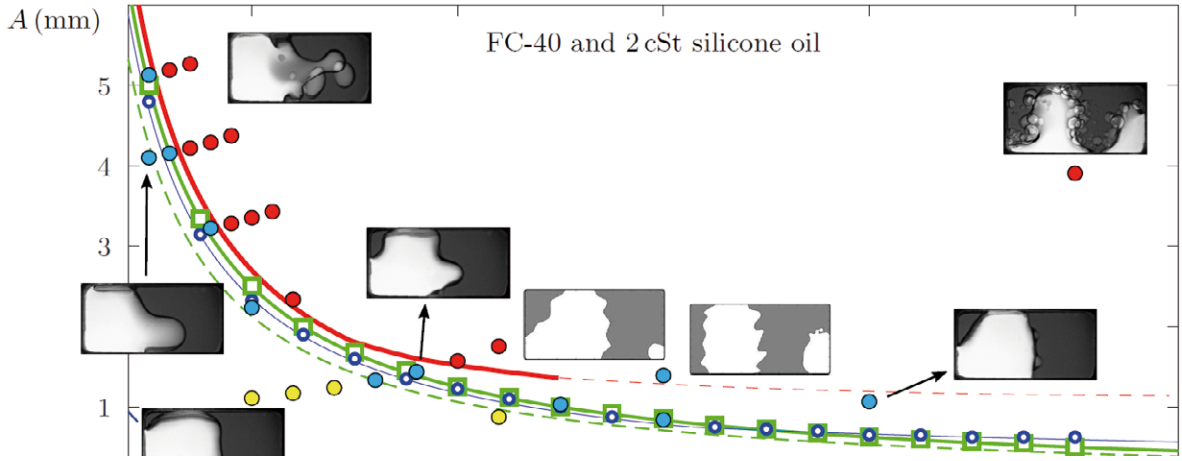

re 2. Response of the fluid interface between FC-40 and 2 cSt silicone oil in microgravity. Solid circles mark experimental points in three nes: harmonic waves (yellow), subharmonic Faraday waves (blue) and drop ejection (red). Open markers denote numerical thresholds for lay waves (blue circles) and frozen waves (green squares). Theoretical onset curves are also shown for Faraday waves (dashed blue) and

low vibrational velocity, residual gravity leads to p-like configurations [see also Fig. 1 (left)] with nonic waves excited on the interface. As the vibrational city is increased, subharmonic Faraday waves are ted. Near onset, these waves oscillate predominantly at uency *f*/2 and tend to grow quickly in size, masking the existing harmonic waves. Pattern selection in this nario depends on both amplitude and frequency.

p ejection follows from the destabilisation of the harmonic mode in the limit of high forcing. Far from et, subharmonic waves reach high amplitude and are very linear, and the interface becomes unstable. Drop ejection ften accompanied by disordered behaviour.

dence of frozen waves, combined with vibroequilibria cts (Fernández et al. 2017), is found for both fluid binations. The results are affected by the airplane urbances (residual gravity) in a critical way.

nclusions

eriments with two pairs of immiscible layers subjected vibrations have been performed in parabolic flights. A e variety of dynamics was observed, depending on the ational velocity. At low driving velocities, residual ity promotes drop-like configurations with harmonic es directly excited on the interface. For higher values, harmonic Faraday waves appear at half the forcing uency and may coexist with frozen waves, which are erved beyond a (different) critical onset value, creating a -scale wave pattern. Finally, disordered behaviour ciated with drop ejection is observed for high vibrational city when the subharmonic surface waves become large ugh for the interface to rupture and eject drops.

nowledgements

work of V.Y., Y.G., A.M. and V.S. was supported by the PRODEX ramme and by ESA through its 63rd Parabolic Flight Campaign. The of P.S.S. and J.P. was supported by the Ministerio de Economía y petitividad under Project no. ESP2015-70458-P.

References

G.H. Wolf, Dynamic stabilization of the interchange instability of a liquid-gas interface, *Phys. Rev. Lett.* 24 (1970) 444–446.

M. Faraday, On peculiar class of Acoustical Figures; and on certain Forms of Assumed groups of particles upon vibrating slastic Surfaces, *Philos. Trans. R. Soc. Lond.* 121 (1831) 299-340.

C.J.R. Garret, On cross-waves. *J. Fluid Mech.* 41 (1970) 837-849.

D.V. Lyubimov, A.A. Cherepanov, Development of a steady releif at the interface of fluids in a vibrational field, *Fluid Dyn.* 21 (1986) 849-854.

E. Talib, S.V. Jalikop, A. Juel, The influence of viscosity on the frozen wave instability: theory and experiment, *J. Fluid Mech.* 584 (2007) 271-304.

A.J. James, M.K. Smith, A. Glezer, Vibration-induced drop atomization and the numerical simulation of low-frequency single-droplet ejection, *J. Fluid Mech.* 476 (2003) 1-28.

V. Shevtsova, Y. Gaponenko, V. Yasnou, A. Mialdun, A. Nepomnyashchy, Two-scale wave patterns on a periodically excited miscible liquid-liquid interface, *J. Fluid Mech.* 795 (2016) 409-422.

P. Salgado Sánchez, V. Yasnou, Y. Gaponenko, A. Mialdun, J. Porter, V. Shevtsova, Interfacial phenomena in inmiscible liquids subjected to vibrations in microgravity, *J. Fluid Mech.* 865 (2019) 850-883.

V. Pletser, S. Rouquette, U. Friedrich, J. F. Clervoy, T. Gharib, F. Gai, C. Mora, The first european Parabolic flight campaign with the Airbus A310 zero-G. *Micro. Sci. Technol* 28 (2014) 587-601.

K. Kumar, L.S. Tuckerman, Parametric instability of the interface between two fluids, *J. Fluid Mech.* 279 (1994) 49-68.

J. Fernández, I. Tinao, J. Porter, A. Laverón, Instabilities of

26th European Low Gravity Research Association Biennial Symposium and General Assembly
14th International Conference on "Two-Phase Systems for Space and Ground Applications"
European Space Agency Topical Teams meetings
Granada (Spain), September 24-27, 2019

Oral 007

The Thermocapillary Effects in Phase Change Materials in Microgravity experiment

P. Salgado Sánchez, J.M. Ezquerro, A. Bello, J. Fernández, J. Rodríguez, I. Tinao

Escuela Técnica Superior de Ingeniería Aeronáutica y del Espacio, Universidad Politécnica de Madrid, Plaza de Cardenal Cisneros 3, 28040 Madrid, Spain;
pablo.salgado@upm.es, jm.ezquerro@upm.es, alvaro.bello@upm.es, jose.ffraile@upm.es, jacobo.rodriguez@upm.es, ignacio.tinao@upm.es

Introduction

By their nature, Phase Change Materials (PCMs) store and release a large amount of energy during phase change, feature that may be put in good use to maintain a system temperature within admissible limits. Such large storage capacity, combined with the thermal stability shown around the melting point, has motivated many industrial applications on ground (Memon, 2014). Space systems, whose operating environment generally results in thermal cycles, have also used PCMs for thermal regulation. Examples of both low and high temperature control systems range from complex engineering applications to daily needs in manned mission (Kim et al. 2013).
Nowadays, a wide variety of PCMs with different working temperatures are available. However, the major disadvantage as thermal control devices, especially in microgravity, is their low thermal conductivity. This leads to long heat storage and discharge phases, reducing their performance. On ground, convection naturally alleviates such constraint, increasing by one order of magnitude the heat transport rate. In microgravity, a fairly well established solution is to place large areas of PCM in contact with high conductive materials (Fernandes et al. 2012). This, however, increases the mass and size of the control devices and, despite of that, it compensates the absence of convection just partially.
We consider here the potential of Marangoni convection for heat transfer enhancement in PCMs in weightless environments. Aiming to measure its influence on the heat transport during the melting process and validate numerical models, the Thermocapillary Effects in Phase Change Materials (TEPiM) experiment was designed. Prior to this project, microgravity experiments of PCMs coupled with thermocapillary convection had not been performed.
The TEPiM experiment was presented to the Fly your Thesis! 2016 programme call for proposals. It was selected to fly in the 65th ESA Parabolic Flight Campaign, November 2016. Throughout the three flights of the campaign, we performed 54 microgravity experiments that explored the melting process varying different experimental parameters. This provided us a perfect starting point to obtain novel experimental data, and gain experience to define and prepare a future sounding rocket or ISS experiment. Here, we describe the scientific objectives and requirements of TEPiM experiment, review the setup and phases, and analyse its performance during the experimental campaign.

Scientific objectives and requirements

The TEPiM experiment proposed to study PCM dynamics and heat transfer features in the presence of Marangoni convection in microgravity. We note that the presence of a liquid-air interface during PCM melting in microgravity has not been analysed extensively. These studies (see e.g., Giangi et al. 2002, Swanson and Birur 2003) were mostly theoretical.
The two main scientific objectives of this work are:

1. Measure the influence of Marangoni convection in the heat transport process.
2. Retrieve novel experimental data to validate the modelling of the underlying phenomena.

These two objectives require a PCM that displays high latent heat, and a phase change temperature above the ground lab temperature (25 ºC) and below the maximum temperature permitted in the flight (90 ºC). We selected the n-octadecane paraffin as the test PCM.
The experiments were carried onboard an aircraft executing parabolic manoeuvres, providing repeated periods of approximately 20 s of microgravity. Thermally, the typical timescales of Marangoni convection and conductive heat transport for the geometries considered are of tens of seconds and various minutes, respectively. Each experiment required a long preparation phase, dominated by conduction, which helps creating a controlled liquid-air interface at the beginning of a microgravity period. Therefore, the subsequent development of Marangoni convection was essentially concentrated during the 20 s of microgravity, isolating its effects from convection. Each experiment was divided accordingly in: *Preheating* and *Final heating* phases.

The experiment: experimental setup and phases

The heart of the experiment is a set of three pairs of *Marangoni* and *Reference* cells of 20, 25 and 30 mm height, filled with n-octadecane. While the *Reference* cells only contains PCM, the *Marangoni* cells have a 5 mm air layer on top that permits the development of Marangoni convection during melting. Both *Marangoni* and *Reference* cells were subjected to similar thermal loads in the (so-called) Monitoring stations.
During the *Preheating phase*, starting roughly 8 min prior to the relevant microgravity period, the test cell was subjected to 0 ºC and 80 ºC temperatures in its upper and lower sides, respectively. This drove the formation of a liquid paraffin bubble surrounded by solid octadecane [see Fig 1 (a,b)], and prevented the liquid to wet the cell interior filled with air. Around 40 seconds before the microgravity period, the *Final heating* phase started and the cell was subjected to 80ºC at both upper and lower sides.

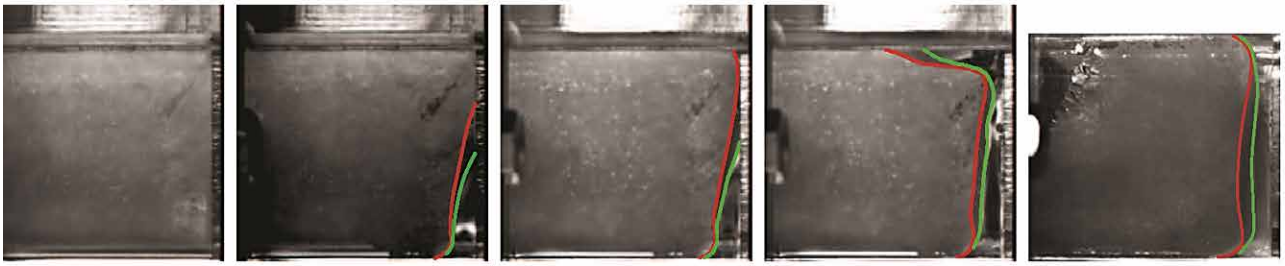

ure 1: (a-d) Snapshots showing the temporal evolution (times and phases labelled) of an experiment using a *Marangoni* cell. (e) Final ɔshot of a *Reference* cell experiment. For visual reference, the (approximate) solid/liquid front in the lateral wall (red line) and central ıe (green line) are highlighted.

solid layer (bridge) separating the liquid paraffin from air was melted [see Fig 1 (c)], creating the liquid-air rface after, roughly, 30 seconds. The convection erated by thermocapillarity in the liquid phase enhanced heat transport; accelerating the melting process and the ion of the solid/liquid front near the liquid-air interface Fig 1 (d)]. During these reduced gravity periods, we trolled the liquid (phase) dynamics by pinning its contact , which permits preserving a (nearly-)flat interface. At experiment completion, the cell was cooled down and Monitoring station prepared for the following run.

ɔ cameras, providing lateral and top views; six mocouples, measuring the experiment temperatures at a ximum rate of 5 Hz in relevant locations; one mometer, to check the cabin temperature and avoid ɔassing the melting point; and the airplane elerometers, monitored each melting process. For the ıera acquisitions, particularly, different sampling rates of roximately 1 Hz for the *Preheating* phase and 10 Hz for *Final heating* phase were selected.

en the experiments duration of roughly 10 minutes, we rated two Monitoring stations in parallel to maximise the eriment outcome. This permitted using three rogravity lapses of each group of five parabolas, and thus ılted in a daily set of eighteen microgravity experiments.

ıclusions: preliminary results and lessons learned

ıough not all the executed experiments provided the ected results, the TEPiM experiment was successful in ıy ways. The main preliminary results and lessons ned are as follows:

As shown in Fig. 1 (d, e), the effect of Marangoni convection can be clearly observed in the region near the liquid-air interface, where a greater advance of the solid/liquid front is achieved. Besides that, the processing of these experiments reveals a heat transfer enhancement of, roughly, a factor of 2 between *Marangoni* and *Reference* cells.

Issues arising from the air retained in the solid PCM suggest that further efforts shall be done to reduce the PCM porosity, e.g., the application of a controlled solidification during the cells filling. PCM porosity further affects the proper observation of experiments, somewhat during microgravity, potentially, due to the presence of microbubbles.

(iii) The contact line pinning performed excellently. It permitted to maintain the liquid-air interface in all but three experiments throughout the campaign.

(iv) We designed a high performance Thermal Control System. It achieved temperature differences of ~80 ºC in the cells, and was capable to nullify these offsets in a very short time (~30 s), while maintaining high temperatures (~80 ºC).

In light of the above considerations, the TEPiM experiment has shown the potential of Marangoni convection for enhancing heat transport in PCMs in microgravity, providing an alternative to develop more efficient thermal control devices in future space missions.

Acknowledgements

This work was supported by the ESA Education Office, in connection with the Fly your Thesis! Programme and the 65th ESA Parabolic Flight Campaign, and by the E-USOC. We thank ELGRA and Novespace for their valuable scientific and technical advice. We thank the ETSIAE at Universidad Politécnica de Madrid, in particular, the research group Ciencias y Operaciones Aeroespaciales, which have supported this Project from the beginning,

References

S.A. Memon, Phase change materials integrated in building walls: A state of art review. *Renew. Sustain. Energy Rev* **31** (2014) 870–906.

T.Y. Kim, B.S. Hyun, J.J. Lee, J. Rhee, Numerical study of the spacecraft thermal control hardware combining solid-liquid phase change material and a heat pipe. *Aerosp. Sci. Technol.* **27** (2013) 10–16.

D. Fernandes, F. Pitié, G. Cáceres, J. Baeyens, Thermal energy storage: "How previous findings determine current research priorities", *Energy* **39** (2012) 246–257.

M. Giangi, F. Stella, E. Leonardi, G. de Vahl Davis, A numerical study of solidification in the presence of a free surface under microgravity conditions. *Numer. Heat Transf. Part A Appl.* **41** (2002) 579–595.

T.D. Swanson, G.C. Birur, NASA thermal control technologies for robotic spacecraft. *Appl. Therm. Eng.* **23**

26th European Low Gravity Research Association Biennial Symposium and General Assembly
14th International Conference on "Two-Phase Systems for Space and Ground Applications"
European Space Agency Topical Teams meetings
Granada (Spain), September 24-27, 2019

Oral 008

Music as a countermeasure in human spaceflights: Music psychophysiological effects under hypergravity stressors

Luque Álvarez Luis [1], Tamás Nagy[2], Loïc Treffel[2]

[1] *Széchenyi István University, Faculty of Art, Győr, Hungary, ESA Education Office, DLR German Aerospace Center, CNES National Centre for Space Studies, MTA-TTK - Hungarian Academy of Sciences*
luisluquewp@gmail.com, nt.nagytamas@gmail.com, Treffelosteopathe@gmail.com

Abstract

Music is often reported as inducing positive psychological and physiological effects in a similar manner to Guided Imagery, a technique often used by professionals in multiple settings such as sports, to reduce stress and anxiety, and improve focus prior to or during an activity, Listening to music has also been reported by trained spaceflight crews during their pressurisation checks of the vehicle prior to launch. Once launched they encounter hypergravity conditions that put physiological and psychological stress upon the body, however it is not documented the effect of this practice of listening to music acts to reduces stress. With commercial spaceflight tourism on the horizon, where a wider population will be exposed to these larger hypergravity stresses for longer periods of time, the potential for non-invasive countermeasures to reduce possible stress would be advantageous. The aim of this study was to understand if music could be used during hypergravity stress to induce a positive psychological state and reduce markers of physiological stress.

We adapted Using an according to a Short Arm Human Centrifuge protocol adapted from the principles of The Bonny Method (GIM) used in Guided imagery, a using music scientifical music selection was devised for use during a controlled hypergravity environment. Experiments were conducted on the selection according to the subjects psychocultural profiles instead of guided imagery. Short Arm Human Centrifuge (SAHC) at DLR, Germany. 11 subjects volunteered for the study and were split into two groups (with music [n=6] and without music [n=5]. Psychocultural questionnaires were utilised to determine and optimise the cultural music style of the subject. Psychological tests, and physiological markers including muscles tone (MyoTone Pro), galvanic skin conductance and stress hormones cortisol/cortisone measurements were performed before, during and after each centrifugation and compared between groups.

In the Music group participants outcome showed a pleasantness tendency to prefer slower rhythmic, lower density and less pitch transposition music. Physiologically the masseter muscle which is the closest measurement to the ears has shown a tendency to decrease tension in comparison with the control group without music. Subjects that experienced hypergravity with music were less stressful or a least without significant differences in tension points and showed a tendency to decrease the psychophysiological stresses.
Hypergravity has affected all the psychological and physiological parameters. Music would improve the stress feeling in this extreme environment.

However, further studies under actual spaceflight permanent microgravity conditions, including the differences between listening to and playing an instrument measurements of the constant listening upon these markers are suggested and the practice of musical instruments in long-term spaceflight might be considered using an extended musical selection including all historical music periods and genres. The outcomes of such studies could reveal the potential of each music period/style and path to the selection and intervention with music as a psychophysiological countermeasure on astronauts extending concentration periods, precision during work hours consequently, symptoms of fatigue and sleep disorders in long-term spaceflight.

The experiment was kindly supported by the European Space Agency (ESA) Education Office and the German Aerospace Center (DLR) as part of the ESA Academy's Spin Your Thesis – Human Edition 2018.

Muscles	Pre	After 1G	After 1.5G	Pre	After 1G	After 1.5G
	Control group without music			Music group		
Biceps Brachii Long	14.67	15.52	15.18	13.54	14.28	14.125
Masseter	14.9 ± 1.06	15.44 ± 1.07	15.83 ± 1.30 (p=0.13 NS)	14.31± 1.48	14.19 ± 0.74	14.26 ± 0.83
Rectus Femoris	15.62±0.86	16.2 ± 0.66 (p=0.07)	16.01	15.35	15.78* (1G vs Pre, p<0.05)	15.89
Rectus Abdominis	14.69	14.94	15.11	12.43	13.26	12.84
Sternocleidomastoid	13.7	12.53	12.54	13.26	12.5	12.53
Tibialis Anterior	22.97	21.05	21.31	22.37	19.1	19.05

Figure 1: Comparison of muscle properties in the control group (n=5 ; without music) to the music group (n=6 ; in green). Oscillation Frequency (in Hertz), before (Pre) after 1G and after 1.5G Mean +/- SEM, each value is the mean of left and right sides per subject. Significant P value when *p<0.05.

Introduction

Music has been widely as a leisure time activity forming part of the cross cultural life of astronauts in space, this is considered a cultural resource useful to decrease the 'stress' experienced during spaceflight (Kanas et al. 2015). This use has been highlighted during interviews with astronauts/cosmonauts, where they have reported both listening to music and performing music on instruments in space (Fries, C. et al. 2015). The effects of music on the brain waves stimulation also has been researched and suggest its capability to stimulate positively physiological responses (Hasminda et al. 2012). This may indicate that a controlled music intervention could have utility for those working in, or going into the space environment, such as tourists.

Hypergravity exposure is conducted during astronaut training to acclimatise them to the launch and re-entry phase of spaceflight. This is conducted using models including centrifugation as well as parabolic flight and aerobatic manoeuvres. The exposure to hypergravity generate alterations on the circadian rhythms combined with psychological stress such as anxiety, depression etc. The anxiety under hypergravity has been previously investigated on a centrifuge to mimic sub-orbital flights for commercial space tourists (Mulcahy et al. 2014). Subject anxiety and psychological measures were recorded and it was suggested that highly anxious subjects are capable of a commercial spaceflight, if accompanied with coaching during the training and spaceflight. Psychological states and profiles can be measured through questionnaires such as the Profile of Mood States (POMS) test and be used in combination with physiological markers.

Physiologically, stress has been documented to generate large-scale neurophysiological changes (Sachs, M. et al. 2016), which activate the autonomic nervous system (sympathetic, parasympathetic systems), triggering catecholamine release (noradrenaline, dopamine), and engaging the hypothalamic–pituitary–adrenal axis, leading to systemic release of glucocorticoids like cortisol (Ulrich et al.). Cortisol is a well-documented marker for stress. Changes in muscle tone have also been reported as a marker for stress and could be used in tandem with psychological tests to document the effects of an activity or intervention.

This study therefore proposed to study the effect of music upon physiological and psychological markers when exposed to a hypergravity environmental stress.

Materials and methods

Program: The ESA- Spin Your Thesis Human Edition is one of the programs of the European Space Agency's Education Office in collaboration with the German Aerospace Center (DLR) in Cologne. The programme allows university students to perform the experiments of their thesis on a Sort Arm Human Centrifuge (SAHC).

Subjects: 11 male volunteers without musical training (i.e. not musicians) volunteers to take part in the study after a medical examination in the DLR facilities. Medical examination including an audiometry to avoid the selection of subjects suffering of hearing-loss or other hearing diseases. Ethical clearance for the study was granted by the German Space Agency Ethical board. 11 male subjects were recruited after a medical examination in the DLR facilities. Medical examination including an audiometry to avoid the selection of subjects suffering of hearing-loss or other hearing diseases. Subjects were selected according to the medical/ethical results and approved by DLR committee under the requirements: normal vision, hearing, no psychological impairments (N=11, no smoker males, aged 27 ± 4 years ; 181 ± 3.3 cm ; 80 ± 7.7 kg ; mean ± SEM). splitted into two groups: **Music group** and **Control group without music**. The subjects were submitted with/without 10' minutes of music to 2 hypergravity sets of 1Gz and 1.5Gz on the Short Arm Human Centrifuge (SAHC) located in the German Aerospace Medicine Envihab facility in Cologne, Germany. The study was registered to the German Clinical Trials Register (DRKS) under number: DRKS00014750.

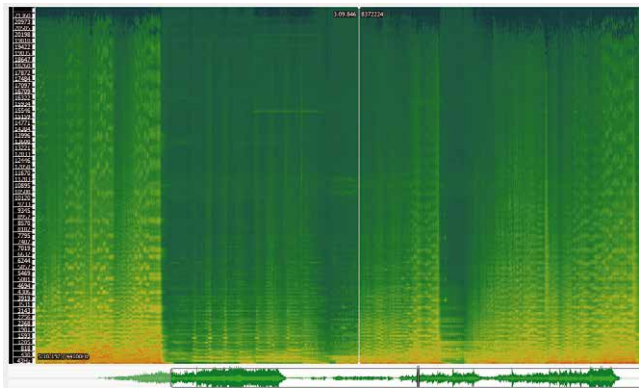

Figure 2: Spectrogram of a music excerpt. Sonic visualizer software allowed to analyze the density of the music before selectin. Orange and red colours indicates dense instrumental, frequencies and dynamics in the music.

Conclusions

Hypergravity has affected all the psychological and physiological parameters. Music would improve the stress feeling in this extreme environment. However, remains unknown the impact of music on brain activity, heart rate and other physiological aspects under hypergravity and microgravity. Further studies in space under permanent microgravity using an extended musical selection from all music historical periods and genres could determine the potential of each music characteristic in order to avoid anxiety, fatigue, sleep loss, optimizing and extending the concentration, precision along the space missions.
It is proposed to test musical intervention as countermeasure for psychophysiological stresses on astronauts before, during and after prolonged spaceflight, including a large selection of different music periods, genres, styles including the measurement of psychophysiological responses performing musical instruments in diverse microgravity environments.

Acknowledgements

Special Thanks to Nigel Savage, Programme Coordinator

for University Student Experiments at ESA Education Office and to David Green, Education Coordinator for the European Astronauts Centre. Thanks to Timo Frett, Guido and Alexandra in DLR-envihab facility for the flexibility to adapt subjects recruitment and the centrifuge audio hardware for this music experiment.

Thankful with ELGRA (European Low Gravity Research Association) and SELGRA for the enormous support and guidance, to Loïc Treffel for serving as endorsed professor coordinating the physiological measurements and for the support to the team, thanks to ESA Education Office and to DLR for organizing the Spin Your Thesis Human Edition 2018 supporting this first endeavour with music as a science in the history of human spaceflight. Thanks to Tamás Nagy and the Hungarian Academy of Sciences coordinating travel/accommodation for Hungarian/Spanish team members and thanks to CNES grant for sub-collaborating with the galvanic skin device and travel/accommodation for French team members.

References

1. Akiyama, K., & Sutoo, D. (2011). Effect of different frequencies of music on blood pressure regulation in spontaneously hypertensive rats. *Neuroscience Letters*, *487*(1), 58–60. https://doi.org/10.1016/j.neulet.2010.09.073

2. Bonny, H. L. (1975/2002). Music and consciousness. In L. Summer (Ed.), Music and consciousness: The evolution of guided imagery and music (pp.77-92). Gilsum, NH: Barcelona Publishers.

3. Burtscher, M., Gatterer, H., Burtscher, J., & Mairbäurl, H. (2018). Extreme Terrestrial Environments: Life in Thermal Stress and Hypoxia. A Narrative Review. *Frontiers in Physiology*, *9*. https://doi.org/10.3389/fphys.2018.00572

4. Bernardi, L., & Sleight, P. (2009). Dynamic Interactions Between Musical, Cardiovascular, and Cerebral Rhythms in Humans. http://circ.ahajournals.org/content/119/25/3171

5. Bonjour, J. (2015). de l'accélération de la gravité sur les réponses cardio-respiratoires à l'exercice chez l'homme. https://tel.archives-ouvertes.fr/tel-00690482

6. Costa-Almeida, R. (2018). Continuous Exposure to Simulated Hypergravity-Induced Changes in Proliferation, Morphology, and Gene Expression of Human Tendon Cells. https://www.liebertpub.com/doi/10.1089/scd.2017.0206

7. Demangel, R., Treffel, L., Py, G., Brioche, T., Pagano, A. F., Bareille, M.-P., … Millet, C. (2017). Early structural and functional signature of 3-day human skeletal muscle disuse using the dry immersion model: Short-term muscle deconditioning. *The Journal of Physiology*, *595*(13), 4301–4315. https://doi.org/10.1113/JP273895

8. Demontis, G. C., Germani, M. M., Caiani, E. G., Barravecchia, I., Passino, C., & Angeloni, D. (2017). Human Pathophysiological Adaptations to the Space Environment. *Frontiers in Physiology*, *8*. https://doi.org/10.3389/fphys.2017.00547

9. De Abreu, S., Amirova, L., Murphy, R., Wallace, R., Twomey, L., Gauquelin-Koch, G., … Navasiolava, N. (2017). Multi-System Deconditioning in 3-Day Dry Immersion without Daily Raise. *Frontiers in Physiology*, *8*. https://doi.org/10.3389/fphys.2017.00799

10. European Space Agency, Human and Robotic Exploraion (2019, April 5). Music For Space. Retrieved from https://www.esa.int/Our_Activities/Human_and_Robotic_Exploration/Music_for_space

11. Fries, C. (3/13/2015). Chronology of Wakeup Calls, NASA History Division. Retrieved from https://history.nasa.gov/wakeup%20calls.pdf

12. Goldberg F. (1992). Images of emotion: The role of emotion in guided imagery and music. Journal of the Association for Music & Imagery, 1,5-17.

13. Garg, A., Xu, D., Laurin, A., & Blaber, A. P. (2014). Physiological interdependence of the cardiovascular and postural control systems under orthostatic stress. *American Journal of Physiology-Heart and Circulatory Physiology*, *307*(2), H259-H264. https://doi.org/10.1152/ajpheart.00171.2014

14. Goswami, N., Evans, J., Schneider, S., von der Wiesche, M., Mulder, E., Rössler, A., … Blaber, A. P. (2015). Effects of

Individualized Centrifugation Training on Orthostatic Tolerance in Men and Women. *PLoS ONE*, *10*(5). https://doi.org/10.1371/journal.pone.0125780

15. Gnyubkin,V. Effects of continuous and intermittent hypergravity on skeleton. https://tel.archives-ouvertes.fr/tel-01539024

16. Hasminda, H. (2012) A preliminary study on the effects of music on human brainwaves. DOI: 10.1109/ICCAIS.2012.6466581

17. Koelsch, S. (2010). Processing Expectancy Violations during Music Performance and Perception. Doi: 10.1162/jocn.2009.21332.

18. Kanas, N. (2015) Humans in Space: The psychological hurdles. Springer Praxis Book. Doi: 10.1007/978-3-319-18868-3

19. Kuan, Garry, Tony Morris, Yee Cheng Kueh, et Peter C. Terry. « Effects of Relaxing and Arousing Music during Imagery Training on Dart-Throwing Performance, Physiological Arousal Indices, and Competitive State Anxiety ». *Frontiers in Psychology* 9 (5 février 2018). https://doi.org/10.3389/fpsyg.2018.00014

20. Ming Yuan, Marc-Antoine Custaud, Zi Xu, Jingyu Wang1, Min Yuan, Carole Tafforin, Loic Treffel, Philippe Arbeille, Michel Nicolas, Claude Gharib, Guillemette Gauquelin-Koch, Laurent Arnaud, Jean-Christophe Lloret, Yinghui Li, Nastassia Navasiolava. (2019),. Multi-system adaptation to confinement during 4-person-180-day CELSS integrated experiment. (submitted in Frontiers in Physiology)

21. Minois, N. (2006). The Hormetic Effects of Hypergravity on Longevity and Aging. https://www.ncbi.nlm.nih.gov/pmc/articles/PMC2477671/

22. Mulcahy RA., (2014). Subject anxiety and psychological considerations for centrifuge-simulated suborbital spaceflight. https://www.ncbi.nlm.nih.gov/pubmed/25199128

23. Masi, A. T., Nair, K., Evans, T., & Ghandour, Y. (2010). Clinical, Biomechanical, and Physiological Translational Interpretations of Human Resting Myofascial Tone or Tension. *International Journal of Therapeutic Massage & Bodywork*, *3*(4), 16-28.

24. Radstaak, M., Geurts, S. A. E., Brosschot, J. F., & Kompier, M. A. J. (2014). Music and psychophysiological recovery from stress. *Psychosomatic Medicine*, *76*(7), 529–537. https://doi.org/10.1097/PSY.0000000000000094

25. Raio, Candace M., Catherine A. Hartley, Temidayo A. Orederu, Jian Li, et Elizabeth A. Phelps. « Stress attenuates the flexible updating of aversive value ». *Proceedings of the National Academy of Sciences of the United States of America* 114, nº 42 (17 octobre 2017): 11241-46. https://doi.org/10.1073/pnas.1702565114

26. Sachs, M. , Elis, R. J., Schlaug, G., Loui, P. (2016) Brain connectivity reflects human aesthetic responses to music. https://www.ncbi.nlm.nih.gov/pmc/articles/PMC4884308/, doi: 10.1093/scan/nsw009

27. Sarchiapone, Marco, Carla Gramaglia, Miriam Iosue, Vladimir Carli, Laura Mandelli, Alessandro Serretti, Debora Marangon, et Patrizia Zeppegno. « The association between electrodermal activity (EDA), depression and suicidal behaviour: A systematic review and narrative synthesis ». *BMC Psychiatry* 18 (25 janvier 2018). https://doi.org/10.1186/s12888-017-1551-4

28. Schneider, S., Peipsi, A., Stokes, M., Knicker, A., & Abeln, V. (2015). Feasibility of monitoring muscle health in microgravity environments using Myoton technology. *Medical & Biological Engineering & Computing*, *53*(1), 57–66. https://doi.org/10.1007/s11517-014-1211-5

29. Sutoo, D., & Akiyama, K. (2004). Music improves dopaminergic neurotransmission: demonstration based on the effect of music on blood pressure regulation. *Brain Research*, *1016*(2), 255–262. https://doi.org/10.1016/j.brainres.2004.05.018

30. Treffel, L., Dmitrieva, L., Gauquelin-Koch, G., Custaud, M.-A., Blanc, S., Gharib, C., & Millet, C. (2016). Craniomandibular System and Postural

Balance after 3-Day Dry Immersion. *PloS One*, *11*(2), e0150052. https://doi.org/10.1371/journal.pone.0150052

31. Trappe, J. Role of music in intensive care medicine. https://www.ncbi.nlm.nih.gov/pmc/articles/PMC3354373/

32. Ulrich-Lai, Yvonne M., et James P. Herman. « Neural Regulation of Endocrine and Autonomic Stress Responses ». *Nature reviews. Neuroscience* 10, nº 6 (juin 2009): 397-409. https://doi.org/10.1038/nrn2647

33. Walsh, R. & Vaughan, F., (Eds.). (1993). Paths beyond ego, The transpersonal vision. Los Angeles, Jeremy P.Tarcher/Perigee.

34. Yang, Y., Baker, M., Graf, S., Larson, J., & Caiozzo, V. J. (2007). Hypergravity resistance exercise: the use of artificial gravity as potential countermeasure to microgravity. *Journal of Applied Physiology*, *103*(5), 1879-1887. https://doi.org/10.1152/japplphysiol.00772.2007

Oral 011

Experimental research on heat transfer enhancement and associated bubble characteristics under high frequency reciprocating flow

Bo Yuan[1], Yonghai Zhang[1], Lei Liu[1], Yang Yang[2], Qian Cao[2], Jinjia Wei[1,3,*]

[1]School of Chemical Engineering and Technology, Xi'an Jiaotong University, 710049 Xi'an, China
[2] Technology and Engineering Center for Space Utilization, Chinese Academy of Sciences, Beijing, 100094, P.R. China
[3] State Key Laboratory of Multiphase Flow in Power Engineering, Xi'an Jiaotong University, 710049 Xi'an, China
Email: jjwei@mail.xjtu.edu.cn

Introduction

Boiling is an efficient way of heat transfer compared to single phase heat transfer methods, and it is a hopeful way to solve the heat dissipation problems of electronic devices. However, under ultra-high heat fluxes, it is difficult to remove bubbles from the heated surface, which may lead to the boiling crisis. To improve the heat transfer performance and increase the critical heat flux (CHF), some methods to change the way of fluid flow were raised by researchers. Pulsating flow in sinusoidal way in one direction was found out to decrease the CHF (Okawa et al. 2009). Heat transfer coefficient was enhanced by flow rate changing in square wave, especially under high frequencies (Mehta et al. 2015, Wang et al. 2016). A higher frequency brings the oscillating flow with a larger core and a thinner boundary layer, which enhance the heat transfer (Xiao et al. 2014). In this study, high frequency reciprocating flow was made to strike bubbles repeatedly and remove them from the surface, and associated bubble characteristics were also studied.

Experimental apparatus

As shown in Figure 1, the closed test loop consists of a centrifugal pump, a heat exchanger, a mass flow meter, a test section, a tank, and four solenoid valves controlled by a PLC. The smooth test chip with surface area of 10×10mm^2 was heated by a DC power. Thermocouples were installed to test the temperature of the chip (T_w) and inlet temperature of the fluid (T_f).

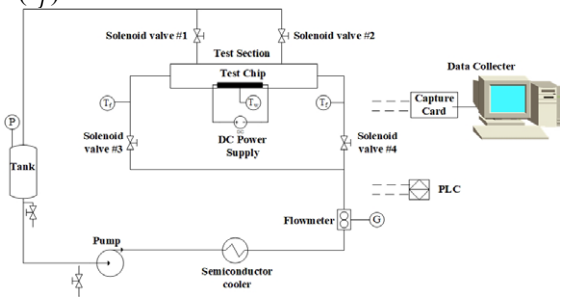

Figure 1: Test loop

PLC programs were made to control solenoid valves to make stable flow or reciprocating flow. When doing experiments under reciprocating flow, valves #1 and #4 were opened, and valves #2 and #3 were closed simultaneously. Liquid was forced to flow from right to left side through the test chip. In the next period, valves #2 and #3 were opened and the other two valves were closed, so liquid was forced to flow in the opposite direction. Flow rate variation in Figure 2 could be made by the alternant open and close of solenoid valves.

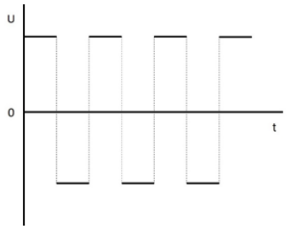

Figure 2: Sketch map of flow rate under reciprocating flow

CHF enhancement under reciprocating flow

Experiments were conducted under four different flow reates: 0.25, 0.5, 0.75 and 0.95m/s and six reciprocating frequencies: 1, 1.25, 1.67, 2.5, 5 and 10Hz. Boiling heat transfer performance under stable flow with corresponding flow rate was also tested. FC-72 was used as the working fluid, and experiments were performed with inlet subcooling, $\Delta t_{sub,}$ of 25℃ and 35℃.

The time-averaged boiling curves under intense reciprocating flow (f=10Hz) with different subcoolings are shown in Figure 3, and the results of corresponding stable flow are also plotted for comparision. It can be found that at low heat fluxes, the boiling curve of reciprocating flow is higher than that of stable flow, implying a higher heat transfer coefficient. And within the high heat fluxes regin, a higher CHF is achieved.

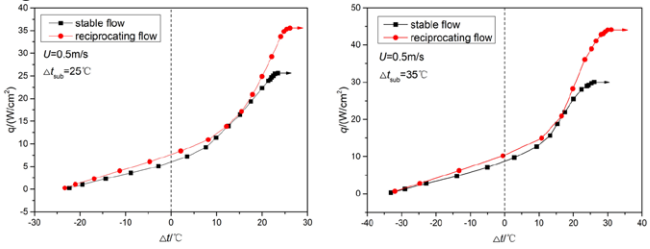

(a). U=0.5m/s, Δt_{sub}=25℃ (b). U=0.5m/s, Δt_{sub}=35℃

Figure 3: Time-averaged boiling curves under stable and reciprocating flow

To make it more clear, the CHF values under different reciprocating conditions with Δt_{sub}=35℃ are plotted in Figure 4. It is clearly shown that, compared to that of stable flow, the CHF increases under all different reciprocating conditions. With the increase of reciprocating frequency, the CHF increases futher more, and reaches the maxmum value when the reciprocating frequency is 10Hz. For the reciprocating flow with flow rates of 0.25, 0.5, 0.75 and 0.95m/s, the CHF is increased by 20.0%, 42.3%, 35.0% and 34.3% respectively.

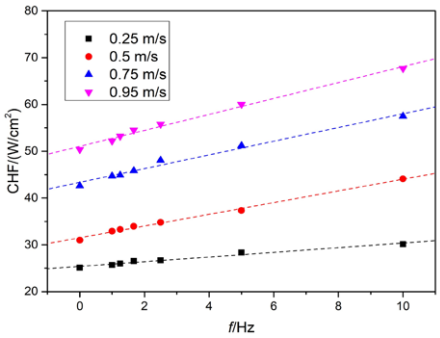

Figure 4: CHF under different reciprocating frequencies (Δt_{sub}=35°C)

As shown in Figure 4, the CHF is almost linearly proportional to the reciprocating frequency, and the linearly fitted lines are also plotted. With the increase of flow rate, the slope of lines also increases, which indicates that the strengthening effect of reciprocating flow is more obvious under high flow rate conditions.

Bubble behaviors under reciprocating flow

To explain the rule of CHF under reciprocating flows, photographic studies have been performed to observe the bubble characteristics. A high speed camera (NacMemrecam HX-6E) with a micro-lens (Nikon AF Micro-Nikkor 60mm f/2.8D) was used. In the present study the recording rate of 5,000 frames/s was adopted, and the frame size was 1,280×720 pixels.

As shown in Figure 5(a), under stable flow, there are many huge bubbles accumulating on the heated surface, which prevents liquid from wetting the surface effectively. However, as a comparasion shown in Figure 5(b), the bubbles generated under reciprocating flow are smaller and more shattered, which are easier to detach from the heated surface. This is because the reciprocating frequency (10Hz) is so high that there is little time left for bubbles to grow up. The flow direction reverses before huge bubbles generate. As a result, the direction of drag force acting on bubbles by flowing liquid also changes repeatedly, which tears the bubbles and pushes them to depart from the heated surface. The stability of flow field would be broken when the flow direction reverses, and the huge bubbles would be impacted directly by the fluid flow without blocking by upstream bubbles under stable flow conditions. In addition, after the reversion of flow direction, there is a region with small bubbles generating rapidly with high heat transfer performance.

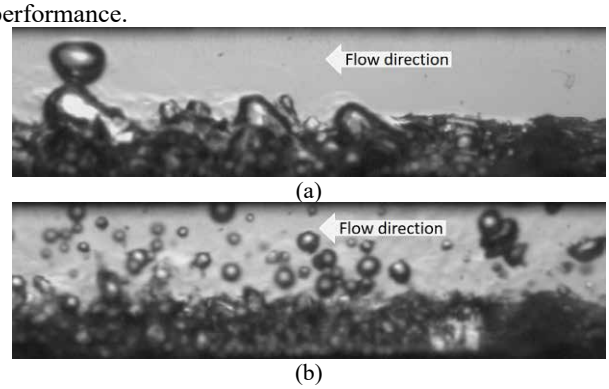

(a)

(b)

Figure 5: bubble behaviors under (a). stable flow and (b). reciprocating flow (U=0.25m/s, Δt_{sub}=35°C, q=25W/cm^2)

The similar phenomenon can also be seen under relatively high flow rate (U=0.95m/s), as shown in Figure 6. There are numberless small bubbles generated on the heated surface under reciprocating flow, which are forced repeatedly by the liquid to detach from the heated surface. As a contrast, the bubbles under stable flow are bigger and adhere to the surface.

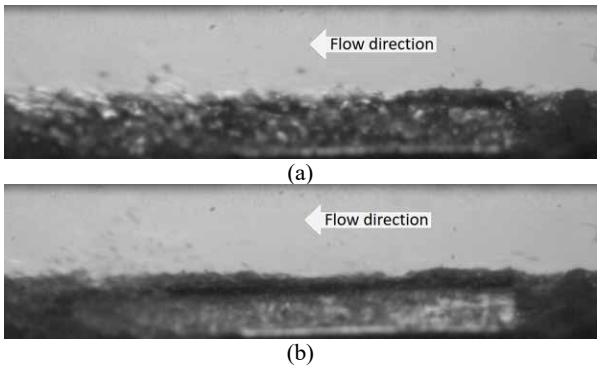

(a)

(b)

Figure 6: bubble behaviors under (a). stable flow and (b). reciprocating flow (U=0.95m/s, Δt_{sub}=35°C, q=50W/cm^2)

The high frequency reversion of flow direction makes the bubbles to suffer an alternant drag force, which tears bubbles to be small and shattered. As a result, the boiling heat transfer performance is improved obviously at high heat flux and the CHF is greatly improved under reciprocating flow.

Conclusions

Experimental research was performed to study heat transfer enhancement and associated bubble behaviors under high frequency reciprocating flow. The major conclusions obtained can be summarized as follows:

1. Reciprocating flow can effectively improve heat transfer performance at high heat fluxes, and the CHF increases by up to 42.3% compared with stable flow with the same flow rate.
2. Because of the alternant drag force, bubbles are much smaller and more shattered under high frequency reciprocating flows, which are easier to depart from the heated surface, leading to the increase of the CHF.

Acknowledgements

The research was supported by the National Natural Science Foundation of China (No.51636006), ESA-CMSA Joint Boiling Project (TGMTYY00-RW-05-1.00) and the Fundamental Research Funds for the Central Universities (No.cxtd2017004).

References

T. Okawa, T. Goto, J. Minamitani, Y. Yamagoe, Liquid film dryout in a boiling channel under flow oscillation conditions, *Int. J. of Heat and Mass Transfer*, 52 (2009) 3665-3675.

B. Mehta, S. Khandekar, Local experimental heat transfer of single-phase pulsating laminar flow in a square mini-channel, *Int. J. of Thermal Sciences*, 91 (2015) 157-166.

X. Wang, K. Tang, P.S. Hrnjak, Evaporator performance enhancement by pulsation width modulation (PWM), *Applied Thermal Engineering*, 99 (2016) 825-833.

G. Xiao, C. Chen, B. Shi, K. Cen, M. Ni, Experimental study on heat transfer of oscillating flow of a tubular Stirling engine heater, *Int. J. of Heat and Mass Transfer*, 71 (2014) 1-7.

Oral 012

A method for simulating subcooled flow boiling CHF in microgravity on the ground

B. Liu[1], B. Yuan[1], Y.H. Zhang[1], J.J. Wei[1, 2], J.F. Zhao[3, 4], Y. Yang[5], Q. Cao[5]

[1] School of Chemical Engineering and Technology, Xi'an Jiaotong University, Xi'an 710049, China, [2] State Key Laboratory of Multiphase Flow in Power Engineering, Xi'an Jiaotong University, Xi'an 710049, China, [3] CAS Key Laboratory of Microgravity, Institute of Mechanics, Chinese Academy of Sciences, Beijing 100190, China, [4] School of Engineering Science, University of Chinese Academy of Sciences, 19A Yuquan Rd, Beijing 00049, China, [5] Engineering and technology center for space applications, Chinese academy of sciences, Beijing 100094, China;
zyh002@mail.xjtu.edu.cn, jjwei@mail.xjtu.edu.cn

Introduction

Flow boiling is widely used in the electronic device heat dissipation and thermal management systems. The critical heat flux (CHF) is a key parameter of flow boiling. However, due to the complexity of the flow boiling CHF experiment and the difficulty of obtaining microgravity conditions, only a few experiments of flow boiling CHF in microgravity have been reported. Since the microgravity flow boiling experiment is difficult to achieve, it is a very convenient and economical method to obtain the CHF of flow boiling in microgravity by the simulation experimental tests conducted on the ground. However, no precise and feasible method for simulating has been reported in the publications yet. This study proposed a method for simulating subcooled flowing boiling CHF in microgravity on the ground. The method was validated by the drop tower experiments, and it was further explained by a modified heat flux partitioning model.

Section 1 The derivation of the method

The component of the buoyancy F_b along the bubble sliding F_{bx} and the bubble life-off F_{by} under different orientations of heating surface θ can be obtained by Eq. (1) - (2), respectively.

$$F_{bx} = F_b \cos\theta \quad (1)$$

$$F_{by} = F_b \sin\theta \quad (2)$$

When $90° < \theta < 180°$, buoyancy is beneficial to bubble sliding, but it is an obstruction for bubble lift-off. Then, the enhancement of flow boiling heat transfer due to the strengthened bubble sliding effect and the deterioration of flow boiling heat transfer due to the weakened bubble lift-off effect can be partially offset. While $F_{bx} = F_{by} = 0$, and the buoyancy has no effect on bubble sliding and bubble lift-off in microgravity. Hence, the flow boiling heat transfer performance in normal gravity is close to that in microgravity at the same conditions. Similarly, when $270° < \theta < 360°$, buoyancy is good for bubble detachment, but it is not conducive to bubble sliding in normal gravity. Therefore, similar conclusion can be obtained under this condition.

The CHF data from literature in microgravity and in normal gravity (Zhang et al. 2002; Zhang et al. 2005; Zhang et al. 2018) with different orientations are shown in **Fig. 1**. It can be observed from **Fig. 1** that the CHF for each case in microgravity ($q_{CHF\text{-}\mu g}$) is in the range of $q_{CHF\text{-}315°}$ and $q_{CHF\text{-}135°}$. In another word, the influence of buoyancy on the flow boiling CHF under microgravity is in the range of that on the flow boiling CHF when θ = 315° and that on the flow boiling CHF when θ = 135°. Therefore, it is possible to be a method that the CHF of subcooled flow boiling can be approximated in microgravity by the range of $q_{CHF\text{-}315°}$ and $q_{CHF\text{-}135°}$ in normal gravity under the corresponding conditions.

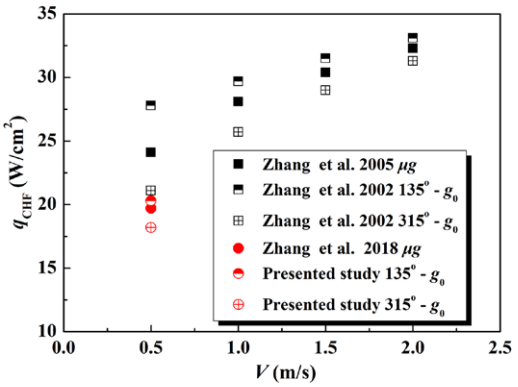

Figure 1: The comparison of CHF data in microgravity and in normal gravity with the orientations of 135° and 315°.

Section 2 Experimental validation

In order to futher verify the feasibility and correctness of the method, a series of subcooled flow boiling CHF data of FC-72 in microgravity were obtained through the drop tower experiment in Beijing. Five cases were validated, as shown in **Fig. 2**. It can be observed that the $CHF_{\mu g}$ is in the range of $CHF_{315°}$ and $CHF_{135°}$ in every calidated case, which proved that the method for simulating subcooled flow boiling CHF in microgravity is feasible and correct under different velocities, channel heights, and heater length.

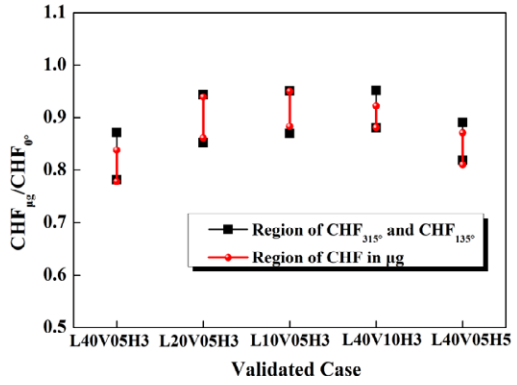

Figure 2: Validation of CHF region by drop tower experiments.

Section 3 Further analysis of the experimental data

To further explain this phenomenon, a modified subcooled flow boiling heat flux partitioning model was developed based on the model proposed by Basu et al. (2005a) and Basu et al. (2005b). The fundamental idea of the modified

model is kept the same with that of Basu et al. (2005a) and Basu et al. (2005b): all the energy from the wall is transferred to the superheated liquid layer immediately adjacent to the wall by transient conduction (q_{tc}) and forced convection (q_{fc}), and then transferred to the bubbles by vaporization and the bulk liquid by the condensation of subcooled liquid (as shown in **Fig. 3**). Therefore, the wall heat flux at CHF can be expressed as

$$q_{w,CHF} = \frac{\kappa_l \left(T_{w,CHF} - T_l\right)}{\sqrt{\pi \alpha_l t}} = q_{tc} + q_{fc} \tag{3}$$

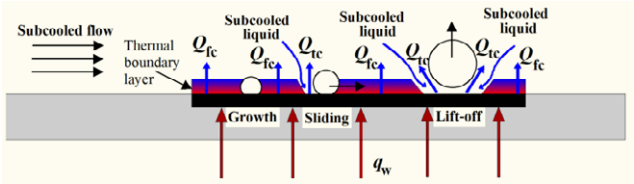

Figure 3: Schematic diagram of heat flux partitioning model for subcooled flow boiling.

In the present study, to obtain the influence of buoyancy on the bubble sliding and bubble lift-off, and hence on the CHF, the heat flux of transient conduction is further divided into two components, which are the contribution caused by bubble sliding (q_{sl}) and the contribution caused by bubble lift-off (q_l), as shown in **Fig. 3**. Then q_{sl} and q_l can be calculated by Eqs. (4) - (5), respectively (Basu et al., 2005a; Basu et al., 2005b).

$$q_{sl} = \frac{1}{t_w + t_g} \int_0^{t_w + t_g} \frac{\kappa_l}{\sqrt{\pi \alpha_l t}} \left(\Delta T_w + \Delta T_{sub}\right) A_{sl} R_f N_a dt \tag{4}$$

$$q_l = \frac{1}{t_w + t_g} \int_0^{t_w + t_g} \frac{\kappa_l}{\sqrt{\pi \alpha_l t}} \left(\Delta T_w + \Delta T_{sub}\right) A_l R_f N_a dt \tag{5}$$

The heat flux due to the forced convection (q_{fc}) in the nucleate boiling heat transfer region can be estimated by

$$q_{fc} = \left(1 - \frac{A_{sl} + A_l}{A}\right) h_{fc} \left(T_w - T_f\right) \tag{6}$$

The active nucleation site *Na* density can be calculated by the fractal model developed by Xiao and Yu (2007) which is given by

$$Na_{tot} = \left(\frac{D_{c,max}}{D_{c,min}}\right)^{d_f} \qquad D_{c,min} \le D_c \le D_{c,max} \tag{7}$$

The parameters of bubble behavior in Eqs. (4) - (6), including the diameter of bubble sliding D_{sl}, the diameter of bubble lift-off D_l, the sliding length l, and the time of bubble growth t_g can be obtained from the bubble force balance model

$$\sum F_x = F_{sx} + F_{qs} + F_{dux} + F_{bx} = 0 \tag{8}$$

$$\sum F_y = F_{sy} + F_{duy} + F_{sl} + F_{by} + F_h + F_{cp} + F_m = 0 \tag{9}$$

where F_s, F_{qs}, F_{du}, F_b, F_{sl}, F_h, F_{cp} and F_m represent surface tension, quasi-steady drag force, unsteady drag force, buoyancy, shear lift force, hydrodynamic pressure force, contact pressure force and Marangoni force, respectively (Klausner et al. 1993).

It can be observed from **Fig. 4** that the ratio of heat flux due to bubble sliding to the CHF in microgravity $q_{sl\text{-}\mu g}/q_{CHF\text{-}\mu g}$ is less than that in normal gravity when θ = 135° but greater than that in normal gravity when θ = 315°. Therefore, it can be inferred that the effects of bubble sliding on CHF in microgravity is weaker than that in normal gravity when θ = 135° but stronger than that in normal gravity when θ = 315°.

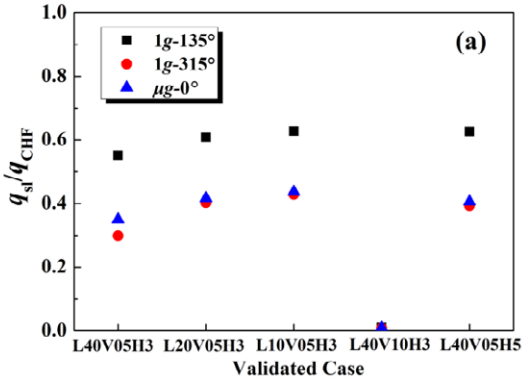

Figure 4: The effect of heater orientation and gravity levels on bubble sliding.

Conclusions

A method for simulating subcooled flowing boiling CHF in microgravity on the ground, which $CHF_{\mu g}$ can be estimated in the range of $CHF_{315°}$ and $CHF_{135°}$ on the ground, was proposed. The experimental results have proved that the method is valid and feasible. A modified heat flux partitioning model was developed to further prove the method. The effects of bubble sliding, bubble lift-off and forced convection on CHF under different orientations and gravity conditions were further explained by this modified model.

Acknowledgements

This work is supported by the project of Young Elite Scientists Sponsorship Program by CAST (2018QNRC001), Joint ESA-CMSA Project (TGMTYY00-RW-05-1.00), National Natural Science Foundation of China (No.51636006), Basic Research Project of Shenzhen Knowledge Innovation Program (JCYJ20180306170627132), the Fundamental Research Funds For the Central Universities (No.cxtd2017004, xjj2017085), and the Postdoctoral Research Project of Shaanxi Province (2016BSHEDZZ131).

References

H. Zhang, I. Mudawar, M.M. Hasan, Experimental assessment of the effects of body force, surface tension force, and inertia on flow boiling CHF, *Int. J. Heat Mass Transf.* 45 (2002) 4079–4095.

H. Zhang, I. Mudawar, M.M. Hasan, Flow boiling CHF in microgravity, *Int. J. Heat Mass Transf.* 48(15) (2005) 3107-3118.

Y.H Zhang, B. Liu, J.F. Zhao, Y.P. Deng, J.J. Wei, Experimental study of subcooled flow boiling heat transfer on micro-pin-finned surfaces in short-term microgravity. *Exp. Therm. Fluid Sci.* 97 (2018) 417–430.

N. Basu, G.R. Warrier, V.K. Dhir, Wall Heat Flux Partitioning During Subcooled Flow Boiling: Part 1—Model Development, *J. Heat Transfer* 127 (2005) 131-140.

N. Basu, G.R. Warrier, V.K. Dhir, Wall Heat Flux Partitioning During Subcooled Flow Boiling: Part II—Model Validation, *J. Heat Transfer* 127 (2005) 141-148.

B. Xiao, B. Yu, A Fractal Analysis of Subcooled Flow Boiling Heat Transfer, *Int. J. Multiph. Flow* 33 (10) (2007) 1126 - 1139.

J.F. Klausner, R. Mei, D.M. Bernhard, L.Z. Zeng, Vapor Bubble Departure in Forced Convection Boiling, *Int. J. Heat and Mass Transfer* 36(3) (1993) 651-662.

Oral 013

On the monitoring of the vibratory environment of DCMIX4 campaign. Preliminary results

D. Dubert[1], M. Marín-Genescà[2], M. J. Simón[2], J.M. Ezquerro[3], Jna. Gavaldà[1], X. Ruiz[1,4], V. Shevtsova[5]

[1] Universitat Rovira i Virgili, Departament de Química Física i Inorgànica, Tarragona, Spain; [2] Universitat Rovira i Virgili, Departament d'Enginyeria Mecànica, Tarragona, Spain; [3]E-USOC. ETSIAE Universidad Politécnica de Madrid, Madrid, Spain; [4]Institut d'Estudis Espacials de Catalunya, IEEC, Barcelona. Spain; [5]Department of Chemical Physics, MRC, Université Libre Bruxelles, Bruxelles, Belgium.

dianacristina.dubert@urv.cat, marc.marin@urv.cat , mariajose.simon@urv.cat , jm.ezquerro@upm.es , fina.gavalda@urv.cat

, josepxavier.ruiz@urv.cat , vshev@ulb.ac.be

Introduction

In the framework of the European Space Agency, all campaigns of the program called "Diffusion and Thermodiffusion Coefficients Measurements in Ternary Mixtures (DCMIX)" aim to accurately measure pure diffusion, thermodiffusion and Soret coefficients of different, but technologically relevant, ternary liquid systems (Shevtsova et al 2014, Triller et al 2018) inside the International Space Station (ISS).

Due to the own nature of the physical processes implied, molecular diffusion and thermodiffusion experiments take a long time, therefore, a careful monitoring of the vibrational environment is thus of capital importance to prevent spurious results potentially related to detectable disturbances occurred during the experiments (Jurado et al 2016, Ollé et al 2017, Dubert et al 2018). Based on this, the present work focused on the preliminary characterization of the DCMIX4 accelerometric environment taking into account the signals coming from the es09006 sensor, nearest to the experiment. The raw accelerometric signals, with a sampling rate of 142 Hz and a cut-off frequency of 6 Hz, were freely downloaded from PIMS NASA website (PIMS website: PIMS 2019). Therefore the signal characterization focuses on the low frequency range which it is known to be the most harmful for the thermodifussion experiments (Shevtsova et al. 2015).

DCMIX4 experiments were performed in five different cells with different mixtures and component concentrations. The first three cells run with the DCMIX2 mixture at different concentrations while cell 4 and 5 run with tetralin-toluene-fullerene and polystyrene-toluene-hexane, respectively. The campaign consisted of 49 runs lasting between 12 and 48 hours. Remark that in the first experiments of each cell, acceleration data are unavailable, due to the malfunction of the sensor. Consequently, it has been analized only the runs in which the sensor was switched on. In addition, all the runs had a missing period data when passing from one day to another. In other words, the signal's recording was always stopped during 10 minutes after midnight.

Metodology, results and discussion

Digital signal processing techniques were systematically applied minute by minute to all the signals, covering both the typical time and frequency analyses: the Root Mean Square (RMS), the Power Spectral Density (PSD), Spectral ENtropy (SEN) and the warning maps (see more details in Ollé et al 2017, Dubert et al 2018). The run 2r07 has been selected as an exemple for the applied techniques.

Fig 1 plots the calculated global RMS values along the whole experiment for the selected run. During the 16 hours of the experiment, two noticeable spikes can be observed. Time domain warnings could be associated to these peaks, therefore the experimentalists should take them into account when interpreting the experimental results. A spike can be considered a warning if its RMS value exceeds the 20% of the mean of all RMS values of the signal (Ollé et al 2017). More details of the spikes found are presented in Table 2.

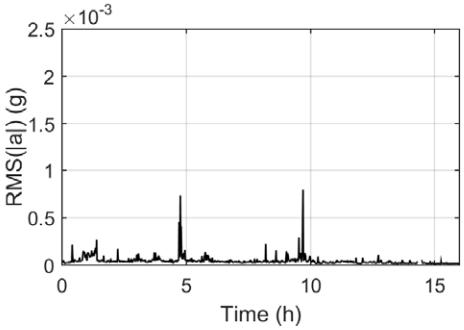

Figure 1: Global RMS (run 2r07)

RMS warning map technique is a quick visual way to display if the vibratory limits have been surpassed or not, along the experiment. The map plots the frequency bands on the X axis and the experiment's duration on Y axis. Symbols in the RMS warning map represent each of the ISS vibratory limits that were exceeded.

To illustrate the above considerations, Fig. 2.a displays the RMS values of the three acceleration components in one-third-octave frequency intervals of the selected signal, calculated for the minute 400. Figure 3.b plots the warning map along all the experiment.

It can be seen that RMS values are quite close to the limit curve below 1 Hz, crossing it at frequency ranges 0.17-0.28 and 0.45-0.58 Hz in x_A and y_A directions, respectively. Moreover, the ISS limit requirements are outdo for almost the entire duration of the experiment and in all three directions, if low frequencies ranges, below 0.6 Hz are considered (see Fig 3.b). Table 1 summarizes the frequency bands that outdo the ISS limits for all the completed runs.

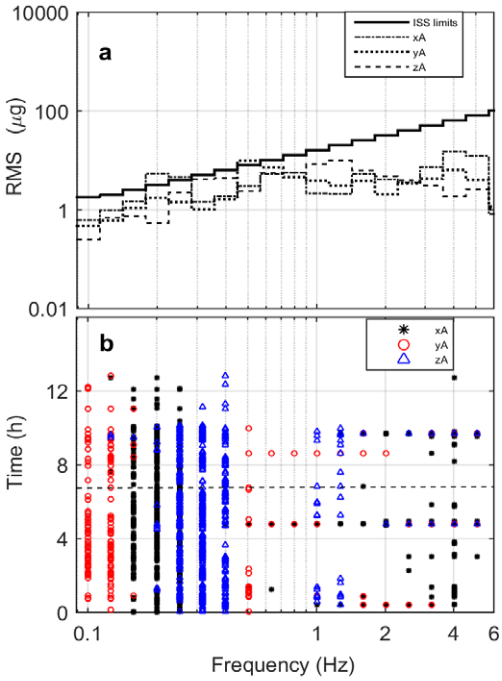

Figure 2: a) RMS acceleration components vs. one third octave frecuency bands calculated in the minute 400, b) Marks indicating when the RMS exceeds the ISS limit curve requirements (Run 2r07).

Table 1: Vibrational observations

Run	Vibrational environmental observations	
	Time domain (time where there are RMS spikes, h)	Frequency domain (range that exceeds the ISS limits, Hz)
Cell #1: Toluene–Methanol-Cyclohexane (0.20 – 0.25 – 0.55 wt%)		
1r04	Small RMS peaks	0.2-0.3
1r05	27.05 h	0.2-0.3
1r06	Small RMS peaks	0.17-0.35
1r07	16.57h, 33.1h, 33.3h, 34.1h, 34.45 h	Correct
1r08	13.93 h, 16.74 h	0.22-0.28
Cell #2: Toluene–Methanol-Cyclohexane (0.35 – 0.25 – 0.40 wt%)		
2r06	Correct	0.28-0.35
2r07	4.758 h, 9.692 h	0.17-0.35
2r08	Small RMS peaks	0.22-0.35
2r09	Correct	Correct
2r10	11.04 h, 12.19 h	Correct
2r11	Correct	0.22-0.28
2r12	5.542 h	Correct
Cell #3: Toluene–Methanol-Cyclohexane (0.55 – 0.25 – 0.20 wt%)		
3r08	Correct	0.22-0.28
3r09	0.525 h, 0.608h, 8.525h	0.17-0.35
3r10	Correct	Correct
3r11	Correct	Correct
3r12	Correct	0.22-0.28
3r14	0.125 h	0.22-0.28 HZ
Cell #4: Tetrahydronaphthalene–Toluene-Fullerene (0.60 -0.3993 – 0.0007 wt%)		
4r04	Correct	0.22-0.28
4r05	15.55 h	0.22-0.28
4r06	9.986 h	0.17-0.35
4r07	17.54 h, 19.92 h	0.17-0.35
4r08	1.508 h, 7.925 h, 20.69 h, 23.67 h	0.22-0.28
Cell #5: Polystyrene–Toluene-n-Hexane (0.02 – 0.49 – 0.49 wt%)		
5r03	6.408 h, 30.41 h, 31 h, 31.01 h,	0.17-0.35
5r04	13.84 h	0.17-0.35

Conclusions

A preliminary accelerometric characterization of the microgravity environment of DCMIX4 runs was performed, enabling further evaluation of its potential impact on the experimental results.

Acknowledgements

The present work has been supported by grants ESP2017-83544-C3-1-P (MCIU/FEDER) and 2018PFR-URV-B2-73 (Rovira I Virgili University).

References

D. Dubert, J. Ollé, R. Jurado, Jna. Gavaldà, A. Laverón-Simavilla, X. Ruiz and V. Shevtsova, *Characterization of the accelerometric environment of DCMIX2/3 experiments*; Microgravity Science and Technology, 30 (2018) 683-697.

https://pims.grc.nasa.gov/html/ISSAccelerationArchive.html

R. Jurado, M.J. Simón, J. Pallarés, A. Laverón-Simavilla, X. Ruiz and V. Shevtsova; *Some considerations on the vibrational environment of the DSC-DCMIX1 experiment onboard ISS*. Acta Astronautica, 129 (2016) 345–356.

J. Ollé, D. Dubert, Jna. Gavaldà, A. Laverón-Simavilla, X. Ruiz and V. Shevtsova; *Onsite vibrational characterization of DCMIX2/3 experiment*s. Acta Astronautica, 140 (2017) 409–419.

V. Shevtsova, C. Santos, V. Sechenyh, J.C. Legros, A. Mialdun; *Diffusion and Soret in Ternary Mixtures. Preparation of the DCMIX2 Experiment on the ISS.* Microgravity Sci Tech. 25 (2014) 275-283.

V. Shevtsova, Y. Gaponenko, V. Sechenyh, D. Melnikov; *Dynamics of a binary mixture subjected to a temperature gradient and oscillatory forcing*. Journal of Fluid Mechanics 767 (2015) 290-322.

T. Triller, H. Bataller, M.M. Bou-Ali, M. Braibanti, F. Croccolo, J.M. Ezquerro, Q. Galand, Jna. Gavaldà, E. Lapeira, A. Laverón-Simavilla, T. Lyubimova, A. Mialdun, J.M. Ortiz de Zárate, J. Rodríguez, X. Ruiz, I. Ryzhkov, V. Shevtsova, S. Van Vaerenbergh, W. Köhler; *Thermodiffusion in ternary mixtures of water/ethanol/triethylene glycol: first report on the DCMIX3-experiments performed on the International Space Station.* Microgravity Sci. Technol, 30(3) (2018) 295-308.

Oral 014

Determination of transport properties of nanofluid C_{60}-THN-Tol in binary mixtures

A. Errarte[1], M. Aginagalde[1], M. Mounir Bou-Ali[1]

[1]Department of Mechanical and Industrial Manufacturing, Mondragon Goi Eskola Politeknikoa, 20500 Arrasate Mondragon, Spain, aerrarte@mondragon.edu, maginagalde@mondragon.edu, mbouali@mondragon.edu

Introduction

Over the last decades, the study of transport properties such as thermodiffusion, molecular diffusion and Soret has considerably increased due to the several fields where they influence (Montel 1994, Rosner 1978, Braun and Libchaber 2004).
Binary mixtures have already been deeply studied (Köhler and Müller 1995, Bou-Ali et al 1998, Kolodner et al. 1988, Bou-Ali et al. 1999). Nevertheless, most of the natural processes where those transport properties are key are composed by more than two components, so during the last years, efforts have been directed toward the study of ternary mixtures. For this purpose, the DCMIX (Diffusion Coefficient Measurements in ternary mIXtures) project was developed together with the European Space Agency, and experiments have been carried out in the International Space Station (Bou-Ali et al. 2015). Actually, the fourth mission of the project has ended; microgravity conditions experiments were onboard from November 2018 to March 2019. In this study, a nanofluid composed by Fullerene (C_{60}), Tetralin (THN) and Toluene (Tol) has been studied for the first time, together with another two ternary mixtures composed by Toluene, Methanol and Cyclohexane, and Polystyrene, Toluene and Cyclohexane.
The present work shows results of the three binary mixtures correspondent to the ternary nanofluid: C_{60}-THN, C_{60}-Tol and THN-Tol at 25 ºC.

Experimental Setup

The thermogravitational technique has been used for the actual work. This technique has been widely used to determine thermodiffusion coefficients of both binary and ternary mixtures (Blanco et al. 2010). With the aim of tracking the concentration variation along the complete column height during the whole time the experiment lasts, a thermogravitational microcolumn was manufactured (Naumann et al. 2012 and Lapeira et al. 2018). The Digital Interferometry optical analysis was applied, allowing determining the thermodiffusion and molecular diffusion coefficients by the transitory and stationary state concentration profile.
The system is based on a Mach-Zehnder interferometer, where two wavelength lasers can be used; 470 nm and 633 nm, depending on the study of binary or ternary mixtures. In the case of studing binary mixtures, it is enough to analyse data with one laser. Nevertheless, in order to verify the obtained results the analysis is carried out for both wavelengths.

Figure 1 shows a scheme of the interferometer installed in Mondragon Unibertsitatea. As it can be seen, the first step is to make a filtering and adecuation of the signal. Then, the beam is divided in two perperndicular beams of the same intensity: one of it passes through the window of the microcolumn and the other acts as reference. In the end of the path, both beams are joined back; the interferometry patterns are generated and captured by the CCD camera.
In order to be able to work with a single laser at each time, a pneumatic cylinder has been placed in front of each of the sources blocking its path.

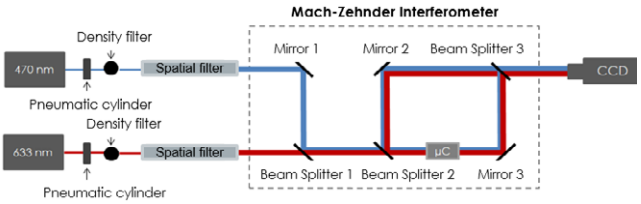

Figure 1: Scheme of the Digital Interfrometer applied to the Thermogravitational .microcolum.

A Labview program is used to control the experiment. First, the system is left to hogomenize at mean temperature, acquiring pictures every few minutes. Then, the temperature gradient is applied, and in order to detect precisely all variations, the image adquisition frequency is increased to every minute.
Once the experiment is finished, the first step of the image processing is to calculate the phase. For this purpose, the 2D Fast Fourier Transform is used. Then, in order to obtain the natural phase of each image unwrapping algorithms are applied. Finally, the phase variation is related to the change of refractive index and transformed to concentration variation as it is shown in expressions (1) and (2).

$$\Delta n(y,z) = \frac{\lambda}{2\pi L}\Delta\phi(y,z) \quad (1)$$

$$\Delta n(y,z) = \left(\frac{\partial n}{\partial c}\right)\Delta c(y,z) \quad (2)$$

These two expressions are applied to each of the images and the variation of the phase and concentrations are calculated as shown in Figure 2 and Figure 3.

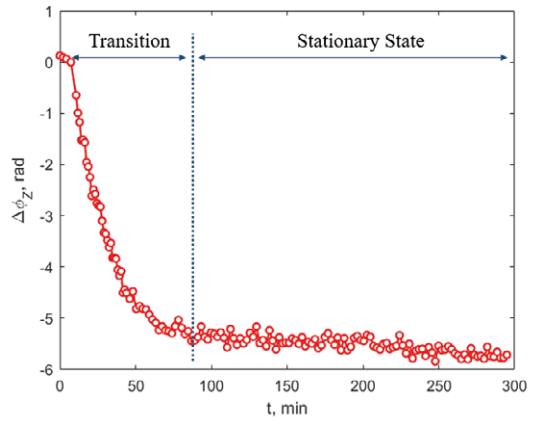

Figure2: Phase variation of C_{60}-THN mixture at c = 0.001 and 25ºC.

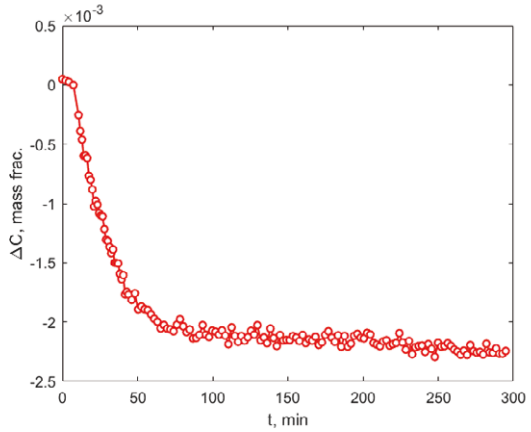

Figure3: Concentration variation of C_{60}-THN mixture at c = 0.001 and 25ºC.

Finally, molecular diffusion (D), thermodiffusion (D_T) and Soret (S_T) coefficients are calculated by expressions (3), (4), and (5).

$$D_T = -\frac{L_x^4}{504}\frac{\alpha g}{\upsilon c_0(1-c_0)}\frac{\partial c}{\partial z} \quad (3)$$

$$t_r = \frac{9!\, L_z^2 \mu^2 D}{(\pi \Delta T g \rho \alpha L_x^3)^2} \quad (4)$$

$$S_T = \frac{D_T}{D} \quad (5)$$

As it can be seen, in order to determine these coefficients previous data about geometrical and thermophysical properties is needed: L_x is the gap, L_z is the column height, α is the thermal expansion coefficient, υ the cinematic viscosity, g the gravitational force, T is the temperature, ρ the density and c_i the concentration of component i.

Conclusions

This work shows new results about thermodiffusion coefficient, molecular diffusion coefficients and Soret coefficients measured by Digital Interferometry applied to a thermogravitational microcolum. This technique allows to determine two first coefficients directly and the third one indirectly. Obtained results show that the presence of fullerene changes the order of magnitude of some of the measured coefficients. This new values could help in the development of new applications.

Acknowledgements

This work has been supported by FETRAFLU (2018-CIEN-000101-01) from Gipuzkoa Program for Science, ATNEMFLU (ESP2017-83544-C3-1-P) of the MINECO, DCMIX (AO-2009-0858/1056) from the European Space Agency, and the Research Group Program (IT1009-16) and µ4Industry from the Basque Government.

References

F. Montel, Importance de la Thermodiffusion en Exploracion et Production Pétrolières, *Entropie*, 184/185 (1994) 86–93.

D. E. Rosner, Thermal (Soret) Diffusion Effects on Interfacial Mass Transport Rates, *Phys. Chem. Hydrodyn.*, 1 (1978) 159–185.

D. Braun and A. Libchaber, Thermal force approach to molecular evolution, *Phys. Biol.*, 1 (2004) 1-8.

W. Köhler and B. Müller, Soret and mass diffusion coefficients of toluene/ n -hexane mixtures, *J. Chem. Phys.*, 103 (1995) 4367–4370.

M. M. Bou-Ali, O. Ecenarro, J. A. Madariaga, C. M. Santamaría, and J. J. Valencia, Thermogravitational measurement of the Soret coefficient of liquid mixtures, *J. Phys. Condens. Matter*, 10 (1998) 3321–3331.

P. Kolodner, H. Williams, and C. Moe, Optical measurement of the Soret coefficient of ethanol/water solutions, *J. Chem. Phys.*, 88 (1988).

M. M. Bou-Ali, O. Ecenarro, J. A. Madariaga, C. M. Santamaria, and J. J. Valencia, Influence of the Grashof number on the stability of the Thermogravitational effect in liquid mixtures with negative thermal diffusion factors, *Entropie*, 218 (1999) 5–7.

M. M. Bou-Ali *et al.*, Benchmark values for the Soret, thermodiffusion and molecular diffusion coefficients of the ternary mixture tetralin+isobutylbenzene+n-dodecane with 0.8-0.1-0.1 mass fraction, *Eur. Phys. J. E*, 38 (2015) 4–9.

P. Blanco, M. M. Bou-Ali, J. K. Platten, D. A. De Mezquia, J. A. Madariaga, and C. Santamaría, Thermodiffusion coefficients of binary and ternary hydrocarbon mixtures. *J. Chem. Phys.*, (2010) 114506.

P. Naumann, A. Martin, H. Kriegs, M. Larrañaga, M. M. Bou-Ali, and S. Wiegand, Development of a thermogravitational microcolumn with an interferometric contactless detection system., *J. Phys. Chem. B*, 116 (2012) 13889–97.

E. Lapeira, A. Mialdun, V. Yasnou, P. Aristimuño, V. Shevtsova, and M. M. Bou-Ali, Digital Interferometry Applied to Thermogravitational Technique, *Microgravity Sci. Technol.*, 30 (2018) 635–641.

Oral 015

The Electromagnetic Levitator (ISS-EML) on the International Space Station – Containerless Electromagnetic Processing on the International Space Station ISS – The ThermoProp/ThermoLab Project

M. Mohr[1], Y. Dong[1], R. K. Wunderlich[1], H.-J. Fecht[1]

[1]Institute of Functional Nanosystems, Ulm University, Ulm, Germany
markus.mohr@uni-ulm.de, yue.dong@uni-ulm.de, rainer.wunderlich@uni-ulm.de, hans.fecht@uni-ulm.de

Introduction

A materials properties are determined by the chemical composition and its microstructure. During the formation of most structural and functional materials, the material is typically molten, followed by cooling and solidification. This step is then defining the resulting microstructure, which could be poly-crystalline, single-crystalline or glassy, dependent on the cooling rate.

Therefore, such solidification processes have to be controlled to obtain the desired microstructure. A progress for the development and optimization of such processes is the advent of casting simulations, which can predict the cooling rate and microstructure formation during solidification.

The most relevant parameters for solidification models are related to the transport of mass and heat in the liquid. These are usually described by dimensionless quantities, namely the Peclét number, the Prandtl number, the Rayleigh number and the Marangoni number. The physical properties behind all these characteristic quantities are the following thermophysical properties of a fluid:

- mass density ρ
- specific heat capacity c_p
- thermal conductivity λ
- viscosity η
- surface tension σ

The measurement of these thermophysical quantities deliver input parameters for numerical solidification models.

Measurement of thermophysical properties of metallic alloys in the liquid phase are difficult in conventional container based methods. Reactions of the melt with the container walls often lead to erroneous results, e.g. for calorimetric measurements.

One approach to overcome this obstacle is the measurement of thermophysical properties using containerless methods, such as electromagnetic levitation (Fecht and Wunderlich, 2017). Due to the relatively high forces necessary to levitate a metallic droplet on ground, excessive heating and turbulences in the sample are caused by the electromagnetic positioning field. Especially samples with relatively low melting points, such as bulk metallic glasses (BMG) can then not be processed in the undercooled liquid range, which would be of scientific interest. The unavoidable turbulent flow makes certain measurements impossible, such as the determination of viscosity. This drawbacks can be avoided in conditions where the force by earths gravitation is balanced by another force, such as on board of parabolic flights (Wunderlich, Fecht and Lohöfer, 2017; Wunderlich *et al.*, 2018; Mohr, Wunderlich, Zweiacker, *et al.*, 2019) or on board the international space station (Fecht and Wunderlich, 2017; Mohr, Wunderlich, Koch, *et al.*, 2019).

We will give an overview over the electromagnetic levitator ISS-EML on board the international space station (ISS) and some results obtained on bulk metallic glasses, recently obtained by the ThermoProp/ThermoLab project.

Thermophysical Properties of BMGs in the Liquid state

Within the last few years, several BMG materials were investigated in the ISS-EML. The two Zr-based glasses Vit106a ($Zr_{58.5}Cu_{15.6}Ni_{12.8}Al_{10.3}Nb_{2.8}$) and LM105 ($Zr_{52.5}Cu_{17.9}Ni_{14.6}Ti_5Al_{10}$) as well as a Fe-based glass former ($Fe_{57.75}Ni_{19.25}Mo_{10.0}C_{5.0}B_{8.0}$) were processed successfully. Some highlights of the results will be presented in this contribution.

Acknowledgements

The authors acknowledge the access to the ISS-EML, which is a joint undertaking of the European Space Agency (ESA) and the DLR Space Administration. The reported work was conducted in the framework of the ESA MAP project ThermoProp (AO-099-022). We further acknowledge funding from the DLR Space Administration with funds provided by the Federal Ministry for Economic Affairs and Energy (BMWi) under Grant No. 50WM1759.

References

Fecht, H. J. and Wunderlich, R. K. (2017) 'Fundamentals of Liquid Processing in Low Earth Orbit: From Thermophysical Properties to Microstructure Formation in Metallic Alloys', *Jom*, 69(8), pp. 1261–1268. doi: 10.1007/s11837-017-2417-4.

Mohr, M., Wunderlich, R. K., Koch, S., *et al.* (2019) 'Surface Tension and Viscosity of Cu50Zr50 Measured by the Oscillating Drop Technique on Board the International Space Station', *Microgravity Science and Technology*, pp. 1–8. doi: 10.1007/s12217-019-9678-1.

Mohr, M., Wunderlich, R. K., Zweiacker, K., *et al.* (2019) 'Surface tension and viscosity of liquid Pd43Cu27Ni10P20 measured in a levitation device under microgravity', *Nature Microgravity*, 5, p. 4. doi: 10.1038/s41526-019-0065-4.

Wunderlich, R. K. *et al.* (2018) 'Surface Tension, Viscosity, and Selected Thermophysical Properties of Ti48Al48Nb2Cr2, Ti46Al46Nb8, and Ti46Al46Ta8 from Microgravity Experiments', *Advanced Engineering Materials*, p. 1800346. doi: 10.1002/adem.201800346.

Wunderlich, R. K., Fecht, H.-J. J. and Lohöfer, G. (2017) 'Surface Tension and Viscosity of the Ni-Based Superalloys LEK94 and CMSX-10 Measured by the Oscillating Drop Method on Board a Parabolic Flight', *Metallurgical and Materials Transactions B*, 48(1), pp. 237–246. doi: 10.1007/s11663-016-0847-y.

26th European Low Gravity Research Association Biennial Symposium and General Assembly
14th International Conference on "Two-Phase Systems for Space and Ground Applications"
European Space Agency Topical Teams meetings
Granada (Spain), September 24-27, 2019

Oral 016

The Electromagnetic Levitator (ISS-EML) on the International Space Station – Thermophysical properties of Ni-based superalloys MC2, LEK94, CMSX-10

M. Mohr[1], Y. Dong[1], R. K. Wunderlich[1], H.-J. Fecht[1]

[1]Institute of Functional Nanosystems, Ulm University, Ulm, Germany
markus.mohr@uni-ulm.de, yue.dong@uni-ulm.de, rainer.wunderlich@uni-ulm.de, hans.fecht@uni-ulm.de

Introduction

Nickel-based superalloys are materials with high strength and high toughness, together with good creep resistance even at high temperatures. This makes them prominent candidates for materials in turbines for power generation or in aircraft engines. The applied casting procedures like the directional solidification casting are time consuming and costly, which makes it imperative to use casting simulations for successful casting development and optimization. Such simulations need input data for the material properties, especially the thermal and material transport properties in the solid and liquid state.
The measurements of these properties in container-based conventional equipment is difficult due to the melts high reactivities. This could lead to contamination of the melt that inhibit precise measurements of surface and bulk properties such as tension and viscosity. Chemical reactions and their associated enthalpies can interfere with precise measurements of thermophysical properties such as the specific heat capacity. Therfore, our approach is to use electromagnetic levitation, a container-less method where the sample is levitated and not in contact with any foreign material.
The levitation force generated by the positioning field are however generating eddy-currents of such density that the sample will experience considerable heating without additional heating. Moreover, in the liquid phase, the liquid will experience turbulent flows, making measurement of viscosity impossible.
In order to obtain a spherical droplet, and control the fluid flow in the droplet (laminar/turbulent flow), one needs to have the equipment in microgravity conditions. This is possible using the TEMPUS facility on board parabolic flights (Lohöfer, Neuhaus, and Egry 1991), as well as the electromagnetic levitator ISS-EML on board the international space station (Lohöfer et al. 2002).

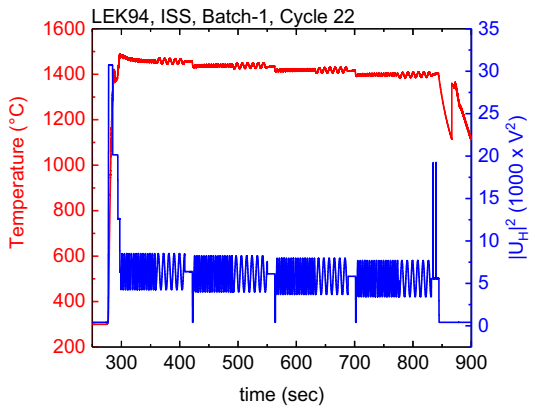

Figure 1: LEK94: typical modulation calorimetry measurement cycle

Results and Discussion

In this contribution we will present thermophysical properties of the Ni-based superalloys MC2, LEK94 and CMSX-10 measured in the ISS-EML.
We present measurements of surface tension and viscosity, as well as density and specific heat capacity. As an example, figure 1 shows a measurement cycle used to determine specific heat capacity at 4 temperatures by modulation calorimetry (Fecht and Johnson 1991; Wunderlich and Fecht 2003; Wunderlich, Fecht, and Willnecker 1993). As can be seen, the experiment held the sample in the liquid state for about 10 minutes. Such long durations of microgravity are presently only available on the international space station.

Conclusions

Thermophysical properties necessary for optimization of industrial casting processes of Ni-based superalloys were measured using the ISS-EML on board the international space station. These properties can be obtained with high precision.

Acknowledgements

The authors acknowledge the access to the ISS-EML, which is a joint undertaking of the European Space Agency (ESA) and the DLR Space Administration. The reported work was conducted in the framework of the ESA MAP project ThermoProp (AO-099-022). We further acknowledge funding from the DLR Space Administration with funds provided by the Federal Ministry for Economic Affairs and Energy (BMWi) under Grant No. 50WM1759.

References

Fecht, H. J. and W. L. Johnson. 1991. “A Conceptual Approach for Noncontact Calorimetry in Space.” *Review of Scientific Instruments* 62(5):1299–1303.
Lohöfer, G., P. Neuhaus, and I. Egry. 1991. “TEMPUS - a Facility for Measuring Thermophysical Properties of Undercooled Liquid Metals.” *High Temperatures - High Pressures* 23:333–42.
Lohöfer, G., J. Piller, G. Lohoefer, and J. Piller. 2002. “The New ISS Electromagnetic Levitation Facility - ‘MSL-EML.’” in *40th AIAA Aerospace Sciences Meeting & Exhibition*. Reston, Virigina: American Institute of Aeronautics and Astronautics.
Wunderlich, R. K. and H. J. Fecht. 2003. “Thermophysical Property Measurements by Electromagnetic Levitation Methods under Reduced Gravity Conditions.” *J. Jpn. Soc. Microgravity Appl.* 20(3):192–205.
Wunderlich, R. K., H. J. Fecht, and R. Willnecker. 1993. “Power Modulation Technique for Noncontact High-Temperature Calorimetry.” *Applied Physics Letters* 62(24):3111–13.

Oral 018

Bénard-Marangoni patterns induced by evaporation in well-defined non-spherical sessile droplet

Tian-Shi Wang[1], Wan-Yuan Shi[1,2], Ji-Long Zhu[1]

[1] School of Energy and Power Engineering, Chongqing University, Chongqing 400044, China,
[2] Key Laboratory of Low-grade Energy Utilization Technologies and Systems, Ministry of Education, Chongqing 400044, China;
cqmr.wang@cqu.edu.cn, shiwy@cqu.edu.cn, 892498678@qq.com

Introduction

Evaporation of a sessile droplet is omnipresent in daily life and this phenomenon plays an important role in a vast variety of industrial and scientific applications. Due to the curved liquid-gas interface, the non-uniform temperature distribution is induced for both the nonuniform evaporation rate and the different length of thermal path and thus the Marangoni convection caused by the surface tension gradient occur in the droplet. The Marangoni convection would lose its stability if the temperature gradient is large enough and corresponding instability patterns would appear. Hydrothermal waves (HTWs) (Sefiane et al. 2008 and Sobac at al 2012) as well as Bénard-Marangoni (BM) (Wang et al. 2019 and Zhu et al 2019) convection cells were observed in sessile evaporating spherical droplets. Recently, the Marangoni convection in the non-spherical droplet (Sáenz et al. 2015) and the evaporation kinetics as well as the flow dynamics of them (Sáenz et al. 2017) were reported. However, the Marangoni convection instability in the non-spherical droplet is still an open question. In this paper, the Marangoni instabilities in some well-defined non-spherical droplets are observed through a series of experiments. Besides, the influences of contact-line curvature, contact angle and substrate temperature on them are studied.

Experimental apparatus

The experimental apparatus is shown in Fig.1. In order to form non-spherical sessile droplets with well-defined geometries, some polished pedestals (height H=2mm±0.1mm) with designed shapes are machined on the upper surface of the brass substrate and their perimeters are artificially fixed to be consistent with P=15mm±0.1mm for all of them. The corners of the pedestals are rounded with radius of R=0.4mm±0.1mm and all the pedestals are constructed with the sharp edges in order to ensure the droplet entirely cover on the small pedestals and the fluid do not overflow along the edge of the pedestals. A droplet of 0.65cSt silicone oil is carefully deposited on the pedestals by a micro-syringe. The temperature of the pedestal surface can be controlled precisely by means of the thermostatic oil bath (PP07R-20-A12Y from PolyScience Inc.) with temperature stability of ± 5mK. The surface thermal pattern of the droplet surface is observed by an Infrared camera (FLIR A655sc, with thermal sensitivity of 30mK and resolution of 640×480) with a microscope lens mounted directly above the droplet. The profile of the droplet is obtained by a contact angle measurement (JC2000DM from Shanghai Zhongchen Digital Technic Apparatus Co., Ltd) with resolution of 0.01°.

Experimental results and discussions

Figure 2 shows a typical case of the Bénard-Marangoni convection patterns of a triangular droplet. When the liquid is deposited onto the pedestal, three convection cells appear at three corners immediately and the flow is arranged in a well-defined three-fold structure with three cold bands connecting the droplet apex with the end of cell (Fig.2a) and more and more cells are generated at the corners (Fig.2b) with droplet evaporating. The droplet is completely filled up with the cells at t=38.03s eventually (Fig.2c). Within next 6 seconds, some new cells are always generated at the middle of three straight sides with deforming and separating and they are always moving outward to the bilateral corner regions. The preferred directions of propagation of these BM cells are illustrated by the arrows in the Fig.2(c). The BM cells located at the middle of the straight sides are perpendicular to the straight sides and the cusp of them point to the apex of the droplet. However, the BM cells near the corners incline to the straight sides with a certain angle and the closer to the corner, the more inclined they are. During this period, these BM cells are almost symmetrically distributed along the cold bands, however, the symmetric structure is broken after t=44.71s. At t=44.71s, one cell is generated at the central region (marked by 'Generated cell' in Fig.2d). However, more and more cells are generated at the central region and the cell patterns become more and more unstable with droplet evaporating. These cells can hardly grow after t=68.16s with their shapes getting close to the polygonal for the droplet is close to a flat thin layer at this time.

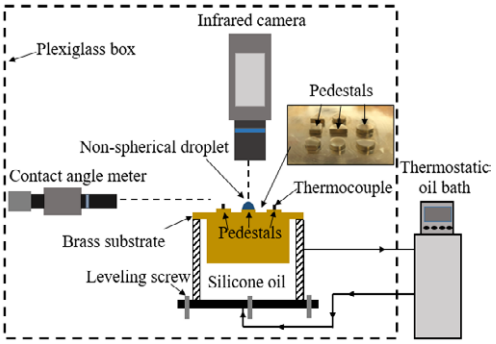

Figure 1: Schematic of the experimental apparatus.

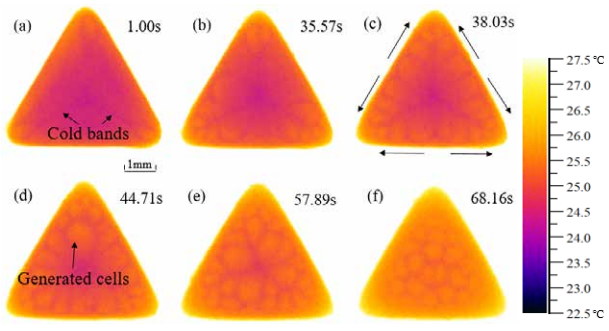

Figure 2: Evolution of the surface temperature patterns of a droplet of triangular geometry at T_w =25.02°C, T_a=23.17°C and the relative humidity of 61%.

Here, Marangoni convection patterns in the droplets of other typical geometries are also observed as shown in Fig.3. Our results showed that the BM cells always appear first at the larger k_{cl} regions (Figs.3a) and serval cold bands exist in the non-spherical droplets. The dimple region is the only region which is free of BM instabilities in the droplet of kidney geometry when the BM cells occupy the whole droplet. It is interesting that the cells will propagate continuously from the smaller k_{cl} region to the larger k_{cl} region which is different from that in the spherical droplet.

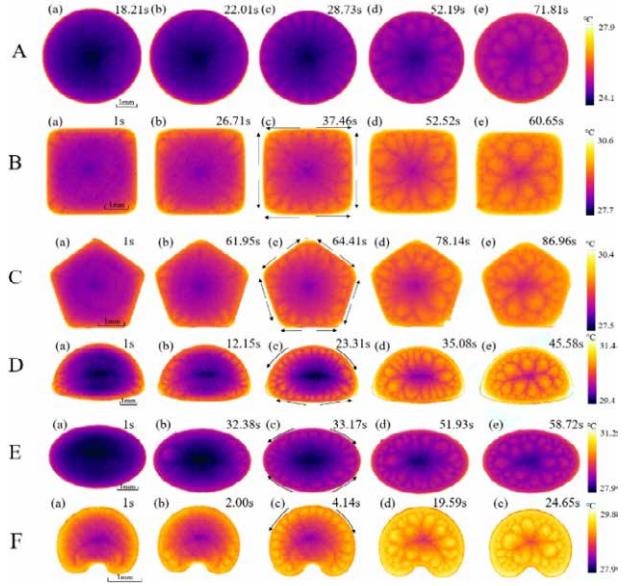

Figure.3: Marangoni convection patterns in the evaporating sessile droplets with different shapes. Here, P=15mm for all the droplets and the initial volume V=7μl.

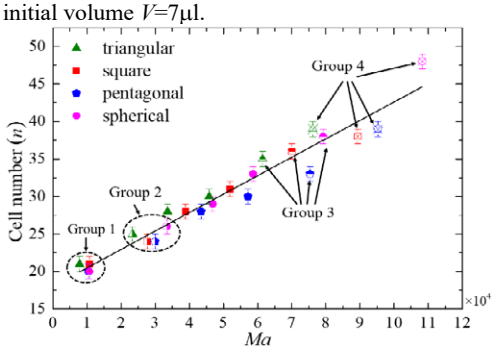

Figure.4: The cell number n versus Ma number in droplets of triangular, square, pentagonal and spherical shapes. Group 1: T_w=24.95°C, T_a=23.01°C. Group 2: T_w=28.85°C, T_a=23.28°C. Group 3: T_w=37.87°C, T_a=23.78°C. Group 4: T_w=41.52°C, T_a=23.54°C.

Here we measure the numbers of cells when the BM instability just fill the whole droplet (Fig.2d and Figs.3c) for different shapes and our experimental results show that they increase linearly with increasing the Ma number as shown in Fig.4. The cell numbers are almost the same (the group 1 and group 2) when the T_w (Ma) is small. When increasing the substrate temperature, the cell number in the spherical droplet is higher than those in polygonal droplets (the group 3 and group 4) and the difference of cell numbers between them becomes larger and larger with increasing the substrate temperature. Our results indicate that the critical contact angles for the onset of the BM convection cells at the middle of the straight side increase linearly with increasing the Ma number as shown in Fig.5. What's more, for the same T_w, the critical contact angle is the largest for the triangular droplet while it is the smallest for the spherical droplet. The critical angles for the polygonal droplet decreases when the shape is close to the circle.

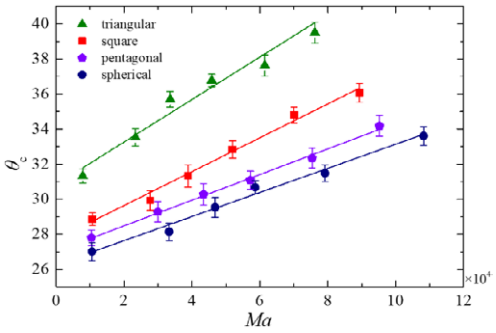

Figure.5: The critical contact angles for the onset of BM cells at the middle of flat sides for the triangular, square, pentagonal and circle droplet.

Conclusions

BM cells always appear first at the larger k_{cl} regions and serval cold bands exist in the non-spherical droplets. After a period of time, the BM cells occupy the whole droplet and these cells are non-uniformly distributed along the azimuthal direction. The BM cells are always preferred propagating from the lower k_{cl} regions towards the larger k_{cl} regions. The cell numbers both in the non-spherical droplet and spherical droplet increase linearly with increasing the Ma number and the spherical droplet is more capable to hold cells especially under a higher Ma number. The critical contact angles for the onset of BM convection cells at the middle of the straight sides in the polygonal droplet increase linearly with increasing the Ma number.

Acknowledgements

This work was funded by the Fundamental Research Funds for the Central Universities (Nos. 2018CDYJSY0055) and National Natural Science Foundation of China (Nos. 51676018 and 51176210).

References

K. Sefiane, J. R. Moffat, O. K. Matar, R. V. Craster. Self-excited hydrothermal waves in evaporating sessile drops. *Appl. Phys. Lett.* 93 (2008) 074103.

B. Sobac, D. Brutin. Thermocapillary instabilities in an evaporating drop deposited onto a heated substrate. *Phys. Fluids* 24 (2012) 032103

T. S. Wang, W. Y. Shi. Influence of substrate temperature on Marangoni convection instabilities in a sessile droplet evaporating at constant contact line mode. *Int. J. Heat Mass Transfer* 131 (2019) 1270-1278.

J.L. Zhu, W.Y. Shi, L. Feng. Flower-like patterns of Bénard-Marangoni instabilities in sessile droplet evaporating at constant contact angle mode. *Int. J. Heat Mass Transfer* 134 (2019) 784-795.

P. J. Sáenz, K. Sefiane, J. Kim, O. K. Matar and P. Valluri. Evaporation of sessile drops: A 3D approach. *J. Fluid Mech.* 772 (2015) 705-739.

P. J. Sáenz, A. W. Wray, Z. Che, O. K. Matar, P. Valluri, J. Kim and K. Sefiane. Dynamics and universal scaling law in geometrically-controlled sessile drop evaporation. *Nature Communications* 8 (2017) 14783.

Oral 019

AtmoFlow – Investigation of atmospheric-like fluid flows under micro-fravity conditions

F. Zaussinger[1], Ch. Egbers[1], P. Haun[1], V. Travnikov[1], P. Canfield[2], M. Meier[1], A. Meyer[1]

[1]Brandenburg University of Technology Cottbus-Senftenberg, Dept. of Aerodynamics and Fluid Mechanics, Cottbus, Germany
[2]Airbus Defence and Space GmbH, Immenstaad, Germany
florian.zaussinger@b-tu.de

A7. Geophysical Fluid Flows

Introduction

The main objective of the *AtmoFlow* experiment is the investigation of convective flows in the spherical gap geometry, (Canfield et al 2018, Zaussinger et al 2018a). Gaining fundamental knowledge on the origin and behavior of flow phenomena such as global cells and planetary waves is interesting not only from a meteorological perspective. Understanding the interaction between atmospheric circulation and a planet's climate, be it Earth, Mars, Jupiter, or a distant exoplanet, contributes to various fields of research such as astrophysics, geophysics, fluid physics, and climatology. AtmoFlow aims to observe flows in a thin spherical gap that are subjected to a central force-field. The Earth's own gravitational field interferes with a simulated central force-field with the given parameters of the model which makes microgravity conditions of $g<10^{-3}g_0$ (e.g. on the ISS) necessary. Without losing its overall view on the complex physics, circulation in planetary atmospheres can be reduced to a simple model of a central gravitational field, the incoming and outgoing energy (e.g. radiation) and rotational effects. Both input parameters are determined by the boundaries of the system. This strongly simplified assumption makes it possible to break some generic cases down to test models which can be investigated by laboratory experiments and numerical simulations. Varying rotational rates and temperature boundary conditions represent different types of planets. This is a very basic approach, but various open questions regarding local pattern formation or global planetary cells can be investigated with that setup. A concept has been defined for developing a payload that could be installed and utilized on-board the International Space Station (ISS). This concept is based on the microgravity experiment *GeoFlow*, which has been conducted successfully between 2008 and 2016 on the ISS, (Egbers et al 2003, Zaussinger et al 2018b). This presentation we addresses the scientific goals, the experimental setup, the concept for implementation of the AtmoFlow experiment on the ISS and first numerical results.

Scientific program and objectives

The evaluation of separated physical processes like rotation, lateral heating and electro-hydrodynamic convection are in the scope of AtmoFlow. The extension of semi-empirical parameterizations of unresolved atmospheric processes, e.g. large-scale / small-scale coupling will be investigated, too. Furthermore, precise parametrization of cell formation will be tested with respect of Rhines scaling. In addition, the findings of AtmoFlow are expected to be of benefit for validation and development of models that deal with climate change. Various initial temperature distributions will be tested to investigate connections between external forcing and climate variability. Furthermore, volumetric heating will be studied as analogy to global warming. This supports extreme value statistics, too. So, it will be possible to deduce warming trends based on time-dependent heating/cooling at the boundaries within the conditions of the experiment. Three scenarios are planned: non-rotation, solid-body rotation and differential rotation. Especially, rotating cases have geophysical and astrophysical equivalents.

Brief description of the experiment

The core of the payload is the fluid cell (see Fig 1), which is composed of an inner sphere (diameter 0.0378m), an outer sphere (diameter 0.054m) and a cooling shell.

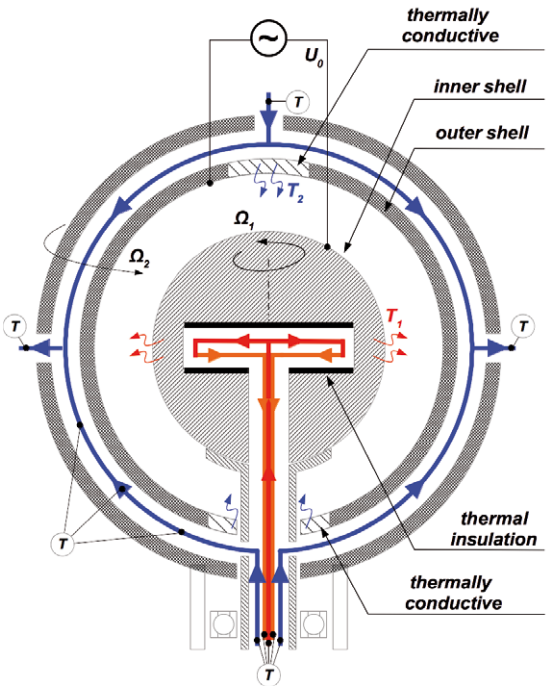

Figure 1: Sketch of the AtmoFlow experiment.

The gap between the inner sphere and the outer sphere is filled with the test liquid 3M Novec 7200 and represents the region of interest for the acquisition of science data. Local temperature boundary conditions are imposed on the poles by cooling plates in the outer shell and at the equator of the inner shell. The mean temperature in the intermediate regions is obtained by a thermalization circuit. The entire fluid cell is supported by a rotating carousel. In addition, the inner sphere can be rotated by a separate drive unit to

impose a differential rotation boundary condition. Visualization of the fluid phenomena is performed using shearing interferometry, see e.g. (Zaussinger et al 2017b). The entire optical setup co-rotates with the outer sphere and observes the test section in a circular region between the polar region of the upper hemisphere and the equator of the inner sphere. A dual camera setup including a beam splitter and dedicated Wollaston prisms allows for simultaneous interferometry in perpendicular planes.

The key feature of AtmoFlow is the thermal boundary condition. Realistic atmospheric boundary conditions are very complex, however, it is possible to break them down to follow three regions: a) a solar-heated equatorial region with absorption of re-radiated infrared radiation; b) heat sinks in the upper atmosphere of the poles and mid-latitudes, c) moderate temperature regions between the polar and the equatorial regions. Imposing these idealized boundary conditions (see Fig. 2) results in a global circulation, which is convectively unstable in the tropics and stable in the mid-latitudes. Hence, the heat transfer from the tropics to the stably stratified mid-latitudes and sub-tropics can be investigated with this setup.

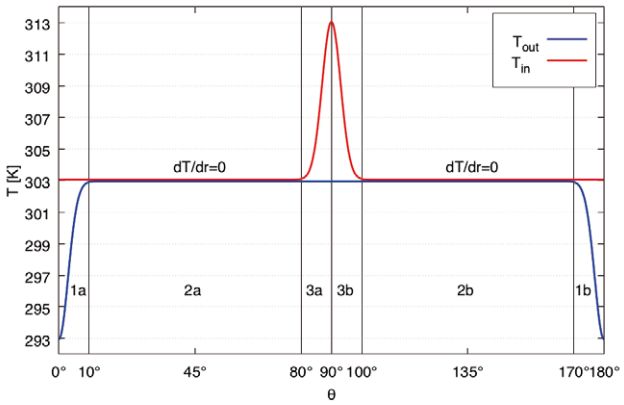

Figure 2: Idealized thermal boundary conditions of Atmoflow.

Expected outcomes

The empirical study of planetary waves, global cell formation and fluid dynamical instabilities are in the focus of the experiment. The experiment results will provide benchmark data for a rich variety of numerical problems, which are still a challenge for scientific research in various fields. The AtmoFlow experiment makes it possible to investigate decoupled flows, which are driven only by internal heating, boundary temperature difference, rotation or complex boundary conditions. This allows the validation of linear stability analysis regarding base flows, onsets and bifurcation scenarios. The main goal is the elucidation of basic aspects of convection in the rotating spherical shell. Especially, the role of mixed heating (internal heating and temperature difference across the gap) in the roating case is not well understood in the spherical gap geometry. These experiments are also accompanied by numerical simulations, (see Fig. 3). Even the non-rotating case has no geo- and astrophysical counterpart, it is of importance for planned technical applications. The construction of optimized heat exchangers, EHD-based pumps and nozzles will profit from this research. Furthermore, the enhancement of convective heat transfer in absence of gravity (e.g. on space stations or spacecrafts) will benefit from from a deeper understanding of EHD driven fluid flows.

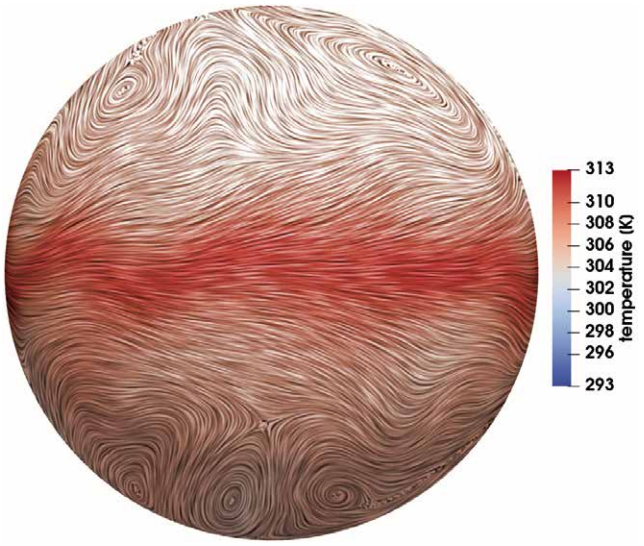

Figure 3: Numerical simulation of an equatorial wave, which is expected in the AtmoFlow parameter space.

Acknowledgements

The AtmoFlow project is funded by DLR Space Administration under contract numbers 50WP1709 and 50WP1809. The GeoFlow research has been funded by the ESA grants AO-99-049, by the DLR grants 50 WM 0122, 50 WM 0822, 50WM1644 and by the SOKRATES / ERASMUS- program LIA-ISTROF (CNRS-cooperation). Furthermore the authors thank the GeoFlow Topical Team (ESA 18950/05/NL/VJ) for intensive discussions.

References

P. Canfield, F. Zaussinger, C. Egbers, and P. Heintzmann. AtmoFlow - Simulating atmospheric flows on the International Space Station. Part I: Experiment and ISS-implementation concept. In 69th **IAC conference proceedings**, volume 18.A2.6.15. International Astronautical Federation, September 2018.

C. Egbers, W. Beyer, A. Bonhage, R. Hollerbach, and P. Beltrame. The GeoFlow-experiment on ISS (part I): Experimental preparation and design of laboratory testing hardware. **Advances in Space Research**, 32(2):171–180, 2003. Gravitational Effects in Physico-Chemical Processes.

F. Zaussinger, P. Haun, M. Neben, T. Seelig, V. Travnikov, C. Egbers, H. Yoshikawa, and I. Mutabazi. Dielectrically driven convection in spherical gap geometry. **Phys. Rev. Fluids**, 3:093501, Sep 2018.

F. Zaussinger, P. Canfield, A. Froitzheim, V. Travnikov, P. Haun, M. Meier, A. Meyer, P. Heintzmann, T. Driebe, Ch. Egbers, AtmoFlow - Investigation of atmospheric-like fluid flows under micro-gravity conditions, under review in **Microgravity Science and Technology**, 2019

Oral 020

The GeoFlow experiment on the ISS: A Review

Ch. Egbers[1], F. Zaussinger[1], P. Haun[1], V. Travnikov[1]

[1]Brandenburg University of Technology Cottbus-Senftenberg, Dept. of Aerodynamics and Fluid Mechanics, Cottbus, Germany
egbers@b-tu.de

A7. Geophysical Fluid Flows

Introduction

The GeoFlow (Geophysical Flow) experiment on the ISS is designed to study convective processes under microgravity conditions in the spherical geometry, (Egbers et al. 2003). By applying a high voltage field between two concentric spherical shells and utilizing a dielectric working fluid, it is possible to maintain an artificial radial force field, which is comparable to a planetary gravitational field. This makes it possible to study convection, as it occurs in the Earth's outer core or in the Earth's mantle. However, the minimum acceleration at the outer shell is $0.1 m/s^2$ and hence too low for Earth bounded execution. This justifies the required microgravity condition on the ISS. Convective processes are triggered by a temperature gradient, which ranges from $0.2K<\Delta T<10K$. This results in Rayleigh numbers from $10^2<Ra<10^6$, thus from the onset of convection to the full turbulent regime. The visualization is realized by a Wollaston shearing interferometry, which is part of the Fluid Science Laboratory (FSL) of the Columbus module.

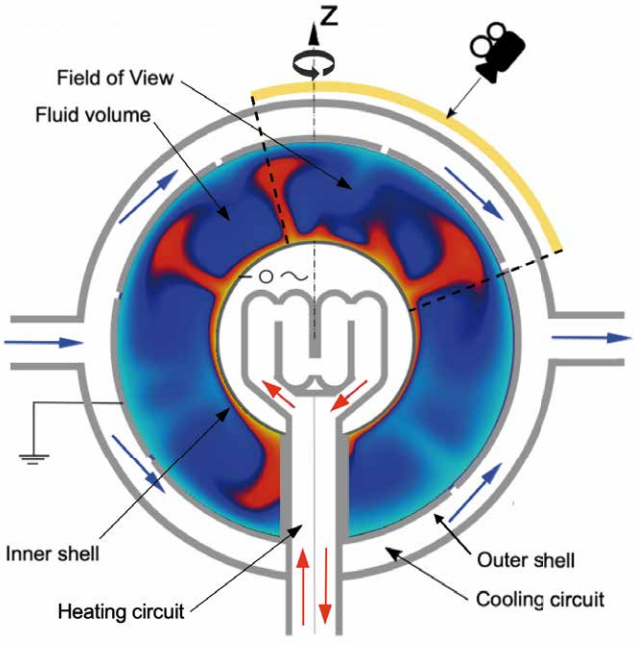

Figure 1: Sketch of the GeoFlow experiment on the ISS.

Two GeoFlow missions have been performed in the last decade. The first mission, GeoFlow I, used an iso-viscous working fluid (M5). The specific parameter regime of the experiment had similarities with convective flows which are assumed in the Earth's core. Not only the stable laminar regime, but the transition to turbulence could be investigated in detail.

The second mission, GeoFlow II, consists of three campaigns, namely GeoFlow IIa-c, however using 1-Nonanol as working fluid. This alcohol has a temperature depended viscosity and hence rheological similarities with the Earth's mantle. The main purpose of the second mission is the investigation of long-term convective flows, which are traced over several hours, as well as highly resolved short-time flows at 10 Hz frame rate. All experiments produced about 1TB of images and several 100GB of telemetry data.

Convection driven by internal heating

The fluid properties of 1-Nonanol feature internal heating, which is based on dielectic heating. Dielectric heating occurs in situations where an alternating electric field is applied on an insulating dielectric material (cf. in domestical micro-wave stoves). This effect can produce thermal convection through the thermo-electric coupling by the dielectrophoretic (DEP) force. It is parameterized by the Rayleigh-Roberts number Ra_H. The onset and the flow properties of the thermal convection are investigated in a spherical gap geometry. The thermo-electro hydrodynamical equations often adopted in the modeling of the DEP-force-driven thermal convection are extended by an additional source term arising from the dielectric heating in the energy equation. Three-dimensional direct numerical simulations are performed, asuming microgravity and without any imposed temperature gradient to highlight the effects of dielectric heating, (Zaussinger et al. 2018). Dielectric heating creates a parabola-shaped mean temperature profile with a maximum in the interior of the spherial gap. The rotating GeoFlow II campaign is the first experiment, which shows global columnar cells (Fig. 2-2c) in the sphere and all transitions from the conductive to the turbulent regime, (Zaussinger et al. 2019). For $Ra_H/Ra<1$ we find a good accordance with patterns known from theory and other experiments. Here the Proudman-Taylor theorem is valid, which results in columnar cells. In case of $Ra_H/Ra>1$ the transitions between the different convective states are shifted towards lower Rayleigh numbers. We show that the presented model reproduces results from the experimental set-up precisely and is able to predict the influence of both, internal heating and convection based on a temperature difference across the gap.

The Geoflow experiment has been dismounted from the ISS and disposed in the orbit in Dez. 2018. The aim of this presentation is a review and summary of the many highlights of both missions. We focus on latest results of rotating cases, which are perfomed in 2016 during the GeoFlow IIc campaign.

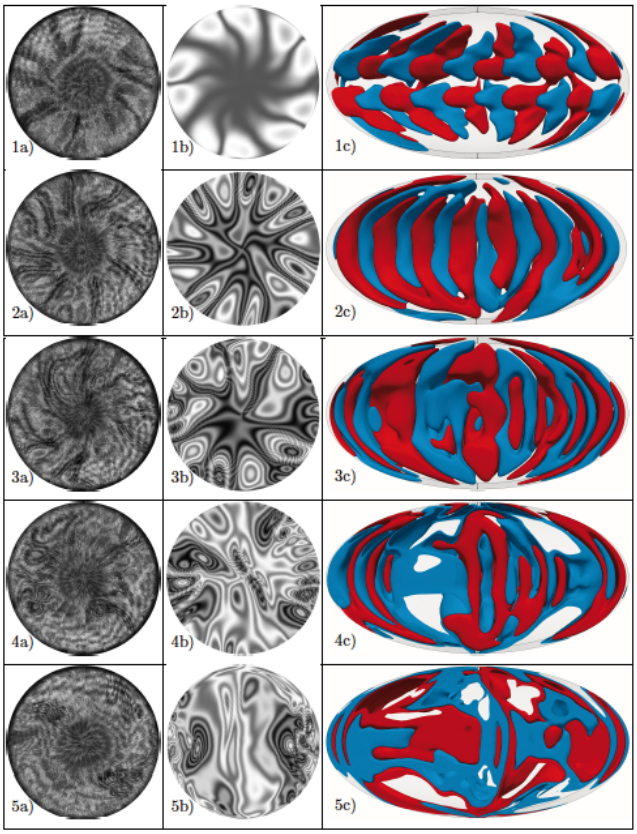

Figure 2: (left column) interferograms for Ra_H/Ra=0.13 (1a-c), Ra_H/Ra=0.38 (2a-c), Ra_H/Ra=0.75 (3a-c), Ra_H/Ra=1.2 (4a-c), Ra_H/Ra=1.8 (5a-c), at Ek = 2.6 10^3 The center is the north pole and the circle is the equator. Convective structures are highlighted by burning. (middle column) numerical interferograms, (right column) Hammer projection of numerical simulations, where red volumes depict positive temperature variations and blue volumes negative temperature variations with respect to the mean temperature field.

Acknowledgements

The GeoFlow research has been funded by the ESA grants AO-99-049, by the DLR grants 50 WM 0122 and 50 WM 0822 and by the SOKRATES / ERASMUS-program LIA-ISTROF (CNRS-cooperation). Furthermore the authors thank the GeoFlow Topical Team (ESA 18950/05/NL/VJ) for intensive discussions. We thank Ahmed Oguzhan Erdogdu for processing GeoFlow interferograms. All simulations have been performed at the Northern German Network for High-Performance Computing (HLRN) and the Heraklit cluster (BTU Cottbus-Senftenberg).

References

Ch. Egbers, W. Beyer, A. Bonhage, R. Hollerbach, and P. Beltrame. The GeoFlow-experiment on ISS (part I): Experimental preparation and design of laboratory testing hardware. **Advances in Space Research**, 32(2):171–180, 2003. Gravitational Effects in Physico-Chemical Processes.

F. Zaussinger, P. Haun, M. Neben, T. Seelig, V. Travnikov, Ch. Egbers, H. Yoshikawa, and I. Mutabazi. Dielectrically driven convection in spherical gap geometry. **Phys. Rev. Fluids**, 3:093501, Sep 2018.

B. Futterer, A. Krebs, A.-C. Plesa, F. Zaussinger, R. Hollerbach, D. Breuer, and Ch. Egbers. Sheet-like and plume-like thermal flow in a spherical convection experiment performed under microgravity. **Journal of Fluid Mechanics**, 735:647–683, Nov 2013.

F. Zaussinger, A. Krebs, V. Travnikov, and Ch. Egbers. Recognition and tracking of convective flow patterns using Wollaston shearing interferometry. **Advances in Space Research**, 60(6):1327–1344, 2017.

F. Zaussinger, P. Haun, V. Travnikov, M. Al Kawwas, Ch. Egbers, Experimental investigation of convection in the internally and boundary heated rotating spherical gap. **submitted to Phys. Rev. Fluids,** March 2019

Oral 021

Linear stability analysis of high-Prandtl-number liquid bridges exposed to an ambient gas stream

M. Stojanovic[1], H. C. Kuhlmann[1]

[1]TU Wien, Vienna, Austria
mario.stojanovic@tuwien.ac.at, hendrik.kuhlmann@tuwien.ac.at

Introduction

The linear stability of thermocapillary flow in a liquid bridge suspendended between two solid rods and exposed to an ambient gas is investigated numerically for zero-gravity conditions. The rods are kept at different temperatures $T_{cold} = T_0 - \Delta T/2$ and $T_{hot} = T_0 + \Delta T/2$, respectively. Due to the temperature dependence of the surface tension $\sigma(T) \approx \sigma_0(T_0) - \gamma(T - T_0)$, where γ is the negative linear Taylor coefficient of the surface tension and the subscript 0 denotes the reference values, the fluid flow is driven by thermocapillary stresses along the liquid-gas interface.
Most previous numerical studies addressed the simplified problem considering only the liquid phase, neglecting viscous stresses from the gas phase. Within these single-fluid models (SFM), the free surface shape is assumed to be merely statically deformed, meaning it is neither affected by the velocity nor by the temperature field (Shevtsova et al. 2011). In addition to that, SFMs require the heat transfer trough the free surface to be modelled, which is commonly achieved either by applying Newton's cooling law with a suitable ambient reference temperature or, even more restrictive, by neglecting the heat transfer into the gas (Nienhüser and Kuhlmann 2002). Among the parameters governing the problem, the effect of heat transfer between the liquid bridge and the ambient gas on the stability characteristics is the least understood.
Therefore, previous numerical investigations on two fluid models (TFM), the geometry is shown in Fig. 1, circumvent the restriction concerning the heat flux through the liquid-gas interface by expanding the computational domain, but still assume a cylindrical, thus non-deformable, shape of the liquid bridge (Shevtsova et al. 2013, Yasnou et al. 2018).
In the present work we address the full two-phase flow problem in which the liquid bridge is placed in a concentric cylinder and exposed to a nominally axial flow field (see Fig. 1). No restrictive assumptions about the boundary conditions at the interface are made, and the balance of normal and tangential stresses as well as the heat transfer between the two phases are taken into account. Our computational model allows the liquid-gas interface to be dynamically deformable, i.e. the exact shape of the interface is part of the solution.

Problem formulation and mathematical model

A liquid bridge of length l_{lb} is kept in place between two concentrical solid rods of radius r_i by surface tension forces. The support cylinders with lengths l_{in} and l_{out} are mounted coaxially in a large cylindrical tube with radius $r_o > r_i$. A gas stream with constant volume flux w_{in} is imposed in the annular gap surrounding the liquid bridge.

The symmetries of the problem allow for an axisymmetric and time-independent basic flow. The basic flow is stably realized for sufficiently small temperature differences ΔT.

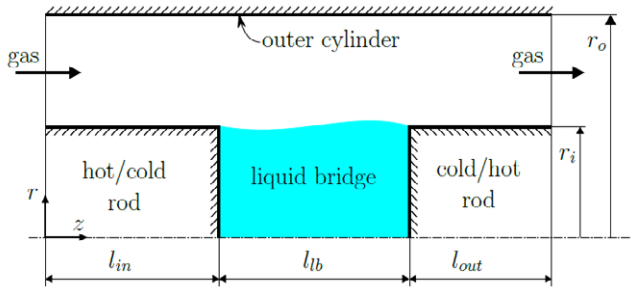

Figure 1: Computational domain: liquid and gaseous phase; dash-dotted line: axis of symmetry; radius of the rods: r_i, radius of the outer cylinder: r_o, length of the liquid bridge: l_{lb}, lengths of the rods at inlet and outlet, respectively: l_{in} and l_{out}.

In our approach, the stationary axisymmetric Navier-Stokes, continuity and energy equations under 0g are solved simultaneously for both, the liquid and the gas phase coupled by the free-surface boundary conditions. For gravity conditions, higher corrections to the Boussinesq equations must be included when taking into account flow-induced surface deformations (Simanovskii and Nepomnyashchy 1993, Kuhlmann 1999), of which our model is capable as well.
The equations governing the basic flow are discretized on a non-uniform deformable grid using a finite-volume method. The resulting system of nonlinear algebraic equations is solved by Newton-Raphson iteration. After the basic-flow solution has been obtained, its linear stability is investigated using a normal-mode ansatz in azimuthal direction.
Figure 2 illustrates the complexity of the linear stability boundary (adopted from Shevtsova et al., 2014). The critical thermocapillary Reynolds number is presented as function of the strength of the gas flow $(w_{in} l_{lb})$ for an indeformable cylindrical interface. As can be seen, the critical curve is made of many different segments of neutral curves belonging to different azimuthal wave numbers. This result for an indeformable interface can serve as reference for further, more refined calculations for a deformable liquid-gas interface und a wider set of paramaters. In particular, the pressure gradient in the gas phase can lead to large interfacial deformations for large gas flow rates.

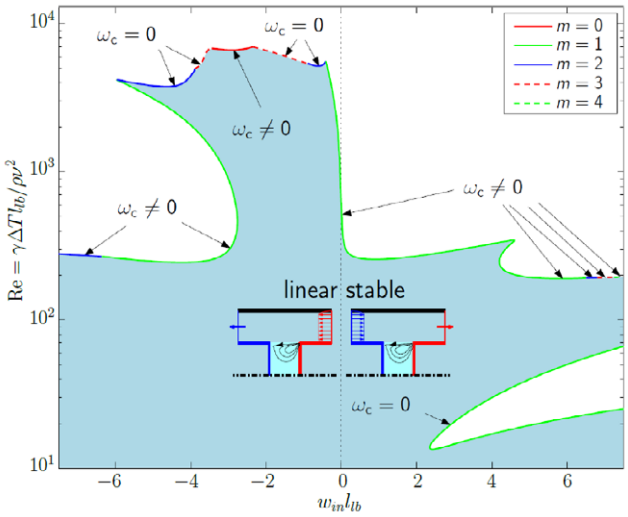

Figure 2: Critical thermocapillary Reynolds number as a function of the product between the mean inlet velocity $\boldsymbol{w_{in}}$ and the height of the liquid bridge $\boldsymbol{l_{lb}}$ for $\boldsymbol{\Gamma = 1}$. The shaded region is linearly stable. Critical azimuthal wavenumbers are denoted by $\boldsymbol{m}$. $\boldsymbol{\rho}$ and $\boldsymbol{\nu}$ are the density and the kinematic viscosity of the liquid, respectively. (reproduced from Shevtsova et al. 2014).

Perspectives

Since the problem involves many parameters, we consider a liquid bridge of 5cSt silicone oil ($\mathrm{Pr} = 68$) and focus on the effect on the critical Reynolds number of the flow rate in the ambient gas. Typically, the supercritical flow arises as a pair of three-dimensional hydrothermal waves in both the liquid and the gas phase.
Using the linear stability analysis, the critical thermocapillary Reynolds number is computed as a function of the mean gas velocity and temperature for different length-to-radius aspect ratios, $\Gamma = l_{lb}/r_i$, which are of interest for the planned space experiment JEREMI (Shevtsova et al. 2014). The corresponding neutral stability curves and other stability characteristics will be presented at the conference.

Acknowledgements

Support by FFG in the framework of ASAP14 through grant number 866027 is gratefully acknowledged.

References

H. C. Kuhlmann, Thermocapillary Convection in Models of Crystal Growth, *Springer Tracts in Modern Physics* 152 (1999)

Ch. Nienhüser, H. C: Kuhlmann, Stability of thermocapillary flows in non-cylindrical liquid bridges, *J. Fluid Mech.* 458 (2002) 35-73

V. Shevtsova, Y. Gaponenko, H. C. Kuhlmann, M. Lappa, M. Lukasser, S. Matsumoto, A. Mialdun, J. M. Montanero, K. Nishino, I. Ueno, The JEREMI-project on thermocapillary convection in liquid bridges. Part B: Overview on impact of co-axial gas flow, *Fluid Dyn. Mat. Proc.* 10 (2014) 197-240

V. Shevtsova, A. Mialdun, H. Kawamura, I. Ueno, K. Nishino, M. Lappa, Onset of Hydrothermal Instability in Liquid Bridge. Exp. Benchmark, *Fluid Dyn. Mater. Process.* 7 (2011) 1-27

V. Shevtsova, Y. A. Gaponenko, A. Nepomnyashchy, Thermocapillary flow regimes and instability caused by a gas stream along the interface, *J. Fluid Mech.* 714 (2013) 644-670

I. B. Simanovskii and A. A. Nepomnyashchy, Convective Instabilities in Systems with Interface, *Gordon and Breach* (1993)

V. Yasnou, Y. Gaponenko, A. Mialdun, V. Shevtsova, Influence of a coaxial gas flow on the evolution of oscillatory states in a liquid bridge, *Int. J. of Heat and Mass Transfer* 123 (2018) 747-759

Oral 022

Sensitivity of Marangoni convection in a high-Prandtl-number liquid bridge to the radiative heat transfer under reduced gravity

T. Yano[1], J. Arinobu[1], K. Nishino[1]

[1]Yokohama National University, Yokohama, Japan;
yano-taishi-gh@ynu.ac.jp, arinobu-junya-sy@ynu.jp, nishino-koichi-fy@ynu.ac.jp

Introduction

Marangoni convection is an interesting subject for heat transfer and fluid dynamics in microgravity (μg, hereafter) because the natural convection due to the density difference diminishes with reducing gravity and the Marangoni convection can play an important role. Two series of μg experiments on the temperature gradient-driven Marangoni convection in a high-Prandtl-number liquid bridge—the so-called *Marangoni Experiment in Space (MEIS)* and *Dynamic Surf*—have been performed on board the Japanese Experiment Module "Kibo" on the International Space Station (ISS) in 2008–2016 to clarify the instability mechanisms of Marangoni convection (Nishino et al. 2015, Yano et al. 2018). Recent investigations with respect to these μg experiments reported significant roles of radiative heat transfer in the Marangoni convection in μg (Melnikov et al. 2018, Shitomi et al. 2018). In this study, the special attention is focused on the following points: the contribution of radiation to the total heat transfer at the liquid bridge free surface, and the effect of radiation to the flow and temperature patterns. The present investigation provides important information for the upcoming μg experiment entitled "Boundary-condition susceptibility and controllability of instability mechanisms in thermocapillary convection," which will be performed on board the "Kibo" on the ISS in 2020.

Effect of radiative heat transfer

The effect of radiative heat transfer on the Marangoni convection in a liquid bridge is investigated through the numerical simulation in this study. A liquid bridge of silicone oil suspended between two concentric disks is placed in a cylindrical chamber filled with argon gas, and the flow and temperature fields both in the liquid phase and in the gaseous phase are analyzed using the commercial CFD software STAR CCM+ (Siemens PLM Software). The simulation domain and the grid are shown in Fig. 1, where the black and grey regions indicate the grid system for the liquid phase and that for the gaseous phase, respectively; the blue, red and green lines indicate the outlines of the cold disk, the hot disk and the chamber wall, respectively. Since the surface tension of silicone oil is a linear decreasing function of the temperature, the Marangoni flow is driven from the hot disk side towards the cold disk side along the liquid bridge free surface. The radiative heat transfer between enclosed multiple grey surfaces (i.e., the surfaces of cold disk, hot disks, chamber wall, and liquid bridge) is considered in the present numerical simulations. A steady and axisymmetric flow is targeted in this study; however the three-dimensional grid system is required in order to cope with the radiation in STAR CCM+.

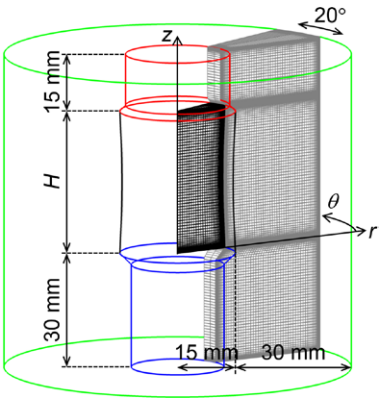

Figure 1: Computational domain and grid system for the numerical simulation.

Figure 2 shows the examples of (1) temperature fields and (2) flow fields obtained from the numerical simulations (a) including and (b) excluding radiative heat transfer. We note that the working liquid is a silicone oil with the kinematic viscosity of 10 cSt, whose Prandtl number at 25°C is Pr = 112; the disk diameter is D = 30.0 mm; the liquid bridge height is H = 37.5 mm; and the cold disk, hot disk, chamber side wall temperatures are T_C = 20.0°C, T_H = 29.1°C, and T_W = 23.0°C, respectively. The hot corner, where the Marangoni convection is mainly driven, is cooled by the radiation because the chamber side wall is cooler than the hot disk. This radiative cooling enhances the flow near the hot corner, and a single convection roll occupies entire flow field inside the liquid bridge. The flow and temperature fields obtained from the numerical simulation excluding radiation show apparently different patterns, and two convection rolls both rotating in the clockwise direction are appeared inside the

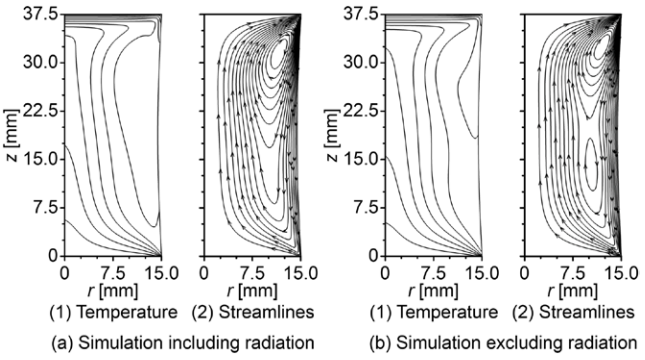

Figure 2: Results of numerical simulations (a) including radiation and (b) excluding radiation: (1) isothermal lines and (2) streamlines on the *r-z* cross section. The working liquid is 10 cSt silicone oil and the temperature conditions are T_C = 20.0°C, T_H = 29.1°C (ΔT = 9.1 K), and T_W = 23.0°C.

liquid bridge. It is confirmed that the results of present numerical simulation including radiative heat transfer show better agreement with the μg experimental data than those excluding radiative heat transfer, indicating the importance of radiative heat transfer under reduced gravity environment.

Conclusions

Marangoni convection in a liquid bridge is investigated numerically under reduced gravity condition. The flow and temperature fields in a liquid bridge and those in an ambient gas are simulated using the commercial CFD software STAR CCM+, and the effects of radiative heat transfer on the Marangoni convection are discussed. The present results indicate that the radiative heat loss enhances the Marangoni flow near the hot corner, and quite different temperature and flow patterns are recognized between the simulation results including radiation and those excluding radiation. The results presented in this study demonstrate the importance of radiative heat transfer to the Marangoni convection in μg.

Acknowledgements

The authors greatly appreciate all members of MEIS and Dynamic Surf for their contributions. The present study is financially supported by the Japan Society for the Promotion of Science (JSPS) KAKENHI (Grant-in-Aid for Scientific Research (C), No. 17K06190).

References

K. Nishino, T. Yano, H. Kawamura, S. Matsumoto, I. Ueno, M. K. Ermakov, Instability of Thermocapillary Convection in Long Liquid Bridges of High Prandtl Number Fluids in Microgravity, *J. Cryst. Growth* 420 (2015) 57-63.

T. Yano, K. Nishino, S. Matsumoto, I. Ueno, A. Komiya, Y. Kamotani, N. Imaishi, Report on Microgravity Experiments of Dynamic Surface Deformation Effects on Marangoni Instability in High-Prandtl-Number Liquid Bridges, *Microgravity Sci. Technol.* 30 (2018) 599-610.

D. E. Melnikov, V. Shevtsova, T. Yano, K. Nishino, Modeling of the Experiments on the Marangoni Convection in Liquid Bridges in Weightlessness for a Wide Range of Aspect Ratio, *Int. J. Heat Mass Transf.* 87 (2015) 119-127.

N. Shitomi, T. Yano, K. Nishino, Effect of Radiative Heat Transfer on Thermocapillary Convection in Long Liquid Bridges of High-Prandtl-Number Fluids in Microgravity, *Int. J. Heat Mass Transf.* 133 (2018) 405-415.

Oral 023

Coherent particle structures in high-Prandtl-number liquid bridges

I. Barmak[1], F. Romanò[1,2], H. C. Kuhlmann[1]

[1]Institute of Fluid Mechanics and Heat Transfer, TU Wien, 1060 Vienna, Austria,
[2] Department of Biomedical Engineering, University of Michigan, Ann Arbor, Michigan 48109-2099, USA
ilya.barmak@tuwien.ac.at, francesco.romano@tuwien.ac.at, hendrik.kuhlmann@tuwien.ac.at

Introduction

Accumulation of small rigid spherical particles is investigated numerically in high-Prandtl-number (Pr=68) thermocapillary liquid bridges under zero-gravity conditions. When the flow arises as a traveling hydrothermal wave, randomly distributed particles can cluster in particle accumulation structures (PAS). This phenomenon has been previously studied in liquid bridges with lower Prandtl numbers, e.g., Pr=4 in Hofmann et al. (2011) and Pr=28 in Romanò and Kuhlmann (2018). The observed PAS are classified as *finite-size coherent structures* (FSCS) and were found to be generic for a class of incompressible flows in which the repulsive particle-boundary interaction (PBI) can transfer the particles from the chaotic region to the regular region of Kolmogorov-Arnold-Moser (KAM) tori of the flow without particles (Romanò et al. 2019a).
In past investigations, different flow and particle parameters have been considered to study the structure and temporal evolution of PAS. Two PBI models have been used. Most investigators have employed the simple inelastic collision model of Hofmann and Kuhlmann (2011). An accurate modeling, however, requires a careful definition of the only parameter Δ of the collision model which, in general, depends on particle size, density and flow parameters (Romanò and Kuhlmann 2018). Recently, Romanò et al. (2019b) introduced another PBI model which is based on the asymptotic form of the lubrication drag acting on the particle in direction normal to the boundary. This latter model is physically more accurate than the collision model and does not require estimating Δ.

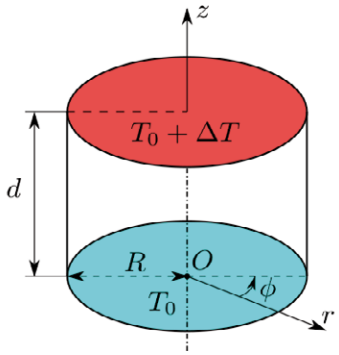

Figure 1: Sketch of a cylindrical liquid bridge.

Problem formulation

A cylindrical liquid bridge of an incompressible fluid with Pr=68 is considered under zero-gravity conditions. The liquid bridge has length d and radius R and it is held between two coaxial rods with temperatures $T_{cold}=T_0$ and $T_{hot}=T_0+\Delta T$ (Fig. 1). The fluid motion is driven by thermocapillary stresses caused by the dependence of the surface tension $\sigma(T)$ on the temperature (thermocapillary effect). The governing Navier-Stokes equations are solved subject to no-slip/no-penetration/constant-temperature boundary conditions on the rods and imposing thermocapillary stresses and adiabatic conditions on the free surface (Romanò and Kuhlmann 2018). Viscous stresses, flow-induced surface deformations, and heat exchange with the ambient gas are neglected. The dimensionless parameters defining the fluid motion are the thermocapillary Reynolds number $\mathrm{Re} = \gamma\Delta T d/\rho_f \nu^2$ (γ: surface-tension coefficient, ρ_f: density, ν: kinematic viscosity), the aspect ratio $\Gamma=d/R$ of the liquid bridge, and Pr. For supercritical Reynolds numbers $\mathrm{Re}>\mathrm{Re}_C=O(300)$ (Shevtsova et al. 2011) the basic axisymmetric flow becomes unstable and the flow $\boldsymbol{u}(\boldsymbol{x}, t)$ arises as a three-dimensional hydrothermal wave (HTW) traveling azimuthally.
In the frame of reference rotating with the same angular velocity $\boldsymbol{\Omega}=\Omega\boldsymbol{e}_z$ as the HTW, the velocity field is steady $\boldsymbol{U}(\boldsymbol{x})=\boldsymbol{u}(\boldsymbol{x}, t_0) - r\Omega\boldsymbol{e}_\varphi$, where $\boldsymbol{u}(\boldsymbol{x}, t_0)$ can be any snapshot of $\boldsymbol{u}$ at any time t_0. In one-way approximation the motion of a small spherical particle (density ρ_p, radius a_p) is approximated by the simplified Maxey-Riley (SMR) equation given by Babiano et al. (2000). The particle's motion is studied in the co-rotating frame of reference, using velocity-matched initial conditions. Additional dimensionless parameters, defining the particle motion, are the particle-to-fluid density ratio $\rho=\rho_p/\rho_f$, and the Stokes number $\mathrm{St}=2\rho a^2/9$, where $a=a_p/d$ is the dimensionless radius of the particle. When the particle is transported close to the boundary the SMR equation breaks down, because PBI forces are not included in the SMR. Therefore, additional wall-normal drag forces according to the Brenner's (1961) solutions for a plane wall and a free surface (truncation order $N=3$) are introduced within a uniform boundary layer of thickness $\Delta_B=3a$ (cut-off distance) on all boundaries.

Results and Discussion

The flow for Pr=68 is computed numerically using a pressure based solver in OpenFOAM, extended to include thermocapillary stresses on the free surface. The simulations are carried out using a block-structured mesh made of ≈21.5 million grid points. The high grid resolution enables identifying various sets of Kolmogorov-Arnold-Moser (KAM) tori in the flow $\boldsymbol{U}(\boldsymbol{x})$.
The topology of the regular streamlines is quite intricate (Kuhlmann and Romanò 2018). As an example, a Poincarè section for $\Gamma=1$ and $\mathrm{Re}=1500$ is shown in Fig. 2 on the plane $\varphi'=\varphi_{max}+\pi/4$, where φ_{max} maximizes $T(r=1,\varphi,z=0.5)$. For these parameters a fundamental wave number of the HTW is $m=1$ and its angular velocity is $\Omega=12.29$ (in the units of ν/d^2).

Two major sets of KAM tori exist. One set is locally close to the hot corner at $(r,z)=(1,1)$ and it is extremely squeezed near the free surface.

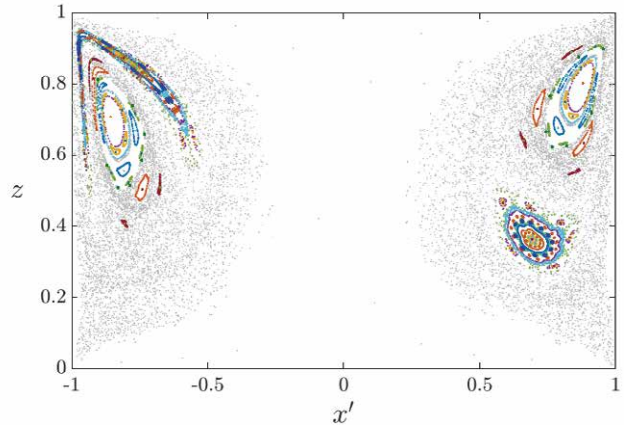

Figure 2: Poincarè section on $\varphi'=\varphi_{max}+\pi/4$, where φ_{max} maximizes $T(r=1,\varphi,z=0.5)$ for Pr=68, Γ=1, Re=1500, and Bi=0. Poincarè points of chaotic (regular) streamlines are indicated in gray (color). For details, cf. text.

The flow topology, in particular the KAM tori, determines PAS for density-matched particles: After $t=340$ (units of d^2/ν) thousand initially randomly distributed particles with $a=0.02$ and $\rho=1$ have clustered on a periodic orbit near a closed streamline of the flow (Fig. 3a). This result, obtained using Brenner's (1961) drag formulae, can also be reproduced using the simpler inelastic collision model with $\Delta=a$. However, the particle dynamics near the boundaries is different and the inelastic collision model can be erroneous in predicting the time evolution of PAS.

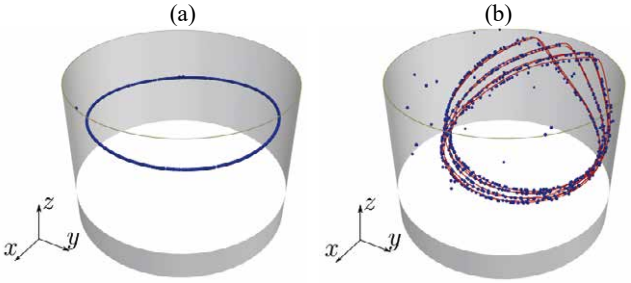

Figure 3: (a) PAS for Γ=1, m=1, Re=1500 and 1000 density-matched particles (ρ=1) with a=0.02 using Brenner's (1961) drag. (b) Closed streamline (red) and PAS (blue) for Γ=1, m=1, Re=2250 and 1000 density-matched particles (ρ=1) with a=0.004 using the inelastic collision model with $\Delta=2a$.

For higher Reynolds numbers the KAM structures are even slenderer near the free surface (Fig. 4). An example for a periodic PAS at Re=2250 in a flow with m=1 is shown in Fig. 3b. In this case, particles cluster near a closed streamline which makes seven revolutions about the axis.

Several extension of this work would be of interest. In addition to the PBI, another effect might contribute to particle clustering. It is based on the amplification of a minute velocity mismatch of density-matched particles by very high strain rates (Babiano et al. 2000). For Pr=68, the strain near the hot corner is very large and has the potential to contribute to particle clustering. Furthermore, current models describe PAS as a single-particle phenomenon equivalent of the attraction of individual non-interacting particles to a periodic attractor. An unsolved problem concerns the late stage of PAS. When the particle volume fraction becomes large locally, particle-particle interactions and the effect of a locally dense particle cluster on the flow may no longer be neglected. It would be interesting to address these collective effects in future investigations.

Acknowledgements

This work has been supported by ESA through contract no. 4000121111/17/NL/PG/pt.

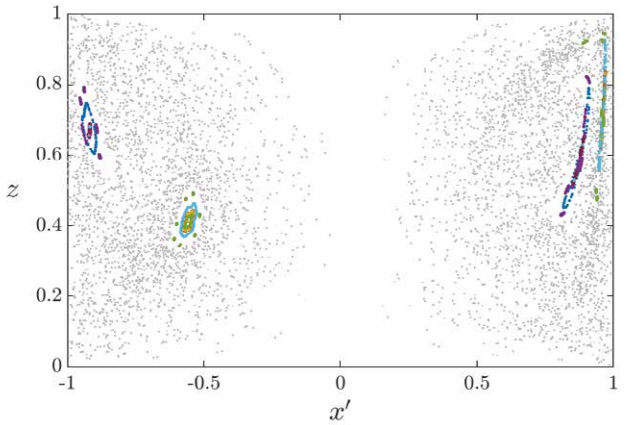

Figure 4: Poincarè section for Pr=68, Γ=1, m=1, Re=2250, and Bi=0. Poincarè points of chaotic (regular) streamlines are indicated in gray (color). The cut is taken at an angle φ' defined in the same way as for Fig. 2.

References

A. Babiano, J. H. E. Cartwright, O. Piro, and A. Provenzale, Dynamics of a small neutrally buoyant sphere in a fluid and targeting in Hamiltonian systems, *Phys. Rev. Lett.* 84 (2000) 5764-5767.

H. Brenner, The slow motion of a sphere through a viscous fluid towards a plane surface, *Chem. Eng. Sci.* 16 (1961) 242-251.

E. Hofmann and H. C. Kuhlmann, Particle accumulation on periodic orbits by repeated free surface collisions, *Phys. Fluids* 23 (2011) 072106.

H. C. Kuhlmann and F. Romanò, Midterm report: Modelling support to ESA-JAXA JEREMI project on ISS., Tech. rep., ESA, 2018.

F. Romanò and H. C. Kuhlmann, Finite-size Lagrangian coherent structures in thermocapillary liquid bridges, *Phys. Rev. Fluids* 3 (2018) 094302.

F. Romanò, H. Wu, and H. C. Kuhlmann, A generic mechanism for finite-size coherent particle structures, *Int. J. Multiphase Flow* 111 (2019a) 42-52.

F. Romanò, P. Kunchi Kannan, and H. C. Kuhlmann, Finite-size Lagrangian coherent structures in a two-sided lid-driven cavity, *Phys. Rev. Fluids* 3 (2019b) 094302.

V. Shevtsova, A. Mialdun, H. Kawamura, I. Ueno, K. Nishino, and M. Lappa, Onset of hydrothermal instability in liquid bridge. Experimental benchmark, Fluid Dyn. Mater. Process. 7 (2011) 1-27.

Oral 025

Measurement of the controlled transition between contact line and microlayer evaporation regimes

K. Schweikert[1], A. Sielaff[1], P. Stephan[1]

[1]Technische Universität Darmstadt, Institute for Technical Thermodynamics, Darmstadt, Germany
schweikert@ttd.tu-darmstadt.de, sielaff@ttd.tu-darmstadt.de, pstephan@ttd.tu-darmstadt.de

Introduction

The study of growing vapor bubbles has revealed that a thin liquid film can form underneath the bubble, leading to large heat flux in this area (Cooper and Lloyd 1969). However, this so called microlayer does not always form and evaporation is then merely concentrated at the contact line. Under what conditions which of these evaporation mechanisms can be expected is therefore topic of large interest within the boiling community. So far a dependency on wall superheat (Kim 2009), system pressure (Fath et al. 1978), contact angle (Urbano et al. 2018) and dewetting velocity (Fischer et al. 2015) on microlayer formation have been suggested, but a controlled change between both evaporation regimes has not been measured.
When a plate is withdrawn from a pool of liquid, films of similar thickness can remain on the solid and can be described by the famous Landau-Levich law (Landau and Levich 1942). When evaporation is introduced to the problem, three regimes can be distinguished and are shown in figure 1.

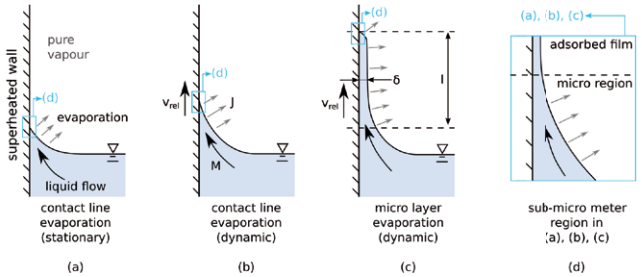

Figure 1: Evaporation at a superheated wall: (a) stationary contact line evaporation, (b) contact line evaporation in dewetting situation, (c) microlayer evaporation in dewetting situation, (d) sub-micrometre region near the 3-phase-contact line.

Since the highest evaporation rate is found near the three phase contact line, the regime illustrated in figure 1a and 1b are referred to as contact line evaporation. In figure 1b wall movement is introduced, changing the apparent contact angle to a dynamic one. If a critical dewetting speed is surpassed, a thin liquid film of finite length l and thickness δ is left on the plate. Since l and δ are comparable to microlayers found underneath growing vapor bubbles, the question arises, if these films are also comparable to those of microlayers underneath vapor bubbles in other respects and if similar laws can be found for their description.

Experimental Techniques

The so called withdrawing plate method, often used study Landau-Levich films in a very controlled manner, is altered to allow wall temperature measurements by infrared thermography. The use of a thin film heater then enables the study of non-isothermal Landau-Levich films. The experimental setup is shown in figure 2.

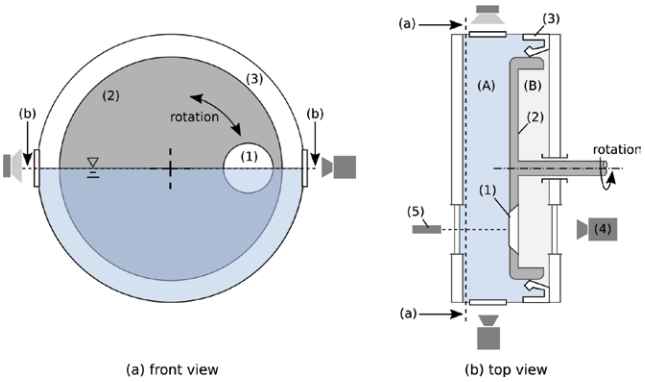

Figure 2: Experimental Setup with Sample (1), disc (2), shaft seal (3), IR camera (4) and interferometric probe (5).

An infrared transparent sample (1) carrying a thin metallic heating coating is mounted eccentrically to a disc (2). Rotation of the disc therefore translates to a vertical motion of the sample. A shaft seal (3) is used to seal both sides of the disc: Side (A) is filled exactly half with liquid, while side (B) is only filled with its gas phase. An infrared camera (4) can then be used to measure the temperature field close to the wetted area of the sample. The film's thickness is measured by an interferometric probe (5).
To overcome the challenge of a moving wall in combination with a stationary infrared sensor, the sample's position is analysed at every frame, which is then calibrated accordingly. From these wall temperature measurements wall superheat, the length of the microlayer and heat flux profiles are calculated. Median steady state values of length and thickness of the microlayer ($\tilde{l}_s$ and $\tilde{\delta}$, respectively) are evaluated for different constant wall superheat and dewetting velocity.

Results

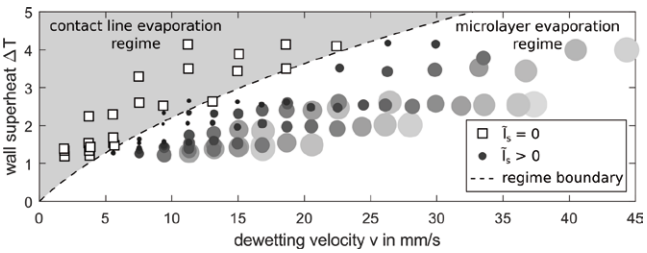

Figure 3: Boundary between both regimes. The size of the square markers represent the microlayer length.

For constant wall superheat ΔT, the thickness of the microlayer increases with increasing dewetting velocity v. A

trend $\tilde{\delta} \sim v^{2/3}$, similar to the Landau-Levich Law, is found. The microlayer length shows a scaling $\tilde{l}_s \sim v^{5/3}$. Both length and thickness of the microlayer decrease with increasing wall superheat. For low ratios $\Delta T/v$ only contact line evaporation is found. Microlayer evaporation is only observed, when a critical dewetting velocity is surpassed for a given wall superheat. A regime boundary is deduced from this data, which is shown in figure 3. In the microlayer regime, the length of the microlayer increases with the distance to the regime boundary, which is indicated by the size of the round markers. A square marker is used for measurements where no microlayer evaporation is observed.
The local heat flux profiles calculated from the temperature measurements show good agreement with those measured underneath growing vapor bubbles.

Conclusions

We can conclude that contact line and microlayer evaporation exist in two different evaporation regimes, which are separated by a critical combination of wall superheat and dewetting velocity. The analysis of the local heat flux profiles shows that the observed microlayers are comparable to those observed underneath growing vapor bubbles. It is therefore likely, that the deduced laws for microlayer length and thickness also hold when applied to microlayers underneath growing vapor bubbles.

Acknowledgements

We kindly acknowledge the financial support by the German Research Foundation (DFG) within the Collaborative Research Centre 1194 "Interaction of Transport and Wetting Processes", Project A01.

References

M. G. Cooper, A. Lloyd, The microlayer in nucleate pool boiling*, Int. J. of Heat and Mass Transfer* 12 (1969) 895-913.

H. S. Fath, R. L. Judd, Influence of system pressure on microlayer evaporation heat transfer, *J. of Heat Transfer* 100 (1978)

J. Kim, Review of nucleate pool boiling bubble heat transfer mechanisms, *Int. J. of Multiphase Flow* 35 (2009)

A. Urbano, S. Tanguy, G. Huber, C. Colin, Direct numerical simulation of nucleate boiling in micro-layer regime*, Int. J. of Heat and Mass Transfer* 123 (2018)

S. Fischer, T. Gambaryan-Roisman, P. Stephan, On the development of a thin evaporating liquid _lm at a receding liquid/vapour-interface*, Int. J. of Heat and Mass Transfer* 88 (2015)

L. D. Landau, B. G. Levich, Dragging of a liquid by a moving plate, *Acta Physicochim* 17 (1942)

Oral 026

Phototropism: Lessons Learned from the Seedling Growth (SG) Spaceflight Project on the International Space Station

John Z. Kiss[1], Joshua P. Vandenbrink[1,2], Richard E. Edelmann[3], F. Javier Medina[4]

[1]Department of Biology, University of North Carolina—Greensboro, Greensboro, NC 27402 USA; [2]School of Biological Sciences, Louisiana Tech University, Ruston, LA 71272 USA; [3]Dept. Biology, Miami University, Oxford OH 45056 USA; [4]Centro de Investigaciones Biológicas (CSIC), Madrid, E28040, Spain
jzkiss@uncg.edu, jpvdb@latech.edu, edelmare@muohio.edu, fjmedina@cib.csic.es

Introduction

Plants on Earth have evolved under the influence of a constant acceleration force of 9.81 $m \cdot s^{-2}$ (or 1-*g*). This persistent and ubiquitous physical force serves as an important input to shape plant growth, development, and morphology at all levels, from the molecular to the whole plant. Removing the gravitational acceleration in the conditions of free fall (or microgravity) that is achieved in orbiting spacecraft can have a profound effect on plant morphology and physiology. Studying plants in the microgravity environment also can provide novel insights into basic mechanisms of growth and development. Thus, in this project, we were able to investigate phototropism in plants grown in microgravity (without the "complications" of gravity) on the International Space Station (ISS) to explore the mechanisms of both blue-light and red-light-induced phototropism.

The Seedling Growth (SG) series of plant biology experiments were part of an agreement between NASA and ESA. The major goals were: (1) to determine how gravity and light responses influence each other in plants, (2) to better understand the cellular signaling and response mechanisms of phototropism and of light stimulation, and (3) to study the factors affecting the proliferation and growth of meristematic cells to analyze in how auxin transport and perception act in the regulation of these cellular functions (Valbuena et al. 2018).

In SG, we utilized the European Modular Cultivation System (EMCS), which arguably has been one of the most successful life science research facilities on the ISS. Three types of data were obtained from the SG experiments: image downlinks of plant seedlings, seedlings frozen on-orbit, and seedlings fixed in aldehydes. Downlinked images were used to provide data on germination, growth, development, and tropistic curvature (Fig. 1). Frozen seedlings were used for gene profiling and RNAseq studies (Correll et al. 2013), and seedlings fixed in aldehydes were used for high-resolution electron microscopic analyses.

While plant growth and development in microgravity environments has been well characterized, considerably less is known about plant growth and development in fractional or reduced gravity environments (less than the nominal 1-*g*; Kiss 2014). The EMCS contains a centrifuge which allows for the creation of gravity vectors to better characterize the interplay between gravitropism and phototropism.

Our previous space experiments examined the phototropic response to red and blue light in microgravity, fractional gravity, and 1-*g* environments (Kiss et al. 2012). Understanding how plants grow and develop in fractional or redcued gravity environments is an important step in successful habitation of the Moon or Mars. In this study, we utilize microgravity as well as a continuum of fractional gravity to better characterize the phototropic responses to red and blue light (Vandenbrink et al. 2016).

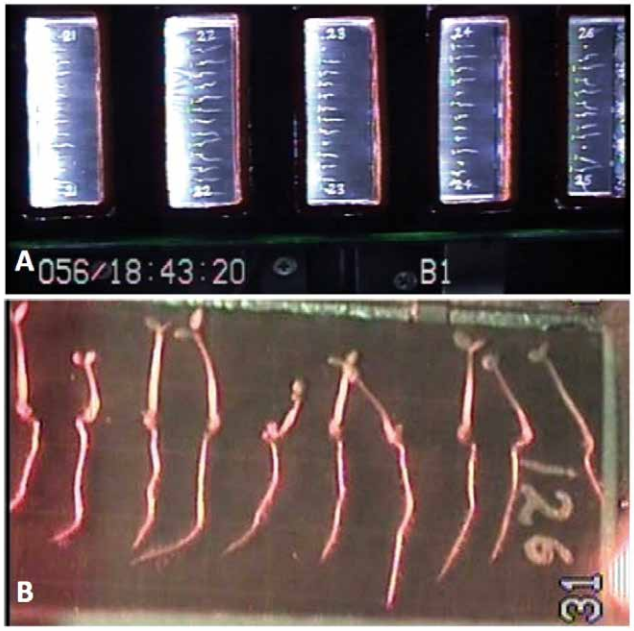

Figure 1. Images of seedlings of *Arabidopsis thaliana* growing on the International Space Station. A) image of 5 seedling cassettes positioned within EMCS. B) Higher magnification view of seedlings growing within a seed cassette.

Results

SG-1 was launched in March 2013 on SpaceX-2 and returned May 2014 on SpaceX-3. **SG-2** was launched in September 2014 on SpaceX-4 and was returned on SpaceX-5 in February 2015. **SG-3** launched on SpaceX-11 in June 2017 and returned on the same mission. In this presention, we will focus on the studies of phototropic curvature in youg seedlings of *Arabidopsis thaliana* (Fig. 1).

A novel positive phototropic response to red light was observed in hypocotyls of seedlings that developed in

microgravity (Fig. 2). This response was not apparent in seedlings grown on Earth or in the 1-*g* control during the spaceflight. Although flowering plants are generally thought to lack red-light phototropism, our data suggest that at least some flowering plants may have retained a red-light sensory system for phototropism. Thus, this discovery may have important implications for understanding the evolution of light sensory systems.

While plant growth and development in microgravity environments have been well characterized since the dawn of the space age, considerably less is known about plant growth in fractional or reduced gravity environments (less than the nominal 1-*g* on Earth). Thus, we examined the phototropic response to red and blue light in microgravity, 0.1-**g**, 0.3-*g*, and 1-*g* conditions, providing insight on how plant development may be affected on the Moon or Mars. Understanding how plants grow and develop in fractional gravity environment (Fig. 2) is an important step in successful habitation of other planets. Furthermore, fractional gravity studies are helpful for the determination of thresholds of gravity sensing.

Time-course studies of positive phototropic curvature in hypocotyls of Arabidopsis seedlings in response to red light were performed during our space-flight experiments (Fig. 2). White circles indicate µg, grey circles indicate 0.1 *g*, hatched circles indicate 0.3 *g* and black circles indicate 1 *g*. The plots represent the mean, and different letters indicate significant differences among the first-order regression plots. Note the magnitude of the positive response at µ*g* and 0.1 *g*. The response at 0.3 g was not significantly different from the value of the 1-*g* control, and there was attenuation of red-light phototropism at 0.3 *g* and 1-*g*.

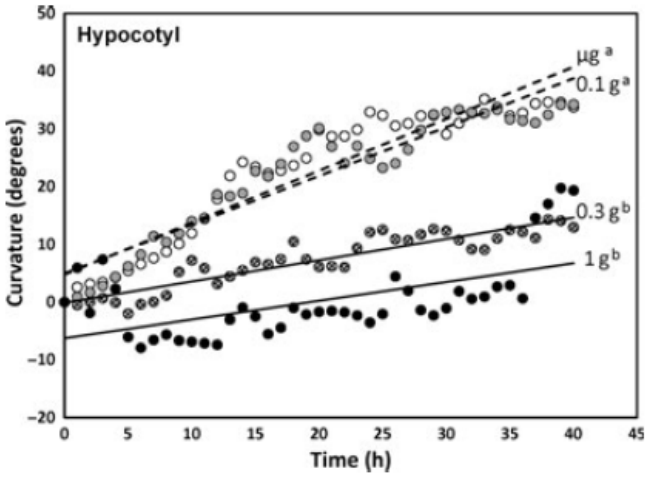

Figure 2. Time-course studies of positive phototropic curvature hypocotyls of seedlings in response to red light during the spaceflight experiment.

Conclusions

A novel positive blue-light phototropic response of roots was observed during conditions of microgravity, and this response was attenuated at 0.1 g (not shown). In addition, a red-light pretreatment of plants enhanced the magnitude of positive phototropic curvature of roots in response to blue illumination. Additionally, a positive phototropic response of roots was observed when exposed to red light, and a decrease in response was gradual and correlated with the increase in gravity. The positive red-light phototropic curvature of hypocotyls when exposed to red light was also confirmed (Fig. 2). Both red-light and blue-light phototropic responses were also shown to be a product of directional light intensity.

To our knowledge, the SG series of experiments provided the first characterization of novel phototropic responses of plants in free fall conditions of low Earth orbit. In addition, SG characterized the relationship between these phototropic responses in fractional or reduced gravity, thus paving the way for the use of plants in bioregenerative life support systems on missions to the Moon and Mars.

Acknowledgements

Funding provided by grant 80NSSC17K0546 from the National Aeronautics and Space Administration (NASA) to John Z. Kiss.

References

Correll M.J., T.P. Pyle, K.D.L. Millar, Y. Sun, J. Yao, R.E. Edelmann, J.Z. Kiss. 2013. Transcriptome analyses of *Arabidopsis thaliana* seedlings grown in space: implications for gravity-responsive genes. Planta 238: 519-533.

Kiss J.Z. 2014. Plant biology in reduced gravity on the Moon and Mars. Plant Biology 16(S1): 12–17.

Kiss J.Z., K.D.L. Millar, R.E. Edelmann. 2012. Phototropism of *Arabidopsis thaliana* in microgravity and fractional gravity on the International Space Station. Planta 236:635–645.

Valbuena M.A., A. Manzano, J.P. Vandenbrink, V. Pereda-Loth, E. Carnero Diaz, R.E. Edelmann, J.Z. Kiss, R. Herranz, F.J. Medina. 2018. The combined effects of real or simulated microgravity and red light photoactivation on plant root meristematic cells. Planta 248: 691–704.

Vandenbrink J.P., R. Herranz, F.J. Medina, R.E. Edelmann, J.Z. Kiss. 2016. A novel blue-light phototropic response is revealed in roots of *Arabidopsis thaliana* in microgravity. Planta 244:1201–1215

Oral 027

Phase Separation in Porous Media Integrated Capillary Channels

Kamal Bisht[1], Michael Dreyer[1]

[1]Department of Fluid Mechanics, Faculty of Production Engineering, ZARM, University of Bremen, Bremen, Germany
kamal.bisht@zarm.uni-bremen.de, michael.dreyer@zarm.uni-bremen.de

Introduction

Phase separation in space is critical for gas free propellant supply, life support systems and refueling of spacecrafts. Surface tension tanks use capillary channels to transport and position the propellant. In the absence of gravity, the stability of the liquid-gas interface depends on the surface tension force. High liquid flow rates, sudden accelerations, and vibrational disturbances can cause the free surface of the liquid to collapse, which results in the ingestion of gas. The presence of the gas degrades the quality of the propellant. Therefore, to manage the gas free propellant supply, it is essential to employ phase separation techniques. In this project work, a capillary channel with an integrated metallic porous screen is used to perform the liquid-gas phase separation.

Theory

A saturated porous screen permits liquid to pass through but acts as a barrier to the gas breakthrough until the differential pressure across the screen exceeds the bubble point pressure. This feature is governed by the porous screen properties such as pore diameter, porosity, wettability, and type of the liquid.

$$\Delta P_0 = \frac{4\sigma\, cos\theta}{D_P} \tag{1}$$

$$\Delta P_{BP} = C_0 \Delta P_0 \tag{2}$$

where σ denotes the surface tension, θ the contact angle, D_P the pore diameter, C_0 the constant which depends on the pore geometry and ΔP_{BP} the bubble point pressure.

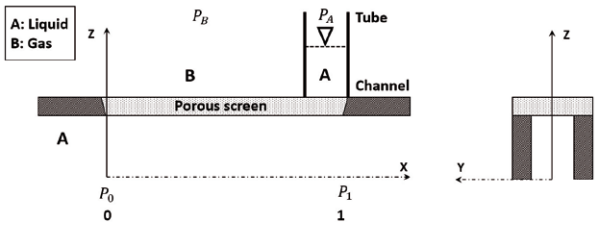

Figure 1: Rectangular groove channel with integrated porous screen

The test section consists of a rectangular acrylic glass channel covered with a DTW 200×1400 porous screen through which component A (liquid) flows (Figure 1). In the capillary tube on the outer side of the porous medium, component A exists. The pressure above the porous medium is P_B in the gas phase, and P_A in the liquid phase. The pressure at the inlet of the channel is P_0. At zero mass flow rate, $P_0 = P_A = P_B$, the system is in equilibrium and no mass transport takes place. If the mass flow rate is increased in positive x-direction, the pressure decreases along the length of the channel and component A enters into the flow channel from the capillary tube. The test liqud used for the experiment is 3M Novec™ Engineering Fluid HFE-7500.

The rate of liquid withdrawal into the channel from the surrounding depends on the cross-flow resistance of the porous medium, the difference in pressure between the channel and the ambient, and on the liquid flow rate in the channel. The cross flow resistance of the screen is predicted as

$$\Delta P = \alpha\left(\frac{\tau B \mu S^2}{\phi^2}\right)u_s + \beta\left(\frac{\tau \rho B}{\phi^2 D_P}\right)u_s^2$$

Where τ denotes the tortuosity of the wires, B the screen thickness, μ the dynamic viscosity, S the surface area to volume ratio, ρ the density, ϕ the porosity, u_s the superficial velocity, α and β the empirical constant. Based on numerical predictions and analytical calculations, an experimental facility was developed to test the concept.

Results

Microgravity and ground experiments performed during drop tower tests and the 33rd DLR parabolic flight campaign successfully validated the principle of the phase separation and provided quantitative data.

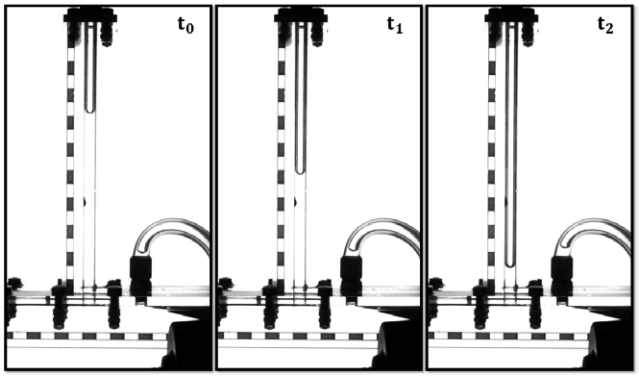

Figure 2: During the microgravity phase, liquid from the surrounding tube is extracted into the channel. No bubble breakthrough occurs across the porous screen.

With the aid of a low-pressure tank and fluid pump, different system pressure and flow rate are implemented to test the device. The images are captured at 41 frames per second by two CMOS camera. At t_0 (Figure 2) during the microgravity phase, the top end of the capillary tube is exposed to the ambient. Due to the differential pressure across the screen, the liquid flows into the channel. The saturated part of the screen prevents the gas breakthrough.

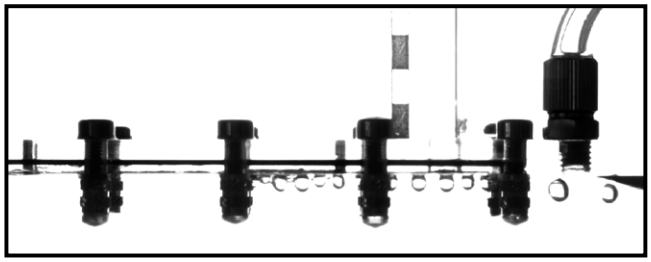

Figure 3: Gas bubbles formation under the screen when differential pressure exceeds the bubble point pressure

However, if the differential pressure exceeds to the bubble point pressure of the screen, the gas breakthrough occurs and the bubbles are ingested into the channel (Figure 3). The obtained experimental and numerical simulation results will be presented in the talk.

Acknowledgements

We acknowledge the funding of the project under the grant number 50WM1745 by the German Aerospace Center (DLR e.V.).

References

1) M. Conrath and M. E. Dreyer, Gas breakthrough at a porous screen, Int. J. Multiphas. Flow, 42 (2012), pp. 29–41

2) P. J. Canfield, P. M. Bronowicki, Y. Chen, L. Kiewidt, A. Grah, J. Klatte, R. Jenson, W. Blackmore, M. M. Weislogel and M. E. Dreyer, The Capillary channel flow experiments on the International Space Station: Experiment set-up and first results, Exp. Fluids, 54 (2013), pp. 1–14.

3) P. Bronowicki, P. Canfield, A. Grah and M. E. Dreyer, Free surfaces in open capillary channels - Parallel plates, Phys. Fluids, 27 (2015), pp. 1–21

Oral 029

Evolution of Marangoni-driven instabilities with temperaute variation of countercurrent gas flow

Y. Gaponenko, V. Yasnou, A. Mialdun, V. Shevtsova

Microgravity Research Center, Université Libre de Bruxelles,Belgium;
ygaponen@ulb.ac.be, vyasnou@ulb.ac.be, amialdun@ ulbac.be, vshev@ulb.ac.be

Introduction

Interfacial flows play an important role in many natural and technological processes. The surface tension gradient due to temperature variation along the free surface drives thermocapillary flow from hot to cold rod near the free surface and in the opposite direction at the axis. Here we consider flows in a cylindrical liquid bridge, which is a drop of liquid held by the action of the surface tension force between two solid rods, and the top rod is hotter than the bottom one. A liquid bridge can be regarded as the simplest half-zone model of the floating zone technique of crystal growth. This connection endows the study of liquid bridges with great interest not only in the field of materials engineering but also in fluid mechanics.

The topic of our study is the influence of gas flow temperature on the dynamics of the liquid bridge induced by interfacial phenomena via thermocapillary (Marangoni). The aim of this investigation is concerned to the space experiment JEREMI (Japanese European Space Research Experiment on Marangoni Instabilities) which is devoted to the study of the threshold of hydrothermal instabilities in two-phase systems in cylindrical geometry. This experiment is planned to be performed in the Japanese module on the ISS using the dedicated FPEF (Fluid Physics Experiment Facility).

We present results of computational and experimental study of a two-phase flow in a liquid bridge that develops under the action of buoyant and Marangoni forces in the presence of weak evaporation and a gas stream parallel to the interface.

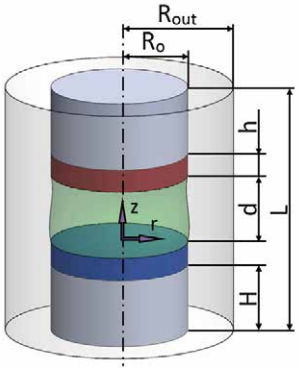

Figure 1: Geometry of the problem.

Problem formulation

The schematic of the system, relevant to the experiment and numerical simulations, is shown in Fig. 1. The system consists of two co-axial cylinders. The outer cylinder is a glass tube of the radius R_{out} = 5.0 mm. The inner cylinder consists of two solid rods of the radius R_0 = 3.0 mm and a liquid bridge between them of the height d = 3 mm, which is kept in its position by the surface tension force. The thickness of the heating/cooling parts of the rods is h = 1 mm. The solid rods are rather long; the distance from the gas inlet to the cold disk is H = 25 mm. It provides a fully developed flow in the gas before reaching the liquid zone. The test fluids were nitrogen (gas) and n-decane (liquid).

In order to study hydrothermal instability in the liquid bridge under action of a parallel gas flow, we have developed a new instrument. In general it consists of different systems: temperature control of heat/cold disks and gas flow, intensity control of gas flow and regulation of liquid bridge volume. The more detailed description of experimental equipment one may found in paper by Yasnou et al. 2018.

Results

Our previous results (Shevtsova et al. 2019) have demonstrated the influence of shear-stress impact of a gas flow blowing along the interface, but here we examine the influence of gas temperature on the instability in the liquid bridge via heat transfer. Depending on the gas temperature of flowing gas we observe a wide variety of flow patterns which correspond to different modes of an oscillatory flow. In Fig. 2, the temperature fields are shown for the case of the oscillatory flow when the temperature difference between the hot and cold rods is the same (ΔT = 7° C) but the temperature of the gas flow is different. An intensive numerical study has been performed in a large range of gas flow temperatures and temperature differences. For each flow regime the heat fluxes through the surface as well as the flow pattern have been analyzed.

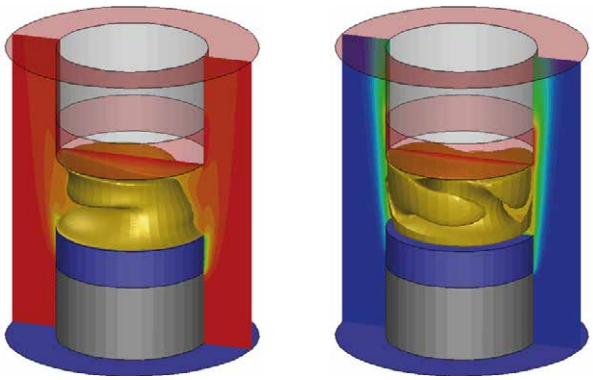

Figure 2: Left: temperature field for cold blowing gas (T_{gas} = 15°C); Right: temperature field for hot blowing gas (T_{gas} = 28° C).

Conclusions

We have performed an extensive study on the effects of the gas temperature of ambient flow on thermocapillary convection in liquid bridge. The sufficiently strong

dependence of liquid oscillatory dynamics on gas flow temperature was noticed in numerical modelling and experiments. The existence of stability gap area, where oscillations in liquid bridge disappear, in certain region of controlled parameters was found.

Acknowledgements

This work is supported by the PRODEX programme of the Belgian Federal Science Policy Office, ESA.

References

V. Yasnou, Y. Gaponenko, A. Mialdun, V. Shevtsova: Influence of a coaxial gas flow on the evolution of oscillatory states in a liquid bridge, *In.l J. of Heat and Mass transfer* 123 (2018) 747–759.

V. Shevtsova, Y. Gaponenko, A. Nepomnyashchy: Thermocapillary flow regimes and instability caused by a gas stream along the interface, *J. Fluid Mech.* 714 (2013) 644–670.

Oral 030

Interplay of diffusion and thermodiffusion fluxes during transport of a binary mixture from free liquid to a porous medium

V. Shevtsova, V. Yasnou, D. Melnikov, A. Mialdun

MRC, CP-165/62, Université libre de Bruxelles (ULB), 50, Ave. F.D. Roosevelt, B-1050 Brussels, Belgium
vshev@ulb.ac.be, vyasnou@ulb.ac.be, Denis.Melnikov@ulb.ac.be, amialdun@ulb.ac.be

Introduction

The heat and mass transfer of liquid mixtures through composite systems, consisting of liquid layers adjacent to porous media, have received significant attention due to environmental (ground-water flow, CO2 leakage through abandoned wells) and industrial applications, especially, in petroleum industry in reservoirs with multiple distinct phases in fractured porous media. Thermodiffusion (also thermal diffusion or Soret) is present in most reservoirs on the geological time scale, since there is a vertical geothermal gradient of about 0.03 K/m.

In laboratory experiments any motion provokes mixing of species and decreases the separation in the direction of the imposed ∇T. To avoid the perturbing effect of gravity, measurements of the Soret coefficient have been performed in microgravity environment on the International Space Station (ISS) to validate ground techniques (Shevtsova et al, 2015; Bou-Ali et al, 2015; Mialdun et al. (2018); Triller et al, 2018). In order to suppress, or to drastically reduce unwanted convection in laboratory experiments, the use of a porous medium was previosulsy tested. The experiments were conducted either in the cell completely filled with porous medium (Platten&Costeseque, 2004) or in a cylinder the largest part of which was filled with a porous medium (Giraudet et al., 2013). However, the validation of either setup showed that the relaxation time to reach the steady state is too long, counted by months for liquids.

Experiment

Knowing the problems of the previous experiments we have created a setup with a totally new design at which the Soret cell consists of two large volumes of free liquid separated by a thin layer of a porous medium. The photo of the setup is shown in Fig.1. The pure ethanol was used for examination of thermal field, and the THN-nC12 binary mixture with mass fraction 50% was used in the Soret experiments. The porosity of the used medium is 0.42.

Advanced optical techniques were used to detect the variations of the refractive index in a transparent liquid in order to describe correctly the thermal and concentration fields. This work provides continuous monitoring of the mass transfer in free liquids and a porous medium during five days, i.e., until the steady state.

The first step was focused on the reconstruction of the accurate temperature distribution in the cell with a layer of a porous medium. A single liquid, ethanol, was used for the purpose.The thermal field in the vicinity of the porous medium is affected by the imbalance of thermal conductivities of free liquid and a saturated porous medium. The spatial distribution of the thermal gradient over the

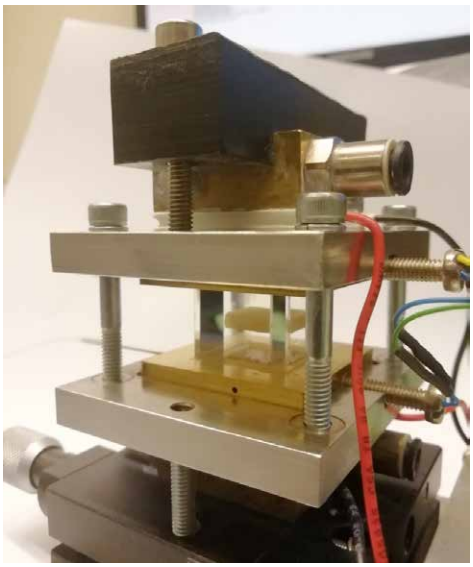

Figure 1. Photo of the experimental cell

surface of the porous medium was refined using tomography. Interestingly, for considered system the resulting thermal gradient through a porous medium is equal to half of that in a liquid without a porous medium.

Next, we examined the concentration field in the steady state in the THN-nC12 binary mixture 50% of mass fraction. The results show that in the regions close to the horizontal walls, the concentration gradient behaves like a gradient in a free liquid and deviates strongly as it approaches a porous medium. The formally obtained Soret coefficient (S_T) from the ratio of the mass and thermal fluxes in the steady state follows the same trend. The value of S_T determined from the data near the cell walls, agrees well with benchmark value while other ones, closer to the porous interface reveal an unfamiliar behavior. The Soret coefficient, determined in a porous medium from the steady state (S_T=10.5x 10^{-3}1/K) is slightly larger than the benchmark value but coincides with the previous measurement using porous medium (Platten&Costeseque, 2004)

Three regimes for the time evolution of the concentration difference (∇C_{pm}) between the interfaces of a porous layer were identified during continuous monitoring of the mass transfer in free liquids and a porous medium. These regimes are shown in Fig.2. It was found that at the beginning of the experiment (the first 24 h) the temporal evolution of the concentration difference between the interfaces of the porous layer looked as if the inverse and strong component separation occurred in the porous medium. It was evidenced that different characteristic times of the thermodiffusion in

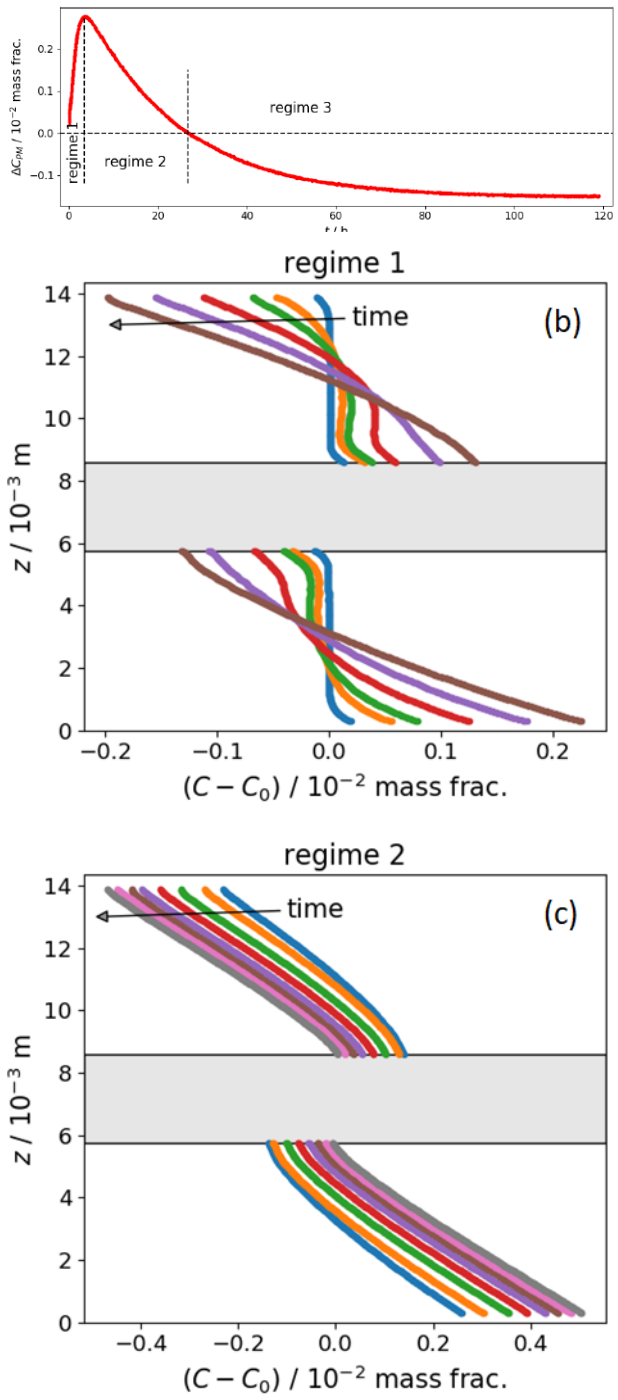

Figure 2: The Soret separation in the THN-nC12 binary mixture at T_{mean}=298K and time regimes. Low row: Evolution of concentration profiles with time in free liquid at different regimes. (b) 1st regime, non-equidistant profiles when Δt varies from 620s to 3 500s (c) 2nd regime, equidistant concentration profiles with Δt=12 000s (d) 3rd regime, equidistant concentration profiles with Δt=60 000s.

free liquids and a porous medium were essential for the formation of apparent inverse separation.

The accurate consideration of mass fluxes evolution in time on the boundary between free liquid and porous layer in transient regime enabled to develop a novel approach for determining diffusion (D_{pm}) and thermodiffusion (D_T) coeffcients from the transient process. Comparison of the obtained diffusion coefficient in porous medium (D_{pm}) with its benchmark value (D) in a free liquid showed that they differ by factor 1.8. Correspondingly, it provides the value of tortuosity 1.36.

Conclusions

The developed experimental approach using digital optical interferometry in combination with tomography yields five coefficients from a single experiment, they are: thermal conductivity k, the Soret (S_T), diffusion (D_{pm}) and thermodiffusion (D_T) coefficients and tortuosity τ. All these coefficients were obtained in the THN-nC12 binary mixture with 50% of mass fraction.

Acknowledgements

The work was supported by the PRODEX programme of the Belgian Federal Science Policy Office, ESA.

Figure 3: The distributions of the Soret coefficient over the compound system: the red line indicates the benchmark value of S_T in free liquid; the blue dotted line shows the measure S_T in porous media; the solid blue line corresponds to the conditional Soret coefficient measured in free liquid.

References

V. Shevtsova, Y. Gaponenko, V. Sechenyh, D. Melnikov, T. Lyubimova, A. Mialdun, Dynamics of a binary mixture subjected to a temperature gradient and oscillatory forcing, *J. Fluid Mechanics* 767 (2015) 290-322.

M. Bou-Ali *et al.*, Benchmark values for the Soret, thermodiffusion and molecular diffusion coefficients of the ternary mixture tetralin+isobutylbenzene+n-dodecane with 0.8-0.1-0.1 mass fraction, *Eur. Phys. J. E* 38 (2015) 30.

A.Mialdun, I. Ryzhkov, O. Khlybov, T. Lyubimova, V. Shevtsova, Measurement of soret cocients in a ternary mixture of toluene-methanol-cyclohexane in convection-free environment, *J. Chem.Physics* 148 (2018) 044506.

T. Triller et al, Thermodiffusion in ternary mixtures of water/ethanol/triethylene glycol: First report on the DCMIX3-experiments performed on the international space station, *Microgravity Sci. and Technology* 30 (2018)

J. K. Platten, P. Costeseque, The Soret Coefficient in Porous Media, J. Porous Media 7 (2004) 317-329.

C. Giraudet, F. Croccolo, G. Galliero, G. Pijaudier-Cabot, S. Van Vaerenbergh, M. Ziad Saghir, F. Montel, H. Bataller, Thermodiffusion of the tetrahydronaphthalene and dodecane mixture under high pressure and in porous medium, *C.R. Méc.* 341 (4) (2013) 340-347.

Oral 032

Axial Sloshing of Liquid Hydrogen at low Bond Numbers with Superheated Walls

Michael E. Dreyer

Department of Fluid Mechanics, Faculty of Production Engineering, University of Bremen
ZARM, Am Fallturm 2, 28359 Bremen, michael.dreyer@zarm.uni-bremen.de

The dynamic behavior of liquids in moving containers with application to space technology, commonly known as sloshing, has been the focus of many studies since the early 60s. Collections and textbooks are dedicated to this topic ([Abraham 1966, Dodge 2000, Ibrahim 2005]). Sloshing is characterized by the ratio of the hydrostatic pressure due to a characteristic acceleration a_C, and the capillary pressure. This ratio is commonly known as the Bond number (or Eötvös number)

$$\mathrm{Bo} = \frac{\rho_L a_C R^2}{\sigma} \tag{1}$$

The density of the liquid ρ_L times the acceleration a_C times a characteristic length, typically the radius R of a container, yields the hydrostatic pressure, whereas the surface tension σ divided by R gives the capillary pressure. Even though the lengths scale for the hydrostatic pressure and the capillary pressure are not the same, usually one scale is used in literature. High Bond number sloshing occurs in the propelled phase of a spacecraft. Theories are available, and testing can be performed at Earth's gravity using sloshing tables. Results are being used to validate and tune the codes, which are used by aerospace industries for the design of liquid filled containers.

Low Bond number sloshing, in particular with perfectly wetting liquids (storable and cryogenic propellants are usually wetting the metallic containers wall), requires a relevant test environment, such as compensated gravity or neutral buoyancy. Theoretical analyses are limited to small surface amplitudes and larger contact angles.

Future launcher concepts use liquid hydrogen (LH2) or liquid methane (CH4) as propellant and liquid oxygen (LOX) as oxidizer. They may experience long ballistic phases with varying acceleration levels. For propellant management purposes, it is important to understand the response of cryogenic fluids (liquid and gas) to these disturbances. Furthermore, superheated tank walls influence the motion of free surfaces, and may cause evaporation and pressure changes. This study investigates the free surface reorientation of liquid hydrogen upon a sudden step reduction of gravity in presence of a superheated wall. The pressure was set around normal pressure leading to a saturation temperature of 20 Kelvin. This test case can be used to validate numerical codes which solve the mass, momentum and energy conservation equations including the thermal behavior of the walls.

The experiment consists of a glass cylinder partly filled with liquid hydrogen enclosed in a cryostat to insulate it from ambient conditions. Temperatures were recorded at several locations along the cylinder and in the gas phase. The pressure inside the cylinder was recorded with a pressure transducer and optical access was enabled with an endoscope. Various heating elements were glued to the cylinder for thermal control of the experiment. Thermal stratification in the liquid phase could be neutralized and wall heating elements were used to establish a wall

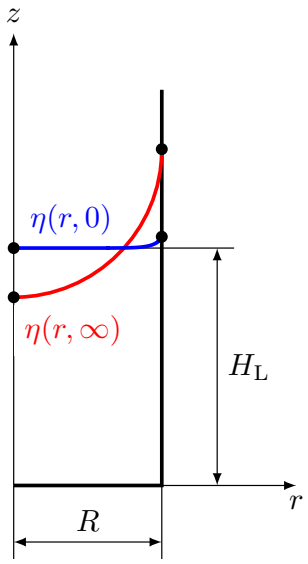

Figure 1: Initial $\eta(r,0)$ and final $\eta(r,\infty)$ interface contour. The container is initially filled up to a height H_{L}.

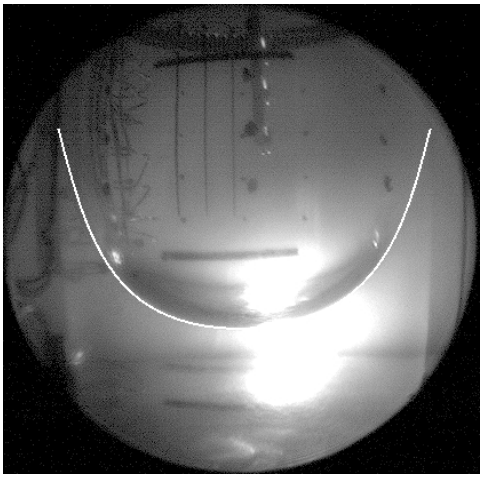

Figure 2: Intermediate surface contour of liquic drogen in a gaseous hydrogen environment. free surface is highlighted in white. The static tact angle is zero but the tangent at the wall is visible due to optical distortions of the cylind container wall.

temperature gradient in vertical direction.

Experiments were carried out in the drop tower at the University of Bremen. Experiment time in microgravity lasted five seconds. Several experiments with varying wall temperature gradients were performed. The reorientation of the free surface could be recorded focusing on wall and center point locations. A final equilibrium surface position could not be achieved due to limited experiment time.

The paper will review previous results with liquid argon and methane ([Kulev et al. 2014]) and liquid hydrogen ([Schmitt and Dreyer 2015]), and present new results ([Friese et al. 2019]). In addition, different numerical codes have been used to get the free surface position, the wall heat transfer, the evaporated mass, and the pressure progression. The results contribute to the understanding of the behavior of cryogenic liquids, such as hydrogen, oxygen, and methane, in launchers, spacecrafts and future orbital propellant depots.

Acknowledgments We acknowledge the funding from the German Aerospace Center (DLR e.V.) through grant number 50RL1621. The funding was provided by the German Federal Ministry of Economic Affairs and Energy, based on a decision of the German Bundestag (German Federal Parliament).

References

[Abraham 1966] Edited by Norman Abra (1966) The Dynamic Behavior of Liquic Moving Containers, NASA SP-106, Washin D.C.

[Dodge 2000] Franklin T. Dodge (2000) The Dynamic Behavior of Liquids in Moving Con ers, Southwest Research Institute, San Ant Texas

[Ibrahim 2005] Ibrahim, R. (2005) Liquid Slos Dynamics, Cambridge University Press, U Kingdom

[Kulev et al. 2014] Kulev, N., Basting, S., Bae E., and Dreyer, M.E. (2014) Interface reo tation of cryogenic liquids under non-isothe conditions *Cryogenics* 62, 48 - 59

[Schmitt and Dreyer 2015] Schmitt, S., Dreyer, M. (2015) Free surface oscilla of liquid hydrogen in microgravity condi *Cryogenics* 72, 22 - 35

[Friese et al. 2019] Friese, P.S., Hopfinger, Dreyer, M.E. (2019) Liquid hydrogen slos in superheated vessels under microgravity, *perimental Thermal and Fluid Science* 106, 118

Oral 034

DCMIX-4 experiment as continuation and extension of DCMIX project

A. Mialdun[1], Yu. Gaponenko[1], V. Shevtsova[1]

[1]MRC, CP165/62, Université libre de Bruxelles (ULB), 50, Ave. F.D. Roosevelt, B-1050 Brussels, Belgium;
amialdun@ulb.ac.be, ygaponen@ulb.ac.be, vshev@ ulb.ac.be

Introduction

Understanding of non-isothermal mass transport phenomena in multicomponent liquid mixtures is of particular interest because of its important role in many natural and industrial processes. Ternary mixtures are the first step in this direction, although even assessing isothermal diffusion in these mixtures is complicated. Non-isothermal thermodiffusion (Soret effect) adds more complexity, making corresponding measurements extremely difficult. It is especially true as non-isothermal diffusion studies are extremely sensitive to tiny disturbances of thermal nature, which cause buoyancy convection and easily destroy the measurement.

To eliminate the main source of disturbances and to establish solid reference data on the ternary thermodiffusion, the DCMIX project of ESA, joined by Roscosmos, was launched in 2009. The modular design of the instrument dedicated to the project made it easy to conduct a set of experiments, targeting different ternary mixtures, each with 5 ternary and 1 binary state points. Up to now, four experimental on-orbit campaigns have been successfully conducted. The first in the series, DCMIX-1, was dedicated to a ternary mixture of hydrocarbons, each presenting a specific chemical family. The choice was motivated by the fact that the mixture had become the main testing subject for the research on ground, though with somewhat contradicting results. The following campaign, DCMIX-2, was aimed at toluene-methanol-cyclohexane ternary mixture that features mostly unstable separation on ground and an extended miscibility gap. Extrapolating from some scarce binary experiments, one may expect in this ternary mixture critical slowing down of diffusion kinetics accompanied by divergence of Soret separation. The third campaign focused on a strongly non-ideal system with extensive hydrogen bonding, consisting of triethylene glycol-ethanol-water. The last campaign, DCMIX-4, which was running on-orbit in December 2018 – March 2019, has more exploratory nature, and apart of the few new state points of the toluene-methanol-cyclohexane mixture, closer targeting the miscibility gap, it also included ternary nanofluid and ternary polymer solution, trying to bridge the thermodiffusion and thermophoresis.

Experimental

The DCMIX experiments on-board the ISS were all performed using Selectable Optical Diagnostics Instrument (SODI), assigned to Microgravity Science Glovebox (MSG) located in the Destiny module of the ISS. SODI is a Mach-Zehnder interferometer simultaneously probing a Soret cell with experiment mixture at two distinct wavelengths, 670 and 935 nm (MR and MN lasers, respectively). Being mounted on a translation stage, the interferometer can sequentially access all 5 cells with ternary mixtures united in a single block (cell array). All experiments consisted of two steps of equal duration: non-isothermal Soret step, when after almost instant creation of the temperature gradient the thermodiffusion separation develops governed by the mass diffusion kinetics, and isothermal step aimed at homogenization of the developed temperature and concentration non-uniformities. In DCMIX-4, the second step was not controlled.

Duration of the steps was liquid-dependent and varied from 12 to 48 h, depending on the cell. Further details on the instrument, principles of operation and runs organization can be found elswere (Ahadi et al. 2013; Mialdun and Shevtsova 2015; Triller et al. 2018).

Communication between the instrument and the science team (commanding of runs and downlink of the evaluation data in near real-time) was performed by Spanish User Support and Operation Center (E-USOC), Madrid.

The main distinction of DCMIX-4 experiment campaign is that it includes not one, but several different ternary mixtures, with several science teams responsible for a particular mixture. Our team was in favour of deeper exploring of the ternary system with demixing zone. The three new state points selected for DCMIX-4 experiment (see Fig.1) aim directly at the critical point of the system, while DCMIX-2 campaign planning was targeting the far side of the miscibility gap.

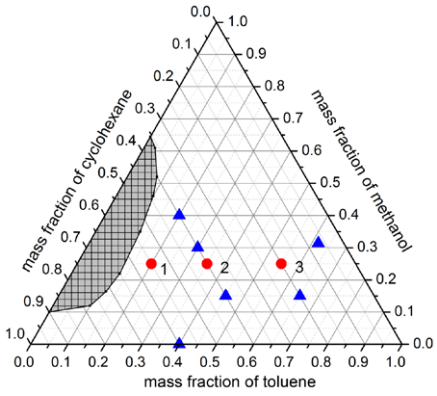

Figure 1: Ternary mixture of toluene-methanol-cyclohexane studied in the frame of DCMIX project. Blue triangles are the points addressed in DCMIX-2 experiment; red circles are the mixtures participated in DCMIX-4 campaign (numbers correspond to the cell identifiers).

Results

The limited amount of data obtained by the direct downlink from the onboard experiments allowed us to verify the performance of the conducted experiments, to check the integrity of the obtained data and to validate the consistency

of the data extraction procedures. Apart of that, we have also performed an exploratory quantitative analysis of selected runs in cells #1-3. The refractive index profiles along the diffusion path, $n(z, t)$, obtained by interferometry and corresponding to the concentration separation caused by thermodiffusion were analysed in different manners with the purpose of characterizing the separation magnitude and the general diffusion kinetics. The separation curves presented in Fig.2 are obtained by evaluating the gradient of the refractive index at the mid-plane of the cell, $(\partial n/\partial z)_{z=H/2}$, reduced to the unit temperature difference.

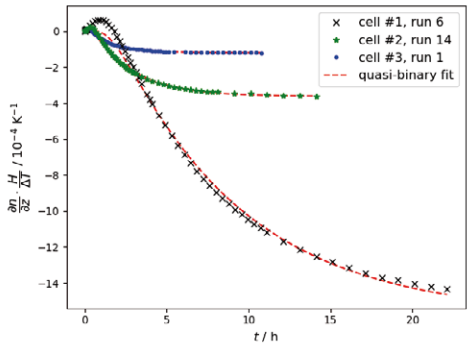

Figure 2: Temporal evolution of the refractive index gradient at the mid-height of the cells, $z = H/2$.

One can clearly see the dramatic separation growth from cell #3 to cell #1, as approaching the critical point.
Due to the shortage in the currently available data, the diffusion kinetics was analysed in a limited manner, by mimicking the mixtures as quasi-binary.

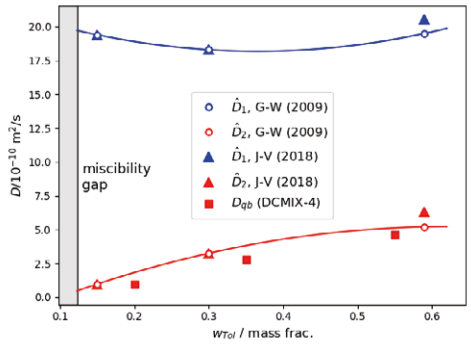

Figure 3: Diffusion in three cells filled with the toluene-methanol-cyclohexane mixture at mean temperature 25°C, compared with eigenvalues of the diffusion matrix from literature (Grossmann and Winkelmann 2009; Janzen and Vrabec 2018). The microgravity results in cells #1-3 for runs 1, 6, 14 (filled squares) are obtained by processing images acquired with MN laser.

As it is seen in Fig.2, the quasi-binary fit provides a very good approximation for the separation curves. According to our previous experience, such obtained diffusion coefficients are typically drawn towards a smaller eigenvalue. It was effectively confirmed by the results of DCMIX-4 (see it in comparison with literature data in Fig.3). The slowing down of the diffusion kinetics as approaching the demixing zone has been successfully confirmed as well.

Conclusions

We present preliminary evaluation of the results of the DCMIX-4 experiment performed on-board the ISS as obtained by analyzing telemetry images downloaded during the on-orbit campaign.
The telemetry images allowed us to qualitatively assess the performance of the experiments by evaluating the amplitude of the signal and the ability of the procedure to extract the relevant information.
The results related to all cells have been assessed as sufficiently good for future complete analysis which will be performed when all images are available by physically downloading data discs from the ISS to Earth.

Acknowledgements

We acknowledge support of this work by the PRODEX program of the Belgian Federal Science Policy Office.

References

A. Ahadi, S.V. Varenbergh, M.Z. Saghir, Measurement of the Soret coefficients for a ternary hydrocarbon mixture in low gravity environment, *J. Chem. Phys.* 138 (2013) 204201.

A. Mialdun, V. Shevtsova, Temperature dependence of Soret and diffusion coefficients for toluene–cyclohexane mixture measured in convection-free environment, *J. Chem. Phys.* 143 (2015) 224902.

T. Triller et al., Thermodiffusion in Ternary mixtures of water/ethanol/triethylene glycol: First report on the DCMIX3-experiments performed on the International Space Station, *Microgravity Sci. Technol.* 30 (2018) 295-308.

T. Grossmann, J. Winkelmann, Ternary diffusion coefficients of cyclohexane + toluene + methanol by Taylor dispersion measurements at 298.15 K. Part 1. Toluene-rich area, *J. Chem. Eng. Data* 54 (2009) 405-410.

T. Groβmann, J. Winkelmann, Ternary diffusion coefficients of cyclohexane + toluene + methanol by Taylor dispersion measurements at 298.15 K. Part 2. Low toluene area near the binodal curve, *J. Chem. Eng. Data* 54 (2009) 485-490.

T. Janzen, J. Vrabec, Diffusion coefficients of a highly nonideal ternary liquid mixture: cyclohexane–toluene–methanol, *Ind. Eng. Chem. Res.* 57 (2018) 16508-16517.

Oral 035

Stabilization of hydrothermal oscillatory flow due to heat transfer from moving gas parallel to the interface

V.Yasnou[1], Y. Gaponenko[1], A.Mialdun[1], V. Shevtsova[1]

[1]MRC, CP-165/62, Université libre de Bruxelles (ULB), 50, Ave. F.D. Roosevelt, B-1050 Brussels, Belgium;
vyasnou@ulb.ac.be, ygaponen@ulb.ac.be, amialdun@ulb.ac.be, vshev@ulb.ac.be,

Introduction

The thermal dependence of surface tension leads to thermocapillary Marangoni stresses that act along the free surface. These stresses are balanced by viscous stresses and the liquid interior is set in motion. In the gravity field, a combined action of the buoyancy and the thermocapillary effect leads to the evolution of a convective flow. This work examines flows in a cylindrical liquid bridge which is a drop of liquid held by the action of the surface tension force between two solid rods where the top rod is hotter than the bottom one.

A two-phase flow in a liquid bridge develops under the action of buoyant and Marangoni forces in the presence of weak evaporation and a gas stream parallel to the interface. The flow at the interface is directed downward from the hot disk to the cold one. At a small temperature difference, the flow is a steady axisymmetric toroidal vortex. However, when $\Delta T = Thot - Tcold$ exceeds some critical value ΔTcr, an instability sets in and gives rise to a number of time-dependent three-dimensional flow regimes.

The novelty of this study with respect to closely related research is substantial due to the innovative design of the set-up, which includes the following issues: (a) the mean temperature of liquid is kept constant; (b) gas temperature is controlled in a large interval, $10°C < T_g < 40°C$; (c) heat transfer between the lateral sides of the rods and gas is absent. Two essential points have been highlighted by our analysis. First, gas temperature produces a weak effect on the threshold of instability but it strongly affects the supercritical flow dynamics. Second, oscillatory instability can be stabilized by choosing specific temperatures and velocities of counter-current gas.

Experiment

For studying hydrothermal instability in the liquid bridge under the action of a parallel gas flow, a new set-up profitably different from the previous models has been developed (Yasnou et al, 2018). In this instrument only the disk-shaped tips of the rods, which are in contact with liquids, are heated or cooled. The temperature of the disks is regulated independently. The major part of the rods is thermally inert and does not produce any influence on the gas temperature. Unlike any other existing instruments, this design allows keeping the gas temperature below the temperature of the cold rod.

Results

A forced gas flow along the interface produces actions on the system via shear stresses and heat exchange. For the experimental fluids (n-decane, nitrogen), the ratio of viscosities is large, about 40, and the gas Reynolds number is moderate, $Re_g < 120$. Thus, the prevailing mechanism by which gas affects the flow in liquid is heat transfer. Correspondingly, this study deals with a supercritical thermocapillary flow in a liquid bridge, where the thermocapillary instability has resulted in diverse oscillatory states depending on the gas temperture. The role of shear streass was previously analysed by means of numerical simultions (V. Shevtsova et al., 2013).

The stability diagram in terms of ΔTcr and the critical frequency fcr as a function of the gas temperature is shown in Figure 1.

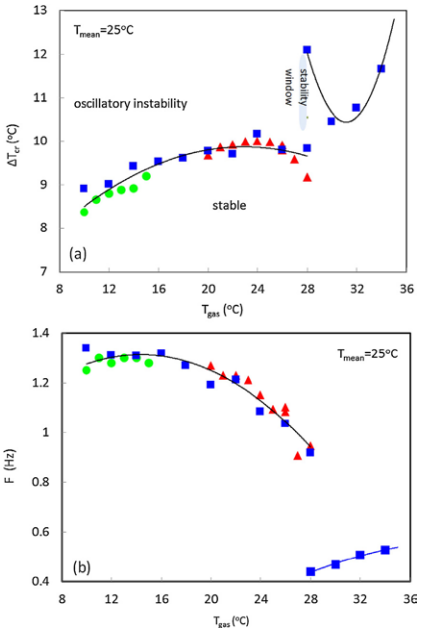

Figure 1: Stability diagram summarizing the experimental observations in n-decane / nitrogen system in terms of ΔTcr and the critical frequency as a function of the gas temperature, $Vg=0.5$ m/s, $V=1.05$. The similar symbols indicate results corresponding to the same experimental campaign.

The critical curve consists of two distinct branches. The major branch, which occurs at $Tg < 28°C$, indicates a weak parabolic dependence of ΔTcr on the gas temperature with a slight maximum at $Tg \approx 23°C$. The second branch has a shape of a narrow parabola and corresponds to the higher ΔTcr.

To understand the gas temperature effect on the evolution of oscillatory flows at the applied ΔT above ΔTcr, the results of all the experiments conducted within several months at the same velocity of gas have been gathered and presented in the form of a map of oscillatory states as a function of the gas temperature and the imposed temperature difference shown in Figure 2.

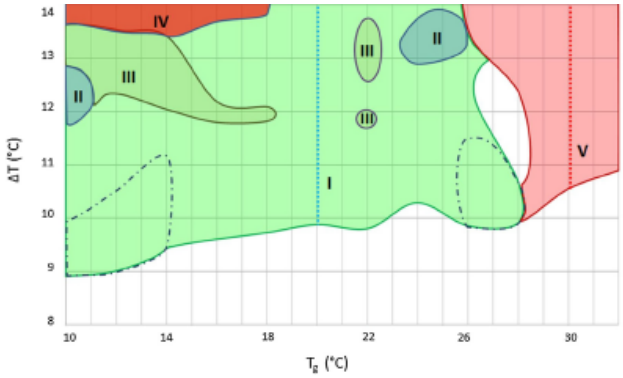

Figure 2: The global view of oscillatory states separated in five regimes in terms of gas temperature (*Tg*) and the imposed temperature difference (*ΔT*). The observed regimes are (I) periodic; (II) quasi-periodic with two frequencies; (III) quasi-periodic with three frequencies**;** (IV) noisy quasi-periodic with three frequencies; (V) periodic. The vertical lines indicate the temperature of the cold and hot disks at the threshold. V_g*=0.5 m/s, V=1.05.*

The study shows that in the supercritical region, $\Delta T > 1.25\ \Delta T_{cr}$, the flow dynamics can be divided in three regimes relative to the gas temperature. When the gas is colder than the temperature of the supporting disk, one can observe multiple transitions between oscillatory states: periodic, quasi-periodic with two frequencies, quasi-periodic with three frequencies and noisy quasi-periodic with three frequencies. In the case, when the gas temperature approaches the temperature of the cold disk and increases to the mean temperature, the flow remains periodic up to the largest tested *ΔT*. In the case of hotter gas, the flow also remains periodic far above the threshold of hydrothermal instability, but the azimuthal mode of the periodic oscillatory flow changes. It has been found that a stability window exists between these two azimuthal modes and its location is sensitive to the gas parameters as well as to the geometry of the liquid bridge. It opens a possibility that oscillatory instability can be stabilized by choosing specific temperatures and velocities of counter-current gas.

Conclusions

In the present work an extensive study of hydrothermal instability and evolution of oscillatory flow states under the action of a gas stream parallel to the interface in the geometry of a liquid bridge has been performed. A new set-up was developed to study the dynamics of thermocapillary and buoyant convection in liquid with moderate Prandtl number, *Pr=12* (n-decane). The major experimental results are presented in terms of Fourier maps at different gas temperatures which then are combined in one global diagram of oscillatory states.

Acknowledgements

This work is supported by the PRODEX programme of the Belgian Federal Science Policy Office, ESA.

References

V. Yasnou, Y. Gaponenko, A. Mialdun, V. Shevtsova: Influence of a coaxial gas flow on the evolution of oscillatory states in a liquid bridge, *In.l J. of Heat and Mass transfer* 123 (2018) 747–759.

V. Shevtsova, Y. Gaponenko, A. Nepomnyashchy: Thermocapillary flow regimes and instability caused by a gas stream along the interface, *J. Fluid Mech.* 714 (2013) 644–670.

Oral 036

Growing Plants in Space

Karl H. Hasenstein[1], Susan John[2]

[1]University of Louisiana at Lafayette, Lafayette, Louisiana 70504-3602
[1]hasenstein@louisiana.edu, [2]spj1554@louisiana.edu

Introduction

So far, most experiments performed in space focused on basic understanding of space effects including microgravity, lack of buoyancy, sensing of gravity and effects of altered atmospheric conditions. The ability of plants to provide food and their long recognized psychological benefits to the crew, and the ability to generate oxygen and recycle waste, leads to a new emphasis of growth optimization under space conditions. While experimental plants, notably *Arabidopsis thaliana*, rarely exceed the seedling stage and therefore do not require space or (recyclable) growth substrate, cultivation of edible plants poses challenges that have not yet been studied. We report on preparations for a space experiment that aims to assess substrate, light and watering conditions of radishes (*Raphanus sativus*) in the Advanced Plant Habitat (APH) on the ISS. The challenge of providing appropriate amounts of water and nutrients, examining mineral and nitrogen accumulation, assessing secondary metabolites, and light effects in combination with elevated CO2 and weightlessness represent complex interactions that must be understood for optimal plant growth in space. We report on ground tests and space-hardware specific challenges.

Plant Cultivation

General space and mass limitations prevent providing regular soil at required depths. In addition, water flow is determined by surface interaction, rather than gravity. Therefore, arcillite (calcined Montmorillonite) was selected. Its porous structure (1 to 3 mm grains), inert properties at neutral pH, low density (~0.69 g×cm^{-3}) and hydrophilicity suggest its suitability as growth substrate. However, its inability to store water and ta limited depth of ca. 5 cm requires a fine-tuned water delivery

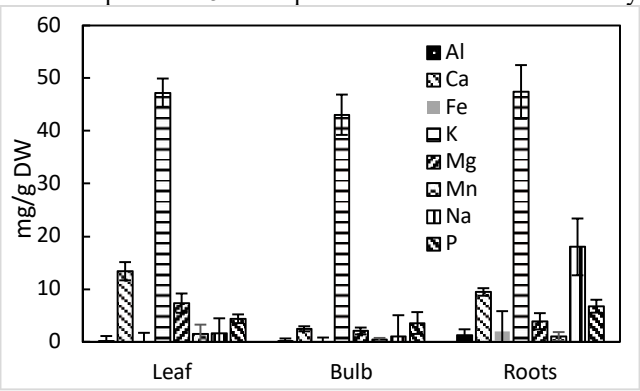

Figure 1: Mineral content of *Raphanus sativus* tissues after growth in modified MS-enriched arcillite. The high potassium content underscores its high nutritional value.

System. The low mineral content necessitates fertilizer supplementation. The initial strategy relied on the use of slow-release fertilizer (Nutricote) as plant nutrient resource. However, the initial slow release (Adams et al., 2013) required a better and more uniform provision of minerals. Because of hardware corrosion sensitivity, we chose modified (chloride-free) Murashige and Skoog (MS) medium that is applied as solution (equal volume as arcillite). After drying, the arcillite can be stored indefinitely. The high K content and consistent mineral profile (Fig. 1) indicate that MS-enriched arcillite is a suitable growth medium. The nitrogen content in MS grown plants was significantly higher than in plants grown in Hoagland medium (data not shown).

Light conditions

Plant development (photomorphogenesis) depends on light intensity and quality. Using a tuneable LED light fixture (Heliospectra RX-30), we determined that elevated red light fluence (>660 nm) resulted in accelerated flower formation while enhanced blue light promotes leaf pigmentation and bulb formation.

Tissue storability

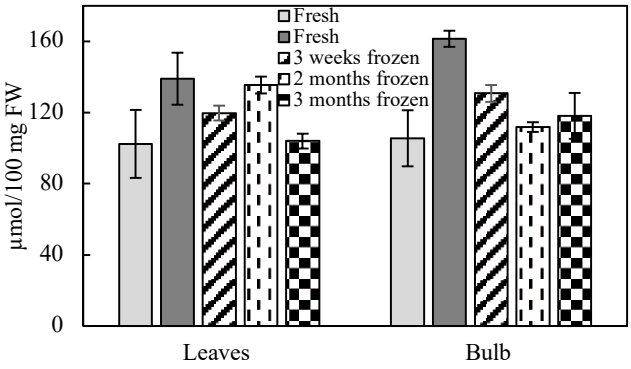

Figure 2: Amount of glucosinolates in fresh and frozen *R. sativus* tissue, expressed a sinigrin equivalent. All data are the average of three replicates per sample. Bulb = storage root. The large variability in fresh samples indicates the sensitivity of plants to the culture conditions

Table 1: RNA extractions of Radish tissue.

Frozen storage, months	RNA Yield (µg per 100 mg FW)		
	Leaves	Radish	Average
3	11.90 ± 1.13	17.82 ± 2.62	14.86 ± 1.57
2	20.56 ± 4.06	13.98 ± 1.24	17.27 ± 2.40
0.75	10.74 ± 3.54	16.50 ± 2.80	13.62 ± 2.40
0	14.08 ± 3.18	11.36 ± 1.19	10.34 ± 1.66

Post-flight analyses require storing tissue on station and subsequent laboratory analyses. Glucosinolates (Fig. 2) and RNA yields (Table 1) after frozen storage are within the range obtained from fresh tissue.

On station experiments will sample photosynthesis data by examining the Quantum Yield (Qy) and Instantaneous Chlorophyll Fluorescence (Ft) using a handheld FluorPen system. These parameters will measure photosynthetic performance of selected leaves over time and provide assessment of photosynthetic performance during leaf development. In combination with comprehensive records of the APH (more than 300 data points per minute) our experiment will provide a thorough data set of plant growth parameters and constraints on the ISS.

Conclusions

The work reported here represents essential preparation for the Science Verification Test (SVT) and Experiment Verification Test (EVT). Additional development of gene expression studies of key metabolic genes will provide the first comprehensive ISS study on plant productivity parameters.

Acknowledgements

This research and a future flight experiment are supported by NASA Grant Number 80NSSC17K0344

References

Adams C, Frantz J, Bugbee B (2013) Macro- and micronutrient-release characteristics of three polymer-coated fertilizers: Theory and measurements. J Plant Nutr Soil Sci 176: 76-88

Murashige T, Skoog F (1962) A revised medium for rapid growth and bio assays with tobacco tissue cultures. Physiol Plant 15: 473-497

Hoagland DR, Arnon DI (1950). The water-culture method for growing plants without soil. University of California Berkeley, College of Agriculture, Agricultural Experiment Station.

Oral 037

On convective stability of a binary mixture with negative Soret effect in a cylindrical thermogravitational column

S. V. Kozlova[1], I. I. Ryzhkov[1], M. M. Bou-Ali[2]

[1] Institute of Computational Modelling, Federal Research Center KSC SB RAS, Krasnoyarsk, Russia,
[2] Mechanical and Manufacturing Department, MGEP Mondragon Goi Eskola Politeknikoa,
Loramendi 4 Apdo. 23, 20500 Mondragon, Spain;
sonique@icm.krasn.ru

Introduction

In recent decades, a thermogravitational column (vertical layer between solid flat walls or co-axial cylinder surfaces maintained at constant temperatures) has been an effective tool for analyzing the Soret effect (thermal diffusion effect) and measuring the thermal diffusion coefficients (Bou–Ali M. et al 1998, Lapeira E. et al 2017). Reliable measurements of the coefficients can be performed only when convective flow is stable in the column. Convective instability can be caused by negative Sore effect, at which the heavier mixture components accumulate in the upper part of the column. However, the experimental observations described in (Bou–Ali M. et al 1999, Bou–Ali M. et al 2000) show that for binary mixtures in a cylindrical column a stable separation is possible in a certain range of the applied temperature difference. This result is not yet explained theoretically.

Section 1

In this paper, a theoretical study of the convective stability of a binary water – ethanol mixture with negative Sore effect in a cylindrical column is performed on the basis of experimental data. This mixture has negative thermal diffusion effect in the range of ethanol concentrations not exceeding 30 % (P. Kolodner et al 1988). In this study, the ethanol mass fraction is 0.2204, which corresponds to the experimental value (Bou–Ali M. et al 1999) and the specified range. The mixture is placed between the walls of co-axial cylinders maintained at different constant temperatures. The inner cylinder is heated by default.

Section 2

The numerical simulation of the mixture separation was performed in Ansys Fluent 14.5 for a column with folowing parameters: height H = 0.42 m, width of gap L=1.53 mm, r_1 = 0.317 cm, r_2 = 0.510 cm. The parameters of the column and the applied temperature differences (4.25, 9, 10.8, 13.5 K) correspond to the experiment (Bou–Ali M. et al 1999, Bou–Ali M. et al 2000). The temperature difference of 16 K was additionally investigated. The mixture physical properties were also taken from (Bou–Ali M. et al 1999, Bou–Ali M. et al 2000) or calculated on the basis of data for pure components. The analytical solution of the problem of mixture separation in a cylindrical column is made taking into account the influence of the ratio of cylinders radii and their curvature on the separation process (S. V. Kozlova, I. I. Ryzhkov 2018). For the studied column, the ratio of cylinders radii is $\delta = r_1/r_2 = 0.6216$. The results of numerical simulation are shown in Fig. 1, where the evolution of the ethanol concentration difference between the bottom and top of the column is shown. According to the experiment, with a small temperature difference between the walls (4.25 K), a small vertical separation disappears due to the development of convective instability in the column. With an increase in the temperature difference (9, 10.8 K), the system reaches the stationary separation regime, but the vertical concentration gradient also vanishes eventually. When the critical temperature difference (13.5) is reached, the observed convective flow in the column becomes stable and the stationary difference in ethanol concentrations between the ends of the column does not change with time. Numerical calculations show that, with a small temperature difference (4.25 K), the separation of the mixture in the column monotonously increases, but disappears, not reaching a stationary state, as it was also shown experimentally. With an increase in the temperature difference, concentration difference reaches the calculated stationary value (S.V. Kozlova, I.I. Ryzhkov 2018), but due to the instability, the separation vanishes. This result was obtained for 13.5 and 16 K, see Fig. 1, at which the maximum value is observed at the beginning of separation process.

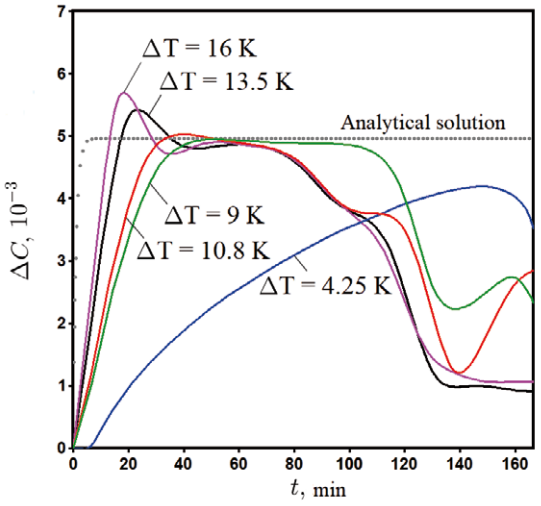

Figure 1: The evolution of the difference of average ethanol concentration ΔC between the bottom and top of a cylindrical column at different ΔT between the walls.

Conclusions

At this stage of the study, the results of numerical simulation are consistent with experimental data for small temperature differences between the walls of the thermogravitational column. With the increase of the temperature difference, a discrepancy in the results appears. Thus, additional verification of the numerical simulation method, refinement

of experimental data, and the linear stability analysis are needed to systematically describe the process of a mixture separation in the cylindrical thermogravitational column.

Acknowledgements

The reported study was funded by Russian Foundation for Basic Research, Government of Krasnoyarsk Territory, Krasnoyarsk Regional Fund of Science to the research project № 18-41-243005.

References

Bou–Ali M., Ecenarro O., Madariaga J. et al, Thermogravitational measurement of the Soret coefficient of liquid mixtures, *J. Phys. Condens. Matter* 10 (1998) 3321–3331.

Lapeira E., Gebhardt M., Triller T. et al, Transport properties of the binary mixtures of the three organic liquids toluene, methanol, and cyclohexane, *J. Chem. Phys.* 146 (2017) 094507.

Bou–Ali M., Ecenarro O., Madariaga J. et al, Stability of convection in a vertical binary fluid layer with an adverse density gradient, *Phys. Rev. E.* 59 (1999) 1250–1252.

Bou–Ali M., Ecenarro O., Madariaga J. et al. Measurement of negative Soret coefficients in a vertical fluid layer with an adverse density gradient, *Phys. Rev. E.* 62 (2000) 1420–1423.

P. Kolodner, H. Williams, C. Moe. Optical measurement of the Soret coefficient of ethanol/water solutions, *J. Chern. Phys.* 88:10 (1988) 6512–6524.

S. V. Kozlova, I. I. Ryzhkov. The study of transient separation of multicomponent mixtures in a cylindrical thermogravitational column, *Int. J. Heat and Mass Transf.* 126 (2018) 660-669.

Oral 038

Correlation of viscosity with atomic packing in $Cu_{50}Zr_{50}$ melt

Q.P. Cao[1], L.Y. Chen[1], M. Mohr[2], R. K. Wunderlich[2], H.-J. Fecht[2], X.D. Wang[1],D.X. Zhang[1] Y. Yang[3], and J. Z. Jiang[1,*]

[1] *International Center for New-Structured Materials, State Key Laboratory of Silicon Materials and School of Materials Science and Engineering, Zhejiang University, Hangzhou 310027, People's Republic of China*

[2] *Institute of Functional Nanosystems, University of Ulm, 89081 Ulm, Germany*

[3] *Technology and Engineering Center for Space Utilization, Chinese Academy of Sciences, Beijing, People's Republic of China*

*Corresponding author: jiangjz@zju.edu.cn

Abstract

The viscosities of $Cu_{50}Zr_{50}$ melt from 1250 K to 1435 K were measured on oscillating droplets using the containerless electromagnetic levitation technique under micro-gravity on board the International Space Station. The excellent stability of microgravity conditions on board the ISS build a stable environment for the verification of ground based measurements of viscosity. The resulting data quality enables the study of effects, such as sample rotations, on the measurement results, without the influence of gravity. The viscosity in the investigated temperature range can be expressed by an Arrhenius temperature dependence $\eta(T) = \eta_0 \exp(E_A/k_BT)$, with $\eta_0 = (0.08\pm0.02)$ mPa·s and $E_A=(0.58 \pm 0.03)$ eV. The temperature dependent viscosity of $Cu_{50}Zr_{50}$ melt is studied by MD simulations in terms of structural mechanism. We find a correlation between the fraction of closer neighboring atoms, *f*, and viscosity, which is described by $\eta=\exp^n f^m$, where n=1.746/Δpe-4.478, m=-0.374/Δpe+0.440, and Δpe is the excess potential energy, indicating that the temperature dependent viscosity during cooling is controlled by the fraction of closer neighboring atoms. This could be a general picture for temperature dependent viscosity of metallic melts.

Oral 039

Effects of Environmental Endotoxins and Microgravity on Normal Human Lymphocytes: Role of ETAS as an Immunomodulation Therapy: Implications for Moon and Mars missions.

Maitreyi Chaganti[1], Elvis Okoro[1], Vivek Mann[1], Marie Doursout[2], Kristina Curry[1], Diana Risin[3], Anil Kulkarni[2] and Alamelu Sundaresan[1]

[1]Texas Southern University, [2] UTHealth, [3] NASA Johnson Space Center, Houston, US

maitreyi.chaganti6@gmail.com, alamelu.sundaresan@tsu.edu

Introduction

Different environmental stressors produce different responses in immune cells depending on their mechanism of action and concentrations. The main objective of this project was to understand how normal Human Peripheral Blood Mononuclear Cells (PBMCs) (Lymphocytes) would respond when exposed to environmental stressors such as Endotoxins and Microgravity. Furthermore, we explored the immunomodulatory effects of a plant-derivative Enzyme-treated Asparagus extract (ETAS) on these stress-induced PBMCs.

Lipopolysaccharide (LPS), an endotoxin, is a common outer membrane component of typical gram-negative bacteria. It is a common airborne environmental and occupational contaminant in agricultural and other industries. In urban areas, LPS is a common constituent of particulate matter such as diesel emissions. Endotoxins have been well recognized as an occupational hazard in numerous occupations, including: swine, poultry and dairy barns; grain and animal feed handling; sawmills, composting and waste handling; metal and fiberglass industry etc. LPS can elicit a strong immune response in host cells, ranging from inflammation and macrophage activation to fever and septic shock (Galanos C. et al. 1993).

Microgravity is one of the challenges astronauts must cope with during space missions. Consequently, long-duration space travel can have detrimental effects on human physiology. Previous studies have demonstrated that microgravity may cause psychological problems, cephalic fluid shifts, neurovestibular issues, and cognitive alterations. The immunological investigations of the astronauts recorded several dysregulations, such as the altered production of cytokines, enhanced sympathetic neuroimmune responses, compromised functions of monocytes, suppressed cytotoxicity of T-cells and Natural Killer (NK) cells, and reduced phagocytic capabilities of neutrophils (Kaur I. et al. 2008).

Closed environments, such as the space station, submarines and high-altitude flights are easily contaminated by gram-negative bacteria containing LPS (Taylor P.W. et al. 2015). Evaluation of these environments is very important to ensure human health and safety in such conditions. An evaluation of the internal environment of International Space Station (ISS) from air, water and surface samples provided a baseline of the contaminant characterization onboard the ISS, which include various bacterial strains capable of producing LPS.

Therefore, understanding the effects of LPS and microgravity on Lymphocytes might provide key insights into immunosuppression in astronauts in a closed space environment. This knowledge will allow scientists to develop systems to maintain crew health during long space flight missions as well therapies to augment immunity in healthy and immunosuppressed individuals.

Previous research studies support that some plant derivatives may be able to provide protection from environmental stressors by augmenting the immune system. In this research project, one such plant derivative was explored for its immunomodulatory activity. ETAS is a functional food ingredient developed as a supplement to alleviate stress. ETAS has demonstrated a clinically validated efficacy for sleep improvement, support of mood and cognitive function, and protection of neuronal cells. Most of ETAS's beneficial effects derive from its capacity to induce cytoprotective heat-shock proteins (Ito T. et al. 2014).

This study would help explore applications of ETAS as an immunomodulation therapy to combat the potential effects of LPS and microgravity on humans, which, we hypothesize, will have applications in protecting immune health in immusuppressed individuals as well as in astronauts bound for long-duration space travel to moon, Mars and beyond.

Methodology

Peripheral Blood Mononuclear Cells (PBMCs) were isolated from whole blood and were treated with different doses of LPS and ETAS at normal earth's gravity conditions (1*g*) and at modeled microgravity (*MMG*). Rotating Wall Vessel (RWV) was used as a microgravity analogue along with high-aspect rotating wall vessels (HARVs). The experiment was set up at three time points: 24, 48 and 72 hours and the cells were terminated after each time point. The cells were observed for morphological changes, cell viability, proliferation and

signaling activity. The RNA and protein were extracted and analysed.

Conclusions

In 1*g*, LPS-induced stress caused significant immunosuppression in lymphocytes and e observed that ETAS may be able to recover these effects. *MMG* caused significant alterations in cell morphology as well as cell's metabolic activity. The immunosuppressive effect of microgravity on lymphocytes was further exacerbated by presence of LPS. ETAS was able to demonstrate its ability to augment immune function in presence of stressors – LPS and ETAS. Signaling results revealed that numerous genes important in lymphocyte function such as ZAP 70 and NFkB were significantly regulated in presence of ETAS, which demonstrates the potential of ETAS as a supplement to maintain immune health even in the presence of stressors.

Acknowledgements

Funding: Grants from Amino Up Chemical (PI-Dr. Alamelu Sundaresan) and NSF TIP 1719318 (PI-Dr. Alamelu Sundaresan)

References

1. Galanos C. and M. A. Freudenberg. Bacterial endotoxins: biological properties and mechanism of action. Mediators of Inflammation 2, 1993
2. Ito T, Sato A, Ono T, Goto K, Maeda T, Takanari J, Nishioka H, Komatsu K, MatsuuraH. 2013. Isolation, structural elucidation, and biological evaluation of a 5-hydroxymethyl-2-furfural derivative, asfural, from enzyme-treated asparagus extract. J Agric Food Chem61:9155–9. doi: 10.1021/jf402010c.
3. Kaur, et al. Effect of Spaceflight on Ability of Monocytes to Respond to Endotoxins of Gram-Negative Bacteria. Clin Vaccine Immunol. 2008 Oct; 15(10): 1523–1528.
4. Taylor PW. Impact of space flight on bacterial virulence and antibiotic susceptibility. Infect Drug Resist. 2015 Jul 30; 8:249-62.

26th European Low Gravity Research Association Biennial Symposium and General Assembly
14th International Conference on "Two-Phase Systems for Space and Ground Applications"
European Space Agency Topical Teams meetings
Granada (Spain), September 24-27, 2019

Oral 042

Bubbles forming under hypergravity accelerations due to degassing of a liquid jet

O. Oikonomidou[1], S.P. Evgenidis[1], C.J. Schwarz [2], J.J.W.A. van Loon[2,3], M. Kostoglou[1], T.D. Karapantsios[1]

[1]Aristotle University of Thessaloniki, Thessaloniki, Greece, [2] European Space Research and Technology Centre, Noordwijk, The Netherlands, [3]Amsterdam UMC and Academic Centre for Dentistry Amsterdam, Amsterdam, The Netherlands;
oikonomid@chem.auth.gr, sevgenid@chem.auth.gr, christian.schwarz@esa.int, j.vanloon@vumc.nl, kostoglu@chem.auth.gr, karapant@chem.auth.gr

Introduction

The process of liquid degassing is encountered in several industrial but also space applications. Aiming to improve the efficiency of wastewater treatment technologies, carbonated beverages production, glass and plastic molding, oil extraction etc., researchers focused on the physics of bubbles formation and growth when triggered by the decompression driven supersaturation of a liquid with dissolved gas (Radzuan et al. 2016; Liger-Belair et al. 2015; Lopes et al. 2009; Birdi and Kleinitz, 1998). Existing research has been conducted exclusively under the gravity of earth and so little is known regading the liquid degassing phenomena at extra terrestrial conditions. The dynamics of deggasing are expected to change under different accelerations conditions, since the acceleration factor interfers with the bubbles buoyancy velocity and the liquid's hydrostatic pressure. Therefore, liquid degassing involved in the cooling and lubrication of workstations and satellite systems, as well as in liquid propellants tanks are expected to affect the processes of thermal regulation, rockets fuel combustion and storage in space (Chen et al. 2001, De Sain et al. 2015, Huang et al. 1994).

This work aims to broaden the existing knowledge and examine the bubble dynamics when liquid degassing takes place under hypergravity conditions. A pressurized liquid that is saturated with dissolved air injects through a nozzle inside a column of stagnant liquid that is open to atmosphere. Upon decompression, the liquid jet becomes supersaturated with dissolved air, forcing gas desorption in the form of bubbles. Experiments are conducted under artificial 2g, 4g, 8g and 12g accelerations at the Large Diameter Centrifuge facility of the European Space Agency (at ESTEC). Experiments under 1g act as a reference. The residence time distribution of the flowing liquid jet inside the column is investigated using conductivity tracers. Combining the flow pattern with bubble characteristics helps the proper understanding of the phenomena. A patented electrical impedance spectroscopy technique is employed for measuring the volume of the desorbed gas phase along the liquid flow. The size of bubbles is studied optically by analysing high resolution bubble images. Dissolved oxygen measurements reveal the total extent of degassing.
Experimental results can be exploited for the improvement of space operations during launching or re-orbiting. Moreover, transferring space technologies in industry may lead to the construction of innovative degassing applications.

Gas phase desorption

Experiments show that the concentration of desorbed gas during the degassing of a flowing liquid jet decreases with acceleration. This is because acceleration increases bubbles buoyancy velocity and therefore limits their residence time in the flow.

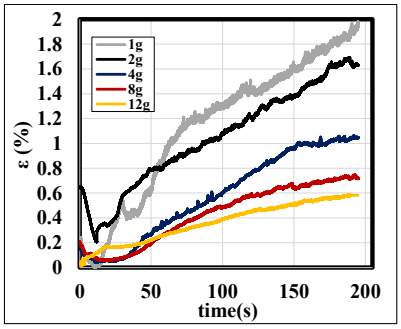

Figure 1: Gas volumetric percentage (ε) evolution in the liquid flow during the injection under various accelerations.

Bubble Size Distributions

Increasing the acceleration during the degassing of a liquid jet limits the residence time of large bubbles in the flow and thus moves the bubble size distributions towards smaller sizes.

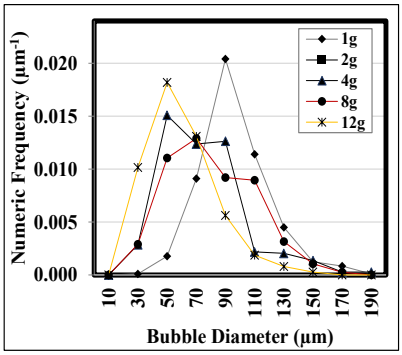

Figure 2: Bubble Size Distributions when a liquid jet degasses under various accelerations

Conclusions

The outcome of this study shows that increasing the acceleration during the degassing of liquid jet results in a less concentrated two phase flow consisting of smaller bubbles. The fact that the total extent of liquid degassing does not change with acceleration shows that the above results are attributed to the increased bubbles buoyancy velocity and not to mass transfer limitations.

Acknowledgements

This study is funded by the European Space Agency (NPI Project: Bubble dynamics during degassing of liquids – contract no.: 4000108790/13/NL/PA) and carried out under the umbrella of COST Action MP1106: 'Smart and green interfaces- from single bubbles and drops to industrial, environmental and biomedical applications' and COST Action MP1305: 'Flowing matter'. We would like to thank Dr. Kostantinos Zacharias for his technical and scientific support regarding the electrical impedance spectroscopy measurements and Mr. Triantafillos Tsilipiras for his contribution in building

the experimental setup. We would also like to thank Mr. Alan Dowson from ES-ESTEC-TEC-MMG for his technical support with LDC during this study.

References

K.S. Birdi, W. Kleinitz, Problems associated with dissolved atmospheric oxygen in crude oil at production facilities. *Oil Gas Eur. Mag*. 24 (1998) 1998.25–28.

Y.M. Chen, S.C.Wu, C.I. Chu, Thermal performance of sintered miniature heat pipes, *Heat Mass Transfer* 37 (2001) 611-616.

Z. Huang, S. Yiming, S. Shiga, H. Nakamura, T. Karasawa, T. Nagasaka, Atomization behavior of fuel containing dissolved gas, *Atomization and Sprays* 4 (1994) 253-262.

G. Liger-Belaira, F. Sternenberg, S. Brunner, B. Robillard, C. Cilindre, Bubble dynamics in various commercial sparkling bottled waters, *J. Food Eng.* 163 (2015) 60–70.

P. Lopes, M.A. Silva, A. Pons, T. Tominaga, V. Lavigne, C. Saucier, P. Darriet, P.L. Teissedre, D. Dubourdieu, Impact of oxygen dissolved at bottling and transmitted through closures on the composition and sensory properties of a sauvignon blanc wine during bottle storage, *J. Agric. Food Chem*., 57 (2009) 10261–10270.

M.R.A. Radzuan, A-B. Belope, R.B. Thrope, Removal of fine oil droplets from oil-in-water mixtures by dissolved air flotation, *Chem. Eng. Res. Des.*, 115 (2016) 19–33.

J.D. de Sain, B.B. Brady, T.J. Curtiss, L.T. Greenberg, M.B. Smith, R.M. Villahermosa, Solubility of pressurant gases in liquid hydrazine at elevated, *J Propul Power* 31 (2015) 1193-1203.

26th European Low Gravity Research Association Biennial Symposium and General Assembly
14th International Conference on "Two-Phase Systems for Space and Ground Applications"
European Space Agency Topical Teams meetings
Granada (Spain), September 24-27, 2019

Oral 043

Passive Phase Separation of Hydrogen under Microgravity Conditions

A. Pingel[1], M. Dreyer[2]

[12] University of Bremen, Faculty of Production Engineering – Mechanical Engineering and Process Engineering, Department of Fluid Mechanics, Center of Applied Space Technology and Microgravity (ZARM), Am Fallturm 2, 28359 Bremen, Germany;
[1]andre.pingel@zarm.uni-bremen.de, [2]Michael.dreyer@zarm.uni-bremen.de

Introduction

The phase separation of hydrogen is a current research theme in the field of space technology which is of special interest concerning two different applications in future cryogenic propulsion systems: on one side for the gas- or vapor-free delivery of the liquid propellant to the combustion chamber and on the other side for the liquid-free venting to condition the propellant. Phase separation can be realized using the retention capability of a screen or double screen against liquid as shown by Behruzi et al. 2013 [1].

Both applications are conceivable with autogenic pressurization in a one species two-phase fluid system consisting of liquid hydrogen and gaseous hydrogen as well as pressurization with a non-condensable gas in a two species two-phase fluid system consisting of liquid hydrogen and gaseous helium.

In this project a cryogenic test facility has been developed which allows to analyze the physical effects which are related to the retention capability of a double screen against liquid hydrogen in gaseous hydrogen environment during ground (1g) and drop tests (0g).

Numerical test predictions

The development of the test facility required the provision of test predictions of the expected physical effects.

Using the commercial computational fluid dynamics program Flow-3D, a first two dimensional, numerical, model could be generated. The model depicts the physical effects radial wicking, capillary rise supported by an external pressurization, bubble point pressure and screen cross flow pressure loss in combination under isothermal, incompressible conditions (**Fig. 1** top right).

Cryogenic test facility

With the aid of the test predictions, the development and building of the cryogenic test facility could be accomplished. The test section is depicted exemplarily in **Fig. 1** (left).

The double screen (a) consists of two cylindrical dutch twilled weave metal screens with 200 warp and 1400 weft wires per square inch. The screens are fixed inside an inner glass cylinder (b), which is immerged into an amount of liquid hydrogen (c) provided inside an outer glass cylinder (d). The cryogenic thermal environment has been provided by a helium bath cryostat which contains the described test section and which can be housed inside a drop capsule.

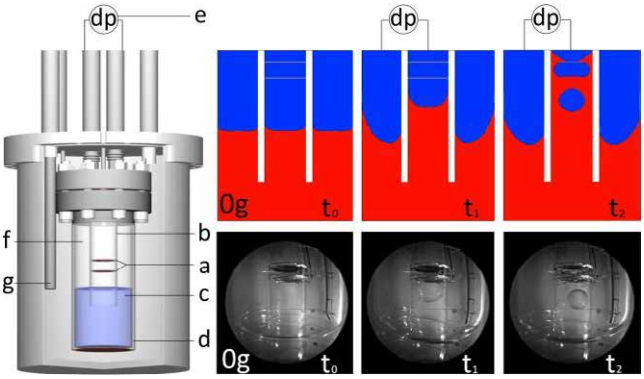

Figure 1: Experimental setup, numerical test predictions and results of a corresponding microgravity experiment.

Experiments

An experimental campaign consisting of 14 tests in earth gravity and three drop tests in microgravity using the drop tower at the University of Bremen has been conducted.

With the aid of an external pressurization system different differential pressures (e) acting at the gaseous phase of the outer glass cylinder (f) have been applied to accelerate the liquid phase inside the inner glass cylinder towards the double screen (**Fig. 1** downright).

During all tests wall temperatures at the outer glass cylinder and at the inner glass cylinder at the height of both screens have been measured. In addition to that the differential pressure of the gaseous hydrogen phases between the inner and outer glass cylinder has been recorded (e) as well as the absolute pressure of the gaseous hydrogen phase in the inner glass cylinder. Using a laser for illumination and an endoscope (g) with connection to a CCD camera, videos could be recorded to track the liquid movement.

Conclusions

The experimental results confirm the predicted governing physical effects. In addition to that, influences due to evaporation and condensation have been observed. Both numerical and experimental results will be presented.

Acknowledgements

The project under the grant number 50RL1621 is funded with means of the German Federal Ministry of Economic Affairs and Energy through the German Aerospace Center (DLR e. V.). We would like to thank Frank Ciecior, Holger Faust, Peter Prengel and Ronald Mairose for their technical support and invested effort for the help of the preparation and conduction of the experiments.

References

[1] P. Behruzi, J. Klatte, G. Netter, Passive Phase Separation in Cryogenic Upper Stage Tanks, AIAA 2013-3905, (2013).

Oral 044

Aerobatic parabolic flights in Barcelona. Review of research and educational activities.

A.Perez-Poch[1,2],D.V. González[2]

[1]UPC BarcelonaTech, Spain,[2] Aeroclub Barcelona-Sabadell, Spain.
antoni.perez-poch@upc.edu

Introduction

We present an innovative method of performing parabolic ights with aerobatic single-engine planes. A parabolic platform has been stablished in Sabadell Airport (Barcelona, Spain) to provide an infraestructure ready to allow Life Sciences and Physical hypogravity experiments to be conducted in parabolic flights. We report on diverse research and educational experiments that have been conducted throughout the last decade.

1. Parabolic Flight Operations

Test flights have demonstrated that up to 8 seconds of reduced gravity can be achieved by using a two-seat CAP10B aircraft, with a gravity range between 0.1 and 0.01g in the three axis. A parabolic flight campaign may be implemented with a reduced budget, and with a very short time-to-access to the platform. Operational skills and proficiency of the pilot controling the aircraft during the maneuvre, sensitivity to wind gusts, and aircraft balance are the key issues that make a parabola successful. Efforts have focused on improving the total zero-g time and the quality of reduced gravity achieved, as well as providing more space for experiments. We report results of test flights that have been conducted in order to optimize the quality and total microgravity time. A computer sofware has been developed and implemented to help the pilot optimize her or his performance (Brigos et al., 2014).

Figure 1: CAP10B aircraft.

2. - Objectives

The objectives of these unique parabolic flights with an aerobatic single-engine aircraft are:

2.1.- Scientific:

- To study different processes in which abrupt changes of gravity workload are applied. In particular: hyper (3 – 3.5g) to hypogravity (0.01g) , and hypo to hypergravity periods.
- To analyse transient phenomena that may occur after short periods of hyper and hypogravity.
- To allow experiments for testing the equipment in a real parabolic flight, with the opportunity to manually interact with the equipment and provide a proof-of-concept before accessing other microgravity research platforms.
- If the experiment can be run in less than 8 seconds of exposure to hypogravity, and the residual acceleration of 0.05 g is acceptable, then quantitative and qualitative measurements can be made, thus providing meaningful data. The parabolic flight can provide 10-15 parabolas in a single flight, and weather permitting the procedure can be repeated in a single day. The facility enables different subjects to test the scientific hypotheses, one by one on board.

2.2. Technological:

- Assessment of technological equipment behaviour in a hyper and hypogravity environment with abrupt changes in a tiny environment.
- Safety assessment of experiments and technological demonstrations within a parabolic flight aircraft 127 cockpit.
- Training of wannabe or future astronauts for foreseen private or public space missions.

2.3. Educational and outreach

- Allowing students to conduct hands-on experiments in a real weightlessness experience.
- Increasing their interest for studying Science, Technology, Engineering and Mathematics (STEM) studies, in particular in the aerospace field.
- Providing students from different backgrounds and nationalities with the opportunity of working as a team with a common goal, while interacting with space professionals.
- Raising public interest in space research.
- Creating the opportunity for students to write and present their space research in relevant journals and congresses, and also to further apply to the space agencies educational programs.

3. Review of Life Sciences experiments.

A number of mainly Life Sciences experiments have been conducted throught the last decade (Perez-Poch et al., 2016). These experiments include some of them which have been conducted by students, who have later presented their results in relevant scientific meetings and journals. Human physiology experiments include validation of numerical models of microgravity effects, effect of gravity loads on brain signals, and more recently, a pioneering study on the effect of microgravity on human sperm samples (Boada et al, 2019).

Student projects include some Bachelor and Master Thesis with technological studies, and three editions of the Barcelona Zero Challenge, which resulted in journal papers and scientific meeting presentations. The topics of these student-led experiments were: reversible images in space, altered perceptions in microgravity, and the effect of mental calculations on the cardiovascular system.

Details of all these research projects will be given in the final presentation, with emphasis in the data outcome of these experiments.

Conclusions

We conclude that aerobatic parabolic flights have proven to be a safe and reliable way to conduct life sciences and physical hypogravity experiments, both for research and educational purposes. This unique platform, a result of a cooperation between a leading Tech University (UPC) and an aerobatic team at the Barcelona Flight School provides a unique testbed for experimentation prior to access to other microgravity platforms. International and multidisciplinar cooperation has been very important to make this platform successful. The platform is permanently open to scientific cooperation.

References

Brigos M., Perez-Poch A., Torner J., Alpiste F., González D.V., "Parabolic flights with single-engine aerobatic aircraft: flight profile and a computer simulator for its optimization.**"** *Microgravity Science and Technology*, 26, **4** ,(2014), 229-239.

Perez-Poch, A.; D. V. González, D. López, "Hypogravity research and educational parabolic flight activities conducted in Barcelona: a new hub of innovation in Europe." *Microgravity Science and Technology*, 28, **6** ,(2016), 603-609.

Boada M., Perez-Poch A., Ballester M., García, S., Alonso, D.V., Rodríguez I., Barri P., Veiga A.,"Effect of microgravity on frozen human sperm samples. Can they be sent to space?". *Proceedings of the European Society for Human Reproduction and Embriology Annual Meeting* (2019), Viena, Austria.

Oral 046

Interfacial tension measurements using electrostatic levitation furnace (ELF) in ISS

M.Watanabe[1]

[1]Department of Phtsics, Gakushuin University, Tokyo, Japan;
masahito.watanabe@gakushuin.ac.jp

Introduction

We planned to measure this interfacial tension using core-shell droplets with an oscillating drop technique in microgravity (Watanabe *et al.* 2016). To execute the measurement of interfacial tension between molten oxide and steel melts forming a core-shell droplet, we are able to use ELF installed in the KIBO module of ISS (Tamaru *et al*. 2015). The interfacial tension values between molten oxides and steel melts requirement in steel industries applications. It is difficult to estimated them, so we must measure them. Because iron melts and molten oxides, however, have high melting temperature, the measurements should be used the non-contact measurements method with containerless technique. We select the electrostatic levitation method to achieve both requirements for the measurement of interfacial tension between molten oxide and iron melts which form core-shell droplet. ELF facilities have been already installed in ISS, therefore, we can use the facilities for our measurements plan. Under microgravity conditions, the shape of two immiscible liquids is dominated by the relationship between surface and interfacial free energies. By selecting the relationship between surface and interfacial free energies, we can make a core-shell droplet under microgravity. This means that we can know the interfacial tension, which is the interfacial free energy per unit area, using the core-shell droplet. We have been measuring the surface tension from thesurface oscillation frequencies using the levitated liquid droplets, which is called drop oscillation technique (Safferen *et al*. 1981). By modifying the technique, we should also be able to measure interfacial tension using a core-shell droplet. The technique can only be applied for the core-shell droplet under microgravity, because on ground conditions we cannot make the core-shell droplet due to the density differences between two immiscible liquids. For ISS experiments using ELF, we performed a short duration microgravity experiment by the parabolic flight of airplane for the decisions of the relationship between surface and interfacial free energies by molten oxides and iron melt. In this paper, we review our preparative research results on ground for ISS experiments using ELF.

ELF-ISS for thermophysical property measurement under microgravity

On ground conditions, ESL needs high voltage input to the electrodes for sample levitation, therefore, the ultra-high vacuum conditions are necessary for avoiding electric spark. This condition makes difficulty of molten oxide levitation experiments. However, under microgravity in ISS, since droplet samples always levitate in the chamber, ELF-ISS is not necessary high voltage for levitation. Therefore, using ELF-ISS we can measure thermophysical properties of molten oxide samples under controlled gas atmosphere conditions. The main configuration shown in Fig.1 is "chamber" which heats and melts the sample, "sample cartridge and holder" which supplies and recovers the sample, "laser" for heating and melting the levitated sample, "Sample observation equipment" for observing sample position and its shape, and “Sample position control equipment"(Tamaru *et al*. 2018). The chamber has a 24-faces polyhedron structure made by Al, and the size of the polyhedral part is about 200mm×200mm. A sample holder filled with the samples for measurement is attached to the sample cartridge and inserted into thechamber by the astronaut. The sample holder can be set 15 samples with the diameter of 2mm. In the sample cartridge, for sample position control 6 electrodes with three axial directions placed at the center are installed. The sample is automatically supplied and recovered from the sample holder with the rotating mechanism. The sample can be uniformly heated and melted by the semiconductor lasers (980nm, 40W) from 4 directions. Laser beam is focused at the sample position, and reproducibility of the condensing position is secured with accuracy of ± 0.1 mm or less even when laser is moved. The sample temperature measures by a single-color pyrometer with the range of 300 to 3000°C in an accuracy of less than 10°C. For sample observation, we use 3 units of overview observation camera, magnifying observation camera, temperature measurement position check camera which is set at the pyrometer view port (Fig.1). The overview observation camera is used for observing the levitation behavior of the sample. In the magnifying observation camera, we can observe the shadow image by the UV-LED backlight system. From the image using this camera, we can obtain the sample shape for the density measurements. For the position control of the levitated sample, parallel light is irradiated using the two semiconductor lasers for the sample position recognition, and the sample position is detected with two facing position sensitive sensors. From the detected sample position signal, the voltage between the electrodes can be changed with high speed PID control to allow stable levitation of the sample.

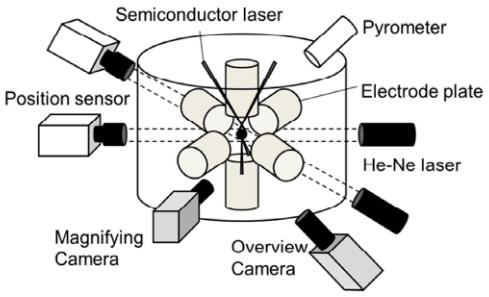

Figure 1: Schematic diagram of electrostatic levitation furnabe (ELF) installed in ISS.

Observation of core-shell droplet formation undershort duration microgravity condition

We must confirm formation of core-shell droplet bymolten oxides and iron melts under the microgravity conditions before on-orbit experiments in ISS. For the requirements, we observed the formation of core-shell droplet under the microgravity condition by parabolic flight experiments using Gulfstream-II (G-II) airplane operated by Diamond Air Service Inc.. On the parabolic flight experiments, we cannot use the electrostatic levitation furnace because it is difficult to keep the sample position during parabolic flight due to rapid change of the gravity level. Therefore, we used electromagnetic levitation for observation of the formation of core-shell droplet by molten oxide and steel melts. We newlydeveloped the compact size electromagnetic levitation facilities specialized for the parabolic flight experiments by G-II airplane. Using the facilities, we succeed to observe the formation of core-shell shape droplet by molten oxides and iron melts (Onodera *et al*. 2016)[8]. Fig. 2 shows timeseries images of the formation of core-shell droplet by molten oxide and metal liquids taken by high-speed camera under microgravity during parabolic flight. Fig.2 (a) shows the case of oxides corresponding to the model oxide composition of blast furnace slag. On the other hand, Fig.2 (b) -(d) shows the model oxide composition of welding flux. In the case of Fig.2 (a), iron melt and molten oxide are separated even after 5 seconds from the complete melting, and about half of iron melt volume is engulfed by molten oxide. We clearly found that iron melt and molten oxide under this condition cannot form the coreshell droplets. On the other hand, Fig. 2 (b)-(d) shows that, after complete melting, molten oxides surround iron melts and finally they form core-shell droplets. For Fig.2 (b) - (d), the oxide composition is the same but their volume is difference under the constant iron volume. The volume differences are indicated by the ratio of the core radius (iron melt) and the shell radius (molten oxide) with (b) 1.01, (c) 1.07 and (d) 1.2. From the results in Fig. 2, for the case where the oxide volume is small and its layer is thin (Fig. 2 (c)), we observed that the fragmented molten oxides pieces coalesce while moving on the surface of the iron melt and gradually covers iron melt surface. As shown in Fig. 2 (c) and (d), when the volume of molten oxide is increased and the oxide layer becomes thick, the core-shell droplet is formed rapidly with molten oxide covering iron melt without fragmentation of molten oxide. In the case of Fig. 2 (d), core-shell droplets are formed in about 20msec after complete melting of both iron and oxide, so that core-shell droplets can be instantaneously formed under microgravity. The amount of oxide in the case of Fig. 2 (d) is same as the condition that clearly observes the two oscillation peaks confirmed from the numerical simulation. Based on the experimental results and numerical simulations, we already prepared for ISS experiment samples as the same conditions for Fig.2(d) experiments with oxide composition and the radius ration to the iron melt.

Conclusions

The preparative research for the project to measure interfacial tension between iron melt and molten oxide using ELF in ISS are shown. In the interfacial tension measurement, it is necessary to form a core-shell droplet in order to measure the surface oscillation frequency of the core-shell droplet. We confirmed that the surface oscillation frequencies of the core-shell droplet show the same fashion as the analytical solutions from the direct observation of core-shell droplet oscillation behaviours on ground and numerical simulation. Based on this numerical simulation, observation of core-shell droplet formation in a short duration microgravity condition. From these preparative researches, we examined the possibility of precise measurement conditions of interfacial tension in ISS using ELF.

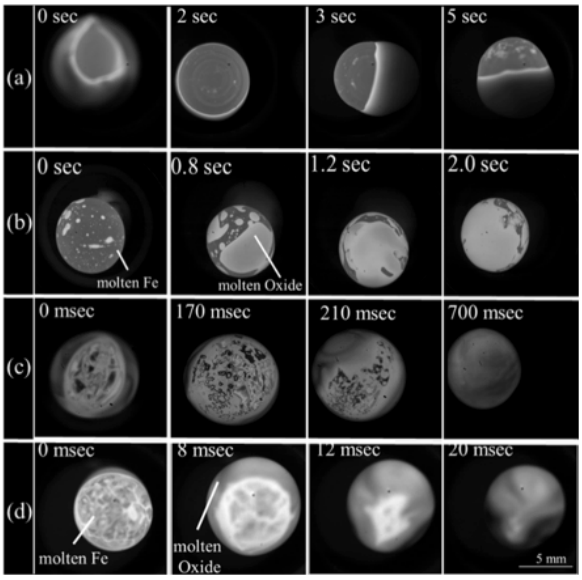

Figure 2: Drop formation of iron melt and molten oxides under microgravity conditions, (a)case of oxide composition with $CaO:Al_2O_3:SiO_2$=14:36:50, and (b)-(d) cases of oxide composition with $CaO:SiO_2:Mn_3O_4:TiO_2:Fe_2O_3$= 25:7:23:18:27. (b)-(d) are cases of different ratio of core radius to outer radius of core-shell drop: (b)1.01, (c)1.07 and (d) 1.2.

Acknowledgements

The author would like to thank Dr. C. Koyama, Ms.H. Tamaru, Mr. H. Saruwatari, Mr. H. Oda (JAXA) for ELF operation and technically supports. INTERFACIAL ENERGY project collaborates with Prof. T. Tanaka (Osaka Univ.), Prof. T. Tsukada (Tohoku Univ.), Prof. T. Ishikawa(JAXA), Prof. S. Ozawa (Chiba Inst. Tech.), Prof. H. Fukuyama (Tohoku Univ.), Prof. J. Lee (Korea Univ), Prof. A. Meyer, Prof. F. Kargle (DLR), Prof. R. H. Hyers, (Massachusetts Univ.), Assoc.Prof. J. Lee (Minnesota Univ.), Prof. A. Jarfors, Assoc.Prof. T. Matsushita (Jönköping Univ.). The author would like to thank their collaborations. This work is financially supported by JAXA, JSPS KAKENHI Grant Numbers JP18H01386 and MEXT-Supported Program for the Strategic Research Foundation at Private Universities (2015-2019).

References

M. Watanabe, T. Tanaka, T. Tsukada, T. Ishikawa, H. Tamaru and A. Mizuno, Int. J. Microgravity Appl., 32(2015)320102-1-6.

H. Tamaru, T. Ishikawa, J. T. Okada, Y. Nakamura, H. Ohkuma, S.Yukizono, Y.Sakai and T. Takada, Int. J. Microgravity Appl., 32 (2015)320104-1-7.

M. Saffren, D. Ellmann and W. K. Rhim, *Proc. 2nd international colloquium on drops and bubbles,* (1981)7-14.

K. Onodera, K. Tanaka, Y. Ishii, Y. Yamada, S. Nishikoori, H. Goto, M. Watanabe, A. Mizuno and T. Tanaka, Int. J. Microgravity Appl., 33(2016) 330218-1-5.

Oral 047

Thermoconvective instabilities during droplet evaporation in microgravity: infrared experimental observations and numerical modelling

Kumar S.[1], Médale M.[1] and Brutin D.[1,2]

[1] Aix-Marseille University, CNRS, IUSTI, Marseille, France
[2] Institut Universitaire de France, Paris, France

Abstract
Our current research is focused on thermal Marangoni instabilities in sessile ethanol and HFE_7100 droplets, which develop spontaneously during evaporation. We detail in the present abstract the numerical modeling in 3D unsteady with moving interface of a sessile droplet under forced evaporation and showing internal flow instabilities. During the presentation, we will compare the numerical results with experimental results obtain with ARLES in microgravity during the ESA SSC MASER-14 campaing.

Introduction

One distinctive type of these thermo-capillary instabilities is called hydrothermal waves (HTW). Conventional HTWs are observed in thin liquid layers whose surface is subject to a lateral temperature gradient. In sessile droplets, however, the HTWs are driven by the process of evaporation which generates these temperature gradients naturally. These instabilities have been observed in droplets of volatile liquids (ethanol, methanol, FC-72) on heated substrates by few researchers [Brutin, 2011; Carle 2012; Sefiane 2013; Sefiane 2008; Sobac, 2012]. It is still not clear what is exactly observed in sessile droplets: is it hydrothermal waves or unsteady Benard-Marangoni (BM) instabilities, or a combination of both? In order to answer this question, it is necessary to understand underlying hydrodynamics and heat transfer, since according to Smith and Davis [Smith, 1983a, 1983b], HTWs are distinguished from other thermo-capillary instabilities by the following attributes: they appear only as a secondary unsteady thermo-convective instability in a basic shear flow (primary thermo-capillary flow) directed along the longitudinal temperature gradient at the liquid surface; the mechanism of HTWs propagation does not require any deflection of the free surface of the liquid layer. The ultimate aim of current research is to achieve both qualitative and quantitative agreement between computer simulations and experiments. Achieving the first one would require a 3D numerical modelling, as the flow observed in drops [Carle, 2012; Sobac, 2012] is essentially three-dimensional. Meanwhile, 2D axisymmetric modelling is quite sufficient for the quantitative validation, because the most appropriate for that purpose and experimentally measurable quantity is the droplet's evaporation rate, which is weakly influenced by the 3D flow pattern inside a droplet.

Experimental Facility / Numerical Methods

In the present paper, we first present the quantitative validation and, therefore, 2D axisymmetric numerical models, which consider all relevant processes of heat and mass transfer, essential for the achievement of quantitative agreement with experiments. The original contribution comprises obtaining a semi-empirical formula for the droplet's evaporation rate, increasing the accuracy of experimental video-data processing (improved fitting of a sessile droplet profile and correction due to non-circular contact perimeter) and, finally, computer simulations reproducing the conditions of three particular microgravity experiments. From theoretical and numerical points of view, current research is a substantial improvement of our previous work [Carle, 2016]. We developed a 3D unsteady semi-analytical model coupling hydrodynamics and heat transfers in a sessile drop of ethanol on a heated substrate. We assume a pinned contact line and a spherical-cap shape of the liquid-gas interface. The computed temperature field is used for post-processing of top-view IR images of a semi-transparent droplet (in IR spectrum), which enabled to validate our model against experimental IR images. Our computations contribute to figure out the internal 3D flow structure in the droplet and also to determine the driving mechanism and energy sources of the observed thermo-convective instability and thus clarifies its nature. A Cartesian system of coordinates (x, y, z) is used, its origin is located at the geometrical center of the droplet-substrate contact area and the z-axis directed perpendicular to the liquid-solid interface pointing upwards. A semi-analytical formula has been previously developed to model the mass flow rate J (in $kg.s^{-1}$) of unsteady diffusion-limited evaporation for a non-isothermal pinned sessile droplet, while accounting for Stefan flow in the gas [Semenov, 2017]. Based on our model published in Semenov et al. [Semenov, 2017a, 2017b] the previous dynamics described in the literature has undoubtedly been erroneously attributed to HTWs, but they are actually BM instabilities. Indeed, the internal flow structure in the droplet reveals that there is no base shear flow directed along the tangential thermal gradient along the interface, basic condition to be satisfied for HTWs to appear according to [Smith, 1983a, 1983b; 1986].

Therefore, these experimentally observed thermo-convective instabilities cannot be classified as HTWs, but actually unsteady Benard-Marangoni instabilities. In order to get quantitative observable comparisons between computations and experimental results, we post-processed simplified IR images based on computed temperature field. Experimental IR was recorded from droplet top view with a camera "VarioCam® hr head" in the mid-wavelength IR range. For the numerical IR post-processing, we considered the semi-transparency of liquid ethanol in the mid-wavelength (MW) bandwidth: according to the spectrophotometer

measurements by Brutin et al. [Brutin, 2011], ethanol's absorption coefficient in the MW range. Using this value, one can compute the intensity of IR radiation arriving at the camera installed above the droplet, which then can be converted into an equivalent blackbody temperature. This computation is done by summing the IR radiation coming from the substrate surface (assumed to be a gray body) with the integral of IR radiation sources distributed across the thickness of a semi-transparent droplet:

$$T^4_{IR,num}(x,y) = \varepsilon T_s^4 e^{-af(x,y)} + \int_0^{f(x,y)} T^4(x,y,z) a\, e^{-a(f(x,y)-z)}\, dz,$$

The governing equations have been implemented in the COMSOL Multiphysics® software, discretized with the finite element method (FEM) using second-order shape functions. Computations start with a uniform initial temperature field (at substrate heating temperature) in the droplet and the imposed heating temperature at the substrate surface. Due to the latent heat of vaporization, the droplet cools down from the liquid-gas interface, meanwhile, the temperature near the contact line remains higher due to heat conduction from the substrate through a thin layer of ethanol. This creates a vertical temperature gradient in the droplet bulk and a tangential one along the droplet surface near the contact line. These temperature gradients promote the development of thermocapillary Benard-Marangoni instability.

On Fig. 1. we display the top view of the time evolution over the first 22s during the evaporation process of the sessile droplet deposited on a heated substrate. First of all, a pattern composed of roughly 10 cells appears within the first second. The central cells cluster in two large ones which propagate radially outward and split into small cells near the rim. The number of cells evolves marginally with time as some cells are merging and then splitting.

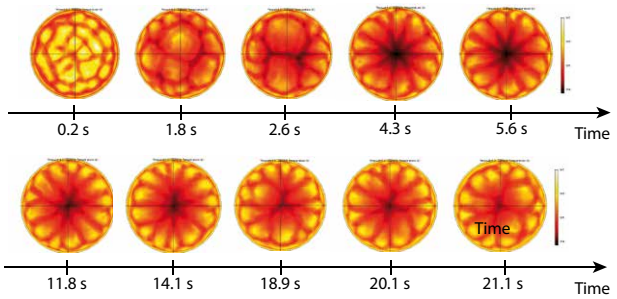

Figure 1: 3D unsteady numerical simulation of an ethanol sessile droplet evaporation evidencing Benard-Marangoni instabilities with cells merging then splitting.

Conclusions

We report a 3D one-sided numerical model of an evaporating sessile droplet of ethanol on a heated substrate. A good qualitative agreement has been obtained leading to quantitative comparison with the experimental data [Semenov, 2016, 2017]. Based on the computed temperature and flow fields we conclude that the experimentally observed thermo-convective pattern in the droplet is an unsteady Benard-Marangoni instability and is different from hydrothermal waves.

Acknowledgements

We would like to thank CNES and ESA for their financial support over the last years. We would like also to thanks SSC and all the scientific team for the contribution to the success of ARLES.

References

Brutin, D., Sobac, B., Rigollet, F., and Niliot, C. L., "Infrared visualization of thermal motion inside a sessile drop deposited onto a heated surface," Exp. Therm. Fluid Sci., 35, (2011).

Carle, F., Semenov, S., Medale, M., and Brutin, D., Contribution of convective transport to evaporation of sessile droplets: Empirical model, Int. J. Therm. Sci. , 101, (2016).

Carle, F., Sobac, B., and Brutin, D., Hydrothermal waves on ethanol droplets evaporating under terrestrial and reduced gravity levels, J. Fluid Mech. , 712, (2012).

Sefiane, K., Fukatani, Y., Takata, Y., and Kim, J., Thermal patterns and hydrothermal waves (htws) in volatile drops, Langmuir, 29, (2013).

Sefiane, K., Moffat, J. R., Matar, O. K., and Craster, R. V., Self-excited hydrothermal waves in evaporating sessile drops,"Appl. Phys. Lett., 93, (2008).

Semenov, S., Carle, F., Medale, M., and Brutin, D. Boundary conditions for a one-sided numerical model of evaporative instabilities in sessile drops of ethanol on heated substrates, Physical Review E., vol. 96, 063113, 2017.

Semenov, S., Carle, F., Medale, M., and Brutin, D., "3D unsteady computations of evaporative instabilities in a sessile drop of ethanol on a heated substrate," App. Phys. Lett., 111(24), pp. 241602–241607, (2017).

Smith, M. K., Instability mechanisms in dynamic thermocapillary liquid layers, Phys. Fluids, 29(10), (1986).

Smith, M. K. and Davis, S. H., Instabilities of dynamic thermocapillary liquid layers. part 1. convective instabilities, J. Fluid Mech. , 132, (1983).

Smith, M. K. and Davis, S. H., Instabilities of dynamic thermocapillary liquid layers. part 2. surface-wave instabilities, J. Fluid Mech. , 132, (1983).

Sobac, B. and Brutin, D., Thermocapillary instabilities in an evaporating drop deposited onto a heated substrate, Phys. Fluids, 24, (2012).

Oral 048

Crystallization of a transparent model alloy under reduced gravity conditions – the MEDI-2 experiment aboard TEXUS-55 sounding rocket

L. Sturz[1], Martin Hamacher[1], G. Zimmermann[1]

[1] *ACCESS e.V., Intzestrasse 5, 52072 Aachen, Germany,*
L.Sturz@access-technology.de, M.Hamacher@access-technology.de, G.Zimmermann@access-technology.de

Abstract

Modeling and understanding crystallization involving microstructure formation is of crucial relevance to improve solidification processes and material properties. In many technical applications, a polycrystalline microstructure consisting of small equiaxed dendritic grains is preferred, because of its isotropic materials properties with good mechanical performance. After nucleation upon cooling, equiaxed dendrites crystallize with growth of a hierarchical solid structure, the dendrite, similar to a snowflake. The dendritic arms grow along preferential crystallographic orientations, often reflecting the crystal symmetry. At later stage of growth, equiaxed dendrites interact mutally and form the final solidified grain structure. Deviations from the simple relationship between crystallographic orientation and crystal structure are well-known even for a single alloy with changing composition and are devoted mainly to a change of surface tension with composition. Up to now, the relationship between crystallographic orientation of the equiaxed dendrites and nucleation behaviour, as well as growth behaviour is largely unknown. We have investigated nucleation and growth in the organic transparent alloy Neopentylglycol-20.0 wt.% (D)Camphor, which crystallizes with a dendritic morphology similar to metallic alloys. The experiment, involving multiple equiaxed dendrites and their interaction (MEDI-2) was carried out aboard the sounding rocket TEXUS-55 mission in 2018. Reduced gravity environment provides conditions without convection in the melt and sedimentation of the equiaxed dendrites. The experimental conditions were chosen such as to obtain diffusive conditions for heat and mass transport during the microgravity period. The microstructure formation was observed in-situ with two different optical systems to analyze the global and the microscopic features of equiaxed crystallization. We obtain equiaxed dendrites with six dendrite arms growing perpendicular to each other, typical for a <100> crystallographic orientation. From the experiment different parameters, like nucleation rate, the growth velocity of the dendrite arms as well as the dendrite undercooling were determined during the whole experiment. The experiment complements the previously performed experiment MEDI, in which a different crystallographic orientation <111> was obtained at higher (D)Camphor composition. Results of both experiments are compared to investigate the effect of crystallographic orientation on the aforementioned phenomena.

26th European Low Gravity Research Association Biennial Symposium and General Assembly
14th International Conference on "Two-Phase Systems for Space and Ground Applications"
European Space Agency Topical Teams meetings
Granada (Spain), September 24-27, 2019

Oral 049

Marangoni instabilities in evaporating sessile droplet on liquid-infused slippery surface

Ji-Long Zhu[1], Wan-Yuan Shi [1,2], Tian-Shi Wang[1]

[1] School of Energy and Power Engineering, Chongqing University, Chongqing, China
[2] Key Laboratory of Low-grade Energy Utilization Technologies and Systems, Ministry of Education, Chongqing, China
892498678@qq.com, shiwy@cqu.edu.cn, CQMr.Wang@cqu.edu.cn

Introduction

Evaporating sessile droplets are ubiquitous in daily life but practically complicated problem involving diffusive and convective vapour transport, evaporative interface cooling, dynamic wetting, buoyancy flow, Marangoni convections, etc. Among them, in past decades, Marangoni convections have received more and more attentions both for the academic and industry communities. For some organic droplets such as methanol, ethanol, FC-72, n-hexane and silicone oil, several kinds of Marangoni instability phenomena were observed, including in hydrothermal wave (Sefiane et al. 2008), Bénard-Marangoni cell(Wang and Shi 2019) and longitudinal roll(Zhu and Shi 2019), and so on. Noticed that the evaporation mode of sessile droplet significantly depends on the features of the substrate. For instance, constant contact line(CCL) mode is obtained of droplets evaporating on PTFE, Macor, titanium, copper (Sefiane et al. 2008) and FC-3120 coating (Wang and Shi 2019). Moreover, constant contact angle(CCA) mode is also successfully achieved on a coated superhydrophobic solid surface(Zhu et al. 2019). Recently, a new type of surface, the slippery liquid-infused porous surface (SLIPS) with low sliding angle(Wong et al. 2011) which exhibits some excellent properties, i.e. self-healing, self-cleaning, hydrophobic and oleophobic, have been received wide attention. However, up to now, to the best of our knowledge, there is actually no report on Marangoni instability phenomenon in droplet evaporating on SLIPS. In this work, the evaporation behaviors and the Marangoni patterns in methanol droplet evaporating on SLIPS were investigated through a series of experiments. Some phenomena different from those on solid surface were observed and analyzed.

Experimental apparatus

The experimental apparatus is illustrated in Figure1 for the evaporation of a sessile droplet of methanol deposited onto a heated cylindrical SLIPS with diameter of 60±0.1mm. A thermostatic oil bath (PP07R-20-A12Y, PolyScience Inc.) was adopted to control the substrate temperature, and the actual temperature of the substrate (T_w) is measured by four bare T-type thermocouples with diameter of 0.25 mm (Omega Engineering Inc.) mounted on the upper surface of the substrate. The SLIPS is formed through 10cSt silicone oil-infused slippery surface based on nanostructured copper compound surface. An infrared camera (FLIR A655sc) with a close-up IR lens is vertically upside down mounted above the droplet to monitor the Marangoni instability patterns on the droplet surface. Meanwhile, a contact angle meter (Powereach JC2000DM) with resolution of 0.01° is used to monitor the side view of the droplet. To reduce the disturbance of surround air flow, an upper open plexiglass box is adopted to enclose the main apparatus.

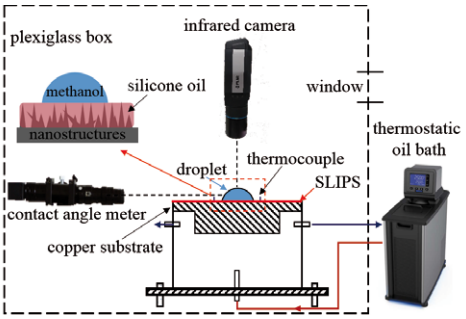

Figure 1:The schematics of the experimental apparatus.

Experimental results and discussions

Figure 2 illustrates the evolutions of contact angle(θ) and the wetting radius(r) of a drople evaporating at substrate temperature T_w=35.78˚C and environment temperature T_a=20.08˚C.With the triple line shrinking after the droplet deposited onto the substrate, the contact agnle increases gradually. The reason is that some of the lubricant are pulled out from the nanostructures by droplet, i.e., the nanostructure under the droplet is not fully filled with the oil. A kind of Cassie−Baxter state thus occurs during this period (McHale et al. 2019). After t=56s, with the wetting radius decreasing, the contact angle decreases again until the droplet vanishes.

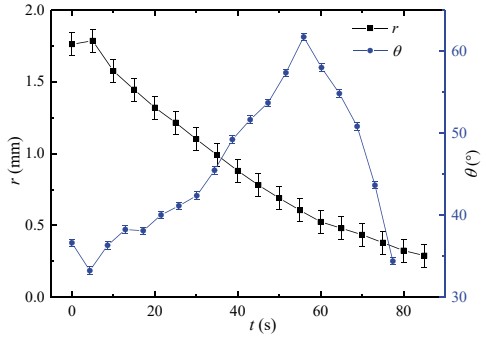

Figure 2: The evolutions of contact angle and the wetting radius of the droplet at T_w=35.78˚C, T_a=20.08˚C and the relative humidity of 55% ± 10%.

Figure 3 shows the evolution of the surface temperature of droplet evaporating at T_w=35.78˚C and ambient temperature T_a=20.08˚C (described in Figure 2). At the beginning, the surface temperature is uniform along azimuthal direction while the temperature near triple line is higher than that of apex (Figure 3a). After a while, a kind of thermal oscillatory waves appear near the triple line (Figure 3b). At about t=5.5s, the waves occupy the whole droplet (Figure 3c). These waves travel from a source to a sink, which are composed of the clockwise propagating waves and the counterclockwise propagating waves. The positions of the source and sink are

not fixed but slowly moved in azimuthal direction during the evaporation (Figures 3d to 3f). Different from the HTWs observed in droplet evaporating on solid surfaces when contact angle is small(<12º)(Sefiane et al. 2008), these waves are wider and the wave number is much smaller due to the larger contact ange(>36º). With the contact angle increasing, the waves become wider and wider and the wave number decreases. At t=31.5s, the HTWs are replaced by a kind of oscillatory convection (Figure 3i). A hot circular region periodically rotates in clockwise or counterclockwise direction. This kind of periodical oscillatory convection is similar as the *oscillatory transition convection* predicted by Shi *et al.* (2017). With increaseing the T_w, the frequency of oscillatory convection first increases slowly and then sharply after T_w >35˚C.

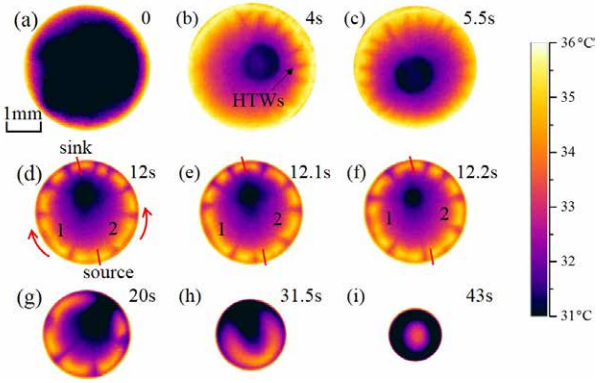

Figure 3: Evolution of the free surface temperature patterns of a droplet with the initial radius r_0=1.76mm at T_w=35.78˚C, T_a=20.08˚C and the relative humidity of 55% ± 10%.

For T_w≥40˚C, the Marangoni patterns transform from BM convection to HTWs and then to the oscillatory convection. One typical example of the Marangoni convection pattern for T_w=40.03˚C is shown in Figure 4. At t=5s, some small cells appear near the triple line(Figure 4b). Slightly latter, totally 21 cells are distributed in the droplet and the outer profile of each cell is circular-arc(Figure 4c). The cell patterns do not propagate and they are the same as the BM cells(Wang and Shi 2019, and Zhu et al. 2019). With the time going on, some bigger BM cells continuously separate into two small cells(Figures 4d-4e). With the receding of wetting radius, when the contact angle increases to 37.8º at 15.6s, the patterns transform from BM cells to HTWs(Figures 4f). After that, the characteristics of Marangoni convection are consist with those under T_w<40˚C(Figures 4f-4h).

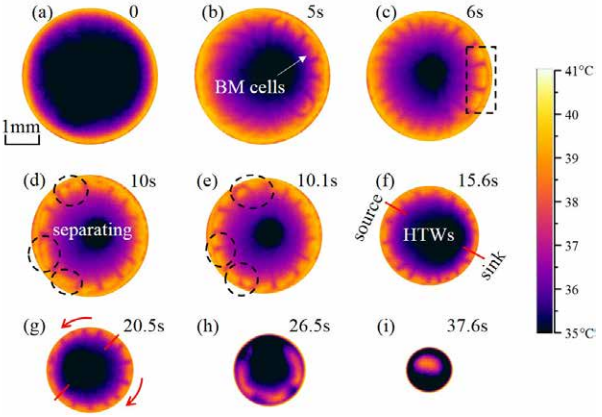

Figure 4: Evolution of the free surface temperature patterns of a droplet with the initial radius r_0=1.94mm at T_w=40.03˚C, T_a=20.22˚C and the relative humidity of 55% ± 10%.

Conclusions

Marangoni patterns in methanol droplet evaporating on liquid-infused slippery surface were investigated through a series of experiments. For T_w<40˚C, two kinds of convection modes occur in sequence, i.e. HTWs and oscillatory convection. With the contact angle increasing, the waves become wider and wider and the wave number decreases. The frequency f of the oscillatory convection increases with T_w. For T_w≥40˚C, with the receding of wetting radius, the Marangoni patterns transform from BM cell to HTWs and then to the oscillatory convection.

Acknowledgements

This work was funded by the National Natural Science Foundation of China (Nos. 51676018 and 51176210) and the Fundamental Research Funds for the Central Universities (No.2018CDXYDL0001).

References

K. Sefiane, J. R. Moffat, O. K. Matar, R. V. Craster. Self-excited hydrothermal waves in evaporating sessile drops. *Appl. Phys. Lett.*, 93(2008) 074103.

T.-S. Wang, W.-Y. Shi. Influence of substrate temperature on Marangoni convection instabilities in a sessile droplet evaporating at constant contact line mode. *Int. J. Heat Mass Transfer*, 131 (2019): 1270-1278.

J.-L. Zhu, W.-Y. Shi. Longitudinal roll patterns of Marangoni instability in an easily volatile sessile droplet evaporating at constant contact angle mode. *Int. J. Heat Mass Transfer*, 134 (2019): 1283–1291.

J.-L. Zhu, W.-Y. Shi, Lin Feng. Bénard-Marangoni instability in sessile droplet evaporating at constant contact angle mode on heated substrate, Int. J. Heat Mass Transfer 134 (2019): 784–795.

T.-S. Wong, S. H. Kang, S. K. Y. Tang, E. J. Smythe, B. D. Hatton, A. Grinthal, J. Aizenberg. Bioinspired Self-Repairing Slippery Surfaces with Pressure-Stable Omniphobicity. *Nature*, 477 (2011): 443−447.

G. McHale, B. V. Orme, G. G. Wells, R. L., Aguilar. Apparent Contact Angles on Lubricant-Impregnated Surfaces/SLIPS: From Superhydrophobicity to Electrowetting. *Langmuir* 35 (2019): 4197-4204

B. Sobac, D. Brutin. Thermocapillary instabilities in an evaporating drop deposited onto a heated substrate. *Phys. Fluids* 24 (2012): 032103.

W.-Y. Shi, K.-Y. Tang, J.-N. Ma, Y.-W. Jia, H.-M. Li, L. Feng. Marangoni convection instability in a sessile droplet with low volatility on heated substrate. *Int. J. Therm. Sci.* 117 (2017): 274–286.

26th European Low Gravity Research Association Biennial Symposium and General Assembly
14th International Conference on "Two-Phase Systems for Space and Ground Applications"
European Space Agency Topical Teams meetings
Granada (Spain), September 24-27, 2019

Oral 050

PACKING GRAINS BY SHEARING

Diego Maza*

Granular Media Lab
Department of Physics and Applied Mathematics
Universidad de Navarra
Irunlarrea S/N, 31080, Pamplona, Navarra, Spain

In this work, we discuss experimental results showing the possibility of compacting an ensemble of cubic particles by alternative shearing the sample instead of tapping it against gravity. This idea has been numerically explored in microgravity conditions. The simulations show that this protocol could be handy to compact granular matter under this condition.

* Corresponding author: dmaza@unav.es

Oral 052

Gravity Effect on Gas Entity Patterns in a Co-Current Two-Phase Flow in a Mini-Tube

Salim Zeguai [1,*], Salah Chikh [2] and Lounès Tadrist [3]

[1] Yahia Farès University, Faculty of Technology, LMP2M Laboratory, Ain d'heb, Médéa 26000, Algeria
[2] USTHB, Faculty of Mechanical and Process Engineering, LTPMP, Alger 16111, Algeria
[3] Aix-Marseille Université, CNRS, Laboratoire IUSTI, UMR 7343, Marseille 13453, France
(*) corresponding author: S. Zeguai, Email adresse: zeguai_salim@hotmail.com

1. Introduction

The influence of gravity of the two-phase flow has received attention during the last decades from both the experimental and numerical points of views (Fukano and Kariyasaki, 1993, Ide and Fukano, 2007, Mehta and Banerjee, 2014). Nevertheless, many questions related to the size of bubbles, slugs and plugs and their evolution in pipes of small diameter remain not addressed.

In this context, an experimental investigation is carried out to visualize and analyze two-phase flow patterns in a 1.5 m long tube of 3 mm inner diameter with horizontal, vertical upward and vertical downward flow orientations and to highlight the evolution of the size of two-phase entities along the tube from the entrance zone (L/D=10) to the far downstream location (L/D=420). Inlet flow rates for both phases are carefully controlled so that superficial velocities are with a range from 0.78×10^{-3} m/s to 79×10^{-3} m/s for the liquid phase and from 2.3×10^{-3} m/s to 3.54 m/s for the gas phase in order to deal with smooth interfaces. A fast camera with 1000 fps is utilized to visualize the flow patterns. The size evolution of the gas entity along the tube is discussed and conclusion may be drawn with regard to breakup or coalescence phenomena along the tube. Two-phase flow maps are then deduced by means of a frequency measurement technique associated with an image processing tool. The transitions from one flow pattern to another are determined for both the entrance region and far downstream and the effect of gravity i.e. flow orientation on the transition curves is highlighted.

2. Experimental operating conditions

In order to control carefully inlet conditions, a coflowing configuration is considered. The gas phase is carried into the entrance tube through an injection system designed for the purpose (see Zeguai et al., 2013).

3. Measurement of gas entity

The equivalent diameter of the gas entity is measured in the inlet zone (L/D=10) after detaching from the injection nozzle and far downstream (L/D = 420). The measurement is based on the use of the frequency measurement method associated with image processing. For each zone explored and to obtain a good sample, 830 images are processed. The volume formation of gas entities is expressed by the following formula: $V_G = Q_G / f$ with Q_G being the gas flow rate, the bubble detachment frequency and $d = (6V_G/\pi)^{1/3}$ the equivalent diameter of the detached gas entities assumed to be of spherical shape, is deduced.

4. Variation laws of gas entity and frequency

The bubble equivalent diameters of gas entities are plotted versus the superficial gas velocity in the two explored zones (L/D=10 and 420) for three orientations of the two-phase flow with respect to gravity for a small value of the superficial velocity of the liquid phase U_{LS}=14.74 x 10^{-3} ms^{-1}.

a. Vertical downwward air-water flow

The variation law of the size of gas entity (Fig.1) evolves similarly in the two zones. It increases linearly with the augmentation of the superficial gas velocity. From a small value until a superficial gas velocity of U_{GS} = 16.4x10^{-3} m.s^{-1}, the bubbly and bubbly/slug structures at L/D=10 evolve towards the slug structure at L/D=420. The slugs are of equal size equidistant and with a regular formation frequency equal to 4.81 Hz. Beyond this superficial gas velocity U_{GS} = 16.4x10^{-3} m.s^{-1}, the slope of the linear variation increases at L/D=420, which means we obtain rapidely bigger slugs. This might be explained by the coalescence phenomenon since for the same inlet velocities, the slugs become bigger at the downstream location.

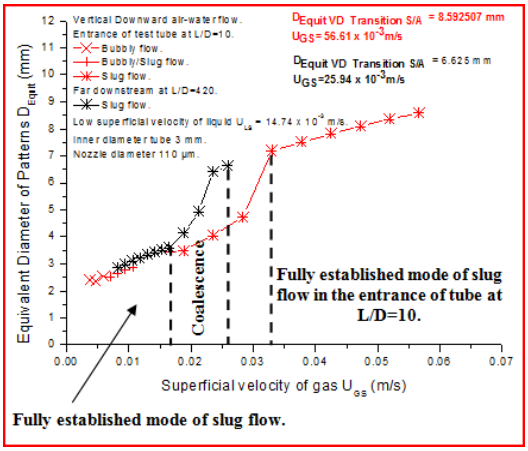

Figure 1. Size variation of gas entity in vertical downward air-water flow at L/D=10 and L/D=420.

By gradually increasing the superficial gas velocity of the gas phase, it is found that the frequency of the gas entity persists at the value of 1.2 Hz and no longer varies. On the other hand, the equivalent diameter of the slugs in the two zones increases towards the slug/annular transition limit with the same slope, up to the respective values of 8.59 mm and 6.62 mm corresponding to gas velocities U_{GS} = 56.6 × 10^{-3}m.s^{-1} and U_{GS} = 26x10^{-3}m.s^{-1} respectively. This behavior means that the effects of coalescence on the gas entities are completely mitigated, the slug regime is fully developed distinctly in each of the two zones at different gas velocities. Beyond these two velocity values, it can be seen that the

two-phase slug flow regime in the L/D=420 zone changes more rapidly towards the annular regime than the downstream one at L/D=10, transiting of course through the slug/annular regime. The slug regime is gradually established later along the pipe with the increase in the apparent velocity of the gas.

b. Horizontal air-water flow

For the horizontal flow, the size evolution of gas entities in the two explored zones reveals a substantial difference in size only for the bubbly flow regime Fig.2. The bubbles may double their size from the inlet zone (1-2 mm) to the far downstream zone (2-4 mm), and the frequency of bubble detachment which is between 10 and 50 hz drops down to an appearance frequency between 2 and 10 hz at L/D=420. In comparison with the vertical case, the limit of the coalescence zone slipped towards the low apparent gas velocities U_{GS}=16.5x10^{-3} m.s^{-1} (Fig.2).

Beyond this zone, the equivalent slug diameter varies linearly both at L/D=10 and 420 giving rise to a fully developed slug flow regime along the pipe to a frequency approximately regular of 6.02 Hz up to a superficial gas velocity equal to 70.9x10^{-3} m.s^{-1}.

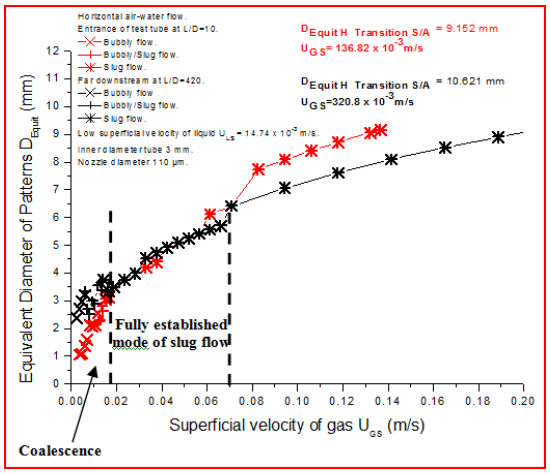

Figure 2. Equivalent diameter of gas entity in horizontal air-water flow at L/D=10 and L/D=420.

c. Vertical upward air-water flow

Similar variation laws are observed for both zones L/D=10 and 420 for the gas entity (Fig.3). At low apparent gas velocity, the size of the dispersed bubbles increases linearly up to an equivalent diameter of 1.64 mm. This peak means that gravity (buoyancy force) helps the bubble detachment and its upward motion.

Beyond this superficial gas velocity, the dispersed bubble structure evolves very rapidly in the two zones towards the slug structure going through the bubbly/slug structure. In this case, the phenomenon of coalescence does not occur. Nevertheless, at higher gas velocity, we may consider probable breakup of slugs as their size is consequently reduced (Fig.3) and their appearance frequency is increased at L/D=420.

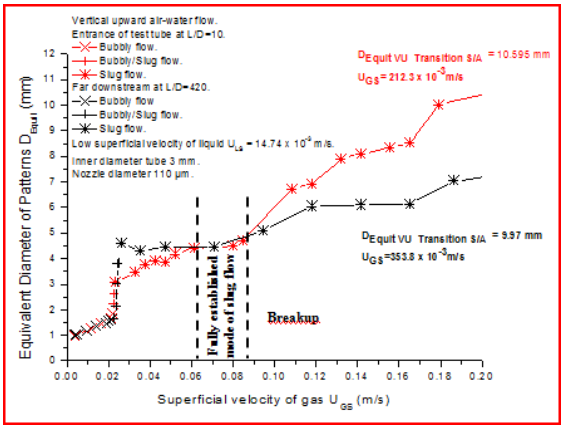

Figure 3. Equivalent diameter of gas entity in vertical upward air-water flow at L/D=10 and L/D=420.

5. Conclusion

Experimental investigation is carried out to analyze the size of bubbles, slugs and plugs in a two-phase flow with different orientations. Coalescence and breakup phenomena could be inferred in certain situations by assessment of equivalent diameter of the gas entities and their detachment and appearance frequency. At L/D=10, the variation laws of the equivalent diameter of gas entities for the three flow orientations evolve in the same way. Flow regimes in the downward vertical case under the influence of gravity and liquid shear are established much more rapidly in comparison with the upward verical case. However, the variation law in the horizontal case is in intermediate position.

References

Fukano. T, Kariyasaki. A, 1993. Characteristics of gas–liquid two-phase flow in a capillary. Nucl. Eng. Des. 141, 59–68.

Ide. H., Kariyasaki. A., Fukano. T., 2007. Fundamental data on the gas–liquid two-phase flow in minichannels. Int. J. of Therm. Sci. 46, 519–530.

Mehta. Hemant. B, Banerjee. Jyotirmay, 2014. An investigation of flow orientation on air–water two-phase flow in circular minichannel. Int. J. Heat Mass Transfer 50, 1353–1364.

Oral 054

A robust treatment of the DCMIX microgravity data

D. Sommermann[1], T. Triller[1], M. Schraml[1], W. Köhler[1]

[1]Physikalisches Institut, Universität Bayreuth, Bayreuth, Germany
werner.koehler@uni-bayreuth.de

Introduction

Within the DCMIX (Diffusion and thermodiffusion Coefficient Measurements In ternary miXtures) project, diffusion, thermodiffusion and Soret coefficients of a series of ternary liquid mixtures have been measured aboard the International Space Station (ISS). One of the main goals of the project is the establishment of reliable reference data that are not affected by gravitation-driven convection. So far, four campaigns, named DCMIX1 to DCMIX4, have been flown between 2012 and 2018, each focusing on different ternary systems.

The experiments aboard the ISS are performed by means of the SODI (Selectable Optical Diagnostics Instrument), which is a two-color digital Mach-Zehnder interferometer that operates simultaneously at 670 and 935 nm wavelength. The concentration changes in a Soret cell subjected to a temperature gradient can be reconstructed from the interferometrically recorded refractive index changes. In this contribution we will mainly focus on the DCMIX3 campaign, where measurements have been performed on ternary mixtures of water, ethanol and triethylene glycol of five different compositions. In particular, we will show how reliable phase data can be extracted even in cases where the usually applied phase stepping technique is hampered by sporadic laser instabilities.

The SODI instrument

The SODI instrument is sketched in Fig. 1. The moveable optical module can individually address the five cells for ternary mixtures. Not shown is the single-color fixed module for the binary reference cell.

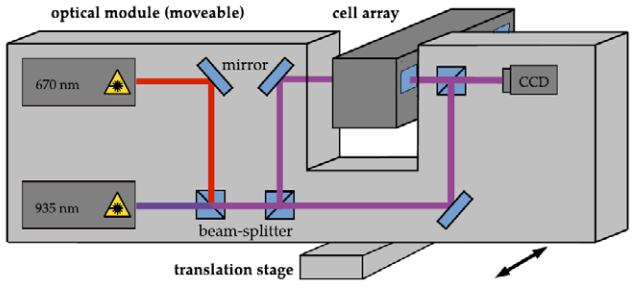

Figure 1: Sketch of SODI interferometer with moveable optical module and cell array with five individually addressable cells for ternary mixtures and one additional companion cell for a binary reference mixture.

Every single "data point" of the SODI interferometer consists of five consecutive fringe images that are phase shifted by π/2. From these five images it is possible to reconstruct a complete 2dim phase map of the entire Soret cell, a technique known as phase shifting interferometry.

Robust phase image analysis

Occasionally, random phase instabilities of the lasers render the temporal phase stepping algorithms, that are based on a well defined phase shift between the consecutive images, impossible. In order not to loose any data gathered in microgravity, we have developed a robust algorithm that can be used to determine diffusion, thermodiffusion and Soret coefficients even in such situations where multi-image temporal phase stepping fails.

In a first step, we do not analyse the entire 2dim phase field but rather determine the phase gradient in the center of the cell.

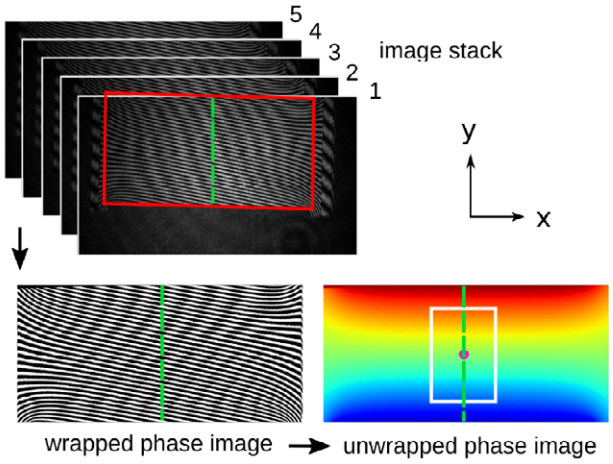

Figure 2: SODI: determination of central phase gradient using temporal phase stepping based on stack of five images.

Fig. 2 shows this approach in the case of intact phase stepping. Since the phase or refractive index gradient in the center of a Soret cell is the quantity that is also sensed in optical beam deflection (OBD), the thus obtained SODI signals can directly by analyzed in the same way as OBD laboratory experiments. In the cases of not properly working phase shifts, it is no longer possible to reconstruct the entire phase field as shown in Fig. 2 as *wrapped* and *unwrapped phase image*. Nevertheless, the central phase gradient can be obtained without resorting to phase stepping by fitting a cosine function with a polynomial argument

$$I(y) = A + B\cos\left(\sum_{k=0}^{n} a_k\,(y - y_0)^k\right)$$

to the intensity along a vertical column of a single image. For practical and stability reasons, somewhat more sophisticated procedures than a direct polynomial cosine fit are employed, which, in principle, yield identical results. This alternative robust technique has been applied to data from DCMIX3 experiments, where we could show that the thus obtained OBD-like transients are practically identical to the ones recorded from the entire image stacks in the case of properly working temporal phase stepping.

Conclusions

Our proposed data evaluation method for interferometric SODI data is robust in the sense that it allows to extract OBD-like time series from single images even in situations where temporal phase stepping does not work as expected due to spurious laser intabilities. These two-color transients can be used to obtain high quality optical data. Their further treatment, in particular the transformation to the composition space for the determination of the Soret coefficients, is identical to the established standard procedures. The method also demonstrates the robustnes and reliability of the SODI instrument, which can deliver fully valid scientific data even in situations where important functions, such as the precise phase stepping, do not work as intended.

Acknowledgements

We thank ESA and Roscosmos for providing the flight and operations opportunity. This work was supported by Deutsches Zentrum für Luft- und Raumfahrt (DLR) (Grants 50WM1130, 50WM1544).

References

T. Triller et al., Thermodiffusion in ternary mixtures of water/ethanol/triethylene glycol: first report on the DCMIX3-experiments performed on the International Space Station, *Microgravity Sci. Tec. 30 (2018) 295.*

D. Sommermann, T. Triller, W. Köhler, A robust evaluation method for the DCMIX microgravity experiments, *Microgravity Sci. Tec. (2019) submitted.*

Oral 056

Surface oscillation of viscous droplet under microgravity and on ground

M. Watababe[1], H. Hasome[1], K. Uchida[1]

[1]Department of Physics, Gakushuin University, Tokyo.Japan;
masahito.watanabe@gakushuin.ac.jp, 18141002@gakushuin.ac.jp, kousuke0127@gmail.com

Introduction

Thermophysical property measurements use the fluid dynamically behaviour of the levitated liquid droplet under the container-less conditions. The levitated liquid without any external forces forms spherical shape by surface tension, therefore we can easy obtain density of sample ρ by the droplet volume V, from its shape at temperature T, as,

$$\rho(T) = M/V(T). \quad (1)$$

M is mass of samples. If the surface oscillation is excited in the levitated droplet, we can obtain surface tension σ using the surface oscillation frequency ω from the following relation (R_0 is radius of droplet, l is integer of oscillation mode number),

$$\omega^2 = l(l-1)(l+2)\frac{\sigma}{\rho R_0^3}. \quad (2)$$

Also, the surface oscillation of levitated droplet is decayed by its viscosity η with decaying constant as τ. Using measured τ, we can obtain viscosity η of sample from the following relation,

$$\frac{1}{\tau} = (l-1)(2l+1)\frac{\eta}{\rho R_0^2}. \quad (3)$$

From these relations, we obtained thermophysical properties of high-temperature liquids using containerless and non-contact methods. Recently, electrostatic levitation (ESL) system was installed in ISS, and we are now using these systems for measurements of thermophysical properties of liquid alloys and molten oxide under microgravity conditions. Microgravity conditions have an advantage for thermo-physical properties measurements using the oscillating drop techniques, because of no deformation of the levitated droplet by large external forces. Therefore, it is expected that thermophysical properties, density, surface tension and viscosity, can be precisely measured under microgravity. However, even under microgravity conditions, we need excite surface oscillation by applying external force with several techniques. The external force for surface oscillation excitation should affect on surface oscillation phenomena with the non-linear effects on oscillation mode and with the internal flow effects on oscillation decaying. These external force effects on surface oscillation have not been examined in details. Because microgravity experiments have several limitations for performing, we cannot perform systematically experiments for performing experiments of external effects on surface oscillation phenomena. Recently, we succeeded to perform oscillating drop experiments on ground by using aerodynamic levitation (ADL) method for the purpose of thermophysical property measurements (Hakamada *et al*. 2017). We improved the unit of nozzle for gas jet flowing to the samples. We combined the improved conical nozzle system and the acoustic oscillation system into the ADL system for measurements of density and viscosity of molten oxides and liquid metals. Using the improved ADL, we can systematically perform oscillating drop experiments to clarify the external force effects on surface oscillation. Using the ground experiments, we can also investigate accuracy of surface oscillation data for thermophysical property measurements obtained under microgravity in ISS. In this paper, we report the results of oscillating drop experiments under microgravity and on ground using different viscosity liquids by molten oxide and liquid metals.

Oscillating drop experiments using levitation facilities under microgravity and on ground

Using ADL technique combined with the acoustic oscillation method, we obtained surface oscillation of molten oxide (Al_2O_3 and CaO-SiO_2-Mn_3O_4-TiO_2) and liquid Fe alloys. Fig. 1 shows the schematic figure of our ADL system for oscillating drop experiments on ground. Spherical shaped solid samples with about 2mm in diameter were levitated by the gas-jet flow from the conical nozzle, and then solid samples were melted under the container-less conditions by CO_2 laser irradiation. For the oscillating drop experiments, we applied two CO_2 laser irradiation to the samples from the top and the bottom in order to reduce the temperature gradient in samples. The sample temperature was measured by the single-color pyrometer with wavelength of 980nm. The droplet shape from the side view was taken by the high-speed camera as the shadow image by the backlight illumination with 200mW He-Ne laser and with the beam shape modification system to make parallel beam (Nakamura *et al*. 2017). Using the static shape of levitated droplet without the surface oscillation, we obtained the volume of droplet with the assumption of symmetrical ellipsoid shape, and then we obtained the density using the average mass of samples measured before and after the experiments. Density was used for the confirmation of sample shape symmetry around vertical axis. It is basic assumption and important for surface oscillation by the oscillating drop experiments. For the oscillating drop experiments, we newly applied the acoustic oscillation system into the gas flow path for the gas jet. Two sound speakers with phase matching were set in the small chamber inserted into gas flow path, then the single wave length signal input into two speakers. By the acoustic oscillation system, the levitation gas-jet flow from the conical nozzle has single wavelength oscillation, as a result the droplet oscillates with the same frequency as the input signal. Moreover, we performed oscillating drop experiments using ESL under microgravity using electrostatic levitation furnace (ELF) installed in ISS. ELF has six electrodes arranged facing each other along the x-y-z axis to make the homogeneous gradient electrical fields. Sample with 2mm in diameter can be kept its position at the center of electrodes by Coulomb force with high-speed feedback position control system using the optical position detecting system and lasers. The sample kept at the center position of electrodes is heated and melted by irradiation of four

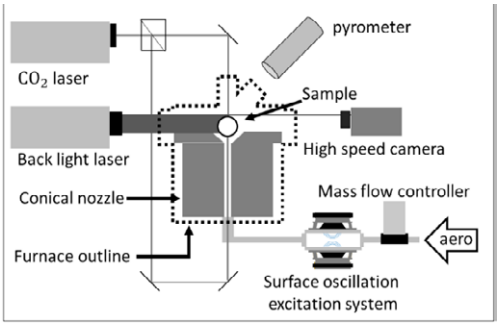

Figure 1: Schematic diagram of ADL system. Main ADL system combined with acoustic oscillation system for surface oscillation excitation.

semiconductor lasers. Details of ELF system was described in elsewhere (Tamaru *et al*. 2018). For ESL technique, surface oscillation of droplet is excited by the applying alternating voltage to the main electrode plates. We performed oscillating drop experiments by ELF using different viscosity and surface tension liquids by molten oxide of CaO-SiO_2-Mn_3O_4-TiO_2-Fe_2O_3 and CaO-SiO_2-Mn_3O_4-TiO_2 system.

We examined the effect of external force on surface oscillation with change the applied acoustic signal power. If the acoustic signal power changes, the amplitude of surface oscillation of droplet is modified with them. We observed the surface oscillation and its decaying of molten Al_2O_3 as show in Fig.2. From the results, we obtained surface tension and viscosity of molten Al_2O_3 by eqs.(2) and (3). Both of surface tension and viscosity agreed with the previous reported values. Agreement of these values with the previous reported values means that the surface of molten Al_2O_3 droplet oscillated with the natural oscillation of l=2 mode as described by eqs.(2) and (3). However, in details of oscillation data the oscillation frequency was changed with the time sequence from acoustic signal off part to end of oscillation part. Using ELF, we observed the same surface oscillation data for molten CaO-SiO_2-Mn_3O_4-TiO_2 system. Molten oxides are high viscosity liquid of about 50mPa·s at closed melting temperature. For molten oxide case, oscillation decay time was not much affected by the input acoustic signal power which corresponded to the surface oscillation amplitude. For the case of low viscosity liquids, we observed surface oscillation of liquid Fe-Si alloys. Fig.3 shows the surface oscillation data of liquid $Fe_{50}Si_{50}$ at 2200K which is high temperature of liquidus temperature of the composition. For low viscosity case, decay time of surface oscillation longer than the high viscosity liquids of molten oxide. We find that the surface oscillation decay time of low viscosity liquids depends on the oscillation amplitude. The relationship between the decay time and the amplitude of surface oscillation well described by the curve using the Reynolds number. This means that the surface oscillation decaying of low viscosity liquids are sensitivity of internal flow conditions. For the excitation of large surface oscillation amplitude, turbulent flow in droplet would be generated and the turbulent flow would be dumped surface oscillation. Therefore, apparent viscosity should be small for the large surface oscillation amplitude excitation case. These results are important for measurement of thermophysical properties measurements of the low viscosity liquids such as liquid metals alloys.

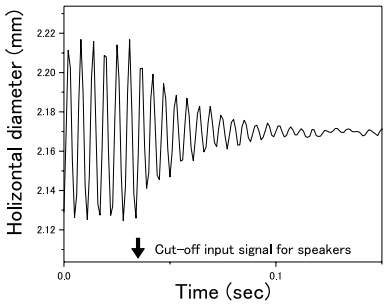

Figure 2: Surface oscillation of molten Al_2O_3 droplet obtained by ADL on ground.

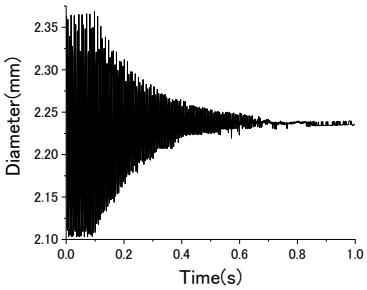

Figure 3: Surface oscillation of liquid $Fe_{50}Si_{50}$ droplet obtained by ADL on ground. This case is large sound signal applying.

Conclusions

The surface oscillation phenomena of levitated droplet were investigated in details using ADL on ground and ELF in ISS under microgravity. The surface oscillation frequency was affected by the external force applying and its decaying was also affected by external force for low viscosity liquids case. For low viscosity liquids, the large surface oscillation amplitude excitation generates turbulent flow inside droplet and the turbulent flow decays surface oscillation. Therefore, for the large amplitude of surface oscillation case, the apparent viscosity would be shown larger than the correct viscosity of sample liquids. From these results, we need the adjustment of surface oscillation amplitude to measure viscosity of high temperature liquid metals alloys samples correctly even under microgravity.

Acknowledgements

The author would like to thank Prof. T. Ishikawa, Dr. C. Koyama, Ms. H. Tamaru, Mr. H. Saruwatari, Mr. H. Oda (JAXA) for ELF operation and technically supports. This work is financially supported by JAXA, JSPS KAKENHI Grant Numbers JP18H01386 and MEXT-Supported Program for the Strategic Research Foundation at Private Universities (2015-2019).

References

S. Hakamada, A. Nakamura, M. Watanabe and F. Kargl, Int. J. Microgravity Appl., 34 (2017) 340403-1-6.

A. Nakamura, S. Hakamada, A. Mizuno and M. Watanabe, Int. J. Microgravity Appl., 34 (2017) 340404-1-6.

H. Tamaru, C. Koyama, H. Saruwatari, Y. Nakamura, T. Ishikawa and T. Takada, Microgravity Sci. Technol. 30 (2018) 643-648.

Oral 057

Finite-size effects on frozen wave pattern selection in microgravity

J. Porter[1], P. Salgado Sánchez[1], Y.A. Gaponenko[2], V. Shevtsova[2]

[1]Escuela Técnica Superior de Ingeniería Aeronáutica y del Espacio, Universidad Politécnica de Madrid, Plaza de Cardenal Cisneros 3, 28040 Madrid, Spain,
[2] Microgravity Research Centre, CP-165/62, Université Libre de Bruxelles (ULB), av. F. D. Roosevelt, 50, B-1050 Brussels, Belgium;
pablo.salgado@upm.es, ygaponen@ulb.ac.be, jeff.porter@upm.es, vshev@ulb.ac.be

Introduction

When two layers of immiscible liquids are separated by an initially flat interface and subjected to horizontal vibrations, quasisteady frozen waves appear at a critical forcing value. If lateral boundaries are ignored and the fluids are assumed to be deep and inviscid, then this threshold is given by (Lyubimov and Cherepanov 1986)

$$(A\omega)^2 = \frac{(\rho_1+\rho_2)^3}{\rho_1\rho_2(\rho_1-\rho_2)}\sqrt{\frac{\sigma g}{\rho_1-\rho_2}}$$

where Aω is the vibrational velocity, ρ_1 and ρ_2 are the lower and upper densities, and σ is the interfacial tension The critical wavelength λ is set by the capillary length, which becomes very large in microgravity conditions, diverging in the limit g=0 while the threshold vanishes. The absence of a gravitational restoring force also facilitates the growth of the initially sinusoidal patterns, which can rapidly develop into large columnar structures (Gandikota *et al.* 2014). The length scale of these structures is determined by the fastest growing perturbation (Lyubimova *et al.* 2017) and the size of the system. After column formation, sufficient forcing can excite Faraday waves on the columnar interfaces, producing a pattern with two length scales (Shevtsova *et al.* 2016).

Results are described from a detailed numerical investigation of frozen wave pattern selection in finite rectangular containers under microgravity conditions with parameters appropriate to silicone oil and FC-40. The pattern selection process is characterized by solution branches that persist over discrete forcing intervals, with a cycle of column growth controlling the transition from one mode to another. In sufficiently long containers, there is a transition from nearly symmetric to asymmetric columnar development at a certain forcing amplitude.

The container aspect ratio plays an important role. Shallow layers suppress the development of long-wave perturbations leading to higher wavenumber patterns whose growth is typically associated with an asymmetric series of collisions between developing columns and container boundaries. In thick layers, lower wavenumbers are observed and the final state is often asymmetric. For container aspect ratios Γ > 2, finite-size effects are relatively weak and the numerically obtained thresholds are similar to, but slightly higher than, the theoretical values from inviscid theory. For Γ < 2, finite-size effects cause a significant delay in frozen wave onset.

Column growth cycle and mode transitions

Immediately after forcing is initiated, the mean vertical velocity is largest near the lateral walls, where the two liquids move up and down. This agitation provides the initial perturbation that activates column growth. As time passes, the frozen wave (column) growth moves inward toward the centre of the container where the perturbations can grow differently depending on their amplitude and the amount of liquid they entrain. The larger lateral columns generally reach the top and bottom walls, but one or more smaller columns located in the interior may be limited before that by surface tension. This can be understood as a kind of wavenumber frustration, where the more rapidly growing lateral columns, with wavelengths closer to the prediction of linear theory, induce a mismatch or defect in the centre of the container.

Figure 1 shows the selected mode in a 30 x 7.5 mm domain as a function of dimensionless forcing. The number of column pairs along the midline is recorded (identifying lateral boundaries), as well as a local wavenumber measured at the location of the emerging column (defect).

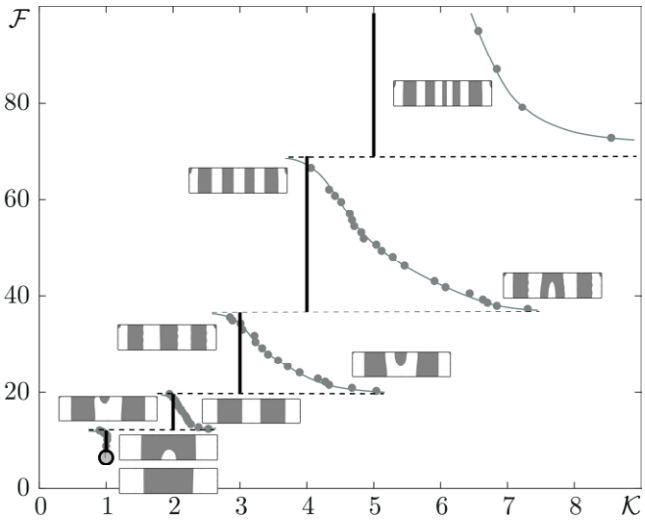

Figure 1. Mode diagram in terms of the vibrational forcing $\mathcal{F}=A\omega\sqrt{(\rho_1-\rho_2)L/\sigma}$ for a container of length L=30 mm and depth 7.5 mm showing the number of column pairs (solid vertical lines) and the wavenumber $\mathcal{K}$ (solid dots) near the defect in the central part of the container. Small insets illustrate the final pattern for selected points on each branch.

At the onset of the frozen wave instability, the interface develops toward a single pair of columns, with the lighter liquid (silicone oil) located in the centre and the denser one (FC-40) divided nearly equally and aligned against the lateral walls. As the vibrational velocity is increased, a new column grows from the centre of the container, eventually splitting the central column of silicone oil. Each mode is found over a certain interval of vibrational velocities, which widens as the wavenumber grows, indicating the increased cost of adding new columnar structures.

The column growth cycle is often nearly symmetric with respect to reflection about the vertical midline of the

container, especially over a range of low to medium strength excitations when the pattern wavelength is on the order of the container length. For sufficiently large containers, a transition from symmetric to asymmetric column growth is observed at moderate forcing values.

Figure 2 shows the final density distribution along the horizontal midline for increasing forcing. As the pattern wavelength becomes smaller than the container length, lateral boundary effects become weaker, the initial growth is more uniform across the interior, and wavenumber frustration can occur at various locations, not always at the centre.

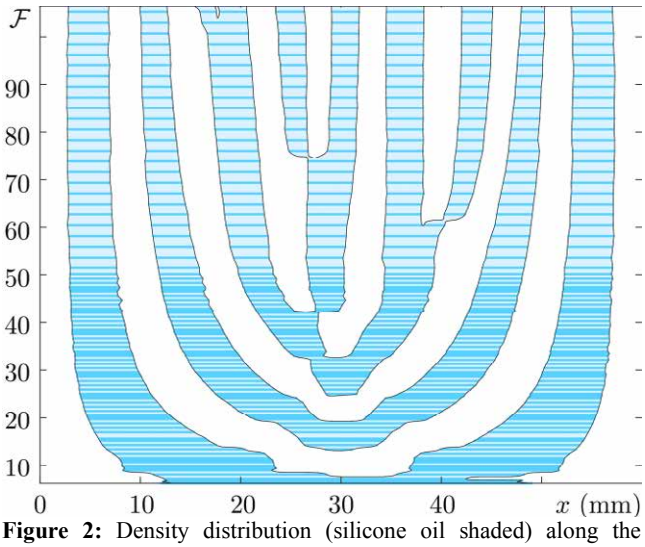

Figure 2: Density distribution (silicone oil shaded) along the horizontal midline of the final steady state as a function of forcing $\mathcal{F}$ in a 60 x 7.5 mm rectangular container; darker lines show the resolution used. The column formation cycle becomes asymmetric at $\mathcal{F} \approx 40$.

The mechanism of column creation in the asymmetric regime is more complicated than in the symmetric case, and often involves a type of fingering or branching during the transient stage as nascent columns of different size merge, either partly or completely. These fingers may branch off to the side of the main column at an angle only to be reabsorbed eventually, sometimes leaving drops behind, or they can reach the upper or lower boundary to form a new column.

The locations of the defects vary, with a tendency to alternate from one side to the other. These defect locations, although seemingly random, are repeatable and continuous, as is the final columnar pattern itself, despite the complicated nonlinear dynamics that precedes it. The locations are likely determined, at least in part, by the temporal form of the forcing function.

Conclusions

Systematic numerical investigations of the columnar patterns triggered by the frozen wave instability in immiscible layers under weightless conditions show that mode transitions are characterized by a column (defect) growth cycle. The final columnar structures are in qualitative agreement with the parabolic flight experiments of Salgado Sánchez *et al.* 2019 in immiscible liquids and with the observations of Shevtsova *et al.* 2016 and Gaponenko *et al.* 2015 in miscible liquids.

The frozen wave threshold decreases with increasing length, consistent with the requirement of inviscid theory (Lyubimov *et al.* 1986, Lyubimova *et al.* 2017) in the infinitely extended case. The onset of frozen waves in short containers is significantly delayed. In longer containers, a transition from approximately symmetric (central) column growth to a more complex, asymmetric column growth cycle is observed.

In thin containers, the development of large wavelength patterns is frustrated by repeated collisions with the upper and lower boundaries, where surface and contact forces play a central role. This highly nonlinear process acts to increase the average wavenumber of the final columnar structure. In thick containers, the asymmetry of the forcing and the associated harmonic surface waves, which are out of phase at the left and right endwalls, is amplified by the longer transient growth time, leading to final structures with more asymmetry.

The vibroequilibria effect clearly plays a part in selecting the final interfacial structure, as demonstrated by the fact that the denser liquid (FC-40) always ends up along the lateral walls although the frozen wave instability itself does not select this. Furthermore, the way the forcing is initiated is important. When the forcing is turned on relatively quickly, as in the parabolic flight experiments (Salgado Sánchez *et al.* 2019), more rapid growth is observed near the lateral walls, with the central column being the last to develop and the most likely to suffer defects due to wavenumber frustration.

Acknowledgements

The work of Y.A.G. and V.S. was supported by the PRODEX programme of the Belgian Federal Science Policy Office. The work of P.S.S. and J.P. was supported by the Ministerio de Economía y Competitividad under Project No. ESP2015-70458-P.

References

D.V. Lyubimov and A.A. Cherepanov, Development of a steady relief at the interface of fluids in a vibrational field *Fluid Dyn. Res*. 21 (1986) 849-854.

G. Gandikota, D. Chatain, S. Amiroudine, T. Lyubimova, and D. Beysens, Frozen-wave instability in near-critical hydrogen subjected to horizontal vibration under various gravity fields, *Phys. Rev. E* 89 (2014) 012309.

T. Lyubimova, A. Ivantsov, Y. Garrabos, C. Lecoutre, G. Gandikota, and D. Beysens, Band instability in near-critical fluids subjected to vibration under weightlessness, *Phys. Rev. E* 95 (2017) 013105.

V. Shevtsova, Y.A. Gaponenko, V. Yasnou, A. Mialdun, and A. Nepomnyashchy, Two-scale wave patterns on a periodically excited miscible liquid-liquid interface *J. Fluid. Mech*. 795 (2016) 409-422.

P. Salgado Sánchez, V. Yasnou, Y. Gaponenko, A. Mialdun, J. Porter, and V. Shevtsova, Interfacial phenomena in immiscible liquids subjected to vibrations in microgravity, *J. Fluid. Mech*. 865 (2019) 850–883.

Y.A. Gaponenko, M.M. Torregrosa, V. Yasnou, A. Mialdun, and V. Shevtsova, Dynamics of the interface between miscible liquids subjected to horizontal vibration, *J. Fluid. Mech*. 784 (2015) 342-372.

Y.A. Gaponenko, M.M. Torregrosa, V. Yasnou, A. Mialdun, and V. Shevtsova, Interfacial pattern selection in miscible liquids under vibration, *Soft Matter* 11 (2015) 8221-8224.

Oral 058

The scientific payload on MASER 14 shared flight

G. Florin[1], C Lockowandt[1]

[1]Swedish Space Corporation SSC, Solna, Sweden
gunnar.florin@sscspace.com, christian.lockowandt@sscspace.com

Introduction

SSC's next microgravity suborbital rocket mission, MASER 14, is scheduled for launch in June 2019 from Esrange Space Center in northern Sweden. The mission will provide the 300 kg scientific payload with 6 minutes of high quality microgravity. The rocket will carry a mixed payload consisting of four experiments from three customers; two ESA scientific experiments; ARLES and XRMON-GF2, one Surface Tension Tank (STT) experiment of Space Solutions in Korea and finally the JAXA/DLR experiment in the field of nucleation of dust (DUST).

ARLES experiment

The ARLES experiment (science coordinator Dr. D Brutin, IUSTI Université Aix-Marseille) intends to mainly study evaporating drops of pure fluids, which contain a low concentration of nanoparticles, under the influence of an electric field. The scientific objectives are dealing with the flow motion and the flow instabilities occurring in the drop, at the droplet interface and in the vapour phase, but also the pattern formation on the substrate after the evaporation of the volatile phase and the consequent substrates' functionalization (nanoparticles organisation/ auto-assembly, the different compaction area in the deposit) as well as the eventual heat transfer enhancement.

XRMON-2 experiment

The XRMON-GF2 experiment (science team coordinator Henri Nguyen-Thi IM2NP, Université Aix-Marseille) aims at studying the directional solidification (columnar and equiaxed dendritic growth in purely diffusive environments) of an Al-Cu system by in-situ real-time X-ray radiography. Special attention will be put on the aspect of nucleation, segregation and impingement. The XRMON program contains a series of in-situ radiography experiments on metallurgical processes related to solidification phenomena under microgravity and terrestrial conditions. A number of experiments have already been carried out in the frame of this program (XRMON-Metal Foam on MASER 11, XRMON-diffusion on MAXUS 8, XRMON-Gradient Furnace on MASER 12, XRMON-Solidification on MASER 13, XRMON-Diffusion on MAXUS 9, six parabolic flight campaigns; two with metal foams and four with gradiant furnaces.

DUST experiment

The DUST experiment is part of the DUST project, which aims at obtaining physical parameters, such as surface free energy and sticking probability, of titanium carbide dust, and their elucidate formation processes of in a gas ejected from a carbon-rich asymptotic giant branch star. It will provide initial data for sciences based on carbonaceous return samples by HAYABUSA 2, OSIRIS Rex and MMX in 2020 and IR data obtained by future observatory such as SPICA and James Webb Space Telescope. The experiment is carried out by Hokkaido and Braunschweig Universities.

STT experiment

The objective of the STT experiment is to study the drainage of a liquid from a pressurized tank equipped with a liquid surface tension and capillary system designed to collect the liquid at the outlet of the tank.

Vehicle overview

The vehicle, with its 300 kg scientific payload, will be propelled by the VSB-30 rocket motor to an apogee of 260 km, and provide more than 6 minutes of microgravity conditions. MASER is part of SSC's new SubOrbital Express flight service. It serves as a system for performing experiments under short-duration microgravity flights, providing the scientific community with an excellent research tool and a full European access to space.

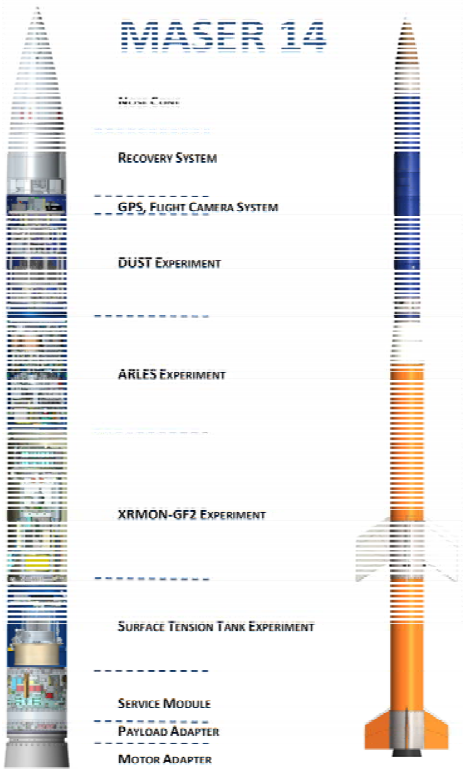

Figure 1: Maser 14 payload and vehicle

MASER legacy

Up till today the MASER programme has provided for 13 successful flights of 6-8 minutes of microgravity, with residual accelerations down to 10^{-6} g. The MASER payload accommodates up to five major experiments of high complexity and offers – with its high speed telemetry system

– real-time digital video monitoring as well as command capabilities from ground during the flight of the scientific experiments. Small payloads of a couple of kilograms can also be accommodated in dedicated compartments.
With the 2015 ALAT/CNES Cryofénix mission, SSC introduced low gravity levels to experiments, in this case 1.75 mg and 7 mg, by applying thrusts of 7 N and 28 N.

Conclusions
The paper provides an overview of SSC's SubOrbital Express microgravity platform as well as a description of the scientific experiments of MASER 14 payload.

Acknowledgements
The accommodation and flight on board MASER 14 of the DUST experiment are carried out under contract with DLR Space Management.
The development and flight of the ARLES and XRMON-GF2 experiments are carried out under a programme of and funded by the European Space Agency. The view expressed in this abstract can in no way be taken to reflect the official opinion of the European Space Agency.
The accommodation and flight on board MASER 14 of STT experiment are carried out under contract with Space Solutions Co. Ltd.
We thank the above referenced organisations for their confidence in SSC for carrying out the development, accommodation and flight of the scientific experiments.

Oral 059

New measurement technique of liquid film thickness distribution with high spatial and temporal resolution: application to convective condensation in microgravity

Pascal Lavieille[1], Marco Azzolin[2], Arianna Berto[2], Patrick Queeckers[3] Andrey Gluschuk[3], Benoit Schlegel[1], Stefano Bortolin[2], Marc Miscevic[1], Carlo Saverio Iorio[3], Davide Del Col[2]

[1]Université Paul Sabatier - Laboratoire Plasma et Conversion d'Energie
118 route de Narbonne, Bat3R1, 31062 Toulouse Cedex 09, France
[2]Università degli Studi di Padova - Dipartimento di Ingegneria Industriale
Via Venezia, 1 – 35131, Padova, Italy
[3]Université libre de Bruxelles - Microgravity Research Centre
Av. F. Roosevelt 50, CP 165/62 - 1050 Brussels - Belgium
Pascal.lavieille@laplace.univ-tlse.fr, davide.delcol@unipd.it, ciorio@ulb.ac.be

Introduction

Prediction of condensing two phase flow (flow pattern, heat transfer and pressure drop) needs an accurate knowledge of liquid film thickness distribution. Indeed liquid film thickness is a key parameter to understand the main mechanisms inducing the instability and governing pressure drop and heat transfer. Unfortunately this liquid film is often very thin and unsteady. This thinness coupled with a highly dynamic change of slope of the interface make challenging the measurements of the liquid thickness. This lack of experimental data limits the validation and improvements of numerical or analytical model and so development of the laws that manage two-phase flow.

The present work proposes a technique to determine accurately with a high spatial and temporal resolution the liquid film thickness distribution inside a tube. This technique combines a high resolution punctual measurement system and high speed image acquisition of the flow inside a tube owning an external specific shape designed in order to magnify small liquid film thickness.

Limitations of standard visualizations

In the 62nd ESA parabolic flight campaign realized in June 2015 a shadowgraph method with a parallel light source has been used in order to determine temporal evolution of liquid film distribution of condensation flows in microgravity. The advantage of this measurement technique is to observe with a high temporal resolution (1500 Hz) the axial film thickness distribution at the top and at the bottom of the tube. In order to obtain quantitative measurements, distorsions induced by the cylindrical shape of the tube have been corrected using a ray-tracing model. This allows to convert the seeming thickness of the image into the real liquid film thickness present inside the tube. Two main limitations reduce the performances of this technique: the resolution of the measurement is limited by the spatial resolution of the camera and the liquid film can not be detected below a threshold value due to light deviation (figure 1). Another limitation induced by the cylindricity of the external shape of the tube is to produce a defocus of light which make ineffective point measurement techniques such as confocal chromatic or interferometric.

In order to overcome these limitations in the 70th ESA parabolic flight campaign realized in Nov. 2018 a glass tube with a specifc external shape has been designed and realized.

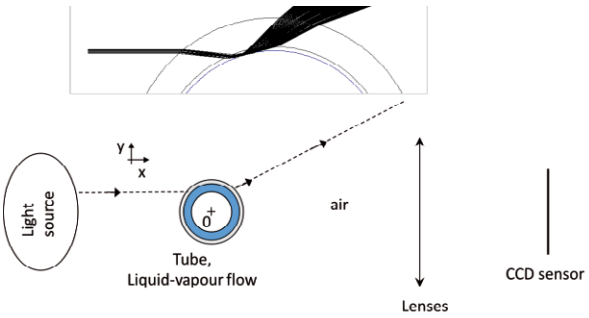

Figure 1: Ray tracing of parallel light inside a tube where a thin liquid film is distributed around the internal wall. The light deviation angle is too high to be collected by the CCD sensor of the camera.

Theoretical optical performances of the specific external tube shape

From the optical properties of the materials and the fluid, the shape of the external surface of the glass tube has been calculated in order to make detectable liquid film down to one micrometer, to produce a magnification of small liquid film thickness and to allow the use of punctual measuring sensors. The theroretical performances deduced from the ray tracing model are presented in figure 2.

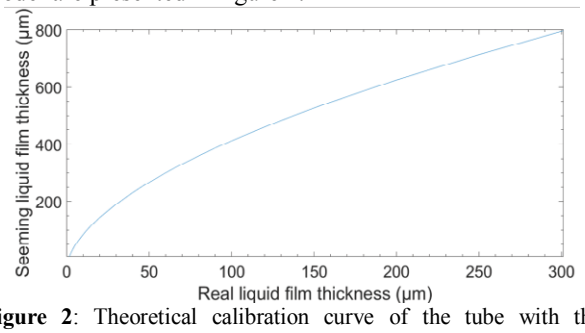

Figure 2: Theoretical calibration curve of the tube with the calculated specific external shape.

Magnification of small liquid film is obtained. Indeed from this calibration curve it can be deducted that when the liquid film thickness inside the tube is 50 µm, the camera will see the liquid film as if its thickness is equal to 267 µm. In that case even if the spatial resolution of the camera is 10 µm/pixel the liquid film thickness will be determined with an accuracy of 6% (knowing that when the seeming thickness is 277 µm the real thickness is 53 µm) instead of 20% when there is no magnifying effect. Figure 3 shows this relative accuracy according to the liquid film thickness inside the tube. With

such a camera resolution the relative accuracy fall down below 10% when liquid film thickness is higher than 20 µm and below 5% for liquid film thickness greater than 100 µm.

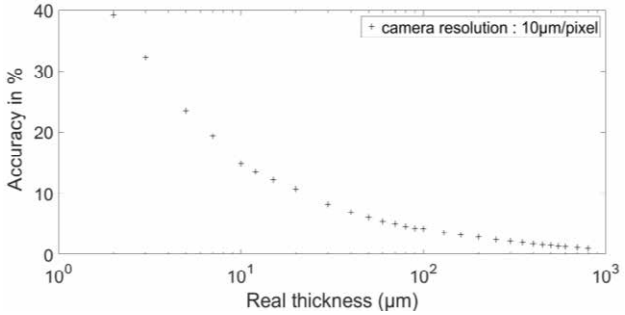

Figure 3: Relative accuracy in measuring film thickness as a function of film thickness inside the tube, using a camera with a resolution of 10 µm/pixel.

Such magnification (figure 4) allows to combine high accuracy and large field of view with a high temporal resolution. For the 70th ESA parabolic flight campaign this optical configuration has been used in order to measure liquid film structures at the top and at the bottom of the tube on a length of 13 mm with a camera frame rate of 1000 Hz.

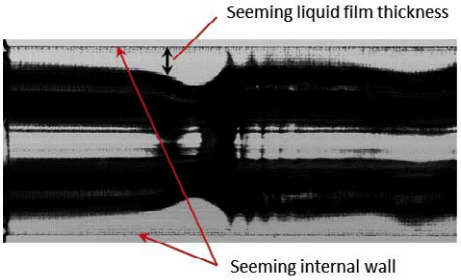

Figure 4: Example of image showing the magnification of liquid film thickness during microgravity inside a tube of 3.4 mm internal diameter.

Punctual measurement techniques

One of the main difficulties of this optical technique is the realization of the calculated external tube shape. Indeed it requires a high accuracy of the shape of the inner and outer surfaces but also of their relative position and roughness. Error in one of these parameters creates a modification of the calibration curve and reduces the capability to determine precisely the liquid film thickness. In order to overcome these difficulties and also to keep the possibility to determine more accurately liquid film thickness, punctual measurement sensors have been added.

The external surface of the tube has two flat surfaces that allow to use techniques analysing the reflected light properties to determine liquid film thickness. A white light interferometer and a confocal chromatic sensor have been placed respectively at the top and at the bottom of the tube. The white light interferometer used, allows to determine liquid film thickness between 0.5 µm to 100 µm with an accuracy of 10 nm. It is particularly well suited for small liquid film thickness. The main limitation is that the angle between the liquid-vapor interface and the tube surface must be small (roughly below 15°). The confocal sensor used can accept slope of the interface up to 28° and can measure liquid film thickness between 20 µm and 300 µm.

Thanks to these sensors and this optical configuration, the liquid film thickness can be measured simultaneously with the camera and one of these sensors at 1000 Hz. This accurate measurement allows to check and eventually correct the theoretical calibration curve of the machinning tube and then create a way to determine accurately the liquid film thickness distribution taking into account the distorsion induced by machining precision.

Such optical measurement set-up was used to study the gravity effect on the condensation of HFE-7000 inside a 3.4 mm internal tube diameter for mass flow rate between 30 and 55 kg m^{-2} s^{-1}.

Experimental set-up

The experimental facility is similar to the one used for the 62nd ESA Parabolic flight campaign (Azzolin et al. 2018) with two main loops: the refrigerant (HFE-7000) loop and the coolant water loop. The optical measurement section is placed between two heat exchangers (figure 5). The first heat exchanger is divided in three sub-sectors, the second one in two sub-sectors. These sub-sectors allow to determine quasi-local heat flux and heat transfer coefficient. The heat flux is obtained thanks to the determination of the water mass flow rate and the temperature difference measured with a copper-constantan three-junction thermopile. For each sub-sector, six T-type thermocouples embedded on the wall allow to deduce the heat transfer coefficient.

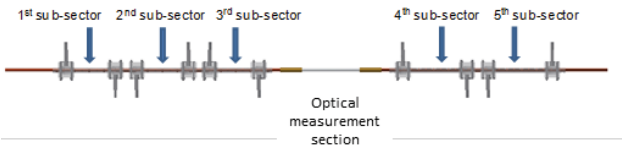

Figure 5: Layout of the experimental test section.

Effect of gravity, mass flow rate and quality on liquid film thickness distribution will be presented in the workshop.

Conclusions

A new technique to accurately measure the liquid film thickness distribution has been proposed and applied during the 70th ESA parabolic flight campaign. A specific designed external tube shape has been realized to magnify the liquid film thickness and to easily detect, with a standard camera resolution, liquid film thickness down to few micrometer. This technique was coupled with confocal and white light interferometric sensors to reach submicrometric precision at a frequency rate of 1000 Hz.

Acknowledgements

The authors acknowledge the financial support of the European Space Agency through the MAP Condensation program ENCOM-3 (AO-2004-096).

References

M. Azzolin, S. Bortolin, L. P. Le Nguyen, P. Lavieille, A. Glushchuk, P. Queeckers, M. Miscevic, C. Saverio Iorio, D. Del Col, Experimental investigation of in-tube condensation in microgravity, *International Communications in Heat and Mass Transfer,* Volume 96 (2018) 69-79.

Oral 060

SubOrbital Express – the new frequent and shared ride flight concept

G. Florin[1], C Lockowandt[1]

[1]Swedish Space Corporation SSC, Solna, Sweden
gunnar.florin@sscspace.com, christian.lockowandt@sscspace.com

Introduction

Suborbital (sounding) rocket missions have in the past decades primarily been used by Space Agencies or major organizations that fly experiments, as the single user of the platform. The cost for development of experiments and the cost for rocket payload integration and launch often exclude organisations with small or single experiments and small budgets from using suborbital rockets as test platform.

SubOrbitalExpress

With SSC's new SubOrbital Express concept, suborbital rocket launches from Esrange Space Center are scheduled frequently. Based on a shared-ride concept accessible to all users, the availability and cost of SSC's suborbital rocket flight becomes affordable for users from different disciplines not filling up a whole payload. This is of particular advantage when it comes to high-performance microgravity missions, where the flight ticket cost is distributed over a handful of customers, each user's cost being significantly less than it would be for a single-user flight.

The shared-ride concept – for everyone

In 2017, SSC introduced a shared-ride concept with a mix of payload customers; agencies, academia and commercial on the same mission. The objective is to provide flight opportunities available to everyone. Experiments are either accommodated into a module provided by SSC and equipped with basic resource systems (e.g. power, lift-off status and telemetry), or the experimenter presents the complete stand-alone experiment module for integration into the payload. With shared-ride concept, it is in addition possible to offer frequent flight opportunities for small payloads as low as a couple of kilogrammes, that otherwise would have to rely on the possibility of piggy-back ride on infrequent larger suborbital rocket missions.

SSC's suborbital microgravity platform

The specific platform in the case of microgravity is the MASER suborbital rocket that accommodates up to 300 kg of experiments in the 17" diameter payload. The microgravity platform, provides up to 6 minutes of high quality microgravity conditions; often as low as 10^{-6} g. The next microgravity mission flight is fully booked with 4 experiments from Asia and Europe (Korea, Japan/Germany and ESA), and will be launched in June 2019.

Frequent flight opportunities

In order to expand flight opportunities for the users, SSC has made an announcement of a microgravity flight opportunity every 18 months, with next launch scheduled for November 2020. The announcement is open to everyone.

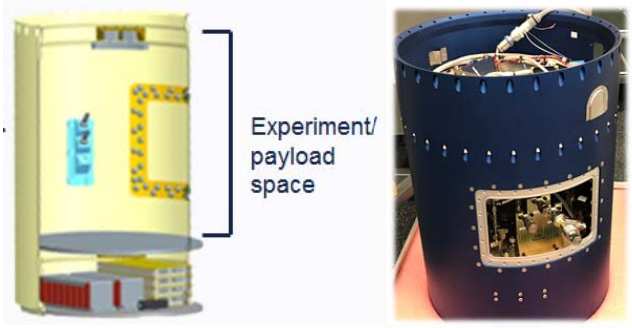

Figure 1: Space available for experiment in SSC's standard payload module (left), and an experiment accommodated in a MASER 14 module (right).

Multi-disciplinary suborbital rocket platform

In parallel with microgravity experiments, the platform can accommodate experiments of other disciplines benefiting from the characteristics of the suborbital flight with high apogee, such as atmospheric research and plasma physics. It can also carry mechanisms for releasing free-flying bodies for drop tests from very high altitude, 250 km, which extends the share-ride concept to other research and technology disciplines.

Esrange Space Center

MASER suborbital microgravity rocket programme is run by SSC, being part of the SSC's new SubOrbital Express concept. The launches of the microgravity platform take place from SSC's launch facility Esrange Space Center in northern Sweden, which offers excellent infrastructure to the science teams, including laboratories for late preparations of experiments. The payload lands safely on ground in a restricted vast impact area, and experiments are recovered within hours after the flight.

Conclusions

This paper elaborates on the shared-ride and flight ticket concepts of SSC's SubOrbital Express concept with launches from Esrange Space Center; from microgravity missions to very basic sounding rocket platforms.

26th European Low Gravity Research Association Biennial Symposium and General Assembly
14th International Conference on "Two-Phase Systems for Space and Ground Applications"
European Space Agency Topical Teams meetings
Granada (Spain), September 24-27, 2019

Oral 064

Dissection of the gene expression profile by RNA-seq of the plant response to partial gravity (Moon and Mars levels on board ISS SEEDLING GROWTH experiment)

R. Herranz[1], A. Villacampa[1], A. Manzano[1], C. Llauro-Berger[2], J.P. Vandenbrink[3], J.Z. Kiss[4], J. Saez-Vasquez[2] and F.J. Medina[1]

[1]*Centro de Investigaciones Biológicas (CSIC), Ramiro de Maeztu 9, 28040, Madrid, Spain,*
[2]*LGDP Laboratory of Genomes and Plant Development, University of Perpignan, Perpignan, France,*
[3]*School of Biological Sciences, Louisiana Tech University, Ruston, LA 71272 USA*
[4] *Department of Biology, University of North Carolina at Greensboro, Greensboro, NC 27402, USA*
r.herranz@csic.es, jpvdb@latech.edu, jzkiss@uncg.edu, saez@univ-perp.fr, fjmedina@cib.csic.es

Introduction

Travelling to near extraterrestrial objects with a reduced gravity level it is becoming a realistic objective for space agencies. The use of plants as part of life support systems will require a better understanding of the interactions among plant growth responses (tropisms) in partial gravity conditions. Here, we utilize several conditions of reduced gravity in the European Modular Cultivation System (EMCS) on board the International Space Station to identify how *Arabidopsis thaliana* wild type and mutant lines cope with increasing levels of partial gravity under different light photostimulation conditions. We assayed 82 samples from the SEEDLING GROWTH series of space experiments on the ISS, using WT, *nuc1* and *nuc2* mutants under blue light, red light and no photostimulation conditions grown in microgravity, several partial *g* levels and 1*g* using RNA-Seq analysis.

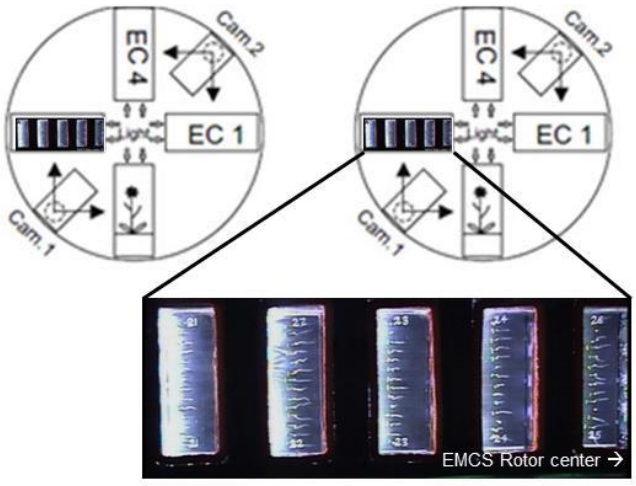

Distance from seedling cassette center to the EMCS center (mm)	150	118	86	54	22
Nominal 0.1*g*	**0.13**	**0.11**	0.10	0.08	**0.07**
Nominal 0.3*g*	**0.39**	**0.34**	0.30	0.25	**0.21**
Nominal 0.5*g*	**0.65**	**0.58**	0.50	0.42	**0.34**
Nominal 0.8*g*	**1.05**	**0.92**	0.80	0.68	**0.55**

Figure 1: Partial gravity levels on the EMCS rotors . The EMCS facility installed in the ISS during the execution of the SEEDLING GROWTH experiment allow us to perform simultaneous experiments in two rotors, normally microgravity (when stopped) and 1*g* control, but also lower g-levels are possible when the centrifugation rate is reduced. Precise *g* levels are shown in the Table for nominal 0.1, 0.3, 0.5 and 0.8*g* ISS samples.

Methods

Transcriptomic analysis was performed using standardized pipelines on 82 RNA samples (pools of 10-15 seedlings). The samples were pooled to reduce the *g*-level interval within biological replicates (Figure 1) as microgravity, low gravity ($0.09 \pm 0.02g$), Moon gravity ($0.18 \pm 0.04g$), Mars gravity ($0.36 \pm 0.02g$), reduced Earth gravity ($0.57 \pm 0.05g$) and 1*g* control ($0.99 \pm 0.06g$).

Results

Differentially expressed genes were further characterized for global responses using Gene Expression Dynamics Inspector (GEDI) tool, gene networks and enrichment for Gene Ontology (GO) terms. Differential gene expression analysis revealed a small amount of differentially expressed gene across all gravity conditions using false discovery rate ($p < 0.05$). The number of variations is similar in microgravity and the Moon *g*-level but increases dramatically at the gravitational load between them (low gravity conditions). Then it is progressively reduced when the difference with the normal Earth gravity is smaller. The GO groups affected also suggest a clearly different response at each partial *g*-level.

Conclusions

Arabidopsis thaliana transcriptional response in the presence of blue-light stimulation suggests that the phototropism can compensate the lack of gravitropism at microgravity conditions. Conflicts between tropisms induce an intense perturbation at the low gravity samples (showing an extensive stress response) and a progressively fading cell wall/membrane remodeling effect from the Moon to Mars gravity levels, potentially related with graviresistance mechanisms. Red-light photostimulation is also able to reduce most of the deleterious gene expression changes that are observed under gravitational stress conditions in darkness. Despite that, the use of a stress-related mutant line (*nuc2*) shows reduced gene expression changes under microgravity, suggesting that reduced stress sensitivity may be a way to cope with exaggerated response to gravitational stress.

Acknowledgements

This work was supported by the Spanish "Plan Estatal de Investigación Científica y Técnica e Innovación" of the Ministry of Economy, Industry and Competitiveness [Grant numbers AYA2012–33982 and ESP2015–64323-R, cofounded by ERDF], by pre-doctoral fellowships to [AM] & [AV] from the Spanish National Program for Young Researchers Training (MINECO, Ref. BES-2013-063933, BES-2016-077976) and the Seedling Growth Project to the ISS LSRA2009-0932/ 1177 of ESA-ELIPS Program. Spetial mention to the funding from ELGRA Gravity Spotlight team grant.

Oral 066

Thermo-electro-hydrodynamic instability of a dielectric fluid in a vertical cylindrical annulus: Earth's gravity and weightless conditions

A. Meyer[1], T. Seelig[1], M. Meier[1], I. Mutabazi[2], C. Egbers[1]

[1]Dept. of Aerodyn. and Fluid Mech., BTU Cottbus-Senftenberg, Cottbus, Germany, [2] Normandie Université, UNIHAVRE, CNRS UMR 6294, Laboratoire Ondes et Milieux Complexes, Le Havre, France;
meyer@b-tu.de, innocent.mutabazi@univ-lehavre.fr

Introduction

When an electric field $\vec{E}$ is applied to a dielectric liquid, the latest undergoes the electrohydrodynamic force which is composed by three terms, namely the electrophoretic force, the dielectrophoretic force, and the electrostrictive force. Under the conditions that a monophasic fluid confined in a rigid container and to which is applied an alternating electric field of high frequency compared to the inverse of all other characteristic times, the only dynamically contributing force is the dielectrophoretic (DEP) force $\vec{F}_{DEP} = -E^2\vec{\nabla}\varepsilon/2$ (Yoshikawa et al. 2013).

This force is proportional to the gradient of the electric permittivity ε which, in our case, is originated by the application of a temperature difference. Considering a permittivity which is linearly dependent on the temperature $\varepsilon(T) = \varepsilon_{ref}\left[1 - e\left(T - T_{ref}\right)\right]$, where T is the temperature, e is the coefficient of thermal variation of the permittivity and the subscript "ref" indicates a choosed reference, the DEP force can be written in the form

$$\vec{F}_{DEP} = -\alpha\left(T - T_{ref}\right)\vec{g}_e \text{ , with } \vec{g}_e = \frac{e}{\alpha\rho_{ref}}\vec{\nabla}\frac{\varepsilon_{ref}E^2}{2} \qquad (1)$$

where ρ is the fluid density. In that form, one can immediately see that the DEP force is a thermal buoyancy generated by an electric gravity $\vec{g}_e$ which expression is given in (1).

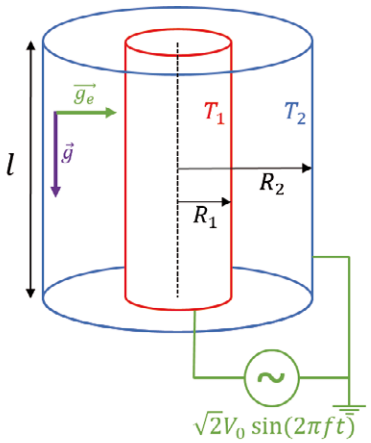

Figure 1: Schematic representation of the annular geometry.

We investigated the convective flow induced by the DEP force in a cylindrical annulus to which is applied a temperature difference between the two cylinders, as well as a difference of electric potential (Fig. 1). Since the inner cylinder is hotter than the outer one, the electric gravity field is centripetal, and instabilities may occur, in analogy to the classical Rayleigh-Bénard instability. The investigation has been done theoretically, numerically and experimentally under Earth's gravity (1g) and microgravity (µg) conditions (Tavnikov et al. 2015, Meyer et al. 2018, Seelig et al. 2019). The main objective is to provide information about the convective flow induced by the DEP force and the corresponding enhancement of the heat transfer. The DEP force could ultimately be used as the driving force for heat exchangers, the main advantage of which is the possibility to have an active control of the heat transfer, simply by the variation of the high voltage under 1g and µg conditions.

Numerical methods

In the cylindrical coordinates, the velocity $\vec{v} = (u, v, w)$, the temperature deviation $\theta = T - T_{ref}$, the generalized pressure π and the electric potential ϕ are solved by the continuity equation, the momentum equations, the energy equation and the Gauss' law for electricity. After non-dimensionalyzing these equations, and adopting the electrohydrodynamic Boussinesq-Oberbeck approximation, one reads:

$$\vec{\nabla}\cdot\vec{v} = 0 \qquad (2a)$$

$$\frac{\partial\vec{v}}{\partial t} + \left(\vec{v}\cdot\vec{\nabla}\right)\vec{v} = -\vec{\nabla}\pi + \Delta\vec{v} + \mathrm{Gr}\theta\vec{e}_z - \frac{\gamma_e \mathrm{V_E^2}}{\mathrm{Pr}}\theta\vec{g}_e \qquad (2b)$$

$$\frac{\partial\theta}{\partial t} + \left(\vec{v}\cdot\vec{\nabla}\right)\theta = \frac{1}{\mathrm{Pr}}\Delta\theta \qquad (2c)$$

$$\vec{\nabla}\cdot\left[(1-\gamma_e\theta)\vec{\nabla}\phi\right] \qquad (2d)$$

In this set of equations, the Prandtl number Pr, the Grashof number Gr, the dimensionless electric potential $\mathrm{V_E}$ and the thermoelectric parameter γ_e have been introduced.

To perform the linear stability analysis (LSA), cylinders of infinite length are considered and the equation are linearized around the base state of the flow which consist on the conductive state for the temperature and the electric potential. The base vertical velocity depends on the considered gravitational condition: in µg there is no base flow while in 1g the gravity acts on the radial density stratification and leads to upward flow near the hot cylinder and downward near the cold one. The unknown quantities are developed into normal modes $\exp(st + in\varphi + ikz)$. The linear equations are transformed into the spectral Chebyshev space, which results in an eigenvalue problem solved by a QZ decomposition.

Experimental set-up

The experiment consists of two concentric vertically aligned cylinders. The gap in-between is filled with a silicone oil. The inner cylinder has radius $R_1 = 5$ mm, the outer cylinder has radius $R_2 = 10$ mm and have a height of $l =$

100 mm. The alternating electric potential $\sqrt{2}V_0 \sin(2\pi f t)$ with $f = 200$ Hz and $V_0 \leq 14$ kV is applied to the inner cylinder while the outer cylinder is connected to the ground. The annulus is placed in a transparent acrylic glass-box and closed by a lower/upper lid that is also made out of acrylic glass. The temperatures T_1 and T_2 are maintained with a heating and a cooling loop of silicone oil, respectively.
The Shadowgraph method is used to visualize the optical index variations which arise due to temperature changes. The cell is illuminated from the bottom with a telecentric homogeneous light source. The light intensity distribution changes with the height and is captured by a camera at the top surface. The PIV technique is used to measure the fluid velocity along a fixed radial-vertical plane. This plane is illuminated with a laser light sheet and particles are mixed into the working fluid. The displacement of the particles, when illuminated by the light sheet, are recorded by a camera mounted normal to the plane. More details can be found in Meier et al. (2018) and Seelig et al. (2019).

Results

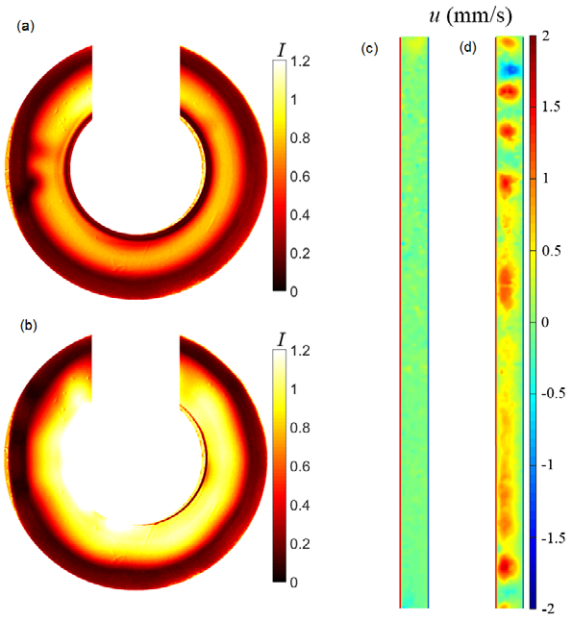

Figure 2: Shadowgraph image at (a) the initial time and (b) the final time of the µg phase for a temperature difference of $\boldsymbol{\Delta T} = 10$ K and an effective electric potential of $\boldsymbol{V_0} = 5$ kV. Radial velocity profiles at (c) the initial time and (d) the final time of the µg phase for $\boldsymbol{\Delta T} = 16$ K and $\boldsymbol{V_0} = 5.7$ kV. For these two parabolas, the voltage was applied only during µg conditions.

It is shown theoretically and numerically that under microgravity conditions the base conductive state destabilizes to counter-rotating pairs of helical vortices. These modes are stationary and increase significantly the heat transfer. Parabolic flight experiments have been performed, providing a microgravity phase of about 22s. The duration of this phase is not sufficient to obtain a fully developed state, but the visualisation methods showed a clear growth of temperature and velocity perturbations. Indeed, we can see in the figure 2 the light intensity profile provided by shadowgraphy and the radial velocity profile provided by PIV at the beginning and at the end of the µg phase. The shadowgraph image at the end of the µg phase shows a dissymmetry in the azimuthal direction and the growth of radial velocity perturbation indicates the occurrence of an instability.
A linear stability analysis showed that under Earth's gravity conditions different modes can be observed depending on the dimensionless electric potential V_E. For low V_E, oscillatory toroidal vortices are originated by the Archimedean buoyancy. For large V_E, the DEP force is the main destabilizing mechanism and induces stationary helical modes. And for moderate V_E, the radial and axial buoyancies contribute together to generate stationary columnar vortices. Numerical and experimental investigation of this problem with an aspect ratio of 20 confirmed the existence of the columnar structure, but the toroidal vortices have never been observed due to the stabilizing effect of the base flow.

Conclusions

The application of the dielectrophoretic force in a cylindrical annulus gives the possibility to modify the stability of the fluid. The vortices have different orientation depending on the presence or absence of a vertical gravity (i.e. the Earth's gravity). It's shown that the occurrence of convective flow is accompanied with a significant increase of the heat transfer, which makes relevant the use of this effect for future devices.

Acknowledgements

The project"Thermoelektrische Konvektion unter Schwerelosigkeit (TEKUS)" is supported by the BMWi via the space administration of the German Aerospace Center DLR under grant no. 50WM1644. We also acknowledge the support of the Centre Nationale d'Etudes Spatiales (CNES), Novespace S.A. in Bordeaux the TEXUS-group of Airbus Defence and Space, Bremen and our technical staff at BTU. T. Seelig was supported by the DFG grant "Thermo-elektrohydrodynamisch TEHD getriebene Wärmetransporterhöhung im vertikalen Zylinderspalt - Experimente und numerische Simulation im Kontext von Messunsicherheiten und optimaler Versuchsplanung (EG 100/20-1)".

References

H.N. Yoshikawa, O. Crumeyrolle, I. Mutabazi, Dielectrophoretic force-driven thermal convection in annular geometry. *Phys. Fluids,* 25 (2013) 024106.

V. Travnikov, O. Crumeyrolle, I. Mutabazi, Numerical investigation of the heat transfer in cylindrical annulus with a dielectric fluid under microgravity. *Phys. Fluids*, 27 (2015) 054103.

A. Meyer, Crumeyrolle, O., Mutabazi, I., Meier, M., Jongmanns, M., Renoult, M.-C., Seelig, T., Egbers, C.: Flow Patterns and Heat Transfer in a Cylindrical Annulus under 1g and low-g Conditions: Theory and Simulation, *Microgravity Sci. Technol.* 30 (2018) 653–662.

T. Seelig, A. Meyer, P. Gerstner, M. Meier, M. Jongmanns, M. Baumann, V. Heuveline, C. Egbers, Dielectrophoretic force-driven convection in annular geometry under Earth's gravity, *International Journal of Heat and Mass Transfer* (accepted in April 2019)

M. Meier, M. Jongmanns, A. Meyer, T. Seelig, C. Egbers, I. Mutabazi, Flow pattern and heat transfer in a cylindrical annulus under 1g and low-g conditions: Experiments, *Microgravity Sci. Technol.* 30 (2018) 699-712.

Oral 067

Frequency jump and associated velocity field of oscillatory thermocapillary flow in a high-Prandtl-number liquid bridge

Y. Mabuchi[1], T. Yano[1], K. Nishino[1]

[1]Department of Mechanical Engineering, Yokohama National University,
79-5 Tokiwadai, Hodogaya-ku, Yokohama, Kanagawa 240-8501, Japan,
mabuchi-yuki-pz@ynu.jp, yano-taishi-gh@ynu.ac.jp, nishino-koichi-fy@ynu.ac.jp

Introduction

Thermocapillary flow in a half-zone liquid bridge (LB) of high-Prandtl-number fluid suspended between differentially heated disks shows a rich variety of transition processes from an initially steady state to a finally chaotic state through several oscillatory states (Preisser et al. 1983, Frank and Schwabe 1997). The first transition from steady state to oscillatory state is detected as an onset of time-dependent behavior of flow and temperature field in the LB. Such a behavior is characterized by the fundamental oscillation frequency and the mode structure that depends on the aspect ratio (AR) and the volume ratio (VR) of the LB (Nishino et al. 2002). It is found that the fundamental oscillation frequency can jump to a lower value with increasing disk temperature difference (ΔT) while the azimuthal mode number (m) remains unchanged (Frank and Schwabe 1997). Recently it is also shown that a small jump (or decrease) in oscillation frequency takes place with increasing ΔT in the supercritical region (Yasnou et al. 2018). The present study focuses on the detailed flow characteristics and their changes associated with the jump of oscillation frequency in the LB of 2-cSt silicone oil.

Experiment

Figure 1 shows the geometry of the present LB. It is formed between two coaxial disks, both 4.0 mm in diameter. The upper disk made of transparent sapphire is heated by a ribbon heater and the lower disk made of aluminum is cooled by a Peltier element. A high-speed CMOS camera (300 fps) is used to observe the internal flow through the upper disk. A green CW laser beam is formed into a 0.2 mm thick light sheet to illuminate horizontal cross sections of the LB. The LB surface temperature is measured with a thermocouple positioned very close to the liquid-gas interface (50 μm apart). The working fluid is silicone oil with the kinematic viscosity of 2 cSt (Pr = 28). The tracer particles of nylon 12 are suspended in the silicone oil. The values of AR, which is the ratio of the LB height to the disk diameter, are varied from 0.30 to 0.60. The value of VR, which is the ratio of the liquid volume to the gap volume between the disks, is either 1.0 or 0.8. The cold disk temperature is kept constant at 20 °C while the hot disk temperature is raised in a stepwise manner, so that $\Delta T / \Delta T_c$ is changed from 1.1 to 2.0 for each AR, where ΔT_c is the critical ΔT at the onset of the oscillatory state.

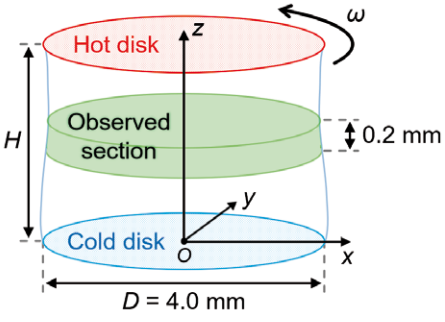

Figure 1: Geometry of the present LB.

Results and Discussion

The thermocouple signals are Fourier transformed to determine the oscillation frequencies. Figure 2 shows the oscillation frequencies for each AR plotted as a function of ΔT. In general, the oscillation frequencies increase with ΔT, but they jump to a lower value under the conditions of $\Delta T \approx$ 17.5 °C for (AR, VR, m) = (0.50, 1.0, 2), $\Delta T \approx$ 20.0 °C for (0.45, 1.0, 2) and $\Delta T \approx$ 22.0 °C for (0.40, 1.0, 2) while the azimuthal mode number of oscillation, m, is unchanged. The values of ΔT corresponding to these jumps are within the range of $\Delta T / \Delta T_c$ = 1.3 - 1.4. Such frequency jumps are not observed under the conditions of m = 1 and 3.

Figure 3 shows the images captured by the high-speed camera before and after the frequency jump for AR = 0.50.

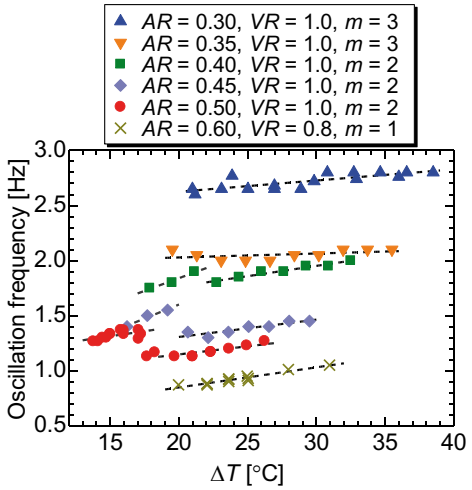

Figure 2: Transition of oscillation frequencies.

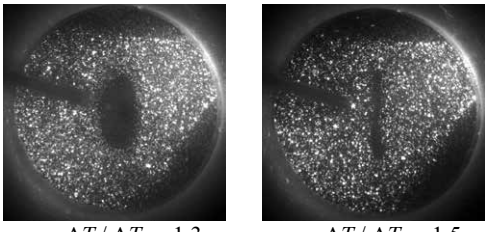

(a) $\Delta T / \Delta T_c$ = 1.3 (ΔT = 17.1 °C) (b) $\Delta T / \Delta T_c$ = 1.5 (ΔT = 19.7 °C)

Figure 3: Images of top view at z = 0.9 - 1.1 mm.

The position of the light sheet is z = 0.9 - 1.1 mm. A remarkable difference is seen in the shape of the void regions which are located in the center of the LB. The void region looks a fat ellipse before the jump at ΔT = 17.1 °C (or ΔT / ΔT_c = 1.3), whereas it changes to a narrow slit after the jump at ΔT = 19.7 °C (or ΔT / ΔT_c = 1.5). For both conditions, the void regions are rotating azimuthally at each constant angular speed, ω.

Entire flow field in the LB from the hot disk to the cold disk is obtained by traversing the laser light sheet in the axial direction at 0.2 mm interval. Instantaneous velocity fields are measured through PIV analysis and they are averaged in a rotating frame of reference which is rotating in the counterclockwise direction at ω. Figure 4 shows the averaged velocity fields at locations of (1) z = 1.5 - 1.7 mm, (2) z = 0.9 - 1.1 mm and (3) z = 0.3 - 0.5 mm for AR = 0.50 for (a) ΔT / ΔT_c = 1.3 and (b) ΔT / ΔT_c = 1.5. Note that the azimuthal phases of these results are aligned uniquely by using the thermocouple signals sampled simultaneously with PIV imaging at each location. The obtained results are explained and interpreted as follows.

(a) Before oscillation frequency jump (ΔT / ΔT_c = 1.3)

The fat elliptical void regions for all z locations are approximately oriented in the y direction and therefore they are not twisted with each other in the axial direction. The large-velocity region colored in red is located near the surface and near the vertex of the void region, but those large-velocity regions appear to change their azimuthal position gradually with respect to the vertex. This indicates the presence of a traveling wave that is rotating azimuthally (in counterclockwise here) with an axially inclined wave front extending from the hot disk to the cold disk. This observation is consistent with the well-known feature of azimuthally traveling wave of surface temperature as reported by, e.g., Nishino et al. (2002).

(b) After oscillation frequency jump (ΔT / ΔT_c = 1.5)

The void regions become into the shape of narrow slit. Their orientation does not change, but the position of the small-velocity regions colored in blue changes in the counterclockwise direction from the hot disk to the cold disk. This suggests that the flow field near the void region has changed. The large-velocity regions colored in red are wider than those for the condition (a) above and they indicate strong inward velocity from the surface to the interior of the LB. Such an inward flow field is particularly evident at z = 0.9 - 1.1 mm. An interesting observation is the velocity fields at z = 0.3 - 0.5 mm (i.e., near the cold disk) for the conditions (a) and (b) resemble with each other. This may suggest that the oscillation frequency jump is associated with the change of velocity (and temperature) field near the hot disk.

Conclusions

This paper presents the frequency jump related to the internal flow structures measured with PIV technique of oscillatory thermocapillary flow in high-Prandtl-number LBs. It is shown that the oscillation frequency jump occurs only under the condition of m = 2 and is associated with the change of internal flow structures.

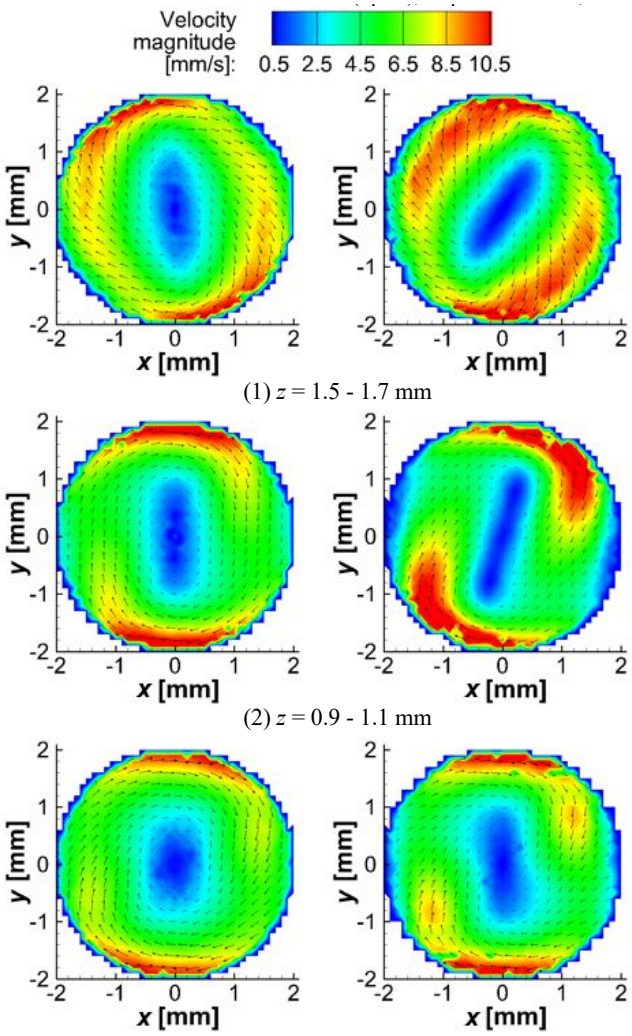

Figure 4: Phase averaged velocity fields at (1) z = 1.5 - 1.7 mm, (2) z = 0.9 - 1.1 mm and (3) z = 0.3 - 0.5 mm for AR = 0.50 for (a) ΔT / ΔT_c = 1.3 and (b) ΔT / ΔT_c = 1.5 seen from a rotating frame of reference.

References

F. Preisser, D. Schwabe and A. Scharmann, Steady and oscillatory thermocapillary convection in liquid columns with free cylindrical surface, *J. Fluid Mech.* 126 (1983) 545-567.

S. Frank and D. Schwabe, Temporal and spatial elements of thermocapillary convection in floating zones, *Exp. Fluids* 23 (1997) 234-251.

K. Nishino, K-H. Ko, M. Yukawa, and S. Yoda, Experimental and numerical study on thermocapillary convection of high Prandtl number fluid in cylindrical bridge, *NASDA Technical Memorandum* NASDA-TMR-020026E (2002) 45-72.

V. Yasnou, Y. Gaponenko, A. Mialdun, V. Shevtsova, Influence of a coaxial gas flow on the evolution of oscillatory states in a liquid bridge, *Int. J. Heat Mass Trans.*, 123, (2018) 747-759.

Oral 069

Effect of Alternating Gravity during a Parabolic Flight on Articular Chondrocytes

Simon L. Wuest[1], Jaro Arnold[2], Sarah Gander[3], Christoph Zumbühl[3], Christina Giger[1], Geraldine Cerretti[1], Martina Caliò[1], Gerhard S. Székely[2], Fabian Ille[1], Marcel Egli[1]

[1] Lucerne School of Engineering and Architecture, Institute of Medical Engineering, Space Biology Group, Hergiswil Switzerland;
[2] Lucerne School of Engineering and Architecture, Institute of Mechanical Engineering and Energy Technology, Horw, Switzerland;
[3] Lucerne School of Engineering and Architecture, Institute of Electrical Engineering, Horw, Switzerland;
simon.wueest@hslu.ch, fabian.ille@hslu.ch, marcel.egli@hslu.ch

Introduction

Adequate mechanical stimulation is essential for cellular health and tissue maintenance. However, to date the molecular mechanisms on how cells incorporate a mechanical force into a cellular response (mechanotransduction) are not fully understood. Among other mechanism the cytoskeleton is thought to play a key role in mechanotransduction (Ingber 2003). The cytoskeleton is involved in numerous cellular functions including proliferation, migration and differentiation and largely determines the mechanical properties of a cell (Ingber 2003). Cytoskeletal rearrangements or adaptations (Vassy, Portet et al. 2001, Aleshcheva, Wehland et al. 2015, Corydon, Kopp et al. 2016) as well as rapid changes in gene expression (Grosse, Wehland et al. 2012, Wehland, Aleshcheva et al. 2015, Thiel, Tauber et al. 2018) have been observed under altered gravity conditions of a parabolic flight in multiple cell types.

In this study we analyze cytoskeletal and gene expression responses during a parabolic flight, in chondrocytes. Chondrocytes are the only cell type found in articular cartilage tissue. This tissue separates the bones in articulating joints (e.g. hips, knees, shoulder, etc.). The pathological breakdown of articular cartilage results in osteoarthritis, which is a wide spread disease in western civilizations and has a major socio-economic impact. To date, cell-based approaches to restore cartilage tissue, had limited success (Marlovits, Zeller et al. 2006). Therefore, osteoarthritis is often treated with partial or total joint replacement. This study should help to better understand mechanotransduction pathways in chondrocytes.

Hardware design

We have developed a novel hardware which allows to chemically fix adherent cells at predefined time points during a parabolic flight. The cells can be fixed with either formaldehyde solution or RNAlater for immunocytochemical stainings or transcriptomic analysis, respectively. The cells are seeded in commercial microscope slides featuring a perfusable channel (ibidi, Germany). The slides are each attached via silicone tubes to a syringe containing the fixative as well as an empty syringe. The fixative is subsequently injected into the slide by a linear actuator replacing the cell culture medium with the fixative within two seconds. Thereby waste medium is collected in the empty syringe.

We designed units, in which up to three slides can be mounted (Figure 1 and 2). The samples are placed on an aluminum plate, which is temperature controlled to 37°C. Each unit runs a microcontroller allowing communication to an external computer via a serial data interface. In addition to controlling the temperature and the injection of the fixative, the microcontroller can also log various housekeeping data such as acceleration, temperature and air pressure.

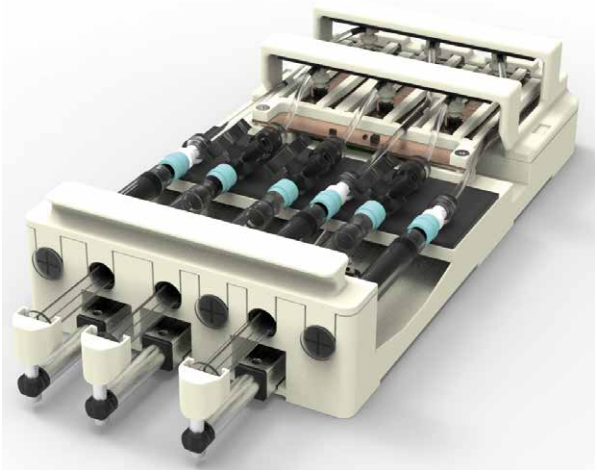

Figure 1: Overview of a unit allowing to chemically fix up to three samples.

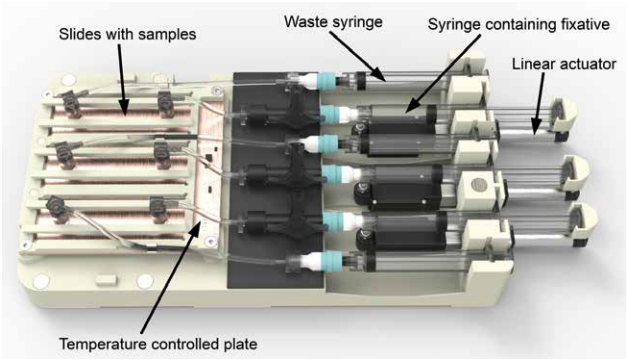

Figure 2: Top view on a unit. Cells are seeded in commercial slides featuring a perfusable channel. A chemical fixative can be rapidely injected by a linear actuator replacing the cell culture medium. Waste medium is collected in an empty syringe.

Outlook

This study will fly during the 71st ESA parabolic flight campaign in May 2019. Thereby, we will examine cytoskeletal adaptations and repid changes in gene expression as the cells are exposed to altered gravity.

Acknowledgements

We thank the European Space Agency (ESA) for the flight opportunity and Novespace for conduction the parabolic flight. We also thank the Swiss Space Office and the Lucerne University of Applied Sciences and Arts for financial support.

References

Aleshcheva, G., M. Wehland, J. Sahana, J. Bauer, T. J. Corydon, R. Hemmersbach, T. Frett, M. Egli, M. Infanger, J. Grosse and D. Grimm (2015). "Moderate alterations of the cytoskeleton in human chondrocytes after short-term microgravity produced by parabolic flight maneuvers could be prevented by up-regulation of BMP-2 and SOX-9." FASEB J **29**(6): 2303-2314.

Corydon, T. J., S. Kopp, M. Wehland, M. Braun, A. Schutte, T. Mayer, T. Hulsing, H. Oltmann, B. Schmitz, R. Hemmersbach and D. Grimm (2016). "Alterations of the cytoskeleton in human cells in space proved by life-cell imaging." Sci Rep **6**: 20043.

Grosse, J., M. Wehland, J. Pietsch, X. Ma, C. Ulbrich, H. Schulz, K. Saar, N. Hubner, J. Hauslage, R. Hemmersbach, M. Braun, J. van Loon, N. Vagt, M. Infanger, C. Eilles, M. Egli, P. Richter, T. Baltz, R. Einspanier, S. Sharbati and D. Grimm (2012). "Short-term weightlessness produced by parabolic flight maneuvers altered gene expression patterns in human endothelial cells." FASEB J **26**(2): 639-655.

Ingber, D. E. (2003). "Tensegrity I. Cell structure and hierarchical systems biology." J Cell Sci **116**(Pt 7): 1157-1173.

Ingber, D. E. (2003). "Tensegrity II. How structural networks influence cellular information processing networks." J Cell Sci **116**(Pt 8): 1397-1408.

Marlovits, S., P. Zeller, P. Singer, C. Resinger and V. Vecsei (2006). "Cartilage repair: generations of autologous chondrocyte transplantation." Eur J Radiol **57**(1): 24-31.

Thiel, C. S., S. Tauber, S. Christoffel, A. Huge, B. A. Lauber, J. Polzer, K. Paulsen, H. Lier, F. Engelmann, B. Schmitz, A. Schutte, C. Raig, L. E. Layer and O. Ullrich (2018). "Rapid coupling between gravitational forces and the transcriptome in human myelomonocytic U937 cells." Sci Rep **8**(1): 13267.

Vassy, J., S. Portet, M. Beil, G. Millot, F. Fauvel-Lafeve, A. Karniguian, G. Gasset, T. Irinopoulou, F. Calvo, J. P. Rigaut and D. Schoevaert (2001). "The effect of weightlessness on cytoskeleton architecture and proliferation of human breast cancer cell line MCF-7." FASEB J **15**(6): 1104-1106.

Wehland, M., G. Aleshcheva, H. Schulz, K. Saar, N. Hübner, R. Hemmersbach, M. Braun, X. Ma, T. Frett, E. Warnke, S. Riwaldt, J. Pietsch, T. J. Corydon, M. Infanger and D. Grimm (2015). "Differential gene expression of human chondrocytes cultured under short-term altered gravity conditions during parabolic flight maneuvers." Cell Communication and Signaling **13**(1): 18.

Oral 070

Results of Microgravity Zero-Boil-Off Tank (ZBOT) Experiment & CFD Model Validation

M. Kassemi [1], S. Hylton, O. Kartuzova

National Center for Space Exploration Research
NASA Glenn Research Center & Case Western Reserve University
Cleveland, Ohio, USA;
[1]Mohammad.Kassemi@nasa.gov

Introduction

Integral to all phases of NASA's projected planetary expeditions is affordable and reliable cryogenic fluid storage for use in propellant or life support systems [1]. Cryogen vaporization due to heat leaks into the tank from its surroundings and support structure can cause self-pressurization that is currently relieved through venting. This leads to undesirable propellant loss. Thus, it is greatly advantageous to develop innovative vent-less pressure control designs based on mixing of the bulk tank fluid with active cooling to allow storage of the cryogenic fluid with zero or reduced boil-off.

The Zero-Boil-Off Tank (ZBOT) Experiments are a series of small scale tank pressurization and pressure control experiments aboard the International Space Station (ISS) that use a transparent volatile simulant fluid in a transparent sealed tank to delineate various fundamental fluid flow, heat and mass transport, and phase change phenomena associated with storage tank pressurization and pressure control in microgravity [2]. The hardware for ZBOT-1 flew to ISS on the OA-7 flight in April 2017 and was installed in the Microgravity Science Glovebox (MSG) as shown in Fig. 1. Operations began in September 2017 and were completed by December 2017, encompassing more than 100 tests. Hand-in-Hand with the experiment a state-of-the-art two-phase CFD model of the storage tank pressurization & pressure control is also developed and validated against the experimental results.

Experimental Results & CFD Model Validation

The ZBOT test cell and the main components of the experimental set up are shown in in Fig 2. In this paper, we present some of the key experimental findings of the microgravity experiment such as [3]:

1. Moderate heat flux strip heating cases produced classic self-pressurization trend at first, but eventually led to boiling at the heaters caused by microgravity thermal stratification resulting in rapid pressure spike.
2. Mixing tests at small jet velocities exhibited a non-intuitive behavior with continuous movement of the ullage towards the nozzle which was more pronounced at lower fill levels (larger ullage sizes).

Figure 1. Astronaut Joe Acaba Installing the ZBOT hardware in the Microgravity Science Glovebox (MSG) aboard the International Space Station (ISS).

3. At larger flow velocities, the ullage was significantly penetrated and deformed by the jet and its downward motion was arrested.
4. During pressure control tests with subcooled jet, surprising and sudden evolution and growth of many small bubbles were observed. Here unexpected boiling at both sides of the screened liquid acquisition device (LAD) during the pressure collapse is suspected.
5. Unique self-pressurization tests during three different ISS reboost/coasting maneuvers showed the effect of the resultant accelerations on the movement and re-positioning of the ullage and on subsequent changes in fluid flow & tank pressurization rate.

Both local temperature and pressure measurements and full field fluid flow captured by Particle Imaging Velocimetry (PIV) are presented to describe the above-mentioned observed phenomena. The important underlying transport/phase change mechanisms associated with these results are discussed using insight provided by two-phase CFD model simulations. The storage tank model is also validated by comparing the CFD predictions with microgravity experimental results for tests involving; (a) self-pressurization by localized and global wall heat heating; (b) Ullage dynamics and deformation and thermal destratification during

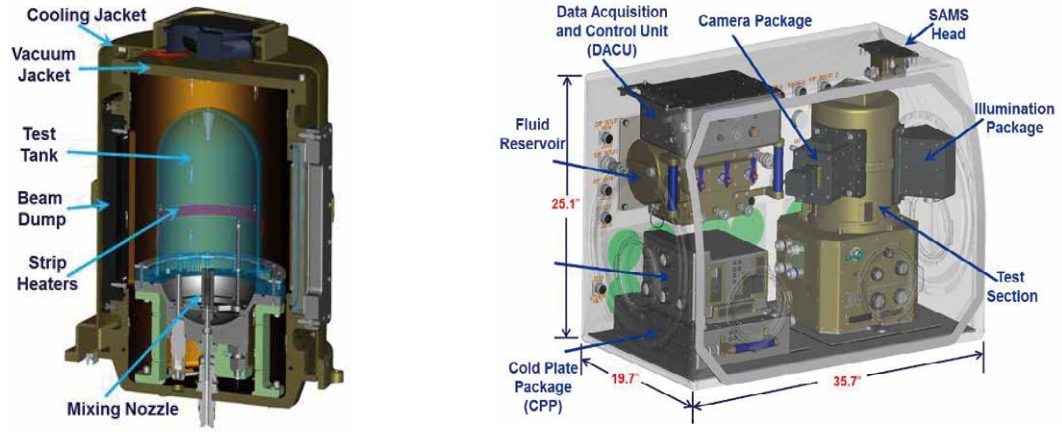

Figure 2. Schematic of ZBOT hardware components in MSG and Cross sectional view of test tank within the vacuum jacket.

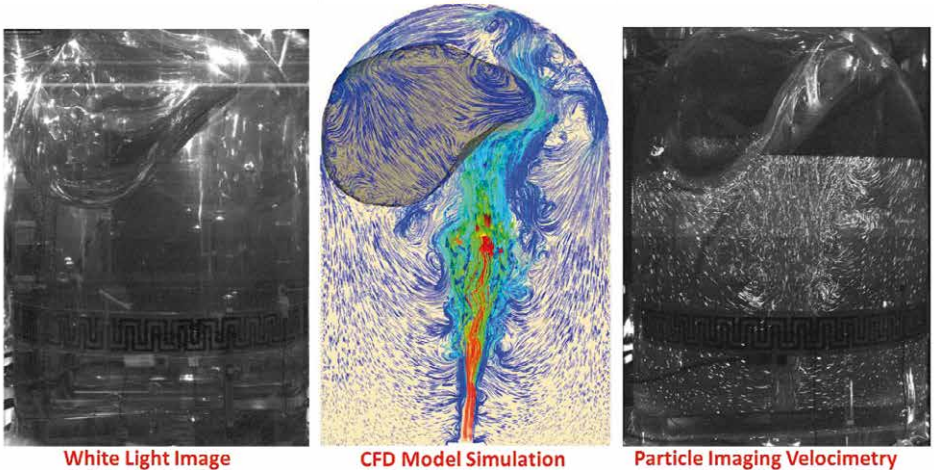

Figure 3. Zero-Boil-Off Tank (ZBOT) Experiment: Depiction of fluid flow and deformation of Ullage (vapor bubble) by the liquid jet during forced jet mixing pressure control in microgravity

isothermal jet mixing; and (c) pressure control using sub-cooled jet mixing.

In Fig. 3, 3D CFD model predictions of fluid flow and ullage deformation are compared to experimentally-captured white light images and particle streakline taken during the PIV flow field measurements. The agreement between CFD predictions and microgravity experimental results is very good with the model simulation depicting the correct dynamic flow structures and ullage deformations that evolve during the isothermal mixing interval.

3D CFD model predictions of tank self-pressurization by global and localized heating in microgravity are also compared to experimental results and agreement was found to be excellent with less than 3% discrepancy between predicted and measure results.

Conclusions

The storage tank pressurization and pressure control data obtained by the ZBOT experiment indicate several interesting intuitive and non-intuitive trends with important implications for Cryogenic Fluid Management of propellant and life support storage tank on Orbit. The data also serves well for validating and verifying the fidelity of a state-of-the-art two phase storage tank CFD model for simulating various aspect of microgravity CFM operations. Without the insight obtained from the computational model understanding the non-intuitive microgravity results would be extremely difficult.

Acknowledgements

Funding from the ISS Microgravity Physical Sciences Program, NASA HQ, and computational and model validation support provided by NASA STMD Evolvable Cryogenic project are greatly acknowledged.

References

1. Salzman, J., "Fluid management in space-based systems," Proceedings of the Engineering, Construction, and Operations in Space, 5th international conference on space, Vol. 1, 1996, p. 521–6.

2. Barsi S. and Kassemi, M. "Investigation of Tank Pressurization and Pressure Control-Part I: Experimental Study", ASME Journal of Thermal Science & Engineering Applications, Vol. 5, No 2, pp- 041005: 1-20, December 2013.

3. M. Kassemi, O. Kartuzova, S. Hylton, Validation of Two-Phase CFD Models for Propellant Tank Self-Pressurization: Crossing Fluid Types, Scales, and Gravity Levels, Cryogenics Vol. 89 pp. 1–15, Jan 2, 2018.

Oral 071

Simple closed ecosystem development for PlantSat nanosatellite mission

V. Brykov[1,2], B. Ivanitskaya[3], Y. Zaplatnikov[4],

[1]M.G. Kholodny Institute of Botany, National Academy of Sciences of Ukraine, Kyiv, Ukraine, [2]RUDN University, Moscow, Russian Federation, [3]M.M. Gryshko National Botanical Garden, Kyiv, Ukraine,[4]ESC "Institute of Biology and Medicine" of T. Shevchenko National University of Kyiv, Kyiv, Ukraine;
vbrykov@gmail.com

Introduction

It is generally accepted that plants are the necessary part of Bioregenerative Life-Support Systems (BLSS) for astronauts' in the future long-term flights in deep space, visiting Mars, building Moon bases, as the sources of oxygen, food, and recycled water. The creation of plant greenhouse BLSS using current technologies used on the ISS and results of previous experiments are not possible. One of the predictable problems is that the use of a large area greenhouse that can provide necessary amount of food and oxygen will require the full involvement of the crew to the process of plant cultivation (Heyenga, 1997; Brykov, 2015). In addition, almost all plants that were grown on board were annuals with a short life cycle (up to 6 months), and unfortunately the duration of many experiments did not exceed 30 days. The results of previous experiments are not enough to predict the behavior of plants in long space flights. So, further investigations of plant responses and adaptation to microgravity are necessary for the further human space exploration. Unfortunately, the opportunities for the realizing of experiments with plants on board the ISS are very limited.

Closed man-made ecological system – a perspective model for biological experiments on nanosatelites

It is known that plants are capable to be in a closed hermetic habitat isolated from the external atmosphere for a sufficient long time. Isolation of living organisms from the atmosphere is called closed man-made ecological system (CMES), and it is a unique tool for research of fundamental processes and interrelations in the global ecosystem (Gitelson, Lisovsky, 2003). Potentially, the CMES can be used to create life-support systems for space exploration and support life outside the Earth's biosphere (Gitelson, Lisovsky, 2003; Nelsonet al., 2003). Biosphere 2 project and several other closed systems are well known. The ability of an orchid *Phalaenopsis pulcherrima* to grow in CMES in 3 dm^2 over 13 years was demonstrated in the M.M. Gryshko National Botanical Garden of the National Academy of Sciences of Ukraine. In order to maintain the viability of plants in CMES, it is only necessary to provide temperature and light conditions and any more manipulations are not required, so they are suitable to use in biological experiments on nanosatellites.

PlantSat mission

Now we are working on the design of a hermetic growth chamber, the selection of perennials, the creation of an autonomous life support system for plants on the CubeSat platform, for realization of the PlantSat mission.The primary scientific purpose of the PlantSat mission is to investigate the influence of microgravity on plant growth and development, its respiration and photosynthetic activity and plant-microbial interactions. To simplify a problem of plant growth support, we propose to develop the miniature CMES using of which requires only corresponding temperature and light regimes. PlantSat will be equipped with sensors of temperature, light, carbon dioxide and oxygen concentration as well as an optical system to detect the plant growth and telemetry. It is planned to test the growth and physiological state of certain plant species selected for space planting in CMES in monoculture (one crop) or polyculture (multiple crops). Currently, we are providing experiments to select plant species suitable for growth in closed system. There are several numbers of plants that are suitable for above-mentioned features and which we chose to grow in small closed ecological chambers: *Chlorophytum comosum*, *Tradescantia fluminensis*, different tomato cultivars, some orchids (*Doritis pulcherrima*, *Bulbophyllum* sp., *Dendrobium crumenatum*, *Coelogyne fimbriata*) as well as *Mammillaria elongata*, *Euphorbia* sp., *Cryptanthus bahianus*.

Conclusions

The results of the PlantSat mission will answer one of the key questions of plant space biology, namely how long higher plants can exist in an active physiological state under the space flight conditions and whether a simple closed ecosystem will be functioning in microgravity.

References

A.G. Heyenga The utilization of passive water and nutrient support systems in space flight plant cultivation and research. 6-th Eur. Symp. Space Environ. Contr. *Syst.*867–871. (1997)

V.O. Brykov, Bioenergetics of plant cells in microgravity, *Space Science and Technology*, 21 (2015) 84-93. (in Ukrainian)

J.I. Gitelson and G.M. Lisovsky, Man-made Closed Ecological Systems. CRC Press, London-New York, 416 p. (2003)

M. Nelson, J. Allen, A. Ailing, W.F. Dempster, S. Silverstone, Earth applications of closed ecological systems: Relevance to the development of sustainability in our global biosphere, *Adv. Space Res*. 31 (2003) 1649-1655.

26th European Low Gravity Research Association Biennial Symposium and General Assembly
14th International Conference on "Two-Phase Systems for Space and Ground Applications"
European Space Agency Topical Teams meetings
Granada (Spain), September 24-27, 2019

Oral 073

Space Transport Efficiency In Nearly Every Regime

P. Clemente, S. Cuevas, D. Martinez, A. Solá. E. Velázquez

EIATA, ETSIT, Universidad Rey Juan Carlos, Madrid, Spain
p.clemente.2017@alumnos.urjc.es s.cuevas.2017@alumnos.urjc.es d.martinezd.2017@alumnos.urjc.es
a.solam.2017@alumnos.urjc.es e.velazquez.2017@alumnos.urjc.es

Introduction

As a result of our participation in the Student Aerospace Challenge, we present the process, ideas, and results of our work in the Aerodynamics and Flight Control work package.

Our goal was to define the aerodynamic and propulsive characteristics for the suborbital vehicle, adapting these to every stage and condition of flight. This would lead to the optimisation of the trajectory in terms of fuel consumption, while reducing environmental impact of the operation.

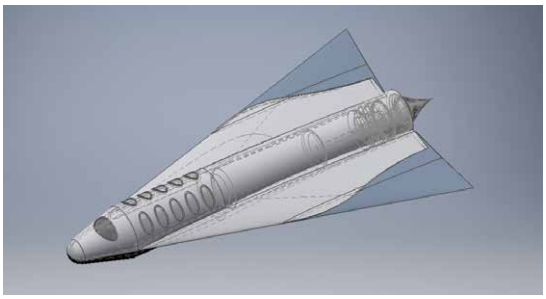

Figure 1: Three-dimensional model of the aircraft and aerospike.

Aerodynamics

(Anderson, 2017 and Weiland, 2013).
We have created a variable-sweep wing design which adjusts the aerodynamic profile of the aircraft to each flight regime. In order to increase efficiency in the transonic regime, we have decided to weaken the drag divergence phenomena with Whitcomb's area rule and by increasing the critical Mach number using the deflection angle.

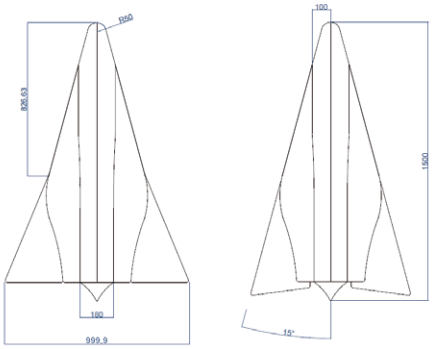

Figure 2: Plan schematic for the variable-sweep wing (cm)

Heat transfer

(Regan et al. 1992).
The vehicle's geometry and stage of flight during re-entry will affect the speed of heat transfer, both through convection and radiation. The choice of materials and the structural design are limited by the heat transfer during re-entry. We have determined the maximum heat flux and applied the Fay-Riddel equation to construct a non-linear system of equations to model the heat transfer.

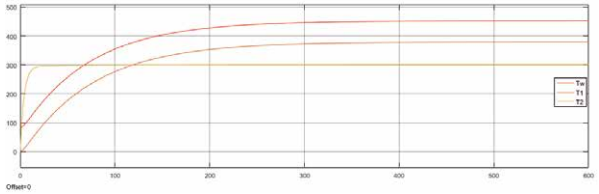

Figure 3: Temperature of the aluminium (underside). Orange for 2024 alloy and red for 5052 honeycomb alloy.

Aerospike engine

In order to increase aerodynamic efficiency at every stage of flight, we have decided to implement a pressure-fed aerospike engine design, using PR-1 and LOX. This increases fuel efficiency, decreaces vehicle size, and improves the aerodynamic profile of the aircraft.

The combustion gasses are constrained on one side by the nozzle's spike, and on the other side by atmospheric pressure. Therefore, the aerospike's plume can widen with the decreasing atmospheric pressure as the vehicle climbs and enters the low pressure in the upper atmosphere.

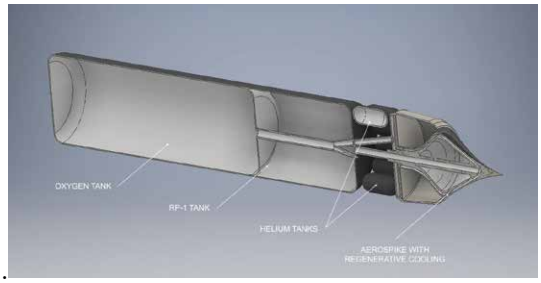

Figure 4: Sectional view of aerospike nozzle, engine, and tanks.

Mechanical model and trayectory

(de Celis, Cadarso. 2018. Gómez Tierno, 2012.)
The objective of the trajectory design process was to obtain a multi-objective optimisation of the vehicle's trajectory. The optimisation of the trajectory has been done using the algebraic optimisation software General Algebraic Modelling System IDE (GAMS), once the underlying mechanical problem was completed.

The mechanical model was constructed using three frame-of-reference systems, applying the Euler angles for

their respective orientations. The final system consisted in three kinematic equations and three dynamic equations. We also introduced the constraints on velocity and accelerations as announced by the challenge. We then made a numerical approximation using the trapezoid method.

For optimization, the critical variables were altitude and range, and the maximisation of these was the objective of the trajectory optimisation. Fuel consumption was also maintained as an objective, so as to not be compromised when achieving maximum range. The solution we have used is the application of non-linear programming algorithms (NLP) This also allows us to gradually add complexity to the model.

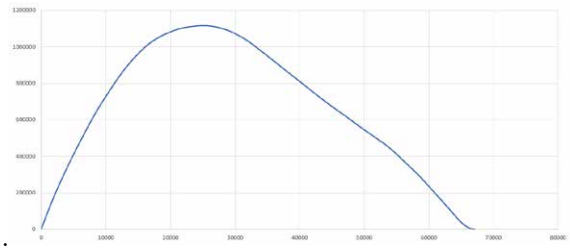

Figure 5: Approximation of optimized trajectory.

Conclusion

A preliminary but complete and accurate design has been proposed. The trajectory optimisation is still in early stages, and yet it has met guidelines, impositions, and boundaries. We have obtained great performance in terms of altitude, range, and fuel consumption, as well as stability and structural integrity. Environmental impact has been established as a critical design variable, selecting recyclable and economically viable alumina, without compromising operational performance.

Education

The design challenge was incredibly nondisciplinary; the reaches of the aerodynamic, thermodynamic, mechanical, and propulsive research that we conducted was a new experience for us. This whole process has forced us, undergraduate aerospace engineering students, to pool our skills, despite the limited education we have received in this field.

It also gives us a glimpse into how the technical knowledge we acquire in lectures and courses is put into practice. It

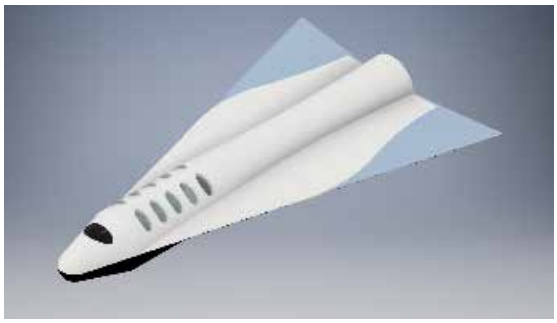

Figure 6: Three dimencional model of aerodynamic profile.

made us aware of how convoluted the design process is, and we learned how to deal with dead ends and bad judgement calls. The level of interconnection between the different fields that we have studied has challenged our capacity for teamwork and transmission of information.

We have also gained an appreciation for how important creativity and out-of-the-box thinking is, often marking the difference when approaching unknown territory and intertwining disciplines. We have created many valuable building blocks for our professional arsenal. We believe that experiences like this help and promote better professionals in the future and encourage us to come together with new ideas for innovative problems.

Acknowledgements

Thank you to our mentor, Pablo Solano, and the EIATA staff.

References

John D. Anderson. *Fundamentals of Aerodynamics.* McGraw-Hill Education, New York, 6th edition, 2017.

Peter Weiand. *Transonic aerodynamics in conceptual aircraft design.* Deutscher Luf-und Raumfahrtkongress, 2013.

Frank J. Regan and Satya M. Anandakrishnan. *Dynamics of Atmospheric Re-Entry.* Washington, DC : American Institute of Aeronautics and Astronautics, c1993, 2nd edition, 1993.

Raúl de Celis and Luis Cadarso. *Attitude determination algorithms through accelerometers, gnss sensors, and gravity vector estimator.* International Journal of Aerospace Engineering, 2018(5394057), 2018.

Miguel Ángel Gómez Tierno and Manuel Pérez Cortés. *Mecánica del Vuelo.* Garceta Grupo Editorial, 2nd edition, 2012.

26th European Low Gravity Research Association Biennial Symposium and General Assembly
14th International Conference on "Two-Phase Systems for Space and Ground Applications"
European Space Agency Topical Teams meetings
Granada (Spain), September 24-27, 2019

Oral 074

External forcing of columnar vortices in thermoelectric convection: a theoretical approach

I. Mutabazi[1], A. Meyer[1], C. Kang[1], H. Yoshikawa[2]

[1]Normandie Université, UNIHAVRE, LOMC, UMR 6294 CNRS, France,
[2] Université Nice Côte d'Azur, CNRS UMR 7010, INPHYNI, Nice, France
mutabazi@univ-lehavre.fr, ckang44@uic.edu,antoine.meyer@b-tu.de, harunori.yoshikawa@unice.fr

Introduction

Thermoelectric convection occurs in a dielectric liquid under the action of a temperature gradient and a high-frequency electric voltage. It is generated by the overwhelming action of the dielectrophoretic buoyancy over dissipative forces in the liquid. In a stationary cylindrical annulus, under microgravity conditions, thermoelectric convection appears in form of stationary helical modes, whose inclination depends only on the radius ratio (Yoshikawa et al. 2013). We show that these helical vortices can be transformed into vertical columnar vortices either by a small Archimedean buoyancy or aCoriolis force.

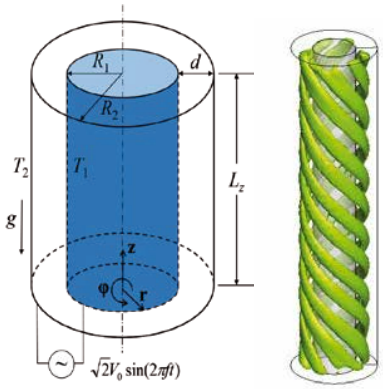

Figure 1: A cylindrical annulus with a dielectrophoretic force under microgravity: critical helical vortices (Travnikov et al., 2015)

Flow equations

We consider a dielectric liquid of density ρ, viscosity ν, thermal expansion coefficient α, thermal diffusivity κ, and permittivity ε, inside a cylindrical annulus with a gap d and subject to a radial temperature difference ΔT and an alternating electric tension with frequency f and an effective voltage V_e. We investigate the robustness of helical vortices by a weak effect of solid body rotation $\boldsymbol{\Omega}$ about the cylinder axis or a weak Archimedean buoyancy. We write the general flow dimesionless equations in the Boussinesq-Oberbeck approximation, as follows

$$\nabla\cdot\mathbf{u} = 0 \qquad (1\text{-a})$$

$$\frac{\partial \mathbf{u}}{\partial t} + (\mathbf{u}\cdot\nabla)\mathbf{u} - 2\tau\mathbf{e}_z\times\mathbf{u} = -\nabla H + \nabla^2\mathbf{u} + \mathbf{B} \qquad (1\text{-b})$$

$$\frac{\partial \theta}{\partial t} + (\mathbf{u}\cdot\nabla)\theta = \frac{1}{Pr}\nabla^2\theta \qquad (1\text{-c})$$

$$\nabla\cdot\{(1-\gamma_e\theta)\mathbf{E}\} = 0, \quad \mathbf{E} = -\nabla\phi \qquad (1\text{-d})$$

where $\mathbf{u}$ is the velocity field, H is the generalized Bernoulli function, θ is the temperature field and $\mathbf{E}$ is the effective electric field and ϕ is the electric potential. The buoyancy term is given by

$$\mathbf{B} = \left(\gamma_e\tau^2 r\boldsymbol{e}_r - \frac{\gamma_e V_E^2}{Pr}\frac{\boldsymbol{g}_e}{\bar{g}_e}\right)\theta, \quad \gamma_e = e\Delta T \qquad (2)$$

where $\boldsymbol{g}_e$ is the electric gravity and $\bar{g}_e$represents the electric gravity at the median cylindrical surface, $\tau = \Omega d^2/\nu$ is the Coriolis number, $V_E = V_0/\sqrt{\rho\nu\kappa/\epsilon_2}$is a dimensionless electric tension.
The equations were investigated by linear stability analysis and by DNS in two cases : weak solid body rotation (case 1) and weak Archimedean buoyancy (case 2). Here are the main results:

Case 1 : Weak solid-body rotation
A weak solid body rotation characterized by the rotation rate $\tau = \Omega d^2/\nu$ transforms the helical vortices into drifiting columnar vortices along the azimuthal direction for $\tau > \tau_c(\eta)$. The value of τ_c is independent of Prandtl number. The threshold of the columnar vortices is higher than that of helical vortices. The heat transfer by columnar vortices transport heat in a less efficient than by helical vortices.

Case 2 : Weak Archimedean buoyancy
We chose a temperature difference ΔT below the critical value (in the absence of the electric tension). Then we apply the electric voltage and increase it until thermoconvection sets in at $L = L_c(\eta)$ which does not depend on Pr. Critical modes appear in form of stationary columnar vortices (Kang et al. 2019).

Conclusion

A weak Archimedean buoyancy or a weak solid-body rotation of a cylindrical annulus with a radial temperature gradient and an alternating electric voltage transforms the helical vortices appearing at the onset of thermoelectric convection under microgravity conditions into columnar vortices.

Acknowledgements

The work was supported by CNES and the Normandy Region.

References

H. N. Yoshikawa, O. Crumeyrolle, and I. Mutabazi, "Dielectrophoretic force-driven thermal convection in annular geometry," *Phys. Fluids* **25** (2013). 024106.
V. Travnikov, O. Crumeyrolle, I. Mutabazi, "Numerical investigation of the heat transfer in cylindrical annulus with a dielectric fluid under microgravity, *Phys. Fluids* **27** (2015), 054103.
C. Kang, I. Mutabazi, Dielectrophoretic buoyancy and heat transfer in a dielectric liquid contained in a cylindrical annular cavity, *J. Appl. Phys*. **125** (2019).

Oral 076

vgBoiling: Study on Gravity Scaling Law of Pool Boiling Phenomena Utilizing VGR of CSS

J. F. Zhao[1, 2], W. F. Du[1], X. Li[3], Z. H. Qiao[3], F. Ye[4], H. Guo[4], H. X. Li[5], J. J. Wei[5, 6]

[1] CAS Key Laboratory of Microgravity (National Microgravity Laboratory), Institute of Mechanics, Chinese Academy of Sciences, Beijing, China; [2] School of Engineering Science, University of Chinese Academy of Sciences, Beijing 100049, China; [3] Technology and Engineering Center for Space Utilization, Chinese Academy of Sciences, Beijing, China; [4] MOE Key Laboratory of Enhanced Heat Transfer and Energy Conservation and Beijing Key Laboratory of Heat Transfer and Energy Conversion, College of Environmental and Energy Engineering, Beijing University of Technology, Beijing, China; [5] State Key Laboratory of Multiphase Flow in Power Engineering, Xi'an Jiaotong University, Xi'an, China; [6] School of Chemical Engineering and Technology, Xi'an Jiaotong University, Xi'an, China
E-mails: jfzhao@imech.ac.cn; duwangfang@imech.ac.cn

Boiling heat transfer realizes the high-performance heat exchange due to latent heat transportation, resulting in its wide applications for high heat flux transfer both on the Earth and in space. It is also a complex and elusive process. Thus, a great amount of empirical correlations and semi-mechanistic models for engineering applications, which are mainly depended upon empirical data obtained from elaborately designed experiments, flood in the literature up to now. Although many empirical correlations and semi-mechanistic models include gravity as a parameter, they usually fail when extended beyond the range of gravity levels they were based on, namely 1g, high-g and low-g.

It is well known that gravity strongly affects boiling phenomenon by creating forces in the systems that drive motions, shape boundaries, and compress fluids. Furthermore, the presence of gravity can mask effects that ever present but comparatively small in normal gravity environment. Advances in the understanding of boiling phenomenon have been greatly hindered by masking effect of gravity.

Microgravity experiments offer a unique opportunity to study the complex interactions without gravity. On the progress in this field, many comprehensive reviews are available now. For example, Straub (2001), Di Marco (2003), Kim (2003, 2009), Ohta (2003), Zhao (2010), among many others, summarized the experimental and theoretical works all over the world.

There is, however, obvious incomparability between the results of different experiments on boiling phenomenon by different authors or even the same authors. This makes the boiling experiments in different gravity conditions often fail to reveal the gravity effect correctly. Raj et al. (2012a) presented a unified framework for scaling heat flux with gravity and heater size based on experimental results acquired for transition periods of approximately 3–5 s when the acceleration varied continuously from hypergravity to low-g and vice versa during parabolic flights. The gravity scaling parameter for heat flux was updated based on high quality microgravity data aboard ISS (Raj et al. 2012b), and its robustness in predicting low gravity heat transfer is further demonstrated by predicting many of the trends in the pool boiling literature that cannot be explained by any single model.

There are still several unsolved problems in the model of Raj et al. (2012a, b). The definition of the dimensionless temperature involves the temperatures of the boiling incipiency and of the critical heat flux (CHF), but the model didn't give a clear rule of their variations with gravity. It implicitly assumed unchangeable values for these two characteristic temperatures in different gravity conditions. There is no theoretical or empirical basis for this assumption. Moreover, recent numerical studies utilizing the lattice Boltzmann method showed that the temperature of CHF decreases with the gravity level (Ma et al. 2017; Feng et al. 2019). Thus, more theoretical and experimental studies are needed on this topic.

A new project, vgBoiling – gravity scaling law of pool boiling heat transfer and relevant bubble thermal dynamic behaviors, has been proposed and passed the relevant expert review. It will be conducted utilizing the Variable Gravity Rack (VGR) aboard the Chinese Space Station (CSS) in the near future.

Fig. 1 shows overview of the VGR (Wang et al. 2019). The VGR has two centrifuges with diameters of 900 mm and can provide the gravity range from 0.01 g_0 to 2 g_0, where g_0 denotes the gravity on Earth.

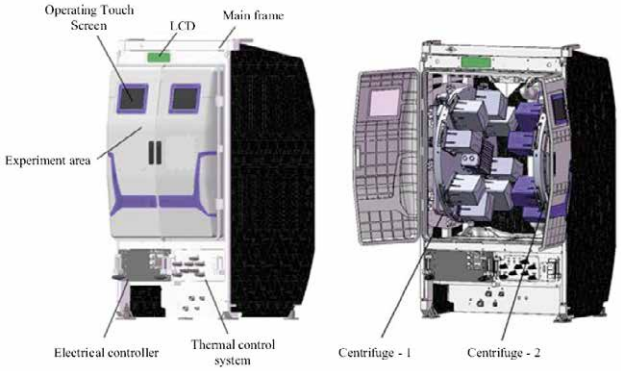

Figure 1: Overview of the VGR.

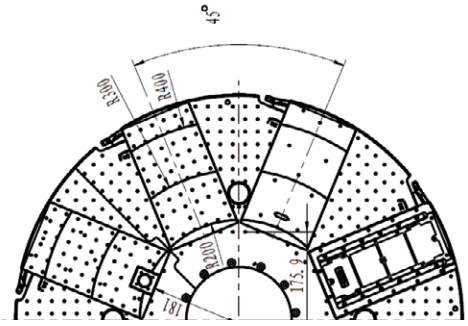

Figure 2: Topview of the centrifuge with standard experimental loads.

The centrifuge is the most important device of the VGR, which can rotate with a certain and varying speed to simulate a variable gravity level. Experiment loads will be locked on the top of the rotator (Fig. 2). A standard experiment load consists of a self-locking part, a container and several connecting rods that can realize the specific motion along radial and axial directions on the centrifuge.

There are two standard experiment loads, namely E-box and C-box, for vgBoiling (Fig. 3). Inside the E-box, there are a boiling chamber (Fig. 4) and a high-speed CCD. A pre-DAB with a novel integrated micro heater is fixed inside the boiling chamber. The integrated micro heater is fabricated by using MEMS technique. The substrate of the integrated micro heater is a $10 \times 10 \times 2$ mm^3 quartz glass wafer. On the back surface of the quartz glass wafer, a serpentine strip of platinum film acts simultaneously as the main heater to provide the input power for maintaining the boiling process and the temperature sensor to measure the average temperature on the back surface. 5 pulse bubble triggers for exciting bubble nuclei by using the method of local overheating are located on the top surface of the integrated micro heater. They can be activated independently and thus can realize different experimental modes including single-, double-, and multi-bubble boiling, as well as normal pool boiling in which no bubble trigger is activated. There are local temperature sensors on the top surface to measure the local temperature distribution underneath the growing bubble(s). Furthermore, inside the quartz glass wafer, there are also several local temperature sensors, which provide more detail information of three dimensional distribution of local temperature in the heating solid and then are more helpful to reveal the influence of the heater thermal parameters on pool boiling performance.

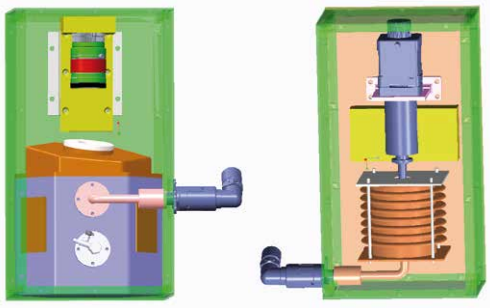

Figure 3: E-box (left) and C-box (right) for vgBoiling.

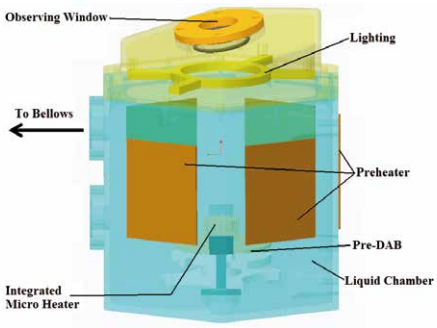

Figure 4: Boiling chamber.

A beryllium bronze bellows, which is fixed in the C-box and connected with the boiling chamber fixed in the E-box, acts as a pressure regulator to maintain the pressure inside the chamber approximately constant during the preheating and boiling processes with the help of constant background pressure environment inside the VGR.

The research contents of this project include: 1) Normal pool boiling in different gravity, focusing on the gravity scaling law of pool boiling heat transfer; 2) Single bubble boiling in different gravity, focusing on bubble dynamics and the influence of the heater thermal parameters on bubble growth and heat transfer performance; 3) Double bubble boiling in different gravity, focusing on bubble dynamics and the interaction mechanism between adjacent nucleation sites; 4) Multiple bubbles in different gravity, focusing on bubble dynamics and the effect of the number density of activated nucleation sites on boiling heat transfer.

The project of vgBoiling is presently in the phase of scheme demonstration. The device of vgBoiling will be installed on the VGR and launched with the CSS Experiment Capsule I "Wentian (WT)" in 2021. Further study is still ongoing.

Acknowledgements

The present study is supported financially by the National Natural Science Foundation of China (NSFC) under the grant of U1738105.

References

P. Di Marco, Review of reduced gravity boiling heat transfer: European research, *J. Jpn. Soc. Microgravity Appl.* 20(2003) 252–263.

Y. Feng, H. Li, K. Guo, X. Lei, J. Zhao, Numerical study on saturated pool boiling heat transfer in presence of a uniform electric field using lattice Boltzmann method, *Int. J. Heat Mass Transfer* 135(2019) 885–896.

J. Kim, Review of nucleate pool boiling bubble heat transfer mechanisms. *Int. J. Multiphase Flow* 35(2009) 1067-1076.

J. Kim, Review of reduced gravity boiling heat transfer: US research, *J. Jpn. Soc. Microgravity Appl.* 20(2003) 264–271.

X. Ma, P. Cheng, S. Gong, X. Quan, Mesoscale simulations of saturated pool boiling heat transfer under microgravity conditions, *Int. J. Heat Mass Transfer* 114(2017) 453–457.

H. Ohta, Review of reduced gravity boiling heat transfer: Japanese research. *J. Jpn. Soc. Microgravity Appl.* 20(2003), 272–285.

R. Raj, J. Kim, J. McQuillen, On the scaling of pool boiling heat flux with gravity and heater size, *J. Heat Transfer* 134(2012a) 011502.

R. Raj, J. Kim, J. McQuillen, Pool Boiling Heat Transfer on the International Space Station: Experimental Results and Model Verification, *J. Heat Transfer* 134(2012b) 011504.

J. Straub, Boiling heat transfer and bubble dynamics in microgravity. *Adv. Heat Transfer* 35(2001) 57–172.

S. K. Wang, K. Wang, Y. L. Zhou, B. Yan, X. Li, Y. Zhang, W. B. Wu, A. P. Wang, Development of the Varying Gravity Rack (VGR) for the Chinese Space Station, *Microgravity Sci. Technol.* 31(2019) 95-107.

J.F. Zhao, Two-phase flow and pool boiling heat transfer in microgravity. *Int. J. Multiphase Flow* 36(2010) 135-143.

Oral 077

Gravity-Related Experiment Programmes for University Students

N. D. L. Savage[1], E. Lageweg[2], N. Callens[3] and P. Galeone[2]

[1]HE Space Operations B.V., Noordwijk, The Netherlands, [2] ESA-ESTEC, Noordwijk, The Netherlands, [3] ESA-ESEC, Transinne, Belgium
nigel.savage@esa.int, evelien.lageweg@esa.int, natacha.callens@esa.int, piero.galeone@esa.int

Introduction

For the past ten years, the ESA Academy Unit (formerly named Tertiary Education Unit) of the ESA Education Office has offered quite a number of programmes and opportunities enabling university student teams from ESA Member States, Canada and Slovenia to design, build, test and perform experiments in state-of-the-art gravity-altering facilities located throughout Europe (Figure 1).

Figure 1. ZARM's Drop Tower (upper left), Novespace's A310 (upper right), ESA's Large Diamter Centrifuge (middle right) and DLR's Short Arm Human Centrifuge (bottom – copyright DLR)

Two new programmes

The programmes traditionally offered almost every year, and for about a decade, include Spin Your Thesis! making use of the Large Diameter Centrifuge based in ESA/ESTEC (NL), Drop Your Thesis! making use of the Drop Tower in Bremen (DE), and Fly Your Thesis! utilizing Novespace's A310 aircraft in Bordeaux (FR). Recently, two additional programmes 'Orbit Your Thesis!' and 'Spin Your Thesis! Human Edition' have been added to the portfolio of opportunities, offering teams access to the International Space Station with the ICE Cubes service from Space Applications Services, and access to use a Short Arm Human Centrifuge in DLR's envihab facilities (DE), respectively.

Designated training

In our drive to constantly improve the hands-on opportunities offered to university students, ESA Academy has introduced four years ago a "Gravity-Related Experiments Training Week" where teams from all programmes are offered basic training to engage more proficiently in the development of their experiment at the ESA Academy's Training and Learning Facility (TLF) in ESEC-Galaxia Belgium (Figure 2). This is a unique and highly valued opportunity for the students who are taught about managing large projects and meet the facility experts as well as past students before starting the design of their experiments.

Figure 2. ESA Academy's Training and Learning Facility in ESEC-Galaxia (BE)

Conclusions

Evaluation of the benefits of participation in the programmes and associated training weeks enables ESA Academy to maintain its high standards. Feedback from the students is meticulously taken into account for each rendition of the programmes to ensure their relevance for the university students who will soon shape the future of gravity related-research in Europe.

Acknowledgements

ESA Academy would like to thank ESA TEC-MMG, ZARM Fab, Novespace, Space Applications Services, DLR and ELGRA for the support to the ESA Academy programmes.

26th European Low Gravity Research Association Biennial Symposium and General Assembly
14th International Conference on "Two-Phase Systems for Space and Ground Applications"
European Space Agency Topical Teams meetings
Granada (Spain), September 24-27, 2019

Oral 078

2C2D-LIF temperature measurements in a micrometric evaporating film

A. Simonini[1], D. Fiorini[1], L. Peveroni[1], J-B. Gouriet[1], S. Soller[2], J. Steelant[3]

[1]von Karman Institute, EA department, chaussée de waterloo 72, Rhode-Saint-Genèse, Belgium
[2] EADS Astrium GmbH, Space Transportation, Propulsion & Equipment 81663 Munich, Germany
[3] ESA-ESTEC, Flight Vehicle and Aerothermodynamics Engineering Section TEC-MPA, P.O. Box 299, Noordwijk, Netherlands
simonini@vki.ac.be

Introduction

MMH as fuel and NTO as oxidizer is a commonly used storable rocket propellant combination. During the propulsion system operation, the large amount of heat released imposes the need of a very effective cooling technology. Large and mid-size engines are regeneratively cooled via cooling channels, using the liquid fuel whereas for small engines, the use of liquid film cooling of the combustion chamber is usually applied as being less complex. The accurate experimental analysis of this technique, supporting the numerical models development, is then mandatory for the optimal design of spacecraft engines. In particular, the exact behaviour of the liquid film temperature is of considerably interest as it is strongly related to the liquid film length (dry-out point) and the wall heat transfer.

Laser-Induced Fluorescence (LIF) is chosen for his non-intrusiveness and ability to measure local temperature. The extremely challenging conditions of the target testing, the micrometric thickness of the film and the presence of evaporation require a careful tuning and adaptation of the technique. LIF for temperature measurements have been successfully applied to many different flows: turbulent jets [1, 2], sprays [3, 4], evaporating droplets [5], liquid meniscus [6], stratified and buoyant plumes [7] and solidification processes [8]. Nevertheless, to best author's knowledge, no works are present in literature presenting LIF measurement in an evaporative thin film.

In this work a 2-Dye, 2-Color LIF has been proved to be able to measure the temperature of a film of liquid ethanol down to 100 μm of thickness.

Technique

LIF is a non-intrusive measurement technique based on creation of an unstable energy state of a fluorophore dissolved in a flow, excited by a certain energy wavelenght. The fluorescent signal is changing with temperature and in some cases shifted towards the red part of the light spectrum, with a distribution which is typical of the fluorophore, independently by the excitation wavelength $\boldsymbol{\lambda}$. The obtained signal F is temperature-dependent according to the following law:

$$\boldsymbol{F^i(T, C, \lambda_i) = K^i_{opt} K^i_{spec} \varepsilon^i V_c I_l C e^{\frac{\beta^i}{T}}} \qquad \textit{Eq. 1}$$

Where C is the concentration of the flurophore, $\boldsymbol{K_{opt}}$ and $\boldsymbol{K_{spec}}$ are the optical and spectral constansts of the measuring system, $\boldsymbol{\varepsilon}$ is the molar exctinction coefficient, $\boldsymbol{V_c}$ is the volume of light collected, $\boldsymbol{I_l}$ is the excitation intensity and $\boldsymbol{\beta}$ is the temperature sensitivity constant. The apex i indicates a single line spectral band. The above expression has then to be integrated over a selected range of spectral bands Δi to reconstruct the signal recorded. The above equation explicits the model of a *Single-Photon fluorescence*.

When the molar exctinction coefficient is dependent on temperature, its behavior can be included in the temperature sensitivity constant. Moreover, to eliminate the dependence on $\boldsymbol{K_{opt}}$, $\boldsymbol{K_{spec}}$, $\boldsymbol{V_c}$ and $\boldsymbol{I_l}$ a reference intensity for which the temperature T_0 is known has to be recorded in the same measuring conditions. Given the interest of applying such technique in evaporative conditions, the problem of the concentration variation occuring when the solvent of the solution is evaporating has to be solved. This can be avoided by using a 2-dyes and 2-color ratiometric approach (2D2C). The first ratiometric LIF developments are due to the work of Coppeta et al. [9] and Sakakibara et al. [10]. A second fluorescent dye, the fluorescence spectral band of which is well separated from the first colorant and which features a different temperature sensitivity, should be dissolved in the fluid. The measurement detects simultaneously a spectral band from each fluorescent emission (one for each of the two dyes). The ratio between the two signals is considered as fluorescent output to cancel the disturbances possibly due to the dyes concentration variations.

The temperature calibration of LIF is based into the determination of the value of β^i for the solution spectral band(s) of interest. Considering the ratio of the equation 1 for for a generic temperature T and the reference temperature T_0, we obtain the expression for $\boldsymbol{\beta}$:

$$\beta^i = \frac{\ln(R^i)}{\frac{1}{T} - \frac{1}{T_0}} \qquad \textit{Eq. 2}$$

where R^i is the ratio of the fluorescent signals $\boldsymbol{F^i(T)}$ with respect to the $\boldsymbol{F^i(T_0)}$.

During this work, the selected dyes were Fluorescein disodium (FL) and Kiton Red (KR). While the single dyes are extensively used in literature, their combination has been used only by Shafii et al. [8] for solidification process of Ammonia. The concentrations in ethanol solution used during this work were of $5 \cdot 10^{-4}$ mol/L for FL and $3 \cdot 10^{-5}$ mol/L for KR. These high concentrations of dye are justified by the necessity of working with a micrometric thickness of film, having a weak fluorescent signal. The excitation source was a Nd:Yag laser with 532 nm wavelength, repetition rate of 15 Hz and a maximum power of 30 mJ. The typical spectra obtained for a film of 100 μm are show in figure 1.

The couple FL-KR was chosen for having a high temperature sensitivity of the solution due to the opposite dependence on temperature of the single fluorophores and their good spectral separation, as it can be seen in figure 1. The spectral bands were selected based on the calculation of the sensitivity as function of the wavelength band with the formula:

$$s^i = \frac{\ln\left(\frac{F^i(T)}{F^i(T_0)}\right)}{T - T_0} \qquad \textit{Eq. 3}$$

In figure 2 the sensitivity is plotted against the wavelength based on equation 3. The spectral bands selected are [540-550] nm for FL, named 1, and [575-585] nm for KR, named 2.

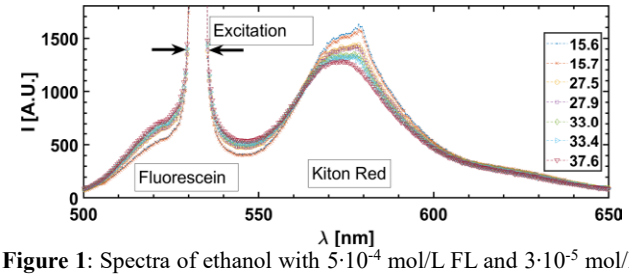

Figure 1: Spectra of ethanol with $5 \cdot 10^{-4}$ mol/L FL and $3 \cdot 10^{-5}$ mol/L for KR with change in temperature.

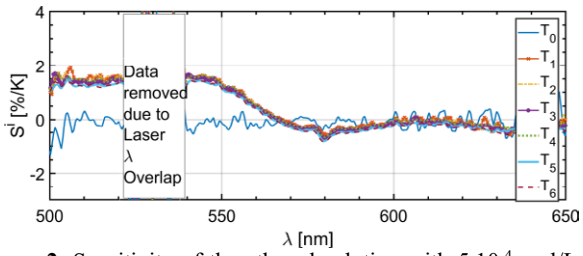

Figure 2: Sensitivity of the ethanol solution with $5 \cdot 10^{-4}$ mol/L FL and $3 \cdot 10^{-5}$ mol/L for KR as function fo the wavelength band.

The calibration of the solution was performed inside quiescent pools of different depths (100 µm, 200 µm and 500 µm) to assess the independency of the calibration in the micrometric range.

Experimental procedures and results.

The feasibility of LIF applied to an evaporative micrometric ethanol film was proved considering the thickness and the evaporating film separately. Indeed, the technique has been applied in copper pools with calibrated depths (100 µm, 200 µm and 500 µm) provided by a flush mounted thermocouple type K with a 250 µm head at the bottom of the pool. A heater was placed below the pool and a thermal pad material was used to ensure good contact with the pool. Several tests (minimum 6) were acquired in each pool, changing 4 different temperatures, starting from room temperature (~15°C) and setting the heater at 30°C, 35°C and 39°C. A value of the total temperature sensitivity of the solution $\Delta\beta = \beta^2 - \beta^1$ was retrieved for each test and their average and standard deviation are shown in table 1.

Table 2: Spectra of ethanol with $5 \cdot 10^{-4}$ mol/L FL and $3 \cdot 10^{-5}$ mol/L for KR with change in temperature.

Pool depth µm	Average **Δβ**	Std **Δβ**
100	2057	76
200	2083	74
500	2111	143

To prove the applicability of the technique in evaporating fluids, the solution was placed in a quartz cuvette 50x50x25 mm^3, heated from below. A copper plate was inserted inside the quartz cuvette in order to assure a homogeneous temperature distribution of the bottom. The fluid was heated by a heater placed below the quartz cuvette and its temperature measured by a thermocouple inserted directly in the fluid. For this assessment the quartz cuvette was open to air allowing evaporation and the liquid layer was initially set at 1 mm. The results of the test are reported in table 2. LIF technique has typically a minimum error of 2.5°C due to the uncertainty on the reference temperature and on the calibration [4] which can partially explain the deviation shown in table 2. Moreover, due to the evaporation condition at the interface, the temperature in the pool was most probably stratified and the thermocouple was acquiring an average value.

Table 2: Results of temperature measurements in evaporation conditions.

Thickness [µm]	**LIF temp. [°C]**	**Thermoc. temperature [°C]**	**Deviation °C**
988	Reference	25.62	-
967	37.97	40.32	2.35
967	41.72	44.15	2.43
967	46.56	50.67	4.11
967	47.32	50.95	3.63
765	48.18	51.65	3.47
765	49.43	51.71	2.28

Conclusions

In this work the feasibility of LIF measurement in an evaporating micrometric liquid film of ethanol using Fluorescein Disodium and Kiton Red as tracers was proven. The tested minimum thickness allowing temperature measurements was 100 µm. Temperature measurements in a film under evaporation were performed retrieving a deviation of maximum 4ºC from the temperature measured by a thermocouple K inserted in the liquid.

The tested experimental technique can be used for temperature characterization of a liquid film under strong evaporation in order to provide data for Validation and Verification of numerical codes.

Acknowledgements

This work has been funded under ESA Contract number 4000114983/15/NL/KML/fg and ESA RFP/3-15270/17/NL/KML/fg.

References

[1] M. Bruchhausen, F. Guillard, and F. Lemoine, "Instantaneous measurement of two-dimensional temperature distributions by means of two-color planar laser induced fluorescence (PLIF)," *Exp. Fluids*, vol. 38, no. 1, pp. 123–131, Jan. 2005.

[2] P. Lavieille, A. Delconte, D. Blondel, M. Lebouch□, and F. Lemoine, "Non-intrusive temperature measurements using three-color laser-induced fluorescence," *Exp. Fluids*, vol. 36, no. 5, pp. 706–716, May 2004.

[3] M. Wolff, A. Delconte, F. Schmidt, P. Gucher, and F. Lemoine, "High-pressure Diesel spray temperature measurements using two-colour laser-induced fluorescence," *Meas. Sci. Technol.*, vol. 18, no. 3, pp. 697–706, Mar. 2007.

[4] M. R. Vetrano, A. Simonini, J. Steelant, and P. Rambaud, "Thermal characterization of a flashing jet by planar laser-induced fluorescence" *Exp. Fluids*, vol. 54, no. 7, 2013.

[5] V. Deprédurand, P. Miron, A. Labergue, M. Wolff, G. Castanet, and F. Lemoine, "A temperature-sensitive tracer suitable for two-colour laser-induced fluorescence thermometry applied to evaporating fuel droplets," *Meas. Sci. Technol.*, vol. 19, no. 10, p. 105403, Oct. 2008.

[6] A. Fenner and P. Stephan "Two dye combinations suitable for two-color/two-dye laser-induced fluorescence thermography for ethanol," *Exp. Fluids*, vol. 58, no. 6, p. 65, 2017.

[7] J.-M. Buchlin, C. Spaccapaniccia, Z. E. Yildirim,P. Planquart, "Study of Thermal Stratification in a Natural Convection Loop by One Color Laser Induced Fluorescence," in *17th International Symposium on Applications of Laser Techniques to Fluid Mechanics*, 2014.

[8] M. B. Shafii, C. L. Lum, and M. M. Koochesfahani, "In situ LIF temperature measurements in aqueous ammonium chloride solution during uni-directional solidification," in *Experiments in Fluids*, 2010, vol. 48, no. 4, pp. 651–662.

[9] J. Coppeta and C. Rogers, "Dual emission laser induced fluorescence for direct planar scalar behavior measurements," *Exp. Fluids*, vol. 25, no. 1, pp. 1–15, 1998.

[10] J. Sakakibara and R. Adrian, "Whole field measurement of temperature in water using two-color laser induced fluorescence," *Exp. Fluids*, vol. 26, no. 1, pp. 7–15, 1999.

26th European Low Gravity Research Association Biennial Symposium and General Assembly
14th International Conference on "Two-Phase Systems for Space and Ground Applications"
European Space Agency Topical Teams meetings
Granada (Spain), September 24-27, 2019

Oral 079

Comparison of the effect of vertical and horizontal fast and slow clinorotation on *A. thaliana* seedlings

A. Villacampa[1], L. Sora [2], F. J. Medina[1], M. Ciska[1]

[1]Centro de Investigaciones Biologicas CSIC, Madrid, [2]Politecnico di Milano, Milan, Italy;
avillacampa@cib.csic.es, ludovico.sora@mail.polimi.it, fjmedina@cib.csic.es, mciska@cib.csic.es

Introduction

The clinostat is one of the most commonly used ground based facility to simulate microgravity. Nevertheless, there is no clear consensus in what are the most optimal settings for microgravity simulation. In general, it is recommended to take into account the specifity of the biological system used and the duration of the experiment, but no clear well-supported user directions are available. The principle of the clinostat is that the constant change of the direction of the gravity vector disables the biological sample from the perception of the gravity vector and, in fact, the gravitropic response of plants is also disabled. Here, we present a mathematical model that enables the selection and adjustment of optimal settings for the experiments with *A. thaliana* plant model. The algorithm was developed based on the known mechanism of gravity perception by specialized cells in the root tip called statocytes. The statocytes are located in the collumella and contain organelles called statoliths which are amyloplasts, filled with starch. These organelles sediment according to the gravity vector due to higher density than the surrounding cytoplasm and, once they reach the bottom of the cell, they trigger a gravitropic response. Up to date, it is not known which receptors are responsible for triggering the gravitropic response, but it is assumed that they are located in the endoplasmic reticulum (ER) or in the cellular membrane (Sato *et al.*, 2015; Su *et al.*, 2017). Therefore, the statoliths do not trigger the gravitropic response until they reach the border of the cell. This mechanism is relatively well known but some data suggest that there is another mechanism of gravity perception at the cellular level, that is probably perceived as the changes of pressure of the cell mass on the cellular membrane at the bottom of the cell (Wayne and Staves, 1996; Wayne *et al.*, 1990). This mechanism is thought to be responsible for the discreet gravitropic response of the cells in *in vitro* cell culture, called gravisensitivity (Kordyum, 2014). Since this mechanism is little known, we have not enough data to develop an algorithm for optimal clinostat settings based in cellular gravisensitivity, and therefore our model does not apply for the *in vitro* culture experiments.

We have verified our mathematical model using as biological system *A. thaliana* seedlings grown for 5 days in optimal conditions and then exposed to clinorotation either for short periods (1, 2, 3 hours), or a long period (24 hours). We have compared the different orientation of the seedlings in reference to the rotation axis using two clinostat speed settings; fast (60 RPM) and slow (1 RPM). The clinorotation was performed in darkness to avoid any light response interference.

Mathematical model for optimal clinostat settings

Taking into account parameters such as the difference between the density of the cytoplasm and statoliths, and cell and statolith dimensions, we developed a mathematical model that relates the speed of the clinostat with the dimensions of the experimental system and the duration of the experiment. In this way, the model enables the choice of optimal settings regarding the duration of the experiment, the dimensions of the experimental container and the clinorotation speed for an experiment, using a plant model system. The model calculates the time that statoliths need to reach the cellular wall starting from the centre of the cell, at a given clinostat rotational speed and in a given position in relation to the centre of the clinorotating plate. We assume that just at the moment when a statolith reaches the cell wall it transmits the information about the direction of the gravity vector and triggers the gravitropic response.

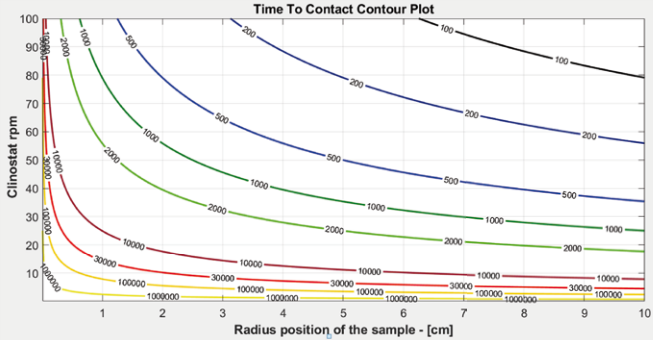

Figure 1: Contour plot of some relevant useful experiment duration isohypses in function of the sample maximum radius (dimension) and clinostat rotational speed. It is a useful tool in future experiments' planning and past experiments' validation

Comparison of fast and slow clinorotation

Our model confirms that a low rotational speed setting enables the performance of longer experiments and allows the use of bigger experimental containers. In case of the high clinorotaional speed, we observed the effect of centrifugal force that substitutes the gravitational vector and causes directional growth of the plants towards the exterior of the experimental container. We also observed differential distribution of the statoliths in columella cells at low and high speeds, although our results suggest that there is no significant difference in the auxin distribution between the two conditions.

Comparison of the vertical and the horizontal clinorotation

In principle, our model can be used for calculating optimal settings for both, vertical and horizontal clinorotation. The path that a statolith is allowed to travel without triggering

gravitropic response is the shortest distance between the centre of the cell and the nearest cell wall. Thus, the limiting value is the width of the cell. Previous studies reported different response in plants grown under vertical or horizontal clinorotation under otherwise identical experimental settings (John and Hasenstein, 2011; Lorenzi and Perbal, 1990). Nevertheless, many studies were performed under vertical or horizontal clinorotation interchangeably (Aarrouf *et al.*, 1999; Brown *et al.*, 1976; Hensel and Sievers, 1980; Smith *et al.*, 1997). Previous data suggest that the biological response is more similar to the real microgravity under vertical clinorotation (Lorenzi and Perbal, 1990). We performed two parallel experiments, one under vertical and one under horizontal clinorotation and compared the root growth rate and direction, position of the statoliths, nucleus and ER in the columella cells, as well as auxin levels and distribution in the meristem.

Conclusions

As confirmed by our mathematical model and biological validation, the best clinostat setting for performing long duration experiments in the plant model is low rotational speed. The vertical and horizontal clinorotation produce differential response in *A. thaliana* seedlings.

Acknowledgements

We acknowledge the support from the Spanish Ministry of Science [ESP2015-64323-R]. Alicia Villacampa was supported by a grant from the Spanish Ministry of Science [BES-2016- 077976]. Clinostat for this study was provided by ZGIP, UNOOSA.

References

Aarrouf J, Darbelley N, Demandre C, Razafindramboa N, Perbal G. Effect of horizontal clinorotation on the root system development and on lipid breakdown in rapeseed (*Brassica napus*) seedlings, *Plant Cell Physiol* 40 (1999) 396-405.

Brown AH, Dahl AO, Chapman DK. Limitation on the use of the horizontal clinostat as a gravity compensator, *Plant Physiol* 58 (1976) 127-130.

Hensel W, Sievers A. Effects of prolonged omnilateral gravistimulation on the ultrastructure of statocytes and on the graviresponse of roots, *Planta* 150 (1980) 338-346.

John SP, Hasenstein KH. Effects of mechanostimulation on gravitropism and signal persistence in flax roots, *Plant Signal Behav* 6 (2011) 1365-1370.

Kordyum EL. Plant cell gravisensitivity and adaptation to microgravity, *Plant Biol (Stuttg)* 16 Suppl 1 (2014) 79-90.

Lorenzi G, Perbal G. Actin filaments responsible for the location of the nucleus in the lentil statocyte are sensitive to gravity, *Biol Cell* 68 (1990) 259-263.

Sato EM, Hijazi H, Bennett MJ, Vissenberg K, Swarup R. New insights into root gravitropic signalling, *J Exp Bot* 66 (2015) 2155-2165.

Smith JD, Todd P, Staehelin LA. Modulation of statolith mass and grouping in white clover (*Trifolium repens*) growth in 1-g, microgravity and on the clinostat, *Plant J* 12 (1997) 1361-1373.

Su SH, Gibbs NM, Jancewicz AL, Masson PH. Molecular Mechanisms of Root Gravitropism, *Curr Biol* 27 (2017) R964-R972.

Wayne R, Staves MP. A down to earth model of gravisensing or Newton's Law of Gravitation from the apple's perspective, *Physiol Plant* 98 (1996) 917-921.

Wayne R, Staves MP, Leopold AC. Gravity-dependent polarity of cytoplasmic streaming in Nitellopsis, *Protoplasma* 155 (1990) 43-57.

26th European Low Gravity Research Association Biennial Symposium and General Assembly
14th International Conference on "Two-Phase Systems for Space and Ground Applications"
European Space Agency Topical Teams meetings
Granada (Spain), September 24-27, 2019

Oral 080

Statolith displacement in root statocytes in real and simulated microgravity

E. Kordyum, V. Brykov

Institute of Botany, National Academy of Sciences of Ukraine, Kyiv, Ukraine
cellbiol@ukr.net

Introduction

To simulate biological effects of microgravity in space flight, different ground-based facilities – slow and fast 2D clinostats, Random Positioning Machine, Free Fall Machine and magnetic levitation – are widely used (Beysens et al. 2011; Herranz et al. 2013) as experiments in "real *μg* are scarce, costly and time consuming" (Krause et al. 2018). Capacities and limitations of various devices to accurately and reliably simulate microgravity conditions, comparable to real microgravity in space, are constantly discussed (van Loon 2007; Herranz et al. 2013; Shinde et al. 2016). Recent comparative studies of the quality of microgravity simulation provided by different operational modes have shown the greatest suitability of fast 2D clinorotation for investigating the graviperception mechanism in *Chara* rhizoids in comparison with slower 2D and 3D clinorotation, and rotation of samples around two axes (Krause et al. 2018). In the given paper, we compare the position of amyloplasts–statoliths in root cap statocytes of higher plants under 1 g, slow and fast 2D clinorotation, real microgravity in space flight, vibration and acceleration in spacecraft launch mode using own and literary data.

1g conditions

Root cap statocytes in angiosperm plants are highly specialized graviperceptive cells and characterized by the structural polarity shown by the position of a blade-shape nucleus in the proximal part of the cell and the endoplasmic reticulum (ER) complex in its distal part, not all investigated species have a massive ER complex. Amyloplasts performing a statolithic function sediment in the distal part of the statocytes in the direction of the gravitational vector at some distance from the plasmalemma and thus not in contact with it (Volkman and Sievers 1979).

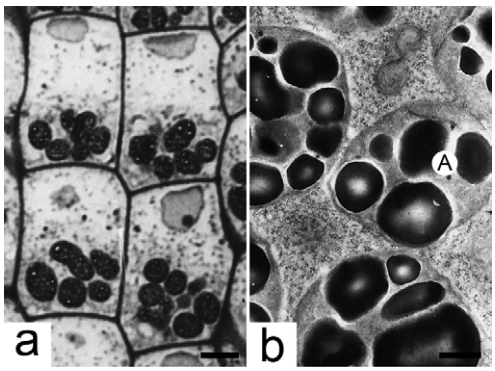

Fig. 1. *Beta vulgaris*. a – general view of statocytes, b – amyloplasts. Scale bar: a – 5 μm, b – 0.5 μm.

This polar arrangement of organelles is achieved and maintain by means of the cytoskeleton (Hensel 1984, 1988). Results of our investigations of *Beta vulgaris, Brassica rapa* and *Pisum sativum* correspond to literary data and show that amyloplasts are in close contact each other with the outgrowths of the outer membrane of the organelle envelope (Fig. 1, a, b).

Vibration and acceleration

To analyze the impact of vibration and acceleration in the space craft launch mode, *P. sativum* seedlings were placed on the installation modeling dynamic factors of space flight in the N.I. Vavilov Institute of General Genetics RAN within 8 min and fixed directly after exposure. Unlike control, mainly round amyloplasts distributed throughout the cytoplasm contacting with the plasmalemma, lomasomes, ER cisterns, and a nucleus.

μg conditions

Histogenesis and cell differentiation in the embryonal root cap of investigated plants occurred normally in real microgravity in space flight as in other species (Volkman et al. 1986; Kiss 2000; Kordyum and Chapman 2007; Perbal 2009; Kordyum 2014). A nucleus was situated in the proximal part of a cell. Amyloplasts, which did not sediment in the distal part of a statocytes in the absence of the gravitational vector, mainly concentrated in the center of a statocyte, organelles could contact in this case, and rarely in the other parts without contacting the plasmalemma (Fig. 2, a,b). There was an increase in vacuolization of the cytoplasm.

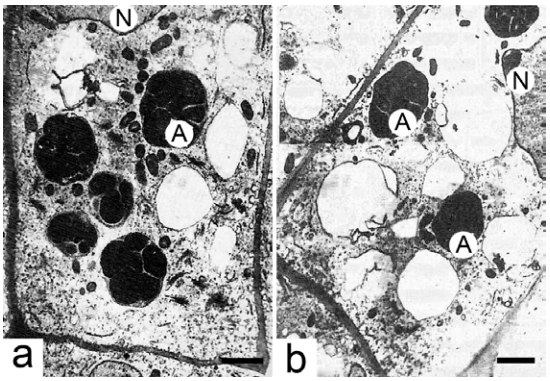

Fig. 2. Statocytes of *Brassica rapa*. a – amyloplasts occupy the cell center, b – scattered amyloplasts. Scale bar 2 μm.

Slow 2D clinorotation (2–5 rpm)

Amyloplasts singly or in groups were situated in different parts of a statocyte, particularly in the nucleus zone,

sometimes showed a tendency to concentrate in the cell center (Fig. 3,a,b). Organelles in groups could touch each other being at some distance from the plasmalemma. Progressive vacuolization of the cytoplasm also occurred.

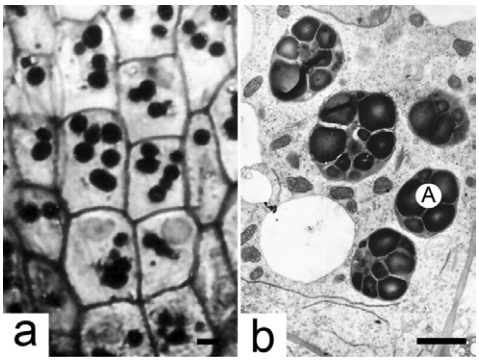

Fig 3. *Beta vulgaris*. a – general view of statocytes, b – amyloplasts. Scale bar: a – 10 µm, b – 5 µm.

Fast 2D clinorotation (50 rpm)

Distribution of amyloplasts throughout the cytoplasm of statocytes partly resembled this. under action of vibration and acceleration. Amyloplasts contacted directly with the plasmalemma or with lomasomes – more or less complex invaginations of the plasmalemma into the cytoplasm, also with a nucleus and ER cisterns, what was the distinguishing feature of amyloplast behavior under fast clinorotation. Most amyloplasts were oval in shape, often one end of organelles narrowed in various degrees, sometimes in the form of an elongated "spout", which contacted with the plasmalemma (Fig 4 a–d).

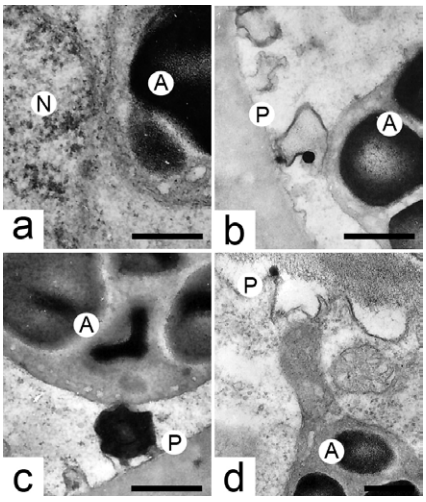

Fig. 4. *Pisum sativum*. Contacts of amyloplasts with the nucleus (a), lomasomes (b, c), plasmalemma (d). Scale bar 0.5 µm.

Conclusions

A comparison of the amyloplast behavior in root cap statocytes in real microgravity and under different speeds of horizontal clinorotation shows that slow 2D clinorotation is the most appropriate tool for its simulation in ground-based experiments. The differences in statolith responses to various modes of microgavity simulation in *Chara* rhizoids and roots of higher plants can be explained by 1) the nature of statoliths – compartments filled with crystallites of barium sulfate in *Chara* and cell organelles in roots of higher plants; 2) unequal sizes of rhizoids and roots, the last are larger and, although seedlings were located strictly on the axis of rotation, may deviate from the axis and perceive acceleration.

References

D. Beysens, L. Carotenuto, J. van Loon, M. Zell, Laboratory Science with Space Data (2011) Springer, Berlin.

W. Hensel, A role of microtubules in the polarity of statocytes from roots of *Lepidium sativum* L., *Planta* 162 (1984) 404-414.

W. Hensel, Demonstration by heavy meromyosin of actin microfilaments in extracted cress (*Lepidium sativum* L.) root statocytes, Planta 173 (1988) 142–143.

R. Herranz, R. Anken, J. Boonstra et al., Ground-based facilities for simulation of microgravity: organism-specific recommendations for their use, and recommended terminology, *Astrobiology*, 13 (2013),1–17.

J. Kiss, Mechanisms of the early stages of plant gravitropism, *Critical Rev. in Plant Sci.* 19 (2000) 551–573.

E. Kordyum, D. Chapman, Plants in Space (2007) Academperiodica Kyiv.

E. Kordyum, Plant cell gravisensitivity and adaptation to microgravity, *Plant Biol*. 16 suppl.1 (2014) 79–90.

L. Krause, M. Braun, J. Hauslage, R. Hemmersbach, Analysis of statolith displacement in *Chara* rhizoids for validating the microgravity-simulation quality of clinorotation modes, *Microgravity Sci. Techn.* 30 (2018) 229–236.

G. Perbal, From ROOTS to GRAVI-1: twenty five years for understanding how plants sense gravity, *Microgravity Sci. Techn*., 21 (2009) 3–10.

V. Shinde, S. Brungs, M. Henry et al., Simulated microgravity modulates differentiation processes of embryonic stem cells, *Cell Physiol. Biochem*. 38 (2016)1483-1499.

J. van Loon, Some history and use of the random positioning machine, RPM, in gravity related research, *Adv. Space Res.* 39 (2007) 1161–1165.

D. Volkman, H. Behrens, A. Sievers, Development and gravity sensing of cress roots under microgravity, *Naturwissenschaften* 73 (1986) 438–441.

D. Volkman, A. Sievers, Graviperception in multicellular organs, *Encycl. Plant Physiol*. New Ser. 7 (1979) 573–600.

S. Wuest, S. Richard, S. Kopp et al., Simulated microgravity: critical review on the use of random positioning machines for mammalian cell culture, *Biomed Res Int.* doi: 10.1155/2015/971474.

26th European Low Gravity Research Association Biennial Symposium and General Assembly
14th International Conference on "Two-Phase Systems for Space and Ground Applications"
European Space Agency Topical Teams meetings
Granada (Spain), September 24-27, 2019

Oral 081

The MAP project EDDI: Understanding the Role of Droplet Interfaces in Emulsion Dynamics

Libero Liggieri[1], Francesca Ravera[1], Eva Santini[1], Giuseppe Loglio[1], Thodoris Karapantsios[2], Margaritis Kostoglou[2], Angeliki Chondrou[2], Reinhard Miller[3], Luigi Cristofolini[4], Fabrizia Salerni[4], Davide Orsi[4], Mickael Antoni[5], Kazutami Sakamoto[6], Yuji Yamashita[7], Takeshi Misono[8], Satoru Hashimoto[8], Boris Noskov[9], James K. Ferri[10]

[1] CNR ICMATE, Genova, Italy; [2]Aristotle University Thessaloniki, Greece; [3] MPI KGF, Golm,, Germany; [4] University of Parma, Italy; [5] Aix-Marseille University, Marseille, France; [6] Tokyo University of Science, Japan; [7] Chiba Institute of Science, Chiba, Japan; [8] COSMOS Nikkol, Tokyo, Japan; [9] St.Petersburg State University, Russia; [10] Virginia Commonwealth University, Richmond VA, USA
libero.liggieri@ge.icmate.cnr.it

Emulsions are dispersions between immiscible liquids widespread in natural and synthetic products and in technologies. Emulsions are thermodynamically unstable systems and, after their preparation, they tend to separate into the liquid phases under the effect of gravity, when the droplets achieve micrometric sizes.

Responsible for the increase of droplet sizes are different fluid dynamic and thermodynamic mechanisms, such as droplet coalescence, droplet aggregation and Ostwald ripening. The latter is a phenomena related to the equilibration of chemical potentials that makes large droplets to grow at the expenses of the smaller ones. These mechanisms can be contrasted by the presence of surface-active additives – overall referred to as emulsifiers – which, adsorbing at the droplet interfaces, changes their mechanical and thermodynamic properties. In spite largely utilized, the mechanisms of action of surface-active emulsifiers remain still to be clarified in many details. The practical use of emulsifiers is, therefore often not fully optimized in qualitative and quantitative terms.

Based on the above motivations, the project EDDI (Emulsion Dynamics and Droplet Interfaces) has been recently submitted and approved by ESA. It has the general aim of a deeper understanding of the role of surfactants in emulsion production and stability, which can lead to a reduction and optimization of the amount of additives utilized and to by-design approaches in emulsion technology. The comprehension of the links between the properties of the droplet interfaces and the mechanisms involved in emulsion formation and stability is a mandatory step to achieve the above target, by validating and developing predictive models.

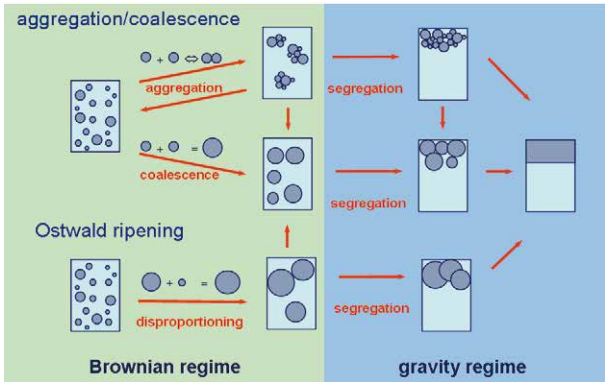

Figure 1: Sketch of the mechanisms involved in emulsion destabilization.

To this aim, within the project, systematic investigations of adsorption layer properties performed on ground will be correlated to benchmark experiments on emulsion aging to be performed under weightlessness (microgravity) conditions. In fact, based on the suppression of droplet buoyancy, microgravity experiments provide an ideal environment to investigate with a superior accuracy all the basic mechanisms involved in emulsions destabilization, under the sole effect of capillary-related features.

These experiments will be executed onboard the International Space Station in the facility FOAM-C, using diagnostics based on the concepts of Diffusion Wave Spectroscopy (DWS).

DWS is a non-invasive optical diagnostics, based on the temporal analysis of the light scattered inside the sample, that allows to study dynamic and structural features of turbid systems, as it is the case for concentrated emulsions.

Here we provide an overview of the concepts and implementation of the EDDI research programme and of the utilized experimental techniques, and also some results related to the preparation of the planned microgravity experiments.

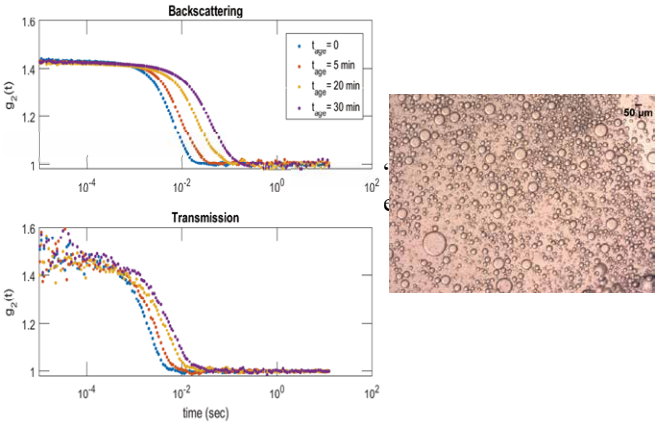

Figure 2: Left: Examples of correlation functions from emulsion at different aging times by the FOAM-C breadboard. Right: Related microscopy picture of the emulsion aged 30 min.

Acknowledgements
European Space Agency MAP Projects "Soft Matter Dynamics" and "Emulsion Dynamics and Droplet Interfaces - EDDI".

Oral 082

Characterization of Three-Dimensional Bone Constructs Derived From Human Fetal Osteoblasts Exposed To the Rotary Cell Culture System

Vivek Mann[1], Maitreyi Chaganti[1], Elvis Okoro[1], Janne E. Reseland[2] and Alamelu Sundaresan[1]

[1]Texas Southern University,[2]University of Oslo
Vivek.mann@tsu.edu,maitreyi.chaganti6@gmail.com,okoro.elvis@tsu.edu,j.e.reseland@odont.uio.no, alamelu.sundaresan@tsu.edu

Introduction

Humans exposed to microgravity conditions experience various physiological changes, including loss of bone mass, muscle deterioration, and immunodeficiency. Long duration space travel subjects' astronauts to microgravity, harmful radiations, immobilization and isolation. All of these can have detrimental effects on human physiology. The lack of weight-bearing forces makes microgravity an ideal physical stimulus to evaluate bone cell responses. In vitro models can be used to extract valuable information about changes in mechanical stress to ultimately identify the different pathways of mechanotransduction in bone cells. Astronauts can lose up to 20% of weight-bearing bone during long duration missions. One of the most significant concerns for NASA today is the deterioration of bone conditions of astronauts exposed to microgravity.

Bone grafts and substitutes are widely used in orthopedic surgeries for numerous applications. Rising cases of orthopedic problems caused due to weakened bones is projected to fuel demand. Although the most heavily investigated area in bone tissue engineering is the creation of appropriate scaffolds from a wide-range of materials, it is becoming increasingly evident that these materials fall short when it comes to mimicking the natural bone healing process, i.e., promoting osteoblast formation and stimulating the vascularization process. In our study here we have employed hFOB cell line using Rotary Cell Culture System (RCCS) a modeled microgravity analog, with the purpose of improving bone engineering properties of 3D scaffolds.

Hfob cells were subjected to simulated microgravity using a RCCS for 21 days. Altered Cytoskeletal findings after exposure to modeled microgravity experiments (21 days) indicated that cells react immediately to the absence of gravity. The investigated cells (Hfob) showed a differential expression of a variety of genes, including extracellular matrix proteins. For quite some time, the cytoskeleton is believed to be a mediator between physical forces (microgravity) and mechanisms of gene regulation. Short-term effects of microgravity are alterations of the cytoskeleton, a change in cell- cell adhesion, altered cytokine release and/or an increase in programmed cell death (apoptosis). It also influences the morphologic appearance of the cells (hFOB) on a longer time scale.

Conclusions

We discovered, that culturing cells for longer time periods In RCCS system forces cells to assemble in 3-dimensional structures (multicellular spheroids). These spheroids exhibit a tissue-specific morphology depending on their origin. In view of long duration interplanetary missions (e.g., Mars Missions) and space tourism where individuals with limited training and experience will be exposed to reduce /microgravity, it is imperative that we extend our knowledge to mitigate neurodegenerative effects of microgravity.

26th European Low Gravity Research Association Biennial Symposium and General Assembly
14th International Conference on "Two-Phase Systems for Space and Ground Applications"
European Space Agency Topical Teams meetings
Granada (Spain), September 24-27, 2019

Oral 083

Prediction of Microgravity Flow Boiling Heat Transfer in the Bubbly Flow Regime

Caleb Hammer[1], Michel Lebon[1], Jungho Kim[1]

[1]University of Maryland, Department of Mechanical Engineering, College Park 20742, USA;
kimjh@umd.edu

Introduction

Phase change processes exist in a wide variety of applications for thermal management due to their potential for high heat transfer and isothermal heat removal. There exists a need to incorporate phase change thermal management in microgravity systems such as satellites and spacecraft (McQuillen 2003; Chiaramonte 2004). However, it has been shown that for flow boiling, one of the most common phase change processes, heat transfer is typically reduced in microgravity when compared to terrestrial gravity. Prior research determined flow convergence limits (Ohta 2003; Colin et al. 1991; Baltis et al. 2012; Zhang et al. 2002) in which the mass flow rate was large enough for inertial forces to overcome buoyancy forces resulting in gravity independent heat transfer, yet the effects of gravity at lower flow rates are still not well understood.

Strongly fluctuating local heat transfer was observed for terrestrial upward and downward flow around areas where bubbles were present (Lebon et al. 2018). This observation implies that turbulent structures dominate heat transfer when the buoyancy force is strong compared to the bulk liquid flow inertia. In microgravity, the reduction in buoyancy force reduces the bubble slip velocity, which in turn significantly reduces the turbulence in bubble wakes. For microgravity bubbly flow boiling, it is hypothesized that single-phase convective heat transfer in the liquid moving at the local liquid velocity is the primary heat transfer mechanism.

Experimental Facility and Numerical Methods

A two-phase flow loop was built for the study of flow boiling of HFE-7000 under terrestrial gravity and microgravity conditions. Local temperature, heat transfer, and visual data were acquired during flow boiling using TSP applied to the inside of a sapphire tube. Data were acquired for a 6 mm ID and a 4 mm ID tube. Bubble positions and diameters were manually tracked throughout the sapphire tube for microgravity conditions. The bubble expansions throughout the tube had coupled effects on the liquid velocity, which in turn affected the bubble velocity along the length of the tube. Time-averaged bubble speeds throughout the tube were used to fit a bubble velocity profile (Fig. 1), irrespective of radial position. The liquid velocity profile was developed by calculating the bubble terminal velocity at measured gravity levels. Associated uncertainties were fit to form upper (+) and lower (-) error margins. It was assumed that the fitted liquid velocity profile was representative of the average mass velocity within the tube.

The accelerating liquid velocity profile was replicated in ANSYS Fluent by simulating single-phase liquid through a heated tube of decreasing diameter. A constant liquid velocity was imposed at the entrance of an unheated entry length upstream of the heated tube. Constant mass flux caused fluid acceleration as the heated tube diameter decreased, simulating the increase in velocity observed in experimental two-phase microgravity flow boiling.

Results and Discussion

Local heat transfer coefficients were acquired for four mass fluxes, five heat fluxes, two subcoolings, and two tube diameters at microgravity and terrestrial gravity conditions. Simulated single-phase heat transfer coefficients were compared for the same cases, where the tube diameter profile, entry length, mass flux, local heat flux profile, and subcooling were imposed as parameters in the simulations. At mass flux G=39 kg/m^2.s, heat flux q"=0.48 W/cm^2, subcooling ΔT_{sub}=9.0°C, and diameter D=6 mm the numerical single-phase results (h_{num}) agree within the error margin of the experimentally acquired (h_{exp}) microgravity two-phase heat transfer coefficients (Fig. 2). A straight tube was simulated for these conditions ($h_{num,str}$) to determine the effect of the flow acceleration. The heat transfer coefficient at the outlet of the straight tube underpredicts the experimental values by about 50%, highlighting the effect of the accelerating flow. At a higher mass flux G = 120 kg/m^2.s, the difference between the outlet heat transfer coefficient for a straight tube and a tube of decreasing diameter was much less, about 10%. This behavior was

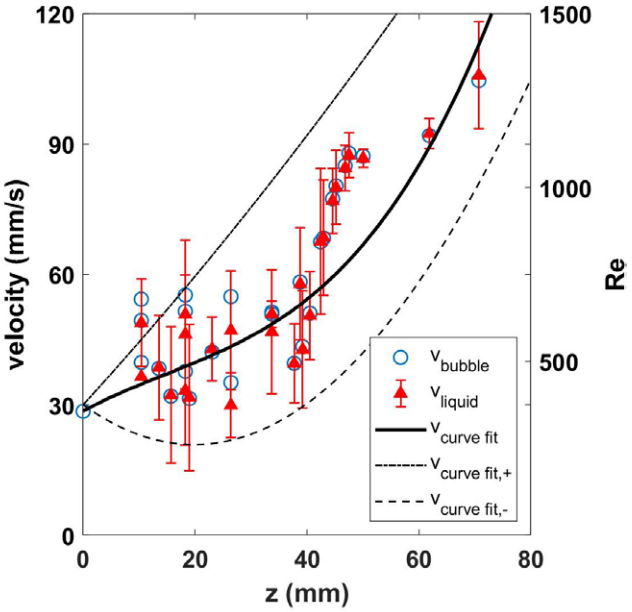

Figure 1: Comparison of local experimental and numerical heat transfer coefficients time-averaged over 2.5 s for G=39 kg/(m^2.s), q"=0.48 W/cm^2, ΔT_{sub}=9.0°C, D=6 mm.

observed for cases with fully laminar Reynolds numbers along the accelerating flow profile at low heat flux. These results reinforce our hypothesis that single-phase liquid convection is the dominant heat transfer mechanism in microgravity flow boiling.

As heat flux increased, bubble diameter and coalescence rate increased, therefore increasing the liquid velocity acceleration. For certain cases in which the accelerating flow entered a transitional Reynolds number, there were noticeable areas along the tube where the frequent merging of bubbles coincided with an increase in heat transfer coefficient. The laminar simulations for these cases significantly underpredict the outlet heat transfer coefficient. The outlet heat transfer coefficient agrees more suitably to single-phase simulations using the k-ω turbulence model. This implies that the bubble coalescence induces wake turbulence within the liquid, thus increasing the local heat transfer coefficient. At the lower tube diameter of 4 mm, bubble coalescence was observed at lower heat fluxes. This implies that the constrainment of bubbles during microgravity flow boiling is an important factor in producing wake turbulence.

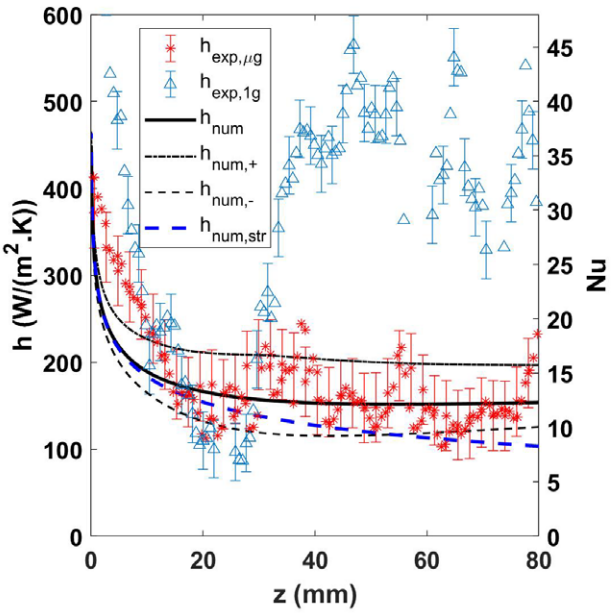

Figure 2: Comparison of local experimental and numerical heat transfer coefficients time-averaged over 2.5 s for G=39 kg/(m^2.s), q"=0.48 W/cm^2, ΔT_{sub}=9.0°C, D=6 mm.

Conclusions

This study showed good agreement between simulated single-phase heat transfer coefficient data of an accelerating flow and microgravity for laminar cases of low mass and heat flux. The results imply that single-phase liquid convection is the dominant heat transfer mechanism in microgravity isolated bubbly flow. This implication is an important step in modeling microgravity flow boiling in regimes where there are significant differences in heat transfer compared to terrestrial flow. Additional studies will be performed comparing heat transfer between 6 mm ID and 4 mm ID results.

Acknowledgements

Support for this research was provided through NASA Grant NNX09AK39A. Mr. Caleb Hammer was funded on a NASA NSTRF Fellowship through Grant NNX16AM94H. The low-gravity flights were supported through the NASA REDDI program through Grant NNX16AP62G.

References

J. McQuillen, E. Rame, M. Kassemi, B. Singh, B. Motil, Results of the Workshop on Two-Phase Flow, Fluid Stability and Dynamics: Issues in Power, Propulsion, and Advanced Life Support Systems. NASA/TM-2003-212598 (2003)

F.P. Chiaramonte, J.A. Joshi, Workshop on Critical Issues in Microgravity Fluids, Transport, and Reaction Processes in Advanced Human Support Technology. NASA/TM—2004-212940 (2004)

H. Ohta, Microgravity heat transfer in flow boiling. *Adv. Heat Transfer* 37 (2003) 1-76.

C. Colin, J. Fabre, A.E. Dukler, Gas–liquid flow at microgravity conditions—I. Dispersed bubble and slug flow, *Int. J. Multiphase Flow*, 17 (1991) 533-544.

C. Baltis, G.P. Celata, M. Cumo, L. Saraceno, G. Zummo, Gravity influence on heat transfer rate in flow boiling, *Microgravity Sci. Technol.*, 24(3) (2012) 203-213.

H. Zhang, I. Mudawar, M.M. Hasan, Experimental and theoretical study of orientation effects on flow boiling CHF, *Int J. of Heat and Mass Transfer* 45 (2002) 4463-4477.

M. Lebon, C. Hammer, J. Kim, Gravity effects on subcooled flow boiling heat transfer, *Int. J. of Heat and Mass Transfer* 128 (2018) 700-714.

26th European Low Gravity Research Association Biennial Symposium and General Assembly
14th International Conference on "Two-Phase Systems for Space and Ground Applications"
European Space Agency Topical Teams meetings
Granada (Spain), September 24-27, 2019

Oral 084

Impact of clinorotation on microtubule regulation by tubulin-associated proteins in plants

G. Shevchenko

Institute of Botany, NAS Ukraine, Tereshchenkivska 2, 01004,

Kiev, Ukraine, e-mail: galli.shevchenko@gmail.com

Introduction

Plant cytoskeleton is highly dynamic structure responsible for cell division, growth and reaction to environmental stimuli. Dynamic nature of the cytoskeleton makes plants highly adaptive to changes. Functioning of two main cytoskeleton components (microtubules (MTs) and actin filaments (AFs) and their dynamic nature is facilitated by numerous associated proteins. Among them are MAP65-1, CLASP and Phospholipase D delta (PLD) known to bundle antiparallel MTs, regulate microtubule plus-end dynamics and stabilize cell wall-plasma membrane-cytoskeleton continuum. Evolutionally development of plant cell cytoskeleton took place under constant 1-g, and it is known that MTs tend to orient along mechanical tension promoting cell form, growth orientation and metabolic processes. However, clear picture of the cytoskeleton dynamics and its regulation is not totally defined. In order to clarify details of plant cytoskeleton regulation, we assume that remove of constant g-impact might decipher details of MT functioning. Therefore, we applied clinorotation and pharmacological approach (tubulin polymerization inhibitor oryzalin (OR)) and investigated *Arabidopsis thaliana* root growth and expression of *TUB6, ACT2, MAP65-1, CLASP* and *PLD delta* after 3 day treatment. Oryzalin was applied in order to enhance MT and AF disorganization which presumably occurred upon clinorotation (Shevchenko et al. 2007; 2009).

Materials and methods

A.thaliana seedling were germinated for 3 days on MS medium and then subsequently transferred on slow rotating (2rpm) 2D clinostats and treated by oryzalin (OR). There were 4 experimental sets: control, control + OR, clinostat and clinostat+OR. Seedlings were treated during 3 days and then proceeded for RNA extraction and qPCR reaction. In each set of experiment expression of *TUA6, ACT2, MAP65-1, CLASP* and *PLD delta* were analyzed both in plants on clinostats and after addition of oryzalin (10uM).

Results and discussion

Network of cortical microtubules (cMTs) undergoes reorganization upon various stresses and it still remains unclear how parallel orientation of MTs in cortical arrays is controlled and what determines whether an array will be oriented transverse or longitudinal relative to the cell axis. Fine network of AFs is co-localized with MTs and is also affected by external stimuli. Fine tuning of all cytoskeletal elements is aimed on plant adaptation to changed surroundings. Our experiments have shown that *A.thaliana* growth was impaired after both type of impact of either clinorotation or both factors on tubulin activity we have analysed expression profiles of *TUA6, ACT2, MAP65-1, CLASP* and *PLD delta*. Factorial analysis ANOVA has revealed that clinorotaton has not affected neither tubulin, not actin gene expression. Oryzalin treatment affected expression of *TUA6, MAP65-1* and *ACT2* evidencing MT disorganization and involvement of MAP65-1 and actin in this process, and therefore, revealing role of these proteins in MT stabilization in control. Thus, one could say that activity of MAP65-1 and actin depends upon the state of MTs (Shevchenko et al. 2008). It should be mentioned that in our previous investigations, application of actin disruptor cytochalasin D also affected both *TUA6* and *ACT2*. Above suggested interrelation between MTs and AFs in growth regulation (Shevchenko et al. 2008; 2009).

At the same time, interaction of both factors – clinorotation and OR does not impact *MAP65-1, CLASP* and *PLD delta* but affected *ACT2*. And this also proves mutual interrelationship between MTs and AFs. It is not excluded that such type of interrelation is regulated in a different way on clinostats.

Conclusions

Analysis of transcripts has shown that clinorotation does not affect expression of *TUA6, ACT2, MAP65-1, CLASP* and *PLDdelta.* At the same time, simultaneous application of both factors – clinorotation and oryzalin changed expression of *ACT2*. Above suggested mutually dependent functioning of cytoskeletal elements (MTs and AFs) and its different regulation upon influence of altered gravity. Our investigation contributes into understanding of plant cell growth regulation by mechanical stress and it helps to clarify cytoskeleton involvement in the mechanism of gravity signaling in plants.

References

G. Shevchenko, Ya.M. Kalinina, E.L.Kordyum, Interrelation between microtubules and microfilaments in the elongation zone of *Arabidopsis* root under clinorotation, Adv.Space Res. 39 (2007) 1171-1175.

G. Shevchenko, Ya.M. Kalinina, E.L.Kordyum, Tubulin cytoskeleton in *Arabidopsis thaliana* root cells under clinorotation, Microgravity Sci. and Technology 21 (2009) 187-190.

treatment, clinorotation and addition of oryzalin (Fig.1).

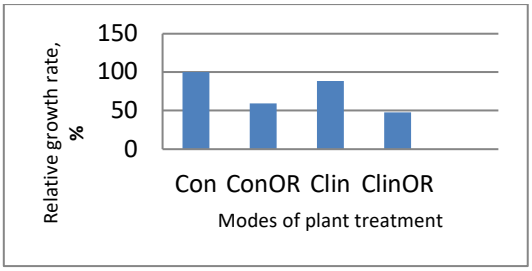

Figure1. Relative growth rate of *A.thaliana* seedlings on clinostats and addition of oryzalin

Common action of clinorotaton and OR affected root growth more severe. In order to decipher

26th European Low Gravity Research Association Biennial Symposium and General Assembly
14th International Conference on "Two-Phase Systems for Space and Ground Applications"
European Space Agency Topical Teams meetings
Granada (Spain), September 24-27, 2019

Oral 086

Simulation of three phase systems in the frame of MAP EDDI

Sergey Semenov[1], Libero Liggieri[2], Mickael Antoni[1]
[1]*Aix-Marseille University - MADIREL - France*
[2] *CNR ICMATE, Genova - Italy*
* m.antoni@univ-amu.fr

Emulsions incorporating gas bubbles - known as bubbly, aerated or foamed emulsions, depending on the amount of gas - are of great practical relevance. Aerated emulsions are particularly common in food and cosmetic industry, with the aim of imparting specific sensorial features (ice creams, skin creams, etc.). The studies of these systems have focussed so far on the general features of the systems, without entering into the details of the interactions between bubbles and drops.

Drop-bubble aggregates can form, which, under ground conditions are subject to creaming. Under microgravity this phenomenon vanishes and the evolution is essentially driven by the ability of capillary forces to bring bubbles and drops together. Although the features and dynamics of such multiphase aggregates share similarities with the floatation of particles, in a bubbly dispersions, the presence of deformable droplets confers specific complexity to bubbly emulsions.

Despite significant progress during the last decades, simulations of three phase systems including capillarity remain still challenging. One reason is the large density difference when dealing with gas and liquids. In this context, the interest of microgravity studies is that they can support the testing of numerical algorithms. In the case of bubbly emulsions under weightlessness conditions, simulations show local coalescence events that trigger abrupt flows in the continuous phase, generating coalescence cascades which make the system highly unstable (see Figure).

These intermittent coalescence phenomena are simulated using two-dimensional system with multiple water droplets and air bubbles in a continuous paraffin oil phase. Conditions are assumed isothermal. A multiphase volume of fluid (VOF) home-made code is employed. It solves the continuity and Navier-Stokes equations for an incompressible medium along with the advection equation for a color function representing phase fraction.

In VOF methods, different immiscible fluids are treated as a unique continuous phase but with changing material properties according to the local value of color function. The interfacial stresses are directly included into Navier-Stokes equations in form of an equivalent body force according to the continuous approach of Brackbill. Interfacial curvature is computed with the aid of height-function. The numerical scheme is based on 2nd order discretization in both time and space. The finite volume method on a staggered computational mesh is used for spatial discretization of all the equations. Heat transfer, action of thermocapillary and solutocapillary stresses as well as reactivity at interfaces will be implemented in future.

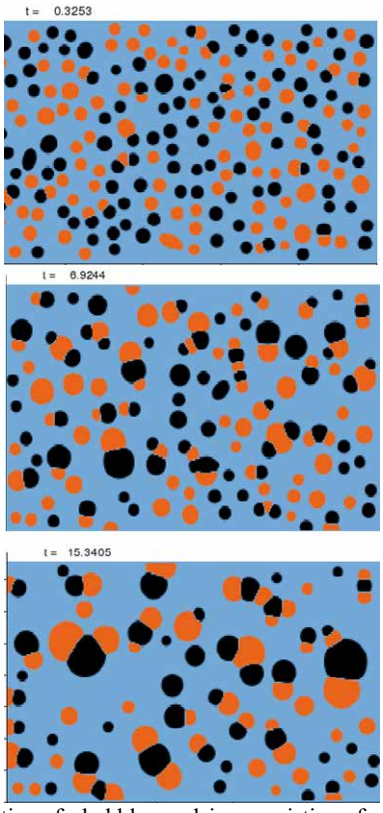

Time evolution of a bubbly emulsion consisting of paraffin oil (blue), water droplets (black) and air bubbles (orange). Size of the system is 30 cm × 20 cm.

Aknowledgements:
CNES Project "*Stabilité des dispersions - mesures et modélisation*" and CEA Project "*Simulation numérique d'un bain de corium*"

Oral 088

Cardiac Response to Sympathetic Activation is altered by long-term microgravity exposure

S. Palacios[1], E.G. Caiani[2], J.P. Martínez[1,3], E. Pueyo[1,3]

[1]BSICoS Group, Aragón Institute of Engineering Research, IIS Aragón, University of Zaragoza, Zaragoza, Spain, spalacios@unizar.es
[2]Electronics, Information, and Bioengineering Department, Politecnico di Milano, Milan, Italy
[3]CIBER en Bioingeniería, Biomateriales y Nanomedicina (CIBER-BBN), Spain;

Introduction

Long-term microgravity exposure induces changes in the cardiovascular system. One of the most commonly reported cardiovascular alterations after landing from a space mission is orthostatic intolerance, which has been associated with impairments in the sympathetic nervous system. The Tilt-Table Test (TTT) is a test used to assess the autonomic nervous system response.

An index of Periodic Repolarization Dynamics (PRD) has been recently proposed to quantify the low-frequency components (≤0.1 Hz) of the beat-to-beat angular changes in the T-wave of the electrocardiogram (ECG), thus representing sympathetic modulation of ventricular repolarization (Rizas et al. 2014).

This study aimed to quantify ventricular responses to TTT, both before (PRE) and after (POST) long-term microgravity exposure simulated by a head-down bed rest (HDBR) model. In addition, the effect of applying a jump-based countermeasure during HDBR is assessed.

Materials and Methods

High-resolution (1000 Hz) 12-lead ECG recordings from 22 male volunteers (29±6 years, 181±5 cm, 77±7 kg), which participated in a 60-day -6º HDBR experiment, were available for this study. Subjects were randomly divided into two groups: countermeasure group (JUMP), who had specific exercises on a sledge jump system (Kramer et al. 2017), and control group (CTRL), who did not perform those exercises. The experiment was part of the European Space Agency (ESA) bed rest studies and was conducted in the *:envihab* facility of the Institute of Aerospace Medicine at the German Aerospace Center-DLR (Cologne, Germany). All subjects gave written informed consent to the experimental procedure, which was approved by the Ethical Committee for Human Research at the host institution.

The whole experiment had three phases: 15-day pre-bed rest control, 60 days of HDBR and 15-day ambulatory recovery period. Two days before HDBR and just after completing HDBR, each volunteer was subject to a TTT. This study analyzed 5-minute intervals prior and immediately following the start of the TTT.

Raw ECG recordings were preprocessed to remove electric and muscle noise, artifacts and baseline wander. QRS detection and ECG wave delineation were performed over the filtered signals to mark onsets and ends of ECG waves. The PRD index was calculated as described in (Rizas et al. 2014), but Cartesian coordinates were used instead of polar coordinates. Continuous wavelet transform using a 4th-order Gaussian wavelet was used to obtain the coefficients for the different scales, which were associated with different pseudo-frequencies. PRD was defined as the average wavelet coefficient between 0.025 and 0.1 Hz.

Results

Results are presented in Table 1. In all cases, PRD increased when measured following TTT as compared to baseline. Additionally, in all cases, simulated microgravity induced PRD increments, with the differences between POST-HDBR and PRE-HDBR being especially remarkable for the CTRL group and, in particular, when evaluated following TTT. The jump-based countermeasure was able to attenuate the increase in PRD following microgravity exposure, but only partially.

Table 1: PRD values for baseline and following TTT, before and after HDBR in the two analysed groups (*significant differences between baseline and tilt in CTRL group at PRE-HDBR, +significant differences between PRE and POST-HDBR at the beginning of TTT for the CTRL subgroup)

CTRL	**PRE**	**Baseline**	* 4.14 [4.42] deg^2
		Tilt	*+ 13.16 [17.80] deg^2
	POST	**Baseline**	6.24 [15.95] deg^2
		Tilt	+ 35.65 [40.33] deg^2
JUMP	**PRE**	**Baseline**	3.98 [2.69] deg^2
		Tilt	4.50 [2.40] deg^2
	POST	**Baseline**	4.59 [4.31] deg^2
		Tilt	8.01 [8.12] deg^2

Discussion and conclusions

This study has shown that PRD, a non-invasive index of low-frequency oscillations in ventricular repolarization, is increased in response to enhanced sympathetic activity induced by TTT. Long-term microgravity exposure exhacerbates ventricular response to sympathetic activation, which could confer higher risk for arrhythmogenecity (Pueyo et al. 2016, Rizas et al. 2017). A jump-based countermeasure was only partially able to reverse microgravity effects on ventricular repolarization.

Acknowledgements

This work was supported by projects ERC-2014-StG 638284 (ERC), DPI2016-75458-R (MINECO) and Aragón Government (Reference Group BSICoS T39-17R) cofunded by FEDER 2014-2020 "Building Europe from Aragon". We also acknowledge the support of the Italian Space Agency (project QT-Bed, PI and recipient EG Caiani).

References

Rizas KD, et al. Sympathetic activity–associated periodic repolarization dynamics predict mortality following myocardial infarction, *J Clin Invest.* 2014; 124(4):1770-1780.

Kramer A, et al. High-Intensity Jump Training Is Tolerated during 60 Days of Bed Rest and Is Very Effective in

Preserving Leg Power and Lean Body Mass: An Overview of the Cologne RSL Study. *PLoS ONE*. 2017; 12(1):1-18

Pueyo E, Orini M, Rodríguez JF, Taggart P. Interactive effect of beta-adrenergic stimulation and mechanical stretch on low-frequency oscillations of ventricular action potential duration in humans. *J Mol Cell Cardiol.* 2016; 97:93-105.

Rizas KD, et al. Prediction of sudden and non-sudden cardiac death in post-infarction patients with reduced left ventricular ejection fraction by periodic repolarization dynamics: MADIT-II substudy, *Eur Heart J.* 2017; 38(27):2110-2118.

Oral 089

Cell Traction Forces Changes at Hypergravity

Jack J.W.A. van Loon [1, 2], Julia Eckert [2,3,4], Lukas M. Eng [4,5], Thomas Schmidt [3]

[1] DESC (Dutch Experiment Support Center), Dept. Oral and Maxillofacial Surgery / Oral Pathology, VU University Medical Center & Academic Centre for Dentistry Amsterdam (ACTA), Amsterdam, The Netherlands, [2] Life & Physical Science, Instrumentation and Life Support Laboratory (TEC-MMG), ESA/ESTEC, Noordwijk, The Netherlands, [3] Physics of Life Processes, Leiden Institute of Physics, Leiden University, Leiden, The Netherlands, [4] School of Science, Department of Physics, Technische Universität Dresden, Dresden, Germany, [5] ct.qmat: Dresden-Würzburg Cluster of Excellence - EXC 2147, TU Dresden, Germany

Introduction

Fundamental biological processes and the cell behavior are modulated under changed gravity conditions. In various studies it has been shown that hypergravity has an effect on the cell shape and elasticity, the cytoskeleton organization and cell motility. However, specific changes of applied traction forces on the extracellular matrix (ECM) under hypergravity conditions have not been explored so far. In the present study, we measured the changes in traction force of 3T3 fibroblasts up to a g-level of 19.5g, generated by the Large Diameter Centrifuge (LDC) of the technology center of the European Space Agency, ESA-ESTEC, in Noordwijk, NL.

Figure 1: 8-meter diameter Large Diameter Centrifuge (LDC) at ESA-ESTEC, Noordwijk, the Netherlands.

To monitor such forces exerted to cells, we used an array of micro pillars, a technology based on the deflection of elastic rods (the micro-pillars of controlled stiffness) that mimic the extracellular environment, to measure cell traction forces. The 3T3 mouse fibroblasts were seeded onto such pillar arrays and exposed to hypergravity at different g-levels. Arrays were oriented in the upright and up-side-down position in order to study the dependency of the direction and magnitude of the g-force on the cell-ECM traction force generation.

Conclusions

The results of our study show that cell traction forces decrease significantly under lower hypergravity conditions, yet increase for higher g-levels. Furthermore we found that cells mounted in the up-side-down position were more affected. These results are in line with earlier studies that showed a respective decrease in actin fiber formation under low hypergravity and an increase at higher g-levels.

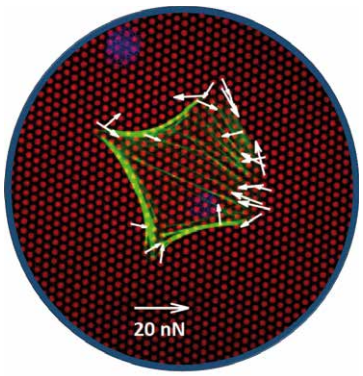

Figure 2: Example of a single cell attached to a bed of flexible PDMS pillars. Deflection of the pillars is a measure of force generated by the cell.

Acknowledgements

We would like to thank ESA and in particular the TEC-MMG section at ESTEC with a special thanks to Robert Lindner, the head of the TEC-MMG and Alan Dowson for his patience and support to make this study possible.

References

van Hoorn, H.; Harkes, H.; Spiesz, E.M.; Storm, C.; van Noort, D.; Ladoux, B.; Schmidt, T.: The Nanoscale Architecture of Force-Bearing Focal Adhesions. *Nano Letters* 14(8) (2014) 4257-62. doi: 10.1021/nl5008773.

van Loon, J.J.W.A.; Dowson, A.:, Large Diameter Centrifuge (LDC) – Experimenter Users Manual, 2016.

van Loon J J.W.A., Krausse J, Cunha H., Goncalves J, Almeida H, Schiller P. The Large Radius Centrifuge, LDC, for Life and Physical Sciences and Technology @ ESA-ESTEC. ESA-ELGRA-ISGP-ASGSB meeting "Life in Space for Life on Earth." 22 - 27 June 2008. Angers – France.

26th European Low Gravity Research Association Biennial Symposium and General Assembly
14th International Conference on "Two-Phase Systems for Space and Ground Applications"
European Space Agency Topical Teams meetings
Granada (Spain), September 24-27, 2019

Oral 091

Pyrocystis noctiluca represents an excellent bioassay for demonstration of shear forces induced in ground-based microgravity simulators

Jens Hauslage[1] and Ruth Hemmersbach[1]
[1]German Aerospace Center, Cologne, Germany, jens.hauslage@dlr.de and ruth.hemmersbach@dlr.de

Abstract
Ground-based facilities, such as clinostats and random positioning machines aim to simulate microgravity conditions in order to prepare space experiments and identify gravity-related signaling pathways. However, they have to be operated in an appropriate manner and potentially induced side-effects, such as shearing forces, have to be taken into account. Dinoflagellates, such as *P. noctiluca*, are fast and sensitive reporter systems for shear stress and hydrodynamic gradients. Deformation of the cell membrane of *P. noctiluca* due to shear stress results in a detectable bioluminescence emission. We exposed them Random Positioning Machine (Dutch office of Airbus), operated either as a 2D clinostat mode (constant rotation around one axis, 60 rpm) or in a 3D random mode, that means rotating around two axes, whose velocity and direction were chosen at random.

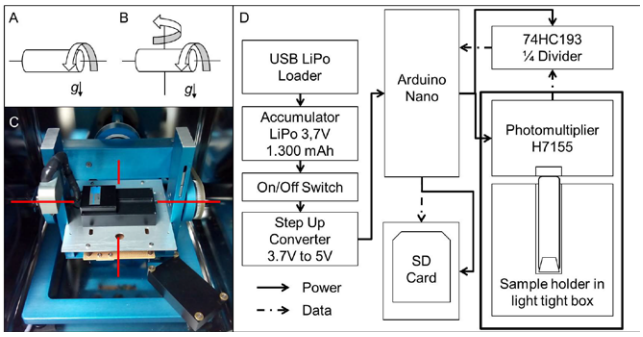

Figure 1: System for monitoring of shearing forces induced in Random Positioning Maschine operated in different modes A: Clinostat mode B: RPM Mode C: picture of the setup and D: technical description of the experimental setup.

Results
Our results show that the amount of mechanical stress is higher on an RPM machine than during constant clinorotation, as indicated by the differences in photon counts (see Figure 2). We conclude that one axis clinorotation induced negligible small side effects in the form of shear forces in contrast to random operation modes tested.

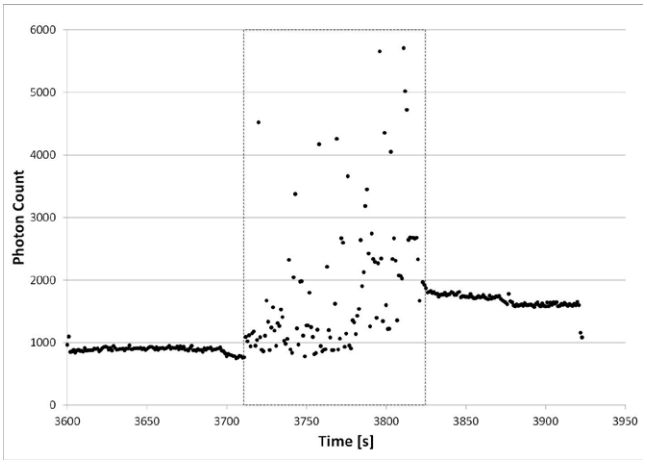

Figure 2: Photons produced by dinoflagellates due to the response towards shearing forces. The shown measurement was taken during clinorotation, interrupted by a period of random positioning (box), demonstrating an increased photon count.

Conclusions
Ground-based facilities provide the opportunity to prepare space experiments and learn about the sensitivity and behavior of the biological system of interest.
However, operation modes should be carefully considered in order to avoid misinterpretation of results impacted by external forces resulting in stress response.

References
J. Hauslage, V. Cevik, R. Hemmersbach, *Pyrocystis noctiluca* represents an excellent bioassay for shear forces induced in ground-based microgravity simulators (clinostat and random positioning machine), *NPJ microgravity*, (2017) *3*(1), 12.

Oral 092

Study on thermocapillary migration of drops by digital holographic interferometry

Li Duan[1,2], Shuoting Zhang[1], Qi Kang[1,2]

[1] Key Laboratory of Microgravity, Institute of Mechanics, Chinese Academy of Sciences, Beijing 100190, PR China
[2] School of Engineering Sciences, University of Chinese Academy of Sciences, Beijing 100049, PR China
duanli@imech.ac.cn

Introduction

The investigation of thermocapillary flow is important for basic research, as well as for material sciences, chemical engineering, and space manufacturing. When the gravity effect is greatly reduced, the interfacial phenomenon becomes important. The motion of drops driven by temperature gradients is related to the Marangoni convection. The Marangoni effects are caused by interface tension changes, typically interface tension becoming decreased with increasing temperatures. Under different conditions, The Marangoni effects can cause a drop to move in the opposite direction.

Experimental installation

The thermocapillary migration of drops in a temperature gradient was studied in the present experiment by utilizing digital holographic interferometry.

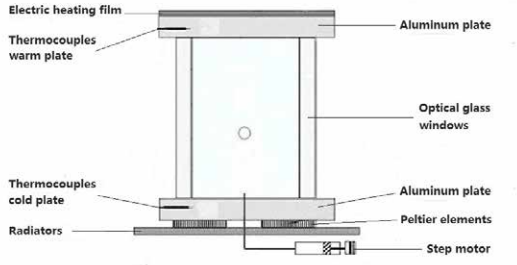

Figure1 Experimental model

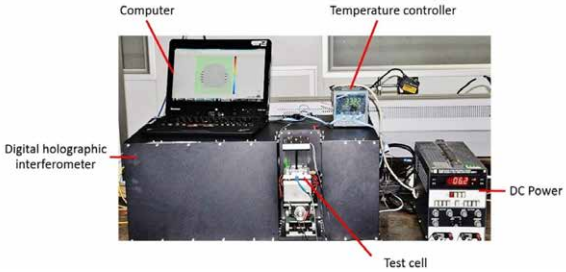

Figure2 Digital holographic interferometry

Experiment result

The temperature distribution around a drop, as well as on the interface of a drop, during migration in a vertical temperature gradient were visualized and provided quantitatively for the first time. The perturbed temperature distribution and the actual temperature distribution around the drop during the thermocapillary migration were obtained, and were discussed in detail in this study. The drop was colder than the continuous phase liquid, and a thermal wake existed behind the drop. The dimensionless interface temperature difference was a monotonically decreasing function of the Marangoni number for the three different temperature gradients. When the Marangoni number was increased, the dimensionless interface temperature difference was found to decrease, which was caused by the decrease of the enhanced convective transport results in the drop's thermocapillary migration velocity. With the increasing Marangoni numbers, the length of the thermal wake region increased, and the thermal wake region was extended.

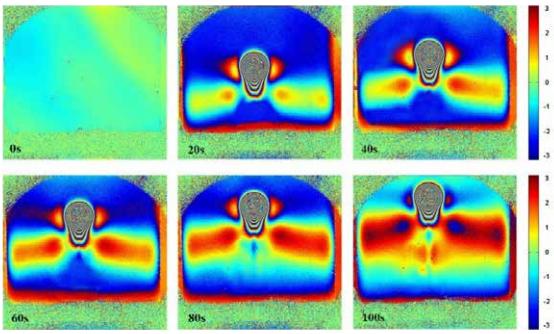

Figure 3 Reconstructed phase distributions at different times

Conclusions

The thermocapillary migration is studied by digital holographic interferometry. The temperature distributions around a droplet are visualized and measured quantitatively for the first time. With the increasing of the Marangoni number, the dimensionless interface temperature difference decreases, the length of the thermal wake region increases. The heat transfer is the coupling of the heat diffusion and the convective transport.

Acknowledgements

This work is funded by the space experimental project of China Manned Space Engineering program.

References

Q. Kang, L. Hu, C. Huang, H.L. Cui, L. Duan, W. R. Hu, Experimental investigations on interaction of two drops by thermocapillary-buoyancy migration, *J. Heat Mass Transfer* 49 (2006) 2636-2641.

L. Duan, Q. Kang, Z.W. Sun, L. Hu, H.L. Cui, H. Lin, G.P. Li, The real-time Mach-Zehnder interferometer used in space experiment. *Microgravity Sci. Tec.* 20 (2008) 91-98.

26th European Low Gravity Research Association Biennial Symposium and General Assembly
14th International Conference on "Two-Phase Systems for Space and Ground Applications"
European Space Agency Topical Teams meetings
Granada (Spain), September 24-27, 2019

Oral 093

Space experimental study on the geometric effect of thermocapillary convection in the liquid bridge

Qi Kang[1,2], Li Duan[1,2], Di Wu[1], Liang Hu[1], Jia Wang[1], Pu Zhang[1], Wenrui Hu[1,2]

[1] Key Laboratory of Microgravity, Institute of Mechanics, Chinese Academy of Sciences, Beijing 100190, PR China
[2] School of Engineering Sciences, University of Chinese Academy of Sciences, Beijing 100049, PR China
kq@imech.ac.cn

Introduction

The experimental study on thermocapillary convection in liquid bridges of large Prandtl number has been carried out on TG-2. The purpose of this experiment is to study the oscillation instability of thermocapillary convection, and to discover and recognize the mechanism of destabilization of thermocapillary convection in microgravity environment in space.

Space experiment

In the space experiments, the liquid bridge is linearly heated or cooled, thermocapillary flows are established, the temperature evolution in fluid is detected by high-accuracy thermocouples. More than 600 sets of space experiments have been finished, and the oscillation and transition laws of thermocapillary convection are analyzed.

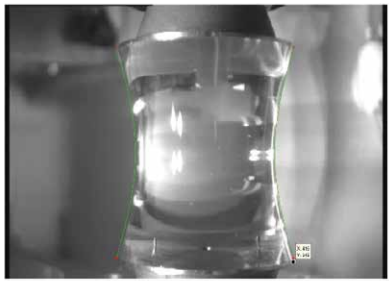

Figure1 Liquid bridge in space

The geometric effect

The geometry of the liquid bridge of half-floating zone is featured by the aspect ratio Ar and volume ratio Vr, and its effect on the critical conditions of the oscillatory thermocapillary convection is studied. The critical conditions and oscillation characteristics of thermocapillary convection instability in the Ar-Vr parameter space have been fully obtained under microgravity conditions for the first time. It is found that the Ar-Vr parameter space is divided into two regions with different critical conditions and oscillation characteristics: the region of low frequency oscillation, and the region of high frequency oscillation. This indicates that both critical curves of volume ratio and aspect ratio are divided into two branches. The more important, the second and the third transition points, have been discovered, we can obtain the complete configuration of these two neutral curves of stability, and find that the low frequency mode is a "Ↄ"type curve.

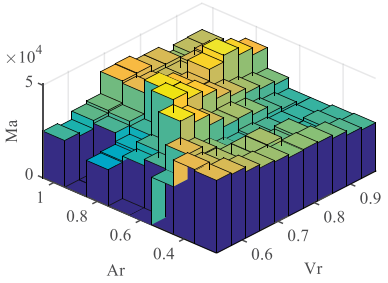

Figure 2 parametric space (Ar, Vr) vs. critical Mac

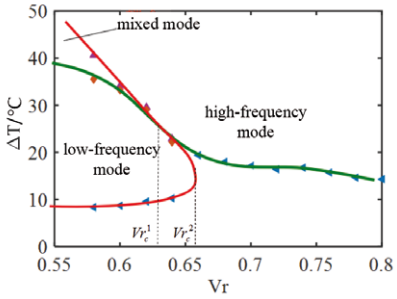

Figure 3 The curves of neutral stability of low-frequency mode and high-frequency mode

Conclusions

The oscillation mode of thermocapillary convection in the liquid bridge is influenced by the aspect ratio effect and the volume ratio effect simultaneously, no matter the aspect ratio effect or the volume ratio effect, both of their critical curves have two branches, and obvious jump change exists.

Acknowledgements

This work is funded by the space experimental project of China Manned Space Engineering program (TG-2).

References

Hu W R, Tang Z M, Li K. Thermocapillary Convection in Floating Zones[J]. *Advances in Mechanics*, 2009, 61(4):415-422.

Wang J, Wu D, Duan L, Kang Q. Ground experiment on the instability of buoyant-thermocapillary convection in large-scale liquid bridge with large Prandtl number[J]. *International Journal of Heat & Mass Transfer*, 2017, 108:2107-2119.

Oral 094

Dynamical clustering of granular materials in microgravity : a review of VIP-GRAN experiments

N. Vandewalle[1]

[1]GRASP, University of Liège, B4000 Liège, Belgium

Summary

The study of the statistical mechanics of an out-of-equilibrium ensemble of solid particles that dissipates due to collisions is of primary interest. Various behaviors are expected and could be compared with classical thermodynamical systems : clustering versus gas-liquid transition, gas versus evaporation, particle motion versus thermal fluctuations. Such experiments can be made with the VIPGRAN (Vibration Induced Phenomena in Granular Materials) instrument, being developed by the European Space Agency (ESA) within the SPACEGRAINS project (spacegrains 2019).

Motivation for low gravity is to achieve an experimental situation in which inelastic collisions between particles are the only interaction mechanism. While the ISS version of VIPGRAN is under development, the parabolic flight version of the instrument has already produced lots of results devoted to the study of dynamical and statistical behaviors of granular matter in low-gravity environment. In this talk, I will give an overview of all experiments done in the PFC using the VIP-GRAN instrument (S.Aumaître et al, 2018).

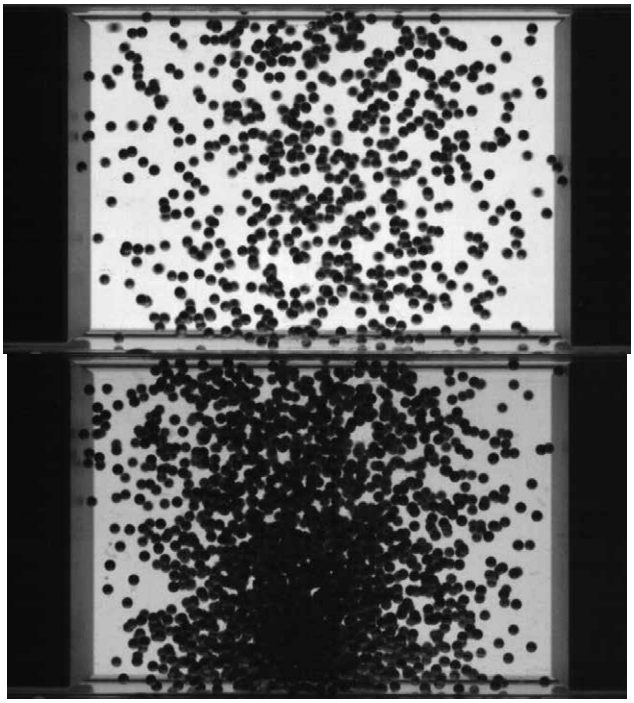

Figure 1: Two extreme states in a driven granular gas in microgravity : (top) dilute gas regime in PFC63, (bottom) cluster in the center of the experimental cell in PFC67.

Figures 1 and 2 show typical granular behaviors that we study in microgravity : gas-cluster transition in Figure 1 and granular mixtures in Figure 2. All behaviors will be discussed during the talk.

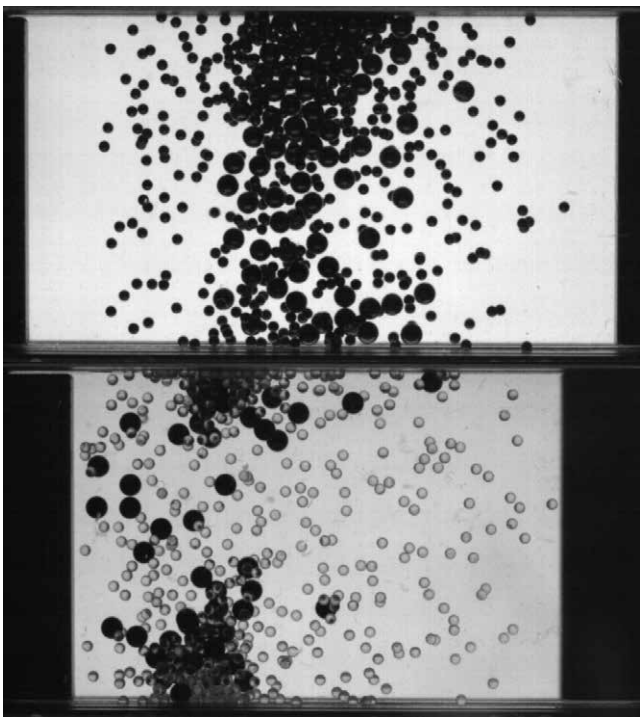

Figure 2: Granular mixtures of large and small grains studied in the VIP-Gran instrument : (top) segregation when all large grains belong to the central cluster while a part of the small grains is still seen in the gas phase in PFC64, (bottom) convection rolls are seen close to non-moving walls of the cell in PFC65.

Acknowledgements

We thank M. Braibanti, O. Minster, and V. Kohne from ESA for fruitful discussions and for the flight opportunity. VIP-Gran-PF was built by DTM Technologies (Modena, Italy).

References

www.spacegrains.org website of the project (2019)

S. Aumaître et al., An instrument for studying granular media in low-gravity environment, *Rev. Sci. Inst.* 89 (2018) 075103.

Oral 097

NUCLEOLIN: Similar and Antagonistic Roles in *Arabidopsis thaliana*

Durut N., Abou-Ellail M., Comella P., Jobet E., de Bures A. and Sáez-Vásquez J*.
LGDP, UMR 5096 CNRS-UPVD, 66860, Perpignan, France.
*saez@iniv-perp.fr

Introduction

NUCLEOLIN (NUC) is an evolutionary conserved and multifunctionary protein present in all eukaryotic cells. NUC is a major nucleolar protein involved in ribosome biogenesis, including RNA Pol I transcription and processing of 45S pre-rRNA and assembly and transport of ribosome particles to the cytoplasm. Noteworthy, NUC protein is involved also in the control of RNA pol II transcription and other activities in the nucleoplasm. NUC protein is encoded by a single gene in yeast (NSR1/ GAR2) and animal (NCL) cells and its activity is controlled at both transcriptional and post transcriptional levels during cell growth and differentiation as well as in response to cellular stresses (Tajrishi et al., 2011; Berger et al., 2015). In contrast, plant genomes encode at least two NUC proteins. Here we described the functional characterization of *NUC1* and *NUC2* from *Arabidopsis thaliana* Col-0 ecotype.

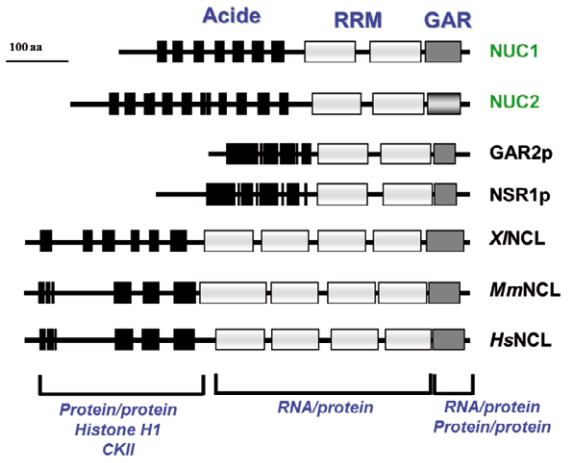

Figure 1: Schematic representation of nucleolin proteins from *A. thaliana* (NUC1 and NUC2), *S. pombe* (GAR2p), *S. cerevisiae* (NSR1p), *X. laevis* (*Xl*NCL), *M. musculus* (*Mm*NCL) and *H. sapiens* (*Hs*NCL). The black boxes correspond to the acidic regions in the N-terminal domain, the white boxes represent the RNA Recognition Motif (RRM) domains and the dark grey boxes the Glycine Arginine Rich (GAR) domain. The light grey box in the NUC2 sequence represents the less conserved GAR domain. The activities or functions of Acidic, RRM and GAR domainsare specified in blue.

Results and Discussion

The *NUC1* gene is constitutively expressed and, is functionally similar to its counterpart yeast NSR1/GAR2 and animal NCL genes. In contrast, *NUC2* gene expression is specifically correlated with seed germination and flowering, and likely plant-specific.

Disruption of *NUC1* gene leads to growth defects and abnormal phenotype characterized by smaller, pointed, scrunched and irregularly shaped leaves. Remarkably, *NUC2* gene expression is up-regulated in *nuc1* mutant plants, suggesting that NUC2 protein might rescue *NUC1* gene disruption (Pontvianne et al., 2007). Concerning *nuc2* plants, the mutation does not affect growth seedlings but induces a delay in flowering but without any obvious floral and/or silique phenotypes (Durut et al., 2014).

Remarkably, disruption of NUC1 protein expression induces 45S rDNA (encoding the 18S, 5.8S and 25S rRNA) chromatin decondensation and transcriptional activation of the most highly represented 45S rDNA variant (Var1), which is inactive in WT plants. Activation is correlated with specific loss of symmetric DNA methylation without affecting histone epigenetic marks. Interestingly, in *nuc2* plants 45S rDNA Var1 is also reactivated, but in contrast to *nuc1*, the expression of Var1 is accompagnied by a CpG hypermethylation and a re-organization of 45S rDNA variants into the Nucleolar Organizer Regions (NORs). We suggested that NUC2 is required to repress specific subset of 45S rDNA located in NOR2 during developmental transitions (Pontvianne et al., 2010; Durut et al., 2014; Durut and Saez-Vasquez, 2015).

In cinstrats to *NUC1* gene, the duplicated *NUC2* gene contains several cis-acting elements related to biotic and abiotic stress responses, including a Heat Shock Element (HSE). At high temperature conditions (37°C/24h), *NUC2* gene expression is up-regulated and the corresponding protein accumulates in the nucleolus. Furthermore, RNAseq analysis of heat-treated and non-treated *nuc2* plants demonstrates that NUC2 is required for expression of specific subsets of protein coding and non-coding genes in response to high temperature conditions.

Acknowledgements

This work was supported by the CNRS; the UPVD (fellowships to ND) and by grant from the ANR (Agence Nationale de la Recherche): RiboStress 17-CE12-0026-01 to JSV. We also acknowledge funding from "ELGRA Gravity Spotlight Team" grant

References

Berger, C.M., Gaume, X., and Bouvet, P. (2015). The roles of nucleolin subcellular localization in cancer. Biochimie **113,** 78-85.

Durut, N., and Saez-Vasquez, J. (2015). Nucleolin: Dual roles in rDNA chromatin transcription. Gene **556,** 7-12.

Durut, N., Abou-Ellail, M., Pontvianne, F., Das, S., Kojima, H., Ukai, S., de Bures, A., Comella, P., Nidelet, S., Rialle, S., Merret, R., Echeverria, M., Bouvet, P., Nakamura, K., and Saez-Vasquez, J. (2014). A duplicated NUCLEOLIN gene with antagonistic activity is required for chromatin organization of silent 45S rDNA in Arabidopsis. Plant Cell **26,** 1330-1344.

Pontvianne, F., Matia, I., Douet, J., Tourmente, S., Medina, F.J., Echeverria, M., and Saez-Vasquez, J. (2007). Characterization of AtNUC-L1 reveals a central role of nucleolin in nucleolus organization and silencing of AtNUC-L2 gene in Arabidopsis. Mol Biol Cell **18,** 369-379.

Pontvianne, F., Abou-Ellail, M., Douet, J., Comella, P., Matia, I., Chandrasekhara, C., Debures, A., Blevins, T., Cooke, R., Medina, F.J., Tourmente, S., Pikaard, C.S., and Saez-Vasquez, J. (2010). Nucleolin is required for DNA methylation state and the expression of rRNA gene variants in Arabidopsis thaliana. PLoS Genet **6,** e1001225.

Tajrishi, M.M., Tuteja, R., and Tuteja, N. (2011). Nucleolin: The most abundant multifunctional phosphoprotein of nucleolus. Commun Integr Biol **4,** 267-275.

Oral 099

Brief on SJ-10 microgravity recoverable satellite mission

Wenrui Hu[1,2], Qi Kang[1,2]

[1] National Microgravity Laboratory, Institute of Mechanics, Chinese Academy of Sciences, Beijing 100190, PR China
[2] School of Engineering Sciences, University of Chinese Academy of Sciences, Beijing 100049, PR China
wrhu@imech.ac.cn, kq@imech.ac.cn

The SJ-10 program provides a mission of space microgravity experiments including both fields of microgravity science and space life science aboard the 24th recoverable satellite of China. Scientific purpose of the program is to promote the scientific research in the space microgravity environment by operating the satellite at lower earth orbit for 2 weeks. There are totally 27 experiments, including 17 ones in the field of microgravity science (microgravity fluid physics 6, microgravity combustion 3, and space materials science 8) and 10 in the field of space life science (radiation biology 3, gravitational biology 3, and space biotechnology 4). These experiments were selected from more than 200 applications.

The satellite was successfully launched in April 6, 2016, and recoverable capsule with all life science facilities and 2 physical facilities was safely received on the ground after 14 days. Then, a research project for research of space experiments is arranged by the National Natural Science Foundation. More than 1000 papers have been published in the scientific journals, and 2 summarized books are printed jointly by Science Press of China and Springer Publishing Co in 2019.

26th European Low Gravity Research Association Biennial Symposium and General Assembly
14th International Conference on "Two-Phase Systems for Space and Ground Applications"
European Space Agency Topical Teams meetings
Granada (Spain), September 24-27, 2019

Oral 100

Experimental study of subcooling mixing jet for thermal vent system

O. Kawanami[1], K. Takeda[1], R. Naguchi[1], R. Imai[2], Y. Umemura[3], T. Himeno[4]

[1] Department of Mechanical Engineering, University of Hyogo, 2167 Shosha, Himeji, Hyogo 671-2280, Japan
[2] Department of Engineering, Muroran Institute of Technology, 27-1 Mizumoto-cho, Muroran, Hokkaido 050-8585, Japan
[3] Japan Aerospace Exploration Agency, 2-1-1 Sengen, Tsukuba, Ibaraki 305-8505, Japan
[4] Department of Aeronautics and Astronautics, The University of Tokyo, 7-3-1 Hongo, Bunkyo-ku, Tokyo 113-8656, Japan

kawanami@eng.u-hyogo.ac.jp

Introduction

For the future space transportation which are currently being under consideration, it is necessary to improve the performance of the propulsion system. Specially, cryogenic propellant should be kept for a long time with as little loss by input heat as possible. Chato (Chato, 2008) reported a thermal management system such as a heat insulation and a pressure control system in the storage tank due to suppress the pressure rise by the heat input is neccessary.

In our project (Imai *et al*, 2019), to privent pressure rising, thermodynamic vent system (TVS) which is a method of destroying the temperature stratification by a mixing jet of subcooled liquid supplied from the lower part of the tank is appried, and here the preliminary study for subcooling mixing jet is carried out.

Experiment

Figure 1 shows the experimental apparatus used in this study. Microgravity experiment was conducted at 50 m drop tower COSMOTORRE in Hokkaido, Japan. COSMOTORRE can provide around 3 seconds microgravity condition. The apparatus consists of a subcooling liquid supply tank, a test vessel, a pump, pressure and temperature sensors. Flow behavior is obverbed by a Schlieren system for ground experiment and CCD camera with back light for microgravity experiment. Volume of the test vessel is H150×W75×D26 mm^3. On the side wall of the vessel, totally 8 heaters for heating up the liquid in the vessel are installed. In order to measure the temperature distribution along the vertically direction inside the vessel, 8 thermocouples are set near the center line and near the side wall, respectively. A SUS 316 tube which has 0.5 mm of inner diameter is used as a jet nozzle, the tube is attached to the center of the bottom of the vessel. Well-degassed FC-72 is used as a test fluid.

Flow behavior under microgravity condition is shown in **Fig. 2**. These images compare fluid behavior at different jet flow rates; without jet mixing, 10.5 ml / min as low flow rate, 70.2 ml / min as a high flow rate. High flow rate is a suitable flow rate of jet for mixing under normal gravity. However, the jet in microgravity at high flow rate penetrates the liquid surface and is not suitable for liquid mixing. On the other hand, we observed that the jet at low flow rate has an effect for liquid mixing.

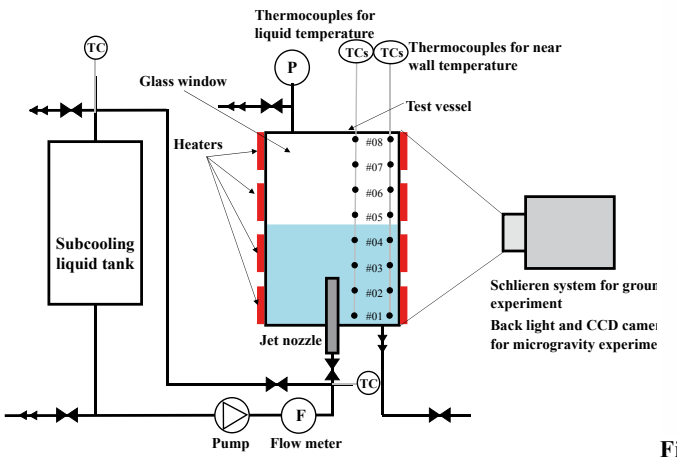

Figure 1: Experimental system.

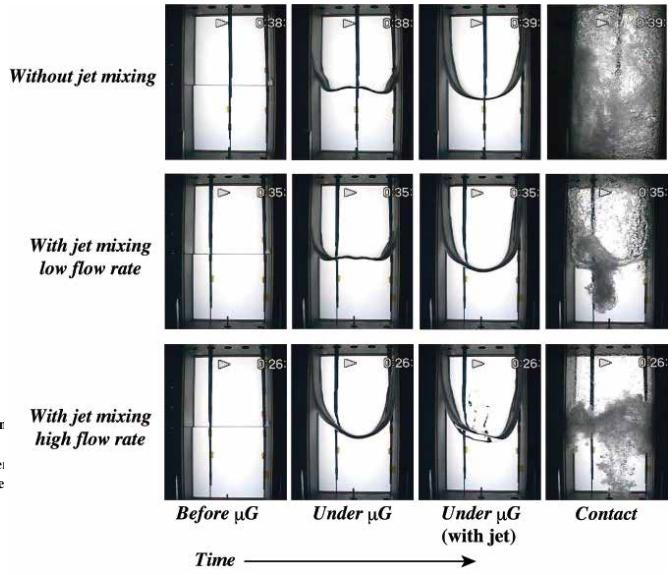

Figure 2: Liquid behavior with or without subcooling jet in microgravity

Acknowledgements

This study carried out as a part of the research project "Development of Innovative Thermal Management Technology to Realize Long-term Storage of Cryogenic Propellant" conducted in the Strategic Basic Development Research of the Space Engineering Committee FY2018.

References

D. J. Chato, *NASA TM-2008-215286* (2008).

R. Imai, O. Kawamami, Y. Umemura, T. Himeno, *IOP Conference Series: Materials Science and Engineering*, **502** (2019) 012082 (5 pages).

Oral 102

Future ESA experiments in Two-phase Heat and Mass Transfer Research on-board the International Space Station

Daniele Mangini[1], Luigi Castiglione[2], Ana Frutos Pastor[3], Balázs Tóth[3], Hans Ranebo[3], Liesbeth De Smet[2], Alessandro De Simone[4] on behalf of ESA's Science, Payload Development and Operations Teams, Science Teams[5] and Space Industries[6]

[1] HE Space Operations BV for ESA, NL-2200AG Noordwijk, The Netherlands, E-mail: daniele.mangini@esa.int
[2] ESA-ESTEC, NL-2200AG Noordwijk, The Netherlands
[3] Space Applications Services for ESA, NL-2200AG Noordwijk, The Netherlands
[5] Science Teams: Aavid Thermalloy (IT), Aerospazio (IT), Air Liquide (FR), AIST (JP), ArianeGroup GmbH (DE), Argotec (IT), AUTh (GR), Beijing University of Aeronautics and Astronautics (CN), Beijing University of Technology (CN), CAS (CN), CCNY (US), CEA (FR), Chongqing University (CN), CSI (DE), Datec Coating (CA), Dream Coating S.A. (BE), Dublin City University (IE), ENEA (IT), ENSMA (FR), EPFL (CH), Eurapo (IT), Euro Heat Pipes (BE), Epsilon (FR), IITK (IN), IMFT (FR), Hexxcell Ltd. (UK), Hephaestus Boiler Makers and Engineering (GR), Interplanetary Expeditions (UK), INSA-LYON (FR), IUSTI (FR), In Quatro srl (IT), KTH (SE), Kutateladze IT (RU), LAPLACE (FR), Liebherr Aerospace (FR), M2P2 (FR), MADIREL (FR), MBSsrl (IT), Nanyang Technological University (CN), NLR (NL), North China Electric Power University (CN), Ònda (IT), Optec (BE), P‘ (FR), Politecnico di Milano (IT), Promete (IT), Selex ES (IT), Shanghai Jiao Tong University (CN), SIT (JP), SMU (US), Southeast University (CN), Sonaca Space GmbH (GE), Solar Tomorrow Inc. (CA), Sun Yat-sen University (CN), Techno System Developments (IT), Thalès Aliena Space (FR), Trinity College Dublin (IE), TU-Darmstadt (DE), UCLA (US), UFSC (BR), ULB-MRC (BE), ULB-TIPs (BE), UNIHEAT (IT), Vangeel Electrical (BE), Xi’an Jiaotong University (CN), York University (CA), ZARM (DE), Universities of Altai State (RU), Brighton (UK), Edinburgh (UK), Granada (ES), Hirosaki (JP), Illinois (US), Kyushu (JP), Liège (BE), Ljubliana (SI), Loughborough (UK), Maryland (US), Mons-Hainaut (BE), Naples (IT), Nottingham (UK), Ochanomizu (JP), Padova (IT), Pisa (IT), Purdue (US), Toronto (CA), Tyumen State (RU), Utsunomiya (JP)
[6] Space Industries: Airbus Defence and Space (Friedrichshafen, DE), Lambda-X (BE), QinetiQ Space NV (BE)

Introduction

Assessing two-phase heat transfer phenomena, where capillary forces play a significant role is often challenging on ground. In the majority of the regimes, gravity masks certain processes making the interpretation of the observations difficult. In some particular cases by creating small scale set-ups, the effect of the gravitational field can be minimised. Nevertheless, this solution imposes further challenges on the diagnostic systems, which are mostly optical.

Therefore, researchers often use reduced microgravity as a tool to minimise the influence of gravity (e.g. buoyancy). To support such studies, in the frame of the *Science in Space Environment* (SciSpacE) programme, the *European Space Agency* (ESA) makes its various reduced gravity platforms (e.g. drop tower, parabolic flights, sounding rockets, space missions) available for scientific research.

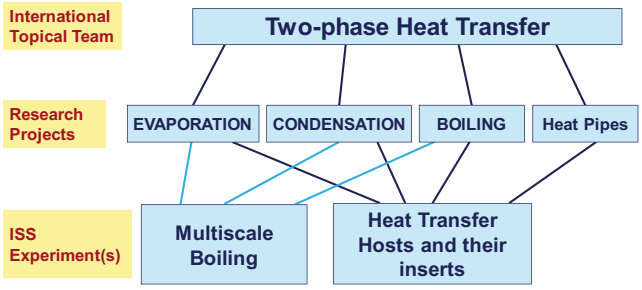

Figure 1: Two-phase heat transfer experiments on the International Space Station (ISS) and research projects

The aim of the present contribution is to provide an update of the two-phase heat transfer experiments envisaged by ESA, focusing on gas-liquid phase change and wettability related phenomena within the frameworks of the utilisation of the *International Space Station* (ISS). The context of these experiments is shown in Figure 1. They serve the objectives of the *EVAPORATION*, *CONDENSATION*, *BOILING* and *Heat Pipes* research projects (further details are given below and in *Tóth, 2012*), which are coordinated in the framework of the *Two-phase Heat Transfer* international topical team. The experiments are planned to be conducted in the *Fluid Science Laboratory* (FSL) and in the second *European Drawer Rack 2* (EDR2) in the Columbus module of the ISS (see Figure 2).

Figure 2: Left: Fluid Science Laboratory (FSL) Right: European Drawer Rack 2 (EDR2)

Multiscale Boiling

The *Multiscale Boiling* experiment aims at addressing the fundamentals of boiling by analysing the behaviour of a single vapour bubble with particular attention to the role and behaviour of the three-phase contact line. Furthermore, *Multiscale Boiling* is designed to quantify the effect of external forces on the bubble dynamics, such as a shear flow or an electric field in the regimes not accessible on other platforms. The hardware is being developed by Airbus Defence and Space (in Friedrichshafen) under ESA contract.

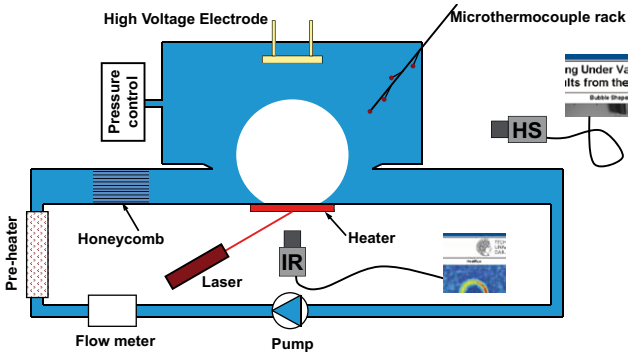

Figure 3: Schematic of the boiling cell of the Multiscale Boiling experiment

Heat Transfer Hosts

To allow a relatively simple implementation of fundamentally similar two-phase flow loops with moderately complicated measurement techniques, the concept of a series of *Heat Transfer Hosts* was initiated.

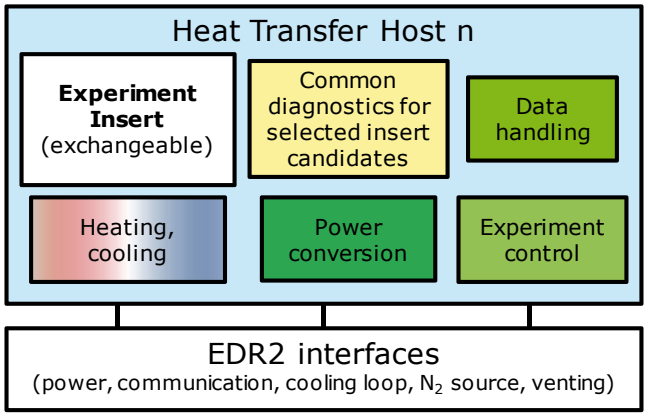

Figure 4: Conceptual schematic of the Heat Transfer Hosts

Installed into the EDR2, one at a time, each Heat Transfer Host will provide for heating and cooling of the test cells, of interchangeable flow loops serving the *Heat Pipes*, *EVAPORATION, CONDENSATION* and/or *BOILING* research projects. The Host facilities will also include (primarily optical) diagnostics commonly required by the target group of insert candidates and provide power, experiment control and data management functions. The experiment inserts are associated to the various Heat Transfer Hosts based on commonalities between their requirements. The philosophy is depicted in Figure 4.

At the time of the preparation of the present abstract the below listed 10 experiment candidates were considered as potential users:

- Insert candidates of Heat Transfer Host 1:
  - *Enhanced Evaporators* targets global heat transfer performance characterisation of multi-scale evaporator structures. Evaporation regimes, wetted area and consequently the three-phase contact line would be characterised together with the critical heat flux (boiling limit) in a capillary pumped loop.
  - *Pulsating Heat Pipes* aims at studying the thermal performance of such innovative devices in weightlessness, flow pattern analysis and local pressure fluctuation with various working fluids and geometries exploring also inertia dominated regimes in large hydraulic diameter tubes.
  - *Self-rewetting Fluid* targets the assessment of the heat transfer performances of self-rewetting liquid mixtures, with particular attention to the vapour-liquid interface temperature, the local liquid composition and liquid film thickness distributions as well as film stability and the dry patch formation. The effect of substrate characteristics and different mixtures will be tested in dedicated inserts.
- Insert candidates of Heat Transfer Host 2 (Heat Transfer Host 2 and its inserts are developed by QinetiQ Space NV under ESA contract):
  - *Drop Evaporation* will investigate thermocapillary convection and vapour diffusion processes as well as the effect of electric field on a series of evaporating sessile drops.
  - *Condensation on Fins* targets liquid film thickness distribution characterisation on a single axisymmetric condenser finger for average and local heat transfer coefficient assessment. Surface roughness and the test liquid are among the envisaged experiment parameters.
  - *Marangoni in Films* aims to better understand heat transport to an evaporating liquid film, through film thickness evolution and dynamics characterisation as well as the vapour concentration distribution. Surfactants are considered as a potential parameter.
- Insert candidates of Heat Transfer Host 3:
  - *In-Tube Condensation* targets void fraction, flow regime and stability characterisation as well as heat transfer coefficient (distribution) measurements and film thickness measurements for annular flow regime in various shapes of tube cross sections.
  - *Flow Boiling* aims at resolving the local heat transfer coefficient distribution in various flow regimes and correlate it with time resolved film thickness measurements and other flow characteristics.
- Insert candidates of future Heat Transfer Hosts:
  - *Boiling* would assess the effect of confinement, shear flow and electric field on a vapour bubble. Particular mixtures and the investigation of non-condensable gas impact are among the most significant objectives.
  - *Shear Driven Film* focuses on determining the heat transfer coefficient, liquid dynamics, film thickness evolution, stability and eventual dry spot formation in liquid films under shear flow influence up-to critical heat flux.

Besides these candidates, in function of the coordinated effort of the scientific community, there may be room for other experiments to utilise the capabilities provided by the Heat Transfer Hosts.

References

B. Tóth, Future Experiments to Measure Liquid-Gas Phase Change and Heat Transfer Phenomena on the International Space Station, Microgravity Science and Technology, Volume 24, Number 3, pp 189-194 (2012)

Oral 103

Steady-state measurements of ternary mixtures in thermogravitational microcolumn

B. Šeta[1], Jna. Gavalda[1], M.M.Bou-Ali[2], X. Ruiz[1]

[1]Universitat Rovira I Vigili, Tarragona, Spain, [2] Mondragon Unibersitatea, Mondragon, Spain;
berin.seta@urv.cat
mbouali@mondragon.edu

Introduction

Thermodiffusion plays an important role in many technological and biological processes of separation (M.M. Bou-Ali et al. 1998). In literature it is possible to find many data about binary mixtures, while focus in ternary mixtures started recently. There are few techniques capable of measuring thermodiffusion coefficients or Soret coefficients and they can be distinguished in those who require convectionless systems and those who use convection to promote separation. Convectionless systems include Soret cell measurements using Optical Digital Interferomety (ODI), Optical Beam Deflection Technique (OBD) and The Thermal Diffusion Forced Rayleigh Scattering Technique (TDFRS). Techniques that include convective coupling are classical Rayleigh-Bernard configuration and thermogravitational column (J.K. Platten 2006). In the present work we will focus on thermogravitational technique with special interest in ternary mixtures measurements.

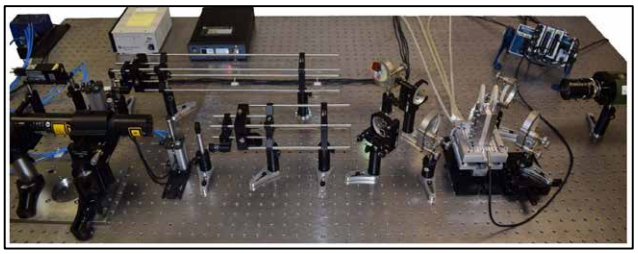

Figure 1: Microcolumn setup

It is possible to find in literature many measurements in binary mixtures using this TG technique, both traditional (E. Lapeira et al.) and microcolumn (B. Šeta et al. 2019), but in ternary mixtures literature is only limited on few studies in traditional thermogravitational columns (Leahy-Dios at al. 2005). In this work, micrcolumn measurements using optical digital interferometry are applied for the first time in ternary mixtures.

Materials and methods

As it is previously mentioned, optical digital interferometry is applied to thermogravitational microcolumn technique in order to obtain thermodiffusion coefficients from steady-state measurements. For the first time such measurements are done in microcolumn for ternary mixtures. In order to do such analysis lasers with two different wavelengths are used. In this case, we used He-Ne red laser with 633nm wavelength and Excelsior Diode-pumped blue lase with 473nm wavelength. By tracking change of refractive indexes through time along the column height it is possible to determine experimentally time when mixture reached steady state. When the two refractive indexes are obtained in steady-state we can transform them into individual concentration differences.

$$\begin{pmatrix}\Delta c_1\\ \Delta c_2\end{pmatrix} = \begin{pmatrix}\frac{\partial n_1}{\partial c_1} & \frac{\partial n_1}{\partial c_2}\\ \frac{\partial n_2}{\partial c_1} & \frac{\partial n_2}{\partial c_2}\end{pmatrix}^{-1} \begin{pmatrix}\Delta n_1\\ \Delta n_2\end{pmatrix} \qquad (1)$$

As it is possible to see from Eq. (1) signal from both lasers impact resulting concentration difference. Later, concentration difference is transformed in corresponding thermodiffusion coefficient using Furry-Jones-Onsager theory

$$D_{T,i} = -\frac{L_x^4}{504}\frac{\alpha g}{\nu}\frac{\Delta c_i}{z} \qquad \text{for i=1,2} \qquad (2)$$

Where L_x is the gap between heated/cooled walls, z is the height of column, α is the thermal expansion and ν is the dynamic viscosity.

In order to resolve contrast factor matrix we used Anton Paar Abemat refractometer which can measure refractive index on seven different wavelengths: 436 nm, 480nm, 513 nm, 546 nm, 589 nm, 633 nm and 655 nm. By measuring refractive indexes in region interest of our mixture, we can possibly obtain contrast factor which assumes linear change of contrast factor with concentration. For laser with 633 nm procedure is straight forward as we directly obtain contrast factor for that wavelength. However, for laser with 473 nm, we need to do an approximation as our refractometer does not measure refractive index on such wavelength. In this case, we apply Cauchy dispersion (Mialdun et al. 2016).

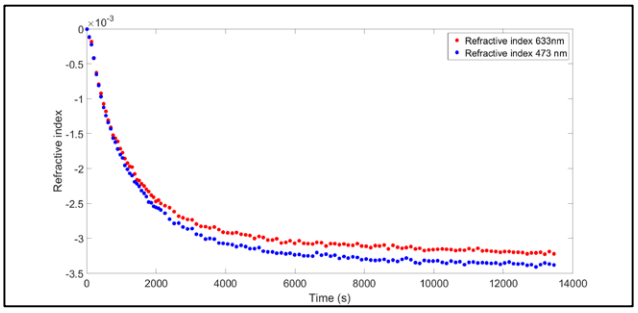

Figure 2: Change of refractive index through time in two lasers of different wavelengths

Selected working mixture was DCMIX1 mixutre which consists of Tetra-Hydro-Naphthalene (THN)- Iso-Butyl-Benzene (IBB)-n-Dodecane(nC12). Mixture is well covered

in literature from different groups and using different techniques. Chosen concentration composition is 0.8(THN)-0.1(IBB)-0.1(nC12).

Results

Thermodiffusion coefficients obtained by thermogravitational microcolumn shown good agreement with literature results (M.M Bou-Ali et al. 2015). However, weak point of the technique is related with ill-conditioned contrast factor matrix which can lead to highly uncertain thermodiffusion coefficients. By introducing small noise in values of refractive indexes, concentrational field undergoes significant change and hence in thermodiffusion coefficients.

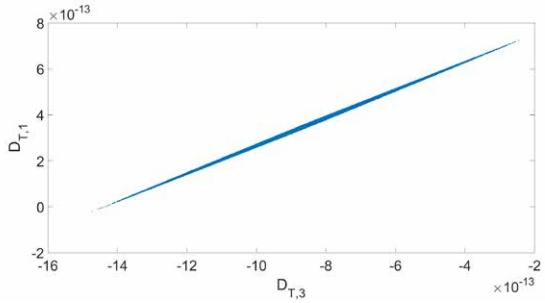

Figure 3: Uncertainty in thermodiffusion coefficients

As it is possible to see from figure 3, uncertainty is developed in one direction due to the shape of contrast factor matrix.

Conclusions

Measurement of thermodiffusion coefficients in ternary mixtures is possible with optical digital interferometry applied to thermogravitational microcolumn. However, contrary to what is found in binary mixtures, large uncertainty is obtained in values of thermodiffusion coefficients. Problem arises from ill-conditioned contrast factor matrix and it is not much different from problems that other optical techniques have. It is possible to apply Monte-Carlo simulation to find most common coefficient, but still some solutions will have quite big deviation from most expected value. Solution could be to use other technique, such as traditional thermogravitational column, which does not take only into account optical data from system, but also density measurements. Contrast factor matrix in most of the cases would not be ill-conditioned and direction of expected results could differ from direction obtained in microcolumn. Intersection of these two directions provides more trustable result.

Acknowledgements

This work was supported by: the Spanish Ministerio de Ciencia, Innovación y Universidades and the European Regional Development Fund (FEDER) (grant numbers: ESP2017-83544-C3-1-P and ESP2017-83544-C3-3-P), DCMIX (AO-2009-0858/1056) from the European Space Agency, the Research Group Program (IT1009-16) from the Basque Government, FETRAFLU (2018-CIEN-000101-01) from Gipuzkoa Program and the Universitat Rovira i Virgili grant number DLRF4741.

References

M.M. Bou-Ali, O. Ecenarro, J.A. Madariaga, C.M. Santamaria, J.J. Valencia, Thermogravitational measurements of the Soret coefficient of liquid mixture, *J. Phys. Condens. Matter 10 (1998) 3321-3331*

J.K. Platten, A Soret Effect: A Review of Recent Experimental Results, J. Appl. Mech. 73 (2006)

E. Lapeira, M.M. Bou-Ali, J. A, Madariaga, C. Santamaria, Thermodiffusion Coefficients of Water/Ethanol Mixtures for Low Water Mass Fractions, Microgravity Sci. Technol. (2016) 28:553-557

B. Šeta, E. Lapeira, D. Dubert, F. Gavalda, M.M Bou-Ali, X. Ruiz, Separation under thermogravitational effects in binary mixtures, Eur. Phys. J. E, (2019)

A. Leahy-Dios, M.M. Bou-Ali, J.K. Platten, A. Firoozabadi, Measurements of moleculare and thermal diffusion coefficients in ternary mixtures, J. Chem. Phys. 122 (2005)

A. Mialdun, V. Shevtsova, Analysis of multi-wavelenght measurements of diffusive properties via dispersion dependence of optical properties, Appl. Opt. 56 (2016)

M.M Bou-Ali, A. Ahadi, D.A. de Mezquia, Q. Galand, M. Gebhardt, O. Khylbov, M. Larranaga, J.C. Legros, T. Lyubimova, A. Mialdun, I. Ryzkhov, Z. Saghir, V. Shevtsova, S. Van Vaerenbergh, Benchmark values for the Soret, thermodiffusion and molecular diffusion coefficients of the ternary mixtures tetralin+isobutylbenzene+n-dodecan with 0.8-0.1-0.1 mass fraction, Eur. Phys. J. E 38 (2015) 113

Oral 105

Granular gases of rod-like particles: 3D experiments and automatic particle tracking

D. Puzyrev[1], K. Harth[1,2], T. Trittel[1] and R. Stannarius[1]

[1]Institute for Experimental Physics, Otto von Guericke University, Magdeburg, Germany
[2]Universiteit Twente, Physics of Fluids and Max Planck Center for Complex Fluid Dynamics, Enschede, The Netherlands
e-mail: dmitry.puzyrev@ovgu.de

Dilute ensembles of granular matter (granular gases) are nonlinear systems which exhibit fascinating dynamical behavior far from equilibrium, including unusual cooling properties, clustering and violation of energy equipartition. So far, most studies have been theoretical or numerical, and only few experiments, mainly in two dimensions (2D), have been performed. Falcon et al. showed dynamical clustering in a first sounding rocket experiment [1], where no analysis on the grain scale level was possible. Currently, an instrument is being prepared for the International Space Station [2].

The experimental realization of low excitation or cooling regimes of granular gases in particular requires microgravity of high quality, e.g. on suborbital rocket flights or in drop towers [3]. Another important issue is the trackability of particles in large ensembles in 3D. In gases of rod-like particles, the mean free path is substantially reduced as compared to gases of spherical grains of identical volume fraction [4]. In addition to that, elongated grains allow the straightforward analysis of rotational degrees of freedom. We have investigated steady states and cooling in ensembles of rod-like particles in the very dilute limit (Knudsen regime) as well as for higher volume fractions, see Fig. 1. The analysis reveals, e.g., a persistent breakdown of energy equipartition between translational and rotational degrees of freedom and strong deviations from Gaussian translational and rotational velocity distributions, beyond the expectation from theory and numerics. In the cooling experiment, Haff's equation [5] describing the energy decay is fulfilled, even though many of its preconditions are violated.

One particular problem in the data analysis is the reliable detection and tracking of the rods in 3D, especially at volume fractions beyond the very dilute limit, see Fig. 1, bottom. Up to now, the experimental data have been analyzed mostly manually. We developed a software for automatic 3D tracking of position and orientation of elongated particles in the ensemble, based on two-perspective video data analysis. Two-dimensional localization of particles is performed with help of the Mask R-CNN neural network [6]. Then, the problem of 3D matching of the particles is solved by minimization of the total reprojection error. Finally, the particle trajectories are tracked and ensemble statistics can be extracted. Depending on the required accuracy, the system can be used fully automatically or serve as a base for subsequent manual correction. The approach can be extended to other 3D and 2D particle tracking problems.

Acknowledgements

The authors gratefully acknowledge funding by the German Aerospace Center DLR, Project No. 50WM1842

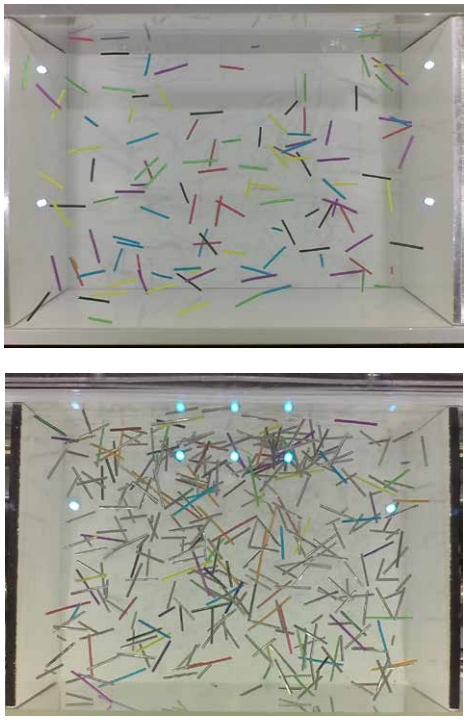

Figure 1: *Top:* Rod-like particle ensemble in very dilute limit (Knudsen regime), image from the drop tower microgravity experiment. *Bottom:* rod-like particle ensemble with higher volume fraction beyond Knudsen regime, image from Blue Origin suborbital flight microgravity experiment.

References

[1] É. Falcon et al., Cluster Formation in a Granular Medium Fluidized by Vibrations in Low Gravity, *Phys. Rev. Lett.*, 83 (1999), 440-443

[2] M. Noirhomme et al., Threshold of gas-like to clustering transition in driven granular media in low-gravity environment, *EPL*, 123 (2018), 14003

[3] K. Harth, T. Trittel, K. May, S. Wegner and R. Stannarius, Three-dimensional (3D) experimental realization and observation of a granular gas in microgravity, *Advances in Space Research,* 55 (2015), 1901 – 1912

[4] K. Harth, T. Trittel, S. Wegner, and R. Stannarius, Free cooling of a granular gas of rodlike particles in microgravity, *Phys. Rev. Lett.*, 120 (2018), 214301; K. Harth, U. Kornek, T. Trittel, U. Strachauer, S. Höme, K. Will, and R. Stannarius, Granular Gases of Rod-Shaped Grains in Microgravity, *Phys. Rev. Lett.*, 110 (2013), 144102

[5] P. K. Haff, Grain flow as a fluid-mechanical phenomenon *Journal of Fluid Mechanics*, 134 (1983), 401-430

[6] K. He, G. Gkioxari, P. Dollár, and R. B. Girshick, "Mask R-CNN", *CoRR*, https://arxiv.org/abs/1703.06870 (2017)

26th European Low Gravity Research Association Biennial Symposium and General Assembly
14th International Conference on "Two-Phase Systems for Space and Ground Applications"
European Space Agency Topical Teams meetings
Granada (Spain), September 24-27, 2019

Oral 106

Emulsion Dynamics by Diffusing Wave Spectroscopy

Luigi Cristofolini[1,2*], Fabrizia Salerni[1], Davide Orsi[1], Eva Santini[2], Francesca Ravera[2], Libero Liggieri[2]

[1]*University of Parma - Italy;* [2]*CNR ICMATE, Genova - Italy;*

* luigi.cristofolini@unipr.it

1. Introduction. Emulsions are ubiquitous, and their properties dominate stability of many foods and drugs, while the ability to form emulsions is determinant in detergents as well as in oil industry. Different processes determine emulsion stability, some related to capillarity and interfacial properties (Ostwald Ripening, disproportionation, coalescence) other to gravity (sedimentation, creaming, phase separation). The latter can be suppressed in microgravity, allowing experiments leading to better understanding of the mechanisms driving the former. The project EDDI (Emulsion Dynamics and Droplet Interfaces) recently submitted and approved by ESA, focuses mainly on experiments on emulsions to be executed onboard the International Space Station in the facility Soft Matter Dynamics (SMD, formerly FOAM-C) using diagnostics based on Diffusion Wave Spectroscopy (DWS).

2. The DWS technique. DWS is a noninvasive technique based on correlation spectroscopy and used to characterize microscopic structure and rheological properties of turbid samples (Weitz et al. 1993). This is achieved by analyzing the time evolution of coherence speckles of light that has been multiply scattered within the sample. Here we evaluate the accuracy of the results providing criteria to establish the time / frequency limits of the technique. These concepts are applied to discuss a laboratory prototype and to address the design and use of the DWS diagnostics suitable for emulsion studies in the SMD facility (Orsi et al., in press).

3. Some results on emulsions. We characterize a paradigmatic emulsion formed by water and dodecane stabilized by the anionic surfactant Sodium Dodecyl Sulfate (SDS). We focus on the regime of low surfactant concentration, well below the Critical Micellar Concentration (CMC). Optimizing emulsion properties in this regime is obviously relevant whenever surfactant might be pollutant. We characterize both structure (drop size) and dynamics (mechanical modulus). Under ageing, no evolution of the mean drop size is found within the sensitivity of the technique, while mechanical moduli strongly evolve. Depending on surfactant concentration, different regimes of ageing are found. For stable emulsions, the shear modulus grows as a power law of ageing time, with an exponent independent on surfactant concentration. This is presumably related to the late stages of the water drainage process.

Interestingly, as a function of surfactant concentration and at constant age, the viscous modulus shows a peak slowdown, corresponding to a maximum in the bulk shear mechanical modulus, around [SDS]=2mM, This is strongly reminiscent of a similar maximum found in the interfacial dilational viscosity, by a completely different technique, namely drop tensiometry, which measures a single interface (see figure).

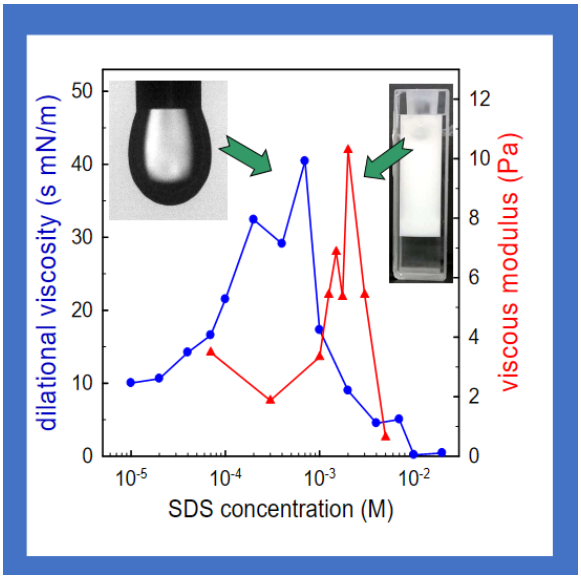

Figure 1: *similar peaks are found in the dependence from surfactant concentration of interfacial dilational viscosity measured by drop tensiometry (blue, left) and in the viscous modulus measured by DWS (red, right).*

4. Conclusions These results suggest a **consistent picture of the mechanisms (de)stabilizing emulsions**, explained in terms of elementary process at the interface. These results show furthermore that DWS can be a reliable diagnostic for the study of the aging and of the mechanical properties of concentrate emulsions. This might be relevant to control stability of emulsions when a low concentration of surfactant is desired, e.g. for economical or environment reasons.

Aknowledgements:

European Space Agency – Projects "Soft Matter Dynamics" and "Emulsion Dynamics and Droplet Interfaces".

References:

D.A. Weitz, D.J. Pine, Diffusing-wave spectroscopy, in: W. Brown (Ed.), Dyn. Light Scatt. Method Some Appl., Clarendon Press, 1993

D. Orsi et al. Colloids and Surfaces A, in press

Oral 107

Transport diffusion in the critical region

R.S. Chatwell[1], G. Guevara-Carrion[1], V. Shevtsova[2] J. Vrabec[1]

[1]Technical University of Berlin, Berlin, Germany;
vrabec@tu-berlin.de
[2]MRC, CP 165/62, Université Libre de Bruxelles, Brussels, Belgium

Introduction

The thermodynamic factor Γ of a binary mixture at infinite dilution is asymptotically constrained

$$\lim_{x_1 \to 0} \Gamma = 1 \,, \qquad (1)$$

irrespective of temperature or pressure. It is common practise, however, to utilise this definition even for finitely diluted mixtures. This works reasonably well for thermodynamic states sufficiently outside the extended critical region. For thermodynamic states in close vicinity to the mixture's critical point, the thermodynamic factor shows significant deviations from unity even for mole fractions as low as 0.01 mol mol^{-1} and even approaches zero on the Widom line (Guevara-Carrion et al. 2019). This phenomenon is experimentally observed in an anomaly of the Fick diffusion coefficient D, which is related via the thermodynamic factor to the Maxwell-Stefan diffusion coefficient $Đ$

$$D = Đ \cdot \Gamma \,. \qquad (2)$$

Diluted benzene in supercritical carbon dioxide

Diluted benzene (C_6H_6) in supercritical carbon dioxide (CO_2) constitutes a relevant test case for $\Gamma \neq 1$ even for very low benzene concentrations. In the present study, the thermodynamic factor was assessed by molecular dynamics (MD) simulations, performed with *ms2* (Rutkai et al. 2017), around the mixture's critical point, i.e. in the temperature range between T = 293.15 and 335 K along the p = 9 MPa isobar. It can readily be seen that Γ approaches zero at T = 320 K and generally tends toward unity for lower benzene concentrations, cf. fig. (1).

The observed anomaly of the Fick diffusion coefficient, cf. fig. (2), can be explained unconstrainedly in light of the thermodynamic factor, while the required Maxwell-Stefan diffusion coefficient was additionally sampled with MD simulations employing the Green-Kubo formalism.

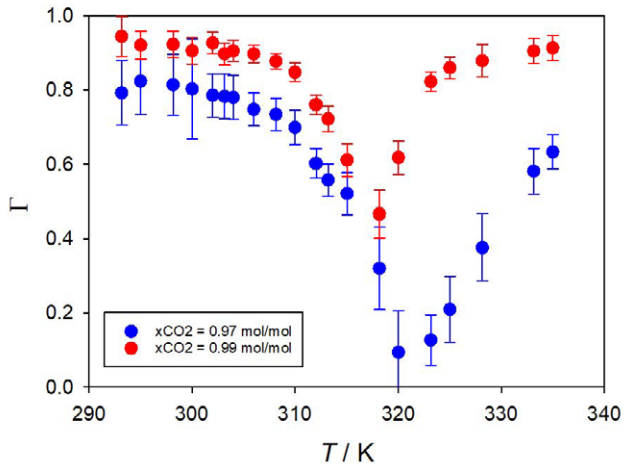

Figure 1: Temperature variation of the thermodynamic factor for diluted benzene in supercritical carbon dioxide at p = 9 MPa for benzene mole fractions x_{C6H6} = 0.03 (blue symbols) to x_{C6H6} = 0.01 mol mol^{-1} (red symbols).

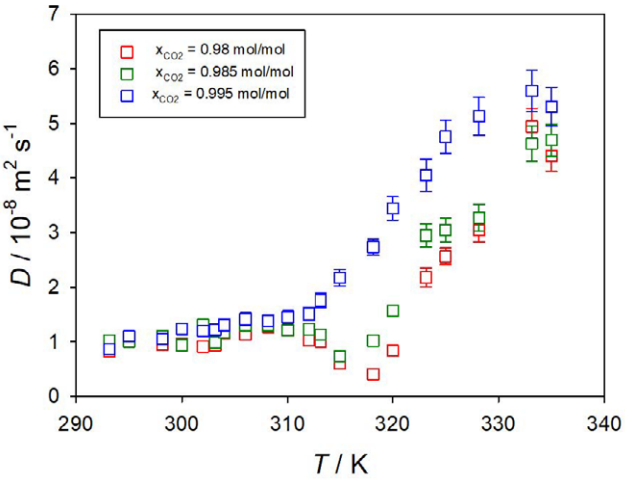

Figure 2: Temperature dependence of the Fick diffusion coefficient of the mixture CO_2 + C_6H_6 along the p = 9 MPa isobar for x_{C6H6} = 0.005, 0.015 and 0.02 mol mol^{-1}.

Acknowledgements

This work was carried out under the auspiecies of the Boltzmann-Zuse society (BZS) and all simulations were performed on Noctua at the Paderborn Center for Parallel Computation (PC²).

References

G. Guevara-Carrion, S. Ancherbak, A. Mialdun, J. Vrabec, V. Shevtsova, Importance of the Widom line on diffusion of methane in supercritical carbon dioxide, *Accepted for publication in Scientific Reports* (2019)

G. Rutkai, A. Köster, G. Guevara-Carrion, T. Janzen, M. Schappals, C. W. Glass, M. Bernreuther, A. Wafei, S. Stephan, M. Kohns, S. Reiser, S. Deublein, M. Horsch, H. Hasse, J. Vrabec, *ms2*: A molecular simulation tool for thermodynamic properties, release 3.0, *Comp. Phys. Commun.* **221**, 343 (2017)

26th European Low Gravity Research Association Biennial Symposium and General Assembly
14th International Conference on "Two-Phase Systems for Space and Ground Applications"
European Space Agency Topical Teams meetings
Granada (Spain), September 24-27, 2019

Oral 108

Intermittency and flow reversals in the spherical Rayleigh-Bénard convection

P. Beltrame[1], P. Chossat[2]

[1]UMR INRA 1114 EMMAH - Avignon Université, Avignon, France, [2] UMR CNRS 7351 Dieudonné - Université de Nice Sophi-Antipolis, Nice, France;
philippe.beltrame@univ-avignon.fr, pascal.chossat@unice.fr

Introduction

This study investigates the thermal convection in spherical shell under a central force field motivated by an experiment carried in the International Space Station: GEOFLOW project (Mutabazi et al. 2016). Our aim in this paper is to investigate intermittent flow reversals by analyzing the dynamics near the onset of convection.

The issue of flow reversal is of great interest to celestial bodies, i.e. stars and planets, for which the magnetic field may reverse its orientation in an aperiodic manner. A simple model is proposed by Pétrélis et al. (2009) to interpret magnetic fields reversal in a von Karman sodium experiment. However, the cylindrical geometry does not correspond to the geo- and gastro-physical framework. In contrast, in this paper we focus on the thermal convection and spherical geometry. The rotation is treated as a small perturbation of the non-rotating case. The advantage of these simplifying assumptions is that they allow the use of the theoretical tools of the bifurcations in the presence of spherical symmetry. Since Friedrich and Haken (1986), it is known that flow reversal between axi-symmetric steady-states may occur when the spherical modes 1 and 2 are in competition. In this paper we study the (3,4) mode intercation because it is relevant for the GEOFLOW experiment. Recently, we showed for the non-rotating case in Beltrame and Chossat (2015) the existence of a complex dynamics with intermittencies involving steady-states with octahedral symmetry.

After a brief recall of the method and theoretical tools, we focus on the existence of flow reversal in the non-rotating case and its small perturbation of the rotating case.

Modeling and Theoretical tools

The Rayleigh–Bénard convection is studied considering an incompressible Newtonian fluid under the Boussinesq approximation. The fluid is confined between two concentric spheres of radii R_{in} and R_{out} ($R_{in} < R_{out}$). A radial force field proportional to $g(r)$ acts on the fluid. When the inner sphere is heated uniformly at T_{in} and the outer sphere is cooled uniformly at $T_{out} < T_{in}$ a temperature gradient appears. The gravity field $g(r)$ encountered in the geophysical context for low-density fluid surrounding a high-density ball (like the Earth's inner core) is mainly proportional to $1/r^2$. In the laboratory, the dielectrophoretic central force field is $1/r^5$-dependent field as for the GEOFLOW experiment. In this work we focused on force fields due either to gravity or dielectrophoretic effect. This latter is produced by applying an periodic high voltage ($V \simeq 10$ kV) between inner and outer sphere on a dielectric fluid (silicon oil).

Due to the buoyancy force, this state may be unstable beyond a critical temperature difference leading to the convection motion. The fluid velocity and the temperature perturbation are governed by the Navier–Stokes equation and the heat transport equation. The non-dimensional equations depend on three numbers: the aspect ratio $\eta = \frac{R_{in}}{R_{out}} < 1$, the Prandtl number Pr (ratio of kinematic viscosity to thermal diffusivity) and the Rayleigh number Ra measuring the buoyancy force. The resulting equations with no-slip boundary conditions can be found in many references in literature e.g. in (Beltrame and Chossat, 2015) and (Travnikov at al. 2017).

For a critical Rayleigh number and aspect ratio, the marginal modes of the linear problem span the space V of eigenmodes with $\ell = 3$ and 4. We shall therefore consider the 2-parameter bifurcation problem with parameters Ra and η. It is a well-established fact that the Rayleigh-Bénard problem satisfies the hypothesis of the center manifold reduction theorem, which allows to reducing the system of Pardial Differential Equarions (PDE) to an Ordinary Differential Equations (ODE) defined in the space V. The idea is that near bifurcation the solutions can be expressed in terms of the marginal modes, the other modes behaving like ''slave variables''. Performing Taylor series expansion of the solution with respect V and parameters, it is then possible to solve the resulting systems step by step from lowest order to get an approximate polynomial ODE (Beltrame and Chossat, 2015).

The spherical symmetry is responsible for the high dimension of the center manifold, i.e. dim V= 16 for the (3,4) mode interaction). The use of concepts and techniques of Equivariant Bifurcation Theory (Chossat and Lauterbach, 2000) will be of crucial importance in the bifurcation analysis. For instance, the isotropy subgroups lattice identifies the possible the bifurcated steady-states and their symmetry and helps to understand the intermittent dynamics. According to (Beltrame and Chossat, 2015), we find out parameters domains where the dynamics do not converge to steady-states or periodic solutions. In the next section, we focus to flow reversals induced by these intermittencies. In particular, we focus on the chaotic behavior of the reversals and its link with the structure of heteroclinic cycles of steady-states.

Results

Intermittent like behavior appears in specific parameter domains: long periods of quasi steady-states (axisymmetric or octahedral pattern) followed by sudden excursions to regimes "far" from equilibrium and relamination to another

dy state. Some of these dynamics result from a cycle of roclinic connections between steady-states. An example this dynamics is displayed in Fig. 1. The plateaux layed in the time evolution correspond to long duration the steady-states with octahedral symmetry. The short sition between reversed steady-states appears with the den 'wake-up' of the mode 3. The symmetry of dy-states is broken during the transitions between ilibria: the first transition corresponds to the di-hedral metry of order 6 and the back transition has the ahedral symmetry (see snapshots in Fig. 1). Let us note the energy of the equilibria is different. Moreover the gy may almost vanish during the transition. Therefore reversal flow mechanism differs to the one proposed by rélis et al. 2009) for which the energy is mainly served during flow reversals.

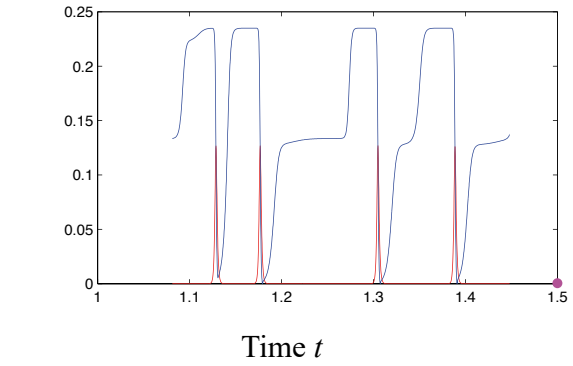

ıre 1: [Top] Time evolution of the energy of the modes 3 and 4 and blue lines respectively) during the heteroclinic cycle. tom] Evolution of the temperature field during the heteroclinic e. Large snapshots represent steady-states with octahedral metry. States-states with octahedral symmetry during flow rsals of steady-states.

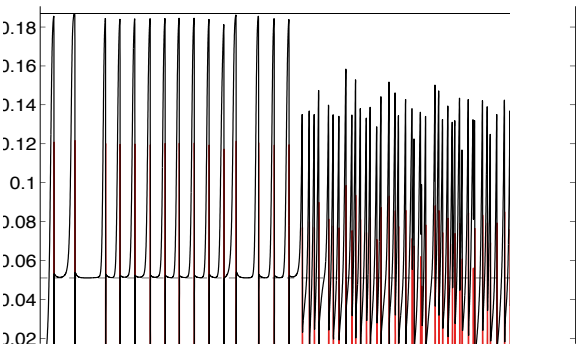

ıre 2: Time evolution of the energy of the mode 3 [red] and e 4 [black]. Firstly, the dynamics is close to a heteroclinic chaotic dynamics takes place.

Most of the heteroclinic cycles are not asymptotically stable. Neverteless, the phase-space trajectories remain in their vicinity. The resulting dynamics can be quite complex. In Fig.2 the time evolution of the (3,4) modes lets appear a dozen of reversals disrupted by an irregular dynamics for which no steady-state is observed during for a long time. Indeed, the heteroclinic cycle is in competition with a chaotic set which has repellent manifolds. Thus, intermittency between the flow reversal dynamics and the chaotic dynamics occurs.
These complex dynamics may remain in the rotating case, as long the rotation rate is small. The equilibria become rotating waves and the axis of these rotating waves coincides with the rotation axis. The consequence of this prevailed axis is that a part of the dynamics complexity vanishes but not the phenomenon of flow reversals.

Conclusion

We showed the existence complex intermittent flow reversals involving octahedral equilibria. The spherical symmetry plays a key role in their existence. The reversal mechanisms differ from the literature regarding the dynamo problem. The persistence of flow reversal in the rotating case spurs to study the case of higher rate rotation that is relevant in the geophysical context.

References

I. Mutabazi, H. N. Yoshikawa, M. T. Fogaing, V. Travnikov, O. Crumeyrolle, B. Futterer, and C. Egbers, Thermo-electro-hydrodynamic convection under microgravity : a review, *Fluid Dyn. Res.* **48**, 061413 (2016).

F. Pétrélis, S. Fauve, E. Dormy and J.-P. Valet., Simple mechanism for reversals of earth's magnetic field, *Phys. Rev. Lett.*, vol. 102, p. 144503 (2009).

R. Friedrich and H. Haken, Static, wavelike, and chaotic thermal convection in spherical geometries, *The American Physical Society* **34**(3), pp. 2100–2120 (1986).

P. Beltrame, P. Chossat, Onset of intermittent octahedral patterns in spherical Bénard convection, *Eur. J. Mech. B/Fluids* 50, pp. 156-174 (2015).

V. Travnikov, F. Zaussinger, P. Beltrame, C. Egbers, Influence of the temperature-dependent viscosity on convective flow in the radial force field, *Phys. Rev. E* 96 (2017) 023108.

P. Chossat and R. Lauterbach, Methods in Equivariant Bifurcations and Dynamical Systems, Advanced Series in Nonlinear Dynamics, vol ; 15, World Scientific, Singapore (2000)

26th European Low Gravity Research Association Biennial Symposium and General Assembly
14th International Conference on "Two-Phase Systems for Space and Ground Applications"
European Space Agency Topical Teams meetings
Granada (Spain), September 24-27, 2019

Oral 109

Coupled non-equilibrium fluctuations in a polymeric ternary mixture involved in the GIANT FLUCTUATIONS space project

L. García-Fernández[1,2], P. Fruton[1], H. Bataller[1], J.M. Ortiz de Zárate[3], F. Croccolo[1]

[1]Laboratoire des Fluides Complexes et leurs Réservoirs – IPRA, UMR5150, E2S-Univ Pau & Pays Adour/CNRS/Total, 1 Allée du Parc Montaury, 64600 Anglet, France, [2]Centre National d'Études Spatiales (CNES), 2 Place Maurice Quentin, 75001 Paris, France,
[3]Departamento de Estructura de la Materia, Física Térmica y Electrónica, Facultad de Ciencias Físicas, Universidad Complutense de Madrid, Plaza de las Ciencias 1, 28040 Madrid, Spain;
loreto.garcia-fernandez@univ-pau.fr, paul.fruton@univ-pau.fr, henri.bataller@univ-pau.fr, jmortizz@ucm.es, fabrizio.croccolo@univ-pau.fr

Introduction

Transport phenomena occur in any fluid present in the nature or the industry when subjected to non-equilibrium conditions, and their comprehension is of great interest for many applications. Far from equilibrium, the thermodynamic variables exhibit non-equilibrium fluctuations (NEFs) and through their analysis, the transport properties of the fluid mixture can be determined (Croccolo et al. 2012). The behavior of NEFs is influenced by gravity, making difficult to perform experiments if convection or sedimentation occur. Therefore, the comparison of ground measurements with the ones performed in microgravity is crucial to fully understand the transport phenomena (Vailati et al. 2011). Many aspects of the behaviour of NEFs in binary liquid mixtures are currently well understood thanks to a large amount of theoretical and experimental work. Ternary systems are the natural next step. Due to the increasing difficulty of a ternary mixture, it is advisable to start with a polymeric mixture providing very different diffusion coefficient eigenvalues (Bataller et al. 2017). For that reason, a polymeric ternary mixture was chosen for one of the experiments of the DCMIX4 as well as the GIANT FLUCTUATIONS space projects (Baaske et al. 2016). A recent study about NEFs in a binary polymeric mixture demonstrated both theoretically and experimentally that temperature and velocity fluctuations are coupled in the presence of gravity inducing the appearance of propagating modes for large fluctuations (Croccolo et al. 2019). This result suggested us to extend the theory of ternary mixtures by taking into account a similar effect, and this is the main purpose of this study.

Fluctuating Hydrodynamics theory of ternary mixtures including the coupling between modes

In a thermodiffusion experiment in a ternary mixture, temperature and concentration gradients coexist inducing NEFs of the thermodynamic variables, i.e. velocity (δv_z), temperature (δT) and the two independent concentrations ($\delta\omega_1$, $\delta\omega_2$). At steady state the evolution equation of these fluctuations taking into account the Boussinesq approximation, neglecting the Dufour effect, writing in the diagonal form and adopting L as a unit of length and $L^2/\widehat{D}_1$ as unit of time ($\widehat{D}_1$ being the smaller eigenvalue of the mass diffusion matrix), can be expressed as follows:

$$\partial_t \begin{bmatrix} \delta v_z \\ \delta T \\ \delta\omega_1 \\ \delta\omega_2 \end{bmatrix} = \begin{bmatrix} LePrq^2 & -1 & 1 & 1 \\ -PrLe^2Ra & Leq^2 & 0 & 0 \\ PrLe^2Ra\psi_1 & \psi_1 q^2 & q^2 & 0 \\ PrLe^2Ra\psi_2 & Dr\psi_2 q^2 & 0 & Drq^2 \end{bmatrix} \begin{bmatrix} \delta v_z \\ \delta T \\ \delta\omega_1 \\ \delta\omega_2 \end{bmatrix} \quad (1)$$

where Le, Pr, Ra are the classical dimensionless numbers, Dr is the mass diffusion eigenvalue ratio and $\psi_{1,2}$ are the diagonal concentration separation ratios. The decay times of the NEFs can then be determined by numerically solving Eq.1.

Experimental methodology

The NEFs of the temperature and concentrations are experimentally studied by the analysis of the induced NEFs of the refractive index of the mixture by dynamic shadowgraphy. The studied polymeric ternary mixture is composed of 2 wt% polystyrene (PS, M_w = 4730 g/mol), 49 wt% toluene and 49 wt% n-hexane. The sample is injected in the thermodiffusion cell placed in a monochromatic shadowgraph set-up, described elsewhere (Giraudet et al. 2014). The sample is sandwiched by two sapphire windows separated by L= 5 mm. The thermodiffusion experiments are carried out at a mean temperature of 25 ºC by imposing a temperature difference of 20 K. Series of images are recorded at three frequencies of 100, 10 and 1 Hz. The Differential Dynamic Algorithm (DDA) analysis (Cerchiari et al. 2012) is performed for each series of images to extract the Structure Functions (SFs), that are then merged to get a single concatenated SF (c-SF):

$$\text{c-SF} = 2\{T(q)S(q)[1 - I_{SF}(q, dt)] + B(q)\} \quad (2)$$

where $T(q)$ is the shadowgraph optical transfer function, $S(q)$ is the static power spectrum, $I_{SF}(q, dt)$ is the intermediate scattering function and $B(q)$ is the background.

Theoretical and experimental results

The theoretical and experimental decay times of the NEFs are shown in Fig. 1. The theoretical results show that for large wave numbers $q \geq 47cm^{-1}$ (i.e. small fluctuations), four real solutions are obtained, demonstrating that all the modes are decoupled in this wave number range. Experimentally, the velocity mode cannot be measured not giving rise to refractive index fluctuations. Therefore, the I_{SF} used to fit the experimental c-SF is defined as the sum of three exponential decays:

$$I_{SF}(q, dt) = a_1 \exp[-dt/\tau_1(q)] + a_2 \exp[-dt/\tau_2(q)] + (1 - a_1 - a_2)\exp[-dt/\tau_3(q)] \quad (3)$$

where a_i and $\tau_i(q)$ are the normalized amplitudes and the relaxation times of the different modes, respectively. By fitting the experimental c-SF through Eqs. 2 and 3 for large q, three modes are clearly distinguished with well-separated decay times. The slowest mode represents the concentration mode of the PS ($\delta\omega_1$), the intermediate one, the concentration mode of the solvent mixture ($\delta\omega_2$) and the

fastest one, the temperature mode (δT). In this range of q, the NEFs relax mainly by a diffusive process. Therefore, the mass diffusion eigenvalues ($\widehat{D}_i$) and the thermal diffusivity (a_T) of the mixture are obtained by fitting the concentration decay times to $\tau_i = 1/\widehat{D}_i q^2$ and the temperature decay times to $\tau_{th} = 1/a_T q^2$.

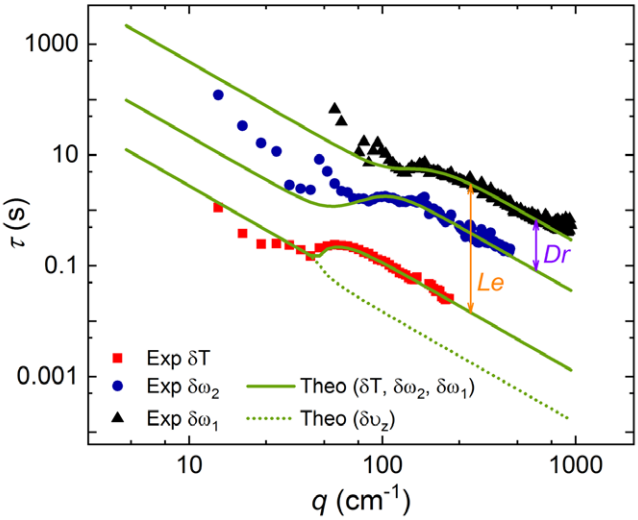

Figure 1: Theoretical and experimental decay times of NEFs on the ternary mixture.

For small wave numbers $q \leq 47cm^{-1}$ (i.e. large fluctuations), two real solutions and a pair of complex conjugate ones are obtained numerically, indicating that velocity and temperature fluctuations are coupled at small q. This coupling induces the propagating modes observed in the experimental c-SF shown in Fig. 2, as oscillations at small q. For this range of small wave numbers an oscillatory term is included in the I_{SF}:

$$I_{SF}(q,dt) = a_1\exp[-dt/\tau_1(q)] + a_2\exp[-dt/\tau_2(q)] + \left\{\frac{1-a_1-a_2}{\cos[\emptyset(q)]}\right\}\cos[\Omega(q)dt + \emptyset(q)]\exp[-dt/\tau_3(q)] \quad (4)$$

where $\Omega(q)$ is the oscillation frequency and $\emptyset(q)$ a phase term. In this range of wave numbers, the experimental decay times are the result of fitting the c-SF to Eqs. 2 and 4. The theoretical results shown in Fig. 1 are in good agreement with the experimental data, as reported in our recent publication (García-Fernández et al. Submitted 2019).

Conclusions

Transport properties of the polymeric ternary mixture PS-toluene-n-hexane involved in the GIANT FLUCTUATIONS project have been measured during a thermodiffusion experiment using the shadowgraph technique. The involved NEFs are analyzed both experimentally and theoretically. The existing theory of fluctuating hydrodynamics for ternary mixtures is further developed including the coupling between temperature and velocity fluctuations. The theory is validated with a very good agreement by comparison with the experimental results. The coupling of fluctuations for small wave numbers induces the appearance of propagating modes visible as oscillations in the structure function.

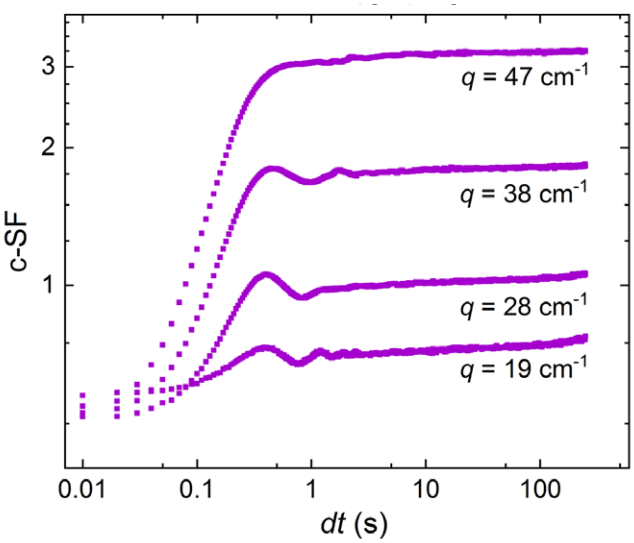

Figure 2: c-SF of the termodiffusion experiment for different small wave numbers.

Acknowledgements

We acknowledge financial support from the Centre National d'Etudes Spatiales (CNES) and from the funding partners of the Industrial Chair CO2ES: E2S-UPPA, TOTAL, CNES and BRGM. L. García-Fernández gratefully acknowledges the CNES for the post-doctoral research grant. The research at the Complutense University was supported by grant ESP2017-83544-C3-2-P of the Spanish Agencia Estatal de Investigación.

References

P. Baaske, H. Bataller, M. Braibanti, M. Carpineti, R. Cerbino, F. Croccolo, A. Donev, W. Köhler, J. M. Ortiz de Zarate, A. Vailati, The NEUF-DIX space project - Non-EquilibriUm Fluctuations during DIffusion in compleX liquids, *Eur. Phys. J. E* 39 (2016) 119.

H. Bataller, T. Triller, B. Pur, W. Köhler, J. M. Ortiz de Zarate, F. Croccolo, Dynamic analysis of the light scattered by the non-equilibrium fluctuations of a ternary mixture of polystyrene-toluene-n-hexane, *Eur. Phys. J. E* 40 (2017) 35.

G. Cerchiari, F. Croccolo, F. Cardinaux, F. Scheffold, Note: Quasi-real-time analysis of dynamic near field scattering data using a graphics processing unit, *Rev. Sci. Instrum.* 83 (2012) 106101.

F. Croccolo, H. Bataller, F. Scheffold, A light scattering study of non equilibrium fluctuations in liquid mixtures to measure the Soret and mass diffusion coefficient, *J. Chem. Phys.* 137 (2012) 234202.

F. Croccolo, L. García-Fernández, H. Bataller, A. Vailati, J. M. Ortiz de Zarate, Propagating modes in a binary liquid mixture under thermal stress, *Phys. Rev. E* 99 (2019) 012602.

L. García-Fernández, P. Fruton, H. Bataller, J.M. Ortiz de Zárate, F. Croccolo, Measurement of transport properties of a ternary mixture by dynamic Shadowgraphy, *Eur. Phys. J. E* Submitted (2019).

C. Giraudet, H. Bataller, F. Croccolo, High-pressure mass transport properties by dynamic near field scattering of non-equilibrium fluctuations, *Eur. Phys. J. E* 37 (2014) 107.

A. Vailati, R. Cerbino, S. Mazzoni, C. J. Takacs, D. S. Cannell, M. Giglio, Fractal fronts of diffusion in microgravity, *Nat. Commun.* 2 (2011) 290.

26th European Low Gravity Research Association Biennial Symposium and General Assembly
14th International Conference on "Two-Phase Systems for Space and Ground Applications"
European Space Agency Topical Teams meetings
Granada (Spain), September 24-27, 2019

Oral 110

Immune-cell responses under microgravity

Ning Li[1,2], Chengzhi Wang[1,2], Shujin Sun[1,2], Yuxin Gao[1], Juan Chen[1] and Mian Long[*,1,2]

[1]Key Laboratory of Microgravity (National Microgravity Laboratory), Center of Biomechanics and Bioengineering, and Beijing Key Laboratory of Engineered Construction and Mechanobiology, Institute of Mechanics, Chinese Academy of Sciences, Beijing, China
[2]School of Engineering Sciences, University of Chinese Academy of Sciences, Beijing, China
[*]mlong@imech.ac.cn

Introduction

Space microgravity can induce immune dysfunction of astronauts in long-term, manned spaceflight and space exploration. Leukocytes and endothelial cells (ECs) are highly sensitive to mechanical forces, which contributes to the microgravity-induced impaired immune function. (Gibbons et al. 2018). The underlying mechanisms remain largely unknown.

Methods

We used a rotary cell culture system (RCCS) to elucidate the effects of simulated microgravity on polymorphonuclear neutrophils (PMN)-like HL-60 cells (Wang et al. 2015), investigated the rolling dynamics of peripheral blood mononuclear cells (PBMCs) in a flow-chamber system during parabolic flight (PF) (Moser et al. in revision), and analysed the effect of space microgravity on the morphological changes and functions of EA.hy926 ECs on board the SJ-10 Recoverable Scientific Satellite (Li et al. 2018). All the samples were analysed off-line for both ground-based tests and space mission.

Results

In the RCCS experiment, we observed the up-regulation of cytokine secretion such as interleukin-6 (IL-6), interleukin-8 (IL-8), and monocyte chemotactic protein 1 (MCP-1) in the supernatant of the PMN-like cells. However, the reduced rolling speed and decreased adhesion of PMN-like cells on ECs under shear stress indicated that PMN recruitment might not be remarkably effective under microgravity.
In the PF experiment, the rolling rate of PBMCs on P-selectin glycoprotein ligand-1 (PSGL-1)-/intercellular cell adhesive molecule-1 (ICAM-1)-immobilized substrate was also decreased under microgravity, suggesting the impaired interactions between leukocytes and ECs.
In SJ-10 mission, space microgravity suppressed the glucose metabolism, modulated the expressions of cellular adhesive molecules such as ICAM-1, vascular cell adhesion molecule-1 (VCAM-1), and CD44, and depressed the release of pro-angiogenesis and pro-inflammation cytokines. Meanwhile, this specialized mechanical microenviroement also induced the depolymerization of actin filaments and microtubules, promoted the vimentin accumulation, restrained the extracellular matrix (ECM) deposition, regulated the mechanotransduction through focal adhesion kinase and Rho GTPases, and enhanced the exosome-mediated mRNA transfer.

Conclusions

This work furthers the understandings in mechanobiological responses of immune cells under microgravity and provides useful information for optimizing the countermeasures to immune suppression in future spaceflight.

Acknowledgements

The authors thank Drs. Alexander Chouker and Oliver Ullrich and their colleagues for the PF campaign. This work was supported by NSFC grants U1738115 and 31661143044, and CAS grants XDA04020202-19, XDA04020416, XDA04073800, and QYZDJ-SSW-JSC018.

References

C.Z. Wang, N. Li, C. Zhang, S.J. Sun, Y.X. Gao, M. Long, Effects of Simulated Microgravity on Functions of Neutrophil-like HL-60 Cells. *Microgravity Science and Technology* 27 (2015) 515-527.
D. Moser, S.J. Sun, N. Li, K. Biere, M. Hoerl, S. Matzel, M. Feuerecker, J.-I. Buchheim, C. Strewe, C.S. Thiel, Y.X. Gao, C.Z. Wang, O. Ullrich, M. Long, A. Choukèr, Cells´ Flow and Immune Cell Priming under Alternating g-forces in Parabolic Flight, *Scientific Reports*, in revision.
N. Li, C.Z. Wang, S.J. Sun, C. Zhang, D.Y. Lü, Q. Chen, M. Long. Microgravity-induced Alterations of Inflammation-related Mechanotransduction in Endothelial Cells on Board SJ-10 Satellite. *Frontiers in Physiology* 9 (2018) 1025.

Oral 111

Contactless manipulation of droplet in reduced gravity condition by counter-faced ultrasonic phased array

K. Hasegawa[1], T. Ito[2], and Y. Abe[2]

[1]Kogakuin University, Department of Mechanical Engineering, 1-24-2 Nishi-shinjuku, Shinjuku, Tokyo, Japan
[2]University of Tsukuba, Graduate school of Systems and Information Engineering, 1-1-1 Tennodai, Tsukuba, Ibaraki, Japan
kojihasegawa@cc.kogakuin.ac.jp[1]

Introduction

In recent years, the container-less processing technique using acoustic levitation method (ALM) has been a focus in the fields of analytical chemistry and biomedical industry. The container-less processing technique can avoid many problems caused by container wall such as a heterogeneous nucleation (T. Vasileiou et al., 2016). For more precise droplet manipulation, Hoshi et al. developed a mid-air acoustic manipulation device by ALM using focused ultrasound and enabled three-dimensional transport of solid particles by controlling the phases of the ultrasonic wave emitted from the transducer (T. Hoshi et al., 2014)). However, the ALM is difficult to handle the liquids because the liquids are deformed caused by the strong acoustic energy. In contrast, a microgravity environment enable us to easily handle the levitated liquid droplets by the ALM. Therefore, we focus on the microgravity experiment on the international space station (ISS). The counter-faced ultrasonic phased array (CUPA) system were developed for the non-contact manipulation in the microgravity environment and evaluated the feasibility of the microgravity experiment by the short-term reduced gravity experiment (D. Kageyama et al., 2014) using the aircraft (MU-300). The purpose of this study is to develop the technology of the contactless fluid manipulation such as levitation, transportation, coalescence, mixing, and evaporation based on the obtained findings on the short-term reduced gravity experiment.

Experimental apparatus and numerical analysis

The CUPA system, desigened and developed by the authors, generated the local acoustic standing waves (L-ASW) using two 12 x 12 ultrasonic phased arrays faced each other and realized the stable droplet levitation and its position control. The FPGA on the CUPA fast generate 40 kHz square waves for the focused ultrasound and controls the ultrasound phases for the L-ASW. The y-direction force F_y acting on a small sphere is defined by Hoshi et al., 2014. The equation of motion of a droplet can be written as

$$\rho \frac{d^2y}{dt^2} = \frac{A^2}{\rho_0 c^2}\frac{6\pi}{w}\left[\frac{\sin\left(\frac{2\pi y}{w}\right)\cos\left(\frac{2\pi y}{w}\right)}{\left(\frac{2\pi y}{w}\right)^2} - \frac{\sin^2\left(\frac{2\pi y}{w}\right)}{\left(\frac{2\pi y}{w}\right)^3}\right] \quad (1)$$

where A is RMS amplitude of the sound pressure, ρ = 998 kg/m^3 and ρ_0 = 1.29 kg/m^3 are the densities of the liquid and air, c = 340 m/s is the density of the air and w is the focal diameter. We used water as a test fluid. Experiments in reduced gravity were also carried out with the aircraft parabolic flights.

Results and discussion

The behaviors of small and large droplets is shown in Fig. 1. As the droplet diameter increased and the sound pressure decreased, both the swing width and the swing cycle are increased. The Droplet behaviors predicted by numerical analysis is shown in Fig. 2. As compared to the behavior of the small droplet in experiment, the behavior of the small droplet in numerical analysis is in good agreement with the experimental result. However, the short swing cycle behavior of the large droplet in numerical analysis is in poor agreement with the experimental result. The numerical analysis indicates the overestimation of the force acting on a large droplet. In conclusion, we evaluated the droplet behavior in the short-term reduced gravity environment and enabled us to elucidate the behavior of the small droplet

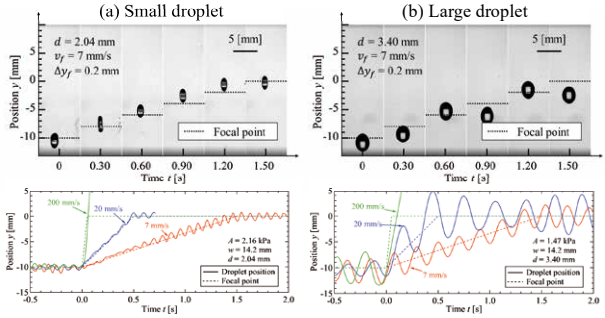

Figure 1: Droplet behaviors in the reduced gravity. (a) d = 2.0 mm, (b) d = 3.4 mm.

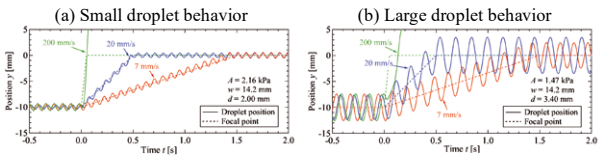

Figure 2: Droplet behaviors predicted by the numerical analysis. (a) d = 2.0 mm, (b) d = 3.4 mm.

References

T. Vasileiou, D. Foresti, A. Bayram, D. Poulikakos, A. Ferrari: *Sci. Rep.*, 6, (2016) 20023.

T. Hoshi, Y. Ochiai, J. Rekimoto: *Jpn. J. Soc. Appl. Phy.*, 53, (2014) 07KE07.

D. Kageyama: Int. *J. Microgravity Sci. Appl.*, 31 (2), (2014) 45-46.

26th European Low Gravity Research Association Biennial Symposium and General Assembly
14th International Conference on "Two-Phase Systems for Space and Ground Applications"
European Space Agency Topical Teams meetings
Granada (Spain), September 24-27, 2019

Oral 113

Preliminary results from vapour cloud measurements in the ARLES sounding rocket experiment

S. Dehaeck[1], A. Rednikov[1] & P. Colinet[1]

[1]Université Libre de Bruxelles (ULB)-Service Transferts, Interfaces et Procédés (TIPs), Brussels, Belgium;
sam.dehaeck@gmail.com, pcolinet@ulb.ac.be

Introduction

The ARLES experiment will fly in June 2019 on board the MASER-14 sounding rocket campaign organized by ESA and SSC. In the experiment, droplet evaporation is studied in microgravity. The module is equipped with multiple diagnostics such as an infrared camera (Semenov et al. 2017) and a side-view interferometer (Dehaeck et al. 2014). In the present abstract, we will have a preliminary look at the results obtained using the interferometer and compare ground with microgravity conditions.

Experimental Setup

A schematic of the Mach-Zehnder interferometric setup in ARLES is shown in Fig. 1. The experimental chamber is a cylinder with an internal volume of 4 L. The substrate is a 2" silicon wafer with a central hole of 0.7mm for injection of the droplet. A groove is etched into the silicon wafer (20µm wide and deep) to stop the spreading of the HFE-7100 droplet. This allows to obtain a contact angle larger than the evaporation-induced contact angle typically obtained for HFE-7100 of ~10° (Tsoumpas et al. 2014). In this way, a constant radius regime is induced in which the droplet diameter remains fixed at 4mm as the contact angle goes from 45° to 10° due to evaporation. Then, the droplet starts retracting with a mostly constant contact angle.

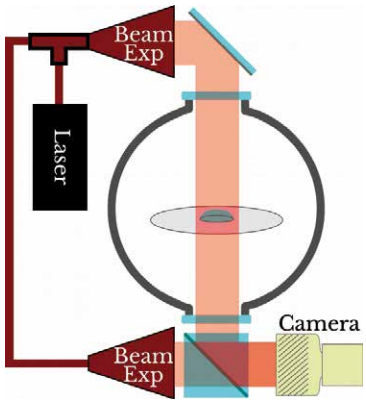

Figure 1: Schematic of the interferometer used in ARLES.

The substrate temperature is kept constant at 28°C, while the environment of pure N2 is kept at 26°C. Five droplets are injected consecutively of which two droplets are additionally subjected to a high voltage electric field (Vancauwenberghe et al. 2013) and the last one is loaded with nanoparticles (Machrafi et al. 2017). In the present abstract, we will only look at the behaviour of the two pure droplets without electric field.

Ground Results

Reference experiments were performed on ground in anticipation of the flight. In Fig. 2, a typical phase field map is shown (modulo 2pi). Note that the central obstruction is the counter-electrode. As there is a hole in this counter-electrode, the vapour should be able to extend above it. Nevertheless, the modulo 2pi contour lines show that the vapour cloud is flattened, which is attributed to gravity-induced natural convection due to density gradients in the gas. Indeed, when studying the evaporation rate of these drops on ground, we noticed that it was equal to 0.22µl/s (and largely independent of the contact angle in the range 10°- 45°). Comparing this to the pure diffusion predicted value of 0.11µl/s, it is clear that natural convection in the vapour cloud has a clear impact on the evaporation rate of the droplet. This will be further confirmed by confronting 1-g results with 0-g ARLES data.

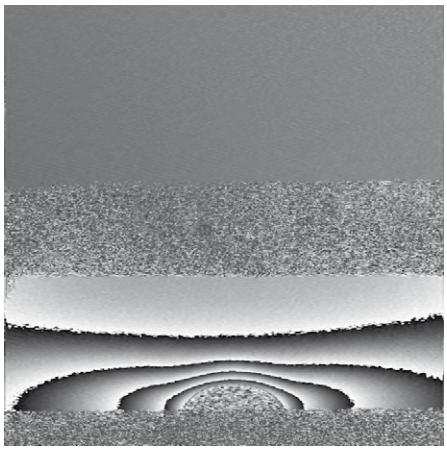

Figure 2: Phase field (modulo 2pi) of a typical vapour cloud measurement during ground tests.

Conclusions

Ground tests on the ARLES sounding rocket experiment have demonstrated the good functioning of the interferometer. These tests show a flattening of the vapour cloud due to gravity, which in turn leads to approximately a doubling of the evaporation rate. The sounding rocket experiment, to be performed in June 2019, is expected to allow a direct comparison between vapour clouds and evaporation rate in absence of gravity.

Acknowledgements

The present work is carried out in the frame of the ESA Research Project EVAPORATION (AO-1999-110). Special thanks to the entire ARLES Science Team for the constant interest and scientific contribution. We would also like to thank the whole ESA sounding rocket staff and the whole ARLES team at the Swedish Space Corporation for their invaluable work during the experiment development and flight. The authors gratefully thank

financial support from the European Space Agency (ESA) and the Belgian Federal Science Policy Office (BELSPO) through PRODEX Evaporation and PRODEX Heat Transfer. P.C. also acknowledges support from the Fonds de la Recherche Scientifique F.N.R.S.

References

S. Semenov, F. Carle, M. Medale, D. Brutin, (2017), 3D unsteady computations of evaporative instabilities in a sessile drop of ethanol on a heated substrate, *Appl. Phys. Lett.* 111, 241602.

S. Dehaeck, A. Rednikov, P. Colinet (2014). Vapor-Based Interferometric Measurement of Local Evaporation Rate and Interfacial Temperature of Evaporating Droplets. *Langmuir*, 30(8), 2002-2008.

I. Tsoumpas, S. Dehaeck, M. Galvagno, A. Rednikov, H. Ottevaere, U. Thiele, P. Colinet. (2014). Nonequilibrium Gibbs' Criterion for Completely Wetting Volatile Liquids. *Langmuir*, 30, 11847−11852.

Vancauwenberghe V., Di Marco P., Brutin D. (2013), Wetting and evaporation of a sessile drop under an external electrical field: A review, *Colloids and Surfaces A: Physicochem. Eng. Aspects*, 432, 50– 56.

H. Machrafi, C. Minetti, P.C. Dauby, C.S. Iorio, (2017), Self-assembly by multi-drop evaporation of carbon-nanotube droplets on a polycarbonate substrate, *Physica E: Low-dimensional Systems and Nanostructures*, 85, 206-213.

26th European Low Gravity Research Association Biennial Symposium and General Assembly
14th International Conference on "Two-Phase Systems for Space and Ground Applications"
European Space Agency Topical Teams meetings
Granada (Spain), September 24-27, 2019

Oral 114

The Seedling Growth (SG) spaceflight project on the International Space Station (ISS): Red light contributes to a better adaptation of plants to the space environment

F. Javier Medina[1], Aránzazu Manzano[1], Alicia Villacampa[1], Miguel A. Valbuena[1,3], Josh Vandenbrink[2], Eugénie Carnero-Diaz[3], Julio Sáez-Vásquez[4], Malgorzata Ciska[1], Raúl Herranz[1], John Z. Kiss[2]

[1]PCNPµG Lab, Centro de Investigaciones Biológicas-CSIC, Madrid, Spain; [2]University of North Carolina at Greensboro, USA; [3]Muséum National d'Histoire Naturelle, Dépt. Systématique et Evolution, Paris, France; [4]Université de Perpignan-Via Domitia, Perpignan, France

[1] fjmedina@cib.csic.es; [2] jzkiss@uncg.edu; [3] eugenie.carnero@mnhn.fr; [4] saez@univ-perp.fr

Introduction

Human space exploration must be accompanied by plants, as essential components of Bioregenerative Life Support Systems. Successful plant growth in space requires full knowledge of the mechanisms of sensing and response to the microgravity environment. In the root, gravity signals are transduced to meristems through the hormone auxin, and they regulate the coordination between cell proliferation (cell cycle progression) and cell growth (protein synthesis, ribosome biogenesis) in the root meristem, the tissue that provides the mother cells for differentiation. This coordination is called "meristematic competence" (Mizukami, 2001). Young plants (seedlings) grown in real or simulated microgravity in darkness show alterations in the root meristematic cells, consisting of an increased proliferation rate (cell cycle acceleration) and a decreased growth rate (reduced ribosome biogenesis). This means the disruption of meristematic competence (Manzano, et al., 2013; Matía, et al., 2010). We also observed accumulation of auxin in root meristems of plants exposed to microgravity conditions, suggesting that auxin transport was disturbed (Herranz, et al., 2014). Furthermore, there is an important reorganization of the general pattern of gene expression (Kamal, et al., 2019; Manzano, et al., 2012). These alterations could seriously compromise the developmental patterns of the plant. However, it has been recently shown that apparently normal adult plants and flowers can be produced in the ISS, revealing that plants eventually adapt to survive in space (Massa, et al., 2013).

The study of the adaptation mechanisms is one of our major challenges for the near future. The adaptation and survival of plants in microgravity could greatly benefit from the substitution of gravity by another external cue, which could play the same or a similar role in driving plant growth and development as gravity does on Earth. Light is a good candidate to be one of such these cues.

Light is indeed a tropistic stimulus. Phototropism complements gravitropism under normal ground conditions with the objective of optimizing the efficiency of the capture of nutrients. In addition, illumination, especially by red light, is sensed and mediated by phytochromes to produce changes in the regulation of auxin responsive genes and many growth coordinators (Vandenbrink, et al., 2014).

The Seedling Growth (SG) Spaceflight Project on the International Space Station (ISS)

In this context, we intended to know to what extent light can act as a signal capable of counteracting the effects caused by the lack of gravity. For this purpose, the series of experiments termed the Seedling Growth (SG) Project was conducted in the International Space Station (ISS) in the European Modular Cultivation System (EMCS). The overall objectives of this project were 1) to understand how gravity and light responses influence each other, 2) to better characterize the cellular signaling mechanisms involved in plant tropisms, and 3) to determine the combined influence of light and gravity on plant development by paying special attention to the effect of these cues on the root meristem.

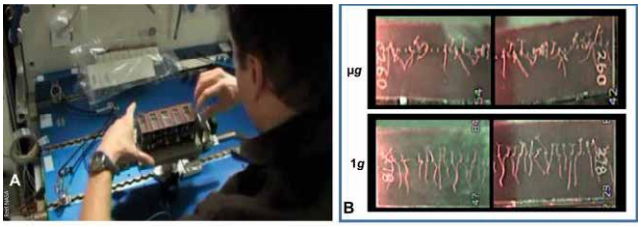

Figure 1: A) A crewmember of ISS operating the culture chambers of SG in which seedlings have grown, in order for their processing and preservation to make possible the post-flight analysis upon their return to Earth. B) Seedlings grown in space. µg: Microgravity. 1g: Control ground gravity, obtained in space by means of a centrifuge. Note the great differences in orientation of seedlings.

The experimental part of SG project was carried out in the ISS in three experiments performed respectively in 2013, 2014 and 2017. The last part, corresponding to the Ground Reference Run, took place in the summer of 2018. The project was the result of the cooperation of NASA and ESA, using a European incubator (i.e., EMCS) combined with an American culture chamber for incubation of seeds and growth of seedlings. Different collections of mutants of *Arabidopsis thaliana,* affecting the phytochromes, nucleolar proteins and auxin responsive genes were used. Seeds germinated in flight, and seedlings grew for six days under different regimes of illumination and gravity (Fig. 1). In addition to microgravity existing in space, seedlings were subjected to different levels of gravity between 0*g* and 1*g*, including the Moon and Mars gravity levels, which were produced by a centrifuge installed in the incubator.

The accomplishment of the space experiments involved technological and methodological developments, which have been validated by different tests. This resulted in significant advances in the reliability of the performance of plant experiments in space. The amount of plant material obtained, with high germination rates, was sufficient to make possible

molecular analyses with global transcriptomic methods (RNAseq). The last phase of SG experiment, SG3, included chemical fixation of samples to enable microscopical analyses. The quality of fixation, using the device developed for this procedure (FixBox), was adequate to allow the ultrastructural analysis of cellular subcomponents, such as the nucleolus, by transmission electron microscopy, as well as the quantity and *in situ* distribution of regulatory proteins of the cell cycle, ribosome biogenesis and other cellular processes involved in the stress response, such as ROS production, by confocal microscopy.

In relation to the first and second objectives of the project, the experiments have identified new phototropic responses to blue light in space, which complement previous findings obtained in the Tropi I and II experiments in the EMCS on the ISS (Vandenbrink, et al., 2016).

Furthermore, a positive effect of red light in counteracting the stress caused by microgravity on cell growth and proliferation in the root meristem has been found (Valbuena, et al., 2018). Photoactivation with red light during the last two days of culture was capable of reverting (totally or partially) the alterations caused by microgravity and of re-establishing meristematic competence, auxin transport and the gene expression patterns to standard values of control environmental conditions.

A full-genome global transcriptomic analysis of red-light-photostimulated plants *versus* plants grown in darkness showed that, in photostimulated plants of the wild type and nucleolin mutant lines *(nuc1* and *nuc2)*, a lower number of genes whose expression is deregulated by microgravity was obtained, in comparison with plants grown in darkness during the same period. Functional gene categories of genes involved in the cell cycle or in ribosome biogenesis are not included among these deregulated genes. The study at the cellular level of these two processes in these plants resulted in values closer to the 1*g* control in those irradiated with red light. Our studies confirmed previous works in the identification of the heat shock complex, the energy/redox processes and the cell wall remodeling as the most affected functions, but we pointed out the existence of a highly significant proportion of genes of unknown function (30-40%) among the genes showing altered expression in response to the simulated microgravity environment.

The study with nucleolin mutants has shown that overactivation of mechanisms of stress response against a situation that the plant is unable of mitigating, such as the lack of gravitational stimulus, may be detrimental. This can be the case for the *nuc2* mutant line, which does not express the nucleolin variant for stress response (NUC2 protein), and is capable of adapting to a microgravity environment by changing the expression of a smaller number of genes than the wild type, showing growth phenotypes equivalent to the latter line in all the experimental conditions studied. Therefore, a mutant line with this attenuated response may constitute an advantage to be taken into account when selecting the most productive plant varieties for Life Support Systems.

These results are very promising since they are a substantial advance in our knowledge on the procedures to succeed in the culture of plants as part of the Life Support Systems for space exploration.

Acknowledgements

This work was supported by the Spanish "Plan Estatal de Investigación Científica y Técnica e Innovación" of the National Agency for Research (AEI) [Grant numbers AYA2012–33982 and ESP2015–64323-R, cofounded by ERDF]. AM, AV and MAV were supported by the Spanish National Program for Young Researchers Training (MINECO, Ref. BES-2013-063933, BES-2016-077976). The Seedling Growth Project was funded by ESA-ELIPS Program (LSRA2009-0932/ 1177). We also acknowledge funding from "ELGRA Gravity Spotlight Team" Grant.

References

Herranz, R., M. A. Valbuena, K. Youssef, F. J. Medina, Mechanisms of disruption of meristematic competence by microgravity in *Arabidopsis* seedlings, *Plant Signaling and Behavior* 9 (2014) e28289. doi: 10.4161/psb.28289.

Kamal, K. Y., J. J. W. A. van Loon, F. J. Medina, R. Herranz, Differential transcriptional profile through cell cycle progression in Arabidopsis cultures under simulated microgravity, *Genomics* (2019). doi: 10.1016/j.ygeno.2019.01.007.

Manzano, A. I., O. Larkin, C. Dijkstra, P. Anthony, M. Davey, L. Eaves, R. Hill, R. Herranz, F. J. Medina, Meristematic cell proliferation and ribosome biogenesis are decoupled in diamagnetically levitated *Arabidopsis* seedlings, *BMC Plant Biology* 13 (2013) 124. doi: 10.1186/1471-2229-13-124.

Manzano, A. I., J. J. W. A. van Loon, P. C. M. Christianen, J. M. Gonzalez-Rubio, F. J. Medina, R. Herranz, Gravitational and magnetic field variations synergize to cause subtle variations in the global transcriptional state of *Arabidopsis* in vitro callus cultures, *BMC Genomics* 13 (2012) 105. doi:10.1186/1471-2164-13-105.

Massa, G. D., G. Newsham, M. E. Hummerick, J. L. Caro, G. W. Stutte, R. C. Morrow, R. M. Wheeler, Preliminary species and media selection for the Veggie space hardware, *Gravitational and Space Research* 1 (2013).

Matía, I., F. González-Camacho, R. Herranz, J. Z. Kiss, G. Gasset, J. J. W. A. van Loon, R. Marco, F. J. Medina, Plant cell proliferation and growth are altered by microgravity conditions in spaceflight, *Journal of Plant Physiology* 167 (2010) 184-93 doi: 10.1016/j.jplph.2009.08.012.

Mizukami, Y., A matter of size: developmental control of organ size in plants, *Current Opinion in Plant Biology* 4 (2001) 533-39. doi: 10.1016/S1369-5266(00)00212-0.

Valbuena, M. A., A. Manzano, J. P. Vandenbrink, V. Pereda-Loth, E. Carnero-Diaz, R. E. Edelmann, J. Z. Kiss, R. Herranz, F. J. Medina, The combined effects of real or simulated microgravity and red-light photoactivation on plant root meristematic cells, *Planta* 248 (2018) 691-704. doi: 10.1007/s00425-018-2930-x.

Vandenbrink, J. P., R. Herranz, F. J. Medina, R. E. Edelmann, J. Z. Kiss, A novel blue-light phototropic response is revealed in roots of Arabidopsis thaliana in microgravity, *Planta* 244 (2016) 1201-15. doi: 10.1007/s00425-016-2581-8.

Vandenbrink, J. P., J. Z. Kiss, R. Herranz, F. J. Medina, Light and gravity signals synergize in modulating plant development, *Frontiers in Plant Science* 5 (2014) 563. doi: 10.3389/fpls.2014.00563.

26th European Low Gravity Research Association Biennial Symposium and General Assembly
14th International Conference on "Two-Phase Systems for Space and Ground Applications"
European Space Agency Topical Teams meetings
Granada (Spain), September 24-27, 2019

Oral 115

Impact of liquid droplets on substrates with high temperature

Song Rong, Longlong Wang, Shiquan Shen, Tianyou Wang, Zhizhao Che*

State Key Laboratory of Engines, Tianjin University, Tianjin, 300072, China
*chezhizhao@tju.edu.cn

Introduction

The phenomenon of droplet impact happens ubiquitously in nature and in a wide range of industrial applications which include but are not limited to spray cooling, painting, inkjet printing, and fuel-spray impingement in internal combustion engines (Yarin 2005, Josserand and Thoroddsen 2016). The contact time of a bouncing droplet is an important parameter in droplet impact process. For the axisymmetric impact of an inviscid droplet on a superhydrophobic surface, the contact time is bounded by the Rayleigh time scale (Richard et al. 2002). Because the contact time controls the mass, momentum and energy transfer between the droplet and the surface, it is important to reduce it in many applications, such as anti-icing, self-cleaning, corrosion-resistance, and maintaining surface dryness. Therefore, many efforts have been made to overcome the theoretical limit and reduce the contact time, for example, by using surfaces with ridges(Bird et al. 2013), pancake bouncing on superhydrophobic surfaces patterned with lattices of submillimeter posts (Liu et al. 2014), asymmetric bouncing on curved surfaces (Liu et al. 2015), egg-shaped droplets(Yun 2018), etc.

In this study of the impact on heated surfaces, we find that a droplet bouncing mode, i.e. *bouncing-with-spray* mode, caused by the burst of vapor bubbles can contribute to a dramatic reduction of the droplet residence time. Comparing with other strategies to reduce the residence time, this approach induced by heat is reliable by avoiding surface degradation and is easy to achieve by avoiding complex fabrication of surface microstructures or surface modification.

Experimental method

Different droplet liquids (water, ethanol, and water/glycerol mixtures) were pushed through an injection tube at an extremely low speed by a syringe pump (Harvard Apparatus, Pump 11 elite Pico plus). Droplets formed at the tip of a blunt syringe needle and detached when the gravitational force exceeded the surface tension force. The droplet then impacted on a polished silicon substrate (silicon wafers, the roughness is less than 0.5 nm) which was heated by a copper holder.

Results and disucssion

Different impact morphologies were observed when varying the substrate temperature and the droplet speed and different kinds of liquids in three boiling regimes, namely nucleate boiling, transition boiling, and film boiling. Figure 1 shows the impact morphologies by taking water as a representative. These different morphologies result in a dramatic difference in the residence time of the droplet on the substrate. Here, the residence time is defined as the interval between the moments that the droplet visually contacts the substrate and that it visually detaches the substrate.

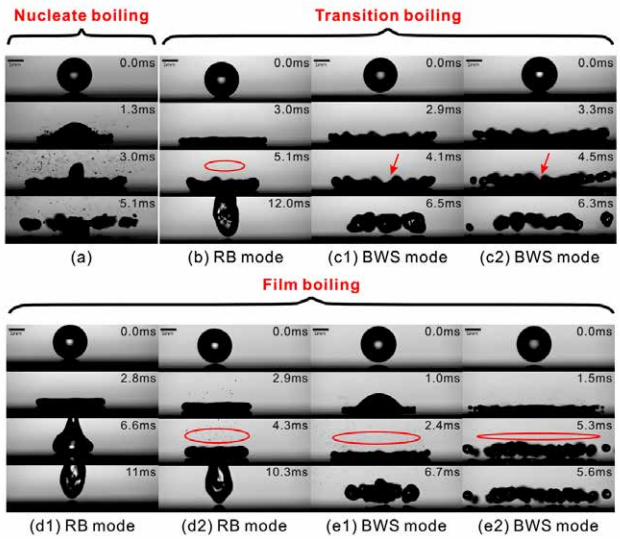

Figure 1: Morphologies of water droplet impacting on heated surfaces in three boiling regimes.

Conclusions

In summary, the impact of droplets on heated surfaces is studied, and a droplet bouncing mode caused by the breakup of the liquid film, i.e., bouncing-with-spray mode, can contribute to a dramatic reduction of the droplet residence time compared to the traditional bouncing mode, i.e., retraction-bouncing mode. The residence time of the bouncing-with-spray mode is independent of liquid's viscosity, and the reduced residence time compared with that of the retraction-bouncing mode is about 40%.

Acknowledgements

This work is supported by the National Natural Science Foundation of China (Grant No. 51676137), the Natural Science Foundation of Tianjin City (Grant No. 16JCYBJC41100), and the National Science Fund for Distinguished Young Scholars (No. 51525603).

References

Bird, J. C., R. Dhiman, H.-M. Kwon and K. K. Varanasi. Reducing the contact time of a bouncing drop. *Nature* **503** (2013): 385.

Josserand, C. and S. Thoroddsen. Drop impact on a solid surface. *Annual Review of Fluid Mechanics* **48** (2016): 365-391.

Liu, Y., M. Andrew, J. Li, J. M. Yeomans and Z. Wang. Symmetry breaking in drop bouncing on curved surfaces. *Nature communications* **6** (2015): 10034.

Liu, Y., L. Moevius, X. Xu, T. Qian, J. M. Yeomans and Z. Wang. Pancake bouncing on superhydrophobic surfaces. *Nature physics* **10** (2014): 515.

Richard, D., C. Clanet and D. Quéré. Surface phenomena: Contact time of a bouncing drop. *Nature* **417** (2002): 811.

Yarin, A. L. Drop impact dynamics: Splashing, spreading, receding, bouncing. *Annual Review of Fluid Mechanics* **38** (2005): 159-192.

Yun, S. Controlling the residence time of a bouncing drop with asymmetric shaping. *Soft Matter* **14** (2018): 4946-4951.

26th European Low Gravity Research Association Biennial Symposium and General Assembly
14th International Conference on "Two-Phase Systems for Space and Ground Applications"
European Space Agency Topical Teams meetings
Granada (Spain), September 24-27, 2019

Oral 116

Cytoskeleton, a major player in endothelial performance in simulated microgravity

Laura Locatelli[1], Alessandra Cazzaniga[1], Valentina Romeo[1], Roberta Scrimieri[1], Monica Zocchi[1], Giorgia Fedele[1], Sara Castiglioni[1] and Jeanette A.M. Maier[1].

1 Dept Biomedical and Clinical Sciences L. Sacco, Università di Milano, Via G.B. Grassi 74, Milano, Italy

Laura.Locatelli@unimi.it; alessandra.cazzaniga@unimi.it; valentina.romeo@unimi.it; roberta.scrimieri@unimi.it; monica.zocchi@unimi.it, giorgia.fedele1@studenti.unimi.it; sara.castiglioni@unimi.it; jeanette.maier@unimi.it

Introduction

Endothelial cells, which are vital for vascular integrity and homeostasis, are very sensitive to mechanical stress, including alterations of gravity [1]. In particular, human primary endothelial cells (hEC) respond to real or simulated microgravity by activating an adaptive response that remodels their performance [2]. Gravitational unloading influences endothelial proliferation, signaling, gene expression, surface adhesion molecules, and causes significant changes in the cytoskeleton [1].

Indeed, several studies showed a significant reduction of the total amounts of the main cytoskeletal components, and fluorescence staining confirmed the early disorganization of actin filaments and microtubules upon endothelial exposure to microgravity [3, 4]. Recent studies have focused on the cytoskeleton as initial gravity sensor [5]. To investigate how cytoskeletal disorganization impacts on hEC, we compared results obtained in simulated microgravity using the Rotating Wall Vessel with data from hEC treated with sublethal concentrations of cytochalasin D, which induces the depolymerization of filamentous actin and inhibits the polymerization of actin.

Methods

To simulate microgravity, hECs from the umbilical vein (HUVEC) were grown in the NASA-developed Rotating Wall Vessels (RWV). Cell morphology and mitochondrial network were assessed by confocal microscopy. Western blot was performed on cell lysates using specific primary antibodies and immunocomplexes were visualized by chemiluminescence [2].

Results

Cytochalasin D was tested for toxicity in a dose dependent fashion and 0.5 μM was identified as the concentration that alters the cytoskeleton without impairing cell viability up to 96 h.

Western blot was performed to assess stress response. We found that cytoskeleton disorganization in hEC exposed to simulated microgravity or induced by 0.5 μM cytochalasin D induces the early accumulation of hsp70 and the late increase of hsp27.

We also wondered whether cytoskeletal remodelling in hEC simulated microgravity or treated with cytochalasin D impacted on cell organelles. We focused on mitochondria and found that a decreased mitochondrial content in both the experimental conditions. We are currently studying the mechanisms responsible for this effect.

Conclusions

Simulated microgravity activates part of endothelial adaptive response through the remodelling of the cytoskeleton.

Acknowledgements

References

1. Maier, J. A., Cialdai, F., Monici, M., and Morbidelli, L. (2015) The impact of microgravity and hypergravity on endothelial cells. BioMed Res. Int. 2015, 434803.
2. Cazzaniga A, Locatelli L, Castiglioni S, Maier JAM (2019). The dynamic adaptation of primary human endothelial cells to simulated microgravity. FASEB J. 33(5):5957-5966.
3. Carlsson, S.I., Bertilaccio, M.T., Ballabio, E., Maier, J.A. (2003) Endothelial stress by gravitational unloading: effects on cell growth and cytoskeletal organization. Biochim Biophys Acta1642, 173-9.
4. Janmaleki, M., Pachenari, M., Seyedpour, S. M., Shahghadami, R., and Sanati-Nezhad, A. (2016) Impact of simulated microgravity on cytoskeleton and viscoelastic properties of endothelial cell. Sci. Rep. 6, 32418.
5. Vorselen D, Roos WH, MacKintosh FC, Wuite GJ, van Loon JJ. The role of the cytoskeleton in sensing changes in gravity by nonspecialized cells. FASEB J. 2014 Feb;28(2):536-47.

Oral 117

Bifurcations in rotating spherical shell convection under the influence of a weak differential rotation between the inner and outer spheres

F. Feudel[1], N. Seehafer[1]

[1] University of Potsdam, Potsdam, Germany ;
ffeudel@uni-potsdam.de, seehafer@uni-potsdam.de

Introduction

This investigation is motivated by the GeoFlow experiment which seeks to investigate thermal convection in a spherical shell under the influence of a central force field at the International Space Station, where such a central force field can be realized under microgravity conditions (Futterer et al. 2008, Feudel et al. 2011). The experimental setup serves as an approximate model for the large-scale convection in planets and in the outer zones of celestial bodies. A comparison of the theoretical predictions and the experimental realizations is of great interest for both experimenters and theorists. Beside numerical simulations which are based on the specific experimental realization of the central force field generated by the action of a dielectric effect more general studies with the usual gravity force of planets are also part of GeoFlow. They serve on the one hand side to evaluate the experimental model and, moreover, to propose further experimental series. Such a principal effect modeling the influence of a weak differential rotation of the inner sphere with respect to the outer one on the heat transfer is subject of this work.

Model and numerical results

We numerically study convection phenomena in a rotating spherical shell which is heated from the inner sphere by imposing a constant temperature difference between its boundaries, and is subject to the action of a radially directed gravity force. In addition to the rotation of the fluid shell with angular velocity Ω, a shear is generated by a weak differential rotation of the inner sphere with respect to the outer one, characterized by the parameter $\varepsilon = \Delta\Omega / \Omega$, where $\Delta\Omega$ is the imposed angular velocity of the inner sphere in the frame rotating with angular velocity Ω. Only small values of ε ($|\varepsilon| < 0.04$), are considered. There are indications that this type of configuration can be realized in astrophysical situation, as e.g. in the convection zones of the Earth-like planets, and can then determine the character of the magnetic dynamo processes there. The Ekman number which characterizes the rotation rate is fixed to a moderately small value of Ek=0.001. Starting from the unperturbed case of ε =0, for which the bifurcations were computed in detail recently {Feudel et al. 2013, Feudel et al. 2015, Feudel et al. 2017}, we study the influence of the imposed shear due to the weak additional rotation of the inner sphere.
Besides purely quantitative modifications of the bifurcations that already occur for ε=0, new branches of rotating waves are found in the case of weak retrograte rotation of the inner sphere. Figure 1 exhibits the bifurcation diagram for the example of ε = -0.02; the negative sign marks the retrograde differential rotation of the inner sphere. The Nusselt number

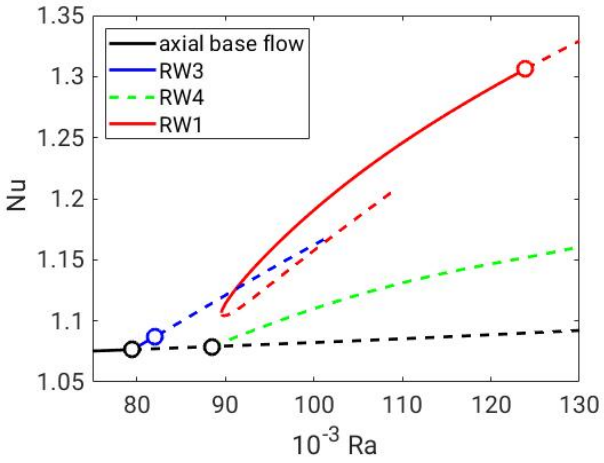

Figure 1: Bifurcation diagram of rotating waves for a differential rotation of the inner sphere with ε=-0.02. Open circles mark supercritical Hop bifurcations. Solid (dashed) lines denote stable (unstable) solutions. The intersections of the blue and red line are no connections of the branches and are only projection effects.

is presented as function of the Rayleigh number which is varied as the relevant bifurcation parameter. In comparison to the rigid rotation of both spheres, in the case of an additional differential rotation no conductive state does exist and already for small Rayleigh numbers a nonvanishing axisymmetric basic flow is generated, drawn as black line in this figure. This axisymmetric solution branch becomes unstable via a symmetry breaking Hopf bifurcations in which rotating waves with a cyclic three-fold rotational symmetry bifurcate, marked by the blue line and denoted by RW3. At higher Rayleigh numbers a further Hof bifurcation generates a four-fold symmetric rotating wave branch (RW4), represented by the green line. Stable branches are drawn by solid lines and unstable branches by dashed lines. The RW4 solutions are unstable at all but also the RW3 branch is stable only over a small inerval of the Rayleigh numbers and ends up with a secondary Hopf bifurcation in which quasiperiodic solutions appear as stable solutions. This quasiperiodic branch is not shown in Fig. 1. The RW3 and RW4 solution branches with a corresponing dominant azimuthal mode numbers m=3 and m=4, respectively, are remnants of the unperturbed situation, ε = 0, which here survive. However the focus of this work is a new type of waves not resulting from a linear instability of the axisymmetric basic flow. They appear via a saddle-node bifurcation in the range $-0.03 < \varepsilon < -0.008$. A particular feature of these bifurcating rotating waves is that their nonaxisymmetric components are weak. However all modes are excited and no axial subsymmetries exist. Since the azimuthal mode m=1 is strongly exited we denote this

branch by RW1 which in Fig. 1 corresponds to the red line. Using a pathfollowing technique we traced the branch around its turning point computing its unstable counterpart and verified the nature of the saddle-node bifurcation. Another feature of this branch is the enhancement of the heat transfer which is clearly visible in Fig. 1 by the values of the Nusselt numbers. In order to give an impression of the convection patterns of the stable RW1 branch Fig.2 shows contour plots of the radial velocity component in the middle of the spherical gap.

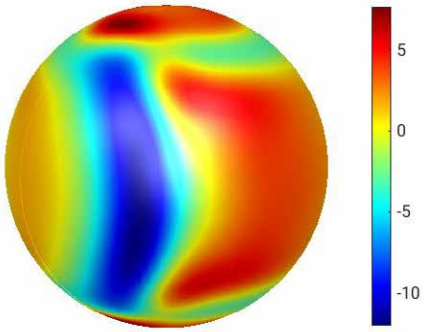

Figure 2: Contour plots of the radial velocity in the middle of the spherical gap of the RW1 branch for $Ra=10^{5.}$.

The bright color (red) can be interpreted as regions of warm ascending fluid and dark color (blue) marks regions of cold descending fluid. On both poles we observe upwelling plumes while only one sharp and strongly downwelling region is visible on the front of the sphere, in accordance with the feature that in particular the m=1 mode is strongly excited.

Conclusions and Outlook

A weak differential rotation of the inner sphere in the rotating spherical Rayleigh-Benard convection generates new flow patterns with an enhancement of the heat transfer. This mechanism may be find applications in the realization of cooling processes in technical devices under microgravity conditions.

Our numerical approach of using both simulations and pathfollowing techniques has been proven to be an effective tool to compute bifurcation diagrams which give a complete survey about the existing flow patterns in dependence of the studied parameters.

As a next step we intend to study, for the case of electrically conducting fluids, the dynamo capabilities of these new rotating waves, in particular with respect to whether they can generate and maintain a magnetic field. This nonlinear dynamo action is already demonstrated for the unperturbed case, $\varepsilon=0$ (Feudel et al. 2017).

Acknowledgements

The fruitful discussions in the Topical Team in the framework of the GeoFlow project are gratefully acknowledged.

References

B. Futterer, C. Egbers, S. Koch, N. Dahley, L. Jehring, Thermal convection in spherical shells: An experimental and and numerical approach within GeoFlow, *Acta Astronautica 62 (2008) 300.*

F. Feudel, K. Bergeman, L.S. Tuckerman, C. Egbers, B. Futterer, M.Gellert, R.Hollerbach, Convection patterns in a spherical fluid shell,. *J. Phys. Rev E* 83 (2011) 046304.

F. Feudel, N. Seehafer, L.S. Tuckerman, M. Gellert, Multistability in rotating spherical shell convection, *J. Phys. Rev E* 87 (2011) 023021.

F. Feudel, L.S. Tuckerman, M. Gellert, N. Seehafer, Bifurcations of rotating waves in spherical shell convection, *J. Phys. Rev E 9*2 (2015) 053015.

F. Feudel, L.S. Tuckerman, M. Zaks, R. Hollerbach, Bifurcations of rotating waves in spherical shell convection, *J. Phys. Rev. Fluids* 2 (2017) 053902.

Oral 120

Flexible single loop PHP preliminar studies

S. Van Vaerenbergh[1], Y.Gabrielloni[2], Q. Galand[1] , T. Maré[2]

[1]Université libr de Bruxelles, Brussels, Belgium,
[2] Université de Rennes UIT St Malo, Saint Malo, France
svanvaer@ulb.ac.be , thierry.mare@univ-rennes1.fr

Introduction

Pulsating heat pipes are emerging in the field of heat transfer and regulation under many geometrical configurations [1] [2] [3]. For space applications, deployable heat pipes are under study in the frame of the MAP TOPDESS initiated in 2019 under ESA auspices. In this frame we studied the signle loop pulsating heat pipes with flexible connections. We present some of the numerous experimental results obtained so far in the section 2, after description of a set up given in section 1.

Set up and procedure

The figure 1 shows a typical setup used to study signle loop heat pipes.

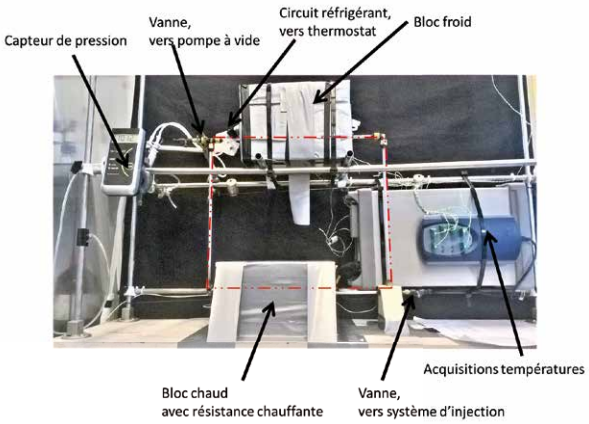

Fig 1: typical setup used for the study of single loop heat pipe

Typically the closed loop is divided into evaporator zone, condensor zone and adiabatic interconnections. The latter are made transparent to visualize the flows and analyze the link between the flows and the heat transfer capability.. The condesor and evaporator are heat blocks with a heat flux meter of the brand CAPTEC. Themocouples are distributed in the loop and a pressure probe provides the initial pressure afete the filling.
In our experiments, the condenser temperature is fixed by an external water loop, and the heat power ois injected in the evaporator with a MINCO resistance that dissipates the injected electrical power.
The different operating parameters are schematized in the well known figure 2

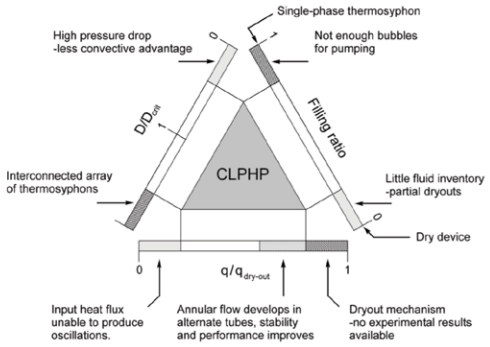

Fig 2 : Main and schematic operating parameters for a closed loop pulsating heat pipe.

The filling ratio in our case is realized at the initial filling under vacuum. The second parameter, usualy given in terms of Bound number is varied in pour systems by v arying the fluid, while keeping the internal fluid section of the loop constant. Finally, the heat power is varied by the electrical power of the electrical MINCO resistance. It is important to not that the mean temeprature is an important parameter not appearing in the figure 2, and this is due to the influence of the phase change, wetting and surface tension.

Results

Except for the start up phase, we can present typical results on the figure 3.

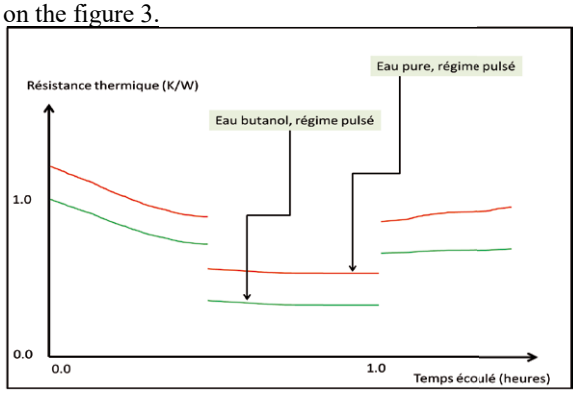

Fig 3: typical results obtained with water (upper curves) and a self rewetting fluid (lower curves)

One observe a significantly better thermal resistances for the self rewetting fluid.
More results will be provided and explained in the full paper

Conclusions

In the fame of the TOPDESS MAP project we initiated single loop heat pipes with flexible connections. Results with self rewetting are significantly better. The fact that flexible connections can be used is a significant step for deployability.

Acknowledgements

Thanks to the TOPDESS MAP auspiced by the European Spâce Agnecy

References

[1] Shafii, M.B., Fahgri, A., Zhang, Y., 2001, "Thermal modelling of unlooped and looped pulsating heat pipes", *Journal of Heat Transfer*, **123**, pp. 1159-1172

[2] K. S. and G. M., "On the definition of pulsating heat pipes: an overview," vol. 3, 2003.

[3] X. Han, X. Wang, H. Zheng, X. Xu, and G. Chen, "Review of the development of pulsating heat pipe for heat dissipation," *Renewable and Sustainable Energy Reviews*, vol. 59. 2016.

Oral 121

Phase-field modelling of the influence of high-frequency vibrations on heterogeous mixtures. Frozen waves

T. Lyubimova[1], A. Vorobev[2]

[1]Institute of Continuous Media Mechanics UB RAS, Perm, Russia, [2]University of Southampton, Southampton, UK;
lyubimovat@mail.ru, A.Vorobev@soton.ac.uk

Introduction

The high-frequency vibrations of a container filled with a fluid induce small-amplitude pulsation motion, that however is hardly-visible with the naked eye, and slow but large-amplitude time-averaged motion that is much more important for practical applications (e.g. microfluidics, control of the crystal growth and other chemical engineering processes). The effective description of high-frequency vibrations is achieved with the use of the multiple-scale method and averaging procedure that could be utilised for splitting the processes that occur on different time scales thus representing the hydrodynamic evolution as small-amplitude pulsations on a background of slower large-amplitude changes, and thus splitting the governing equations for the separate, although coupled, sets of the pulsation and averaged equations. The use of the averaged equations allows the time integration with the much larger time steps as the need to resolve the short-scale oscillatory motion is eliminated.

In the present work, we develop a theoretical model for a heterogeneous binary mixture of two slowly miscible liquids that are enclosed in a container subjected to the high-frequency small-amplitude mechanical vibrations.

The traditional description of the multiphase system is given within the Laplacian approach, when the phases are divided by infinitely thin boundaries endowed with surface tension. To describe the hydrodynamic processes in the multiphase system, conventionally, the governing equations are separately solved within each phase, and then the obtained solutions are matched by using the appropriate boundary conditions imposed at the interfaces.

The traditional description becomes inconvenient if the interfaces experience strong topological transformations, or may even emerge or disappear during the evolution (which may occur e.g. due to dissolution of existent inclusions or due to nucleation of new phase inclusions). An alternative description is to represent the interface as a transition layer of a finite thickness across which almost all variables experience sharp but still continuous changes. One set of the governing equations is solved for the whole multiphase system including the interface.

Time-averaged equations

In our work, we examine the action of uniform vibrations (defined by the velocity $a\omega\vec{j}cos(\omega t)$, where a is the amplitude of vibrations, ω is the frequency of vibrations, and $\vec{j}$ is the unit vector that defines the direction of the vibrational forcing). The phase-field (Cahn-Hillliard) approach is employed for the description of evolution of a multiphase mixture of two liquids. The use of the multiple-scale method for the analysis of time scales involved into the full Cahn-Hilliard-Navier-Stokes equations with additional vibration term allowed us to derive the following equations for the average flow fields,

$$\frac{\partial \vec{u}}{\partial t} + (\vec{u}\cdot\nabla)\vec{u} = -\nabla\left(\frac{\Pi}{\rho}\right) + \frac{\eta}{\rho}\Delta\vec{u} - C\nabla\mu - \frac{\varphi}{2}(\vec{w}\cdot\vec{w}_0)\nabla C,$$

$$\frac{\partial C}{\partial t} + (\vec{u}\cdot\nabla)C = \frac{\alpha}{\rho}\Delta\mu,$$

$$\nabla\cdot\vec{u} = 0.$$

Here t denotes time, $\vec{u}$ is the vector of the average velocity, $\vec{w}_0 = a\omega\vec{j}$ is the amplitude of the vibrational forcing, $\vec{w}$ is the induced pulsation velocity, η is the coefficient of dynamic viscosity, ρ is the mixture density, C is the concentration (mass fraction) of one of the components in a mixture, $\varphi = (\rho_2 - \rho_1)/\rho_2$ is the density contrast, and α is the mobility coefficient. The chemical potential, μ, is determined from the following equation,

$$\mu = -\varphi(\vec{g}\cdot\vec{r}) + \frac{df_0}{dC} - \varepsilon\Delta C,$$

where $\vec{g}$ is the gravity acceleration, $\vec{r}$ is the radius-vector, f_0 is the classical part of the specific free energy function that determines the thermodynamic behaviour of a mixture, and ε is the capillary constant.

The set of equations for the pulsation velocity takes the following form,

$$\nabla\times\vec{w} = \varphi\vec{w}_0\times\nabla C, \qquad \nabla\cdot\vec{w} = 0.$$

The derived set of the governing equations are to be supplemented with the boundary conditions. For the average velocity, the no-slip boundary condition needs to be imposed, $\vec{u} = 0$. For the pulsation velocity, the normal component is to be set zero at the wall, $w_n = 0$. The zero value of the normal derivative of the chemical potential, $\frac{\partial\mu}{\partial n} = 0$, is imposed to exclude the diffusive flux through the wall. One additional condition for the concentration field is also needed to define the wetting properties at the wall. There are two simplest cases, (i) the walls are neutral to the molecules of the mixture components, and thus the contact line is orthogonal to the wall, $\frac{\partial C}{\partial n} = 0$, and (ii) the walls are perfectly wetted by one of the liquids, and in this case the value of the concentration needs to be maintained at the wall.

The details of the derivation of the mathematical model can be found in our recent work (Vorobev & Lyubimova 2019). The obtained theoretical model describes the slow diffusive and convective evolution of the binary mixture with the account of the dynamic (varying over the duration of the process) surface tension effects. The diffusion term is defined on the basis of the extended Fick's law, and thus the model includes the effect of barodiffusion. The averaged vibrational force and the equations for the pulsation flow coincide with the standard equations that determine the effects of the

uniform high-frequency vibrations on a single-phase fluid flow (Gershuni & Lyubimov 1998).

Frozen waves

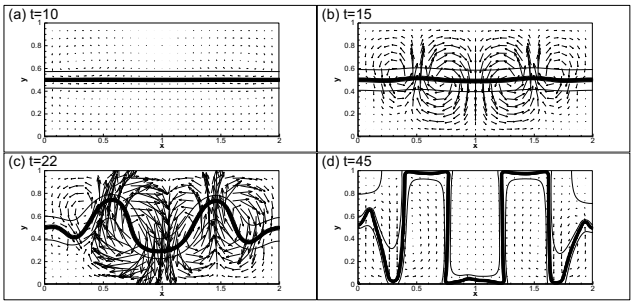

Figure 1: Formation of frozen waves.

To validate the derived equations we aimed to reproduce the results of the recent experiments (Gaponenko et al. 2015). Namely, we assume that two miscible liquids, that are taken in equal volumes and that are initially separated by a thin flat boundary, occupy a closed 2D rectangular container (with the aspect ratio of 2:1). A container is subjected to translational vibrations along its larger dimension. The weightlessness conditions are assumed.

The phenomenon of the frozen waves in a mixture of two miscible liquids was earlier studied with the use of the approach, that represented a heterogeneous binary mixture as a single-phase fluid with an impurity and that disregarded the surface tension effects for miscible interfaces (Gaponenko et. al 2015). This simplified approach produced the results that were in a generally good agreement with the experiments, in terms that the experimentally observed frozen patterns could be reproduced. However, in accordance with the linear stability theory of an interface subjected to high-frequency vibrations, the instability should occur unconditionally (Lyubimov et. al 2003), and in the experiment, the start of the instability was characterised by a threshold level of vibrations. In order to match the experimental observations with the theory, it was earlier proposed to introduce the effective surface tension for a miscible interface, which was missing in the classical model.

In our work, we undertake the modelling of the experiment on the basis of the phase-field approach, taking into account the surface tension effects. We managed to reproduce all experimental observations, including the threshold ignition of the instability. The threshold is determined by the value of the effective surface tension coefficient that is associated with a miscible boundary. The time needed for setting up the frozen waves increases for the parameters near the threshold. This imposes a substantial restriction on the minimum duration of the experiment. We also observe that upon further increase of the vibrational forcing (which intensity is determined by the square of the vibrational velocity) the frozen pattern may change (additional frozen waves appear in the container).

We fulfilled quite long numerical calculations that described the evolution of a binary mixture for the period of about 1 hour. The frozen wave patten remains stable during the whole run, no additional instabilities within a transitional layer, that were previously expected (Wolf 2018), were noticed. Depending on whether the liquids are fully or partially miscible, the pillar's walls either smear until they become completely indistinguishable, or remain sharp indefinitely long. In the latter case the diffusion process ends when the concentrations in the neighbouring components reach the equilibrium values, so the binary mixture attains the state of mechanical and thermodynamic equilibrium.

Further details can be found in our recent work (A. Vorobev & T. Lyubimova 2019).

Conclusions

In our work, we derived the theoretical model to describe the averaged effects of uniform high-frequency vibrations on an isothermal evolution of a heterogeneous (with interfaces) mixture. The resultant model includes the effects of molecular diffusion and barodiffusion, the dynamic interfacial stresses, and the generation of the hydrodynamic flows by non-homogeneities of the concentration field (when they are combined with the effects of gravity and vibrations).

To validate the theoretical model and to investigate the role of interfacial stresses in the evolution of miscible boundaries we studied the action of high-frequency vibrations on a heterogeneous binary mixture that fills in a closed container. An experimental study reports the threshold ignition of the frozen waves at a miscible interface even under weightlessness conditions, which cannot be explained on the basis of the classical approach that represents a binary mixture as a single phase fluid with impurity. This effect, however, can be well explained on the basis of the phase-field equations.

An agreement of the results with the previous experimental and theoretical studies makes the derived equations a powerful computational tool for tracing the dynamics of miscible (completely or partially miscible) and immiscible liquids with the account of the surface tension effects.

Acknowledgements

The work is financially supported by the Russian Foundation for Basic Research (grant 18-01-00782).

References

Y.A. Gaponenko, M. Torregrosa, V. Yasnou, A. Mialdun & V. Shevtsova, Dynamics of the interface between miscible liquids subjected to horizontal vibration, *J. Fluid Mech.,* 2015, 784, 342-372.

G. Gershuni, D. Lyubimov, Thermal Vibrational Convection, Wiley & Sons, 1998

D.V. Lyubimov, T.P. Lyubimova & A.A. Cherepanov, Dynamics of interfaces subject to vibrations, FizMatLit., 2003

A. Vorobev & T. Lyubimova, Vibrational convection in a heterogeneous binary mixture. Part 1 Time averaged equations, *J Fluid Mech.* 870 (2019) 543-562

A. Vorobev, T. Lyubimova, Vibrational convection in a heterogeneous binary mixture. Part II. Frozen waves, *J. Fluid Mech.*, 2019, 870, pp. 563-594

G.H. Wolf Dynamic stabilization of the rayleigh-taylor instability of miscible liquids and the related "frozen waves". Phys. Fluids, 2018, 30, 021701.

Oral 123

Soret induced convection of ternary fluid with small value of the net separation ratio in closed cavity

T. Lyubimova[1], S. Prokopev[1], V. Shevtsova[2]

[1]Institute of Continuous Media Mechanics Ural Branch RAS, Perm, Russia,
[2] MRC, CP165/62, Université libre de Bruxelles (ULB), 50, Ave. F.D. Roosevelt, B-1050 Brussels, Belgium
lubimova@psu.ru, prokopev.s@icmm.ru, vshev@ulb.ac.be

Problem formulation. Governing equations

We study Soret-driven convection of a ternary fluid in a rectangular cavity with the aspect ratio of 3:1 (the horizontal size is 3 times larger than vertical one). The liquid under consideration is toluene-methanol-cyclohexane with mass fraction 0.62/0.31/0.07 respectively. The boundaries are assumed to be rigid and impermeable. The case of heating from above is considered. The axis x of the Cartesian coordinate system is directed horizontally and z-axis in vertical direction.
The governing equations in the dimensionless form are:

$$\frac{\partial \mathbf{v}}{\partial t} + \mathbf{v}\cdot\nabla\mathbf{v} = -\nabla p + \Delta\mathbf{v} - \frac{Ra}{\mathrm{Pr}}(T + \mathbf{C})\boldsymbol{\gamma} \qquad (1)$$

$$\frac{\partial T}{\partial t} + \mathbf{v}\cdot\nabla T = \frac{1}{\mathrm{Pr}}\Delta T \qquad (2)$$

$$\frac{\partial \mathbf{C}}{\partial t} + \mathbf{v}\cdot\nabla\mathbf{C} = SC(\Delta\mathbf{C} + \boldsymbol{\psi}\Delta T) \qquad (3)$$

$$\mathrm{div}\ \mathbf{v} = 0 \qquad (4)$$

Equations (1)-(4) contain the following parameters: $\mathrm{Pr} = \nu/\chi$, $Ra = g\beta_T\,\Delta T\,h^3/(\nu\chi)$, $SC_{ij} = -(\beta_i/\beta_j)Sc_{ij}^{-1}$, $Sc_{ij} = \nu/D_{ij}$, $\psi = -(\beta_i/\beta_T)(D^{-1})_{ij}D_{Tj}$, $\Psi = \sum_i \psi_i$. The following scales are used: h for the length, ν/h for the velocity, h^2/ν for the time, $\rho_0\nu^2/h^2$ for the pressure, ΔT for the temperature and $\beta_T\Delta T B^{-1}$ for the concentration. Here $\mathbf{v}, p, T, \mathbf{C}$ are the dimensionless velocity, pressure temperature and vector of concentrations, ν is the kinematic viscosity, χ is the thermal diffusivity, D is the diffusion matrix, $\mathbf{D_T}$ is the vector of thermal diffusion coefficients, β_T, β_i are the thermal expansion and solutal expansion coefficients, $\boldsymbol{\gamma}$ is the unit vector along the gravity, g is the gravity acceleration.

The boundary conditions are

$$z = 0,1:\ \mathbf{v} = 0,\ \mathrm{T} = z,\ \frac{\partial \mathbf{C}}{\partial z} + \boldsymbol{\psi}\frac{\partial T}{\partial z} = 0 \qquad (5)$$

$$x = 0,3:\ \mathbf{v} = 0,\ \mathrm{T} = z,\ \frac{\partial \mathbf{C}}{\partial x} + \boldsymbol{\psi}\frac{\partial T}{\partial x} = 0 \qquad (6)$$

In the experiment the refractive index is measured which is described by the relation

$$\Delta n = \frac{\partial n}{\partial C_1}\Delta C_1 + \frac{\partial n}{\partial C_2}\Delta C_2 \qquad (7)$$

The values of $\partial n/\partial C_1$ and $\partial n/\partial C_2$ were measured in advance (Mialdun et al. 2018) for $\lambda = 670$ nm. ΔC_1 and ΔC_2 are the differences of concentrations between the top and bottom walls in the middle of the cavity, which should be determined from the experiments at two different wave lengths. The optical separation, that is the variation of refractive index between hot and cold walls is presented in Figure 1.

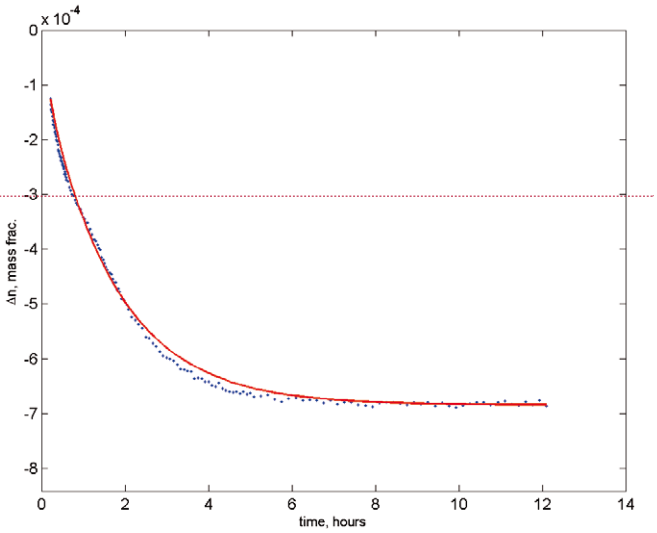

Figure 1: The refractive index variation between hot and cold walls measured in (Mialdun et al. 2018) for the mixture toluene (0.62) - methanol (0.31) - cyclohexane (0.07).

Numerical calculations

The numerical calculations were performed using the finite difference method in the stream function - vorticity formulation. In (Mialdun et al. 2018) two data sets are presented which are measured by two different research groups. In both cases the value of the net separation ratio is close to zero but in the first case it is positive ($\Psi > 0$) and in the second case negative ($\Psi < 0$). It the present paper we consider these two cases and also the case with average value of the net separation ratio. We performed the calculations for three types of initial temperature distribution: the linear vertical temperature profile, uniform temperature equal to the mean value between the top and

bottom and uniform temperature equal to the temperature of cold bottom. The types of the regimes observed in the calculations for all above cases are briefly described in the Table 1.

Table 1: .Identified regimes for different initial distributions and separation ratios.

	RAS, $\Psi > 0$	ULB, $\Psi > 0$	Average, $\Psi > 0$
T_{linea}	Stability 1	Instability 4	Stability 1
T_{mea}	Stability 1	Instability 4	Stability 1
T_{cold}	Stability 1	Instability 3	Stability 2

The stable regime 1 was observed in a ternary mixture with positive net separation ratio in five cases presented in Table 1. Temporal evolutions in all these cases are similar to each other and result in the motionless state with linear vertical temperature and concentration distributions. Slight difference was observed only at t<1.

The stable regime 2 occurs at the initially cold mixture with the net separation equal to the average value. Finally, this regime comes to the same state as Regime 1, but at very small time scales small fingers appear in the concentration fields, which are then transformed into a cat-eyes pattern that occupies the entire cavity.

The regime 3 is similar to the previous one, however “cat eyes” do not fade with time but transform into another regime which is unstable and we see single vortex global motion. The unstable regime 4 comes to the same state as regime 3 but much faster skipping the “cat eyes” stage.

Taking into account the data obtained in the numerical calculation we can conclude that regime 1 corresponds to the data from the experiment. In Fig. 2 the evolution of the refractive index with. time is plotted for this case. The refractive index is calculated using the same relation (7). This case is in a good agreement with the experimental data shown in Fig.1.

Conclusions

The evolution of DCMIX-2 ternary system with the Soret effect has been studied for different initial distributions of the temperature inside the closed cell.

Three different values of the net separation ratio, although small but of different signs, were examined for all initial thermal conditions. Two types of evolution were found for $\Psi > 0$, both types lead to the steady state with linear temperature and concentration gradients. The concentration difference in this state corresponds to the value for purely diffusive (convectionless) transient process. Two types of evolution were found for $\Psi < 0$ depending on the initial thermal conditions. Both types demonstrate the development of instability. Due to development of convection, the concentration difference in steady state is much smaller than that for purely diffusive transient process.

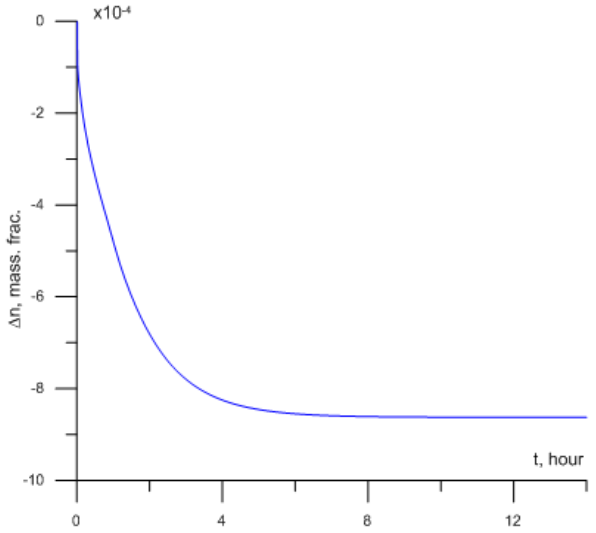

Figure 2: The refractive index variation between hot and cold walls obtained in the direct numerical calculation.

Acknowledgements

This work was performed in the frame of DCMIX project (ESA-Roscosmos) and supported by FGUP TSNIIMASH. VS acknowledges support of this work by the PRODEX program of the Belgian Federal Science Policy Office.

References

A. Mialdun, I. Ryzhkov, O. Khlybov, T. Lyubimova, and V. Shevtsova, Measurement of Soret coefficients in a ternary mixture of toluene-methanol-cyclohexane in convection-free environment, J. Chem. Physics 148, 044506

Oral 127

Diffusion and Soret coefficients measurement of the triethylene glycol and water binary mixture by dynamic Shadowgraphy

A.T. Ndjaka[1], M. Burtin[1], P. Fruton[1], L. García-Fernández[1,2], F. Croccolo[1] and H. Bataller[1]

[1]Laboratoire des Fluides Complexes et leurs Réservoirs – IPRA, UMR5150, E2S-Univ Pau & Pays Adour/CNRS/Total, 1 Allée du Parc Montaury, 64600 Anglet, France,
[2]Centre National d'Études Spatiales (CNES), 2 Place Maurice Quentin, 75001 Paris, France
ange-tatiana.ndjaka@univ-pau.fr

Introduction

Transport phenomena occur in any multicomponent fluid present in the nature and/or the industry subjected to non-equilibrium conditions. Its comprehension is of great interest for many applications. Due to experemintal and mathematical difficulties, only a limited number of diffusion and thermodiffusion coefficients of ternaries are so far available and often, measurements by different techniques do not agree. To overcome these problems, the European Space Agency (ESA) is carrying on the DCMIX (Diffusion and thermodiffusion Coefficients measurements in ternary MIXtures) project on board the International Space Station. DCMIX is organized into four measurements campaigns, each focusing on particular ternary systems. The third campaign, DCMIX3, which focused on aqueous systems with water/ethanol/triethylene-glycol, was flown in 2016 and is coordinated by the team of Pr Werner Köhler (Triller et al. 2018, 2019) at the University of Bayreuth (DE). In order to predict the limit behaviors of the ternaries, it is also necessary to know the values of the diffusion and Soret coefficients of the associated binaries. This work aims at determining the transport coefficients of one binary triethylene glycol (TEG) and water mixture.

Our group has developed a shadowgraph set-up to measure the transport coefficients by analyzing the non-equilibrium fluctuations (NEFs) of binary and ternary mixtures (Croccolo et al. 2012, Giraudet et al. 2014, Bataller et al. 2017). Until present, essentially non-associative mixtures were studied. In order to calibrate and develop a measurement methodology for the associative mixture, the 30 wt% TEG concentration was first studied and the obtained results are presented in this communication.

Shadowgraph experiment

The NEFs of the temperature and concentration are experimentally studied by analysis of the light scattered by the NEFs of the refractive index. The studied mixture is composed by 30 wt% of TEG (Sigma-Aldrich, T59455-1L, 99%) and 70 wt% of ultra pure water. Mixture is injected in a thermodiffusion cell placed in a monochromatic shadowgraph set-up, described elsewhere (Croccolo et al. 2012). The sample is sandwiched by two sapphire windows separated by a vertical distance L=2 mm and illuminated by a super-luminous diode at wavelength 675 nm. The sensor placed at about 10 cm from the cell is a scientific-CMOS camera. Three thermodiffusion experiments are carried out at mean temperatures of 20, 25 and 30°C by imposing a temperature difference of 20 K. Series of 10000 images of 1024x1024 pixels are recorded at 20 Hz. The Differential Dynamic Algorithm analysis (Cerchiari et al. 2012) is performed for each series of images, resulting in the corresponding Structure Functions (SF), theoretically given by:

$$\mathrm{SF} = 2\{T(q)S(q)[1 - I_{SF}(q,dt)] + B(q)\} \quad (1)$$

where $T(q)$ is the shadowgraph optical transfer function, $S(q)$ is the static power spectrum, $I_{SF}(q,dt)$ is the intermediate scattering function and $B(q)$ is the background.

Data analysis

The analysis was carried out for wave numbers $50\ cm^{-1} < q < 400\ cm^{-1}$. Assuming that the relaxation modes of the fluctuations are decoupled, the I_{SF} used to analyze the experimental SF is defined as a sum of two exponential decays:

$$I_{SF}(q,dt) = a\exp[-dt/\tau_T(q)] + (1-a)\exp[-dt/\tau_S(q)] \quad (2)$$

where a is the normalized amplitude and $\tau_T(q)$ and $\tau_S(q)$ are the relaxation times of the thermal and solutal NEFs, respectively.

The fitting of the calculated SF with Eqs. 1 and 2 allows to obtaine the values of the relaxations times. The fitting of the massic mode is thereafter done with the following equation which takes into account the confinement effect:

$$\tau_s(q) = \frac{1}{Dq^2\left[1+\left(\frac{q_S^*}{q}\right)^4\right]} \times \left[1+\frac{\left(\frac{q_S^*}{q}\right)^4}{\left(1+\frac{\left(q_S^* L\right)^4}{720}\right)}\right] \quad (3)$$

where D is the diffusion coefficient and q_S^* is the solutal roll-off wave number. This one is given by:

$$q_S^* = \left(\frac{\beta g \overrightarrow{\nabla c}}{\nu D}\right)^{1/4} \quad (4)$$

where β is the mass expansion coefficient, g the gravity acceleration and ν the kinematic viscosity.

At the steady state the separation of the components in the mixture is related to the Soret coefficient which is obtained from Eq. 4:

$$S_T = \frac{q_S^{*4}\nu DL}{\beta g c_0(1-c_0)\Delta T} \quad (5)$$

where c_0 is the equilibrium concentration of the denser component.

For the three temperatures, the viscosity has been measured by a capillary viscometer (Ubbelohde Schott). β is indirectly determined after measuring at the three temperatures the mixture density at different concentrations around c_0 =0.3 by using a density meter (Anton Paar DMA 5000).

Results

In Figure 1 we report the values of the diffusion and Soret coefficients as a function of temperature.

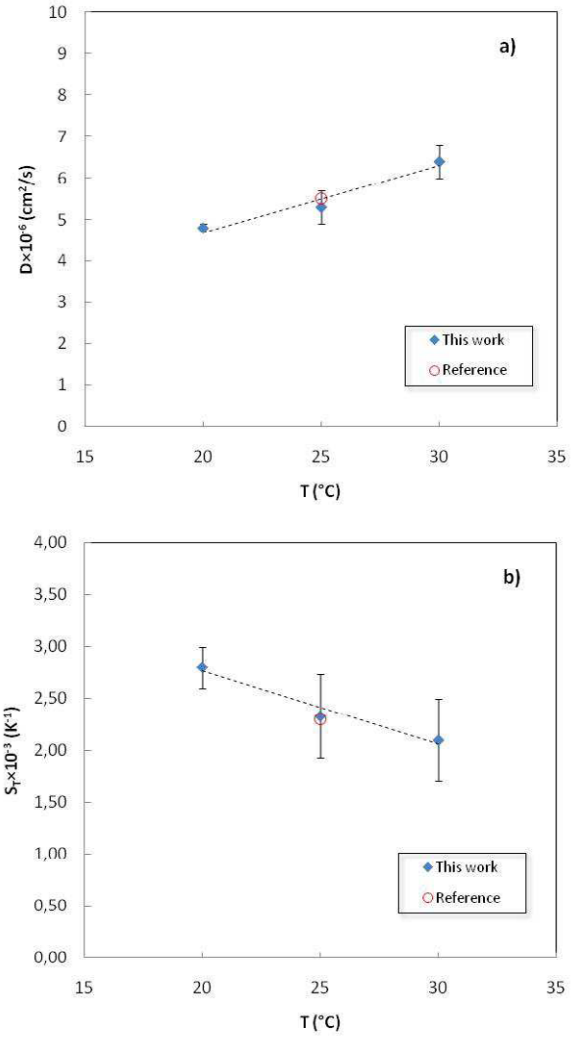

Figure 1: Diffusion a) and Soret b) coefficients as a function of the temperature of the 30 wt% TEG and 70 wt% water binary mixture.

Furthermore, the reference values at 25 ° C are reported (Legros et al. 2015, Bauer 2015). Our measurements are in good agreement. A linear increase of the diffusion coefficient as a function of the temperature is consistent with a decrease of the viscosity, as a function of temperature. The Soret coefficients present an opposite tendency.

Conclusions

In order to complete the databases of the binaries associated to the ternary mixture of water/ethanol/triethylene glycol involved in the DCMIX project, we proceeded to the measurement of the diffusion and Soret coefficients of the triethylene glycol/water mixture. For that, we analyzed the decay times of the concentration NEFs in a thermodiffusion experiment by Shadowgraphy. In order to develop a measurement methodology, the 30 wt% triethylene glycol concentration was first studied. Both coefficients are obtained at the same time. We estimate that the accuracy on the diffusion coefficient is about 2%, while the accuracy on the Soret coefficient is of the order of 10%. A preliminary study indicates an increase of the diffusion coefficient with temperature, while the Soret coefficient decreases. Future work will focus on other compositions of the same mixture, mainly those for which the Soret coefficient is negative.

Acknowledgements

We acknowledge financial support from the Centre National d'Etudes Spatiales (CNES) and from the funding partners of the Industrial Chair CO2ES: E2S-UPPA, TOTAL, CNES and BRGM. L. García-Fernández gratefully acknowledges the CNES for the post-doctoral research grant.

References

C. Bauer, Transportkoeffizienten des ternären DCMIX-3-Systems Wasser/Ethanol/Triethylenglykol längs des binären Randes Triethylenglykol/Wasser, Bachelor thesis, University of Bayreuth (2015)

C. Giraudet, H. Bataller, F. Croccolo, High-pressure mass transport properties by dynamic near field scattering of non-equilibrium fluctuations, *Eur. Phys. J. E* 37 (2014) 107.

F. Croccolo, H. Bataller, F. Scheffold, A light scattering study of non equilibrium fluctuations in liquid mixtures to measure the Soret and mass diffusion coefficient, *J. Chem. Phys*. 137 (2012) 234202.

G. Cerchiari, F. Croccolo, F. Cardinaux, F. Scheffold, Note: Quasi-real-time analysis of dynamic near field scattering data using a graphics processing unit, *Rev. Sci. Instrum*. 83 (2012) 106101.

H. Bataller, T. Triller, B. Pur, W. Köhler, J. M. Ortiz de Zarate, F. Croccolo, Dynamic analysis of the light scattered by the non-equilibrium fluctuations of a ternary mixture of polystyrene-toluene-n-hexane, *Eur. Phys. J. E* 40 (2017) 35.

J. Legros et al., Investigation of Fickian diffusion in the ternary mixtures of water-ethanol-triethylene glycol and its binary pairs, Phys. Chem. Chem. Phys. 17 (2015) 27713

T. Triller et al., Thermodiffusion in Ternary mixtures of water/ethanol/triethylene glycol: First report on the DCMIX3-experiments performed on the International Space Station, *Microgravity Sci. Technol.* 30 (2018) 295-308.

T. Triller et al., The Soret effect in ternary mixture of water+ethanol+triethylene glycol of equal mass fractions: ground and microgravity experiments, *Eur. Phys. J. E* 42 (2019) 27.

Oral 128

Spaceflight-Associated Alterations in Drug Metabolism Gene Expression: Implications for Personalized Medicine

V. E. Wotring

Center for Space Medicine and Department of Pharmacology and Chemical Biology, Baylor College of Medicine, Houston TX, USA

Introduction

The spaceflight environment has been shown to affect mammalian physiology in nearly every system studied. Certain systems demonstrate relatively acute negative changes and were the focus of study in the earlier days of spaceflight missions (loss of bone mineral density, atrophy of leg and trunk muscles, neurovestibular adaptation to microgravity). With upcoming exploration missions of up to 3 years in duration, it is prudent to expand physiological research to include the study of physiological systems that might experience chronic effects associated with spaceflight. The liver is the seat of much metabolism of xenobiotics. Despite its importance to overall health, its function in the spaceflight environment has not been comprehensively studied. Changes in liver function have been noted in animals after spaceflight including: increased hepatocyte size1, decreased total P450 enzyme activity, decrease in activity of 3-hydroxy-3-methylglutaryl-CoA reductase, the rate-limiting enzyme of steroid biosynthesis, and decrease in the amount of the liver enzymes catalase and glutathione reductase (both involved in antioxidant activity), as well as GSH sulfur-transferase, a Phase II drug-metabolizing enzyme.

Individually, the relevance of each of these results for future astronauts cannot be determined. However, taken together, these results suggest potential for alterations to liver during spaceflight that, although the experimental animals above were reported to be in satisfactory health, could develop into more serious conditions over the durations of longer missions.

Methods

Experimental design

This experiment was made possible through a joint tissue sharing experiment aboard shuttle mission STS-135. Experiment and procedures were approved by the NASA Ames Research Center (ARC) and Kennedy Space Center (KSC) institutional animal care and use committees. Female 9-11 week-old C57BL/6 mice were assigned to one of two groups (n=15 each): those that experienced spaceflight (FLT) and ground controls that remained on Earth in conditions similar to those in flight (CON). Mice were flown on the STS-135 mission that lifted off at 11:29 a.m. EDT on July 8th and landed at 5:57 a.m. on July 21st, 2011. The mission duration was 12 days, 18 hours, 28 minutes. Due to post-flight errors, some of the animals were not made available for tissue sharing, leaving the FLT group with n=7 and the CON with n=5.

Animals

Both groups of mice were housed in Animal Enclosure Modules (AEM), self-contained environment that controls lighting (14 lux on a 12 hour light/dark cycle), ventilation, food, water and waste management. The FLT AEMs were on the middeck of the shuttle where environmental dosimetry measured about 5 mGy radiation over the duration of the flight and temperature was set at 3-8°C above the environmental temperature. After landing, animals were euthanized and dissections completed within 8 hours. Livers were removed immediately and flash-frozen in liquid nitrogen. Ground control animals were sacrificed the next day on a time schedule matching the flight animals' sacrifice and handling. Frozen samples were hand-carried back to JSC on dry ice and stored at -80 until analysis.

RNA Protocol

Total RNA was extracted from frozen rat liver tissue using the Agilent RNA Miniprep kit (Santa Clara, CA) according to manufacturer's spin protocol for animal tissue. Briefly, rat liver tissue was homogenized and frozen (flash frozen in liquid nitrogen) in lysis buffer with mercaptoethanol added. Total RNA was purified from the samples with the spin column method (Agilent RNA miniprep kit; Santa Clara, CA) Samples were aliquoted and frozen at -80°C. Concentrations were then measured with Thermo Scientific NanoDrop 2000c (Thermo Fisher Scientific, Wilmington, DE). RNA samples that met the quality control standards (RIN $\geq$ 8) were reverse transcribed to cDNA (RT2 First Strand Kit, SABiosciences). First strand cDNA samples were aliquoted and stored at -80°C.

PCR Protocol

qRT-PCR was performed using a BioRad C1000 Thermal Cycler and commercially available gene expression arrays for the investigation of drug metabolism (SABiosciences Drug Metabolism Array PAMM-002Z). Change in expression was measured by relative mRNA concentration at the time of sacrifice determined by normalizing test gene expression to the mean expression of a set of genes empirically determined to be unaffected by treatment: hypoxanthine guanine phosphoribosyl transferase (Hprt), β-actin (b-Act), and glyceraldehyde-3-phosphate dehydrogenase (GAPDH). The ΔΔCt method was used for calculations.

Data analysis

There were 5 animals in the control group and 7 in the flight group. One liver sample from each animal was analyzed with qRT-PCR. For qPCR experiments, data were normalized to a set of reference genes (run on every plate), whose expression was not altered by any treatment (Hprt, b-Act, and GAPDH). All data are expressed as % change in gene expression normalized to reference gene expression (2 (-ΔCt), mean ±

SEM). The data presented are means of the samples ± SEM. Significance at $p < 0.05$ was determined by Student's T - test.

Results

Changes in gene expression were measured in 22 of the 84 drug metabolism genes tested (some detailed in Table 1). These included genes that code for cytochrome p450 enzymes, drug transporters, and enzymes involved in steroidogenesis as well as those involved in maintenance of reduction-oxidation homeostasis.

Table 1: Livers of flight animals exhibited altered gene expression compared to controls, expressed as fold-change.

Gene	Gene expression, Flight/Control
Abcb1a	1.95
Abcb1b	2.75
Adh5	2.04
Aldh1a1	1.78
Cyp11B2	1.79
Cyp2E1	1.87
Cyp19A1	1.86
Gstm3	-1.71
Pon1	1.5

Each of these results was significant at $p < 0.05$.

Exposure to the spaceflight environment includes elevated exposure to space radiation, microgravity, elevated carbon dioxide and other factors related to life in a closed system. This experiment, as with many spaceflight experiments, cannot determine which of these factors might be causal. It is notable that changes were detectable after only 12 days exposure to the spaceflight environament. Although this preliminary study did not include examination of all possible drug metabolic genes, one of the most strongly affected genes, Abcb1b, codes for the drug transporter glycoprotein, which eliminates ISS medications tobramycin, glycopyrrolate, hydromorphone and ceftriaxone (Stingl, 2015).

Conclusions

In the livers of mice exposed to the spaceflight environment for 12 days, there were measurable changes in gene expression. One of the most important drug transporters (Abcb1b) exhibited almost 3-fold increase in gene expression. Other genes that code for drug metabolizing enzymes (21 of 84 tested) exhibited significant changes. This preliminary result highlights the possibility of altered pharmacokinetics during spaceflight missions, which could affect treatments given to astronauts. Further study in humans is warranted, particularly with respect to those enzymes responsible for metabolism of medications used on spaceflight missions.

Acknowledgements

Access to excess liver tissues from control mice on the STS-135 mission was graciously provided by the Amgen Corporation.

References

Stingl JC, Welker S, Hartmann G, Damann V, Gerzer R. Where Failure Is Not an Option -Personalized Medicine in Astronauts. PLoS One. 2015 Oct 21;10(10).

Oral 129

Preliminary analysis of Diffusion Coefficient Measurements in ternary mIXtures 4 (DCMIX4) experiment on-board the International Space Station

F. Croccolo[1], H. Bataller [1], M. M. Bou-Ali[2], M. Braibanti[3], A. Errarte[2], J.M. Ezquerro[4], J.J. Fernández[4], Yu. Gaponenko[5], L. García-Fernández[1,6], A. Mialdun[5], J. Rodríguez[4] and V. Shevtsova [5]

[1]Laboratoire des Fluides Complexes et leurs Réservoirs (LFCR) – IPRA, UMR5150, E2S-Univ Pau & Pays Adour/CNRS/Total, 1 Allée du Parc Montaury, 64600 Anglet, France,
[2]Mechanical and Manufacturing Department, Mondragon Goi Eskola Politeknikoa, Loramendi 4, Apdo. 23, 20500 Mondragon, Spain,
[3]European Space Agency (ESA), ESTEC, Noordwijk, The Netherlands,
[4]E-USOC, Ciencias y Operaciones Aeroespaciales, Center for Computational Simulation, DAVE, ETSIAE, Universidad Politécnica de Madrid, Plaza de Cardenal Cisneros, 3, 28040, Madrid, Spain,
[5]Microgravity Research Center (MRC), CP 165/62, Université libre de Bruxelles (ULB), 50, Ave. F.D. Roosevelt, B-1050 Brussels, Belgium,
[6]Centre National d'Études Spatiales (CNES), 2 Place Maurice Quentin, 75001 Paris, France.
fabrizio.croccolo@univ-pau.fr

Introduction

In the frame of the Diffusion Coefficient Measurements in ternary mIXtures (DCMIX) project, thermodiffusion experiments are conducted on the International Space Station (ISS) by means of the Selectable Optical Diagnostics Instrument (SODI), which is on orbit since 2009. We describe here the results of preliminary analysis of images downloaded during the execution of the latest campaign DCMIX4 in order to check the quality of the running experiments and adjust the experiment parameters for the following runs. The quick analysis of raw data showed that they are meaningful and allow obtaining the transport coefficients of examined ternary and binary mixtures.

Experiment description

The aim of the Diffusion Coefficient Measurements in ternary mIXtures" (DCMIX) series of experiments is to provide quantitative measurements of mass diffusion and Soret coefficients during thermodiffusion experiments on ternary mixtures performed in gravity-free environment.
Up to now DCMIX1, DCMIX2 and DCMIX3 campaigns have already been completed and results have been published mostly for the first series of experiments (Galand 2019).
DCMIX4 campaign involves quite different samples including: three samples with different concentrations of the ternary mixture toluene – methanol – cyclohexane for its fundamental interest as it exhibits a miscibility gap and a large region with negative Soret coefficients; a mixture of fullerene – tetrahydronaphthalene – toluene, as the first complex mixture including nanoparticles and the ternary mixture of polystyrene – toluene – cyclohexane as model sample because the two eigenvalues of its mass diffusion coefficient matrix are separated by a factor larger than 10; and finally a reference binary mixture of polystyrene – toluene. The present abstract will focus on the two samples including polystyrene that are coordinated by the team at the University of Pau (FR).
The DCMIX4 campaign has successfully run on the ISS between 12th December 2018 and 6th March 2019, but the disks containing the acquired images have currently not been physically downloaded yet. However, a limited set of images have been downloaded through telemetry during the execution of the experiment itself.

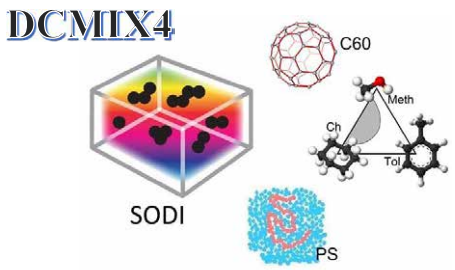

Figure 1: SODI-DCMIX4 logo.

As described in more details in the literature (Galand 2019), in DCMIX campaign each cell array contains five ternary samples and one binary reference sample. The two-colour interferometer is equipped with two lasers of wavelength λ_1 = 670nm (moving red, MR) and λ_2 = 935nm (moving near-infrared, MN), while the single colour setup only contains the red source (fixed red, FR). The recorded interferograms allow obtaining information about the refractive index change within the sample. By proper processing, one can separate the 'fast' thermal variation from the 'slow 'concentration' one. The latter can then, in principle, be divided into the two signals for the two independent component concentrations and provide information about the transport properties of the investigated system. This requires previous knowledge of the so-called optical contrast factors.

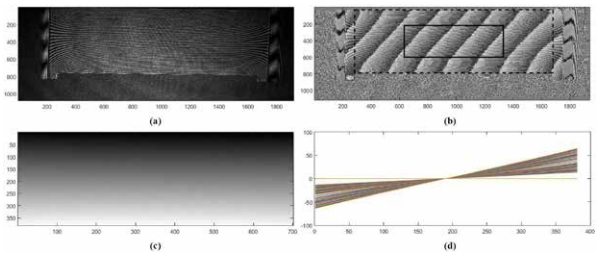

Figure 2: Capture of the software output. From top to bottom, from left to right; (a) 1 image of a stack of one run recorded with the MN laser, (b) rotated wrapped phase map, (c) unwrapped phase map, (d) phase profiles averaged over all the horizontal length of the ROI vs. height.

Data analysis

Apart from the qualitative analysis of raw optical phase of all the cells, we have also performed an exploratory quantitative analysis of selected cells and runs. In this analysis, we have focused exclusively on the Soret separation step of a run and evaluated only the optical signal related to the phase variations in the studied mixtures by means of the MN signal.

In Fig.3 we report the phase change at the borders of the ROI shown in Fig.2b as a continuous rectangle for cells #5 and #6.

The main points of such preliminary analysis are the following:

- all the experiments have been successfully performed with no bubble formation;
- the cell containing the ternary mixture (cell #5) shows an initial rapid decrease of the phase induced by the imposition of the thermal gradient and a succesfull and slower change of the phase induced by the change in the concentration profile within the investigated cell;
- in cell #5 two different kinetics can be clearly distinguished for the concentration signal with opposite directions. That is attributed to the negative Soret coefficient of the toluene – n-hexane component of the mixture. Two distinct mass diffusion coefficient eigenvalues can be determined;
- in cell #6 only one kinetic appears, as expected for a binary mixture.

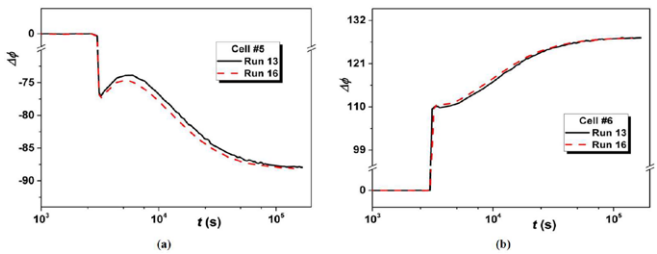

Figure 3: Log-lin plot of the phase difference between top and bottom of the ROI vs. time recorded with the MN laser for cells #5 and FR laser for cell #6.

Conclusions

We have presented preliminary evaluation of the results of the DCMIX4 experiment performed on-board the ISS as obtained by analyzing telemetry images downloaded during the first weeks of the on-orbit campaign. First, visual inspection of the images allowed us to check that no gas bubble was present in any sample cell. The telemetry images allowed us to assess qualitatively the performance of the experiments by evaluating the amplitude of the signal and the ability of the procedure to extract the relevant information. Moreover, from studying these images we could judge whether the time prescribed for the experiments was sufficient to reach the steady state of thermodiffusion process, necessary to get a full quantitative measurement of the transport coefficiants. Results related to cells #5 and #6 have been assessed as of sufficiently quality for future complete analysis when all images will be available by physically downloading data discs from the ISS to Earth.

Acknowledgements

The authors of the University of Pau kindly thank the financial support from the Centre National d'Etudes Spatiales (CNES) and from the funding partners of the Industrial Chair CO2ES: E2S-UPPA, TOTAL, CNES and BRGM. L. García-Fernández gratefully acknowledges the CNES for the post-doctoral research grant. The authors from ULB acknowledge the financial support from the PRODEX program of the Belgian Federal Science Policy Office. The authors from MU acknowledge support of FETRAFLU (2018-CIEN-000101-01) from Gipuzkoa Program for Science, ATNEMFLU (ESP2017-83544-C3-1-P) of the MINECO and the Research Group Program (IT1009-16) from the Basque Government. The authors are also very grateful to ESA and Roscosmos for providing the flight and operations opportunity.

References

Q. Galand, S. Van Vaerenbergh, W. Köhler, O. Khlybov, T. Lyubimova, A. Mialdun, I. Ryzhkov, V. Shevtsova, T. Triller, Results of the DCMIX1 Experiment: Experiment Description and Measurement of Soret Coefficients in Ternary Hydrocarbons Systems under Microgravity Conditions on ISS, *J. Chem. Phys.* (2019) submitted

A. Mialdun, H. Bataller, M. M. Bou-Ali, M. Braibanti, F. Croccolo, A. Errarte, J. M. Ezquerro, J.J. Fernández, Yu. Gaponenko, L. García-Fernández, J. Rodríguez, V. Shevtsova, Preliminary analysis of Diffusion Coefficient Measurements in ternary mIXtures 4 (DCMIX4) experiment on-board the International Space Station, Eur. Phys J. E, submitted

Oral 130

Comparison of wearable monitoring based on ballistocardiography with MRI to evaluate cardiovascular changes during two months of bed rest

J. Rabineau[1], A. Hossein[1], F. Landreani[2], R. Egoriti[2], E. G. Caiani[2], J. Tank[3], P. van de Borne[1], P.F. Migeotte[1]

[1]Université libre de Bruxelles, Brussels, Belgium, [2] Politecnico di Milano, Milan, Italy, [3] DLR (German Aerospace Center), Cologne, Germany;
Jeremy.Rabineau@ulb.ac.be

Introduction

Long duration head-down (-6°) bed-rest (HDBR) induces cardiovascular changes that simulate those occurring during space flights (Dorfman et al. 2007, Levine et al. 1997). On Earth, the gold standard to evaluate cardiac inotropic function is cardiac MRI, while ultrasound echocardiography is also used extensively. However, such technics are operationally difficult to use in space, either for material reasons or because they require a trained external operator to perform the measurement, or at least to assist the astronaut in the case of tele-operated echocardiography (Hamilton et al. 2011). In contrast, ballistocardiography (BCG) and seismocardiography (SCG) are much less well-known techniques for inotropic state assessment and that have the advantage to be non-invasive and easy to perform by non-medically trained operators. They are based on the measure of body displacement and/or accelerations consecutive to the cardiac contraction and blood flow through the major vessels. The development of tiny accelerometers based on micro-electro-mechanical-systems (MEMS) for the smartphone industry led to solutions that are more and more sensitive and affordable, which initiated a regain of interest or this field in the biomedical engineering community (Inan et al. 2015)

The effects of a 60-day HDBR on the cardiovascular system were assessed with Cardiovector, a non-invasive wearable system combining multi-dimensional (6D) BCG and SCG, measuring cardiac induced vibrations on the surface of the skin (Migeotte et al. 2014). Cardiac MRI protocols were conducted in parallel, with the hypothesis that the expected decrease in stroke volume (SV) and left ventricle (LV) mass would correspond to a decrease in the different BCG and SCG metrics. In addition, efficiency of the ESA-RSL JUMP countermeasure was evaluated.

Methods

24 healthy males were enrolled in the ESA-RSL-BR study (including one who discontinued at the very beginning for medical reason) and randomly assigned to either a training group, performing regular sessions of physical exercise (JUMP), or to a control group (CTRL). Participants of the JUMP group performed 48 training sessions during the 60 days of HDBR. The average time spent for each training session was 3 minutes, during which the participants performed squats and heel raises as well as countermovement jumps and repetitive hops. The training system was equipped to pull the participant toward their feet by the force generated by low pressure cylinders during the exercise (Kramer et al. 2017). Protocols were approved by the local ethical review boards and informed consents were obtained.

After a training session, measurements were conducted using the Cardiovector device during baseline data collection (BDC-4), as well as at day 5, 21, and 58 of HDBR (HDT5, HDT21, and HDT58, respectively), and during recovery, 1 and 4 days after the 60-day HDBR (R+1 and R+4, respectively). A controlled breathing protocol (4-, 6-, 8-, 10-second cycles) was imposed while recording 6D BCG (in the lumbar region) and dorsoventral SCG (at the apex) in parallel to ECG and plethysmography. Ensemble average was computed for all channels and respiratory protocols. The linear accelerations and angular velocities recorded were converted to kinetic energy signals. The integral of the linear and rotational kinetic energies transferred to the BCG sensor by cardiac activity during an average heartbeat provided KE_{Lin} and KE_{Rot} metrics, respectively. Here, only these two Cardiovector-based metrics will be analyzed and only for the 8-second breathing protocols.

Cardiac MRI protocols took place at BDC-4, HDT21, HDT58, and R+4. Blood velocity was integrated over the aortic lumen area to allow computation of SV, while ventricle short-axis images were used to compute LV mass.

Linear mixed-effects models' analysis was performed to compare data collected at BDC-4, HDT58, and R+4, which are the days when data was collected both with the MRI and Cardiovector protocols. p-values < 0.05 were considered statistically significant.

Results

After 58 days of HDBR, significant changes ($p < 0.05$) are seen in the CTRL group as compared to BDC-4. This is the case for SV (-22%), LV mass (-9%), BCG KE_{Lin} (-37%), and BCG KE_{Rot} (-26%) (see Figure 1 & 2). HDT58 vs. BDC-4 changes in the JUMP group are less important and significant only for SV (-12%), BCG KE_{Lin} (+14%), and BCG KE_{Rot} (-23%). Interestingly, the evolution of BCG KE_{Lin} seems opposed between the training and the control group and this is confirmed when looking at the other data points (see Figure 1). At R+4, the different metrics tend to go back to their baseline values in both groups, while LV mass (-7%) and BCG KE_{Lin} (-24%) in CTRL remained significantly lower.

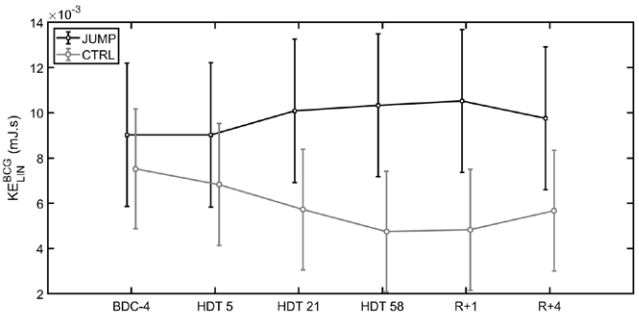

Figure 1: Evolution of BCG KE_{Lin} during the ESA-RSL-BR study. Black: JUMP group; Grey: CTRL group. KE_{Lin} corresponds to the integral over the whole heartbeat of the linear kinetic energy caused by cardiac activity and transmitted to the BCG sensor.

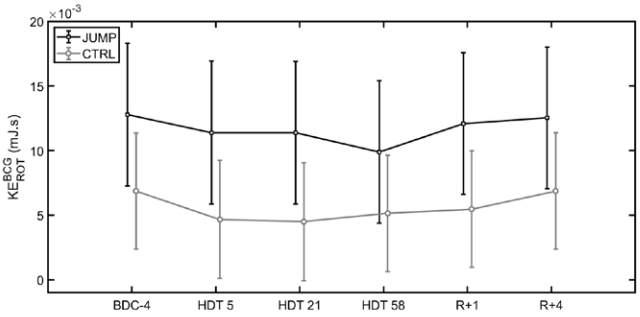

Figure 2: Evolution of BCG KE_{Rot} during the ESA-RSL-BR study. Black: JUMP group; Grey: CTRL group. KE_{Rot} corresponds to the integral over the whole heartbeat of the rotational kinetic energy caused by cardiac activity and transmitted to the BCG sensor.

Conclusions

This is the first study assessing the efficiency of multidimensional BCG as a marker of altered cardiovascular inotropic state together with cardiac MRI during a 60-day HDBR campaign. Consequences of cardiovascular deconditioning were observed with all these techniques, with enough sensitivity to differentiate the control and training groups. This study can be used as a validation for the ISS Cardiovector protocol and opens the path for such non-invasive wearable systems to be used for the follow-up of cardiovascular condition in planetary exploration, but also on Earth.

Acknowledgements

This research is supported by the Belgian Federal Science Policy Office via the European Space Agency PRODEX program.
J. Rabineau is supported by the F.R.S.-FNRS via a "mandat aspirant".
We thank the nurses, staff, and entire research team at DLR for their exceptional contribution to make this bed rest a real scientific success. We also thank the 23 outstanding participants who volunteered for this bed rest investigation.

References

T.A. Dorfman, B.D. Levine, T. Tillery, R.M. Peshock, J.L. Hastings, S.M. Schneider, B.R. Macias, G. Biolo, A.R. Hargens, Cardiac atrophy in bed rest following bed rest, *J Appl Physiol* 103 (2007) 8-16.

B.D. Levine, J.H. Zuckerman, J.A. Pawelczyk, Cardiac Atrophy After Bed-Rest Deconditioning, *Circulation* 96 (1997) 517-525.

D.R. Hamilton, A.E. Sargsyan, D.S. Martin, K.M. Garcia, S.L. Melton, A. Feiveson, S.A. Dulchavsky, On-Orbit Prospective Echocardiography on International Space Station Crew, *Echocardiography* 28 (2011) 491-501.

O.T. Inan, P.F. Migeotte, K.S. Park, M. Etemadi, K. Tavakolian, R. Casanella, J. Zanetti, J. Tank, I. Funtova, G.K. Prisk, M. Di Rienzo, Ballistocardiography and Seismocardiography: A Review of Recent Advances, *IEEE J Biomed Health Inform* 19 (2015) 1414-1427.

P.F. Migeotte, L. Lejeune, Q. Deliere, E. Caiani, C. Casellaot, J. Tank, I. Funtova, R. Baevsky, G.K. Prisk, P. van de Borne, Three dimensional ballistocardiogram and seismocardiogram: What do they have in common?, *Conf Proc IEEE Eng Med Biol Soc 2014* (2014) 6085-6088.

A. Kramer, A. Gollhofer, G. Armbrecht, D. Felsenberg, M. Gruber, How to prevent the detrimental effects of two months of bed-rest on muscle, bone and cardiovascular system: an RCT, *Sci Rep* 7 (2017) 13177.

Oral 132

Nature-Inspired, Multi-Functional Surface Coatings for Space Applications

Malica Schmidt[1, 2], Marcos Cruz[2], Marc-Olivier Coppens[1]

[1] CNIE, Department of Chemical Engineering, UCL, London, UK, [2] Bio-ID, Bartlett School of Architecture, UCL, London, UK
m.schmidt.17@ucl.ac.uk, m.cruz@ucl.ac.uk, m.coppens@ucl.ac.uk

Introduction

Air and water are available on Earth to survive and support life. The conditions in space, however, are extreme including low atmospheric pressure, low gravity, space debris, meteoroids, and ionizing radiation. Nevertheless, the goal for the indoor environment on the International Space Station (ISS) remains the same as on Earth: to provide comfort and a healthy quality of life. The environmental control and life-support system (ECLSS) is, among others, responsible for the absorption of humidity from cabin air, which is treated, purified, stored, and re-used (Kitmacher 2006).

Issues with life support system

However, efficiency could be improved, as only 70-93% of water is recyclable, i.e. 6000-9000 litres have to be resupplied from Earth every year, which costs between M$16-44. With the Deep Space Gateway (DSG) in cislunar space, water resupply will be more problematic by mid-2020 (ISECG 2018) as for plans to go to Moon and Mars, it will be required, to take all water and oxygen without the possibility to send additional supplies (Jernigan et al. 2018).

Additionally, astronauts on the ISS experience 0.5 Sv of ionizing radiation, consisting of solar particle events (SPE) containing low- to medium-energy protons and galactic cosmic rays (GCR) containing high energy protons (hydrogen nuclei), particles (helium nuclei), and high-energy charged nuclei (Thirsk et al. 2009). Beyond Earth's magnetic field, this can increase immensely due to potential solar flares. It is, therefore, becoming the biggest risk to astronauts' health (Chancellor et al. 2014), but, furthermore, threatens future bio-regenerative life-support systems (Moeller et al. 2007).

Some bacteria, however, are able to survive the harsh environments in space and the hampered immune system of astronauts reinforces the requirement to strictly control microbial contamination.

Furthermore, it is essential to monitor the microbial flora and reduce a variety of microorganisms or inhibit their growth to biofilm formations to minimize biofouling (Bruce et al. 2005).

Currently, neither water reclamation, nor radiation protection mechanisms or anti-bacterial properties are feasible for future missions to Moon, Mars, and beyond. Therefore, finding new approaches for regenerative life support through passive systems, is crucial.

Nature-inspired, multi-functional surface coating

We develop a nature-inspired (Coppens 2012), multi-functional surface coating to improve the existing ISS ECLSS and enhance the DSG ECLSS by taking advantage of the humidity produced by astronauts' indoors activities. The surface coating consists of cicada wing, human and month eye inspired hydrophobic microstructures that are able to transport humidity passively through the structures and guide the collected water to microchannels (Figure 1).

The microstructures are fabricated by additive manufacturing techniques and experiments with water droplets including and excluding fluorescence as well as relative humidity tests were carried out. After discharging water droplets onto the fabricated surface (Figure 2a), the surface shows hydrophobic adhesive behaviour (Figure 2b). After several seconds, the droplets sink into the structures (Figure 2c), which indicates passive water transport through the narrow neck into the vase-shaped structure via capillary action. Similar promising results are shown with fluorescence tests (Figure 3a-c). At 5% of relative humidity (Figure 4a), there was no sign of condensation formed near the vases. By increasing the humidity to 95% (Figure 4b), humidity formed first in the close proximity outside of the microstructures.

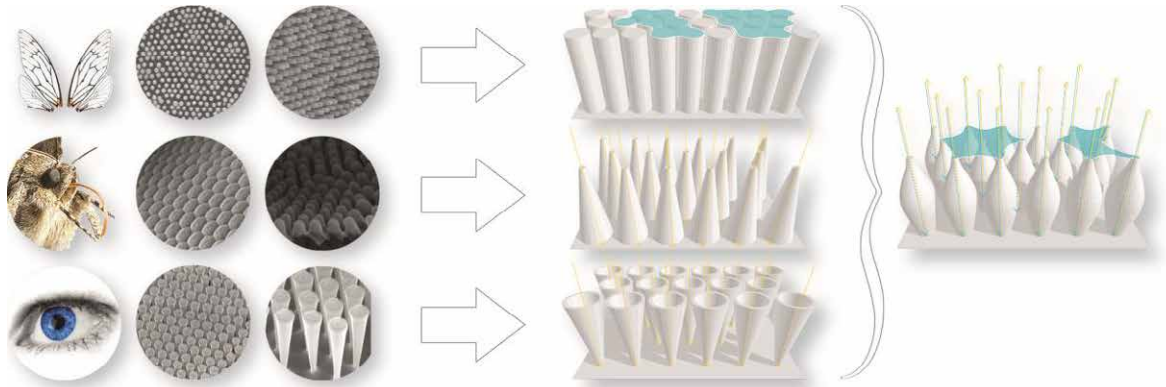

Figure 1: From cicada wings, moth and human eyes as natural inspiration to concept and design of the multifunctional microstructures.

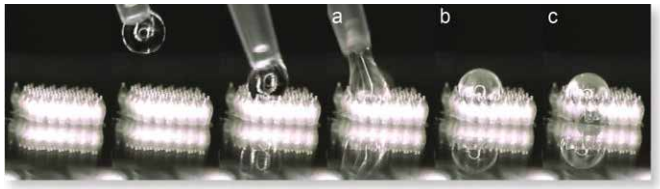

Figure 2: Water droplet experiments under gravity conditions.

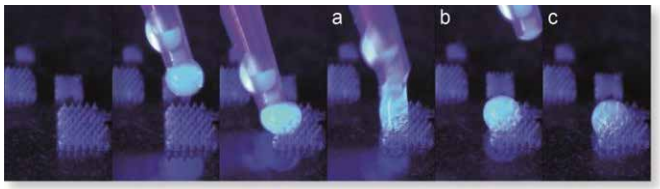

Figure 3: Fluorescent water droplet experiments under gravity conditions.

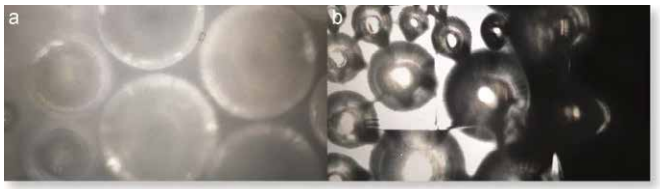

Figure 4: Relative humidity experiments under gravity conditions.

After ground-based experiments, it can be estimated that the microstructures' increase in performance under microgravity conditions as capillary-dominated systems are supported in space and several of the existing fluid management systems on the ISS rely critically on this advantage (Weislogel et al. 2009).

Additionally, water and polymer, such as the proposed IP-S, are effective shielding mechanism against ionozing radiation as hydrogen stops protons in SPE, fragments heavy ions in GCR, and slows down neutrons formed as secondaries originating from contact of SPE and GCR with the ISS (Thibeault 2012). Furthermore, the structures could absorb or repel bacteria due to the self-cleaning and anti-microbial properties of the natural inspiration of cicada wings.

Conclusions

This project improves the understanding on passive water systems and humidity absorption in space, which leads to a better use of water resources and minimizes transport costs for water. It contributes to a better understanding of life comfort and health for astronauts such as room quality, anti-bacterial properties, and shielding of ionizing radiation. Due to its passivity, less energy resources need to be consumed for the space industry, which leads to a greener environment, the reduction of CO_2 and greenhouse gases, and, therefore, to a positive contribution towards the issues of climate change.

Reclaimable water is crucial for astronauts, but more importantly, for human survival on Earth. People around the world still lack access to water. This project could further help improving passive water collection in humid areas on Earth and the commercialization would benefit areas worldwide.

Acknowledgements

We gratefully acknowledge the support from the Engineering and Physical Sciences Research Council (EPSRC) via a Doctoral Training Partnerships (EP/R512400/1) with the project number 1926173. The authors thank R. Möller and the researchers at the Space Microbiology Research Group from the German Aerospace Centre (DLR) as well as A. Cowley from the European Space Agency (ESA) for technical support.

References

Kitmacher, G. Reference guide to the International Space Station. (2006).

International Space Exploration Coordination Group (ISECG). The Global Exploration Roadmap. 1–36 (2018).

Jernigan, M., Gatens, R., Joshi, J. & Perry, J. The Next Steps for Environmental Control and Life Support Systems Development for Deep Space Exploration. *48th Int. Conf. Environ. Syst.* 1–8 (2018).

Thirsk, R., Kuipers, A., Mukai, C. & Williams, D. The space-flight environment: the International Space Station and beyond. *Can. Med. Assoc. J.* **180,** 1216–1220 (2009).

Chancellor, J., Scott, G. & Sutton, J. Space Radiation: The Number One Risk to Astronaut Health beyond Low Earth Orbit. *Life* **4,** 491–510 (2014).

Moeller, R., Stackebrandt, E., Reitz, G., Berger, T., Rettberg, P., Doherty, A. J., Horneck, G. & Nicholson, W. L. Role of DNA Repair by Nonhomologous-End Joining in Bacillus subtilis Spore Resistance to Extreme Dryness, Mono- and Polychromatic UV, and Ionizing Radiation. *J. Bacteriol.* **189,** 3306 LP – 3311 (2007).

Bruce, R. J., Ott, C. M., Skuratov, V. M. & Pierson, D. L. Microbial Surveillance of Potable Water Sources of the International Space Station. *SAE Trans.* **114,** 283–292 (2005).

Coppens, M.-O. A nature-inspired approach to reactor and catalysis engineering. *Curr. Opin. Chem. Eng.* **1,** 281–289 (2012).

Weislogel, M. M., Jenson, R., Chen, Y., Collicott, S. H., Klatte, J. & Dreyer, M. The capillary flow experiments aboard the International Space Station: Status. *Acta Astronaut.* **65,** 861–869 (2009).

Thibeault, S. Radiation Shielding Materials Containing Hydrogen, Boron, and Nitrogen: Systematic Computational and Experimental Study. (2012).

Oral 133

Acoustic propulsion of metallic nano-cylinders: contribution of the local vertical acceleration from micro to hyper gravity

G. Dumy[1,2], X. Benoit-Gonin, M. Hoyos[1], J-L. Aider[2]

[1] PMMH Lab, ESPCI Paris, Paris Sciences et Lettres, Sorbonne Universités, Paris, France
[2] Université Paris Descartes, Paris, France
gabriel.dumy@espci.fr, mauricio.hoyos@espci.fr, jean-luc.aider@espci.fr

Introduction

Acoustic manipulation of microscopic objects can be performed using ultrasonic standing wave resonators and is called acoustophoresis. Provided that the wavelength λ of the acoustic field (generated in this case by a piezoelectric transducer) and that one of the cavity dimension h verify $\lambda = 2h$, an ultrasonic stationary wave can be generated between two opposite walls of said cavity. This field can have two effects on the cavity components: on scattering particles it will exert a net body force on scattering particles, and it will transfer momentum to the fluid filling the cavity resulting in a streaming flow. Thus, a suspension of microscopic objects submitted to such a field will see its constituents driven towards the pressure nodes (or antinodes depending on particles properties), where they can be trapped. The typical size of the objects that can be moved by acoustophoresis ranges usually from 500 nm to several tens of microns.

A surprising finding in ultrasonic manipulation of micron-sized objects is the auto-propulsion of metallic nano-cylinders when trapped in such a field (Wang et al. 2012): instead of aggregating like spherical particles, they start to swim while being confined in the pressure node of the acoustic field. The phenomenon has first been described with gold nano-cylinders (1µm long and 200nm in diameter). Trajectories ranging from straight lines to circular trajectories is observed. It is an intriguing phenomenon, since these quite small particles can propel up to hundredth of sizes per seconds (Ahmed et al 2016), while while moving into a Re ~ 10^{-4} flow (see Figure 2. d)). In addition, these particles can organize themselves in chains hundredth of microns long because of their rotation, showing interesting self-assembling properties. Moreover, the power levels used here are on par with medical echography devices, and these nanorods have proven to be active even in cells, showing interesting potential for bio-oriented applications. In the present work we investigated the contribution of the local acceleration of the gravity field on the orientation of the nano-cylinders, and its potential role in the propulsion of these objects.

Reorientation of metallic nano-cylinders under different vertical accelerations

Indeed, in standard gravity conditions, the aggregating position differs from the geometrical pressure node because of the equilibrium between the acoustic force and buoyant forces, which are non-negligible for metallic particles. As depicted on Figure 1, for metallic particles the aggregating plane is lower than the geometric center of the acoustic field. Calculations show that for gold microparticles with a typical acoustic energy of 10 to 100 J.m^{-3} under regular gravity, the levitation plane is 5 to 10% lower than the pressure node.

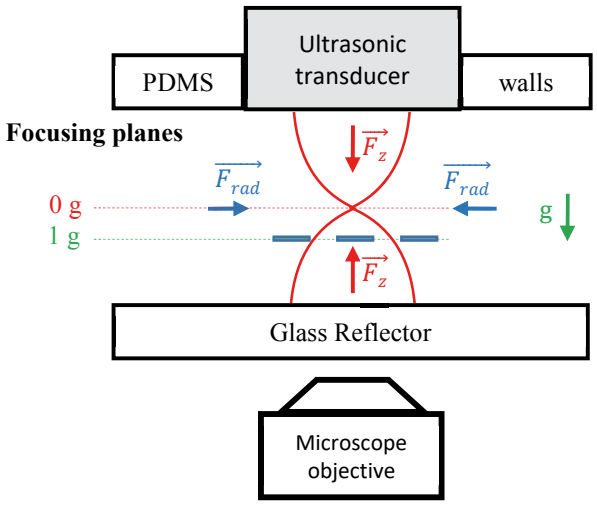

Figure 1: Sketch of the acoustic resonant cavity. The cavity height is 200 µm leading to an acoustic resonant frequency f_{ac} = 3.65 MHz. The cavity upper wall is directly the quarter-wave layer of a packaged transducer, embedded in PDMS walls. When the ultrasounds are turned on the micro-rods gather at the equilibrium focusing plane and form a swarming cluster. The equilibrium focusing plane is lower than the nodal plane because of the gravity. The distance from the nodal plane is larger for high-density micro-rods, like gold micro-rods. In micro-gravity, the micro-rods are expected to gather in the nodal plane.

Thus, we carried out a micro-gravity experiments campaign, to test the influence of the local vertical acceleration, and thus the effect of the vertical aggregating position on the behavior of our objects.

Figure 2 presents a striking feature of our findings. An aggregate of gold nano-cylinders is formed under a 3.65 MHz acoustic field, and its behavior during the 1g and 2g phases of the experiment is comparable to what we observe in the laboratory. However, as soon as we start the microgravity phase, its appearance changes. It becomes darker, which we interpreted as a reorientation of the nano-rods. Indeed, in every acoustic propulsion of these objects we know of, the long axis of the rods is always parallel to the observation plane, which leads to the visualization of bright nanorods. Since we mostly perform reflection observation experiments, these objects always appear brighter than the background. However, if one considers that the rod long axis is now perpendicular to the observation plane, then the effective are reflecting the light becomes much smaller, leading to a darker object.

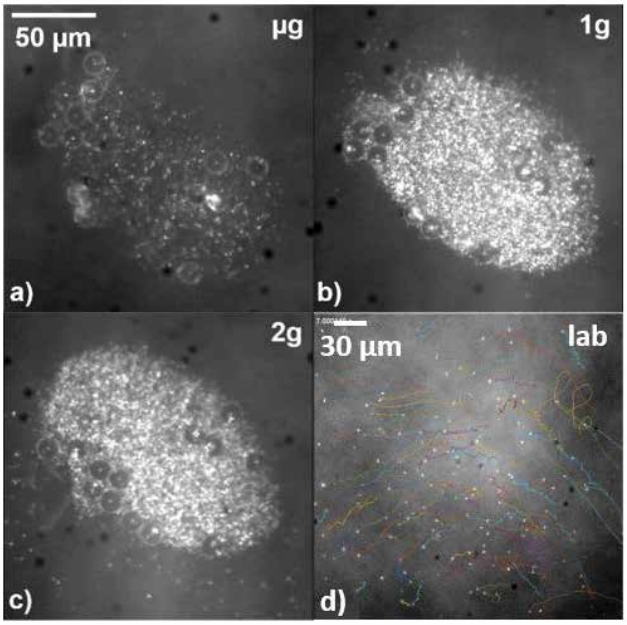

Figure 2: Visualizations of a large aggregate of self-propelled micro-rods in acoustic levitation in micro-gravity (a), 1 g (b) and hyper-gravity (c). The large circles observed in the aggregates are 15 micrometers polystyrene particles that were used to find the equilibrium positions of aggregates before the experiment, and that were not completely washed by the buffer. (d) In standard gravity conditions, the micro-rods are self-propelled by the ultrasounds once they have reached the acoustic levitation plane. Here, micro cylinders of pure gold (1µm length, ~200 nm radius) are propelled in a 3.6 MHz acoustic field, with an acoustic energy density of 25 $J.m^{-3}$. Tracks denoting their trajectories over a few seconds are plotted in color, propulsion velocities typically reach ~30 $\mu m.s^{-1}$.

A contribution of the transversal acoustic radiation force component?

Why should these objects change orientation when the vertical acceleration changes? An interesting additional observation, as denoted before, is that in every visualization we know of, the rods present their long axis parallel to the aggregation plane. Up to now, this observation has been taken for granted. Our experiments show that this is in fact not trivial, and can be explained only if they are forced to do so by the vertical component of the acoustic radiation force. As the vertical component of the acoustic force vanishes in the nodal plane of the resonator (Whitworth et al 1991, Tuziuti et al 1999), only the transverse one remains, which will then force the rods to reorient themselves along the observation axis.

The vertical position of aggregation for these high-density objects seems then to have a role to play in their acoustic response, a hypothesis that has not been much considered before. It also means that the orientation and propulsion is linked to the transverse component of the acoustic field, which is a hypothesis currently under investigation.

Conclusion

We compared laboratory and microgravity experiments, to correlate between the vertical position of the aggregate and the propulsion speed of the swimmers. We observed a different behavior of the cylinders in each case, which leads to reconsidering the classic hypothesis used to study self-acoustophoresis. This result suggests that the transverse component of the acoustic force plays an important role in the propulsion mechanism of these objects.

Acknowledgements

We would like to thank the foundation Bettencourt and the doctoral school FIRE for funding Gabriel Dumy's PhD.

References

W. Wang, L.A. Castro, M. Hoyos, T.E. Mallouk, Autonomous motion of metallic microrods propelled by ultrasound, *ACS Nano*, **6**, 7, 6122 (2012).

S. Ahmed, W. Wang, L. Bai, D.T. Gentekos, M. Hoyos, T.E. Mallouk, Density and Shape Effects in the Acoustic Propulsion of Bimetallic Nanorod Motors, *ACS Nano* **10**, 4, 4763 (2016).

G. Whitworth, M.A. Grundy, W.T. Coakley, Transport and harvesting of suspended particles using modulated ultrasound, *Ultrasonics*, **29**, 439 (1991).

T. Tuziuti, T. Kozuka, H. Mitome, Measurement of distribution of acoustic radiation force perpendicular to sound beam axis, *Japanese journal of applied physics*, **38**, 3297 (1999).

Oral 134

Stability of steady flow excited by inner core oscillation in a rotating cavity

V. Kozlov[1], S. Subbotin[1], M. Shiryaeva[1]

[1]PSHPU, Perm, Rusiia
kozlov@pspu.ru, subbotin_sv@pspu.ru, davydovapsu@gmail.com

Introduction

The structure of steady flow caused by inner core oscillation in a rotating spherical cavity with fluid and the stability of this flow is an actual hydrodynamic problem with geophysical and technological aspects. In case of free inner core, the axially symmetrical steady flow excited by oscillating core is accompanied by the core differential rotation (Kozlov et al. 2017). With increase of intensity, the flow loose stability. To define the role of the core differential rotation in flow structure and its stability we study the flow stability in case of nonrotating core. The differential rotation of the core is deactivated, for that one of the core poles is connected with the nearest cavity pole by a torsionally elastic fish-line. The inner core oscillation relative to the cavity is caused by external field, directed transversally to the rotation axis; thus, the frequency of circular oscillation is equal to the rotation frequency of the system. The comparative analysis shows that the differential rotation of inner core is not an essential condition for the appearance of instabilities. The mechanism for the instabilities is related with inflection points in azimuthal velocity profile of steady flow excited by the core oscillation relative to the cavity.

Experimental setup & technique

The spherical core of radius $R_1 = 1.77$ cm and density $\rho_C = 0.22$ g/cm^3 is located in the spherical cavity of radius $R_2 = 3.60$ cm with fluid. As a working fluid we use a water glycerin mixture, its kinematic viscosity varies. Rotation of the cavity is set by the stepper motor. The cavity rotation speed varies within the range $\Omega = 60 - 240$ s^{-1} and set with an accuracy 0.1 s^{-1}. During the experiment, the rotation speed is being changed gradually. At every step, the azimuthal flow structure is studied. For this, the azimuthal velocity fields (of fluid differential rotation) are examined by PIV method in different cross-sections, which are transversal to the axis of rotation.

Experimental results

The core oscillations in the cavity frame results in excitation of quasi-two-dimmensional steady flow (Fig.1). As follows from the theoretical analysis of the light-weight cylindrical core dynamics in filled with fluid cylinder which rotates around the horizontal axis (Kozlov and Kozlov 2007), the radial shift from the axis of rotation is determined by the parameter $\Gamma(1-\rho)$. Here $\Gamma = g/(\Omega^2 R_1)$ is dimensionless acceleration of the gravity field, $\rho = \rho_C/\rho_L$ is relative density of the core. It follows from the experiment with the free light-weight spherical core (Kozlov and Subbotin 2018) that the core shift from the axis of cavity rotation b/R_1 increases linearly with the parameter $\Gamma(1-\rho)$. As the intensity of steady flow is determined by the amplitude of the core oscillation, for its characteristic it is handier to use the parameter $\Gamma(1-\rho)$.

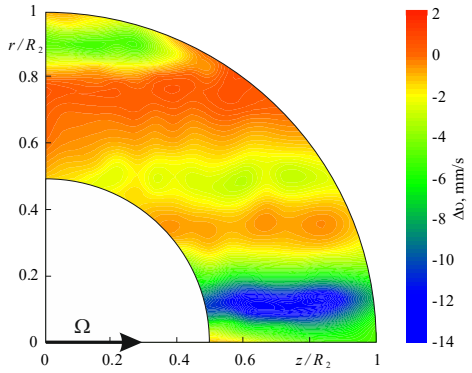

Figure 1: Distribution of the fluid azimuthal velocity $\Delta\upsilon_L$ in an axial section of the cavity at $\nu = 5.4$ cSt and $\Omega = 201$ s^{-1}. The color indicates the fluid velocity value.

With decrease of the cavity rotation speed Ω (with increase of the parameter $\Gamma(1-\rho)$) the differential rotation speed of fluid grows, that leads to instability of the axisymmetric flow. Initially a pair of vortices is generated near the cavity rotation axis, where one can observe the fastest differential rotation of fluid. The PIV measurements demonstrate that the vortices are crescent-shaped and move relative to the cavity in anticyclonic direction, herewith $\Delta\Omega_v \equiv (\Omega_v - \Omega) < 0$. Herein Ω_v is rotation velocity of the vortex system in the laboratory frame.

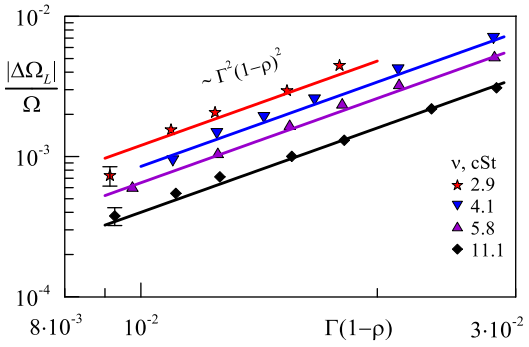

Figure 2: Velocity of retrograde differential rotation of the fluid depending on the dimensionless parameter $\Gamma(1-\rho)$ at different fluid viscosity values.

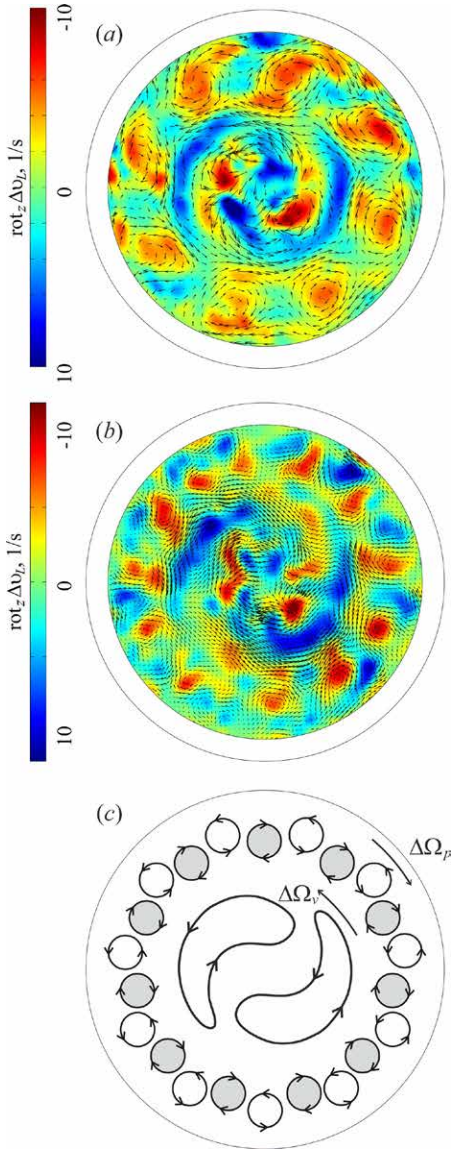

Figure 3: The field of the mean differential velocity of fluid at $\Omega = 157$ s^{-1} and $\nu = 3.3$ cSt (*a*) and $\nu = 2.5$ cSt (*b*). The color indicates z-component of the vorticity field (*z* axis is directed from us). On the section (*c*) the scheme of flow in the cavity reference frame, when the rolls system executes prograde drift (*b*), is presented.

With consequent increase of $\Gamma(1-\rho)$ at the distance $r/R_2 = 0.68$ we can see the appearance of the system of rolls extended along the axis of rotation (Fig. 3 *a*). The fluid in rolls is rotating in cyclonic direction, at this time the whole system drifts relative to the cavity in backward direction at the speed $\Delta\Omega_w \equiv (\Omega_w - \Omega) < 0$ (Ω_w is speed in the laboratory reference frame). The dimensionless velocity of azimuthal motion of the rolls system $\Delta\Omega_w / \Omega$ does not depend on the fluid viscosity and is fully specified by the wave number. The analysis of results indicates that in this case $\Delta\Omega_w / \Omega \sim m^{-2}$, it corresponds to the dispersion relation for Rossby waves. The same waves were observed in the case of steady flows, which are caused by oscillation of the free core (Kozlov et al. 2017). Besides, the generation of Rossby waves was followed by violation of the Taylor column axially symmetrical boundary. The column had the form of polygonal prism.

With further increase of the parameter $\Gamma(1-\rho)$ the system (Fig. 3 *b*) replaces the rolls system, which executes the retrograde motion. The azimuthal rotation speed of the new system exceeds the cavity rotation speed, $\Delta\Omega_P \equiv (\Omega_P - \Omega) > 0$ (Ω_p is the speed in the laboratory reference frame). The transition to such structure is followed by disruption of Rossby wave. According to the PIV measurements, the flow consists of pairs of rolls, which are rotating in alignment; besides the vortex system near the cavity center continues its rotation at speed $\Delta\Omega_v$ (Fig. 3 *c*).

Conclusions

We experimentally investigated the stability of steady flow in the rotating spherical cavity. The fluid motion in the cavity frame is caused by circular oscillation of the core in the absence of its own differential rotation relative to the cavity. The cavity is rotating around the horizontal axis, the oscillations of the core in the rotating system are caused by the gravity force and takes place at a rotation frequency.

It is shown that the loss of stability of axisymmetrical flow is related with the nonmonotonic radial distribution of azimuthal velocity, which is specified by a few inflection points. With increase of the flow intensity, one finds several instabilities. Initially near the axis of rotation the generation of the vortex system which performs a retrograde drift takes place. On further increase of the steady flow speed outside the core one finds an excitation of Rossby wave. Therein the excitation of Rossby wave does not affect the vortex system near the axis of rotation. Both structures exist independently of each other and rotate at different phase velocities. Finally, by further increase of the flow intensity one finds out another kind of instability. To replace the Rossby wave a system of rolls comes which performs a prograde rotation. The remarkable thing is that similar instabilities had been observed before in the experiments with free core, which executed differential rotation apart from oscillation.

One can conclude that the instability modes observed are not related with differential rotation of the core. They are defined by existence in the profile of inflection points, for which only the core oscillation relative to the cavity is responsible.

Acknowledgements

The research was supported by the Russian Science Foundation (project No. 18-71-10053).

References

V.G.Kozlov, N.V. Kozlov, S.V. Subbotin, Instabilities and pattern formation in rotating spherical cavity with oscillating inner core, *Eur. J. Mech. B-Fluid* 63 (2017) 39–46.

V.G.Kozlov, S.V. Subbotin, Steady flows generated by a core oscillating in a rotating spherical cavity, *J. Appl. Mech. Tech. Phys.* 59 (2018) 22–31.

V.G.Kozlov, N.V. Kozlov, Vibrational hydrodynamic gyroscope, *Dokl. Phys.* 52 (2007) 458–461.

Oral 135

Introduction of frame-invariant diffusion matrices in multi-component systems by rewriting Fick's law

J.M. Ortiz de Zárate

Facultad de Ciencias Físicas, Universidad Complutense de Madrid, Plaza de las Ciencias 1, 28040 Madrid, Spain.
jmortizz@ucm.es

A complete description of diffusion in multi-component systems, starting with ternaries, requires the introduction of cross-diffusion coefficients which, in general, are not zero (Bou-Ali et al, 2015). Hence, for isotropic systems, diffusion is quantified by a so-called diffusion matrix, of dimension $(N-1)\times(N-1)$, where N is the number of components of the mixture. An associated complication is that diffusion matrices are frame-dependent; meaning that the numerical value of the various diffusion coefficients depends on which representation is used to specify the composition of the mixture: either mole fractions, mass fractions or molarities (Taylor & Krishna, 1993). Notice that this complication does not exists in binary mixtures, where the single (scalar) diffusion coefficient is invariant upon change in the concentration representation.

Diffusion in multi-component mixtures is difficult to measure, and quite often measurements by different experimental groups or by different techniques do not agree (Bardow, 2007). On this regard, sometimes it is unclear which frame of reference is used for the theory supporting a given experimental technique (Ray & Leaist, 2010). In addition, experimentalist reporting diffusion matrices very seldom describe in which reference frame their measurements are performed (Grossmann & Winkelmann, 2009).

A similar frame-dependence issue also exists for thermodiffusion coefficients in ternary and multi-component mixtures. However, it has been recently illustrated (Ortiz de Zárate, 2019) how frame-independent thermodiffusion coefficients may be defined by adopting appropriate concentration matrices as prefctors. As a corollary of those developments, new formulas were obtained for swithching diffusion matrices between the mole center reference frame and the center-of-mass reference frame. The purpose of the current communication is to show how these developments (Ortiz de Zárate, 2019) can also be used to define frame-independent diffusion matrices at the cost of rewriting Fick's law.

Specifically, for a ternary mixture, one introduces matrices

$$\mathsf{X}=\begin{bmatrix} x_1(1-x_1) & -x_1x_2 \\ -x_1x_2 & x_2(1-x_2)\end{bmatrix}, \qquad (1)$$

and

$$\mathsf{W}=\begin{bmatrix} w_1(1-w_1) & -w_1w_2 \\ -w_1w_2 & w_2(1-w_2)\end{bmatrix}, \qquad (2)$$

where the x_i represents the concentrations of the mixture in mole fraction and w_i in mass fraction. Then, the proposal is to rewrite Fick's law such that in the mole frame of reference,

$$\begin{bmatrix}\mathbf{J}_1^{(x)}\\ \mathbf{J}_2^{(x)}\end{bmatrix}=-c_t\,\mathsf{X}\cdot\mathsf{D}\cdot\mathsf{X}^{-1}\cdot\begin{bmatrix}\nabla x_1\\ \nabla x_2\end{bmatrix}, \qquad (3)$$

while in the center of mass frame of reference:

$$\begin{bmatrix}\mathbf{J}_1^{(w)}\\ \mathbf{J}_2^{(w)}\end{bmatrix}=-\rho_t\,\mathsf{W}\cdot\mathsf{D}\cdot\mathsf{W}^{-1}\cdot\begin{bmatrix}\nabla w_1\\ \nabla w_2\end{bmatrix}. \qquad (3)$$

In these equations ρ_t and c_t represent, repectively, the total mass density of the mixture and the total mole density of the mixture, while $\mathbf{J}_i^{(x)}=c_t x_i(\mathbf{v}_i-\mathbf{v}_{\mathrm{M}})$ and $\mathbf{J}_i^{(w)}=\rho_t w_i(\mathbf{v}_i-\mathbf{v}_{\mathrm{CM}})$ are, in turn, the mole diffusion flux of component-i with respect to the center of mole velocity $\mathbf{v}_{\mathrm{M}}=\Sigma x_i\mathbf{v}_i$ and the mass diffusion flux of component-i with respect to the center of mass velocity $\mathbf{v}_{CM}=\Sigma w_i\mathbf{v}_i$.

The important thing about Eqs. (3) and (4) is that the new diffusion matrix, D, is frame-invariant meaning that both equations hold for exactly the same numerical coefficnts in D. This fact can be readily verified by using the formulas to switch between diffusion fluxes and concentrations gradients. Further note in Eqs. (3) and (4) that, for a binary mixture, when matrices reduce to scalars, the product is commutative and one recovers Fick's law in its usual form. Another advantage of Eqs. (3) and (4) is that most concentration dependence of diffusion is expected to be carried out by the concentration matrices, so that the new D is expected to depend only slightly on composition. Indeed, the cancelation of some diffusion coefficients in the binary limits of the concentration triangle (Gupta & Cooper, 1971) is automatically carried out by the concentration prefactors.

Although for clarity reasons the proposal has been explicitly presented here only for ternary mixtures, it can be generalized for arbitrary multicomponent mixtures. Diffusion is also often discussed in the volume frame of reference and corresponding molar concentrations. Whether the current proposal could be extended to the volume frame of reference, or not, still needs to be worked out in detail.

Acknowledgements

This research has been supported by grant ESP2017-83544-C3-2-P of the Spanish Agencia Estatal de Investigación. This research has been performed as contribution to the ESA Space Science projects DCMIX and Giant Fluctuations

References

A. Bardow, Fluid Phase Equilib. **251**, (2007) 121.

Bou-Ali, Ahadi, Alonso de Mezquia, Galand, Gebhardt, Khlybov, Köhler, Larrañaga, Legros, Lyubimova, Mialdun, Ryzhkov, Saghir, Shevtsova, Van Vaerenbergh Eur. Phys. J. E **38** (2015) 30.

T. Grossmann, J. Winkelmann, J. Chem. Eng. Data, **54**, (2009) 405–410.

P. K. Gupta, A. R. Cooper, Physica, **54** (1971) pp 39-59.

J. M. Ortiz de Zárate, Eur. Phys. J. E **42** (2019) 43.

G.B. Ray, D.G. Leaist, J. Chem. Eng. Data **55**, (2010) 1814.

R. Taylor, R. Krishna, *Multicomponent mass transfer*. Wiley, New York, 1993

26th European Low Gravity Research Association Biennial Symposium and General Assembly
14th International Conference on "Two-Phase Systems for Space and Ground Applications"
European Space Agency Topical Teams meetings
Granada (Spain), September 24-27, 2019

Oral 138

Nuts & Bolts: Bringing Science and Hardware Together for Spaceflight

Richard E. Edelmann[1], John Z. Kiss[2], Joshua P. Vandenbrink[2,3], Raúl Herranz[4], F. Javier Medina[4]

[1]Center for Advanced Microscopy & Imaging, Miami University, Oxford OH 45056 USA; [2]Department of Biology, University of North Carolina-Greensboro, Greensboro, NC 27402 USA; [3]School of Biological Sciences, Louisiana Tech University, Ruston, LA 71272 USA; [4]Centro de Investigaciones Biológicas (CSIC), Madrid, E28040, Spain
edelmare@miamioh.edu, jzkiss@uncg.edu, jpvdb@latech.edu, rherranz@cib.csic.es, fjmedina@cib.csic.es

Introduction

In performing science on Earth, assembling and setting up the equipment and hardware is generally straight forward and easy. Our laboratory shelves are full of equipment and supplies, and if needed there are global manufacturers, custom fabricators and even basement workshops. For setting up the experiments we have large laboratory spaces, electrical power, water and refrigeration readily available. Ultimately in the worst cases we have windows to open and vent experimental failures.

Unfortunately, this is not the scenario for spaceflight experimentation. Nearly all equipment and hardware needs to be custom manufactured, and everything fully tested including chemical reactivity, off gassing, durability, sharp edges, electromagnetic interference, and potential effects on human and biological safety. It has to have minimal mass, spatial volume, and resource utilization (Gases, water, electricity, heating, cooling, etc.). Further replaceable parts, repairs, and human intervention are very limited if available at all. It must noted that all of these requirements are external to the actual scientific experimental goals. Development, manufacture and testing can take years and cost millions of euros.

This leads to two results. First, control of the engineering variables and requirements means that hardware is designed for a specific scientific goal. Secondly, once designed, built, and tested the hardware must be used as much as possible to gain the highest benefits from the time and financial expenses. This creates a new "problem", once a scientific goal is successfully completed, the expensive hardware's specific task is also done. The "problem" becomes what new questions can be answered, and experiments performed with the same (or nearly the same) hardware?

Experimentation

The European Modular Cultivation System (EMCS), was designed with the specific goal of growing whole plants, in individual experimental chambers (EC's), under photosynthetic lighting, with variable centrifugal gravity, and collection of video and digital data. EMCS has arguably been one of the most successful life science research facilities on the International Space Station (ISS). The first experiments perform in this system were TROPI, which studied the interactions of light and gravity tropisms in *Arabidopsis* (Kiss et al. 2009, Millar et al. 2010). To accomplish this each original EC was subdivided into 5 "mini-cassette" growth chambers, with orthogonal, unidirectional illumination, dedicated hydration and gas exchange systems (Fig. 1). Re-purposing the original EMCS design goals in the very first experiment. These experiments were followed up in 2010 with TROPI-2, which used the same mini-cassette hardware but with improved ethylene scrubbing, new genotypes and gravity levels (Kiss et al. 2011 & 2012).

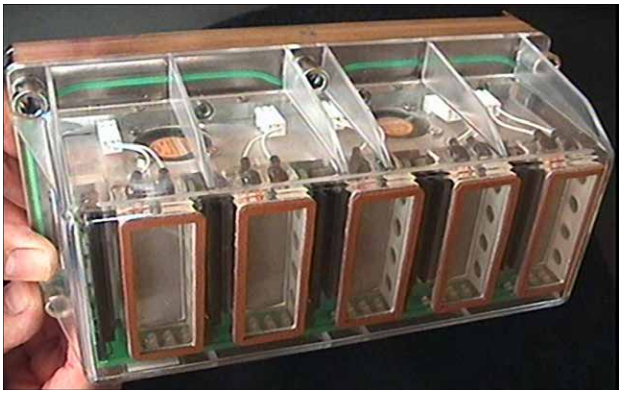

Figure 1 Re-envisionsing the design goals of EMCS by sub-dividing the EC into five "Mini-containers."

The TROPI experiments were followed up with the Seedling Growth (SG) series of experiments, which were part of an agreement between NASA and ESA. Data collection from the SG experiments were time-lapse images of the seedling growth responses to combinations of gravity and light stimulations, molecular data collection of cryogenically preserved samples, and chemical aldehyde fixative preservation of cellular and tissue for microscopic analysis. A number of hurdles needed to be accounted for in designing the experimentation, such as photostimulation light contamination between the rotating platforms within the EMCS. During SG-1 flight very unexpectedly, severe imaging issues arose. By 2013 the EMCS had been in orbit on ISS for nearly five years and the CCD cameras had been accumulating radiation damage. Due to the low intensity of the unidirectional SG mini-cassette lighting this presented a severe signal to noise problem. The solution was to use the EMCS infrared (IR) illumination. The IR illumination did not impact the photostimulation of the plants, but did provide superior imaging illumination (Fig 2).

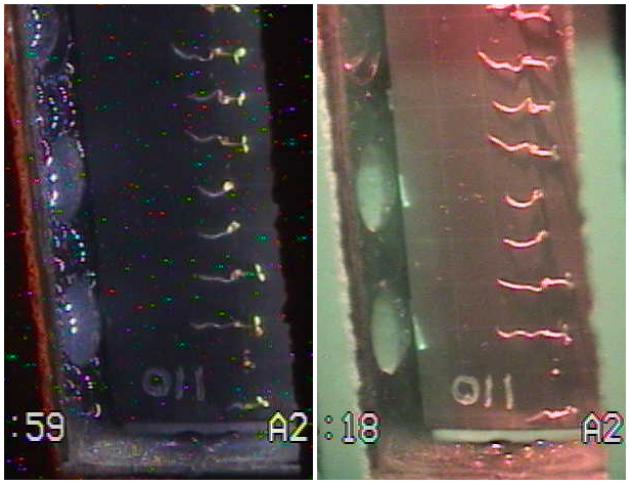

Figure 2 Comparison of EUE Illumination vs EMCS Infrared illumination. The reduced camera sensitivity was due to long term radiation damage to the CCD sensors.

The largest problem was the science requirment for aldehyde fixation needed to adequately preserve the tissue for microscopy analysis. One of the considerations of the original TROPI hardware design was that it would not used for liquid fixation at any point. The solution eventually required a combination of the development of a new hardware FixBox, as well as pre-flight and on-flight modificaitons for the mini cassttes. On orbit, the mini-cassettes were removed from the EC's, mounted into the FixBox hardware, sealed and flooded with fixative (Fig 3). Following further processing upon return to ground, this provided for imaging of the ultrastructural morphology of the microgravity grown samples fixed in microgravity (Valbuena et al. 2018).

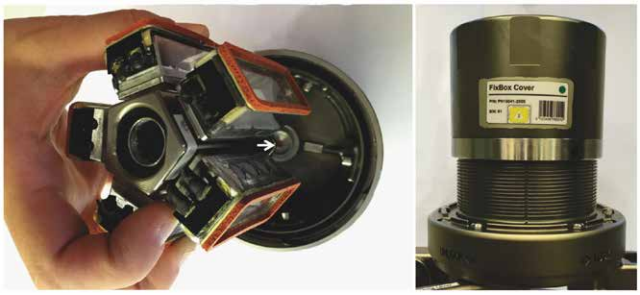

Figure 3 Mini-Cassettes mounted in FixBox hardware.

Conclusions

It is time costly, financially expensive and rare to have the opportunity to develop completely new spaceflight experimentation hardware for a unique and singular scientific goal. It is far more research and cost effective to take existing hardware and creatively conform the experiments to accomplish the science, but you may have to accept some compromises, and be willing to perform equally good science via a slightly different vision. The original TROPI hardware successfully completed 6 different sets of EMCS experiments on ISS over 10 years. These experiments were beyond those envisioned in the original EMCS design concepts. Further more we able successfully complete chemical fixation in SG-3, with the TROPI hardware, despite the decision in its original designs that the hardware would never to be used for such fixation.

Acknowledgements

Funding for this work was provided by grants NCC2-1200, and 80NSSC17K0546 from the National Aeronautics and Space Administration (NASA). We appreciate the fine support provided by several NASA centers (ARC, KSC, JSC, and MSFC) and European facilities (ESTEC and N-USOC). Thanks are due to NASA for continued financial support of our spaceflight research and to ESA for providing excellent research laboratories for space research.This contribution is part of the "Gravity Spotlight Team" activity with funding and support by ELGRA.

References

Kiss, JZ , P. Kumar, KDL Millar, RE Edelmann, MJ Correll. 2009. "Operations of a spaceflight experiment to investigate plant tropisms." J. Adv. Space Res. 44: 879-886. [DOI:10.1016/j.asr.2009.06.007]

Millar KDL, P Kumar, MJ Correll, JL Mullen, RP, Hangarter, RE Edelmann, JZ Kiss. 2010. "A Novel Phototropic Response to Red Light Is Revealed in Microgravity." New Phytologist 186 : 648–656 [DOI: 10.1111/j.1469-8137.2010.03211]

Kiss, JZ, KDL Millar, P Kumar, RE Edelmann, MJ Correll. 2011. "Improvements in the re-flight of spaceflight experiments on plant tropisms." Advances in Space Research 47: 545–552. [doi:10.1016/j.asr.2010.09.024]

Kiss JZ, KDL. Millar, R.E. Edelmann. 2012. "Phototropism of Arabidopsis thaliana in microgravity and fractional gravity on the International Space Station". Planta 236:635–645 [doi: 10.1007/s00425-012-1633-y].

Valbuena, MA, A Manzano , JP Vandenbrink, V Pereda-Loth, E Carnero-Diaz, RE Edelmann, JZ Kiss, R Herranz, FJ Medina. 2018. "The Combined Effects of Real or Simulated Microgravity and Red.light Photoactivation on Plant Root Meristematic Cells." Planta (2018) 248:691–704, [DOI: 10.1007/s00425-018-2930-x]

26th European Low Gravity Research Association Biennial Symposium and General Assembly
14th International Conference on "Two-Phase Systems for Space and Ground Applications"
European Space Agency Topical Teams meetings
Granada (Spain), September 24-27, 2019

Oral 139

Evaporation across a planar vapor-liquid interface and droplet coalescence investigated by large scale molecular dynamics simulation

M. Heinen[1], J. Vrabec[1]

[1]Technische Universität Berlin, Berlin, Germany;
vrabec@tu-berlin.de

Introduction

Evaporation of condensed matter and droplet coalescence are ubiquitous processes both in nature and in many engineering fields. To take advantage of those processes in technical applications, a good understanding is indispensable. Molecular Dynamics (MD) simulation is a valuable approach to explore the phenomena involved in such processes in full atomistic detail. Based on a molecular force field model that describes the interactions between two particles, no further assumptions are made so that the observed process itself can evolve naturally under the given boundary conditions. For this purpose, the MD code *ls1 mardyn* (Niethammer et al. 2014) was employed to investigate the evaporation process across a planar vapor-liquid interface and the coalescence of two droplets. For both studies the Lennard-Jones truncated and shifted fluid was used, which can be parameterized to mimic the thermophysical behavior of the noble gases and methane (Vrabec et al. 2006). This fluid has the advantage that particle interactions have to be considered only within a comparatively small cutoff radius of 2.5 particle diameters, and long range corrections, which are a challenging issue in two-phase systems (Werth et al. 2014), are omitted per definition. Hence, simulations considering this fluid are straightforward and computationally cheap.

Evaporation across a planar vapor-liquid interface

The evaporation process across a planar vapor-liquid interface was studied in a cuboid system consisting of a liquid and a vapor phase with an extent of $L_l = 100$ and $L_v = 400$ particle diameters, cf. Fig. 1. The interface between the phases had a comparatively large cross-sectional area of $A = 140^2$ particle diameters to the square, to obtain statistically sound simulation results, which is particularly important for the sampling of the velocity distribution. In total, the system contained $N = 1.5 \cdot 10^6$ particles.

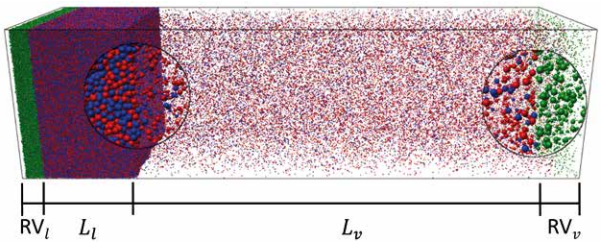

Figure 1: Snapshot of a stationary simulation of evaporation. The system consisted of a liquid and a vapor phase with an extent of $L_l = 100$ and $L_v = 400$ particle diameters. At both outer boundaries, the phases were extended by reservoir volumes RV$_l$ and RV$_v$. Particles constituting the reservoirs, forward flux j^+ and backward flux j^- are colored green, red and blue, respectively. Magnifying glasses (circles) are intended to support visualization.

The evaporation process was studied under stationary conditions. Therefore, at both outer boundaries, the phases were extended by reservoir volumes RV$_l$ and RV$_v$. The reservoir RV$_l$ was intended to replenish the liquid phase with the same rate as particles evaporate, which was measured at the boundary of RV$_v$ on the vapor side. Thereby, mass conservation was attained so that the interface position was constant. Hence, classical profiles of temperature, density, force and hydrodynamic velocity could be averaged over the entire time period of the production runs. To gain a better understanding of the mechansims of the evaporation process, also partial profiles were sampled, distinguishing between particles constituting the forward flux j^+ and backward flux j^-.

The extent of the vapor phase L_v was chosen to be large enough to cover the entire Knudsen layer emerging under evaporation conditions (Gusarov et al. 2002). In contrast to the conditions at the interface, the vapor flow beyond the Knudsen layer can assumed to be in local thermodynamic equilibrium (Euler regime). Hence, reservoir RV$_v$ was employed to emit a backward flux j^- into the system, according to a shifted Maxwell velocity distribution, to maintain a vapor flow with a constant target hydrodynamic velocity. The target velocity was varied from zero (vapor-liquid equilibrium) to the speed of sound (vacuum).

Droplet coalescence

The coalescence of two argon droplets with a diameter of $d = 50$ nm, each containing $N = 10^6$ particles, was investigated. The droplets were in equilibrium with their surrounding vapor at a temperature of $T = 110$ K and had an initial distance between their interfaces of $\delta = 1$ nm, cf. Fig. 2. Already within a fraction of a nanosecond, a rapidly growing liquid bridge between the two droplets was formed spontaneously. Due to the large particle ensemble and rotationally symmetric sampling, the changing curvature of the interface could be pinpointed, allowing for a direct and quantitative comparison with results of other methods, e.g. Dynamic Density Functional Theory (DDFT). It should be noted that the surface tension, which drives the coalescence process, is a property that is solely determined by the interactions between particles and hence can also be sampled by MD simulation (Werth et al. 2014). The present simulation results can thus be considered as a benchmark for other methods that include more assumptions and approximations.

One of the interesting results of the study was, that the outer boundaries of the droplets, cf. $z = -50$ and $z = 50$ in Fig. 2 started to move only after the liquid bridge almost reached the droplet diameter. This effect is a consequence of mass inertia.

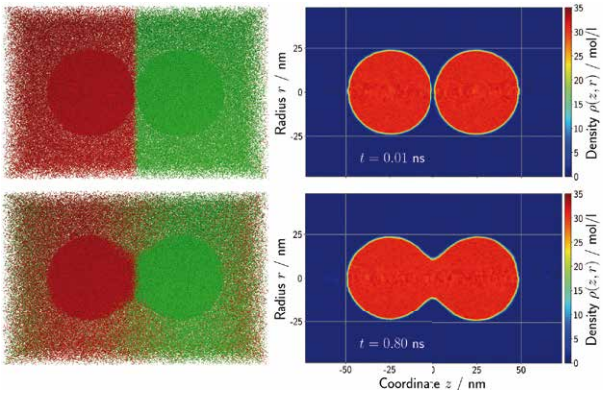

Figure 2: Two argon droplets with a diameter of $d = 50$ nm, each containing $N = 10^6$ particles, in equilibrium with their vapor at a temperature of $T = 110$ K. The left column shows snapshots from the cross-platform visualization framework MegaMol (Grottel et al. 2015), considering every single particle of the system. The colors red and green were selected to observe the diffusive mixing of particles that were initially located either in the left or right half of the system. The right column shows two-dimensional density fields, employing a colormap. The sequence shows a time period of $\Delta t = 0.8$ ns.

Conclusions

For the investigation of the evaporation process across a planar interface, an efficient method was introduced, allowing for simulations with large particle ensembles to be sampled on modern High Performance Computer (HPC) architectures. The obtained results are of high statistical quality so that the particle velocity distribution could be evaluated precisely. Highly accurate profiles were sampled, distinguishing between the forward and backward flux deepening the understanding of the mechanisms of evaporation processes. Since a vapor volume extent spanning to the boundary of the Euler regime was considered, the simulation results can be compared to those of Computational Fluid Dynamics (CFD) simulations that are operating on macroscopic scales.
From the simulations of droplet coalescence, sharp two-dimensional profiles of the rapidly varying vapor-liquid interface were obtained. Naturally evolving effects, like mass inertia, were observed. Revealing such effects with other methods, e.g. DDFT is not yet necessarily straightforward. Hence, present results of the MD study could serve as a benchmark for such approaches.

Acknowledgements

The present work contributes to the Collaborative Research Center (SFB) 75 of Deutsche Forschungsgemeinschaft (DFG) and was funded under the grant VR 6/9-2. All computations were performed either on the HPC cluster OCuLUS at the Paderborn Center for Parallel Computing (PC²) or on the Cray XC40 system Hazel Hen at the High Performance Computing Center Stuttgart (HLRS) with resources allocated according to grant MMHBF2. This work was carried out under the auspices of the Boltzmann-Zuse society.

References

C. Niethammer, S. Becker, M. Bernreuther, M. Buchholz, W. Eckhardt, A. Heinecke, S. Werth, H.-J. Bungartz, C. Glass, H. Hasse, J. Vrabec, and M. Horsch, ls1 mardyn: The massively parallel molecular dynamics code for large systems, *Journal of Chemical Theory and Computation* 10 (2014) 4455.

J. Vrabec, G.K. Kedia, G. Fuchs, H. Hasse, Comprehensive study of the vapour–liquid coexistence of the truncated and shifted Lennard–Jones fluid including planar and spherical interface properties, *Molecular Physics* 104 (2006) 1509–1527.

S. Werth, G. Rutkai, J. Vrabec, M. Horsch and H. Hasse, Long-range correction for multi-site Lennard-Jones models and planar interfaces, *Molecular Physics* 112 (2014) 2227–2234.

S. Grottel, M. Krone, C. Müller, G. Reina, T. Ertl, MegaMol - A Prototyping Framework for Particle-Based Visualization, *IEEE Transactions on Visualization and Computer Graphics* 21 (2015) 201–214.

A.V. Gusarov and I. Smurov, Gas-dynamic boundary conditions of evaporation and condensation: Numerical analysis of the Knudsen layer, Physics of Fluids 14 (2002) 4242–4255

26th European Low Gravity Research Association Biennial Symposium and General Assembly
14th International Conference on "Two-Phase Systems for Space and Ground Applications"
European Space Agency Topical Teams meetings
Granada (Spain), September 24-27, 2019

Oral 141

Autonomous vision-based tracking via fusion of multimodal imaging techniques

Helia Sharif[12], Michael Suppa[1]

[1]Universität Bremen, Bremen, Germany, [2] German Aerospace Center (DLR), Bremen, Germany;
helia@uni-bremen.de, suppa@uni-bremen.de

Introduction

One of the main robotic challenges is the communication delays and limited uplink opportunities. In this context, the technological development regarding vision-based techniques towards autonomous detection and tracking is cruicial for ensuring the success of future long durational space exploration missions. Guidance via visible and infrared imagery are currently used mainly for remote operations. This paper demonstrates with two applications, the fusion of visible and infrared imagery to complement their shortcomings and perform pose estimation tracking of subject towards autonomous tracking.

Methodology

In this work, Oriented Fast and Rotated Brief (ORB) feature detector was employed to visually track the subject. This robust technique was selected as it has proven to require low compuatational power and memory (Sharif and Hölzel 2017). The feature detector technique uses a 2D reference image of the subject to compare with the rest of the images that were acquired during the study. Once the features are extracted from each set of images, their respective binary descriptors are matched using RANdom SAmple Consensus (RANSAC) (Fischler et al. 1981) and projected onto the reference image to establish the pose estimation of the subject relative to the reference image.

Data Acquisition and Results

For the first application, dataset from team Space Farmers' study from European Space Agency (ESA)'s 40th Parabolic Flight Campaign were employed (ESA's Erasmus Archives 2019). Four spinach were monitored during 21 parabolas per flight to evaluate the photosynthesis of the plant during the span of about 2.5hrs of the flight (as shown in Figure 1 and Figure 2). It is evident that the leaf is slightly moving during each parabola. The leaf surface was imaged at 1Hz with FlirOne visible and infrared cameras of 480x690 and 240x320 pixel resolution respectively.

Since the leaves shifted during the flight, the movements were tracked using the feature detector and later correlated with the specific pixel position from the infrared images to consistenly evaluate the temperature at the same position on the leaf surface. The leaf movement is the most visible along the 2D axis as they were using nylon thread along the horizontal axis. So the leaves predominantly shifted from side to side in between the threads but maintained a fixed height relative to the other two axis' displacement.

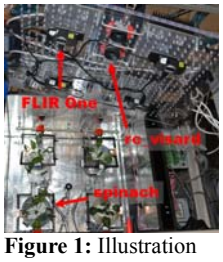

Figure 1: Illustration of imaging instruments and the subjects inside the rack.

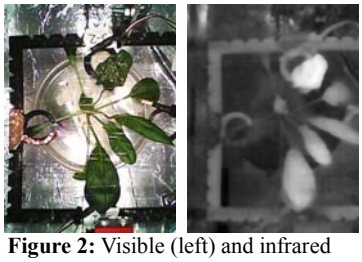

Figure 2: Visible (left) and infrared (right) image of spinach in microgravity.

Moreover, in order to maintain a consistent reference, a copper coated ring was imaged next to the subject. Copper has a high thermal conductivity (Yoshida and Morigami 2004), so it should maintain a consistent thermal signature throughout the flight. The temperature at the leaf surface was subtracted each time from the temperature of the copper in the frame to better evaluate its accuracy.

The prelimenray results indicate a sudden rise of temperature at approximately when the experimental rack was opened after the first set of parabolas. Thus it is speculated that the cabin temperature and humidity may have contributed to the rise of average temperature. Further analysis will be carried out to cross-correlate the measuremnts from the thermocouples, CO_2, and humidty sensors inside the enclosure to better understand the cause of the temperature increase.

For the second application, due to lack of available infrared and visible images of a spacecraft in orbit, a 75:1 scale model of SpaceX Dragon was 3D printed to be used as the fixed reference target. The model was printed via PolyLactic Acid (PLA) and coated in select regions with aluminium foil to emulate contrasting thermal emissivities (as illustrated in **Figure 3**) of solar panels and the remainder of the spacecraft.

Extreme illumination impedes the visual tracking due to false detections that are introduced. So infrared and visible images of the subject were averaged together to compensate for the shortcoming.

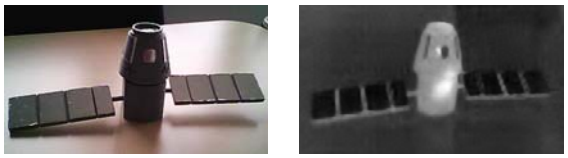

Figure 3: Visible (left) and infrared (right) image of the Dragon model.

FlirOne acquired infrared images with 240x320 pixel resolution, while rc_visard 65c acquired visible images that were cropped down to 632x238 pixel resolution to only display the image observed from the left camera lens of the 3D camera. Moreover, the FlirOne and rc_visard camera were fixed together and acquired images at 1Hz frequency while approaching the subject in a simulated randezvous maneouver.

During the feature tracking, various feature detection techniques were considered. Ultimately, ORB feature detector was selected as it is ideal for the type of application it was used due to its characteristics of being rotation and orientation invariant. So the target spacecraft can be approached and visually tracked from any angle of approach.

Monocular cameras suffer from scale uncertainty due to the feature detector's characteristcs. So additionally, the built-in Inertial Measurement Unit (IMU) of rc_visard 65c recorded the acceleration and gyrospe measurements of the camera movement at 200Hz. IMU are traditionally a great navigation instrument. However, IMUs are known to accumulate drift overtime. So the pose estimation and IMU measuremts were fused together using Error-State Kalman Filter (ESKF), as it is a proven navigation filter to further improve the autonomous navigation (Roumeliotis et al. 1999).

IMU measurements from the rc_visard 65c were employed as the ground truth, while the average pose estimations derived from the tracked features from visible and infrared image were applied as the visual odometry, to obtain their fusion as the visual inertial odometry. The prelimenrary results suggest that the filter improves the performance of tracking and is a viable technique to be applied in future applications.

Conclusions

The preliminary results demonstrate that a fusion of infrared and imagery improved the robustness of the feature-based tracking of the subject. The benefit of fusing the two sensors, enable the user to detect and track the subject even in harsh lighting conditions.

Acknowledgements

Special thanks to Lucie Poulet, Antoine Vernay, and Vasiliki Kondyli at Space Farmers, Raphael Schaller at Roboception, and everyone at Novespace for your guidance and support. This research was made possible with financial support of CNES, CNRS, ESA, Université Clermont Auvergne, and Universität Bremen.

References

ESA's Erasmus Experiment Archive (2019). Experiment Record N° 9601: ANTHEMS - ANdroid-based THErmal Monitoring of Spinach. Retrieved May 21, 2019, from http://eea.spaceflight.esa.int/portal/exp/?id=9601.

Lasseur, C., Brunet, J., De Weever, H., Dixon, M., Dussap, G., Godia, F., ... & Van Der Straeten, D. (2010). MELiSSA: the European project of closed life support system. Gravitational and Space Research, 23(2).

Sharif, H., & Hölzel, M. (2017). A comparison of prefilters in ORB-based object detection. *Pattern Recognition Letters*, *93*, 154-161.

Fischler, M. A., & Bolles, R. C. (1981). Random sample consensus: a paradigm for model fitting with applications to image analysis and automated cartography. Communications of the ACM, 24(6), 381-395.

Yoshida, K., & Morigami, H. (2004). Thermal properties of diamond/copper composite material. Microelectronics reliability, 44(2), 303-308.

Roumeliotis, S. I., Sukhatme, G. S., & Bekey, G. A. (1999). Circumventing dynamic modeling: Evaluation of the error-state kalman filter applied to mobile robot localization. In Proceedings 1999 IEEE International Conference on Robotics and Automation (Cat. No. 99CH36288C) (Vol. 2, pp. 1656-1663). IEEE.

26th European Low Gravity Research Association Biennial Symposium and General Assembly
14th International Conference on "Two-Phase Systems for Space and Ground Applications"
European Space Agency Topical Teams meetings
Granada (Spain), September 24-27, 2019

Oral 143

Liquid film structure of annular flows under microgravity - Results of TPF experiments onboard International Space Station -

H. Asano[1], H. Nakase[1], O. Kawanami[2], K. Inoue[3], K. Suzuki[4], R. Imai[5], S. Matsumoto[6], H. Ohta[7]

[1]Kobe University, Kobe, Japan, [2]University of Hyogo, Himeji, Japan, [3]The University of Kitakyushu, Kitakyushu, Japan,
[4] Tokyo University of Science, Noda, Japan, [5]Muroran Institute of Technology, Muroran, Japan,
[6]Japan Aerospace Exploration Agency, Tsukuba, Japan, [7]Kyushu University, Fukuoka, Japan
asano@mech.kobe-u.ac.jp

Introduction

Two-phase flow loop cooling system will be required for increasing heat transfer rate, heat transfer distance, and cooling heat flux in thermal control of space structures. The understandings on thermo-fluid dynamics of gas-liquid two-phase flows with phase change under microgravity is necessary for the design of the system. In order to realize one-component gas-liquid two-phase flows under stable microgravity condition, two-phase flow experiments had been carried out as a JAXA project named TPF experiment in Japanese Experimental Module "KIBO" of International Space Station (ISS). The detail information on TPF experiment was reported by Ohta, et al. 2016.

In this report, gas-liquid two-phase flow behaviors observed in the adiabatic observation section just at the downstream of the copper heating section, especially liquid film structure of annuar flows, are shown.

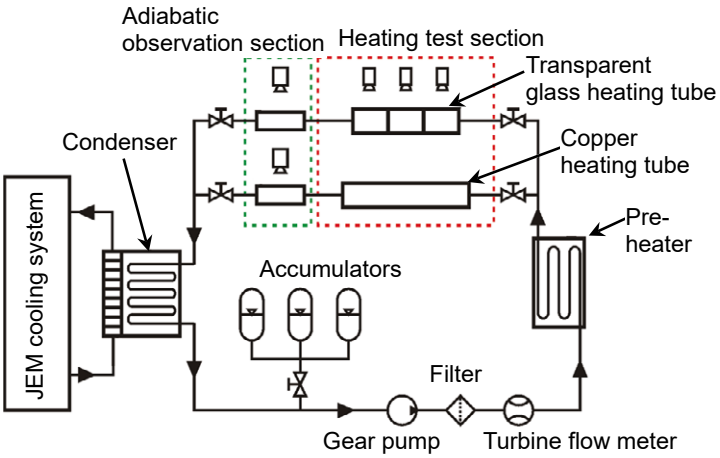

Figure 1: Schematic diagram of experimental apparatus of TPF experiment.

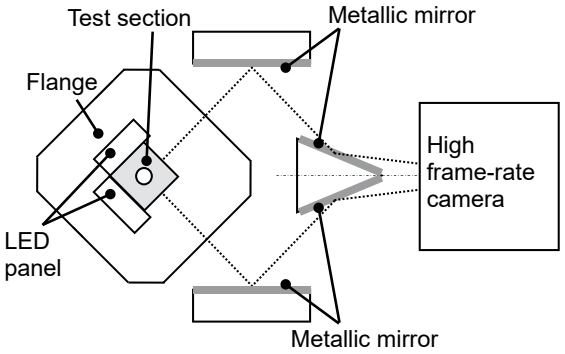

Figure 2: Arrangement of optical system for stereoscopic imaging mounted at the adiabatic observation section.

Experimental apparatus

A schematic diagram of the experimental apparatus of TPF experiment is shown in Figure 1. The loop is a pump driven two-phase flow loop, in which the fluid pressure is maintained by mechanical accumulators with bellows. The back pressure of the accumulators was opened to the cabin environment. The system pressure can be kept around the atmospheric pressure. Perfluoro-hexane that is the main component of the fluorocarbon FC-72 was selected as the working fluid. The experimental loop has two kinds of heating section with the inner diameter of 4 mm in parallel; a copper heating tube and transparent glass heating tube. Boiling heat transfer coefficient and critical heat flux can be measured in these heating sections, and boiling flow behaviors can be visualized in the glass heating tube.

In addition, it is required for understanding the phenomena to measure interfacial structures of boiling two-phase flows in more detail, especially 3D structure must be important. For the purpose, an adiabatic observation section is introduced just at the downstream of each heating section. The observation section was made of transparent polycarbonate resin. To make the effect of refraction at the outside wall smaller, the exterior shape was formed into a square, and then a circular channel with a diameter of 4 mm was drilled. For 3D observation, a method of stereoscopic photography by which two images from two orthogonal directions can be photographed by one camera was applied. The optical system consists of one compact high frame-rate camera whose maximum frame-rate is 1000 fps, four metallic mirrors, and two flicker-free LED panels for the back-lighting as shown in Figure 2. It was confirmed that the actual liquid film thickness can be measured from the photographed image within ± 4 % accuracy (Gomyo and Asano 2016). Continuous image of 750 frames was recorded for each condition.

Experimental results and discussion

Example frame extracted from continuous images recorded by the high frame-rate camera are shown in Figure 3. The flow pattern was annular flow. Strong axial asymmetry in circumferential liquid film thickness distribution was not obserbed. In order to visualize the behaviour of disturbance wasves, an image of time strips at the center of tube, and the example is shown in Figure 4. The vertical and horizontal

length show the position in the axial diretion and the number of frames, respectively. Since the brightness becomes lower at disturbance waves due to reflection and refraction on the disturbed interface, disturbance waves could be visalized as black lines. Coalescence and division of disturbance waves were not observed under this condition. From Figure 4, velocity and passing frequency of disturbance waves can be measured.

Velocity of disturbance waves are shown in Figure 5. Bold symbols are calculated values by Sekoguchi et al.'s equation for vertically upward annular flows under normal gravity (Sekoguchi et al. 1973). It was shown that the velocity of disturbance waves was higher than those under normal gravity. The velocity increased with increasing mass flux and increasing vapor volumetric flux.

Liquid film thickness on the side walls can be measured at four points for a horizontal line in an image. Measured results of base liquid film thickness are plotted against vapor quality in Figure 6. These results are average at the center in the axial diection. Base liquid film thickness decreased with increasing quality.

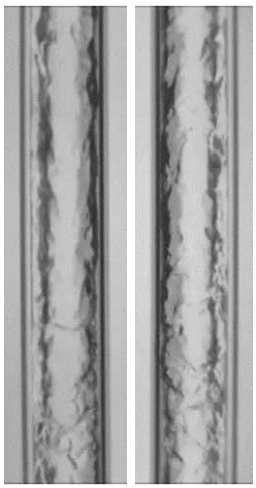

left right

Figure 3: Annular flow.

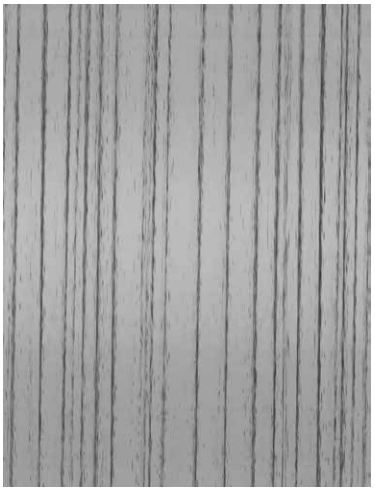

Figure 4: Time strips at the center of tube.

Conclusions

Liquid film structures of annular flows obtained in TPF experiment onboard ISS were analysed. As a result, the velocity and passing frequency of disturbance waves were higher under microgravity than normal gravity. The base liquid film thickness was thinner under microgravity.

Acknowledgements

The authors would like to thank Mr. Ukena, Mr. Fujii, Ms. Semba, Mr. Miyawaki for their support in TPF experiment, and also thank JAMSS and JSF for the support of TPF project, and also thank IHI aerospace for the fabrication of the apparatus.

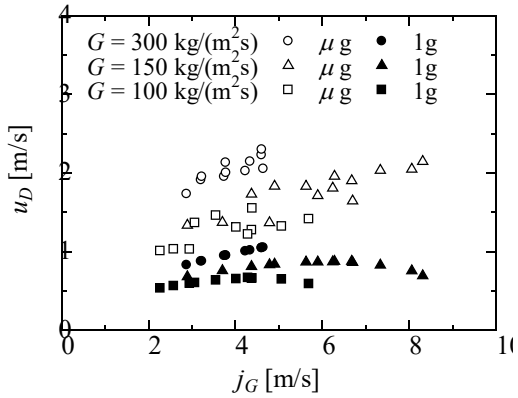

Figure 5: Velocity of disturbance waves.

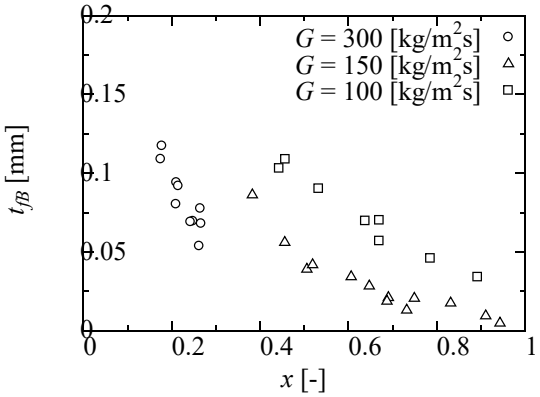

Figure 6: Thickness of base liquid film.

References

H. Ohta, et al., Development of Boiling and Two-Phase Flow Experiments on Board ISS, *Int. J. of Microgravity Science and Application,* 33(1) (2018) paper No. 330102 to 330107.

T. Gomyo and H. Asano, Void Fraction Characteristics of One-Component Gas–Liquid Two-Phase Flow in Small Diameter Tubes, *Interfacial Phenomena and Heat Transfer*, 4(1), (2016) pp. 1-18.

K. Sekoguchi, et al., Transactions of the JSME, 39(317) (1973), pp. 313-323. (in Japanese)

Automated control system for aerosol cloud levitation in microgravity

D. Balapanov[1], A. Vedernikov[1], , Raffaele Romagnoli[2], Emanuele Garone[2]

[1]Microgravity Research Center of Brussels Free University, Belgium
[2]Control Engineering and System Analysis, Brussels Free University, Belgium
dbalapan@ulb.ac.be, avederni@ulb.ac.be

oduction

microgravity experiments with multiphase media often ire a quiescent state of the mixture, e.g. for precise surements of transport coefficients. We developed and cessfully tested a system providing levitation of particle ids in gas at low pressure. The work is done within the he of ICAPS project of European Space Agency. The goal he project is to observe non-perturbed agglomeration of wnian particles for times no less than 3 minutes.

real experiment conditions, there are always non- pensated temperature gradients, and it leads to the cloud t from the cold region to the warm one due to the mophoresis. The proposed system can compensate ntual disturbances in real time and in 3D space. In ition, it is capable to increase the cloud concentration ng the experiment to study collective effects of the icle motion, and to increase the particle agglomeration . We refer the system as Automated Cloud Manipulation tem (Automated CMS).

tem description and test results

proposed system uses four concentric ring-shaped Peltier lules to drive particles in any direction due to mophoresis, gas flow created by thermal creep and mal expansion/contraction. The motion mechanisms are -sensitive to the particle size, so they move the cloud as a d body. The big rings are divided by 4 sectors (see Figure) create potential for horizontal positioning, and two small s are used for vertical positioning. In the squeezing mode, riodic temperature variation is applied to the rings, so that particles follow a periodic trajectory with secular tendency he system center.

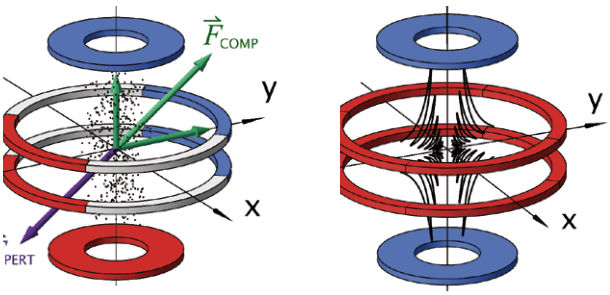

ıre 2: CMS geometry and working modes. Left – the levitation e with compensation of ZY-perturbation. Right – squeezing e with antiphase change of big ring and small ring temperature. ectories of four probe particles are shown.

architecture of automated CMS and dataflow scheme are ented in **¡Error! No se encuentra el origen de la**

separate current sources that are controlled by housekeeping computer; 2) two high-resolution digital cameras observing two mutually perpendicular planes illuminated by laser light sheets; 3) single-board computer that performs real-time processing of the images from two cameras. Images of particle cloud grabbed by the cameras are analysed using the Particle Image Velocimetry technique (simplified fast version - Parallel Projection Correlation) that allows quantifying in real time the eventual 3D cloud displacement between two consecutive frames. This displacement is controlled by three decoupled digital controllers (one per each space axis) running on the single-board PC. Each controller provides a proportional, integral and derivative (PID) action on the discrepancy between the measured and the cloud position and required "home point". Then, the control action is transformed into electrical current values that are applied to the CMS Peltier rings by the housekeeping computer. Thus, we have a closed control loop.

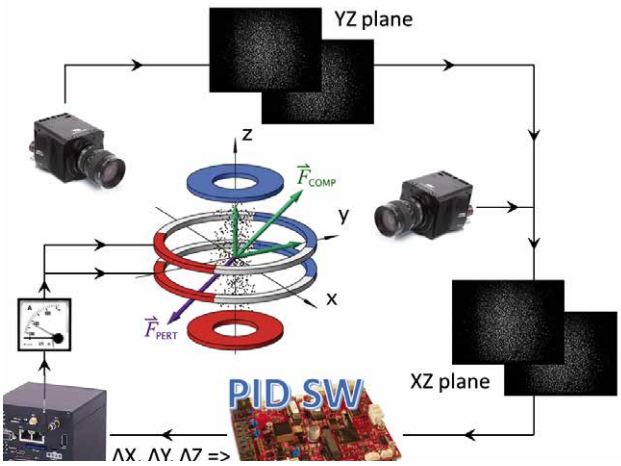

The system we developed is to perform following tasks for the ICAPS experiment. First, the system controls the quality of the particle *injection*. It is important, since the high cloud density is required for the agglomeration observation. Special software is capable to count and measure particles on camera image in real time using highly efficient Connected Component Labeling approach. If the cloud density appears too low, the injection is repeated. Besides the main task, levitation, there is necessity to regularly move the cloud there and back in one direction. It is done to increase the amount of particles observed by fine optics (not discussed here) having field of view about 1mm^3. By this cloud *scanning* we significantly increase the scientific output of the experiment. Another important mode of automated CMS is agglomerate *targeting*, which means detection of biggest agglomerate after

agglomerate to the fine optics field of view for further study of the agglomerate structure.
Functioning of the PID controllers is verifed by numerical cloud dynamics simulator with taking into account possible process disturbances, sensor noise, and model uncertainties.
The automated CMS has been tested in microgravity at the Bremen Drop Tower. We have proved cloud levitation against an external disturbance along the z-axis. The disturbance was simulated by the gas stream from a gas flow controller or by big ring sectors that can produce slow cloud motion in axial direction. The disturbance compensation was clearly observed and the measured cloud trajectory is in good accordance with predictions of the CAP simulator, as shown in Figure 3

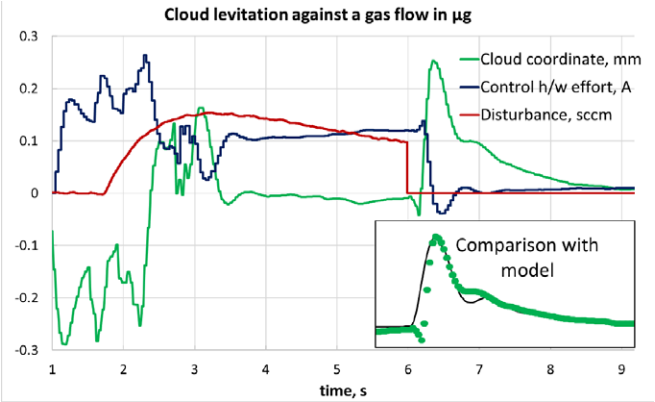

Figure 3: Proof of the cloud levitation: cloud coordinate vs time compared to theory.

To prove the cloud scanning a cloud displacement there and back by 3mm was performed. For this, the set point of the cloud home position was changing by 3mm, and the system moved the cloud to the new equilibrium points. By this approach it is guaranteed that the cloud returns to the home position. This is important, because in case of even small hysteresis, resultant cloud displacement can become too large after many scanning cycles.
The cloud velocity during such scanning is not constant: in the middle of the displacement the velocity is maximal (about 3mm/s) and it tends to zero in the end of scanning.
Squeezing mode is tested in previous drop tower campaigns, and the test showed ability of CMS to create large particle agglomerates (up to 1mm size) during several seconds.
The Automated CMS is applicable for cloud levitation at normal gravity, which has been proved by laboratory tests.

Conclusions

We present a new scientific instrument for microgravity research: Automated Cloud Manipulation System developed within the frame of ESA ICAPS project. The system allows various contactless manipulations with aerosol clouds at low gas pressures. Most important function is levitation of the entire cloud against perturbations of arbitrary nature. In addition, the system allows quick positioning the cloud in any spatial direction. The particle concentration in the cloud can be increased, and this allows creating large particle agglomerates in short time. Facility of cloud levitation at normal gravity has been proved as well.

Acknowledgements

ESA PRODEX program, the Belgian Federal Science Policy Office and ZARM Drop Tower Operation and Service Company Ltd. are greatly acknowledged. We acknowledge companies QinetiQ Space Belgium and Lambda-X for their contribution in the implementation of the system.

26th European Low Gravity Research Association Biennial Symposium and General Assembly
14th International Conference on "Two-Phase Systems for Space and Ground Applications"
European Space Agency Topical Teams meetings
Granada (Spain), September 24-27, 2019

Oral 145

Effect of the Ekman number on mean flow excited by inertial modes in liquid filled librating cylinder

S. Subbotin

Perm State Humanitarian Pedagogical University, Perm, Russia;
subbotin_sv@pspu.ru

Introduction

The oscillating motion in a rotating fluid is a source for support of inertial waves (Greenspan 1968). If the oscillation frequency σ is less than twice rotation rate of the system 2Ω, these waves propagate in the fluid bulk along the characteristic surfaces formed by the free shear layers. At some frequencies as a result of spatial resonance, inertial waves can excite so-called inertial modes. These modes are the natural frequencies of the rotating fluid and strongly depend on the cavity geometry. At the same time, it is known that the phase or spatial inhomogeneity of the oscillating component of the flow velocity leads to the appearance of a nonzero average (Riley 2001). This paper is devoted to the experimental study of steady flow excited by inertial modes in a rotating cylinder.

Experimental setup and technique

The cuvette is a cylinder of circular cross section with a length of $L = 102.0$ mm and a radius of $R = 26.0$ mm. The cuvette rotation speed changes in the laboratory frame by law $\omega(t) = \Omega(1+\varepsilon\cos\Omega_l t)$, where Ω is the average angular velocity, Ω_l is the libration frequency, and ε is the libration amplitude. In the experiments the dimensionless libration frequency and amplitude varies in the range of 0–2.00, and 0–0.300 respectively. The Ekman number varies in the range $\mathrm{E} \equiv \nu/\Omega R^2 = 2\cdot10^{-4} - 2\cdot10^{-3}$. The experiments are carried out as follows. The cuvette is driven in a rapid uniform rotation around the horizontal axis. After the establishment of solid-state rotation at a given frequency σ, corresponding to one of the inertial modes, the amplitude ε smoothly increases. The velocity field is investigated by the PIV method.

Experimental results

The eigenfrequencies of inviscid inertial modes in a cylindrical cavity can be calculated as follows $\sigma^2 = \left(4\pi^2 n^2 / \left(\pi^2 n^2 + \xi_{nmk}^2 L^2/R^2\right)\right)$, where ξ_{nmk} is the m – th positive solution of a transcendental equation $\xi \frac{d}{d\xi} \mathrm{J}_{|k|}(\xi) = 0$ (Greenspan 1968). When the libration frequency coincides with one of the natural frequencies a large-scale oscillating motion is resonantly excited.

At the frequency $\sigma = 1.563$ the instantaneous structure of the flow consists of six pairs of toroidal vortices, the direction of rotation in which is reversed during the libration period (Fig. 1*a*). The oscillating motion of the fluid leads to the appearance of mean flow in the viscous boundary layers close to the cylinder side wall. The mean flow is a system of toroidal vortices, the position of which is consistent with the position of oscillating vortices (Fig. 1*b*). An exception is the area near the junction of the side and end walls, where mean corner flow is associated exclusively with the angular oscillations of the cavity.

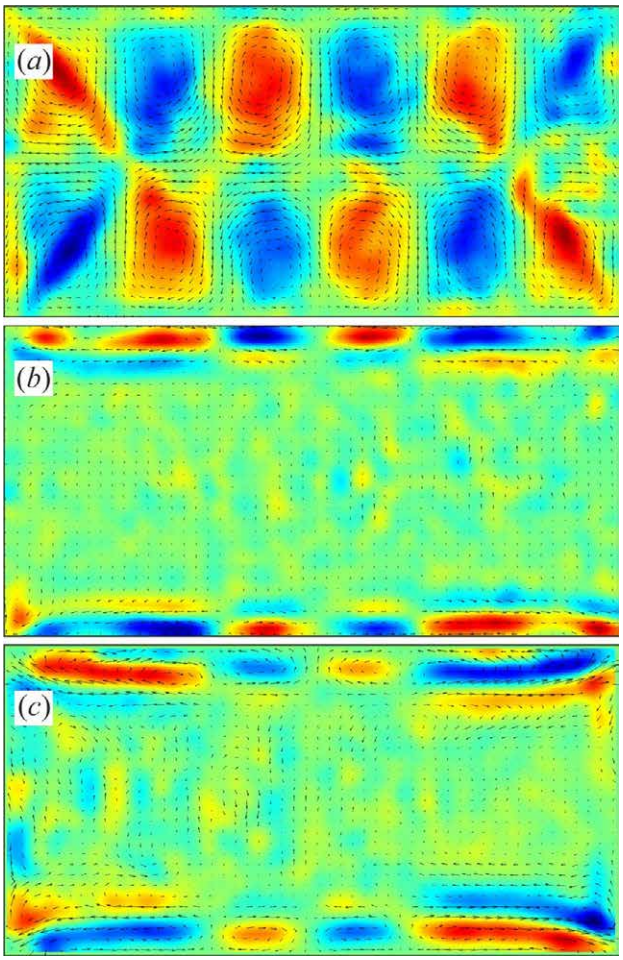

Figure 1: Instantaneous (*a*) and averaged velocity field (*b*, *c*) in the axial section at $\sigma = 1.563$ and $\mathrm{E} = 2.2\cdot10^{-4}$ (*b*) and $\mathrm{E} = 2.2\cdot10^{-3}$ (*c*).

With an increase in the Ekman number E inviscid inertial modes dissipates. This leads to a decrease in the intensity of the mean flow according to the law $\sim \mathrm{E}^{-1/2}$. At $\mathrm{E} > 10^{-3}$ the flow associated with inertial modes becomes so weak that corner flow suppress it, penetrating deeply along the side wall (Fig. 1*c*).

Acknowledgements

The research was supported by the grant of the President of the Russian Federation (project No. MK-1994.2018.1).

References

H.P. Greenspan, *The theory of rotating fluids* (University Press, Cambridge, 1968).

N. Riley, Steady streaming, *Annu. Rev. Fluid Mech.* 33 (2001) 43–65.

S. Subbotin, V. Dyakova, Inertial waves and steady flows in a liquid filled librating cylinder, *Microgravity Sci. Technol.* 30 (2018) 383–392.

26th European Low Gravity Research Association Biennial Symposium and General Assembly
14th International Conference on "Two-Phase Systems for Space and Ground Applications"
European Space Agency Topical Teams meetings
Granada (Spain), September 24-27, 2019

Oral 146

Experimental Study on the Nanofluids Thermal Performance for Ethanol Condensation

A. Banisharif [1], S. Van Vaerenbergh [1], P. Estellé [2]

[1] Microgravity Research Center (MRC), Université Libre de Bruxelles, Brussels, Belgium, [2] Université Rennes 1, Rennes, France,
abanisha@ulb.ac.be, svanvaer@ulb.ac.be, patrice.estelle@univ-rennes1.fr,

Introduction

The process of evaporation and condensation involves the transfer of heat to and from the product stream, and then the change of the alcohol phase from the liquid to the vapor and vice versa. This phase change requires a lot of added/removal heat at a constant temperature (McCabe et al. 2005). Heat exchangers are performed this process efficiently. The literature survey demonstrates that nanofluids as a two-phase stream significantly enhance the heat transfer capability of conventional heat transfer fluids in heat exchangers such as water by suspending nanoparticles in the base liquid (Kakaç et al. 2009). In the convention heat transfer mechanism of nanofluids, thermal conductivity and dynamic viscosity of the fluids involved play an important role (Pérez-Tavernier et al. 2019). In this context, the present research intends to introduce an experimental study in the performance of the alcohol condensation process taking into consideration the heat and mass transfer phenomena, studying the effects of thermo-physical and transportation properties, temperature and volumetric flow rate.

Experimental Method

Copper (Cu) synthesized by reducing of the metal salts, Fe_3O_4 produced by the precipitation method, Nanoporous Graphene and MWCNT synthesized using a CVD method over were chosen for preparing nanofluids as metallic, metal oxides, nonmetallic nanoparticle, respectively. All nanofluid batches have been prepared with half hour ultrasonication at 0.01, 0.05 and 0.1 vol. % via suitable surfactants. They are investigated from -20 ºC to 20ºC. The thermal conductivity was carried out by a THW-L2 Portable thermal conductivity meter. Experimental investigations of the dynamic viscosity of stable nanofluids were studied by a Malvern Kinexus Pro stress controlled shear rheometer. In order to perform HTC test, the construction of a set-up for measuring the heat transfer coefficient (h), which was discussed in the schematic below, and discussed in detail in the proposal, was essential as displayed in Figure 1.

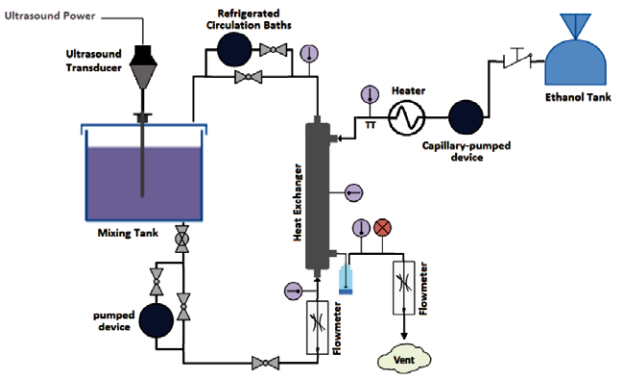

Figure 1: Diagram for the HTC experimental set-up for condensation of Ethanol.

Water- and WEG-based nanofluids are used to measure the local Nusselt numbers. Ethanol is chosen to test the HTC. At first, the ethanol is evaporated by heater and then it is condensed by the heat exchanger.

Results and discussion

In agreement with the literature, the viscosity increases faster than higher at lower temperatures. Except at the lower temperature, there is no significant difference between MWCNT and the base fluid. The viscosity is significantly reduced by adding nanoparticles for Cu and Fe_3O_4 nanofluids at all temperatures to surfactant-base fluids. For 0.1 vol% of Fe_3O_4 viscosity is lower than the water and ethylene glycol mixture, and the reduction of viscosity at lower temperature is also increased. Such behavior should be attributed as previously reported to the lubricating effect of nanoparticles (Phouc et al. 2011).

The measured thermal properties of the nanofluids are presented in Figure 2 for the water-based and water ethylene glycol-based, respectively and for all tested volume fractions. There is no significant difference in the thermal conductivity of different surfactant solutions. But the thermal conductivity enhancement of nanofluids is observed, especially for Fe_3O_4 WEG-based nanofluid.

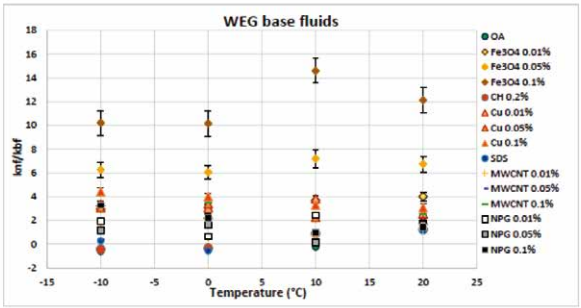

Figure 2: Relative thermal conductivity water-based nanofluids s in function of nanoparticle volume fraction and temperature.

The results of a heat exchanger set-up for codenstation of ethanol that are undertaken at -20°C and 20°C for water and WEG-based nanofluids, indicated heat transfer coefficient enhancement.

Conclusions

The main result shows the positive effects of adding nanoparticles on thermo-physical properties of water and water-ethylene glycol based fluids to condense ethanol in the designed heat exchanger at low concentration and temperature. Compared to the base fluid, the enhancement of nanofluid thermal transport properties is obtained.

Acknowledgements

We acknowledges EU COST for the STMS grant ref. COST-STSM CA15119-42469 as well as Microgravity Reseach Center at ULB.

References

J. Pérez-Tavernier, J.P. Vallejo, D. Cabaleiro, J. Fernández-Seara, L. Lugo, Heat transfer performance of a nano-enhanced propylene glycol:water mixture. *International Journal of Thermal Sciences*, 139 (2019) 413-423.

S. Kakaç, A. Pramuanjaroenkij Review of convective heat transfer enhancement with nanofluids. *Int. J. of Heat and Mass Transfer* (2009) 3187–3196.

T.X. Phuoc, M. Massoudi, And R. Chen, Viscosity and thermal conductivity of nanofluids containing multi-walled carbon nanotubes stabilized by chitosan. *International Journal of Thermal Sciences*, 50(1) (2011) 12–18.

W.L. McCabe, J.C. Smith, P. Harriott, Unit operation of Chemical Engineering, 7th edition, *McGrawHill,* (2005), New York, USA.

26th European Low Gravity Research Association Biennial Symposium and General Assembly
14th International Conference on "Two-Phase Systems for Space and Ground Applications"
European Space Agency Topical Teams meetings
Granada (Spain), September 24-27, 2019

Oral 147

Onset of Non-Equilibrium Fluctuations induced by thermophoretic diffusion

M. Carpineti[1], M. Sabato[1], F. Croccolo[2], A. Vailati[1]

[1]Dipartimento di Fisica, Università degli Studi di Milano, I20133 Milano, Italy, [2] Laboratoire des Fluides Complexes et leurs Reservoirs, IPRA, UMR5150 E2S-Université de Pau et des Pays de l'Adour, CNRS, TOTAL, F-64600 Anglet, France;
marina.carpineti@unimi.it

Introduction

We present the results of a preliminary investigation of the kinetics of growth of non-equilibrium fluctuations (NEF) in a sample approaching a steady state condition during a thermodiffusion process.

Theories and experiments give a detailed description of non-equilibrium fluctuations under ideal conditions: in the quasi-stationary case of free diffusion, or, at steady state in the presence of a constant concentration profiles in thermally driven processes. These results show that NEFs are long range correlated, with a structure factor diverging as q^{-4} as a function of the wave vector q. NEFs can be orders of magnitude larger than equilibrium fluctuations, but in the presence of gravity there is a maximum fluctuation length, due to buoyancy, that frustrates the diffusive relaxation.

However, there is a limited number of studies predicting the way these fluctuations develop when a temperature gradient is applied to a sample. A model based on an adiabatic approximation of the equations of linearized hydrodynamics describes the onset of NEFs for thermodiffusion processes in systems where the macroscopic state changes are very slow with respect to the fluctuations (Vailati et al. 1998). Recent simulations (Cerbino at al 2015) describe the onset of NEFs induced by thermophoretic diffusion in microgravity, predicting a spinodal-like growth of the fluctuations, leading to a peaked structure factor with scale invariance at large wave vectors.

In this work, we present the results of a study, performed with a quantitative Shadowgraph technique, of the onset of the fluctuations induced by a thermophoretic process (Carpineti et al. 2019).

Experimental results

We study the kinetics of growth of the concentration fluctuations' modes during a transient leading to a stationary state in a solution of polystyrene polymer in toluene. As the onset of the fluctuations is a quite elusive process, we use a polymer with large molecular weight $M_w = 7.06 \times 10^5$ *g mol*$^{-1}$ at a concentration approximately three times the overlap concentration, in order to slow down the kinetics of the process. We start from a condition of uniform concentration, with the sample at fixed temperature, and then we apply suddenly a temperature gradient ΔT in the vertical direction. The gradient induces a net mass flow due to Soret effect that lasts until a uniform concentration gradient is formed inside the sample cell and a steady state is reached. We take images of the sample during the transient, using a highly sensitive shadowgraph technique (Croccolo et al. 2007; Vailati et al. 2011), collecting the light transmitted and scattered along a direction parallel to the temperature gradient.

In Fig. 2 we show the time evolution of the structure factor of the concentration fluctuations, obtained from the shadowgraph images, where it is appreciable the rapid growth in the first stages of the process.

From these curves we determined the time evolution of the growth rate of fluctuations for different wave vector ranges, and we find the interesting result that the rate of growth does not show the presence of any typical time scale, but follows a power-law behavior $Rc(q; t) \propto 1/t$.

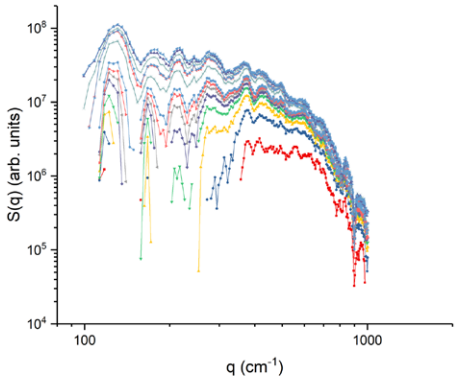

Figure 2: Time evolution of the static structure factor of non-equilibrium concentration fluctuations taken during the transient phase.

A final analysis performed on the data is the study of the variance of the shadowgraph images that is proportional to the total intensity scattered by the sample and collected by the sensor. The growth of the variance gives us a further evidence of the onset of the fluctuations inside the sample. We propose a phenomenological model in good agreement with the data that allows to relate the growth of the fluctuations to the growth of the macroscopic concentration difference at the boundaries of the cell.

Conclusions

Our study represents a first attempt at investigating the onset of non–equilibrium concentration fluctuations in the presence of a temperature gradient. We have developed a first phenomenological model in good agreement with the experimental data. Due to the relevance of buoyancy effects, affecting the amplitude of NEFs at small q-values, a more complete understanding of the kinetics of fluctuations growth would benefit of experiments in microgravity conditions.

This represents one of the main goals of the Giant-Fluctuations (NEUF-DIX) project of the European Space Agency (Baaske et al, 2016).

Acknowledgements
Work partially supported by the European Space Agency.

References

P. Baaske, H. Bataller, M. Braibanti, M. Carpineti, R, Cerbino, F. Croccolo, A. Donev, W. Köhler, J. M. Ortiz de Zàrate, and A. Vailati, *Eur. Phys. J. E* 39, (2016), 119.

M. Carpineti, M. Sabato, F. Croccolo, A. Vailati, *Eur. Phys. J. E*, 42, (2019) 25.

R. Cerbino, Y. Sun, A. Donev, A. Vailati, *Sci. Rep*. 5, (2015) 14486.

F. Croccolo, D. Brogioli, A. Vailati, M. Giglio, D.S. Cannell, *Phys. Rev. E* 76, (2007), 041112.

A. Vailati, M. Giglio, Phys. Rev. E 58, (1998), 4361.

A. Vailati, R. Cerbino, S. Mazzoni, C.J. Takacs, D.S. Cannell, M. Giglio, *Nature Comm* 2, (2011), 290.

26th European Low Gravity Research Association Biennial Symposium and General Assembly
14th International Conference on "Two-Phase Systems for Space and Ground Applications"
European Space Agency Topical Teams meetings
Granada (Spain), September 24-27, 2019

Oral 148

The ESA Topical Team on: "Tissue Healing in Space: Techniques for Promoting and Monitoring Tissue Repair and Regeneration"

M. Monici[1], C. S. Iorio[2]

[1] ASAcampus Joint Laboratory, ASA Res. Div. & Dept. of Experimental and Clinical Biomedical Sciences "Mario Serio", University of Florence, Florence, ITALY; [2] Service de Chimie-Physique E.P. Microgravity Research Center, Universitè Libre de Bruxelles, Av. Paul Heger, 1050 Bruxelles, CP 165/62, BELGIUM
monica.monici@unifi.it, ciorio@ulb.ac.be

Currently, the procedure for the management of medical and surgical emergencies on board the International Space Station (ISS) is the temporary stabilization of the patient, followed by return to Earth in a time as fast as possible.
Until now, the management of surgical emergencies and trauma, as well as the treatment of wounds and burns on the ISS was not considered a top concern. In fact, during current space missions, the occurrence of injuries, traumatic events and surgical emergencies is considered unlikely.
But, future space exploration programs require long-term missions beyond LEO. In this case, surgical emergencies and traumas on board cannot be excluded, while medical evacuation times to Earth could become too long and the delay in communication would make it useless to guide the crew's actions remotely. Therefore, the planning of medical assistance for future space exploration missions should include the concepts of emergency surgery and trauma care. Furthermore, as wound healing is essential for survival, in-depth studies on tissue repair and regeneration processes in space are needed. Therefore, the space agencies have given impetus to efforts to organize studies and experiments on these issues.
The European Space Agency has created a Topical Team (TT) on: "Tissue Healing in Space: Techniques for Promoting and Monitoring Tissue Repair and Regeneration". The TT is composed of: 26 research groups from 12 different countries, 13 companies (of which 12 do not operate in the space field) from 7 different countries, 16 internationally recognized experts from 10 different countries. The TT is organized in two subgroups, one for life sciences, which addresses the biomedical problems, and the other for physical sciences, which addresses physical and technological problems.
After two years of intense activity, the TT elaborated a document, which has been submitted to ESA. In the document, three main topics have been identified and discussed:

1) Potential problems in the management of surgical emergencies, traumas, wounds and burns on board vehicles/space stations, both in terms of diagnostic/therapeutic procedures to be applied and for the evolution of the healing process. It must be also considered that the healing mechanisms may be affected by systemic alterations induced by space environment.
2) Possible countermeasures or strategies to be implemented in order to prevent/mitigate the above mentioned problems.
3) Research activities aimed at:
   a. increase knowledge on the healing process of wounds / burns in space (study of the mechanisms involved, suture behavior, healing times, quality of scar tissue);
   b. assess the effectiveness of countermeasures and strategies aimed at increasing the ability to manage surgical emergencies, severe traumas, burns and wounds in environments other than Earth, and to favor tissue repair and regeneration processes. It will be necessary to define the requirements for the application of "countermeasures" in space environment and also the feasibility of the related procedures. The "spatialization" of suitable devices will require significant technological efforts.

In vitro, ex vivo and in vivo experimental models particularly suitable for use in space research have been selected/developed to implement the activities at point (3).
The TT not only has the aim to address the multifaceted problem of wounds, sutures, and their healing but also to ensure an integrated approach for the development of:

1) Strategies to promote tissue repair both in space and terrestrial environment.
2) Devices to monitor repair processes and suture behaviour.
3) Synergies between Life and Physical Sciences in order to develop an integrated research programme capturing both the biological aspect of tissue regeneration and its monitoring through advanced and innovative devices
4) Virtuous partnerships between basic and applied sciences by connecting industrial partners and universities/research centers in a poly-disciplinary frame.
5) Fruitful environment for enhancing the technology transfer towards market applications.

Acknowledgements

The authors would like to thanks the European Space Agency Topical Team "Tissue Healing in Space: Techniques for Promoting and Monitoring Tissue Repair and Regeneration" for the financial and moral support.
All TT members actively participated in the TT activities and preparation of the Report.

References

Miskovic V, Traettino S, Minetti C, Machrafi H, Amirfazli A, Dubois F, Iorio CS, Fabrication and characterization of

polystyrene colloidal photonic crystals on soft sodium alginate film, *J. Nanoelectron. Optoelectron*, (2017)

Machrafi H, Minetti C, Miskovic V, Dauby P, Dubois F, Iorio CS, Self-assembly of carbon nanotube-based composites by means of evaporation-assisted depositions: Importance of drop-by-drop self-assembly on material properties, *Materials Chemistry and Physics* 218, (2018)

ESA-TT on Tissue Healing in Space: Techniques for Promoting and Monitoring Tissue Repair and Regeneration - Report on open problems concerning tissue healing in space, includingemergency surgery and trauma care, possible countermeasures and experimental models, (2019)

Riwaldt, S.; Monici, M.; Petersen, A.G.; Jensen, U.B.; Evert, K.; Pantalone, D.; Utpatel, K.; Evert, M.; Wehland, M.; Krüger, M.; Kopp, S.; Frandsen, S.; Corydon, T.; Sahana, J.; Bauer, J.; Lützenberg, R.; Infanger, M.; Grimm, D. Preparation of A Spaceflight: Apoptosis Search in Sutured Wound Healing Models. *Int. J. Mol. Sci.* (2017), *18*, 2604

Cialdai F, Vignali L, Morbidelli L, Colciago A, Celotti F, Santi A, Caselli A, Cirri P, Monici M. Modeled Microgravity Affects Fibroblast Functions Related to Wound Healing. *Microgravity Sci. Technol*. 10.1007/s1221701695327, (2017)

Cialdai F, Monici M. Wound healing: what happens in microgravity?.CURRENT BIOTECHNOLOGY, ISSN: 2211-5501, doi: 10.2174/22115501113026660025, vol.2, p. 250-256, (2013).

26th European Low Gravity Research Association Biennial Symposium and General Assembly
14th International Conference on "Two-Phase Systems for Space and Ground Applications"
European Space Agency Topical Teams meetings
Granada (Spain), September 24-27, 2019

Oral 149

Photoelastic Granular Materials as a Tool for Experimental Studies on Impacts and Interaction with Regolith Covered Surfaces in Low Gravity

J.E. Kollmer[1,2] Corinna Krause[1], Tabea Bogdan[1], Maximilian Kruss[1], Jens Teiser[1], Joshua E. Colwell[2], Karen E.Daniels[3] and Gerhard Wurm [1]

[1]Universität Duisburg-Essen, Duisburg, Germany
[2]University of Central Florida, Orlando, FL, USA
[3]North Carolina State University, Raleigh, NC, USA

jonathan.kollmer@uni-due.de

Introduction

Photoelastic techniques (Daniels2017) are used to make both qualitative and quantitative measurements of the forces within idealized granular materials. The method is based on placing a birefringent granular material between a pair of polarizing filters, so that each region of the material rotates the polarization of light according to the amount of local stress. We apply these materials to adress two questions about regolith covered surfaces

1. Splashes from slow impacts

Splashes from slow impacts into granular materials, which play an important role in the sculpting of asteroid surfaces and for the structures formed in wind blown sands. We present results from two experiments that explore the ejecta generation and material redistribution from slow impacts into a granular bed. The impactors are selected to have the same size and material as the grains that make up the target. We find that for small grains the ejecta will stay close to the impact site under conditions realistic for a small asteroid. (Bogdan2019). We further find that buckling introduced by the impact can create ejecta away from the impact site. (Krause 2019)

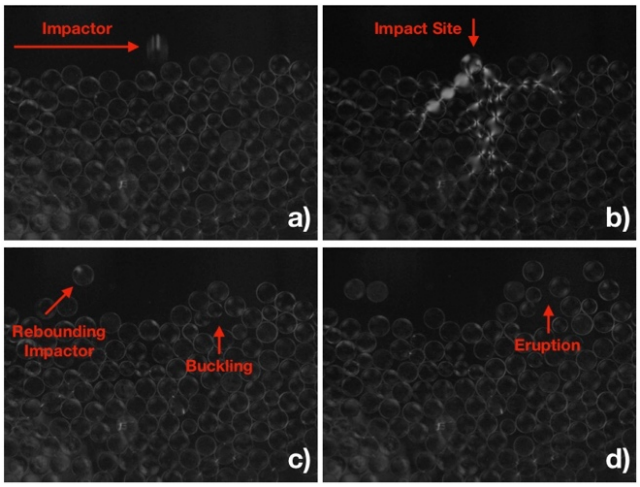

Figure 1: A cm sized impactor hitting a bed of photoelastic particles at ~10m/s and creating a buckling induced splash away from the impact site.

2. Interacting with Regolith Covered Surfaces

With recent sucesses in visiting asteroids and other poorly-consolidated near-earth-objects (NEOs), it has become important to safely interact with the granular materials at the surface of these objects. A particular concern is the low elastic modulus of granular materials: rubble-pile asteroids are only held together by weak gravitational and van der Waals forces. This means that both the escape velocity and the sound velocity are low compared to their values on earth. To better predict the dynamics of the granular flows resulting from surface explorations such as digging, sample-collection, anchoring, or lift-off, we develop microgravity experiments which are able to predict the circumstances under which the NEO material will remain intact or become unstable (Kollmer 2017). In our EMPANADA (Ejecta Minimizing Protocols for Applications Needing Anchoring or Digging on Asteroids) experiment, we insert a flexible probe into a granular material under low gravity. We show that low-speed interactions reduce the effects of shock wave creation and observe that thinner diggers allow the grains to rearrange and minimize the possibility of ejecta.

.

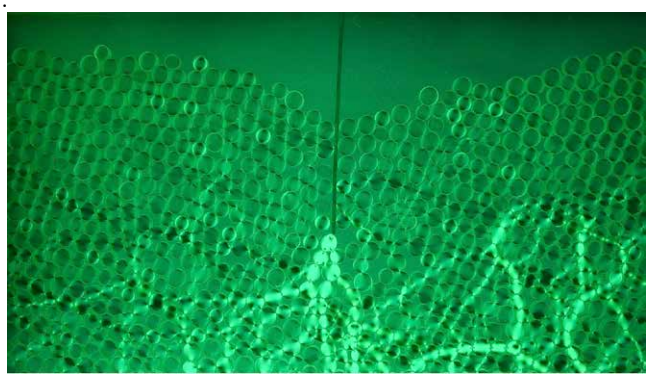

Figure 2: A flexible rod is inserted into a bed of photoelastic materials under lunar gravity during a parabolic flight. Brighter regions indicate stronger forces.

Conclusions

Photoelastic granular materials are a valuable tool for studying the granular aspects of regolith behaviour. Using these materials we identiefied a buckling ejection regime for slow impacts and we show that we can use them to successfully study the dynamics of surface probing in microgravity experiments.

Acknowledgements

Slow impact splash work was partially funded by DFG grant WU 321/12-1.
EMPANADA was funded by NASA Flight Opportunities Program

References

K.E. Daniels, J.E. Kollmer, J.G. Puckett, *Review of Scientific Instruments* 88 (5), 051808 (2017)

J.E. Kollmer, S.M. Lindauer, K.E. Daniels, *ASCE Earth & Space (2016)*

T. Bogdan, J.E. Kollmer, J. Teiser, M. Kruss, G. Wurm, *in prep.* (2019)

C. Krause, MSc Thesis, Universität Duisburg-Essen, Duisburg, Germany (2019)

Oral 150

Plant-on-a-Chip Platform for Secondaru Metabolites

Münire Ekmekçigil[1], Sinan Güven[1]

[1]Izmir Biomedicine and Genom Center, Turkey, Izmir
munire.ekmekcigil@ibg.org.tr, sinan.guven@ibg.org.tr

Introduction

Plant biotechnology is a set of techniques used to adapt plants for specific needs and products. Plant cell, tissue and organ culture techniques enable to in vitro cultivation of plant cells or tissue under aseptic and controlled enviromental conditions, in liquid or on semi-solid well-defined nutrient medium for the production of secondary metabolites or to regenerate plant.

Microfluidics is commonly defined as the science and technology that process minute volumes of fluids using channels with dimensions of a few to hundreds of micrometres.

The field of microfluidic technology is interdisciplinary and covers a wide spectrum of disciplines including physics, chemistry, engineering and biotechnology. The applications of microfluidics in the food, agriculture and biosystems sector are relatively recent, it grows rapidly as evidenced by the number of relevant publications and patents over the last decade

Our project based on obtaining secondary metabolites of naphtaquinones from *Onosma alboroseum* spp. through the microfluidic systems.

Figure 1**: Caption.**

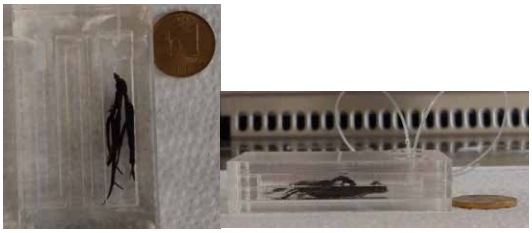

Figure 2**: Caption.**

Section 1

Therefore, We designed the suitable microchips and microbioreactors for plant studies. Naphtaquinones found a large amounts in the Boraginace family.

Natural and synthetic naphthoquinones derivatives are compounds that exhibit important biological activities, including antibacterial, antifungal, anti-parasitic and antiviral properties.

In our project, we were using *Onosma alba-roseum* belonging to this plant family for the production of naphthoquinones

The genus contain alkaloids, phenolic compounds, naphthoquinones, flavones while most important are shikonins and onosmins

Traditionally used as laxative, anthelmintic and also eye, blood diseases, bronchitis, abdominal pain, itch, fever, wounds, burns. Besides the medicinal effcts, the roots are used for coloring food stuffs, oils and dying wool and in traditionally

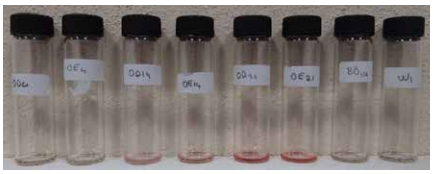

Figure 3: Caption.

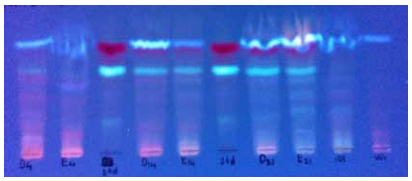

Figure 4:**Caption.**

Conclusions

Çalışmamızda steril koşullarda hücre kültürlerinde rejenerasyonu sağlanan köklerden alınan eksplantlardan, uygun tasarıma sahip mikroçipler aracılığıyla kinon grubu sekonder metabolit eldesi gerçekleştirilmiştir. Konvensiyonel bitki hücre kültürü tekniklerine göre daha modern ve etkili olan mikroakışkan sistemlerde bitki gelişimi ve metabolit eldesinin avantaj sağlaması konusunda ileri çalışmalar gerçekleştirilecektir.

Acknowledgements

We would like to thanks to Prof. Dr. Erdal Bedir from Department of Bioengineering, Izmir Institute of Technology for TLC analyses

References

https://nifa.usda.gov/plant-biotechnology

Oral 151

Giant Fluctuations induced by thermal diffusion in complex liquids

Alberto Vailati[1], Philipp Baaske[2], Henri Bataller[3], Marco Braibanti[4], Marina Carpineti[1], Roberto Cerbino[5], Fabrizio Croccolo[3], Aleksandar Donev[6], Loreto Garcia Fernandez[3], Fabio Giavazzi[5], Werner Köhler[7], José M. Ortiz de Zárate[8], Shenghua Xu[9], Daniel Zapf [7]

[1]Dipartimento di Fisica "A. Pontremoli", Università degli Studi di Milano, Milano, Italy, [2] Nanotemper Technologies GmbH, Munich, Germany, [3] Laboratoire des Fluides Complexes et leurs Réservoirs, Université de Pau et des Pays de l'Adour, Anglet, France, [4] ESA-Estec,Noordwijk, The Netherlands, [5] Dipartimento di Biotecnologie Mediche e Medicina Traslazionale, Università degli Studi di Milano, Segrate (MI), Italy, [6] Courant Institute of Mathematical Sciences, New York University, New York, USA, [7] Physikalisches Institut, Universität Bayreuth, Bayreuth, Germany, [8] Department of Applied Physics I, Universidad Complutense, Madrid, Spain, [9] Institut of Mechanics, Cjinese Academy of Sciences, Beijing, China
alberto.vailati@unimi.it

Introduction

The presence of a non-equilibrium condition in a fluid, such as a temperature or concentration gradient, gives rise to long-ranged fluctuations, whose amplitude is orders of magnitude larger than that of equilibrium ones (Ortiz de Zarate 2006). On earth the development of fluctuations is affected by the gravity force, which quenches them below a critical wave vector. The Gradflex experiment of ESA has shown that under microgravity conditions a stationary thermodiffusion process is accompanied by non-equilibrium fluctuation with size as large as the size of the container hosting the fluid (Fig. 1) (Vailati 2011).

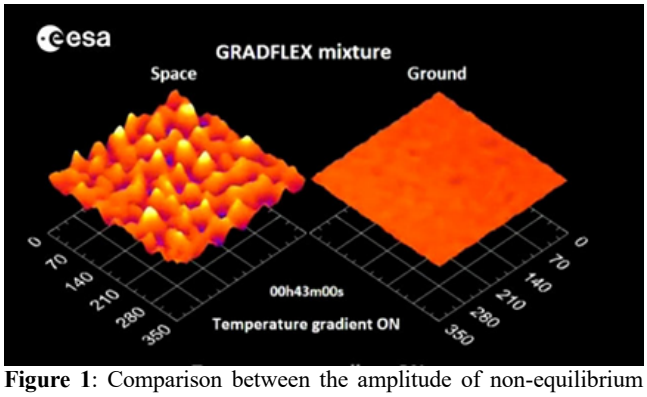

Figure 1: Comparison between the amplitude of non-equilibrium fluctuations is space (left) and on earth (right). Results were obtained during the Gradflex experiment of ESA on Foton M3. The sample was a polystyrene polymer in toluene under the action of a 13K temperature difference.

Thermal diffusion and fluctuations in the absence of gravity

Gradflex provided unambiguous evidence that thermodiffusion processes in space are accompanied by large non-equilibrium fluctuations, whose features can be described by means of linearized hydrodynamics. However, the linear models are not suitable to describe cases of practical interest, such as fluctuations induced by large gradients and under non-stationary conditions. Moreover, the investigation of non-equilibrium fluctuations has mainy involved single component fluids and binary mixtures, but recently transport processes in ternary mixtures have attracted increasing interest, due to the experiments performed on the International Space Station in the framework of the DCMIX project (Shevtsova 2018, Triller 2018).

The Giant-Fluctuations space project

The experience gathered with Gradflex, together with the identification of novel outstanding scientific problems, allowed to develop a new series of projects aimed at the fundamental understanding of the role of fluctuations during thermodiffusion in complex fluids and at the developments of innovative diagnostic methods based on these fluctuations (Fig. 2). The Giant Fluctuations (Neuf-Dix) project of ESA will investigate non-equilbrium fluctuations occurring in complex multicomponent mixtures, including a macromolecular component such as a polymer, a colloid or a protein. An important objective will be the understanding of how the fluctuations affect the interactions between macromolecules. The project is currently entering the C/D phase and is scheduled for flight on the International Space Station in 2021.

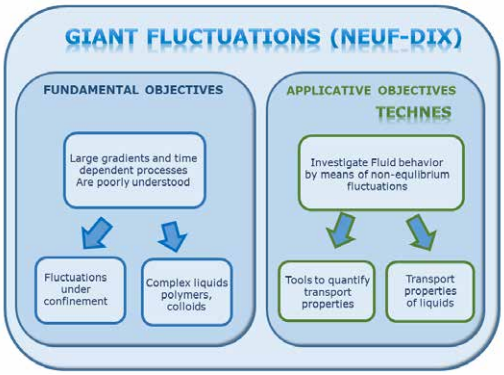

Figure 2: Main fundamental and applicative objectives of the Giant Fluctuations space project.

The opportunity of developing advanced diagnostic tools based on non-equilibrium fluctuations will be investigated within the TechNES (Technologies for Non-Equilibrium Systems) project of ESA. The rationale behind these methods is that non-equilibrium fluctuations reproduce at the mesoscopic scale the transport properties occurring at the macroscopic scale. Therefore, the statistical investigation of their relaxation allows the determination of transport coefficients.

Conclusions

Long-ranged fluctuations develop spontaneously during transport processes in fluids, but their investigation has been previously mostly focused onto fluctuations occurring during transport processes in single component fluids and binary mixtures under ideal conditions. The investigation of non-equilibrium fluctuations in multicomponent complex mixtures represents an innovative challenge that will be tackled within the Giant Fluctuations project of ESA during a long series of experiments aimed at understanding the behaviour of macromolecules under non equilibrium conditions.

Acknowledgements

Work supported by the ESA, CNES and DLR

References

J. M. Ortiz de Zárate and J. V. Sengers, *Hydrodynamic Fluctuations in Fluids and Fluid Mixtures* (Elsevier, Amsterdam, 2006).

P. Baaske, H. Bataller, M. Braibanti, M. Carpineti, R. Cerbino, F. Croccolo, A. Donev, W. Köhler, J. M. Ortiz de Zárate and A. Vailati, *Eur. Phys. J.* E39 (2016) 119.

V. Shevtsova, C. Santos, V. Sechenyh, J. C. Legros, and A. Mialdun. *Microgravity Sci. Technol.,* 25 (2018) 275.

T. Triller et al. *Microgravity Sci. Technol.,* 30 (2018) 295.

A. Vailati, R. Cerbino, S. Mazzoni, C. J. Takacs, D. S. Cannell, and M. Giglio, *Nat. Commun.* 2 (2011) 290

Oral 152

Effects of red light stimulation on plant growth and on auxin polar transport under microgravity condition in *Arabidopsis thaliana.* A morphometric study

Eugénie Carnero Diaz[1], Miguel A. Valbuena[1,2], Isabel Le Disquet[1], F. Javier Medina[2], Aránzazu Manzano[2], Alicia Villacampa[2], Josh Vandenbrink[3], Julio Sáez-Vásquez[4], Malgorzata Ciska[2], Raúl Herranz[2], John Z. Kiss[3]

[1]Muséum National d'Histoire Naturelle, Dépt.Systématique et Evolution, Paris, France;[2]PCNPµG Lab, Centro de Investigaciones Biológicas-CSIC, Madrid, Spain; [3]University of North Carolina at Greensboro, USA; [4]Université de Perpignan-ViaDomitia, Perpignan, France

[1]eugenie.carnero@mnhn.fr; [2]fjmedina@cib.csic.es; [3]jzkiss@uncg.edu; [4]saez@univ-perp.fr

Introduction

In the context of the space conquest of Mars, a controlled life-support system must be developped to revitalize atmosphere (liberate oxygen and fixe carbon dioxide), purify water (via transpiration), and provide human food. Photosynthetic higher plantes will be an essential element in this system. Due to their sessil nature, plants utilize environmental cues to growth and respond to their enviroment. Two of these cues, light and gravity, play an essential role both in the growth (phototropism and gravitropism, respectively) and in the nutrition of plants (photosinthesys).
Previous experiments showed that microgravity produces the disruption of meristematic competence, i.e., affecting the regulation of cell cycle and cell growth (Manzano et al., 2013, Matia et al., 2010). Light irradiation, especially red light (RL), mediated by phytochromes has an activating effect on these processes (Vanderbrink et al., 2014, Valbuena et al., 2018). Phytohormones, and more precisely the auxin, also are key mediators in these alterations (Herranz et al., 2014, Vanderbrink et al., 2014, Valbuena et al., 2018).

Morphometrical analysis of *Arabidopsis thaliana* seedlings cultivated in ISS during the SG3 experiment.

The Seedling Growth (SG) experiment aims to understand the combined influence of light and gravity on plant development through the identification of changes in the mechanisms and regulation of essential cellular functions. Proliferation and growth of root meristematic cells as well as auxin transport and perception have been analyzed. This project carried out onboard the ISS and it was divided into three experiments: SG1 (2013), SG2 (2014) and SG3 (2017). The contribution of this study was mainly to perform a morphological characterization of *Arabidopsis thaliana* Wild Type (WT) seedlings and mutants affected in the transport (*eir1.1* and *aux1-7*) and perception (*tir1*) of auxin. Indeed, special attention has been paid here to auxin because auxin is known to be a mediator of the transduction of the gravitropic and phototropic signal. It is also a regulator of the rates of growth and proliferation in meristematic cells, as well as of their further differentiation. Therefore, gravitropism, phototropism, auxin levels, and meristematic competence are mutually interrelated. In this study we focused on the transport polarity and the perception of this hormone using mutants deficient in these cellular processes: the *aux1.7* mutant (Stepanova et al., 2007, Li et al., 2015) is affected in auxin influx, the mutant *eir1.1* (Luschnig et al., 1998), is affected in the auxin efflux and the mutant *tir1.1* (Ruegger et al., 1998) is affected in the intracellular recognition of auxin.
The SG3 experiment has been carrying out on the European Modular Cultivation System (EMCS) located in the European Columbus module. Seeds of different *Arabidopsis thaliana* strains were hydrated and germinated in the EMCS. Throughout all steps of Figure1, images were taken from samples to downlink to the Earth for the analysis of tropisms and morphometric parameters (Kiss et al. 2012; Vandenbrink et al. 2016).

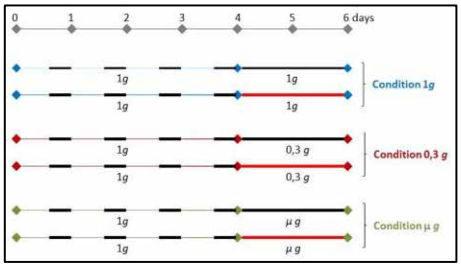

Figure 1: The time line of the spaceflight experiment as performed in the International Space Station (ISS). Seedlings of the different genotypes were grown either under microgravity (µg), partial gravity (0.3*g*) or 1*g* gravity level. All samples were exposed to photoperiodic (16 h light/8 h darkness) white light for 4 days, from top of the cassette and with continuous red light (RL) (red bars).

Morphometric analysis was performed on the last photo of each culture chamber (Figure 2). For this, we measured the length of the main root and the angle formed between the last mm of the root tip and the vertical. These inclination angles correspond to the gravitropic response of roots.

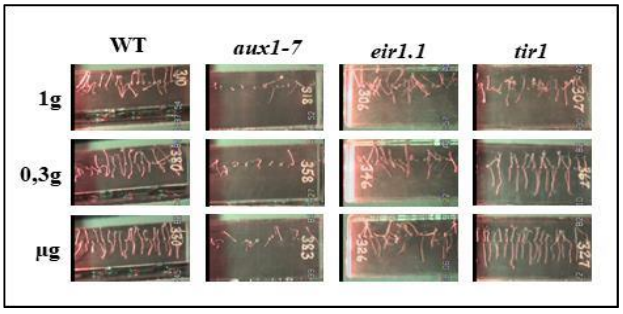

Figure 2: Images of 6-day-old seedlings from experiment performed on the ISS in different gravity conditions (µg, 0.3g and

1g). One culture chamber per experimental condition is shown at the end of the experiment in red light (RL).

The results of root growth of *Arabidopsis* wild type after 48 hours of photostimulation showed that root growth is not affected by μg in the presence of RL. Like WT, *aux1* mutant is not affected by μg significantly. On the other hand, root growth is stimulated by mini- and micro-gravity. Mutant *eir1* is not affected by either mini- or micro-gravity or RL. These results show that polarized transport is involved in controlling the response of plants to both factors (gravity and light), whether isolated or combined with each other. Regarding the mutant *tir1.1*, it presents a response to altered gravity and to RL similar to that of WT. Therefore, the perception of auxin by TIR1 does not appear to be an essential mechanism for the plant's response to the combined action of microgravity and LR

The measurement of the angle of inclination of the WT shows a significant positive photropism at the μg which decreases when the degree of gravity increases. This confirms the previous results of Vanderbrink *et al.* (2016). The mutant *aux1.1* has a positive phototropism independent of the level of gravity and the mutant *eir1.1* has a totally inhibited phototropism. These results highlighted the importance of polarized auxin transport in the plant response to the combined action of μg and RL. It seems that the auxin influx plays a less important role here than the efflux. The mutant *tir1* has a total absence of curvature irrespective of the level of *g*. Thus, the perception of auxin by its Tir1 receptor is crucial in the phototropic response of the plant in the absence of gravity.

These results have shown that the cross-regulation of gravitropism and photomorphism is largely due to polarized transport and auxin perception. Thus, RL induces a change in the distribution of auxin in the plant. At the meristem level, this new distribution would restore the meristematic cell competence interrupted by microgravity and at the level of the elongation **zone;** this new distribution of auxin would reveal the positive phototropism of the roots to the RL usually masked by the gravity earthly.

Conclusions

In conclusion, this research contributes to better understand the mechanisms of plant development and their large adaptability to their environment. This work opens up the perspective for some continuity between the understanding of past plant adaptation to gravity, after them exit from the water 400 million years ago, and their future adaptation to weightlessness in the framework of the space exploration (Moon, Mars) when the plants will not be subject anymore to gravity and they will be used as life support to Man

Acknowledgements

This work was supported by the French Space Agency "Centre National d'Etudes Spatiales"[Grant number DAR–4800000972], by post-doctoral fellowship to [MAV] from the French Space Agency CNES and the Seedling Growth Project to the ISSLSRA2009-0932/ 1177 of ESA-ELIPS Program. We also acknowledge funding from "ELGRA Gravity Spotlight Team" Grant.

References

Herranz, R., M. A. Valbuena, K. Youssef, F. J. Medina, Mechanisms of disruption of meristematic competence by microgravity in *Arabidopsis* seedlings, *Plant Signaling and Behavior* 9 (2014) e28289. doi: 10.4161/psb.28289.

Kamal, K. Y., J. J. W. A. van Loon, F. J. Medina, R. Herranz, Differential transcriptional profile through cell cycle progression in Arabidopsis cultures under simulated microgravity, *Genomics* (2019). doi: 10.1016/j.ygeno.2019.01.007.

Li, J. et al. 2015. Ethylene Inhibits Root Elongation during Alkaline Stress through AUXIN1 and Associated Changes in Auxin Accumulation. Plant physiology 168(4): 1777-91. PubMed ID: 26109425.

Luschnig, C., Gaxiola, R.A., Grisafi, P., and Fink, G.R., EIR1, a root-specific protein involved in auxin transport, is required for gravitropism inArabidopsis thaliana, *Genes & Dev.* (1998). 12: 2175-2187. doi: 10.1101/gad.12.14.2175.

Manzano, A. I., O. Larkin, C. Dijkstra, P. Anthony, M. Davey, L. Eaves, R. Hill, R. Herranz, F. J. Medina, Meristematic cell proliferation and ribosome biogenesis are decoupled in diamagnetically levitated *Arabidopsis* seedlings, *BMC Plant Biology* 13 (2013) 124. doi: 10.1186/1471-2229-13-124.

Manzano, A. I., J. J. W. A. van Loon, P. C. M. Christianen, J. M. Gonzalez-Rubio, F. J. Medina, R. Herranz, Gravitational and magnetic field variations synergize to cause subtle variations in the global transcriptional state of *Arabidopsis* in vitro callus cultures, *BMC Genomics* 13 (2012) 105. doi:10.1186/1471-2164-13-105.

Massa, G. D., G. Newsham, M. E. Hummerick, J. L. Caro, G. W. Stutte, R. C. Morrow, R. M. Wheeler, Preliminary species and media selection for the Veggie space hardware, *Gravitational and Space Research* 1 (2013).

Matía, I., F. González-Camacho, R. Herranz, J. Z. Kiss, G. Gasset, J. J. W. A. van Loon, R. Marco, F. J. Medina, Plant cell proliferation and growth are altered by microgravity conditions in spaceflight, *Journal of Plant Physiology* 167 (2010) 184-93 doi: 10.1016/j.jplph.2009.08.012.

Mizukami, Y., A matter of size: developmental control of organ size in plants, *Current Opinion in Plant Biology* 4 (2001) 533-39. doi: 10.1016/S1369-5266(00)00212-0.

Ruegger, M. et al. 1998. The TIR1 protein of Arabidopsis functions in auxin response and is related to human SKP2 and yeast grr1p. Genes & Development 12(2):198-207. PubMed ID: 9436980.

Stepanova, A.N. et al. 2007. Multilevel interactions between ethylene and auxin in Arabidopsis roots. The Plant Cell 19(7):2169-85. PubMed ID: 17630276.

Valbuena, M. A., A. Manzano, J. P. Vandenbrink, V. Pereda-Loth, E. Carnero-Diaz, R. E. Edelmann, J. Z. Kiss, R. Herranz, F. J. Medina, The combined effects of real or simulated microgravity and red-light photoactivation on plant root meristematic cells, *Planta* 248 (2018) 691-704. doi: 10.1007/s00425-018-2930-x.

Vandenbrink, J. P., R. Herranz, F. J. Medina, R. E. Edelmann, J. Z. Kiss, A novel blue-light phototropic response is revealed in roots of Arabidopsis thaliana in microgravity, *Planta* 244 (2016) 1201-15. doi: 10.1007/s00425-016-2581-8.

Vandenbrink, J. P., J. Z. Kiss, R. Herranz, F. J. Medina, Light and gravity signals synergize in modulating plant development, *Frontiers in Plant Science* 5 (2014) 563. doi: 10.3389/fpls.2014.00563.

Oral 154

Faraday waves under weightlessness on liquid-vapor bands

D. Beysens[1], T. Lyubimova[2,3], A. Ivantsov[2,3], Y. Garrabos[4], C. Lecoutre[4]

[1]Physique et Mécanique des Milieux Hétérogènes, CNRS PSL-ESPCI Sorbonne Université Paris Cité, 10 rue Vauquelin, 75005, Paris, France, EU, [2]Institute of Continuous Media Mechanics of the Ural Branch, RAS, 1, Koroleva Str., 614013, Perm, Russia, [3] Perm State University, 15, Bukireva Str. 614990, Perm, Russia, [4 4] CNRS, Univ. Bordeaux, Bordeaux INP, ICMCB, UMR 5026, F-33600 Pessac, France; daniel.beysens@espci.fr; lyubimovat@mail.ru, aivantsov@gmail.com, yves.garrabos@cnrs.fr, carole.lecoutre@cnrs.fr

Introduction

In the space environment, gravity effects are not present and a number of phenomena, of marginal effect on earth, can become predominant. This is particularly the case for a number of fluid instabilities triggered by vibrations when the stabilizing effect of gravity is not present any more. It is of both industrial and academic interest to investigate such instabilities.

When subjected to vibration, the shape and stability of the interface between two fluids depend on the relative direction of the vibration and the interface. It is known that in a gravity field a quasi-stationary wave pattern (frozen wave instability (Wolf 1969) can develop at the interface when the applied vibration is parallel to the initially horizontal fluid interface. This phenomenon was studied by Lyubimov and Cherepanov (1986) for the case of two superposed infinite horizontal layers of inviscid fluids. Because of the difference in densities of the fluids, the base flow velocities in the two layers are different, thus a tangential velocity jump across the interface appears, leading to a shear-driven Kelvin-Helmholtz (K-H) instability. The interface is immobile ("frozen") in average in the reference frame of the oscillating boundaries (Fig.1). Under zero-g, when the stabilizing effect of gravity is absent, the amplitude of the frozen waves thus diverges, forming bands oriented perpendicularly to the vibration direction (Fig. 1c, d) as observed in CO_2 (Lyubimova et al. 2017; Beysens et al. 1998, 2009, H_2 (Beysens et al. 2007; Gandikota et al. 2014), liquid mixtures of FC-40 and silicone oil (Salgado Sánchez et al. 2019) and miscible mixtures of water–isopropanol with water (Shevtsova et al. 2016).

When the band pattern is established, the fluid interface becomes perpendicular to the vibration direction and Faraday waves are expected when the vibration intensity exceeds a critical value (see Fig. 1c,d). Faraday instability has indeed been observed at the liquid-vapor interface in H_2 near its critical point (Gandikota et al. 2014) and at the interface of miscible water-alcohol mixtures (Shevtsova et al. 2016).

We analyze these Faraday waves on band patterns, analytically, numerically and compare with new data obtained in CO_2 (sounding rocket Maxus 7). The two-phase system used in our experiments is characterized by very low surface tension and viscosity of each fluid phase. In this case, the wavelength of the most dangerous perturbations are small, i.e. formation of thin bands is expected. Therefore, differing from the previous studies, the interaction between the interfaces should be important, which can substantially modify the instability characteristics. We here study the excitation of Faraday waves on the band pattern by taking into account this new particular situation.

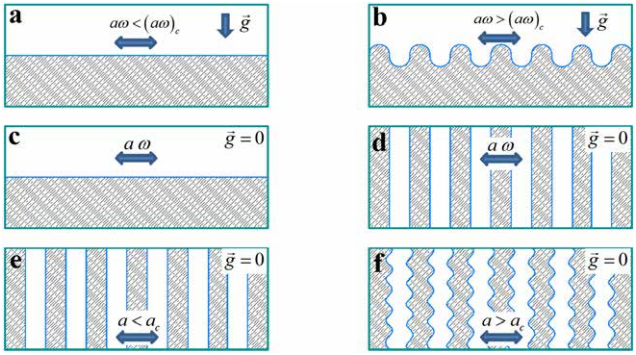

Figure 1: Interface between two fluids in a container of thickness $2h$: (a), (b) in a gravity field, (c), (d), (e), (f) in zero gravity conditions; (a), (c), (e) base states, (b), (d), (f) supercritical regimes: (b) frozen waves at $a\omega > a\omega_c$, (d) band pattern, (f) Faraday waves on bands at $a > a_c$.

Experimental observation

The use of fluids in the vicinity of their liquid-vapor critical point is particularly appealing for such investigations. In addition to its use by the space industry in near supercritical conditions, the thermodynamic properties of fluids when expressed under reduced temperature or density distance from the critical point can be conveyed under universal, scaled functions (Stanley 1987). In addition, the fact that surface tension σ and liquid-vapor density difference $\rho_2 - \rho_1$ vanish when nearing the critical point enhances the effect of accelerations and highlights the mechanical instabilities. Experimentally speaking, another interest of considering the critical point vicinity is the possibility to vary the fluid parameters simply by changing temperature.

Experiments have been performed with CO_2 in cylindrical samples on board of sounding rockets. Details on the experimental setup can be found in Beysens et al. (2009; 2010). The experimental module is of TEM-FER type (Beysens et al. 2009). Figure 2 reports a typical pattern where the interface between bands is subjected to Faraday instability.

Direct numerical simulations (DNS)

The numerical simulations were performed for a system of two immiscible fluids filling a rectangular container of length l and height $2h$. The container is subjected to vibrations at amplitude a and frequency ω. The initial state corresponds to the band structures with interfaces perpendicular to vibration axis.

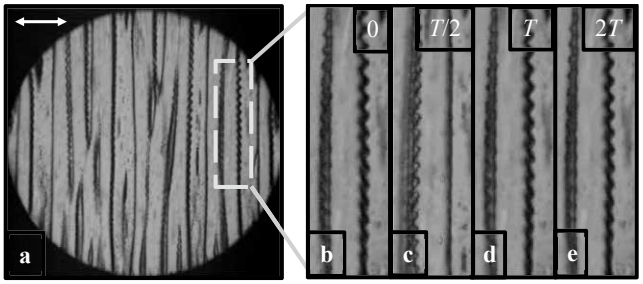

Figure 2: (a) CO_2 sample (10.0 mm diameter and 2.189 mm thickness) under a=0.7 mm, f=25.25 Hz vibrations (direction: double arrow. The window is enlarged in (b-e). The black lines correspond to the interfaces between the liquid and vapor phases, which order as "bands" perpendicular to the vibration direction. (b-e) Different times in units of vibration period T (see text) showing subharmonicity by the interface deformation phase as highlighted by the white dotted line). Time origin corresponds to amplitude maximum on the right. Interface deformation occurs on half period on one side of the band (b, d, e) and on the other half period on the other side (c).

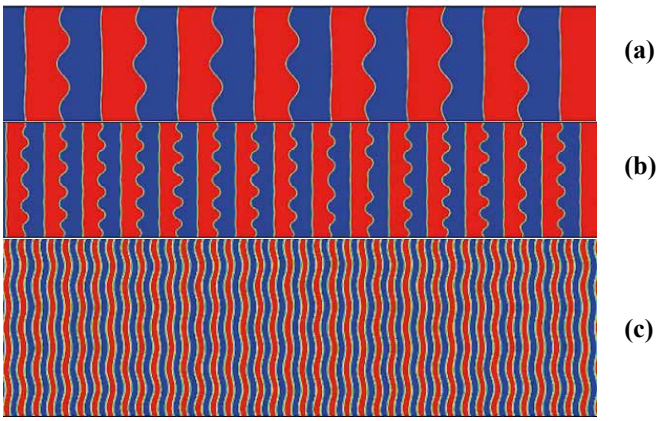

Figure 3: Faraday waves for different parameters of vibrations: (a) f = 5 Hz, a = 2.5 mm, band pattern period = 0.8 mm, (b) f = 25 Hz, a = 1.1 mm, band pattern period = 0.4 mm, (c) f = 20 Hz, a = 1.6 mm, band pattern period = 0.1 mm.

Theoretical analysis of Faraday instability on bands

The critical conditions for the Faraday instability uses the approach of Kumar & Tuckerman (1994) taking into account the very low viscosity of fluids. Minimizing the neutral curve with respect to the wave number, one obtains the critical vibration amplitude a_c above which Faraday waves can develop: $$a_c = \frac{2\sqrt{2e^{-2H}+\sqrt{6e^{-2H}+1}}}{(\rho_2-\rho_1)(1-e^{-2H})}\sqrt{\frac{(\rho_2+\rho_1)(\eta_1+\eta_2)}{\omega}},$$

Here $H = kh$ is the dimensionless spatial period of the band pattern, with k the band wavenumber (Figs. 1e and 2). In the case of large H, when interaction of interfaces is negligible, this formula is different and reduces to $a_c = \frac{2}{\rho_2-\rho_1}\sqrt{\frac{(\rho_2+\rho_1)(\eta_1+\eta_2)}{\omega}}$.

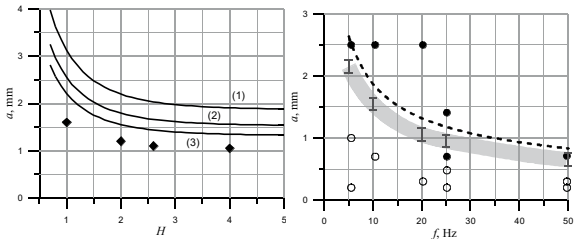

Figure 4: Left: Dependences of a_c on $H=kh$ for (1) f=10 Hz, (2) f=15 Hz, (3) f=20 Hz. The parameters correspond to CO_2 experiments. Diamonds correspond to the stability boundary obtained in the numerical simulations for f=20 Hz. Right: Stability map for experimental, analytical and DNS results. Circles are experimental results (open circles: stable states; filled circles: Faraday instability). The grey line shows DNS results (the line width corresponds to the accuracy of the stability boundary determination). The dashed line corresponds to analytical stability estimation.

Conclusions

Periodical pattern (bands) can develop in near critical fluid under zero gravity or in liquid mixtures. Depending on the vibration parameters, an instability can be observed on the bands, which leads to the development of Faraday waves. In the present study, Faraday instabilities in a thin band pattern, a novel situation, have been studied taking into account the interaction between the bands.

Acknowledgements

We thank ESA and CNES for providing space access and laboratory support. Theoretical analysis and numerical calculations were supported by the Russian Foundation for Basic Research (Grant No. 15-01-09069).

References

G.-H. Wolf, Z. Phys. B 227 (1969) 291.
D. V. Lyubimov and A. A. Cherepanov, Fluid Dyn. 21 (1986) 849. (2017).
D. Beysens, R. Wunenburger, C. Chabot, and Y. Garrabos, Microgravity Sci. Technol. 11(1998) 113.
D. Beysens, Y. Garrabos, D. Chatain, and P. Evesque, EPL 86 (2009) 16003.
D. Beysens, D. Chatain, Y. Garrabos, C. Lecoutre, F. Palencia, P. Evesque, and V. Nikolayev, Acta Astronaut. 61 (2007) 1002.
G. Gandikota, D. Chatain, S. Amiroudine, T. Lyubimova, and D. Beysens, Phys. Rev. E 89 (2014) 013022.
P. Salgado Sánchez, V. Yasnou, Y. Gaponenko, A. Mialdun, J. Porter, and V. Shevtsova, J. Fluid Mech. 865, 850 (2019).
H. E. Stanley, Introduction to Phase Transitions and Critical Phenomena (*Oxford University Press,* 1987).
K. Kumar and L. S. Tuckerman, *J. Fluid Mech.* 279 (1994).

Oral 155

5 Years of SELGRA: Past, Present and Future

T. Ribeiro[1], M. Ferreira[2], J. Rabineau[3], J. Attias[4], L. Luque Álvarez[5]

[1] Faculdade de Ciências da Universidade do Porto, Porto, Portugal; [2] The University of Manchester, Manchester, UK; [3] Université libre de Bruxelles, Brussels, Belgium; [4] Research Centre for Musculoskeletal Science & Sports Medicine, Manchester Metropolitan University, UK; [5]Széchenyi István University, Győr, Hungary
selgra@elgra.org

Introduction

SELGRA (Student European Low-Gravity Research Association) is a non-profit European student association whose main objective is to promote gravity-related research between university students across Europe. It was created in 2013 as a student chapter of ELGRA (European Low-Gravity Research Association), born out of a need to encourage student's engagement and further European cooperation in the field.

Figure 1: SELGRA badge for the commemoration of 5 years.

In this presentation we will introduce SELGRA, its evolution and challenges. Moreover, the importance of maintaining such a community will be discussed in parallel with our perspective for the future of gravity-related research.

The community

Since its inception, SELGRA has grown steadily. Members are mainly university students from all over Europe working in different fields from life to physical sciences and engineering. They all have in common the interest towards gravity-related research. Within the community, members can share their work and experiences, promote scientific events in their countries, look for opportunities in the field of gravity-related research and find financial support to attend conferences.

Project and Activities

Through a branch of different outreach tools our members can have an overview of the current research under microgravity and hypergravity conditions. Members have access to newsletters, where they can share their experiences and read about a variety of topics. In addition, SELGRA is now organizing webinars to promote interaction between students and experts in the field. The scientific level of the webinars will be adapted so every member can benefit from it. We have been present in several scientific events and through social media we have promoted the interaction with the general public.

Acknowledgements

We gratefully acknowledge the continuous financial support of ELGRA. Furthermore, many thanks to all the members that contributed to the SELGRA newsletter and shared opportunities over the past 5 years.

References

SELGRA website: www.elgra.org/selgra

ELGRA website: www.elgra.org

Oral 156

Understanding the Effectiveness of Countermeasure Exercises in Human Spaceflight: Individual Variation

Scott JPR[1,2,3]

[1] Wyle Laboratories GmbH; [2] ESA Space Medicine Team; [3] ESA Topical Team on Personalised Medicine

Exposure to microgravity (μG) and the space environment results in a profound multi-system adaptation, characterised by both short- and long-term changes, including reductions in maximum oxygen uptake (VO_{2max}), muscle size and strength, and bone mineral density (BMD) As these changes appear to reflect those that occur with prolonged inactivity or the absence of gravitational loading, since the early days of human spaceflight, exercise training has been used as a potential method of managing the adaptation process and today is the cornerstone of the International Space Station (ISS) μG countermeasure (CM) programme. Technological developments in exercise devices has, on average, reduced the magnitude of adaptations, but these improvements mask a significant variation between individual astronauts.

In 'personalized medicine', certain types of analysis purport to quantify individual differences (ID) in intervention response and identify ‘responders’ and ‘non-responders’, and thus justify the exploration of response moderators or mediators. However, it has been argued that, because of the influence of within-subject variation, true ID can only be quantified by comparing the standard deviations of changes between ‘intervention’ and ‘comparator’ arms (Atkinson & Batterham, 2015). This poses a significant challenge in the study of the effectiveness of CM exercise programmes, as true intervention studies are rarely performed and, historically, some form of CM exercise has always been used resulting in the absence of any comparator group, either past or present. Inter-individual differences also appear to exist in responses to long-term bed rest (LTBR) – considered to be the ‘Gold-Standard’ ground-based model of spaceflight adaptation – and LTBR-tested interventions, but LTBR studies frequently have control groups and control many of the factors that may confound space flight studies.

As such, LTBR may help to ‘prove’ that true ID exist in response to unloading and countermeasures/interventions and whether humans might have different degrees of ‘sensitivity’ (Pickering & Reily, 2019) to BR and BR-tested exercise interventions. This paper describes the 1) challenges of understanding the effectiveness of CM exercise and the importance of understanding ID in operational space medicine; 2) the value of LTBR in understanding ID, and; 3) the current work of the ESA Topical Team on Personalised Medicine and ESA in advancing understanding in this area.

References

1. Atkinson G, Batterham AM. True and false interindividual differences in the physiological response to an intervention. Exp Physiol (2015) 100:577–88.
2. Pickering & Reily. Do Non-Responders to Exercise Exist—and If So, What Should We Do About Them? Sports Medicine (2019) 49:1–7.

Oral 158

Experimental analysis of ternary mixture with Soret effect at the border of hydrodynamic stability

A. Mialdun[1], A. Arrate[2], M. Bou-Ali[2], V. Shevtsova[1]

[11]MRC, CP165/62, Université libre de Bruxelles (ULB), 50, Ave. F.D. Roosevelt, B-1050 Brussels, Belgium
[2]Mechanical and Manufacturing Department, Mondragon Goi Eskola Politeknikoa, Loramendi 4, Apdo. 23, 20500 Mondragon, Spain,
amialdun@ulb.ac.be, mbouali@mondragon.edu, vshev@ ulb.ac.be

Introduction

Thermodiffusion (also known as thermal diffusion or Soret effect) refers to a transport mechanism in which temperature gradients cause mass transfer in mixtures. The experimental techniques for the measurement of Soret coefficients in liquid binary mixtures are well established and the scientific focus moved towards ternary mixtures. The thermo-diffusion coefficients retrieved from the experiment with ternary mixtures are extremely sensitive to the precise values of mass diffusion coefficients and optical contrast factors. In addition, ternary systems are further complicated by the fact that the sign of the Soret coefficients of the various components can be different and this can lead to convective instability, which difficult to recognize and quantify.

In the framework of the international DCMIX (Diffusion Coefficients Measurement in ternary mIXtures) project, scientists expect to obtain reliable benchmark results on the International Space Station (ISS) for the validation and calibration of present and future ground based measure-ments. Here we are aimed at the study of the mixture which was examined in DCMIX2 experiment, which is composed by toluene, methanol, and cyclohexane. This highly non-ideal system is of particular interest due to the existence of a miscibility gap and a large region of compositions with negative Soret coefficients.The measurements onboard of the ISS have shown that only one of the five examined ternary state points, i.e., with mass fractions of Tol-Meth-CH → 0.61-0.32-0.07 can be gravitationally stable. The Soret coefficient of the denser component, toluene, is positive but the Soret coefficient for methanol, which present in excess, is negative. However, this state point is on the border of stability and the present research is aimed at the investigation of its transport properties.

Methodology

The ternary mixture was analysed using two different techniques: the Optical Digital Interferometry (ODI) and the Thermogravitational column (TG).

Two different mixtures of Tol-Meth-CH, one with concentrations of 0.60-0.35-0.07, and another one with slightly shifted composition 0.61-0.32-0.07 were examined using both techniques. In the thermogravitational column [1], the mixture is placed between two vertical walls and a horizontal temperature gradient is applied. Afterwards the concentration variation of each component along the column height is determined.

Here, in order to analyse the stability of the mixture, two different types of columns were used: the short Thermogravitational Column (STC) and the Thermogravitational μColumn.

The thermodiffusion coefficient in the case of the STC is obtained from the analysis of the concentration in stationary state [1]. Various samples are extracted at different height-points of the column and composition at these points is determined from the measurements of density and refractive index in samples.

The ODI technique have been used onboard of the ISS and in ground laboratory and its description can found elsewhere [2, 3].

The thermogravitational μColumn combines both, STC and ODI. It is convection based technique as STC but with optical windows which enalble the application of the ODI technique [4]. The system is equipped with two lasers ($\lambda_1 = 470$ nm and $\lambda_2 = 633$ nm) forming Mach-Zehnder interferometer, and the concentration variation of the species of the mixture is tracked by changes in the refractive index. The variations of the refractive index are determined from the captured interferograms.

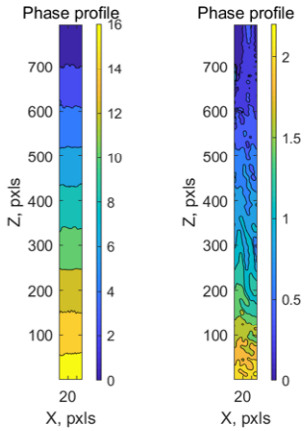

(a) (b)

Figure 1: Red laser phase profile for (a) stable stationary state and (b) unstable stationary state. We carried out the experiments at 25ºC.

Results

The results of the STC show that in both mixures the toluene migrates toward the bottom wall. For the mixture with the 5% CH in mass, both methanol and cyclohexane are displaced toward the top part on the column. However in the mixture with 7%, of cyclohexane, methanol migrates toward the top part while cyclohexane, the less dense component, migrates in the opposite direction.

Microcolum results using the red laser helped in the determination of the mixture stability. For the mixture with

5% CH, once the temperature gradient is built up separation starts and remains constant in the stationary state. However, for the mixture with 7% CH, even if separation states when ΔT is applied, the system does not reach to a stable stationary state, it keeps oscilating on time.

The ODI results reveal that the mixture with 7% of CH is conditionally stable, the fringes on the wrapped phase map in Fig2a are not parallel but here is no motion and the picture is stable. However, traces of secondary instability can be noticed.

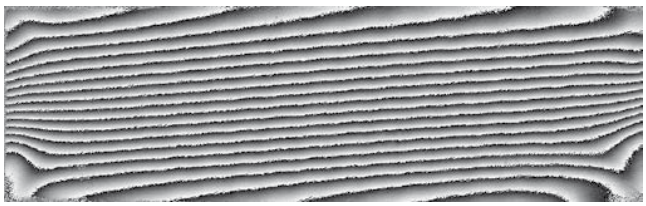

(a) Tol/Meth/Ch mixture with mass fr. 0.62/0.31/0.07

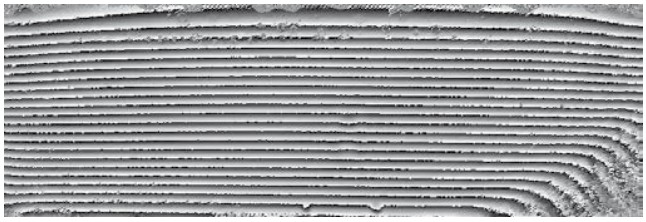

(b) Tol/Meth/Ch mixture with mass fr. 0.62/0.31/0.05

Figure 2: The wrapped phase maps correspond to 12h of separation with ΔT=6K as observed by 670nm laser by ODI.

The wrapped phase map for the mixture 0.60/0.35/0.05 shown in Fig. 2b clearly indicates the stable hydrodynamic behavior.

In addition to the hydrodynamic stability of the DCMIX2 mixture, 0.62/0.31/0.07, we have analyzed the quantitative characteristics of diffusion and thermodiffusion by the ODI technique. For this purpose, variation of Δn/ΔT in the steady state and effective diffusion was examined along the concentration path with 60% toluene. The starting point is the binary mixture composed by Tol/Met with mass fraction 0.6/0.4. The optical separation per unit of a temperature, Δn/ΔT, is proportional to the Soret separation and it is shown by the blue curve in Fig.3. It displays strong dependence on the mass fraction of cyclohexane. Taking into account that, the Soret sepation and Δn have opposite signs, it means that the Soret separation increases with the mass fraction of cyclohexane. The effective diffusion coefficient grows continuously with the increase of cyclohexane content in the mixture.

Conclusions

We studied the hydrodynamic stability of the ternary mixture Tol-Meth-CH at two different compositions by using different experimental approaches: the short thermo-

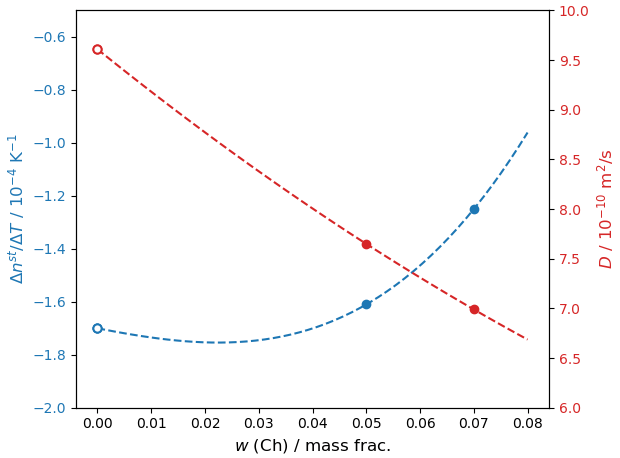

Fig.3. The optical separation and effective diffusion coefficient measured by ODI technique along the path with 60% of toluene in mass fraction.

gravitational column (STC), the thermogravitational μColumn and optial digital interferometry.

All results converge that the mixture with composition 0.60-0.35-0.05 is completely stable. However, for the mass fraction 0.61-0.32-0.07, the mixture is conditionally stable displaying features of secondary instability. The Soret separation and diffusion was tracked along the path with 60% of toluene.

Acknowledgements

The authors from ULB acknowledge support of this work by the PRODEX program of the Belgian Federal Science Policy Office. The authors from MU thank FETRAFLU (2018-CIEN-000101-01) from Gipuzkoa Program for Science, ATNEMFLU (ESP2017-83544-C3-1-P) of the MINECO, DCMIX (AO-2009-0858/1056) from the European Space Agency, and the Research Group Program (IT1009-16) and μ4Industry from the Basque Government.

References

[1] P. Blanco, M. M. Bou-Ali, J. K. Platten, D. A. De Mezquia, J. A. Madariaga, and C. Santamaría, "Thermodiffusion coefficients of binary and ternary hydrocarbon mixtures," *J. Chem. Phys.*, vol. 132, no. 11, 2010.

[2] A. Mialdun, V. Shevtsova, Temperature dependence of Soret and diffusion coefficients for toluene–cyclohexane mixture measured in convection-free environment, *J. Chem. Phys.* 143 (2015) 224902.

[3] A. Mialdun, I. Ryzhkov, O. Khlybov, T. Lyubimova, and V. Shevtsova, Measurement of Soret coefficients in a ternary mixture of toluene–methanol–cyclohexane in convection-free environment, J. Chem Physics 148, 044506 (2018);

[4] E. Lapeira, A. Mialdun, V. Yasnou, P. Aristimuño, V. Shevtsova, and M. M. Bou-Ali, "Digital Interferometry Applied to Thermogravitational Technique," Microgravity Sci. Technol., vol. 30, no. 5, pp. 635–641, 2018.

Oral 159

Two-liquid system in a rotating cylindrical cavity under the transverse vibrations

N. V. Kozlov[1], I. E. Karpunin[2]

[1] Institute of Continuous Media Mechanics UrB RAS, Perm, Russia, [2] Perm State Humanitarian Pedagogical University, Perm, Russia;
kozlov.n@icmm.ru, vankarpunin@yandex.ru

Introduction

Vibrations are an efficient tool for the control of nonlinear mechanical systems due to various average effects (Blekhman 2000). For example, vibrations can have a strong effect on the hape and dynamics of the interface between miscible liquids (Gaponenko et al. 2015). Rotating hydromechanical systems posses a large number of interesting properties because of inertia forces (Greenspan 1968). Applying vibrations for the control of rotating fluids in low gravity has a great potential for application in modern technologies.

A centrifuged two-liquid system is prone to the excitation of waves (Scott 1973, Bauer 1982). At vibrations parallel to the cylinder axis a standing wave and a frozen relief are observed (Lapin et al. 1990, Ivanova and Salnikova 2007). At vibrations perpendicular to the rotation axis, in cylindrical two-liquid systems centrifugal waves and steady flows are excited in a resonant manner (Ivanova et al. 2005, Kozlov and Shuvalova 2016).

Vjatkin et al. (2019) studied the dynamics of nonisothermal fluid in a rotating cylindrical container at transversal vibrations. An electric current passed through the liquid parallel to the cylinder axis. As a result, a parabolic radial temperature profile was formed. Due to the radial fluid stratification the vibrations excite its inertial oscillations. In particular, it was shown experimentally and theoretically that vibrations whose radian frequency is equal to the rotation rate lead to the transformation of the centrifugal field.

The present work considers a rotating two-liquid system subject to transverse vibrations with the radian frequency Ω_v equal to the rotation rate Ω_r.

Experimental method

Experimental model is a cylindrical container entirely filled with two immiscible liquids of different density (Fig. 1). The walls of the container are made of acrylic glass and are transparent. Its inner dimensions are radius $R_o = 3.5$ cm, length $L = 13.5$ cm. The container is rotated by a stepper motor FL86STH80-4208A sufficiently fast, so that the liquids are steadily distributed in the form of the core with radius R_i and the annulus.

The container *1* is installed horizontally in supports with bearings on the platform of a mechanical vibrator *2* that is brought in motion via a crank-and-rod mechanism *3* by an electric motor *4* (Fig. 1). The motion of fluids is studied by means of video registration and consequent digital image processing. For this a high-speed camera Optronis CamRecord CL600x2 and a personal computer are used.

In the absence of vibrations, the column of light liquid is situated near the rotation axis. Its interface has the circular shape and rotates slower than the cavity due to the steady flows generated under the effect of gravity (Kozlov et al. 2016).

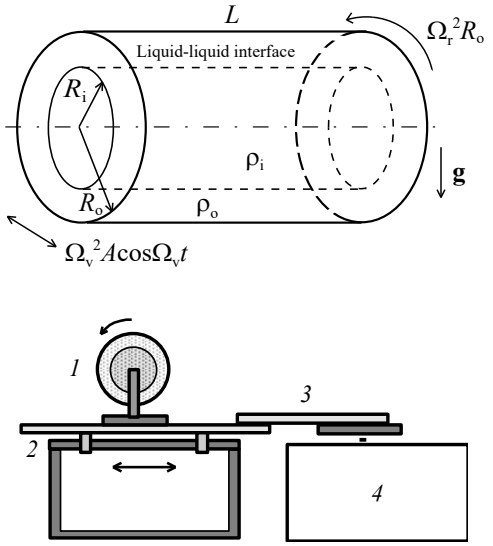

Figure 1: Experimental model.

Experimental results

Vibrations with the relative frequency $n \equiv \Omega_v / \Omega_r = 1$ lead to the radial shift of the light-liquid column by the distance b_1. Meanwhile its position in the rotating reference frame is stationary. In the laboratory frame, the column center orbits about the cavity axis with the angular rate equal to the rate of container rotation. At deviation of n from 1, the column drifts relative to the container wall in the leading or lagging direction. The gravity field makes the fluid oscillate with the frequency of rotation, while the column-center coordinate periodically changes with the amplitude b_2. In experiments, the gravity contribution is small compared to the action of vibrations, $b_2 / b_1 \sim 0.1$.

With an increase in the vibration amplitude A the magnitude of the column radial shift b_1 increases. Gradually, on the interface waves can be distinguished that propagate in the azimuthal and axial directions. In Fig. 2, the instantaneous position of the light-liquid column in the rotating container at vibrations is shown. The column is shifted radially, and waves propagate on its boundary. In Fig. 3, one can see the wave crests periodic along the rotation axis. At the same time, the fine particles that initially seeded the interface accumulate in thin rings that are spaced regularly along the axis. The waves do not alter the dynamics of the liquid column as a whole, its radial displacement remaining the same.

Figure 2: Photograph of the two-liquid system at rotation taken through the front flange at some angle to the rotation axis.

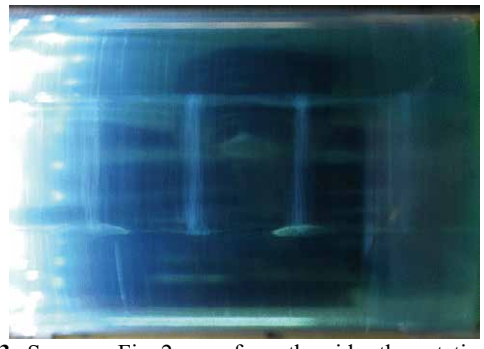

Figure 3: Same as Fig. 2 seen from the side, the rotation axis is oriented from left to right.

The following parameters were varied in experiments: rotation rate Ω_r, column relative radius R_i / R_o, viscosity ratio ν_i / ν_o, radian frequency Ω_v and amplitude A of vibrations. At condition $n = 1$, in all experiments the relation $b_1 / A \approx 0.5$ held. Thus, vibrations lead to the radial shift of the light-liquid column by the distance that depends only on the vibration amplitude. This result agrees with the one found in the work (Vjatkin et al. 2019) for the nonisothermal liquid. Results of the present experiments support the conclusion made by Vjatkin et al. (2019) in respect that the shift of the light inclusion from the container's symmetry axis is caused by the averaged field of inertia. The present results also point to the fact that the theory (Vjatkin et al. 2019) may be generalized for a wider class of rotating systems inhomogeneous in density. It is interesting to notice that the centrifugal waves propagate in the reference frame of the light-liquid column.

Conclusions

The dynamics of a system of two immiscible liquids in a rotating cylindrical container has been studied experimentally at vibrations perpendicular to the rotation axis. The case when the vibration frequency coincides with the rotation rate has been considered. Under vibrations the light liquid shifts radially by the distance equal to the half of vibration amplitude. This result demonstrates that vibrations lead to an average transformation of inertia field.

Acknowledgements

The work was supported by the Russian Science Foundation (grant No. 18-71-10053).

References

H. F. Bauer, Coupled oscillations of a solidly rotating liquid bridge, *Acta Astronaut.* 9(9) (1982) 547–563.

I. I. Blekhman, *Vibrational mechanics: nonlinear dynamic effects, general approach, applications* (Singapore: World Scientific, 2000).

Y. A. Gaponenko, M. Torregrosa, V. Yasnou, A. Mialdun, V. Shevtsova, Dynamics of the interface between miscible liquids subjected to horizontal vibration, *J. Fluid Mech*. 784 (2015) 342–372.

H. Greenspan, *The Theory of Rotating Fluids*, (University Press, Cambridge, 1968).

A. A. Ivanova, V. G. Kozlov, D. A. Polezhaev, Vibrational dynamics of a centrifuged fluid layer, *Fluid Dyn*. 40(2) (2005) 297–304.

A. A. Ivanova, A. N. Salnikova, Dynamics of a Two-Fluid System in a Rotating Horizontal Cylinder under Longitudinal Vibration, *Fluid Dyn.* 42(3) (2007) 369–375.

N. V. Kozlov, D. A. Shuvalova, Effect of vibration on two-liquid system in rotating cylinder, *Acta Astronaut.* 127 (2016) 561–571.

N. V. Kozlov, A. N. Kozlova, D. A. Shuvalova, Dynamics of immiscible liquids in a rotating horizontal cylinder, *Phys. Fluids* 28 (2016) 112102.

A. Yu. Lapin, D. V. Lyubimov, T. P. Lyubimova, The numerical study of the quasi-equilibrium forms of rotating liquid interface in an axial vibration field, in *Nonlinear problems of viscous fluid dynamics* (UB AS USSR, Sverdlovsk, 1990) 90–97. (in Russian)

W. E. Scott, Inertial wave frequency spectrum in a cylindrically confined, inviscid, incompressible, two-component liquid, *Phys. Fluids* 16(1) (1973) 9–12.

A. A. Vjatkin, V. G. Kozlov, R. R. Sabirov, Convection of a heat-generating fluid in a rotating cylindrical cavity subject to transverse vibrations, *Int. J. Therm. Sci.* 137 (2019) 560–570.

Oral 160

Selective particle transport in a microgravity environment via ratchet effect

P. Beltrame[1]

[1]UMR INRA 1114 EMMAH - Avignon Université, Avignon, France;
philippe.beltrame@univ-avignon.fr

Introduction

Sorting suspended particles in a fluid is an issue in many domains as the food industry, the medical analyses or in the treatment wastewater. Many processes are based on the microfiltration using a membrane. Nevertheless at high permeation rates this method suffers from accumulation of non-permeating particles above the membrane surface, thereby blocking the pores. The last decades, alternative techniques using flow in a periodic and asymmetric structure of micro-channels are rising. Begin of 2000's, micro-devices for which a particle is obtained without net flux are proposed. In particular, Matthias and Müller (2003) realized an experiment where two basins are connected via modulated microchannels filled with a liquid. A periodic pumping confers a back and forth fluid motion dragging the particle in suspension. The experiment showed the existence of an effective transport in specific ranges of parameter values. Among the many mechanisms which may explain these results, the authors interpret the slow particle drift as a ratchet effect called *drift ratchet* (Kettner et al. 2000). "Ratchet effect" refers to the possibility of transporting particles even if the mean force is zero (zero bias). Therefore the selective transport via ratchet effect can arise in microgravity environment.

Nevertheless, further experiments reveal that the thermal fluctuation are negligible in the experiment of Matthias and Müller (2003) and does not proof a selective.
In (Beltrame et al. 2016) we analyzed the possible deterministic mechanisms of such a device with 1D model. We found out two main mechanisms depending on the particle characteristics.
The goal of this paper is to determine if the 1D transport mechanisms described in (Beltrame et al. 2016) exist for a more realistic axi-symmetric 3D model and if it can be applied to particle sorting in microgravity.

Modeling

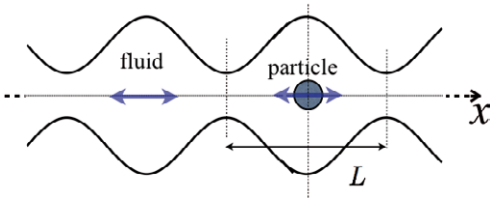

Figure 1: Sketch of the problem: the particle translates along the *x*-axis of a periodic distribution of pores. It is dragged by a periodic motion of a viscous fluid. The particle weight is oriented to the negative *x* direction.

Let us consider a L-periodically modulated channel infinitely extended along the line (Ox) and is filled by a newtonian fluid with the viscosity μ. We call 'pore' the channel portion of length L (fig. 1). We consider the axis-symmetric problem where the particle of mass m in suspension in the fluid moves only along the axis and the particle does not rotate. The pressure amplitude $A(t)$ of the fluid pumping is T-periodic and defined by:

$$A(t) = \begin{matrix} 1-\alpha & \text{if} \quad 0 \le t \ (\mathrm{mod}\, T) < T\alpha \\ \cos\left(2\pi \frac{t-T\alpha}{T-T\alpha}\right) - \alpha & \text{if} \quad \alpha T \le t \ (\mathrm{mod}\, T) < T \end{matrix} \quad (1)$$

The parameter α takes values in the range $[0,1[$. If $\alpha = 0$ then $A(t)$ is sinusoidal. Otherwise, the pressure difference is constant during the first step in the interval $[t_0, t_0 + \alpha[$ following by a sinusoidal pumping in the interval $[t_0 + \alpha, t_0 + T[$. The advantage of the temporal asymmetry compared to the asymmetric geometry is to control the particle direction by changing only the pumping.
We assume that the flow is a quasi-static Stokes' flow. The consistency of this approximation with the parameter domains of the transport solution is discussed in the last section. Under these assumptions, the position of the particle center is x(t) governed by the dimensionless ODE's

$$\ddot{x} + \boldsymbol{P_\gamma}\gamma(x)\dot{x} = \boldsymbol{P_\gamma}\,\boldsymbol{P_v}\,\gamma(x)u_{eq}(x)A(t) \quad (2)$$

where the dimensionless parameters are

$$\boldsymbol{P_\gamma} = \frac{LT\mu}{m}, \quad \boldsymbol{P_v} = \frac{[p]T}{\mu},$$

The effective pressure difference between the inlet and outlet of a pore is noted $[p]$. The fields $\gamma(x)$ and $u_{eq}(x)$ depend on the pore boundary and the particle shape and they are computed using a Boundary Element Method (Makhoul et al. 2015). Note that for the limiting case of a point particle in an infinite medium, the field $\gamma(x)$ becomes the Stokes drag coefficient of a sphere.

Due to the low particle inertia, bounded oscillations are expected. However, for specific parameter values, a transport may occur. To find these domains, in addition to the time integration of the evolution equation (2) we employ the tools of bifurcation analysis and continuation of periodic orbit. This gives a broad overview of the dynamics in the parameter space (Beltrame 2018).

Results

We show that a transport arises via an intermittent transition from a periodic and bounded trajectory to quasi-periodic

drift. In the latter case, the stroboscopic time evolution of the particle position at every period (Fig. 2) displays a regular descending staircase for different values of α. The plateaux correspond to oscillations close to the threshold. The plateaux become longer when α approaches the onset of bifurcations. Such a dynamics is similar to the phase slip of a desynchronisation transition (Beltrame et al. 2016). The drift velocity increases till $\alpha = 0.5$ which corresponds approximatively to the maximal velocitiy. In the following, we fix α parameter to 0.5.

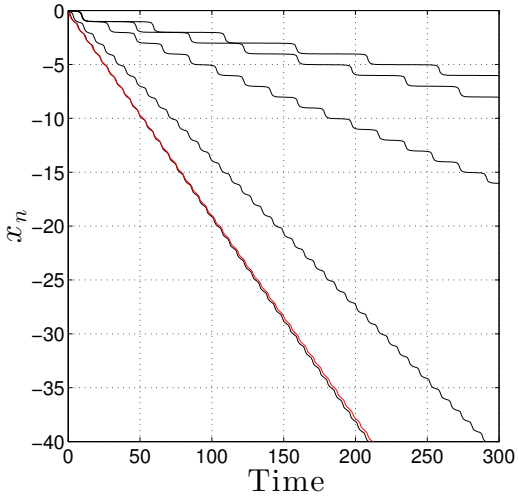

Figure 2: Discrete particle positions $\boldsymbol{x_n = x(n)}$ at entire times n in the transport region for different values of $\boldsymbol{\alpha = 0.283; 0.285; 0.300; 0.400; 0.500}$ and 0.600. The red line displays the particle dynamics for α=0.5.

We explore the domain transport by varying the parameters $\boldsymbol{P_v}$ and $\boldsymbol{P_\gamma}$. The bifurcation analysis shows that the transport solution exists in intervalls of $\boldsymbol{P_v}$ for fixed $\boldsymbol{P_\gamma}$ value. Therefore in the parameter plane $(\boldsymbol{P_\gamma}, \boldsymbol{P_v})$ the existence domains of periodic solutions are delimited by bandd which end in a minor value $\boldsymbol{P_\gamma}$ unless $\boldsymbol{P_v}$ is about 1000 (Fig. 3). Thus, transport arises in the region outside these bands when the bands do not overlap. In a general way, the transport domain range is when $\boldsymbol{P_v}$ is larger i.e. when the pumping amplitude is larger.

Nevertheless large pumping amplitude implies an increasing Reynolds number. Therefore, the consistency of the results with the Stokes approximation has to be checked. Concretly the fine lines in Fig. 3 correspond to the limit of validity of the Stokes approximation for two different particle densities. The parameters $(\boldsymbol{P_\gamma}, \boldsymbol{P_v})$ at the left of this line are consistent with the Stokes approximation with a density 1000 and 10000 larger than the fluid. Then the transport of metal particles is possible in a gaz.
Since there is a tapered space between the bands for specific $\boldsymbol{P_v}$ values, a very selective transport of the particles can be obtained. Such a micro-pump device constitutes an interesting way to filter micro-particles in the air in mirogravity environment.

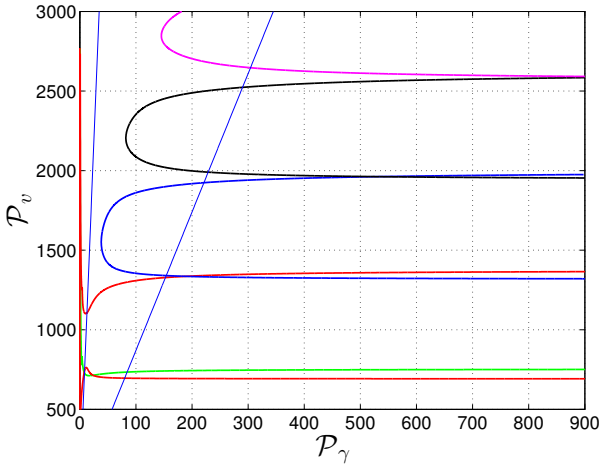

Figure 3: Boundary of the periodic solutions in the $(\boldsymbol{P_\gamma}, \boldsymbol{P_v})$ parameter plane. Outside these boundaries an intermittent transport occurs. The straight lines correspond to the limite of validity of the Stokes approximation for particle density 10000 (larger slope) and 1000 times (smaller slope) larger than the fluid density.

Conclusion

We have shown the existence of a deterministic transport of micro-particles in a Stokes flow through micro-channels. Depending on the parameters, only certain particles are transported in a chosen direction.
By taking the pore size about ten microns, a fluid as air and metal particles, it would be possible to observe this selective transport during the short duration of micro-gravity experiments such as in a drop tower or in a zero-g flight. The study of the influence of noise is paramount because of significant *g*-jitter in a zero-g flight. Beltrame (2018) showed that the noise triggers the transport for specific parameters in ratchet systems. Therefore, the particle transport could still be effective even in the presence of *g*-jitter.

References

S. Matthias and F. Müller, Asymmetric pores in a silicon membrane acting as massively parallel Brownian ratchets, *letters to nature,* **424**, 53 (2003).

C. Kettner, P. Reimann, P. Hänggi and F. Müller, Drift ratchet, *Phys. Rev. E*, **61**, 312-323 (2000).

P. Beltrame, M. Makhoul, M. Joelson, Deterministic particle transport in a ratchet flow, *Phys. Rev. E* **93**, 012208 (2016).

M. Makhoul, P. Beltrame and M. Joelson, Drag force on a confined particle: particle transport, *Int. J. Mechanics* **9**, pp. 260-271 (2015).

P. Beltrame, Absolute Negative Mobility in ratchets: Symmetry, *Chaos and Noise, J. of Chotic Modeling and Simulation* **1**, pp. 101-114 (2018)

Oral 161

Dynamics of a deformable cylindrical drop in a density-stratified liquid subjected to vibrations

T. Lyubimova[1,2], A. Ivantsov[1,2]

[1]Institute of Continuous Media Mechanics UB RAS, Perm, Russia;
[2]Perm State University, Perm, Russia;
lyubimovat@mail.ru, aivantsov@gmail.com

Introduction

If a solid inclusion is suspended in a liquid which fills a vibrating container then a non-zero average vibrational force acting on the inclusion from oscillating liquid arises if the densities of inclusion and host liquid are different [1]. For the translational vibrations, the average vibrational force acting on the inclusion from oscillating fluid is subjected to the fast decrease with the growth of distance between the inclusion and wall [1-2]. The formula for average vibrational attraction force in the case of non-deformable inclusion was obtained analytically in [3-4] neglecting the viscosities of media. Appearance of the vibrational attraction of inclusion to the nearest wall is attributed in these works to the Bernoulli effect. In the case of deformable inclusion translational vibrations of container could also influence the average shape of inclusion, compressing it in the direction of vibrations [5].

Governing equations

Let us consider the behavior of a cylindrical liquid drop in density-stratified fluid completely filling oscillating container in zero gravity conditions. Vibration axis is parallel to the density gradient of the external fluid. Container undergoes harmonic oscillations according to the law: $\vec{r} = a\vec{j}\cos\omega t$, where $\vec{r}$ is the coordinate of the container mass center, a and ω are the vibration amplitude and frequency, $\vec{j}$ is the unit vector in the direction of vibration axis (i.e. also in the direction of the density gradient of the external fluid).

Equations describing the dynamics of system in the reference frame of oscillating container have the form:

$$\frac{\partial \vec{v}_s}{\partial t} + \vec{v}_s \cdot \nabla \vec{v}_s = -\nabla p_s + \frac{1}{\Omega}\Delta \vec{v}_s + \lambda \vec{j}\cos t, \quad \operatorname{div} \vec{v}_s = 0$$

Here the subscript $s = 1, 2$ numerates the fluids.

The drop shape is determined by the equationv $\zeta(x, y, z, t) = 0$. At the fluid interface we impose the continuity conditions for the normal and tangential stresses and the kinematic condition:

$$(p_1 - p_2)n_i = \frac{1}{\Omega}(\sigma_{ik}^{(1)} - \sigma_{ik}^{(2)})n_k + \frac{1}{\mathrm{We}} n_i \operatorname{div}\vec{n},$$

$$\vec{v}_1 = \vec{v}_2, \quad \frac{\partial \zeta}{\partial t} + \vec{v}_1 \cdot \nabla \zeta = 0,$$

where $\vec{n}$ is the unit vector normal to the interface, directed to the less dense fluid; $\sigma_{ik}^s = \eta_s\left(\partial v_{s,i}/\partial x_k + \partial v_{s,k}/\partial x_i\right)$ is the viscous stress tensor. The no-slip conditions are set at the container wall.

Equations and boundary conditions are written in non-dimensional form, the following quantities are used as the scales: drop radius R for the length, inverse vibration frequency $1/\omega$ for the time, average density of the external stratified fluid near the drop ρ for the density, dynamic viscosity of the external fluid η for the viscosity, $\eta^2/\left(\rho^2 R^3\right)$ for average acceleration of the drop. The problem contains the following dimensionless parameters: dimensionless vibration amplitude and frequency $\lambda = a/R$ and $\Omega = \rho\omega R^2/\eta$, Weber number $\mathrm{We} = \rho R^3\omega^2/\alpha$ (α is the surface tension coefficient), dimensionless density and viscosity of the drop $\mathrm{P} = \rho_1/\rho$ and $N = \eta_1/\eta$, dimensionless density gradient of the external fluid $\beta = R\nabla\rho_2/\rho$.

Numerical investigation of the dynamics of the drop was carried out in a non-averaged approach using the Volume of Fluid method implemented in the Ansys Fluent package. To improve the accuracy of the solution near the interface, a non-uniform grid was used, which dynamically adapts in the process of iteration of equations. The stratification of the external fluid was specified by an additional scalar function for which the transport equation was solved. The spatial discretization of the equations was performed using the third-order method of accuracy, and a second-order scheme was used to approximate the time derivative. The time step was 0.02 of the period of vibrations. The average values of the functions were calculated by averaging over five periods of vibrations.

Numerical results

The calculations have shown that the stratification of external fluid substantially changes the average dynamics of the drop. As in the absence of stratification, there arises average vibrational force acting to the drop from the surrounding fluid. In the case of stratified external fluid this force leads to the average displacement of the drop in the direction of the density gradient of external fluid. (Fig. 1).

Vibrations lead to the generation of average flows near the interface. Fig. 2a shows the vector field of the average flow velocity obtained by averaging of numerical data over vibration period. In the directions perpendicular to the vibration axis the flow away from the drop is observed and along the axis of the vibrations, the liquid moves to the drop. Because of the presence of stratification, the intensity of vortices in the domains of denser fluid is larger than that in less dense fluid domains. The displacement of the drop to the container wall results in a considerable transformation of the density distribution in the external fluid. External fluid is involved in the motion together with th drop, as the result the area is formed where the density is smaller than far from the

drop. In this case, the average flowss generated near the drop are also considerably changed (Fig. 2b).

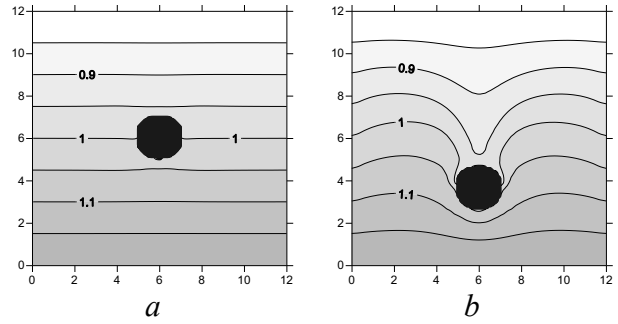

Рис. 1. *Density distribution at* $We = 40$, $\lambda = 0.2$, $\Omega = 63$, $P = 2$, $\beta = 0.03$ *at different time moments: (a)* $t = 6$, *(b)* $t = 60$

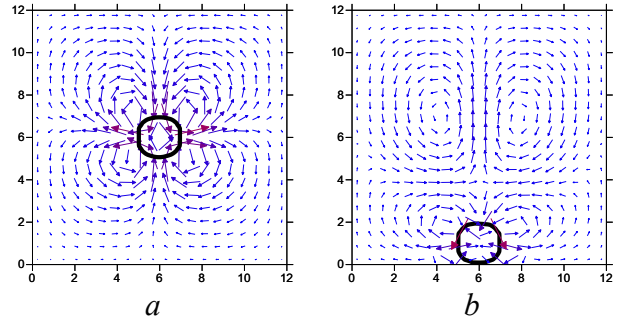

Fig.2. *Velocity of average flow and average shape of the drop at* $We = 40$, $\lambda = 0.2$, $\Omega = 63$, $P = 2$, $\beta = 0.03$: *(a)* $t = 6$, *(b)* $t = 200$

The dependencies of average force acting to the drop on the vibration parameters and density gradient in the external fluid are obtained. It is found that at initial stages of the process, when the density field is not transformed yet, this force grows linearly with the density gradient in external fluid. Dependence of the average force on the vibration frequency is quadratic and on the vibration amplitude it is linear. Thus, in the considered range of the parameters (at finite amplitude and frequency of the vibrations and finite viscosities of fluids) the verage force acting to the drop is proportional to the density gradient in external fluid and to the vibrational acceleration.

Conclusions

The behavior of a cylindrical liquid drop in a stratified liquid filling an oscillating container in zero gravity conditions is studied numerically. It is supposed that the axis of vibrations and the density gradient of the external fluid are co-directed. At the initial time moment, the drop is located in the center of the container. The calculations show that the drop moves in the direction to more dense fluid, while in the absence of stratification of external fluid, the average position of the drop is not changed. The dependences of the average force acting to the drop on the external fluid density gradient and the vibration parameters are obtained. It is found that at the earlier stages of the process, when the density field varies linearly in the direction of vibrations, this force is proportional to the density gradient in the external fluid and to the vibrational acceleration. The motion of a drop to the wall of the container causes a substantial modification of the density field. The average flows generated near the drop are studied.

The effect of stratification on average shape of the drop is weak; as in the absence of stratification, at not too large surface tension the drop flatterned in the direction of vibrations.

The average flow generated by vibrations near the drop in the absence of stratification has the form of four vortices of the same intensity; in directions perpendicular to the axis of vibration, there is a flow directed from the drop and along the axis of vibrations, the fluid moves to the drop. In the presence of stratification, the intensity of the vortices in a denser fluid decreases. As the result, the flow from the side of the less dense fluid turns out to be more intense than that from the side of the more dense fluid.

Acknowledgements

The work is financially supported by the Government of Perm Region (grant C 26-788 for the support of Scientific schools of Perm Region).

References

1. D.V. Lyubimov, T.P. Lyubimova, A.A. Cherepanov, On a motion of solid body in a vibrating fluid. Convective Flows, Perm, pp.61-70 (1987).
2. D.V. Lyubimov, A.A. Cherepanov, T.P. Lyubimova, The motion of solid body in a liquid under the influence of a vibration field, Reviewed Proc. of the First Int. Symp. on Hydromechanics and Heat/Mass Transfer in Microgravity, Gordon and Breach, pp. 247-251 (1992).
3. B.A. Lugovtsov, V.L. Sennitskii, On a motion of a solid in a vibrating liquid, Dokl. AN SSSR, Vol. 289-2 pp. 314-317 (1986).
4. D.V. Lyubimov, A.A. Cherepanov, T.P. Lyubimova, B. Roux, Vibration influence of a two-phase system in weightlessness conditions, J. Physique IV, Vol. 11-Pr6 pp. 83-90 (2001).
5. D.V. Lyubimov, A.A. Cherepanov, T.P. Lyubimova, B. Roux, Deformation of gas or drop inclusion in high frequency vibrational field, Microgravity Quarterly, Vol. 6/2-3 pp. 69-73 (1996).

Oral 162

Fluid mixing by steady streaming in an annulus with deflectors

N. V. Kozlov

Institute of Continuous Media Mechanics UrB RAS, Perm, Russia;
kozlov.n@icmm.ru

Introduction

The control of heat and mass transfer in liquids in low gravity is of great practical importance for space industry. Steady streaming (Riley 2001) is an efficient tool for this, because it is independent of gravity (Gershuni and Lyubimov 1998). Non-translational oscillations are an approach to generate steady time-average flows in a closed container (Gershuni and Lyubimov 1998, Ivanova and Kozlov 2003)

The present work includes experimental study and direct numerical simulation of dynamics of an isothermal low-viscosity fluid in a specially-shaped annulus making rotational vibrations relative to its axis. On the inner surface of the outer container's wall, semicircular deflectors are placed regularly. At vibrations, the fluid oscillates tangentially about the deflectors. Due to the activators shape this leads to the generation of steady streaming in the viscous boundary layers (Schlichting 1968).

In experiments, a container with large aspect ratio (height to radius) is used (Fig. 1). In the simulation a two-dimensional configuration is considered, excluding the end-walls effects. The details of experimental and numerical methods can be found in (Kozlov et al. 2016).

Figure 1: Experimetnal setup: *1* – container, *2* – rocking platform, *3* – motor, *4* – crank, *5* – rod.

Steady flows in the anulus

On each deflector, outside the boundary layer, a symmetric vortical pattern is formed (Fig. 2). The steady flows in the annulus consist of a regular system of rolls with the azimuthal periodicity. Comparison of the experiment and the simulation reveals an agreement. The flows produce a rather regular fluid mixing; the maximum average velocity is localized in thin regions on the deflector walls (Fig. 3). With an increase in the vibration intensity, due to the competition between the vortices, the flows lose stability and transform.

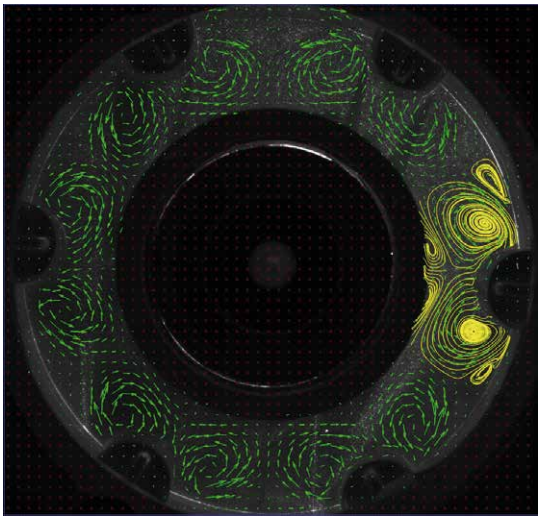

Figure 2: Steady time-average flows in the cross section. Experiment, PIV.

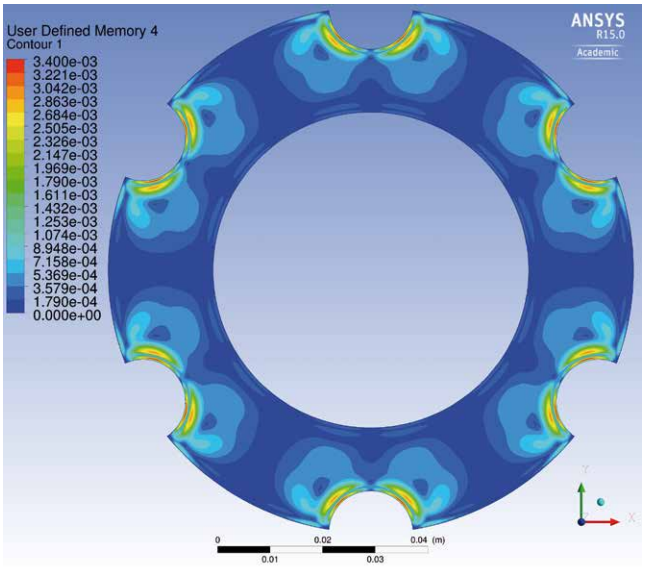

Figure 3: Color map of time-average velocity magnitude. Numeric simulation.

Analysis of the flow-velocity field reveals that the fluid mixing can be achieved at relatively low shear rate. This feature can be important for processing some sensitive substances (Mitsuhashi et al. 1994). Also, because of the two-dimensional configuration (invariance along the z axis), regimes are found when the mixing is homogeneous along the container height and this makes it independent of the gravity.

Conclusions

Steady streaming excited by vibrations can be applied for mass transfer intensification. The studied oscillating container may be considered as a concept of a reactor suitable for some special operating conditions. The studied hydrodynamic mechanisms assure two important features: low shear stress and independence of the gravity.

Acknowledgements

The work was supported by the Ministry of Education of Permskii Krai (project C-26/174.9).

References

G. Z. Gershuni, D. V. Lyubimov, *Thermal Vibrational Convection* (New York: Wiley, 1998).

A. A. Ivanova, V. G. Kozlov, Vibrational convection in nontranslationally oscillating cavity (isothermal case), *Fluid Dyn.* 38 (2003) 186–192.

N. V. Kozlov, D. Pareau, A. Ivantsov, M. Stambouli, Steady flow instability in annulus with deflectors at rotational vibration, *Fluid Dyn. Res.* 48 (2016) 061416.

S. Mitsuhashi, M. Fujimoto, H. Muramatsu, K. Tanishita, Effect of simple shear flow on photosynthesis rate and morphology of micro algae, *Acta Astronaut.* 33 (1994) 179–187.

N. Riley, Steady streaming, *Ann. Rev. Fluid Mech.* 33 (2001) 43–65.

H. Schlichting, *Boundary-Layer Theory* (New York: McGraw-Hill, 1968) (re-edited in 1979).

Oral 164

Testing of a Capillary Device to Separate Blood and Air for Future Spaceflight Medical Care

S. H. Collicott[1] and C. Marsh Cuttino[2]

[1]Purdue University, School of Aeronautics and Astronautics, West Lafayette, Indiana, USA
collicott@purdue.edu
[2]Orbital Medcine, Richmond, Virginia, USA
orbitalmedicine@gmail.com

Introduction

Medical procedures in future long-duration human spaceflight are anticipated to include chest suction. Piston pumps driven by DC-motors already in use on Earth for portable systems are expected (and proven) to function well in weightlessness, but the resulting flow from suction is a mixture of liquid blood and air. It is important to note that both the blood and the air are vital and limited resources in a human spacecraft. Thus, both fluids need to be recovered and separated, so that blood can be transfused back into the patient and all astronauts can breathe the air. Unlike a well-equipped hospital on Earth, in a spacecraft there will not be a large blood bank.

Methodology

Ideal hardware for this phase separation task – liquid from gas – would be passive and compact. Passive in that it should use no power, as power is also always going to be a limited resource, and it should be able to be stored for years in smaller form before simple deployment for emergency use. A suitable design and the successful zero-gravity flight testing on parabolic aircraft flight and on commercial re-usable sub-orbital rocket flight are described. The Flight Opportunity Program in Spaceflight Technology Mission Directorate at NASA provided funding for flight testing, the first author's undergraduate students in Aerospace Engineering designed and built the hardware, and the second author provided expert understanding of the need and of a variety of 1-g surgical operations and tools. Flight test operations were performed jointly by the authors and students.

The basic 1-g operation of chest suction is sketched in Figure 1. Note that gravity easily separates blood from air and that blood never reaches the suction pump, which pumps only air. To transfer this well-proven 1-g system to 0-g, separation of the blood and air must be achieved by some mechanism other than gravity. The present prototype exploits the good wetting physics of human blood on common plastics to create a capillary device which wicks blood into a retention region and passes air out of the device. The basic design approach mimics that of a half century of surface tension propellant management device designs for spacecraft fuel tanks.

The separator is approximately a cone with tangent spherical end-cap and internal conical shells tangent to one wall of the outer cone, as shown in Figure 2. Cusps rather than the corners typical of PMDs were chosen based on previous work with other bio-fluids (Ginter et al., 2005) but the blood was found to wet well and corners should also suffice for good functioning of a blood-air separator.

Testing the device in 0-g adds one level of complexity. Each vehicle that the authors have tested the separator on requires multiple layers of containment of liquids. Thus, the open-air venting shown in Figure 1 must be replaced by closing the loop as shown in Figure 3. That is, air exhausted from the pump becomes the air that enter the "patient" jar to replace the volume of fluids removed by suction. Thus, the operation of the separator and pump becomes a closed loop for the air. Additional one or two levels of containment, depending on flight vehicle, were also implemented.

A series of three flight tests was performed. The first flight test was parabolic aircraft flights with a rigid prototype of the separator on June 13 and 14, 2016. The second test was again the rigid separator prototype but in high quality 0-g on the Blue Origin New Shepard sub-orbital rocket on December 12, 2017. The third test was again on New Shepard but with a sub-scale flexible stowable version of the separator on May 2, 2019.

Conclusions

The prototype separators worked perfectly in all three flights. The blood was collected in the separator and the air was expelled. There was no blood in the air tube leaving the separator, as shown in Figure 4. The safety sponge was dry after every flight test. Additionally, there were no leaks of blood from the first level of containment during any of the flight tests. Testing of the stowable version of the separator in the third test highlighted clearly why human-tended sub-orbital experiments will have significant value. Specifically, automating the deployment of devices designed for hand-held use by astronauts adds significant complexity to what is otherwise a fairly simple and unpowered mechanism. With a human in the New Shepard crew capsule, multiple prototypes could be tested rapidly in one flight.

Acknowledgements

Thank you to the NASA Flight OpportunityProgram for providing the flights and support.

References

R. W. Ginter, J. R. Morell, and S. H. Collicott, Liquid Waste Control in Micro-G: Designing a Capillary-Wicking Liner for the Specimen Chamber of the Advanced Animal Habitat

\H). 2005 SAE International Conference On
/ironmental Systems, paper number 2005-01-2785

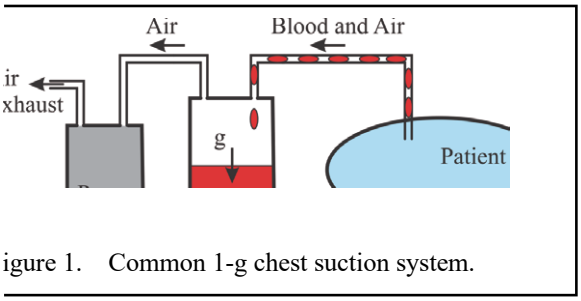

igure 1. Common 1-g chest suction system.

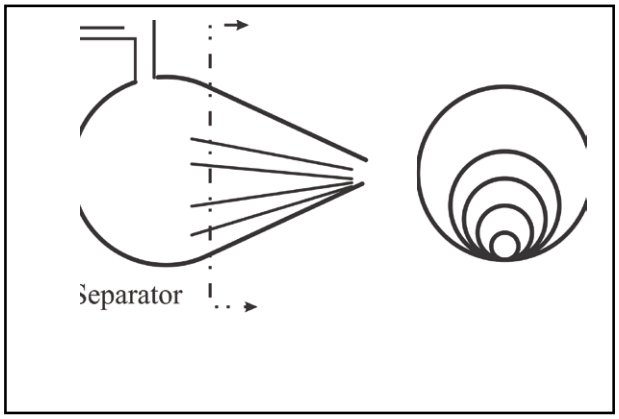

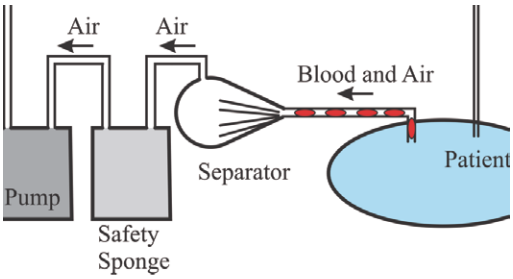

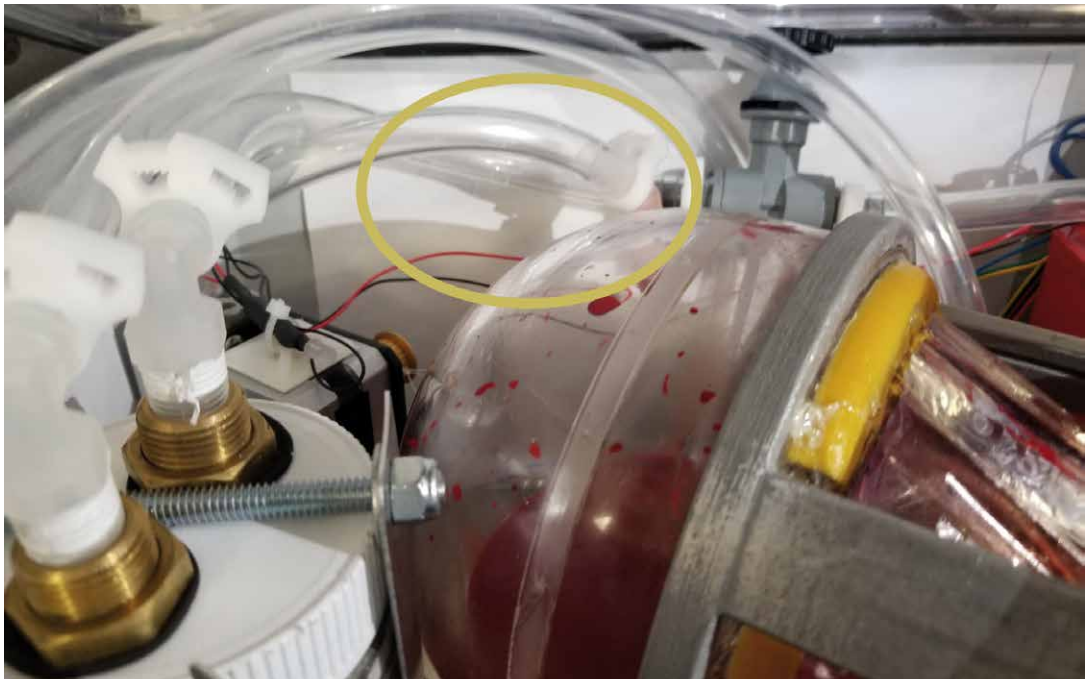

'igure 4. Post-flight condition of the third test. The gold ellipse highlights the air vent from the separator /hich is clean of all blo0d.

Oral 165

Effect of carbon-based coatings on film-wise condensation

A. Glushchuk[1], E. Barakhovskaia[1,2], S. Fiore[3], C. Minetti[1], C.S. Iorio[1]

[1]Microgravity Research Center, Université libre de Bruxelles, Brussels, Belgium,
[2]Novosibirsk State University, Novosibirsk, Russia, [3]Università Degli Studi Di Napoli Federico II, Naples, Italy;
Andrey.Glushchuk@ulb.ac.be, sElla.Barakhovskaia@ulb.ac.be, simo.fiore@studenti.unina.it,
Christophe.Minetti.@ulb.ac.be, Carlo.Iorio@ulb.ac.be

Introduction

Heat transfer of filmwise condensation has been researched extensively since the original work of Nusselt (Nusselt, 1916), who analysed laminar film condensation on vertical plates under free convective conditions. Film-wise condensation carries out at vapour-liquid interface and released heat goes through the condensate film. Therefore, the intensity of the condensation process depends on the film thickness. In order to enhance this process, a way to thin the condensate film should be found. A lot of various methods are published in the literature. Most of the methods are based on usage of different forces affecting the film or film-vapour surface: gravity, stationary electrical field, centrifugal force, vapour flow stress, surface tension. There is one more method, which is underestimated in case of film-wise condensation: modification of surface topology.

Analysis of the available works does not give a clear idea about roughness, porous, or other types of coating effect on film-wise condensation. The results of one author come contrary to the observations of others, and most of the experiments were done with water that has very high surface energy. This fact complicates experiments because both drop-wise and film-wise types of condensation can exist on the same surface. Only the appropriate detection of film thickness distribution can reveal these situations.

In this work, two different surface coating (Carbon Nano Tubes and Graphene) were tested and compared with the non-coated surface because they provided different microstructures of coated surface and thermal conductivity behaviour. Considerable attention was given to achieve a stable condensation for each acquisition period and accurate measurements of film thickness distribution.

Experimental setup

The investigation of vapour condensation on cylindrical samples having different surface coatings had been carried out. Methoxy-nonafluorobutane (trademark HFE-7100) had been used in all experiments because of its relatively low latent heat value (111 kJ/kg) and low boiling point (61°C at 1 atm), with respect to water.

The concept of the experiment is shown in **Figure 1**. The sample was placed in a tight container with pure vapour inside. Pressure and temperature of the vapour were maintained constant. The sample temperature was maintained lower than the vapour temperature with the help of a cooling platform. These settings created a good condition for the condensation process. The condensed liquid was flowing along the surface under the action of gravity. The distribution of the film thickness and the temperature field in the sample body were measured. The sample had an axisymmetric shape in order to employ an afocal optical system, which consisted of a collimated light source and an image projection system, for accurate measurements of condensate thickness distribution. Two optical windows provided a precise observation of the condensed liquid on the sample. Detailed description about used experimental set-up can be found in (Glushchuk et al. 2017)

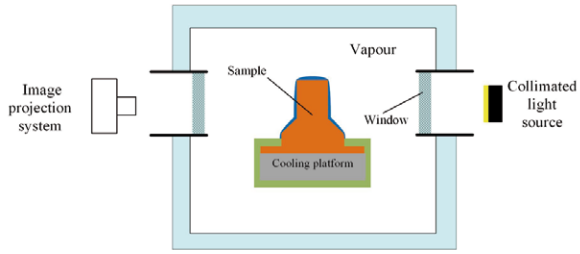

Figure 1: Concept of the experiment

Three samples were used in the experiment. The samples consisted of a specially crafted cylindrical fin, a conical-cylindrical pedestal and a base. The total height of the fin samples was 24 mm. The base had dimensions 40x40x3 mm^3. The pedestal diameter was 18 mm, and the total height was 12 mm, the height of the conical part was 6.2 mm. The cylindrical fin had dimensions Ø6 x 9 mm^2.

Coated fins had peculiars surface qualities whose performances in heat transferring were tested. Black&White images (**Figure 2**) show results of Scanning Electron Microscope (SEM) measurements of the surface of each sample.

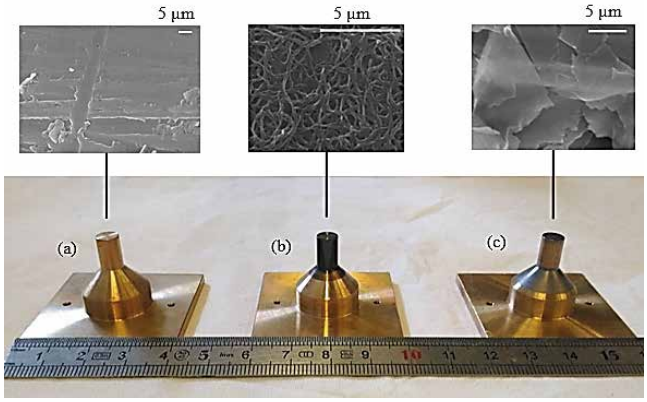

Figure 2: Fin samples and SEM images of the surfaces: (a) no coating, (b) CNT coating, (c) Graphene coating

The coating was made by dipping procedure using a motorized setup. With a special software, up-down cycle parameters were set in a definite way to achieve the lowest

speed, in order to create fewer vibrations as possible to the liquid solution.
Two solutions were used in the experiment. The first was water-based solutions of CNT; the second was water-based solutions of Graphene. Ultra-pure water L0020 from Merck Millipore was used to prepare solutions. The concentration 0.3% was used in the experiments because for higher concentrations the increase in the solutions' viscosity will avoid obtaining a uniform coating. On the other hand, with a lower concentration, a large number of layers is needed to have a good coating (Machrafi et al. 2018).
It should be mentioned that the CNT coating is a deep black, while the Graphene coating is grey and even transparent (**Figure 2**), probably because the Graphene flakes present there were well aligned during the dipping procedure because of the gravity.
As observed with the SEM, the coatings severely affected the surface quality. In particular, the CNT coating resembled a porous media, and its behaviour could be expected to be similar to what H. Wang et al. observed in their experiment (H. Wang et al. 2016).

Results
The comparison of the condensation capability of each sample was made using two parameters: temperature gradient inside the sample body and film thickness distribution.
The temperature gradients were evaluated thanks to the sensors installed inside each fin sample bodies. It is worth noticing that for all the studied cases, in the cylindrical part of the sample, the temperature gradient of the Graphene coated sample was the biggest one, which indicated very intensive condensation. At the same time, CNT had more mediocre performances (smaller temperature gradient) above a certain temperature drop between vapour and the base.
Figure 3 shows the film thickness distributions in regards to the totality of set points. Both CNT and Graphene coated samples showed smaller film thickness in comparison with uncoated one.

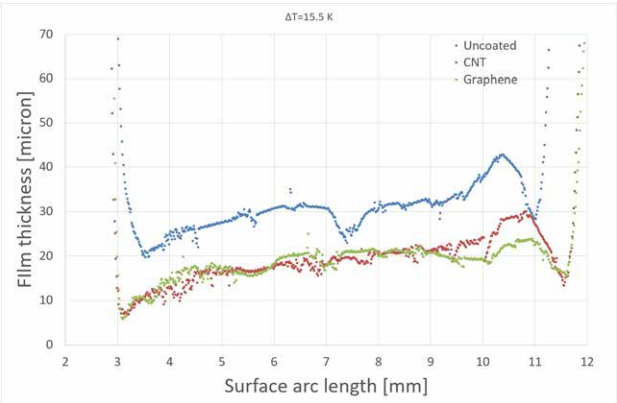

Figure 3: Film thickness comparison

Smaller condensate thickness of Graphene case means that the coating provides a higher heat transfer coefficient. This result correlates very well with the evidence obtained by the temperature gradients analysis. At the same time, the CNT coating showed quite confusing results. Temperature gradients analysis showed smaller heat of condensation, while the condensate film is thinner than for uncoated samples.

Conclusions
In conclusion, Graphene coating showed very promising results, while further investigations are needed for the CNT coating. This might be explained if one consider that coatings can affect heat transfer capabilities of the samples in two ways:
1. The hydrodynamical effect, which invalidates the no-slip condition on the boundary between the condensate film and the sample surface, since portions of liquid can be trapped in the coating layer.
2. The thermal effect, because these carbon-based coatings have higher thermal conductivity coefficient than the condensate film, so the total conductivity coefficient it is a mean between the two.

Since Graphene gave such unmistakably good results, both effects could be presented in the improvement of the heat transfer capabilities, while for CNT the thermal effect might be non-existent or conflicting with the other one.

References

W. Nusselt, The surface condensation of water vapour, *Z. Vereines Deutscher Ingenieure* 60, (1916), 541-575.

Glushchuk, C. Minetti, H. Machrafi, C.S. Iorio, Experimental investigation of force balance at vapour condensation on a cylindrical fin, *Int. J. of Heat and Mass Transfer* 108, (2017), 2130-2142.

H. Machrafi, C. Minetti, V. Miskovic, P.C. Dauby, F. Dubois, C.S. Iorio, Self-assembly of carbon nanotube-based composites by means of evaporation-assisted depositions: Importance of drop-by-drop self-assembly on material properties, *Materials Chemistry and Physics* 218 (2018), 1-9.

H. Wang, J. Wu, Q. Yang, X. Zhu, Q. Liao, Heat transfer enhancement of ammonia spray cooling by surface modification, *Int. J. of Heat and Mass Transfer,* 101 (2016) 60-68.

Oral 166

Stabilization of condensate flow from curvilinear surface by means of porous media

E. Barakhovskaia[1,2], P. Queekers[1], C.S. Iorio[1], A. Glushchuk[1]
[1]Microgravity Research Center, Université libre de Bruxelles, Brussels, Belgium,
[2]Novosibirsk State University, Novosibirsk, Russia,
Ella.Barakhovskaia@ulb.ac.be, Patrick.Queeckers@ulb.ac.be, Carlo.Iorio@ulb.ac.be, Andrey.Glushchuk@ulb.ac.be

Introduction

A widely used intensification method of vapour condensation is the finning of a condenser surface. The enhancement is provided not only by increasing the contact area between the vapour and the cold surface but also by the action of surface tension forces, which help to move condensate from the fin additionally to other forces (gravity, shear stress, etc.). If a liquid-vapour interface is curved, a pressure difference across the interface must be present to establish a mechanical balance. The balance is described by the curvature of the liquid-vapour interface within the Young-Laplace equation. Any curvature variation along the interface induces a pressure inhomogeneity within the liquid, which leads to fluid redistribution. This pressure variation is known as the surface-tension pressure gradient (*STPG*). Thus, the enhanced surfaces should work not only on earth but also under weightless condition.

Film-wise condensation on curvilinear extended fins has been the subject of numerous publications. Gregorig (1954) was the first to notice that, on curvilinear fins, surface tension would generate large pressure gradients inside the liquid film due to the change in curvature. (Mori et al. 1981) concluded that a parabolic fin profile could give the high condensing heat transfer performance. (Kedzierski and Webb 1990) proposed a new class of two-dimensional fins with a small fin tip radius and a gradually increasing curvature radius along the fin surface, based on an approximate analysis of condensate flow on the curved portion of the fin surface. (Zhu and Honda 1993) proposed another class of 2D fin with a small fin tip radius, a gradually increasing radius of curvature near the fin tip, and a constant fin thickness near the fin root. (Valenzuela et al. 1993) described a high performance condensing surface with internal drainage, developed for use under weightless condition.

Recent experiments of (Glushchuk et al. 2017) showed that any flat section of the fin surface could cause a dramatic decrease of *STPG* and, as a result, destabilization of the condensate film. Because of the limitation of manufacturing methods, it is impossible to create the fin with continuously changing surface curvature. The goal of this work is to test the condenser, which combines the capability of the curvilinear surface to drive liquid and a porous media to collect and store condensed fluid.

Experimental set-up

The investigation of vapour condensation has been carried out during the 69th ESA parabolic flight campaign. Methoxy-nonafluorobutane (trademark HFE-7100) had been used in all experiments because of its relatively low latent heat value (111 kJ/kg) and low boiling point (61°C at 1 atm) relative to water. A parabolic flight is a ballistic trajectory by a modified aircraft during which a short period of around 22 seconds of low gravity at 0.05 g_0 is experienced. Just before and after the low gravity period, two periods of around 20 seconds each of hypergravity at around 1.5 – 1.8 g_0 are also experienced. A detailed description of the gravity conditions during one parabolic maneuver is presented in the paper of (Pletser 2013).

Figure 1 shows the concept of this experiment. The single fin having a height of 18 mm is placed in a tight container with pure vapour inside. Pressure and temperature of the vapour are constant. The fin base temperature is maintained lower than vapour temperature using a cooling platform. That creates a good condition for condensation process. The condensed liquid is flowing along the fin surface only under the action of the capillary pressure gradient. A porous media is placed around the fin. The porous media plays two roles. First, it works as a liquid trap in microgravity condition thanks to capillary pressure inside the pores. Moreover, secondly, it dumps any fluctuations generated by a liquid retraction system and gravity level changes during one parabolic maneuver of the airplane. The distribution of the film thickness and the temperature field in the fin body is measured in this experiment. Enhanced shadow optical system (ESS) consisted of a collimated light source, and an image projection system is used to measure the thickness. Detailed description about used experimental set-up can be found in (Glushchuk et al. 2017)

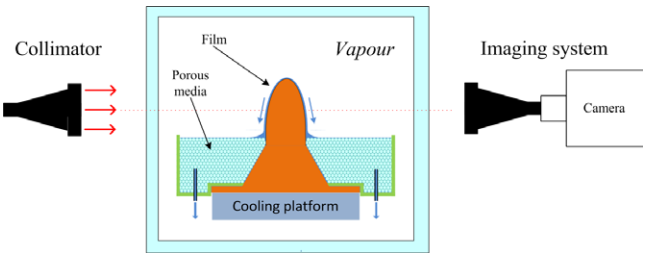

Figure 1: Concept of the experiment

Results and conclusion

Three porous media with different values of the pore size and material were tested: polypropylene with average pore size 100 µm and 150 µm and polyethylene with pore size 140 µm. **Figure 2** shows the typical shadow image of the fin with the film observed during the experiment. The condensate flowed from the fin tip toward the porous media by the surface-tension pressure gradient caused by continuous changes of fin surface curvature. Eventually, the liquid was captured and accumulated by the tested porous

lia. The growth of the condensate film thickness was erved during the weightless period of the parabolic neuver. However, there was no observable film surface ormation. The present experiment has shown that gration of the porous media between curvilinear fins ld help to stabilize the condensate flow and get a ximum condensation capability from the curvilinear ace.

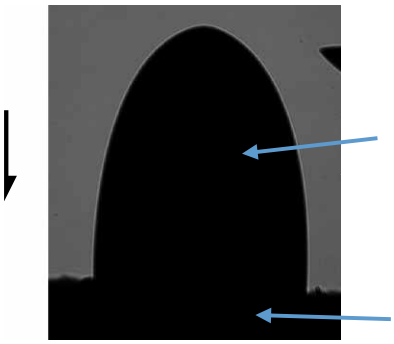

ıre 2: Shadow image of the fin with the film under weightless lition.

knowledgments

work was done in the framework of HEAT TRANSFER PRODEX ct under financial support of the BELGIAN FEDERAL SCIENCE ICY OFFICE. The authors thank the European Space Agency for the Parabolic Flight Campaign and the financial support through MAP lensation project AO-2004-096. The authors express their gratitude to Novosibirsk State University for assistance in preparing experiments discussing the obtained results. The authors also appreciate the help the team at NOVESPACE for invaluable help in the preparation of the riment and the parabolic flight campaign.

References

R. Gregorig, Hautkondensation an feingewellten Oberflächen bei Berüksichtigung der Oberflächenspannungen., *Zeitschrift für angewandte Mathematik and Physik* 5 (1954) 36 – 49.

J. Mori, K. Hijikata, S. Hirasawa and W. Nakayama, Optimized performance of condensers with outside condensing surface, *Journal of Heat Transfer* 103 (1981) 96 – 102.

M.M. Kedzierski and R.L. Webb, Practical fin shapes for surface tension drained condensation, *Journal of Heat Transfer* 112 (1990) 479 – 485.

H.R. Zhu and H. Honda, Optimization of fin geometry of a horizontal low finned condenser tube, *Heat Transfer —Japanese Research* 22(4) (1993) 372 – 386.

J.A. Valenzuela, J.A. McCormick and J. Thornborrow, Design performance of an internally drained condenser surface, *Condensation and Condenser Design Conference*, ASME (1993) 557 – 568.

A. Glushchuk, C. Minetti, H. Machrafi, C.S. Iorio, Experimental investigation of force balance at vapour condensation on a cylindrical fin, *Int. J. of Heat and Mass Transfer* 108 (2017) 2130-2142.

V. Pletser, Are aircraft parabolic flights really parabolic? *Acta Astronautica* 89 (2013) 226 – 228.

Oral 168

Sloshing of propellant in partially filled storage tank under reduced gravity

Kai Li[1,2], Ji-Cheng Li[1,2], Hai Lin[1], Jian-Fu Zhao[1,2] Wen-Rui Hu[1]

[1] Key Laboratory of Microgravity, Institute of Mechanics, Chinese Academy of Sciences, Beijing 100190, China;
[2] School of Engineering Sciences, University of Chinese Academy of Sciences, Beijing 100049, China.
likai@imech.ac.cn

Introduction

The sloshing of propellant in a partially filled storage tank caused by an abrupt change of gravity level is of critical importance for the management of fluids in space. The dynamic behaviors of the propellant, determined by its thermo-physical properties, the configuration of the storage tank and circumstances of space, is mostly responsible for the safety, stability, fuel supply, etc., which is a topic of high interest in many applications

Numerical models

We present, in this paper, numerical simulations of liquid sloshing in capsule storage tanks under reduced gravity which changed from g_0 to $10^{-3}g_0$ and $0g_0$. g_0 is the normal gravity acceleration 9.8 m/s^2. The gravity level 10^{-3} g_0 corresponds to the experimental gravity level in Beijing Drop Tower and $0g_0$ is the microgravity condition. As shown in equations 1 and 2, dynamic contact angle (DCA) model (Kistler 1993) was adopted to capture the sloshing behaviors of liquid in capsule storage tanks under the abrupt gravity reduction.

$$\theta_D = f_{\mathrm{Hoff}}\left[Ca + f_{\mathrm{Hoff}}^{-1}(\theta_e)\right] \quad (1)$$

$$f_{\mathrm{Hoff}}(x) = \arccos\left\{1 - 2\tanh\left[5.16\left(\frac{x}{1+1.31x^{0.99}}\right)^{0.706}\right]\right\} \quad (2)$$

in which θ_D and θ_e are the dynamic and static contact angle, respectively. The volume of fluids (VOF) method (Hirt and Nichols 1981) was adopted for the capture of free surface of liquid, the continuous surface force (CSF) model for the coupling of surface tension and the piecewise-linear method (Young 1982) for the geometry reconstruction. The ethanol and FC-72 were used as the tes fluid.

Results

The effect of dynamic contact angle (DCA) was discussed by comparing with the results with static contact angle (SCA). The results show that for the case with the gravity reduction to $10^{-3}g_0$, the vapor phase distribution is ellipsoidal rather than spherical vapor phase distribution for the case with the gravity reduction to $0g_0$. The results considering the dynamic contact angle show more significant damping effects on the time evoltuions of the moving contact line. The results considering the dynamic contact angle agreed much better with the corresponding experiments than the reults with the static contact angle. Based on the verified numerical model, numerical simulations were conducted for the capsule storage tanks with different filling ratios ranging from 10% to 90%. As shown in fig. 1, the dynamic behaviors of liquids were probed time-dependently, which shows different sloshing characteristics with different filling ratios and fluids. Meanwhile, analysis on the oscillation frequency of the free surface was conducted. As shown in fig. 2, the results show that the oscillation frequency, for both cases whether moving contact line climbed up to the top of storage tank or not, increases with the increasing of filling ratio of the liquid. Finally, we also detail the comparison between ethanol and FC-72 on both sloshing patterns and frequency analysis.

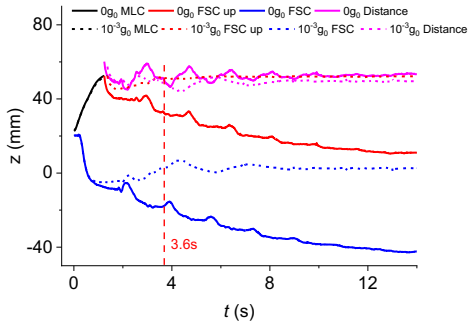

Figure 1. Time dependent dynamic behavior of free surface under different gravity level with the filling ratio 75%.

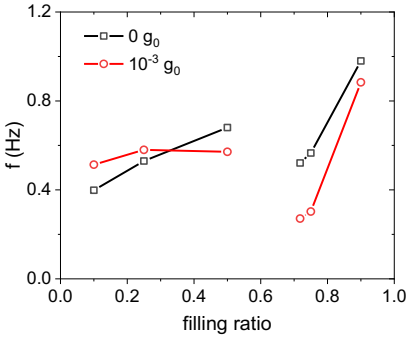

Figure 2. Oscillation frequency of ullage with different filling ratios for different gravity levels.

Acknowledgements

This work is supported by the National Nature Science Foundation of China (11672311) and the Key Research Program of Frontier Sciences, CAS (QYZDY-SSW-JSC040).

References

S. F. Kistler, Hydrodynamics of wetting. Wettability 6 (1993) 311-430.

C.W. Hirt, B.D. Nichols, Volume of fluid (VOF) method for the dynamics of free boundaries. J. Comput. Phys. 39, (1981) 201-225

D.L. Youngs, Time-dependent multi-material flow with large fluid distortion. In: Morton W., Baines M.J. (eds.) Numerical Methods in Fluid Dynamics (1982) 273-285. Academic Press.

26th European Low Gravity Research Association Biennial Symposium and General Assembly
14th International Conference on "Two-Phase Systems for Space and Ground Applications"
European Space Agency Topical Teams meetings
Granada (Spain), September 24-27, 2019

Oral 169

A method of condensation length measurement with Fiber Bragg gratings

YUN-SHENG CHEN [1,3], LI-PING HUANG[1], SHI-ZHE WEN [*1,2], , ZHEN-HUI HE [*1,2,4]

1Center for space technology, Sun-Yat Sen University, Zhuhai 519000, P.R, China
2 School of physics and astronomy, Sun Yat-Sen University, Zhuhai 519000, P.R, China
3 School chemical engineering, Sun Yat-Sen University, Zhuhai 519000, P.R, China
4 state key laboratory of optoelectro materials and technologies, Sun Yat-Sen University, Guangzhou 510275, P.R, China
*correspondent author: E-mail: stshzh@mail.sysu.edu.cn(He);wenshizhe@mail.sysu.edu.cn(Wen)

Introduction

Compared with the single-phase loops, the two-phase loops have the characteristics of high heat-exchange efficiency, and are widely used in various heat exchangers or temperature control systems. A two-phase loop is mainly composed of an evaporation section and a condensation section. There have been much researches on the evaporation section, while not enough in the condensation section[1].

Condensation length is one of the important parameters that describe the condensation heat transfer efficiency, yet difficult to be measured accurately. At present, there are two methods to obtain the condensation length[2]. The first is by numerical calculations based on established correlation equations for the condensation process; the second is by direct measurement of a two-phase flow condensation. In many cases, these two methods are used simultaneously. Relevance is often based on a large amount of experimental data[3-6].

The large error (20%) of the two research methods mentioned above can not meet the requirement of precise researches[7-9]. We developed a method of measuring the condensation length with higher spatial resolution (3.0cm), which mainly uses a plurality of fiber Bragg gratings (FBG) to measure the temperature distribution of the fluid in the pipe of the condensation section, thereby to determine the condensation length. The repeatability and reliability of this method were investigated in this paper.

When a laser beam passes a fiber Bragg grating, the wavelength of the reflected beam by the grating will change with the change of temperature and stress. One can use these characteristics to measure the temperature after calibration[10].

To measure the temperature distribution at the same time, a fiber with 30 Bragg grating sensors, called distributed fiber Bragg gratings was employed and sealed in a stainless tube. It was then inserted into the horizontal double-pipe heat exchanger for the measurement of condensation length.

Temperature-wavelength static calibration

Temperature-wavelength calibration for the distributed fiber Bragg gratings are carried out with R134A liquid flow pumped in a loop in a temperature range of 20.0 to 40.0 °C. The calibration was repeated two days and one month after respectively to investigate its repeatability.

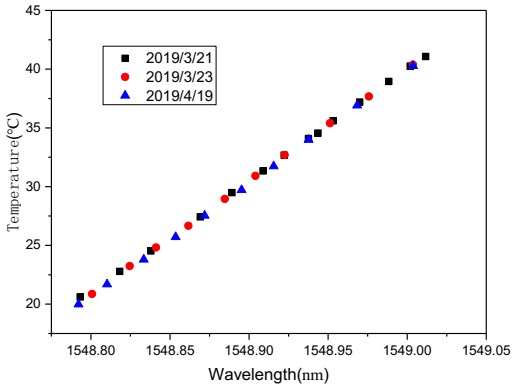

Figure 1: Calibration curve of the 20th grating sensor (Solid black square: First calibration experiment on March 21, 2019; Solid red circle: Second calibration experiment on March 23, 2019; Solid blue triangle: Third calibration experiment on April 19, 2019)

The linear relationship between temperature and the reflect light wavelength for the 20th sensors is shown in Figure 1. The linear correlation coefficient exceeds 0.999. All the other relationship of the 29 grating sensors are similar. The data showed that within one month, the temperature measurement repeatability of the grating sensor is 0.3°C. and the random error of the temperature measurement is 0.2°C. This is within the temperature uncertainty (0.3°C) measured with a sealed thermol couple. Although repeatability range of the temperature measurement with the distributed fiber Bragg gratings was higher than the temperature measurement error, the measured temperatures within a month were reliable and can be regarded as repeatable. Therefore, it can accurately measure the condensation length in pipes.

Condensation length measurement

We define the length of the two-phase fluid as the condensation length. The principle of obtaining condensation length by measuring the temperature distribution of the fluid is: the temperature of the fluid in two-phase state, is the saturation temperature. However, when the two-phase fluid is completely condensed into liquid phase, the temperature of the liquid phase drops quickly. Therefore, as long as the temperature transition point can be located, the condensation length can be determined.

Condensation length measurement was performed using R134A two-phase fluid pump driven loop. The condensation length was adjusted by changing the heating power of the evaporator.

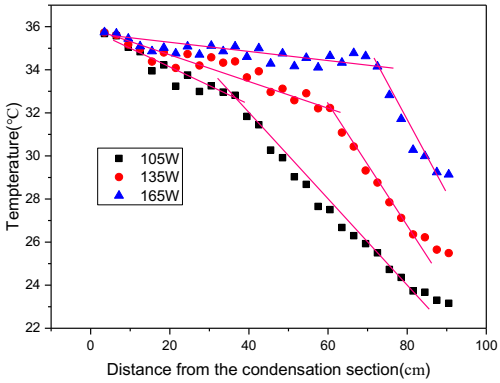

Figure 2: The temperature distribution measured by the Fiber Bragg Gratings in series after calibration. (Saturated temperature:36℃, cooling water temperature:18℃, heating power of the evaporator: Solid black square-105W、Solid red circle -135W、Solid blue triangle-165W)

The measured fluid temperature of the two-phase flow decreases slightly along the flow direction. The pressure drop of the condensation tube was less than 300Pa. It is too small to attribute to the decrease of the saturation temperature. Owning to the gravity, the thickness of the liquid layer of the stratified flow gradually increases along the flow direction. The fiber drawn to the bottom of the tube by the gravity was immersed in the liquid layer thicker and thicher, so the measured temperatures of the two-phase section is indeed the liquid temperatures of the stratified flow, showing a slightly inclined line. When the two-phase fluid is completely condensed into liquid phase fluid, the temperature drops significantly.

The condensation length is defined by the intersection of the two fitted lines of the two-phase flow and the liquid flow, respectively, as shown in the Figure 2, which is 72.5 cm. It is close to the value predicted by Rhosenow's correlation[2] (72.0 cm) and higher than the Dobson's correlation[3] (66.0 cm).

The comparison between the measured values of the condensation length at different heating powers and the predicted value is shown in the table 1.

Table 1: Comparison of condensation lengths between the measurements and predictions (HP:Heating Power, M:Measurement, R: Rhosenow model, D: Dobson model)

HP (W)	M(cm)	R (cm)	D (cm)
105	39.5	48.0	41.0
135	66.5	61.0	54.0
165	72.5	72.0	66.0
195	75.5	83.0	77.0

Conclusions

Current measured data show that the method of measuring the condensation length using distributed fiber Bragg gratings has a high repeatability within one month. The spatial resolution of the condensation length measurement can reach 3.0 cm

Acknowledgements

This work was supported by the project under grant No.09010-32031708 for State Key Laboratory of Optoelectronic Materials and Technologies. It was also supported by the project under Grant No. 71000-42080001 for Zhuhai Key Laboratory of Center for Space Technology.

References

[1] S. Lips, J. P. Meyer, Two-phase flow in inclined tubes with specific reference to condensation: A review, *Int J of Multiphase Flow* 37.8 (2011) 845-859.

[2] V. García, O., Review of In-Tube Condensation Heat Transfer Correlations for Smooth and Microfin Tubes, *Heat Transfer Engineering* 24.4 (2003) 6-24.

[3] M. K. Dobson, Heat Transfer and Flow Regimes During Condensation in Horizontal Tubes, (1994).

[4] M. K. Dobson, J. C. Chato, Condensation in Smooth Horizontal Tubes. *Journal of Heat Transfe*r 120.1 (1998) 193-213.

[5] A. Cavallini, G. Gensi, et al., Condensation inside and outside smooth and enhanced tubes-a review of recent research, I*nternational Journal of Refrigeration* 26.4 (2003) 373-392.

[6] F. Illán-Gómez, A. López-Belchí, et al., Experimental two-phase heat transfer coefficient and frictional pressure drop inside mini-channels during condensation with R1234yf and R134a, *International Journal of Refrigeration* 51 (2015) 12-23.

[7] S. Koyama, K. Kuwahara, et al., An experimental study on condensation of refrigerant R134a in a multi-port extruded tube. *International Journal of Refrigeration* 26.4 (2003) 425-432.

[8] K. W. Moser, R. L. Webb, et al., A New Equivalent Reynolds Number Model for Condensation in Smooth Tubes, *Journal of Heat Transfer* 120.2 (1998) 410.

[9] A. Cavallini, D. DelCol, et al., Condensation in Horizontal Smooth Tubes: A New Heat Transfer Model for Heat Exchanger Design, *Heat Transfer Engineering* 27.8 (2006) 31-38.

[10] K. O. Hill, Fiber Bragg Grating Technology Fundamentals and Overview, *Journal of Lightwave Technology* 15.8 (1997) 1263-1276.

26th European Low Gravity Research Association Biennial Symposium and General Assembly
14th International Conference on "Two-Phase Systems for Space and Ground Applications"
European Space Agency Topical Teams meetings
Granada (Spain), September 24-27, 2019

Oral 171

Asymptotic model of bubble growth in pool boiling: further developments

A. Rednikov[1], N. Hollander[1], M. Hernando Revilla[1], P. Colinet[1]

[1]TIPs Lab, Univérsité libre de Bruxelles, Brussels, Belgium;
aredniko@ulb.ac.be, pcolinet@ulb.ac.be

Vapor bubble growth on a superheated substrate is an elementary act of the boiling process. Given a long-standing interest to this fundamental problem, the literature dedicated to its modelling does not seem to be overly too vast. Quite a number of numerical studies come from the members of our ESA Topical Team (e.g. Kunkelmann & Stephan 2010, Huber et al. 2017), and more activity will be stimulated by the forthcoming RUBI experiment organized by ESA onboard the ISS. One of the difficulties of the modelling is associated with the presence of a (moving) contact line, where the well-known hydrodynamic and heat-flux singularities need to be resolved at a microscopic level. In the present study, we make use of a multiscale approach, similarly to many other authors. However, a distinctive feature here is that we push it even further, by formally and consistently considering the asymptotic limit of small contact angles. Furthermore, it is the case of a perfectly wetting liquid (zero Young's angle) that is explicitly implied here, when (small) finite contact angles are actually just dynamic, evaporation-induced ones.

The consideration generally involves four regions: i) microregion, where the contact line singularities are resolved and the evaporation-induced contact angles are established (cf. e.g. Rednikov & Colinet 2017 for various microregion models), ii) Cox-Voinov region, iii) foot of the bubble, and iv) macroregion. It is only in the latter region, which remarkably appears to leading order in the form of the exterior of a sphere touching a planar surface in one point (hence a fixed geometry even for variable contact angles), that the full Navier-Stokes and heat equations are to be numerically resolved (Hollander 2013, Hernando Revilla 2014, Rednikov et al. 2014); cf. Fig. 1. In the first three regions, the analysis is either carried out analytically (ii and iii), or as a separate numerical module (i). The increase of the mass of the bubble is due to the evaporation mass flux into its interior, which is a sum of the contributions from the mentioned four regions:

$$4\pi\rho_v R^2\dot{R} = J_{(i)} + J_{(ii)} + J_{(iii)} + J_{(iv)} \qquad (1)$$

with $R = R(t)$ being the bubble radius as a function of time t, $\dot{R} \equiv dR/dt$, $\rho_v \approx pM/(R_g T_w)$ the vapor density (assumed constant on account of the superheat being much smaller than the wall temperature: $\Delta T = T_w - T_{sat} \ll T_w$ and the pressure change in the bubble being much smaller than ambient pressure p), M the molar mass, and R_g the universal gas constant. J is the mass flux given by

$$J = \frac{\lambda_l}{L}\int \frac{\partial T}{\partial n}\, dS$$

where λ_l is the liquid thermal conductivity, L [J/kg] the latent heat of evaporation, $\partial T/\partial n$ the (external) normal temperature gradient, S is the area, while the integration is performed over the regions indicated by the subscripts on the right-hand side of (1). Note that, as the problem is here treated by means of asymptotic matching, the right-hand side of (1) naturally does not depend on a concrete choice of the boundaries between the regions involved, even if each term taken apart does.

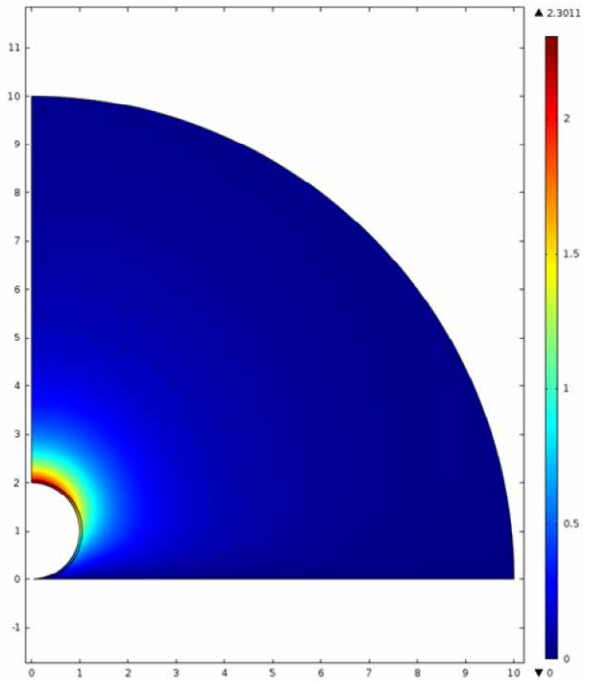

Figure 1: Velocity field (absolute value; in units of $\dot{R}$) within the computation domain (R being the unit of length) for HFE-7100 at 1 atm and a superheat $\Delta T = 10$ K.

An extensive parametric study has been carried out assuming a locally superheated liquid environment at T_w and highlighting the role of various effects and parameter values. Some results are shown in Figs. 2—5.

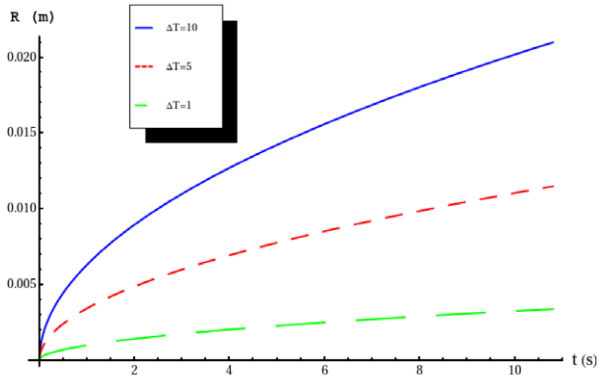

Figure 2: Evolution of the vapor bubble radius with time starting from an initial condition R_0=100 μm at t =0 for HFE-7100 at 1 atm and various values of the superheat (ΔT =1, 5 and 10 K).

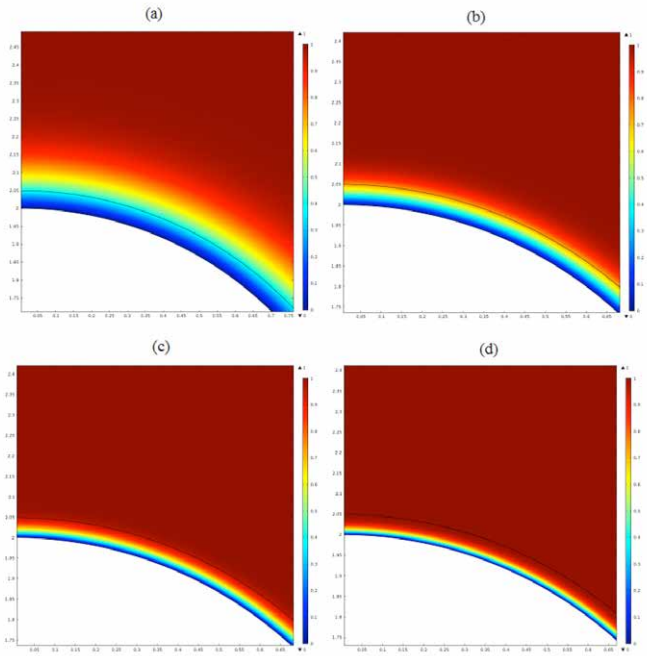

Figure 3: Thermal boundary layer at the surface of a growing vapor bubble for (a) $\Delta T = 1$ K, (b) $\Delta T = 3$ K, (c) $\Delta T = 6$ K and (d) $\Delta T = 10$ K, the liquid being locally superheated in the vicinity of the bubble. The boundary layer is thin in accordance with the large values of the Peclet number obtained (cf. Fig. 4).

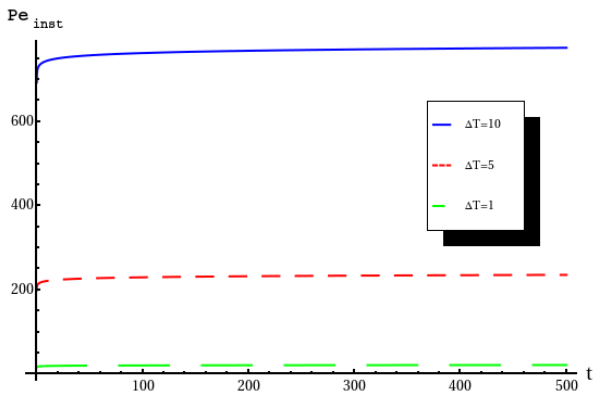

Figure 4: The instantaneous Peclet number (defined as $R\dot{R}/\kappa_l$, where is the thermal diffusivity of the liquid) for the vapor growth versus the dimensionless time for the same cases as those shown in Fig. 1. The dimensionless time is defined in terms of the dimensional one as $\lambda_l \Delta T t/(R_0^2 L \rho_v)$. The instantaneous Reynolds number can be inferred as $Re_{inst}=Pe_{inst}/Pr$, where Pr is the Prandtl number (Pr=7.6 for HFE-7100 at the boiling point at 1 atm).

Further work is related to lifting certain limitations still contained in the model, such as an insufficient account for the velocity dependence of the receding contact angle. The analysis is extended to include the possibility of a subcooled liquid environment for bubble growth. Substrate configuration is adapted closer to RUBI. The results of such further developments will be reported at the conference.

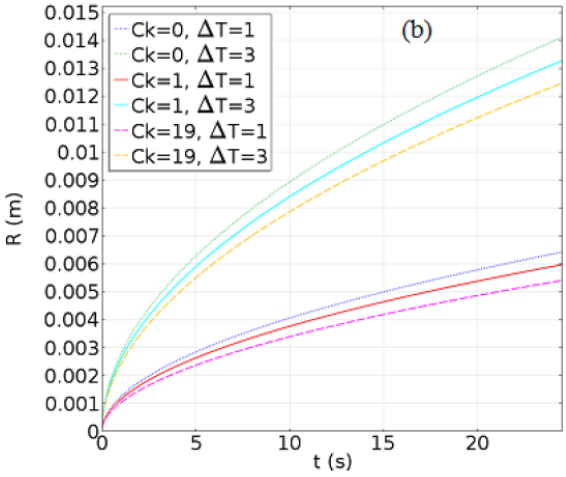

Figure 5: Investigation of the influence of the accommodation coefficient C_k in the evaporation kinetics on the computed bubble growth rate (HFE-7100 at 1 atm and $\Delta T = 1$ K or $\Delta T = 3$ K). The accommodation coefficient is one of the material properties that is difficult to determine or to measure, hence an inherent uncertainty from the modelling viewpoint. Here $C_k = 0$ symbolically represents the case when a local thermodynamic equilibrium is imposed throughout (instantaneous kinetics), $C_k = 1$ correponds to an ideal value of this coefficient, whereas higher values of C_k are expected in reality.

Acknowledgements

Support from BELSPO PRODEX and ESA MANBO Projects as well as from the Fond de la Recherche Scientifique -- FNRS is gratefully acknowledged.

References

M. Hernando Revilla, Modelling of Nucleate Boiling: Single Vapor Bubble Growth on a Superheated Surface, *Master Thesis*, Université libre de Bruxelles (2014).

N. Hollander, Contribution à la Modélisation de la Croissance d'une Bulle de Vapeur sur une Plaque Surchauffée : Acte Élémentaire d'Ébullition, *Master Thesis*, Université libre de Bruxelles (2013).

G. Huber, S. Tanguy, M. Sagan, C. Colin, Direct Numerical simulation of Nucleate Pool Boiling at Large Microscopic Contact Angle and Moderate Jacob Number, *Int. J. of Heat and Mass Transfer* 113 (2017) 662-682.

C. Kunkelmann, P. Stephan, Numerical Simulation of the Transient Heat Transfer during Nucleate Boiling of Refrigerant HFE-7100, *Int. J. Refrigeration* 33 (2010), 1221–1228.

A. Rednikov, N. Hollander, M. Hernando, P. Colinet, Computation of Bubble Growth on a Hot Substrate: Asymptotic Scheme for Small Contact Angles, *Ninth International Conference on Two-Phase Systems for Ground and Space Applications,* Baltimore, Maryland, USA, Sept. 22-26 (2014).

A. Rednikov, P. Colinet, Asymptotic Analysis of the Contact-Line Microregion for a Perfectly Wetting Volatile Liquid in a Pure-Vapor Atmosphere, *Phys. Rev. Fluids* 2 (2017) 124006.

26th European Low Gravity Research Association Biennial Symposium and General Assembly
14th International Conference on "Two-Phase Systems for Space and Ground Applications"
European Space Agency Topical Teams meetings
Granada (Spain), September 24-27, 2019

Oral 172

Evaporation, boiling and dry spots dynamic in shear–driven thin liquid films under intense heating

O. Kabov[1,2], E. Tkachenko[1,2], V. Belosludtsev[1,2] and D. Zaitsev[1]

[1] Kutateladze Institute of Thermophysics SB RAS, 630090 Novosibirsk, Russia
[2] Novosibirsk State University, 630090 Novosibirsk, Russia
kabov@itp.nsc.ru

Introduction

One of the most important problems of thermal physics today is cooling of microelectronic equipment. Currently, the production of processors changes over from the 14 nm manufacturing process technology to the 7 nm technology. The average heat flux on the chips of commercially available computers and other electronic devices is up to 200-300 W/cm^2. In local areas from 100 μm^2 to few square millimeters, the heat flux reaches values of 1 kW/cm^2 or higher. Devices of the next generation may have even higher heat fluxes (Bar-Cohen and Holloway, 2016).

There are three known methods of heat removal from localized heat sources of high intensity: 1) boiling in microchannels, 2) spray cooling, and 3) microfluidic cooling. The authors propose the fourth method of effective cooling, in which heat removal is due to intensive evaporation of a thin liquid film, moving in a flat micro-/minichannel under the action of gas flow (Kabov et al. 2007, 2009). Recent experimental investigations (Zitsev et al. 2017) proved possible removal of heat fluxes with density of up to 1 kW/cm^2 from the heating area of 1x1 cm^2 using this method.

In the present work with the help of high-speed imaging we study the dynamics of liquid film driven in a minichannel under the action of shear stress of gas, under intense local heating.

Methods

The main part of the test section is a stainless-steel plate with a pressed-in copper rod. The rod surface has a shape of a square head 1x1 cm^2, imitating the surface of a computer chip. The rod is heated using a nichrome coil, wound around its lower part. The working surface (stainless steel plate with copper rod) was rough polished. The root mean square (RMS) surface roughness was found to be 0.79 μm. The working area is covered with a transparent cover of optical glass, thus forming a flat channel. The channel height is 0.17 – 2.0 mm, and the width is 35-40 mm. Gas is introduced into the working area from a compressor. The working liquid is supplied from the thermostat, enters the channel through the liquid nozzle and moves over the stainless steel plate as a film under the influence of gas friction. After passing the working area the gas is vented to atmosphere, and the fluid flows back to the thermostat. Distilled water with initial temperature of 24˚C is used as the working fluid. Air with temperature of 24-27˚C and relative humidity of 15-30% is used as working gas.

The dynamics of vapor microbubbles and dry spots are investigated with high-speed camera (FASTCAM SA1.1, 5400 frames per second at a resolution of 1024x1024 pixels and up to 675000 frames per second at lower resolutions, optical system of high spatial resolution: 2.5 μm per 1 pixel of the camera sensor).

Experimental results

With the help of high-speed imaging, it was found that the maximum intensity of heat removal from the heater is achieved in the mode, when the film flow continuity is broken. The heater is covered with small (of about 100 microns in size) dry spots with the lifetime on the order of 1/1000 s. At that, the number of spots that exist simultaneously on one square centimeter of the surface can reach several hundred (Fig. 1).

The dynamics of formation of a typical dry spot is as follows. At the initial moment, we observe a continuous film of liquid, then a microscale bubble arises in the film, then film rupture occurs very rapidly, which leads to the formation of a dry spot. Then development of the spot is observed, after which, the spot is washed out. Fig. 2 shows the scheme of dry spot formation. It was estimated that at the heat flux of 450 W/cm^2, during 1 s up to 1 million dry spots appear and disappear at the area of 1 cm^2 (the surface of the heater). With increasing heat flux, the number of dry spots and the frequency of their formation increase. Fig. 3 shows the time dependence of the average diameter of 10 dry spots at the same parameters of the experiment. Totally, we analyzed 158 consecutive dry spots from one video. It was found that about 50% of dry spots have lifetime less than 0.5 ms.

Figure 1: The flow of a water film moving under the action of gas in a 1.5 mm high channel with a heater of 1x1 cm^2. Reynolds number of liquid Re_l = 14, superficial gas velocity U_{Sg} = 34 m/s, heat flux q=240 W/cm^2, temperature of the heater surface T_w=126°C. The flow is directed from top to bottom.

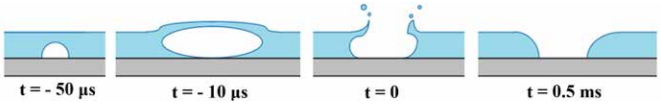

Figure 2: Scheme of dry spot formation (side view).

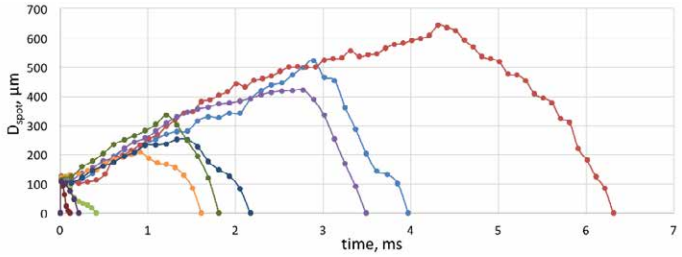

Figure 3: Time dependence of the average diameter of 10 different dry spots. $Re_l = 40$, $U_{Sg} = 19.5$ m/s, q = 450 W/cm^2, $T_w = 130$°C.

As the heat flux is increased, the total area of dry spots increases, but when the heater reaches a certain temperature (≈100°C), the total area begins to decrease. Fig. 4a shows the photo processing results in the form of the total area of dry spots on the heater, divided by the area of the heater, vs. heat flux for $Re_l = 45$ and $U_{Sg} = 7.4$ m/s. In contrast to the area of dry spots, the total length of contact line on the heater increases with increasing heat flux and reaches a maximum in the pre-crisis regime. The dependence of the total length of the contact line on the heat flux is shown in Fig. 4b for two different runs. It is seen that for Run 2 in pre-crisis regime the total area of the contact line on the heater reaches 30 cm.

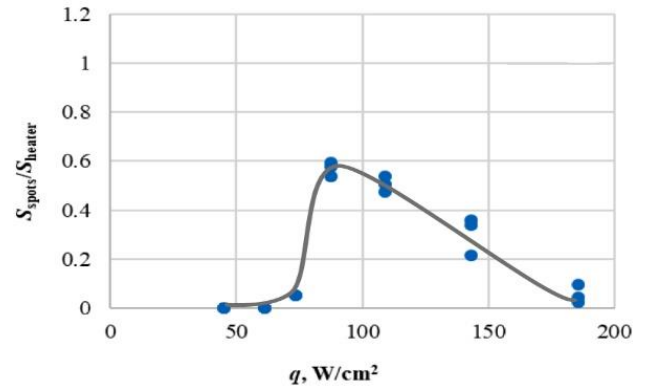

a

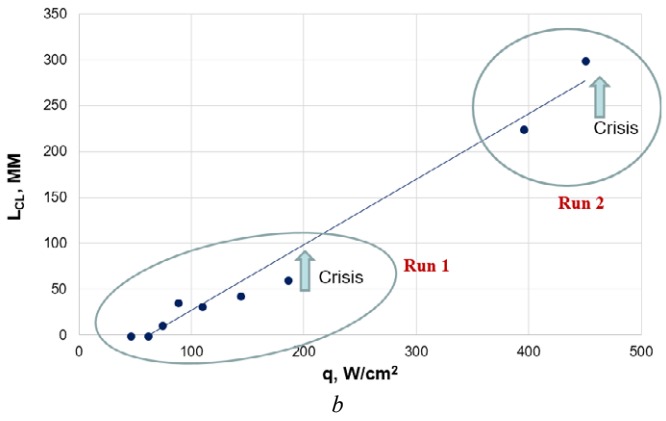

b

Figure 4: (a) The dependence of the total area of dry spots (relative to the area of the heater) on the heat flux at $Re_l = 45$ and $U_{Sg} = 7.4$ m/s. (b) Dependence of the total length of contact line on the heat flux. Run 1: $Re_l = 45$; $U_{Sg} = 7.4$ m/s; CHF = 200 W/cm^2. Run 2: $Re_l = 40$; $U_{Sg} = 19.5$ m/s; CHF = 470 W/cm^2.

Conclusions

Systematic experimental studies of the flow and destruction of a water film, shear-driven in the channel, under heating from a local heat source with size of 1x1 cm2, have been performed.

For a microchannel with the height of H=170-250 mm the critical heat flux was found to be weakly dependent on the superficial gas velocity, while for a minichannel with the height of H=1-2 mm the critical heat flux was found to strongly decrease with the decrease of the superficial gas velocity. Thus, we conclude that cooling systems with shear-driven liquid films in microchannels are more reliable than those with shear-driven liquid films in minichannels.

Experiments have resulted in the values of heat flux and heat transfer coefficient, which are a record for a thin liquid film (~1 kW/cm^2 and ~300 kW/m^{2}K, respectively). The value of the critical heat flux is by an order of magnitude higher than the corresponding values for falling water films and several times higher than CHF for channel flow boiling obtained on the same test section. The CHF values reached for shear-driven liquid film are close to the CHF for full evaporation of liquid. This confirms the prospects of using thin liquid films, moving under the influence of the gas flow friction in modern systems of equipment cooling with high local heat release.

With the help of high-speed imaging, it was found that the maximum intensity of heat removal from the heater is achieved in the mode, when the film flow continuity is broken. During the experiment, the total area of dry spots increases with increasing heat flux, but when the heater reaches a certain temperature (≈100°C), the total area starts to decrease. In contrast to the area of dry spots, the length of contact line increases with increasing heat flux and reaches a maximum in the pre-crisis regime. Intensive evaporation in the region of the contact line (Kabov et al. 2017) may explain high heat fluxes achieved in the experiment.

Acknowledgements

This work was supported by the Russian Science Foundation (Project No. 19-19-00695).

References

Bar-Cohen A., Holloway C., *Journal of Physics: Conference Series*, 745, 022002, (2016).

Kabov, O.A., Lyulin, Yu.V., Marchuk, I.V. and Zaitsev, D.V., *International Journal of Heat and Fluid Flow*, 28, pp. 103-112, (2007).

Kabov O.A and Zaitsev D.V., *Multiphase Science and Technology*, 21, pp. 249-266, (2009).

Kabov O.A., Zaitsev D.V., Kirichenko D.P., Ajaev V.S., *Nanoscale and Microscale Thermophysical Engineering*, 21, p. 60, (2017).

Zaitsev D., Tkachenko E. and Kabov O., *EPJ Web of Conferences* 159, 00054 (2017).

26th European Low Gravity Research Association Biennial Symposium and General Assembly
14th International Conference on "Two-Phase Systems for Space and Ground Applications"
European Space Agency Topical Teams meetings
Granada (Spain), September 24-27, 2019

Oral 173

Isolated bubble growth and detachment in a shear flow

I. Layouni[1], M. Lebon[1], J. Sebilleau[1], C. Colinr[1]

[1]Institut de Mécanique des Fluides, Université de Toulouse, Toulouse, France;
colin@imft.fr

Introduction

The most advanced model for the prediction of heat transfer coefficient in convective nucleate boiling are based on heat flux partitioning taking into account the contribution of phase change, rewetting of the wall after bubble lift-off or in the wake of the sliding bubble, convection between the nucleation sites (Judd and Hwang, 1976; Kurul and Podowski, 1990). These models require a good prediction of the diameter and frequency of bubble detachment.

In the case of quasi-static bubble growth on a horizontal wall in a quiescent liquid, the bubble shape can be easily calculated by integrating the Young-Laplace equation (Oguz and Prosperetti 1993, Di Bari and Robinson, 2013). Bubble detachment occurs when the bubble shape becomes unstable. In the case of bubble growth in a shear flow, the bubble is no longer axisymetrical and its radius at detachment R_{det}, is often calculated by using point force models (Thorncroft *et al.*, 2001, Yeoh and Tu 2005, Van der Geld, 2009, Mazocco *et al.,* 2018). The main difficulty is the lack of knowledge in the hydrodynamic forces for a deformed bubble growing on a wall in a large range of bubble Reynolds numbers (20 to 1,000).

To improve the modeling of the hydrodynamic forces a detailed analysis at the scale of individual bubbles is required. This is the objective of the Experimental set-up RUBI (Reference mUltiscale Boiling Investigation), which has been designed for more than a decade by several European teams involved in the ESA Project MANBO (Multiscale Ananlyis of Boiling). In this experiment, IMFT is especially involved in the study of vapour bubble growth and detachment in a shear flow.

Experimental set-up

The experimental set-up consists of a test cell (Figure 1) with a heating plate on its lower part including an artificial nucleation site to ensure the generation of a isolated bubble. This cavity is activated thanks to a laser beam pulse. RUBI Experiment provides measurements of wall temperature and heat flux distribution underneath vapour bubbles with high spatial and temporal resolutions by means of IR thermography. These data are synchronised with the bubble shape observation by a high-speed video. Furthermore, the fluid temperatures in the vicinity and inside the bubbles are measured by an array of four thermocouples. In order to study bubble detachment or sliding on the heating surface, an electrical field can be also applied and a shear flow is created by a forced convection loop. The entrance part of the test section is a rectangular channel of 40mmx5mm. The flow in the RUBI test cell, in the convection loop and in the honey comb upstream have been calculated by numerical simulation using the software STAR CMM+.

Recent experiments with the flight model of RUBI have been performed in horizontal configuration with upward facing and downward facing heating plate At the Belgian User Support and Operations Centre. RUBI should be launched on the International Space Station on July 2019 and be operated until the end of the year.

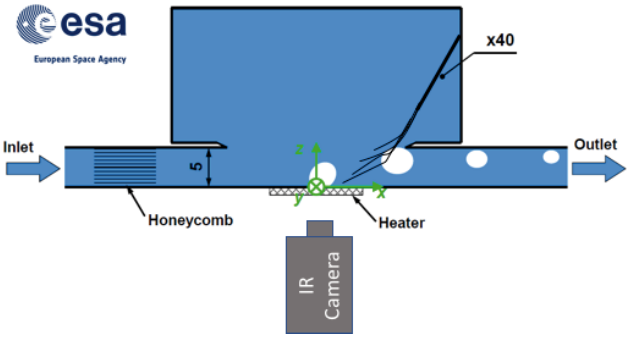

Figure 1: Sheme of RUBI test cell.

Prelimiary results

On ground and parabolic flight experiments have been performed with a model of the RUBI test cell in collaboration with the University of Pisa. High-speed video images of the bubble have been recorded. After image processing the geometrical parameters of the bubble during its growth are determined: bubble equivalent radius, radius of the bubble foot in contact to the heated wall, coordinates of the center of gravity, bubble height, upstream and downsteam contact angles. The experiments shows that in microgravity conditions the bubble growth time is longer, the bubble radius at detachment is larger (figure 2) and the bubble foot elongates on the heated plate.

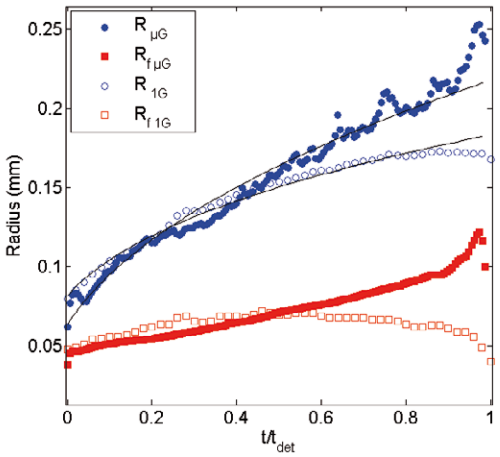

Figure 2: time evolution of the bubble radius R and the bubble foot radius R_f in normal gravity (1G) and microgravity (μG).

From the evolution of the geometrical parameters of the bubble during its growth, the static and hydrodynamic forces are evaluated. Using a classical point force approach (Thorncroft *et al*., 2001 ; Duhar *et al*., 2009 ; Van der Geld 2009), a balance on the forces acting on the bubble can be written as: $\boldsymbol{F_B + F_C + F_{CP} + F_D + F_L + F_I = 0}$

where $\boldsymbol{F_B}$ is the Archimedean force, $\boldsymbol{F_C}$ the capillary force, $\boldsymbol{F_{CP}}$ the contact pressure force, $\boldsymbol{F_D}$ the drag force, $\boldsymbol{F_L}$ the lift force, and $\boldsymbol{F_I}$ the inertia force or added mass force. The buoyancy force $\boldsymbol{F_B}$ vanishes under microgravity. In the direction perpendicular to the wall, $\boldsymbol{F_{CP}}$ will act to detach the bubble, whereas the capillary force will keep it attached to the wall. More interesting is the force balance in the direction parallel to the wall where the inertia force induced by large bubble growth rate can becomes of the same order of magnitude of the drag force to promote the bubble detachment.

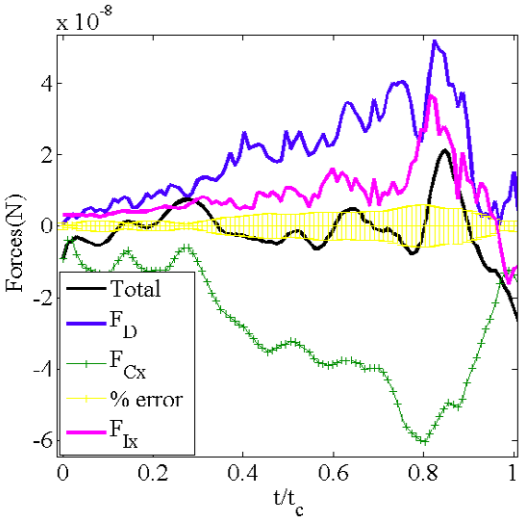

Figure 3: time evolution of the forces acting on bubble in the direction parallel to the wall in microgravity condition in a shear flow with a bulk velocity of 0.1 m/s (t_c is the growth time).

Conclusion and perspectives

RUBI experiments will allow to investigate the bubble growth and detachment in a wide range of flow velocities up to 0.4m/s, wall heat fluxes from 0.5 to 2 W/cm^2, liquid subcooling from 10K to 1K. The processed data will be used as reference data to validate theoretical and numerical models of the phase change and hydrodynamics of the bubble in a shear flow.

Acknowledgements

The authors would like to thank the French Space Agency CNES and the European Space Agency for the organisation of the parabolic flight campaings, their financial support through GDR MFA and MAP project MANBO and for their support in the development of RUBI.

References

R. Judd, K. Hwang, A comprehensive model for nucleate pool boiling heat transfer including microlayer evaporation, J. Heat Transf. 98 (4) (1976) 623–629.

N. Kurul, M.Z. Podowski, Multidimensional effects in forced convection subcooled boiling, Proceedings of the Ninth International Heat Transfer Conference, vol. 2, Hemisphere Publishing, New York, (1990), 19–24.

S. Di Bari, A.J. Robinson, Experimental study of gas injected bubble growth from submerged orifices, Experimental Thermal and Fluid Science 44 (2013) 124–137.

G. Duhar, G. Riboux, C. Colin, Vapour bubble growth and detachment at the wall of shear flow, Heat and Mass Transfer 45 (2009) 847-855.

T. Mazzocco, W. Ambrosini, R. Kommajosyula, E. Baglietto. A reassessed model for mechanistic prediction of bubble departure and lift off diameters, International Journal of Heat and Mass Transfer 117 (2018) 119–124.

N. Oguz, A. Prosperetti, Dynamics of bubble growth and detachment from a needle, Journal of Fluid Mechanics 257 (1993) 111–145.

G. Thorncroft, J.F. Klausner, R. Mei, 2001, Bubble forces and detachment models, Multiphase Science and Technology 13 (2001) 35-76.

C. Van der Geld, C., The dynamics of a boiling bubble before and after detachment, Heat and mass transfer 45 (2009) 831–846.

G. Yeoh, J. Tu, 2005, A unified model considering force balances for departing vapour bubbles and population balance in subcooled boiling flow, Nuclear Engineering and Design, 235 (2005) 1251–1265.

Oral 174

Thermocapillary stability of a thin viscoelastic film with deformable surface coating a thick wall: competition between stationary and oscillatory convection.

Luis A. Dávalos-Orozco

Universidad Nacional Autónoma de México, Instituto de Investigaciones en Materiales, Departamento de Polímeros
Ciudad Universitaria, Circuito Exterior S/N, C.P. 04510, Ciudad de México, México
ldavalos@unam.mx

Thermocapillary convection has been the subject of research since many years ago due to the interest it has from the fundamental point of view and because of the large number of important applications (Ruschak 2004, Quéré 1999). Such applications include consideration of Newtonian fluids and in particular of non-Newtonian fluids whose mechanical properties have a special interest.

Advances in isothermal and non-isothermal flow have been done in the recent years. In cylindrical coordinates examples are the flow down rotating cylinders (Dávalos-Orozco and Ruiz-Chavarría 1993, Ruiz-Chavarría and Dávalos-Orozco 1996, 1997). The stability of films down heated cylinders was investigated (Dávalos-Orozco and You 2000, Dávalos - Orozco 2018, 2019). In the absence of gravity the nonlinear instability was investigated (Dávalos - Orozco 2017). The case of a viscoelastic film was investigated in the presence and in the absence of gravity in by (Moctezuma - Sánchez and Dávalos - Orozco 2008, 2015).

When the film flows on deformed surfaces it was possible to when the stabilizing effect of wavy deformation in case the wavelength of the free surface deformations present a resonance with the wavelength of the wavy wall by (Dávalos - Orozco 2007, 2008, see reviews 2013a, 2016) and for a viscoelastic fluid by (Dávalos - Orozco 2013b). The thickness of the wall was assumed in the problem by (Dávalos - Orozco 2012) for a film falling down a heated wall. These results had a very important influence when the thickness of the hot wall was taken into account in the presence of wavy deformation at the fluid wall interface (Dávalos - Orozco 2014, 2015).

Viscoelastic liquids present a different response to perturbations. The linear thermocapillary instability of a flat viscoelastic liquid film coating a thick wall with finite thermal conductivity was investigated by (Hernández-Hernández and Dávalos-Orozco, 2015). It is well known that viscoelasticity promotes oscillatory convection. However, when the thickness and thermal conductivity of the wall vary the conditions change and stationary convection may prevail. In that paper it was shown that stationary and oscillatory instabilities compete to be the most unstable when the free surface is assumed to be flat and different condition of the wall.

The general interest is to present results of competition of stationary and oscillatory instabilities of a thin film with free surface deformation and for different conditions of the heated wall. This is in contrast to previous work (Hernández-Hernández and Dávalos-Orozco, 2015) for a flat surface. Here a sample is presented in this abstract in which the small wave number approximation is used to investigate the stability of a viscoelastic film under these conditions. It is interesting that under this approximation the flow instability is stationary and not oscillatory as could be expected. Therefore, more results will be presented to show for which parameters this instability could be oscillatory.

It is found that the frequency of oscillation is $\omega = 0$. The growth rate varies as shown in Fig. 1a and 1b. It is clearly shown the stabilizing influence of the ratio d/Qc. d is the wall liquid film thicknesses ratio and Qc the corresponding thermal conductivities ratio. The solid curves correspond to viscoelastic Deborah number De = 0.1 and the dashed curves to De = 0.3. The Deborah number is a destabilizing factor. The Marangoni number increases from 0.1, 1 and 10. The lowest curve corresponds to Ma = 0.1. The Marangoni number also has a destabilizing effect. All these results correspond to stationary convection and show the influence of the parameters.

References

L. A. Dávalos-Orozco, "Nonlinear instability of a thin film flowing down a smoothly deformed surface" *Phys. Fluids* **19** (2007) 074103.

L. A. Dávalos-Orozco, "Instabilities of thin films flowing down flat and smoothly deformed walls" *Micrograv. Sci. and Tech* **20** (2008) 225 - 229.

L. A. Dávalos-Orozco, "The effect of the thermal conductivity and thickness of the wall on the nonlinear instability of a thin film flowing down an incline" *Int. J. Non-Linear Mech.* **47** (2012) 1 – 7.

L. A. Dávalos-Orozco, "Stability of thin liquid films falling down isothermal and nonisothermal walls" *Interfacial Phenomena and Heat Transfer* **1** (2013a) 93 – 138.

L. A. Dávalos-Orozco, "Stability of thin viscoelastic films falling down wavy walls" *Interfacial Phenomena and Heat Transfer* **1** (2013b) 301 – 315.

L. A. Dávalos-Orozco, "Nonlinear instability of a thin film flowing down a smoothly deformed thick wall of finite thermal conductivity" *Interfacial Phenomena and Heat Transfer* **2** (2014) 55 – 74.

L. A. Dávalos-Orozco, "Nonlinear instability of a thin film flowing down a cooled wavy thick wall of finite thermal conductivity" *Physics Letters A* **379** (2015) 962 – 967.

L. A. Dávalos-Orozco, "Thin liquid films falling down heated walls; a review of recent results" *Interfacial Phenomena and Heat Transfer* **4** (2016) 109 – 131.

L. A. Dávalos-Orozco, "Sideband thermocapillary instability of a thin film coating the outside of a thick walled cylinder with finite thermal conductivity in the absence of gravity" *Interfacial Phenomena and Heat Transfer* **5** (2017) 287-298.

L. A. Dávalos-Orozco, "Sideband thermocapillary instability of a thin film flowing down the inside of a thick-walled cylinder with finite thermal conductivity" *Interfacial Phenomena and Heat Transfer* **6** (2018) 239-251.

L. A. Dávalos-Orozco, "Sideband thermocapillary instability of a thin film coating the outside of a thick walled cylinder with finite thermal conductivity in the absence of gravity" *Int. J. Non-Linear Mech.* **109** (2019) 15 - 23.

I J. Hernández-Hernández and L. A. Dávalos-Orozco, "Competition between stationary and oscillatory viscoelastic thermocapillary convection of a film coating a thick wall" *Int. J. Thermal Sci.* **89** (2015) 164 - 173.

L. A. Dávalos-Orozco and G. Ruiz-Chavarría, "Hydrodynamic instability of a fluid layer flowing down a rotating cylinder" *Phys. Fluids A* **5**, (1993) 2390 – 2404.

G. Ruiz-Chavarría and L. A. Dávalos-Orozco, "Stability of a liquid film flowing down a rotating cylinder subject to azimuthal disturbances", *J. Phys. II France*, **6** (1996) 1219 - 1227.

G. Ruiz-Chavarría and L. A. Dávalos-Orozco, "Azimuthal and streamwise disturbances in a fluid layer flowing down a rotating cylinder", *Phys. Fluids* **9**,(1997) 2899 – 2908.

M. Moctezuma - Sánchez and L. A. Dávalos – Orozco, "Linear Three dimensional instability of viscoelastic fluid layers flowing down cylindrical walls" *Microgravity Sci. Technol.* **20** (2008) 161 – 164.

M. Moctezuma - Sánchez and L. A. Dávalos – Orozco, "Azimuthal instability modes in a viscoelastic liquid layer flowing down a heated cylinder" *Int. J. Heat Mass Transfer* **90** (2015) 15 - 25.

D. Quéré, "Fluid coating on a fiber", *Annu. Rev. Fluid Mech.* **31** (1999) 347 – 384.

S. J. Weinstein and K. J. Ruschak, "Coating flows", Annu. *Rev. Fluid Mech.* **36**, (2004) 29 - 53.

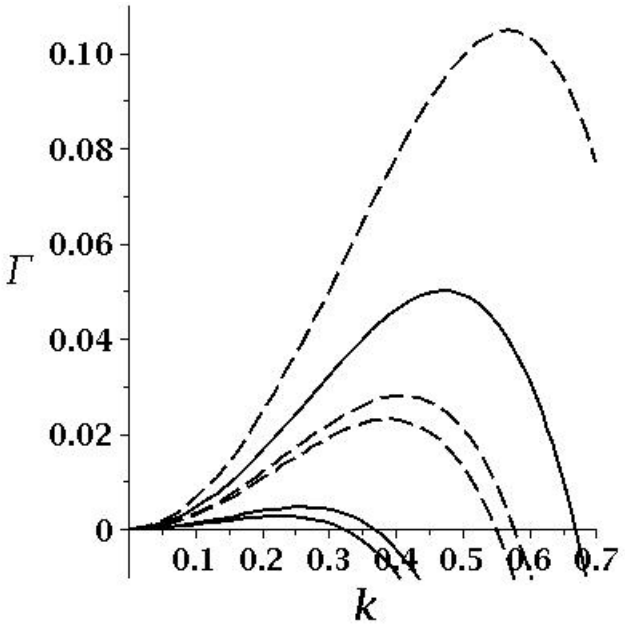

Fig. 1a

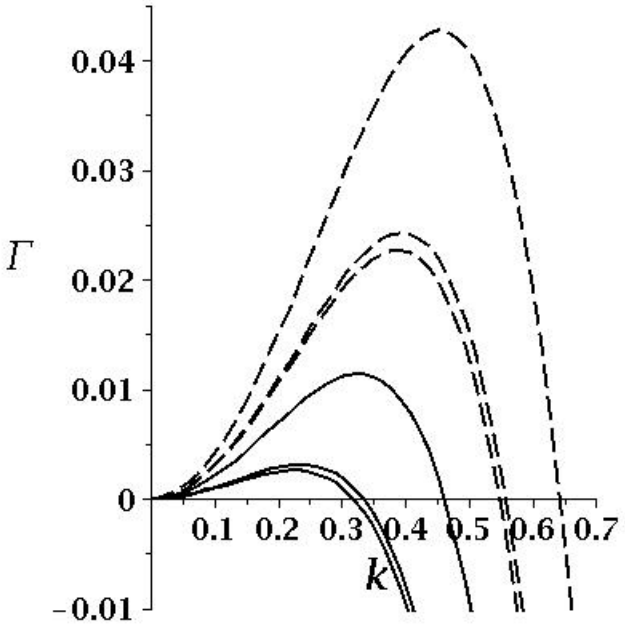

Fig. 1b

Figure 1: Growth rate against the wavenumber. Thin viscoelastic film coating a hot thick wall with finite thermal conductivity. Bi = 0.1, S= 1: Fig. 1a: d/Qc = 1 and Fig. 1b d/Qc = 10. De = 0.1 (solid) and De = 0.3 (dashed) for three Ma = 0.1, 1, 10 (the lower curves are for Ma = 0.1).

26th European Low Gravity Research Association Biennial Symposium and General Assembly
14th International Conference on "Two-Phase Systems for Space and Ground Applications"
European Space Agency Topical Teams meetings
Granada (Spain), September 24-27, 2019

Oral 176

Numerical investigations on droplet shapes with electric field

Vishwa K. Rajan[2], Alekos I. Garivalis[1], Paolo Di Marco[1]

[1]DESTEC, Università di Pisa, Pisa, Italy;
[2]School of Mechanical Engineering, SASTRA Deemed University,Thanjavur, India-613401
vishwak08@gmail.com, alekosioannis.garivalis@phd.unipi.it, p.dimarco@ing.unipi.it

Introduction

The current work focuses on numerical study on dynamics of a droplet with electric field under adiabatic conditions in order to understand the pure effect of electric stresses on droplet movement along with its deformation. A numerical study implementing axisymmetric finite element modelling and adopting level set framework of tracking interface is created. The electric force model combining the techniques available in literature is used. Simple boundary conditions have been specified at each and every boundary. High potential is applied to washer shaped electrode and this analysis is focused on droplet deformation under 6 kV. To validate this with experiments, droplet profiles computed numerically is matched to experimental profiles taken through MATLAB code. Local electric force and average electric force have been computed in order to quantify the forces in interface. The analysis showed that electric force is higher for the droplet of higher volume and several oscillations are seen across the thin interface line.

Experimental apparatus, procedures and computational domain

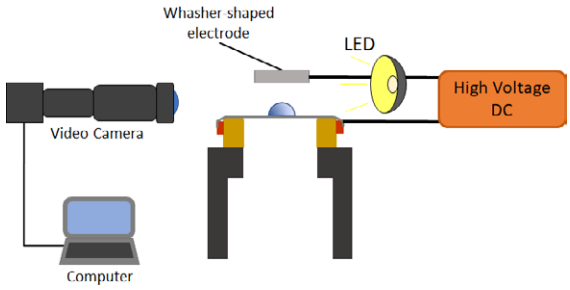

Figure 1: Experimental apparatus.

The experimental set-up is similar to the one described by Gibbons (Gibbons et al. 2018). Fig. 1 illustrates the experimental layout. The test section is a coated stainless steel foil. A washer shape electrode is placed at a distance of 6 mm from the surface. The washer shaped electrode is connected to high voltage power supply, and voltage of 8 kV can be applied to the test section. Images are captured using high speed camera with microscopic lens, utilising shadowgraphic technique. The illumination necessary for capturing images are supplied by a led lamp. Droplet of deionized water is deposed through a syringe by dismantling the electrode configuration. The electrode is connected to power and images of droplet are captured for different voltages. The solid surface on which the droplet is in contact, is cleaned after taking each set of data in order to fetch images for different droplet volume. The captured images are processed using MATLAB software. The droplet interface is converted to an interpolation function and it is utilized to draw initial droplet profile for computations.
Computational domain is designed in order to mimic the actual experimental apparatus and its dimensions are shown in Fig. 2 for droplet V1 (similar trends for V2 and V3). The steady state profile of initial shape of the droplet interface without electric fields is extracted from experimental setup through MATLAB code followed by fitting a trendline for the actual droplet surface. The trendline fitted is approximately 0.99 times the actual droplet surface.

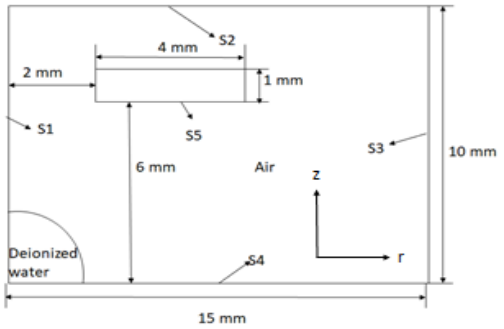

Figure 2: Computational domain.

In order to calculate interfacial forces and curvatures accurately, level set formulation is adopted to track the interface. The mass and momentum conservation for incompressible fluids are written. The surface tension forces acting at interface between two fluids is formulated by continuous surface modeling approach. The electric force is formulated combining the techniques of Brackbill modelling of surface tension (Brackbill et al. 2007) and electric stress expression derived by Di Marco (Di Marco 2012). Interfaces are taken into account in the model using a Level set variable φ and its transport equation: at the interfaces the value of Level set variable ranges from 0 to 1, it is 0 in droplet and 1 in air.
Governing equations such as mass, momentum, level set and charge conservation for a dielectric incompressible fluid are solved simultaneously to calculate dependent variables using the following boundary conditions:

- Line S1 is an axisymmetric boundary.
- Line S2 is given an outflow boundary condition.
- Line S3 and S5 is given no-slip boundary condition and S5 is given an electric potential.
- Line S4 is given a static contact angle taken from experiments.

The commercial finite element modeller COMSOL Multiphysics is implemented to solve the above governing

equations. In order to control the convergence, the relative tolerance is set as 0.01.

Results and discussion

The analysis for the current work was performed for three different droplets ($V_1 = 43.13$ mm^3, $\theta_1 = 82.4°$; $V_2 = 95.92$ mm^3, $\theta_2 = 87.5°$; $V_3 = 42.59$ mm^3, $\theta_3 = 74.9°$) under a high voltage for 6 kV. The volume is computed by integrating the φ along the interfacial boundary of liquid-air. The error in mass conservation is limited to 7%.
The simulations are performed for 250 ms. At the end of each simulation, it was observed that the average accelerating force on the liquid-air interface was found to be less than 200 N/m^3. In the current simulation it is assumed to be the steady state.

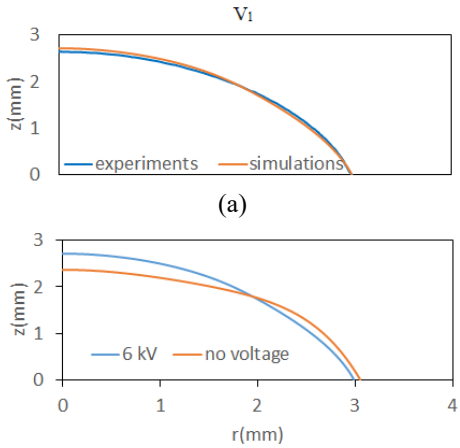

Figure 3: Comparison between calculated and experimental profiles (a) and differences between profile with and without electric field (b) for droplet V_1.

The results of the simulations are compared after the droplet has achieved its approximate steady state as stated earlier. Fig. 3 (a) shows the comparison of computed profile with experiments for the droplet V_1. Blue profile shows the profile of experiments and orange profile shows the results of simulations. The computed profile is in good agreement with the experimental profile. It was observed that vertical height of droplet is increased upon the action of electric fields with droplet diameter almost being constant. The deformation is a result of normal electric stresses at the liquid-air interface thereby pushing the droplet (having higher permittivity) to a region of higher electric field. Fig. 3 (b) shows the difference between the interface with and without electric field.

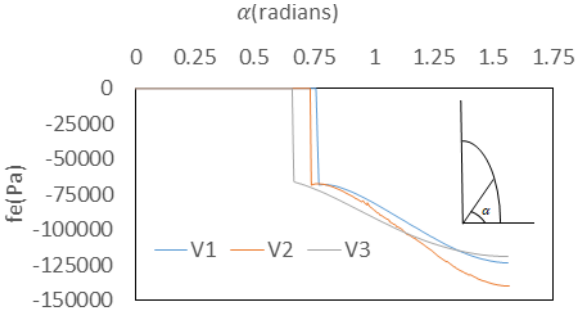

Figure 4: Local vertical electric stress versus angle.

Fig. 4 shows local vertical electric stress calculated at the end of simulation versus the angle α measured in radians. The electric stress is almost zero near the three phase contact line and there is a sudden jump after 0.5 radians for all the three droplets. This can be explained by the higher permittivity gradient of two fluids created in these regions. As we go to the droplet apex, we observe that the stress value grows, and it is higher for droplet V_2 and almost the same for the other two droplets, which have similar volumes. The value of stress at the apex is related to the droplet volume. The difference in stresses in angular region of droplet V_1 and V_3, that have similar volumes, can be explained by differences in contact angle which produce some differences in droplet shapes.
The local vertical electric stress is used to compute average vertical electric force on interface vesus time to understand its effect on droplet height. Fig. 5 shows average electric force (left) and height (right) versus time. It is seen that average electric force oscillates with time and its oscillation reduces as the time increases. This creates an oscillation in height of the droplet. It is seen that average electric force for droplets V_1 and V_3 are almost equal and it is quite high for droplet V_2. This observation was similar to the one explained earlier.

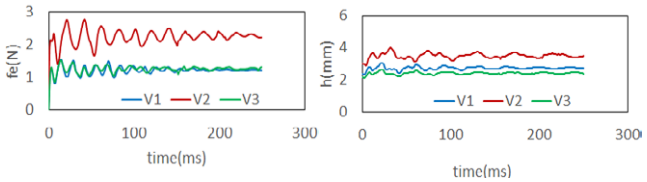

Figure 5: Average electric force (left) and height (right) vs time.

Conclusions

The current study is focused on understanding the pure effect of electric stresses on droplet movement along with its interface. A numerical model is created using Level set technique. An electric force model combining the techniques of Brackbill modelling of surface tension (Brackbill et al. 2007) and electric stress expression derived by Di Marco (2012) is used. The droplet computed numerically is very well matching with experimental profile. The analysis on electric force shows that electric force is almost negligible near the three phase contact line and droplet apex. The electric force acts in the region after 0.5 radians. Further, oscillations in average electric force with time can be seen as an evidence for oscillations of height of droplet.

Acknowledgements

This work is partially funded by ESA under the MAP-Evaporation (AO-1999-110) project.

References

J.U. Brackbill, D.B. Kothe, C. Zemach, A continuum method for modeling surface tension, *Journal of computational physics*, 100(2), (1992) 335-354.

P. Di Marco, The use of electric force as a replacement of buoyancy in two-phase flow, *Microgravity Science and Technology*, 24(3), (2012) 215-228.

M. Gibbons, P. Di Marco, A.J. Robinson, Local Heat Transfer to an Evaporating Droplet, *Int. J. of Heat and Mass Transfer* 121 (2018) 641-652.

26th European Low Gravity Research Association Biennial Symposium and General Assembly
14th International Conference on "Two-Phase Systems for Space and Ground Applications"
European Space Agency Topical Teams meetings
Granada (Spain), September 24-27, 2019

Oral 177

Droplet population during dropwise condensation of steam

D. Del Col, S. Bortolin, M. Mirafiori, R. Parin

Department of Industrial Engineering, University of Padova, Via Venezia 1, 35131 Padova, Italy
davide.delcol@unipd.it

Introduction

Condensation is a phase-change process that is present in nature and in a wide range of industrial applications. Condensation can take place in filmwise mode (FWC) or in dropwise (DWC) mode. During DWC, condensed liquid forms discrete droplets instead of a continuos film and this mechanism leads to higher heat transfer coefficients compared to FWC mode. To develop updated heat transfer correlations and to better understand the DWC process, information about the droplet population are very important.
The droplet population is divided in two parts: the small droplet population, where the dominant growth mechanism is direct condensation and the large droplet population where the dominant growth mechanism is coalescence. To statistically describe the droplet distribution, Le Fevre and Rose (1966) introduced the drop-size density distribution $N(r)$ function. The drop-size density distribution function has been evaluated in semi-empirical mode by means of photos taken during the DWC phenomenon. Observations become very difficult when focusing the attention on small radius droplets.
In the present paper, the experimental investigation of droplet population is extended from few millimeters to tens of microns where the expression proposed by Le Fevre and Rose (1966) is supposed to be still valid. Several samples at different heat fluxes have been considered. A toroidal homemade LED and a high-speed camera have been used to detect the droplets. Experimental data have been obtained with saturated steam (around 100°C saturation temperature) flowing in the test section at 2.7 m s^{-1}. A wide range of heat flux conditions (between 89 and 544 kW m^{-2}) is considered and four different coatings are investigated. Video analysis has been performed on around six millions of droplets by a homemade MATLAB® program.

Image analysis

Videos have been recorded during DWC of steam using a high-speed camera (Photron FASTCAM UX100 coupled with zoom lens). Figure 1a shows an image of the DWC: the investigated area is a square window 13.6 mm x 13.6 mm. Particular attention has been paid to reduce vibrations between the experimental apparatus and the high speed camera. The camera focus has been controlled by a programmable board to avoid any disturb. Since the conventional lighting techniques are unable to highlight uniformly the contours of drops, which is essential for a precise droplet dimension detection, a toroidal-shape LED has been designed and built. The toroidal-shape LED projects its torus pattern onto each drop and this pattern can be put in relation with the droplet radius itself. An example of the resulting illumination is showed in Figure 1a. The image is then post-processed by a MATLAB® program.

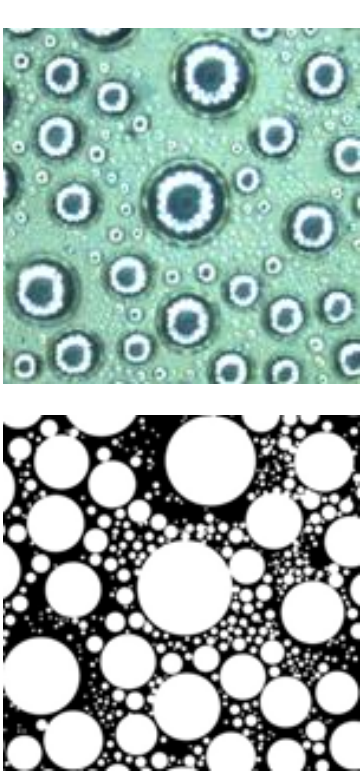

Figure 1. Droplet population visualized during DWC. (a) Image of the DWC process taken with the high-speed camera and the toroidal LED (visualization window 3.6 mm x 13.6 mm). b) Reconstructed image after post-processing.

The result of the post-process is illustrated in Figure 1b. Then the number of droplets whose radius is included in a given interval can be automatically determined.

Experimental results

Four different aluminum samples have been tested in the experimental apparatus which consists of a two-phase thermosyphon loop. Saturated steam is used as operative fluid. The system is made of four main components (boiling chamber, test section, cooling water loop and post-condenser) and it allows simultaneous visualization of the dropwise condensation process and heat transfer measurements. A detailed description of the experimental apparatus can be found in Del Col et al. (2015, 2017).
Video analysis has been performed with four aluminum samples, treated with different hydrophobic layers. Wetting measurements (advancing and recedings contact angles) and operating conditions (heat flux) at which samples have been tested are listed in Table 1.
The evaluation of the maximum drop radius in the drop-size density distribution for large droplet population is an

important issue since it is the only parameter on which $N(r)$ depends. In theoretical models, the common assumption is that the steam is in quiescent state without the presence of vapor shear stress. Since the present experimental data are taken with non-zero steam velocity, the departing radius has been directly measured by visualizations. Figure 2 shows the droplet distribution around the maximum departing radius. It has been found that the droplet departing radius is not affected by the heat flux: each coating shows the same departing radius regardless the test operating conditions.

Table 2. Advancing/receding contact angles and heat flux range for the different coatings considered in the present study.

	θ_a [deg]	θ_r [deg]	q [kW m^{-2}]
Coating #1	89 ± 1	64 ± 3	167 - 509
Coating #2	83 ± 3	57 ± 6	144 - 544
Coating #3	77 ± 4	45 ± 5	89 - 346
Coating #4	76 ± 5	53 ± 11	111 - 464

a)

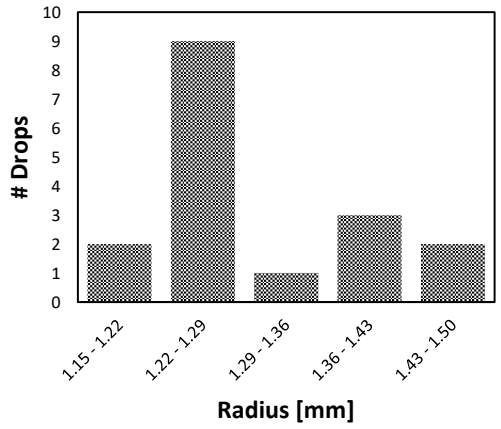

b)

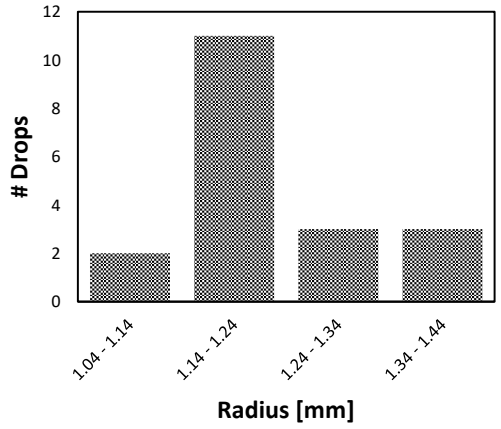

Figure 2. Number of drops for each radius interval measured with coating #2 (a) and coating #4 (b).

During the experimental campaign, for all the four tested coatings, high-speed videos have been recorded covering all the heat fluxes reported in Table 1. The experimental data have been interpolated with a power-law equation having the same functional form as the Le Fevre and Rose formula (1966), $N(r) = A\, r^B$ (where r is the droplet radius, A and B are the constants obtained from the data regression analysis). The data, in total around six million droplets, are aggregated for each sample since different heat fluxes led to a similar droplet population. The two power-law parameters A and B are compared with the constants proposed by Le Fevre and Rose (1966) in their equation showing good agreement.
The minimum measured radius is around 15 μm: these droplets are still growing by coalescence (as it can be inferred from videos), meaning that such droplets should still be considered into the large droplet population.

Conclusions

The drop-size density distribution during dropwise condensation in different operating conditions has been studied and compared to the existent literature. Drop-size density distribution has been analysed using the experimental apparatus available at the Two-Phase Heat Transfer Laboratory of the University of Padova. A new illumination system, a torus-shaped LED, has been developed. The analysis has been performed on four different coatings tested varying the heat flux. An excellent agreement was found with the large droplet population theory proposed by Le Fevre and Rose (1966) provided that the measured value of the maximum droplet radius is used in their equation. The analysis of the different samples demonstrates that the drop-size density distribution is not influenced by the different operating conditions of the condensation tests and this validates experimentally the distribution theory proposed by Le Fevre and Rose (1966).

Acknowledgements

The authors acknowledge the financial support of the the European Space Agency through the MAP Condensation program ENCOM-3 (AO-2004-096).

References

E. J. Le Fevre and J. W. Rose, A theory of heat transfer by dropwise condensation, in *Proceedings of the 3rd International Heat Transfer Conference,* Vol. 2 (1966).

A. Bisetto, S. Bortolin, D. Del Col, Experimental analysis of steam condensation over conventional and superhydrophilic vertical surfaces, *Exp. Therm. Fluid Sci*. 68 (2015) 216–227.

D. Del Col, R. Parin, A. Bisetto, S. Bortolin, A. Martucci, Film condensation of steam flowing on a hydrophobic surface, *Int. J. Heat Mass Transf*. 107 (2017) 307–318.

26th European Low Gravity Research Association Biennial Symposium and General Assembly
14th International Conference on "Two-Phase Systems for Space and Ground Applications"
European Space Agency Topical Teams meetings
Granada (Spain), September 24-27, 2019

Oral 178

Structured 2D droplet arrays levitating over liquid and solid surfaces

D. Zaitsev[1], D. Kirichenko[1], A. Shatekova[1], V. Ajaev[2] and O. Kabov[1]

[1] Kutateladze Institute of Thermophysics SB RAS, 630090 Novosibirsk, Russia
[2] Department of Mathematics, Southern Methodist University, Dallas TX 75275, USA
zaitsev@itp.nsc.ru

Introduction

As first described by Schaefer (1971), microscale droplets of condensed liquid may levitate over a hot liquid-gas interface. Such levitation can be sometimes observed over a hot surface of tea or coffee. The main mechanism of levitation is the Stokes force acting onto a drop from the flow originated at the interface. The levitating droplets can also be seen organizing themselves into 2D regular structures near liquid and solid interfaces (Zaitsev et al. 2017), as shown in Fig. 1.

Understanding the criteria for levitation of microdroplets near interfaces is important for practical applications such as spray cooling, drug delivery using aerosols, and containerless synthesis of amorphous chemicals. A promising practical application is the use of levitating microdroplets as natural tracers for determination of local gas flow on microscale. Kabov et al. (2017) carried out detailed analysis of trajectories of levitating microdroplets and used the results to find local velocities of the moist air flow above a heated layer of liquid with a dry patch. A substantial increase of the flow velocity was observed in the vicinity of the contact line.

Here we present our recent experimental and theoretical results on droplet arrays levitating over liquid surfaces as well as over dry solid substrates.

Methods

A sketch of the experimental set-up is shown in Fig. 2. The substrate is a copper block heated from below. In order to achieve pinning of the contact line at the substrate, the working surface was rough with the root mean square (RMS) roughness of 0.50 μm. The surface temperature of the block T_w is measured by thermocouples at several points with the accuracy of 0.1 K and frequency of 1 Hz. According to the measurements, the condition of constant temperature, is satisfied along the copper surface. In the experiments, T_w varied from 50 to 100°C. The test section is installed horizontally and open to the atmosphere. Degassed ultra-pure water (Merck Millipore) is used as the working liquid. Optical recording is made at 5400 fps using a high-speed CCD camera equipped with a microscope objective of high resolving power (resolution of up to 0.781 μm per pixel). The camera was oriented either for top view or for side view.

The experimental procedure is as follows: 1) A pre-determined volume of the liquid is deposited with a syringe onto the substrate to form a liquid layer (with the initial thickness, H_0, varying from 0.40 to 1.00 mm). 2) The heater is switched on. Provided T_w is becoming above 50°C, an ordered array of levitating microdroplets forms over the free surface of the liquid (Fig. 1). The optical recoding of the array is made. 3) With a short pulse of air jet, a dry spot (about 0.5-1 mm in size) is formed on the copper surface, Fig. 2. 4) Under the action of gravity, the droplet array moves down the slope of the interface toward the dry area. Once the droplets reach the dry spot, the optical recording is made again.

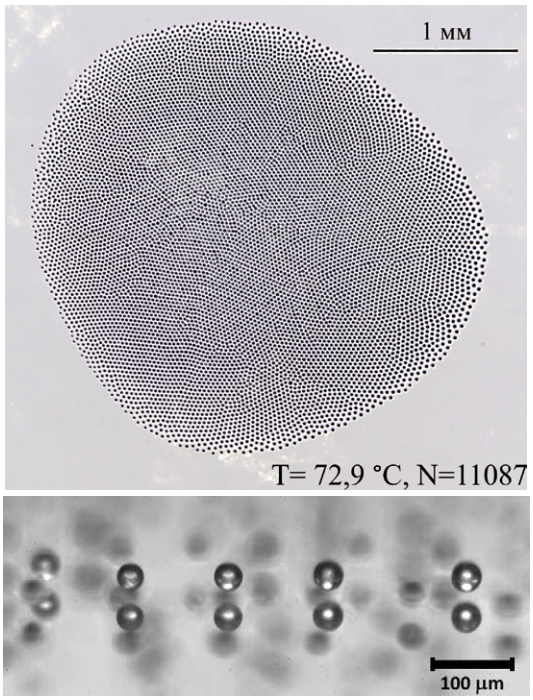

Figure 1: Top and side view photographs of a structured array of microdroplets levitating over a thin layer of water heated from below.

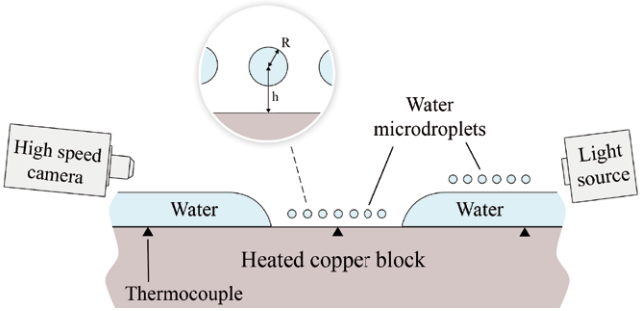

Figure 2: Sketch of the experiment with definition of h and R.

Results

We started by observation of droplet levitation over the liquid-air interface. It was found that as the substrate temperature grows the number of droplets in the array, N, increases to a certain value, following which the number of droplets practically does not change, Fig. 3. The size of the array increases almost linearly with temperature from roughly 1 to 3 mm. The interdroplet distance was found to increase with the substrate temperature, with the distance from the center of the array, and also with the droplet size.

When the array moves to the dry spot, the droplets continue to levitate over the solid dry surface, Figs. 4,5. Even though the life-time of the array is shorter over the dry surface, its geometric characteristics are remarkably similar to the case of droplets levitating over liquid-gas interface, Fig. 1.

We demonstrated experimentally for the first time that a structured array of levitating liquid microdroplets can form over a dry substrate with temperature below the saturation temperature, Figs. 4,5. The minimum temperature of the substrate at which levitation of water microdroplets occurs was found to be about 50°C. There is a narrow dry region near the contact line ("forbidden zone"), where no levitating droplets are observed, Fig. 5. The width of this region substantially increases with the substrate temperature, Fig. 6.

A simple model is developed that explains the droplet levitation over the solid substrate by the reflection of the flow, created by the evaporating droplet, off the substrate. Dependence of the relative height of droplet levitation $\hat{h} \equiv h/R$ on the dimensionless radius of the droplet is shown in Fig. 7 (experiment and theory). It is seen that above $\hat{h} \sim 2$ the experimental data are in good quantitative agreement with the model predicting power law $\hat{h} \sim R^{-3/2}$. At $\hat{h} \sim 2$, a crossover to a different regime is observed. In this regime, the geometry is similar to the one used in studies of Leidenfrost droplets, so the distance between the droplet and the wall is the key parameter; this distance (h - R), scaled by R, is plotted in the inset of Fig. 7 and follows the power law $\hat{h} - 1 \sim R^{-2}$.

We then used the same approach to model droplet levitation over liquid surfaces. A new power law is found and shown to be in agreement with the experimental data from both our experiments and previously published study of a small-sized array of levitating droplets.

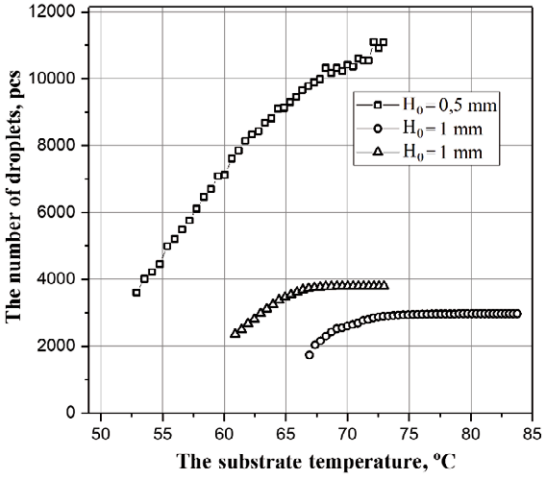

Figure 3: Number of levitating microdroplets in the array vs. substrate temperature. Data for three different arrays is presented.

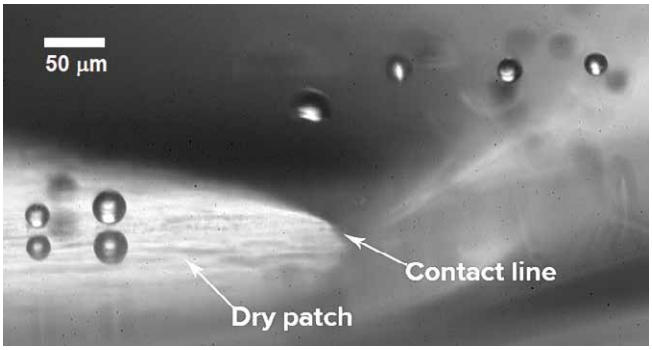

Figure 4: Side view photograph of droplets flying over the contact line towards dry spot (T_w=95°C).

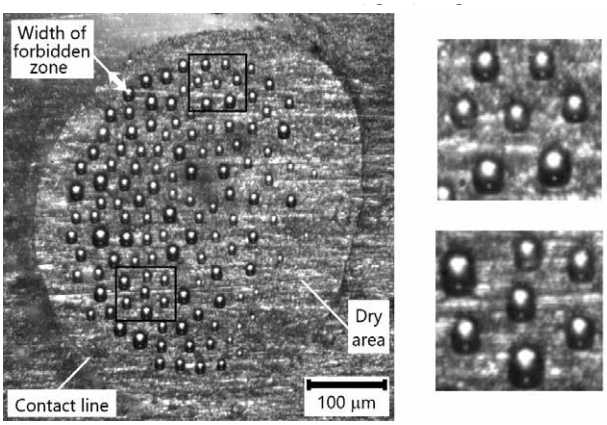

Figure 5: Left: array of microdroplets levitating over dry spot (T_w=85°C). Right: two zoom-in images of parts of the droplet array with high regularity (corresponding to two black rectangles in left image).

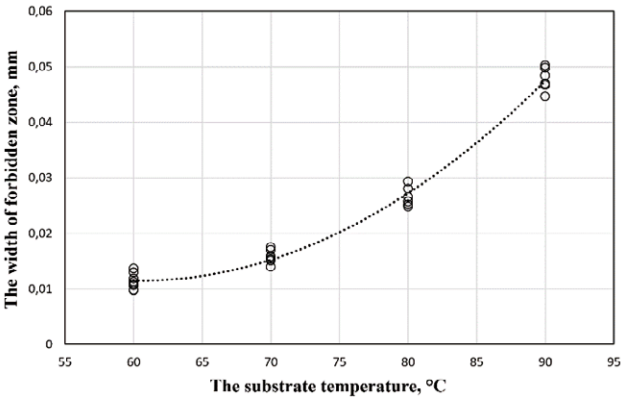

Figure 6: The minimum distance from the contact line to the array of droplets levitating over dry spot vs. substrate temperature.

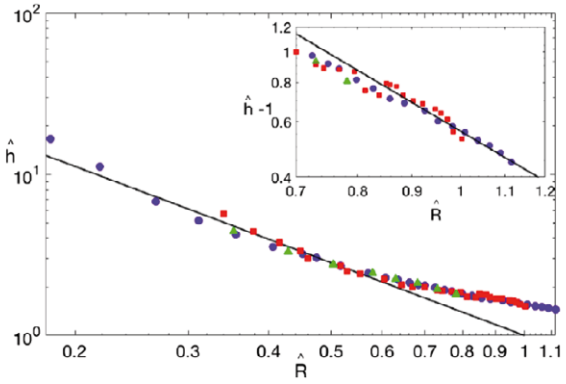

Figure 7: Comparison between experiment (three different droplets at T_w = 85°C) and theory (solid line) for droplets levitating over dry substrate. Inset illustrates the power law corresponding to Leidenfrost-type situation at lower $\hat{h}$.

Acknowledgements

This work was supported by the Russian Science Foundation (Project No. 18-19-00538).

References

Kabov, O.A., Zaitsev, D.V., Kirichenko, D.P., Ajaev, V.S., *Nanoscale and microscale thermophysical engineering*, vol. **21**, pp.60-69, 2017.

Schaefer, V. J., *Am. Sci.*, vol. **59**, pp. 534–535, 1971.

Zaitsev, D.V., Kirichenko, D.P., Ajaev, V.S., Kabov, O.A., *Physical Review Letters,* vol. **119**, 094503, 2017.

26th European Low Gravity Research Association Biennial Symposium and General Assembly
14th International Conference on "Two-Phase Systems for Space and Ground Applications"
European Space Agency Topical Teams meetings
Granada (Spain), September 24-27, 2019

Oral 179

The effect of a seven day period of whole body unloading with hyper-bouyancy floatation (HBF) on the spine and intervertebral disc height

P. Carvil[1,2], TE. Morris-Paterson[1], EJ. Jones[1], T. Gkouvinas[1], C-C. Tsai[3,4], H. Hasegawa[3,4], S. Halson-Brown[5], ZA Puthucheary[6], DA Green[7], SB Zanello[1], I Rosenzweig[3,4], SDR Harridge[1]

[1] Centre for Human and Applied Physiological Sciences, King's College London, UK. [2] Science and Technology Facilities Council – UK Research & Innovation, UK. [3] Sleep and Brain Plasticity Centre, Department of Neuroimaging, IoPPN, King's College London, UK. [4]Sleep Disorders Centre, Guy's and St Thomas' Hospital, UK. [5]Department of Women's and Children's Health, King's College London, UK. [6]Institute of Health and Human Performance, University College London, UK. [7]KBRWyle, European Astronaut Centre, Germany.
Philip.carvil@stfc.ac.uk

Introduction

Analogues are currently utilised to study the effects of unloading induced by microgravity upon the. This provides a platform to assess the efficacy of countermeasures for human spaceflight. However current analogues may prove unsuitable for the evaluation of spinal countermeasures. Head-down tilt (HDT), the most commonly used analogue for spaceflight has been shown to induce stature significant elongation of up to 2cm after 3 days [1]. However it has also shown to cause compression of the thoracic intervertebral discs (IVD) and cervical muscles associated with the weight bearing of the head [2]. It has also suggested that this analogue does not best represent the haemodynamic situation in microgravity [3].

Dry immersion uses a lined barrier between the participant and water. Participants are placed on the surface of this 'barrier', before being lowered into the water via inbuilt hydraulic lifts. Similar to wet immersion, the participant's head remains out of the water, but the body sinks and becomes flexed at the hips. Three-days of dry immersion has been found to induce significant lumbar IVD [4]. Participant accessibility is, however, limited with immersion, making measurements whilst immersed impractical.

Originally conceived by John Lilly in the 1970's, immersion tanks filled with salt water, termed restricted environmental stimulation technology (REST) flotation has been used in therapeutic situations as a relaxation tool. Participants are placed in a darkened tank filled with mixed water and Epsom salt (Magnesium sulphate; 1.7gcm^3), induces flotation [5]. However, participants cannot stay in the tank for longer than a few hours, due to skin maceration and risk of drowning when asleep.

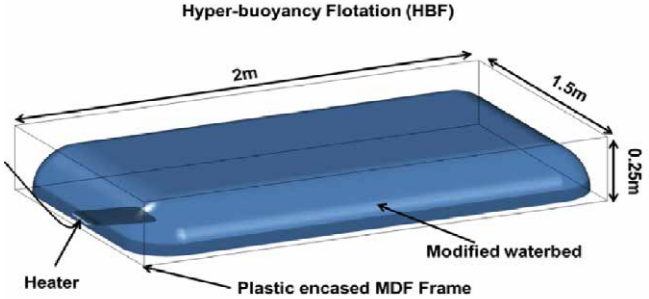

Figure 1: Schematic of Hyper-buoyancy flotation. Image Credit – King's College London.

Using a combination of dry immersion and REST flotation, a new analogue was devised at King's College London termed hyper-buoyancy flotation (HBF). This comprises of a waterbed partially filled with hypersaline water using the same mixture of Magnesium sulphate and water to a ~1.7gcm3 density as REST, which is maintained at a thermo-neutral temperature (Figure 1).

Previous studies using 8 hour flotation have indicated that HBF induces significant increases in stature and small increase in spinal measures [6]. However no long term data exists on the effects of HBF to understand its utility as a spaceflight-unloading analogue.

Aims

The aims of this study were:-

- Investigate how seven-day unloading using the HBF analogue would affect stature elongation and anterior IVD height over time using the in-flight NASA ultrasound protocol.
- Understand the effect of 7 day (pre vs. post) HBF on spinal length, curvature and Intervertebral disc height using MRI.

Methods

The study was conducted as part of a larger clinical trial (NCT03195348). Twelve male participants gave written informed consent to partake in the seven day study.

Participants were fully familiarised with all procedures before commencing their seven day bed rest trial. On study commencement participants attended the sleep centre in the morning where they were prepared to lie on the HBF. For this study standing stature measurements were recorded every day when the participants came off the HBF for their allotted 15minute comfort break.

Ultrasound was performed whilst participants were on the HBF, imaging the anterior IVD heights of the cervical spine (C4/C5 - C7/T1) and lumbar spine (L2/L3 - L5/S1) laterally. This was done at midday on all 3 occasions (day 1, 3 and 7). A 12-4 MHz linear array probe at 6cm depth was used for imaging the cervical spine, parallel to the right of the oesophagus starting just above the manubrium and running cranially up. For the Lumbar spine, a 5-2 MHz curvilinear array probe was positioned sagittal using the sacral shelf at L5/S1 as the first reference marker (Figure 2).

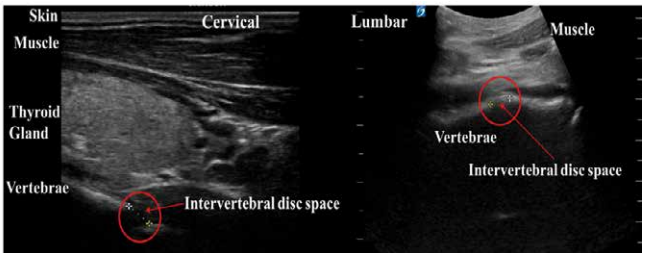

Figure 2: Acquired images of the cervical (left) and lumbar (right) disc spaces and placement of markers for anterior IVD height. Image Credit - King's College London.

Pre and post imaging seven day flotation spinal scans were taken using magnetic resonance imaging (MRI). Sagittal slices were taken from the top of the cervical spine to the base of the lumbar spine. Total spinal length, lumbar length, curvature and intervertebral disc height were measured.

Results were assessed for normality and statistical analysis undertaken. Stature was compared over time using a repeated measures ANOVA. Ultrasound data taken on time point's day 1 and day 7 was plotted individually and compared using a paired samples Wilcoxon test. Ultrasound data collected on days 1, 3 and 7 was grouped and averaged (mean and standard deviation) and compared using a one-way ANOVA with Geisser-Greenhouse correction. MRI data was plotted individually for spinal measures and compared pre vs. post using a paired samples t-test. IVD data was grouped and compared at each level pre vs.post with a t-test.

Results

Following seven-day HBF there was a significant difference in total stature (Day 0:180.3±8.8 vs. Day 7: 182.1±8.8cm). Throughout the seven days, the average daily stature measurements incrementally increased from the first measure on day 1.

Anterior IVD measurements of both cervical and lumbar vertebrae (taken via ultrasound whilst participants were on the HBF between day 1 and 7), were significantly higher in all four cervical vertebrae and two lumbar vertebrae (L3/L4, L5/S1). When looking at change over time in anterior disc height with US between day 1, 3 and 7, there was an increase over time in C3/C4 and C4/C5 and in three lumbar vertebra (L2/L3, L3/L4, L5/S1).

Total spinal length (C2-S1:59±3.2 vs. 59.6±3cm) was significantly (p=0.011), but marginally increased post seven-day flotation. Lumbar length was similarly increased (L1-S1:17.4±1 vs. 17.6±0.9cm) following flotation (p=0.005). Significant reductions (p=0.048) in lumbar curvature were observed post flotation (L1-S1:44.5±8.9 vs. 52.2±8.1°), through 3 of the 12 participants had marginal increases in curvature following flotation (Figure 3).

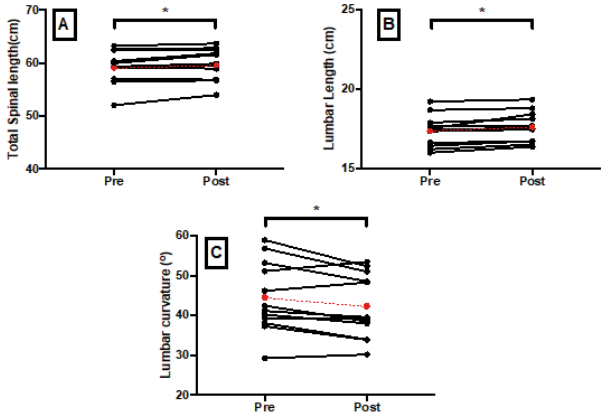

Figure 3: Individual data plotted (pre vs. post 7-day HBF) for total spinal (panel A), lumbar length (panel B) and lumbar curvature (panel c). * = Significant difference pre vs. post 7-day HBF ($p<0.05$. Average highlighted in red

There was a significant increase in the average IVD height at L1/L2 (+0.44mm, p=0.033), L4/L5 (+0.38mm, p=0.015) and L5/S1 (+0.51mm, p=0.032) with a trend for an increase at L3/L4 (+0.37mm, p=0.071). No significant differences were observed at L2/L3 (+0.15mm, p=0.425). When examining the constituent components of average IVD height (anterior, middle and posterior), significant increases in height were observed in the middle of all lumbar discs.

Conclusions

HBF for 7 days provides a novel platform that provides levels of stature and spinal elongation greater than that observed with 8h flotation and head down tilt studies. As such, this supine buoyant position enabled by HBF may provide an alternative microgravity analogue for studying the effects of spinal unloading.

Acknowledgements

We would like to thank the technical staff from King's College London, the imaging teams and the sleep disorders centre at Guys' and St Thomas Hospital for their assistance with the project.

References

[1] Styf JR, Ballard RE, Fechner K, et al (1997) Height increase, neuromuscular function, and back pain during 6°head- down tilt with traction. Aviat Sp Environ Med 68:
[2] Belavý DL, Miokovic T, Armbrecht G, et al (2013) Hypertrophy in the cervical muscles and thoracic discs in bed rest? J Appl Physiology.
[3] Hargens AR, Vico L (2016) Long-duration bed rest as an analog to microgravity. J Appl Physiol 120
[4] Treffel L, Mkhitaryan K, Gellee S, et al (2016) Intervertebral disc swelling demonstrated by 3D and water content magnetic resonance analyses after a 3-day dry immersion simulating microgravity. Front Physiol 7
[5] Hill S, Eckett MJ, Paterson C, Harkness EF (1999) A pilot study to evaluate the effects of floatation spa treatment on patients with osteoarthritis. Complement Ther Med 7:235–8
[6] Carvil, P (2017). Axial loading as a countermeasure to microgravity-induced deconditioning; effects on the spine and its associated structures. Thesis. King's College London

Oral 180

Tolerability of plyometric exercises on a short-arm centrifuge

Timo Frett[1], David Andrew Green[2, 3, 4], Jens Jordan[1, 6], Alexandra Noppe[1], Michael Arz[1], Guido Petrat[1], Uwe Tegtbur[5]

[1.] Institute of Aerospace Medicine, German Aerospace Center, Cologne, Germany
[2.] Space Medicine Team (HRE-OM), European Astronaut Centre, European Space Agency, Cologne, Germany
[3.] KBRwyle GmbH, Cologne, Germany
[4.] King's College London, London, UK
[5.] Institutes of Sports Medicine, Hannover Medical School, Hannover, Germany
[6.] Chair of Aerospace Medicine, University of Cologne, Cologne, Germany
E-Mail: Timo.frett@dlr.de
Web: www.dlr.de/me

Abstract –Artificial Gravity generated by Short Arm Human Centrifuges is a promising multi-system countermeasure for physiological deconditioning during long duration space flights [1, 2]. However, motion sickness symptoms could limit the tolerability of the approach due to cross-coupled forces. Therefore, we determined the feasibility and tolerability, particularly occurrence of motion sickness symptoms, during reactive jumping exercises on a short-arm centrifuge.

In a cross-over randomized study, we assessed motion sickness symptoms during reactive jumping exercises on a short-arm centrifuge in 15 healthy men at different +Gz-level (0.5, 0.75, 1.0, 1.25 and 1.5 +Gz referenced to Center of Mass). On the centrifuge, a jumping sledge was attached with low friction bearings that allowed horizontal movements and around pitch axis along the radius. Head movements were not restricted. Vertical jumping in Earth´s Gravity was used as control.

The results showed good tolerability of the jumping exercises. Motion sickness ratings (using Motion Sickness Assessment Questionnaire pre/post conditions) were in general low in all conditions, post-hoc analysis only showed higher ratings ($z = 2.527$, $p = 0.034$) for condition +1Gz on the Short-arm centrifuge compared to control. Further related effects of motion sickness like mood changes or increased sleepiness recorded with PANAS and Epworth Sleepiness Scale were not significant higher after jumping exercises during centrifugation compared with control.

Our study demonstrates that repetitive plyometric exercises are tolerable at different +Gz-levels during short-radius centrifugation.

The finding is remarkable given the significant head yaw, pitch, and roll velocities being generated in all conditions that are excess of those previously defined as being associated with comfort zones [3].

References

[1] Clément, G. and A. Bukley, Artificial Gravity. Vol. 20. 2007: Springer Science & Business Media. [2] A. Author, B. Author and C. Author, "Proposal of a unique theory," *21th Annual Meeting of the International Society for Magnetic Resonance in Medicine (ISMRM 2013)*, April 20-26, Salt Lake City, UT, USA, Session on Novel RF Coils, pp. 2775, 2013.

[2] Frett, T., et al., DLR-AG Facilities & Research Plans, in International Workshop on Research and Operational Considerations for Artificial Gravity Countermeasures. 2014: Kalifornien, USA.

[3] Hall, T. W. Artificial gravity and the architecture of orbital habitats. Journal of the British Interplanetary Society, 52, 290-300 (1999).

Diminished Glial Scar Formation at Hypergravity

C. Liemersdorf, Y. Lichterfeld, T. Frett and R. Hemmersbach

German Aerospace Center (DLR), Cologne, Germany
Department of Gravitational Biology
christian.liemersdorf@dlr.de ; ruth.hemmersbach@dlr.de

Preferred Session: B2 Cell Biology

roduction

turbed neuronal connectivity is the ultimate cause of bility in individuals with neurological disease including al cord injury, head trauma, and stroke. Functional rological recovery is limited through an unfavorable nce between neuronal regrowth and glia scar formation. prevalent type of glial cells are astrocytes, providing rons with growth factors, nutrients and other promoting ors in the extracellular environment. In addition, these s are predominant in the formation of the so-called glial , which not only sterically hinders neuronal re-growth actively inhibits axonal regeneration processes.
ronal growth as well as astroglial function and migration uire dynamic cytoskeletal protein rearrangements. ause hypergravity stabilizes microtubules while tabilizing actin filaments, we hypothesized that erimental hypergravity would shift the balance between ronal and astroglial growth *in vitro*.

thods: Hypergravity-Exposure and Live-Cell Imaging

exposure of cells to a defined level of hypergravity, erably in the physiological range that would be tolerable to human subjects, is the aim of the Multi-Sample ubator Centrifuge (MuSIC) of the DLR (Fig. 1). This trifuge was designed to create hypergravity environments vibration-free manner in controlled incubation setups able for living samples.

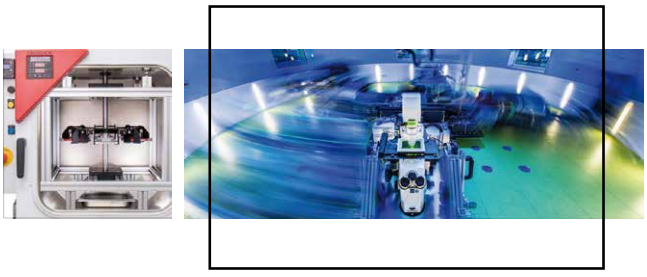

ure 1: The Multi-Sample Incubator Centrifuge (MuSIC) oles researchers to expose a variety of samples in different nats to hypergravity in the range of 2-50g in a defined and ation-controlled setup. To visualize cellular responses on the ecular level during hypergravity exposure, we installed a -cell imaging microscope, the Hyperscope (B), on the :envihab rifuge at DLR, Cologne, Germany. This setup serves as a atile and fast imaging system mounted onto a swing-out form equipped with improved focus stabilization and cell bation methods.

Moreover, observing cellular responses live during exposure to altered environmental stimuli is the key to yield a deeper understanding on underlying mechanisms and time frames, in which cells react and possibly adapt. Thus, we employed the DLR short-arm human centrifuge to install a live-cell imaging microscope system on a swing-out platform onto the centrifuge (Fig. 1).

Results: Impaired Mechanisms of Glial Scar Formation

The formation of the glial scar requires dynamic cytoskeletal rearrangements, which are induced upon exposure of astrocytes to increased gravitational loads in the physiologically tolerable range of 2g. Under these conditions changes in astrocytic properties can already be observed. Astrocytes fail to spread as under normal conditions and show a reduced cell area. This reduction in cell spreading is not coincidental with a diminished proliferation rate, but correlated to impaired migratory behavior (Fig. 2). Impairment in migration behavior is an important mechanism that will have a direct impact on glial scar formation and thus on neuronal regeneration in general.

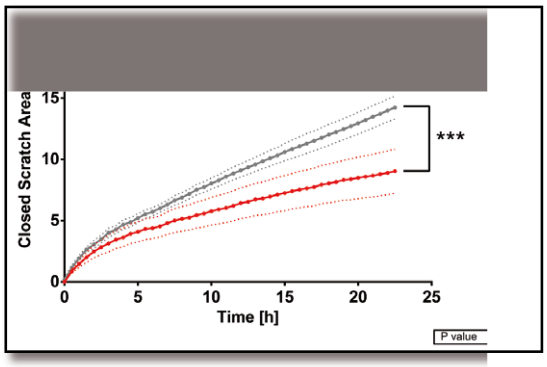

nitial 24h of inished (ca. 20%) migration rate followed by an adaptation phase during later time frames that will last for up to one week.

Acknowledgements

Supported by the ELGRA Research Prize 2017, DLR Project NeuroSpace and the ESA Ground-Based Facility Program

Oral 183

ESA/ELGRA Gravity-Related Research Summer School

P. Carvil[1,2], R González-Cinca[3], N. Callens[4]

[1] Science and Technology Facilities Council, Daresbury, UK. [2] CHAPS – King's College London, London, UK. [3] Department of Physics, UPC-BarcelonaTech, Castelldefels, Barcelona, Spain. [4]ESA Education Office, ESEC-Galaxia, Transinne, Belgium.
Philip.carvil@stfc.ac.uk, ricard.gonzalez@upc.edu Natacha.callens@esa.int

Introduction

The European Low Gravity Research Association (ELGRA) [1] and the European Space Agency (ESA) [2] co-organise since 2016 an annual Summer School on gravity-related research. The main objective of the Summer School is to promote gravity-related research amongst future scientists and engineers. These young minds are introduced to the benefits of performing research at different gravity levels and offered an overview of current research under microgravity and hypergravity conditions in both life and physical sciences. Over four and a half packed days they attend stimulating lectures and work within small groups to devise ideas for prospective experiments.

The Summer School takes place, every June, at the ESA Academy´s Training and Learning Facility in ESEC-Galaxia, Transinne (Belgium) and is opened to 30 Bachelor and Master students in science or engineering disciplines from ESA Member States, Canada and Slovenia not yet involved in the space sector. The trainers are ELGRA and ESA experts from across Europe, sharing their experience and know-how with the students, including their day-to-day work and research experience in biology, human physiology, and physics. The participating students and trainers (Fig. 1) are sponsored by ESA and ELGRA to cover their travel, accommodation and meals.

Figure 1: Group picture at ESA/ELGRA Gravity-Related Research Summer School, 2016

Each year, ELGRA contacts their members to offer them the opportunity to participate in the Summer School by submitting an abstract for a lecture in life or physical sciences (Fig. 2). SELGRA (the student association of ELGRA) is also supporting the Summer School by presenting their activities and offering students the opportunity to join the association.

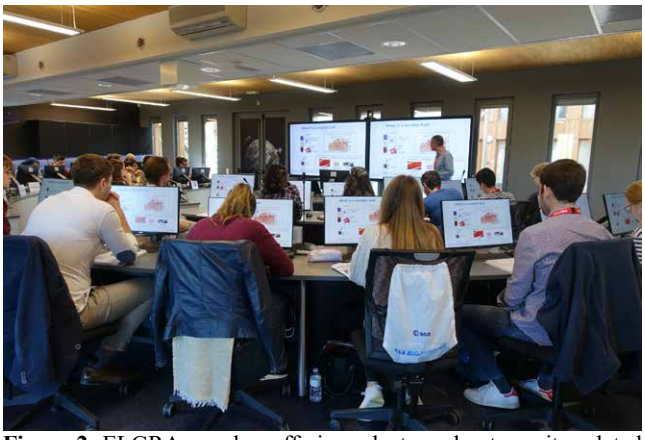

Figure 2: ELGRA member offering a lecture about gravity-related research during the ESA/ELGRA Gravity-Related Research Summer School, 2018

Summer school contents

The Summer School programme includes lectures in the following topics:

- Gravity-related research and gravity-related platforms
- Hands-on opportunities for university students
- Introduction to project management
- Gravity-related experiment development
- Experiment life cycle
- Physical sciences at different g levels
- Life sciences at different g levels
- Human physiology at different g levels

The lectures are complemented by three testimonials from university students who have designed, built, tested and performed a gravity-releated scientific experiment in the frame of ESA Academy's hands-on programmes [3].

Throughout the Summer School, the students are asked in groups of five to generate an idea for a future gravity-related experiment. They are asked to come up with a scientific or engineering objective, to choose a gravity-related platform and propose a preliminary experimental setup and procedure. Students take advantage of the continuous presence of experts to discuss their ideas. In the final day of the Summer School, as shown on Fig. 3 the student groups get the opportunity to present their projects and are evaluated by experts from ELGRA and ESA.

Figure 3: Student group presenting their project to ESA and ELGRA experts during the ESA/ELGRA Gravity-Related Research Summer School, 2017

Aside from the lectures and group project, students have the opportunity to visit ESEC-Redu [4] and the Euro Space Center [5].

At the end of the Summer School the students are presented with a certificate of participation and a course transcript including their evaluation to allow them to claim ECTS credit(s) for their participation to their respective universities.

Conclusions

The summer school aims at complementing what future scientists and engineers learn at university, inspire them and attract them into the space sector and its multiple research opportunities. Feedback from the participating students and trainers is very positive. Proposed improvements are taken into account by ELGRA and ESA for each rendition to improve the quality of the Summer School.

Acknowledgements

ESA and ELGRA would like to thank trainers who supported the four editions of the Summer School and shared their knowledge and enthusiasm with the university students.

References

[1] www.elgra.org
[2] www.esa.int
[3] N. Callens, L. Ha and P. Galeone, Benefits of ESA Gravity-Related Hands-on Programmes for University Students' Careers", Microgravity Science and Technology, Volume 28, Issue 5, 2016, pp 519–527
[4] www.esa.int/About_Us/Welcome_to_ESA/ESEC
[5] www.eurospacecenter.be

Oral 186

Heat Loss Analysis for Accurate Evaluation of Fluid Conditions at Test Section in Flow Boiling Experiments onboard International Space Station

Koichi Inoue[1], Haruhiko Ohta[2], Hitoshi Asano[3], Osamu Kawanami[4], Ryoji Imai[5], Koichi Suzuki[6], Yasuhisa Shinmoto[2], Yuuki Toyoshima[7], Satoshi Matsumoto[8]

[1]The University of Kitakyushu, Kitakyushu, Japan, [2]Kyushu University, Fukuoka, Japan, [3]Kobe University, Kobe, Japan, [4]University of Hyogo, Himeji, Japan, [5]Muroran Institute of Technology, Muroran, Japan, [6]Tokyo University of Science, Noda, Japan, [7]Japan Manned Space Systems Corporation, Tsukuba, Japan, [8]Japan Aerospace Exploration Agency, Tsukuba, Japan
inoue-k@kitakyu-u.ac.jp

Introduction

Boiling and two-phase flow thermal systems have a great potential for realizing high-efficiency heat exchange and heat transportation in future space systems. Boiling and two-phase flow phenomena can change with gravity level and therefore reliable fluid flow and heat transfer data under microgravity are essential for the thermal design of the space systems. Systematic flow boiling experiments have been carried out in the International Space Station (ISS) as a JAXA project named "TPF (Two-Phase Flow)" experiment. The detailed information on TPF experiment was reported by Ohta, et al. (2016).

For the precise analysis of the gravity effects, accurate evaluation of fluid conditions at the heating test section are quite important and the development of thermal models of heat loss from test fluid to the ambient is needed. In this paper, the heat loss characteristics of the TPF flight model (FM) in ISS are reported.

Experimental apparatus

A schematic diagram of test loop is shown in Fig. 1. The test loop consists of a circulating gear pump, a preheater, heating test sections, adiabatic observation sections, a condenser, accumulators, which are packed with auxiliary systems for power supply, data acquisition and image recording into the TPF FM with a size of 670mm × 810mm × 510mm. The TPF FM is mounted in the multi-purpose small payload rack (MSPR) in the Japanese experimental module "KIBO". Electric power, cooling water, avionics air, etc. are supplied from MSPR to TPF FM. Because the test loop is densely packed and avionics air passes through the inside of TPF FM for preventing local excessive temperature rise, the heat loss paths from the test loop to the ambient are very complicated and unknown.

The test fluid selected is perfluoro-hexane for the reduction of power supply and tube size. Subcooled test fluid is pumped into the preheater. The liquid subcooling or vapor quality at the inlet of the heating test sections is adjusted by the preheater. The system pressure is maintained at almost atmospheric pressure by the operation of mechanical accumulators.

The test loop has two heating test sections of a copper heating tube and a transparent glass heating tube. These two heating tubes are connected in parallel with valves and test fluid flows through either of heating tubes according to the experimental objects. In the present report, the heat loss from the test loop is analyzed for the copper heating tube. The copper heating tube has an inner diameter of 4.0mm and a heated length of 368mm. Electric heater and ten K-type thermocouples are attached to the copper heating tube. The copper heating tube is installed between stainless steel brackets and is covered by thermal insulation materials.

The preheater consists of a copper tube with outer diameter of 3/8inch, a thickness of 1mm and a length of approx. 1.6m. The preheater is operated by electric heaters and covered by thermal insulation materials.

Heat loss model development

For the accurate evaluation of fluid conditions at the test section of a copper heating tube, two heat loss models for $\dot{Q}_{loss,012}$, $\dot{Q}_{loss,345}$ are considered as shown in Fig. 2. To develop the heat loss models, preliminary experiments for single-phase liquid flow were performed. Test fluid was heated below the saturation temperature by the preheater and was introduced to the heating test section. When the test fluid is not heated at the copper heating tube, the heat loss $\dot{Q}_{loss,012}$, $\dot{Q}_{loss,345}$ can be calculated as

$$\dot{Q}_{loss,012} = \dot{Q}_{PH} - \dot{Q}_{f012} \quad (1)$$

$$\dot{Q}_{loss,345} = \dot{Q}_{f,345} \quad (2)$$

$$\dot{Q}_{f,012} = \dot{m}(h_2 - h_1) \quad (3)$$

$$\dot{Q}_{f,345} = \dot{m}(h_3 - h_2) \quad (4)$$

where $\dot{m}$ is mass flow rate of test fluid. $\dot{Q}_{PH}$ is power generation of the preheater. h_1, h_2, h_3 are liquid enthalpy estimated from T_1, T_2, T_3 as shown in Fig. 2.

$\dot{Q}_{loss,012}$ is well correlated by the temperature difference between the surface temperature of preheater $T_{PH,s}$ and avionics temperature T_{avio}, ($T_{PH,s}$ - T_{avio}), and is independent

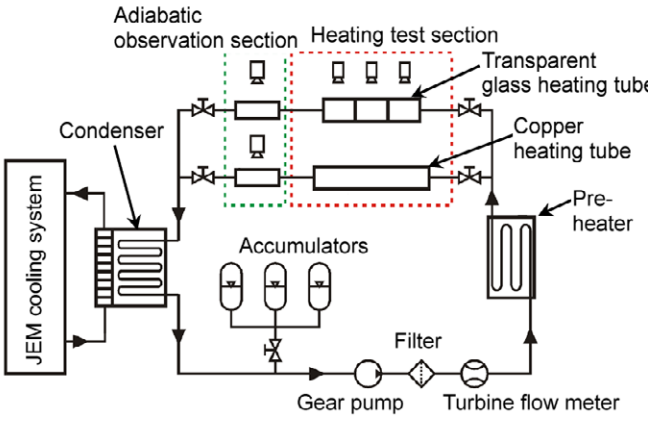

Figure 1: Flow boiling test loop for TPF experiment

of mass velocity G. Hence, it is conjectured that $\dot{Q}_{loss,012}$ can be estimated by Fig. 3 even for the case of liquid-vapor two-phase flow.

Figure 4 shows the relation between the heat loss $\dot{Q}_{loss,345}$ and the logarithmic mean temperature difference $\Delta T_{lm,345}$. $\Delta T_{lm,345}$ is calculated as

$$\Delta T_{lm,345} = \frac{T_2 - T_3}{ln\frac{T_2 - T_{avio}}{T_3 - T_{avio}}} \qquad (5)$$

$\dot{Q}_{loss,345}$ can be correlated by $\Delta T_{lm,345}$ and G. To develop the heat loss model for $\dot{Q}_{loss,345}$, four thermal resistance in series is considered.

$$R_{total} = R_1 + Y_1 + Y_2 + X \qquad (6)$$

where R is thermal resistance for convection heat transfer at the inner tube wall. Y_1 and Y_2 are thermal resistance for conduction in the copper tube wall and thermal insulation, respectively. X is surface radiation and convection resistance at the outer surface of thermal insulation. The value (X+Y_2) is influenced by the installation conditions in the rack to which the avionics air is introduced. Figure 5 shows the evaluation of (X+Y_2) by single-phase liquid flow experiments at higher mass velocity (G=300, 600 kg/m^{2}s). The value (X+Y_2) is regarded as almost constant.

Conclusions

Heat loss models of FM for ISS experiment have been developed to evaluate fluid condition at the copper heating test section. The improvement of the model at the heating test section will be performed to evaluate local heat transfer coefficients with high accuracy.

Acknowledgements

The authors would like to thank Mr. Ukena, Mr. Fujii, Ms. Semba, Mr. Miyawaki, Mr. Nakase, Mr. Inoue for their support in TPF experiment. The authors also thank JSF for the support of TPF project and IHI aerospace for the fabrication of the experimental apparatus.

References

H. Ohta, et al., Development of Boiling and Two-Phase Flow Experiments on Board ISS, Int. J. of Microgravity Science and Application, 33(1) (2016) paper No. 330102 to 330107.

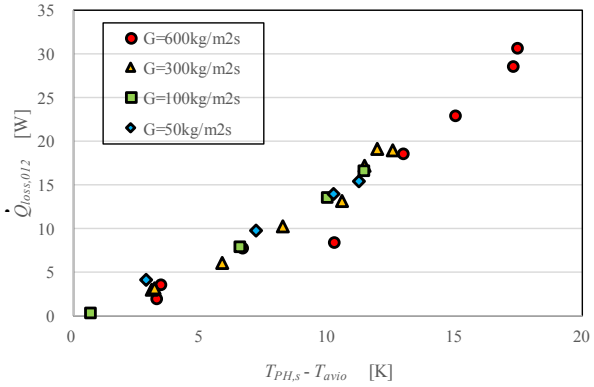

Figure 3: Heat loss $\dot{Q}_{loss,012}$

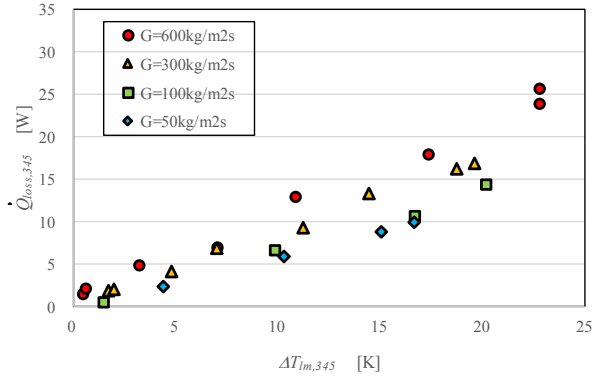

Figure 4: Heat loss $\dot{Q}_{loss,345}$

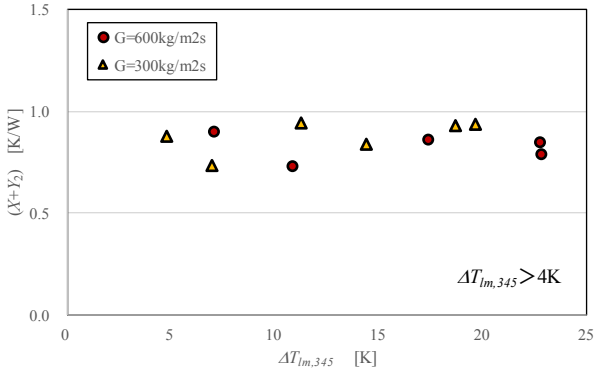

Figure 5: Thermal resistance of insulation materials for $\dot{Q}_{loss,345}$

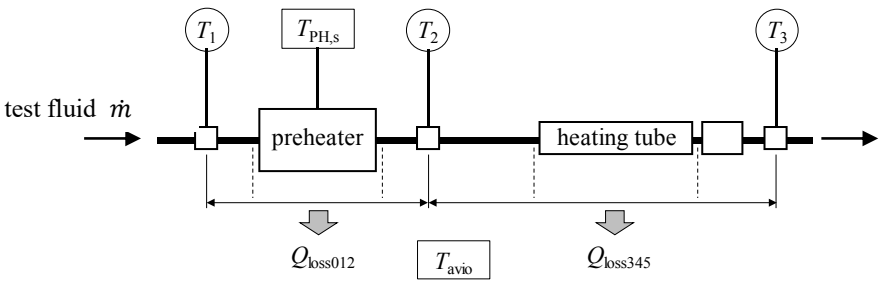

Figure 2: Heat loss models between preheater and copper heating test section

Oral 189

Heat transfer in the drop during evaporation

V. V. Cheverda[1,2], T. G. Ponomarenko[1,2]

[1]Kutateladze Institute of Thermophysics SB RAS, Novosibirsk, 630090, Russia, [2]Novosibirsk State University, Novosibirsk, 630090, Russia,

Introduction

The silicon-based technology gains in performance become less expensive to produce, are more plentiful and capable. With increasing transistor density of processors, heat dissipations from processors is increasing. In particularly for space applications - electronic cooling devices becomes are very important for successful space missions.

The thickness of liquid in this region with the width of about several microns, often called the microregion, decreases from 1–3 μm to 10–20 nm, i.e., to the thickness of the adsorbed film. Theoretical and experimental studies confirm that the heat flux in this microregion contact line region can be more than an order of magnitude higher than the average one (about 1 kW/cm2). Now it is impossible to measure directly the heat flux density in the microregion, so various indirect methods and numerical procedures are using. It was found that the local heat flux density in the contact line region is about 5 times higher than the average heat flux density on the surface for a meniscus of HFE7100 liquid, evaporating between two vertical heated plates of metal foil [Ibrahem et al., 2010]. The spray cooling system is one of the most promising solution for heat transfer problem and this requires a deeper study of the physics of heat transfer for drop evaporation. [Pautsch and Shedd, 2006; Roisman et al., 2007].

To estimate the heat flux density near the contact line more precisely, the statement of Cauchy problem for an elliptic equation (stationary heat conductivity) was formulated. The temperature distribution on the foil underside is measured by IR scanner, the sidewalls were assumed adiabatic and electrical power is measured by power supply. The Cauchy problem for the Laplace equation of the general form is one of the famous ill-posed problems and its solution is unstable. Instability of solution to the Cauchy problem becomes obvious at implementation of any numerical method for solving it. In this work, we used the method that reduces the Cauchy problem solution to the solution of the moment problem [Karchevsky et al., 2016].

Experimental setup

The experimental setup is demonstrated in Fig. 1. A metallic foil (constantan - CuNi) with the thickness of 25 μm and size of 88x35 mm^2 was used as a substrate. The electrical power of heat release in experiments was from 0.25 to 2.5 W. The photo of a droplet profile was taken using an optical shadow system with resolution of 8 μm/pixel.. The temperature distribution on the lower surface of foil was measured by a Titanium 570M IR-scanner. To increase the minimal solvable temperature difference when using the IR-camera, the backside of foil was covered with a layer of black paint. The wettability by water of foil surface is measured by Kruss DSA-100 and equal for advancing contact angle 109° and receding contact angle 21°, so hysteresis is about 88° measured by the sessile drop method (Fig. 2). The glass syringe (1 ml) is used to impact liquid drop on the foil surface.

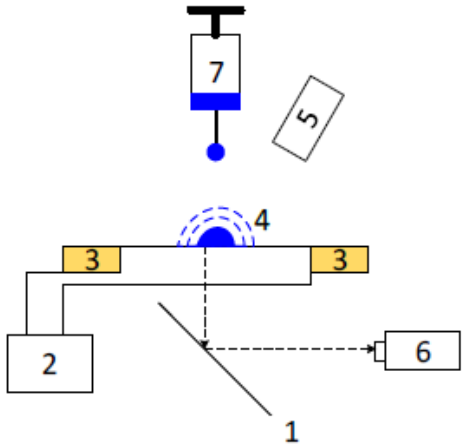

Figure 1: The scheme of experiment: 1 - mirror with gold deposition, 2 - power source, 3 - brass electrodes, 4 – liquid drop, 5 - video camera, 6 - IR-scanner, 7 – syringe with liquid.

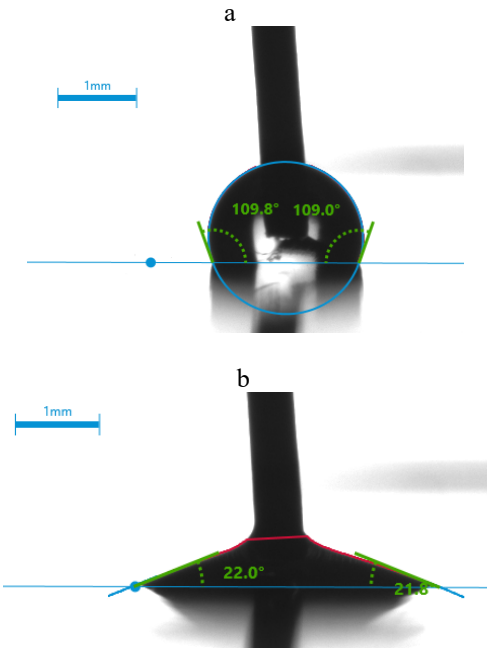

Figure 2: Determination of the contact angle of wetting of water using sessile drop method by Kruss DSA-100 (advanced-a and receding-b).

Experimental results

The proposed mathematical method for solving the Cauchy problem will be used to solve non-stationary heattransfer distribution in constantan foil during drop

evaporation. The temperature distribution measured with the help of an IR-scanner versus time (Fig. 3) and diameter of the water drop (Fig. 4) are demonstrated below.

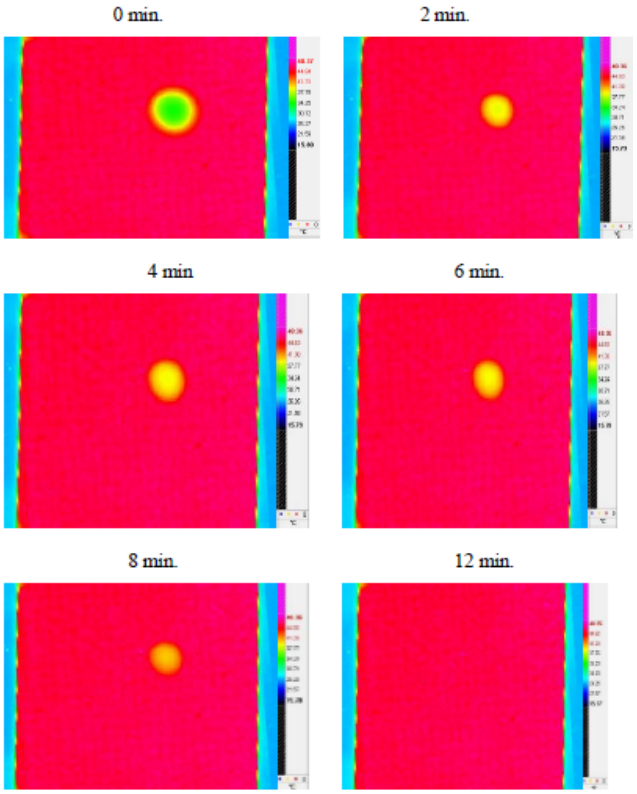

Figure 3: Thermal images of water drop 0.5 ml, qS = 489.56 W/m2.

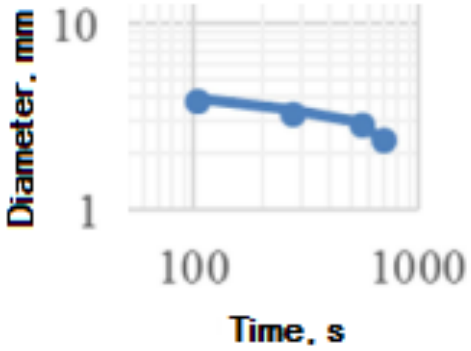

Figure 4: Diameter versus time for water drop.

Conclusions

In the present paper heat transfer in a sessile liquid drop on the heated constantan foil has been studied experimentally. These data will be used to find heat flux distribution in the contact line of the studied drop during evaporation process.

Acknowledgements

The experiments were carried out with financial support by the Russian Science Foundation grant (Agreement No. 18-19-00538)

References

K. Ibrahem, M.F.A. Rabbo, T.G. Roisman, and P. Stephan, Experimental investigation of evaporative heat trans-fer characteristics at the 3-phase contact line, Experimental Thermal and Fluid Sci. 34 (2010) 1036–1041

A.L. Karchevsky, I.V. Marchuk, and O.A. Kabov, Calculation of the heat flux near the liquid-gas-solid contact line, Appl. Math. Modelling 40 (2) (2016) 1029–1037.

A.G. Pautsch, T.A. Shedd, Adiabatic and diabatic measurements of the liquid film thickness during spray cooling with FC-72, International Journal of Heat and Mass Transfer 49 (2006) 2610– 2618.

I. V. Roisman, T. Gambaryan-Roisman, O. Kyriopoulos, P. Stephan and C. Tropea, Breakup and atomization of a stretching crown, Physical Review E 76 (2) (2007) 26302-1 - 26302-9.


POSTERS

Poster 009

The Soret effect in ternary mixtures of water+ethanol+triethylene glycol: Ground and microgravity experiments

M. Schraml[1], T. Triller[1], D. Sommermann[1], F. Sommer[1], E. Lapeira[2], M.M. Bou-Ali[2], and W. Köhler[1*]

[1]Institute of Physics, University of Bayreuth, Bayreuth, Germany,
[2] Mechanical and Manufacturing Department, MGEP Mondragon Goi Eskola Politeknikoa, Mondragon, Spain;
*werner.koehler@uni-bayreuth.de

Introduction

Diffusive flows in a non-isothermal multicomponent fluid are characterized by complex cross-coupling phenomena between all concentration and temperature gradients. Beside the well known Fickian diffusion, a mass flux due to a concentration gradient, there is another contribution to the total mass flux, the so-called Soret effect or thermodiffusion. Since the number of unknown coefficients increases quadratically with the number of components, such multicomponent systems quickly become intractable, and today's research focuses mainly on ternary mixtures as multicomponent model systems.
Within the ESA/Roscosmos DCMIX program, measurements are performed under microgravity conditions aboard the International Space Station ISS to generate a benchmark system as a comparision to ground-based laboratory experiments.

DCMIX3 program

On the poster we will discuss the results of a sample with a symmetric composition of the DCMIX3 program, which consists of a mixtures of water, ethanol and triethylene glycol. We are going to compare ground measurements with the data one obtained by the ISS experiments. Furthermore, we will have a look on the ongoing evaluation and measuremts.

Experiments in the laboratory

In order to resolve all components, optical multicolor beam deflection (OBD) and the thermogravitational column technique (TGC) are employed. Optical beam deflection uses a Soret cell which is filled with the sample. Between the upper and lower side of the cell a temperature gradient is applied. The Soret effect causes a demixing of the fluid and, depending of the refractive indices of the pure components, a refractive index gradient. A laser beam orthogonal to the gradient gets deflected. The most critical step in the data analysis is the transformation from the multicolor refractive index space to the compositions, for which the so-called contrast factor matrix must be inverted. Since this matrix is frequently ill-conditioned, extremely precise measurements of the partial derivatives of the refractive index with respect to the composition variables and the temperature are required.
In the thermogravitational column setup the sample is placed between two vertical walls with different temperatures. In comparison to the OBD, the temperature gradient is perpendicular to the gravitational force. The arising concentration gradient leads to convective flows due to differences in the densities of the components, which amplifies the seperation. After the stationary state is reached, one takes different samples at different hights of the column and measures the refractive index and density, respectively.

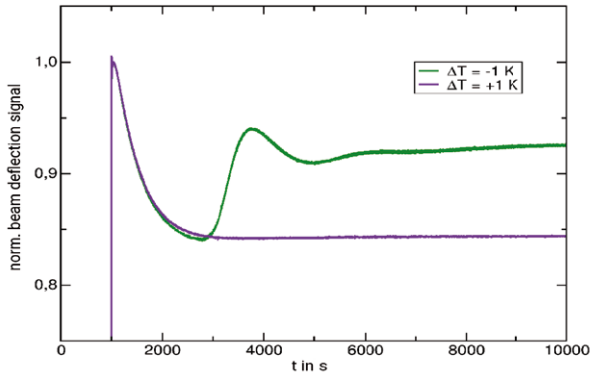

Figure 1: Normalized 2-OBD transients of the red laser (635 nm). $\Delta T = -1$ K heated from below, $\Delta T = +1$ K heated from above. Mean temperature 298 K.

Microgravity experiments aboard the ISS

Depending on the sign of the Soret coefficient and the densities of the components, the demixing due to the Soret effect can cause convective instabilities which inhibit evaluable OBD signals on ground as seen in Fig. 1.
On the ISS different samples were measured in four different campains (up to now) to create a benchmark system. The experiments take place in the microgravity science glove box (MSG) in the Columbus module. It contains, inter alia, the selectable optical diagnostics instrument (SODI) which is a setup of two Mach-Zehnder interferometers, one single-color and one two-color. The first one has one fixed sample cell containing a binary reference sample, the second one has a movable cell array with 5 ternary mixtures.

Conclusions

All in all the three different experiments agree. In particular, they yield the same sign of the thermodiffusion coefficients and Soret coefficients, respectively.
For an ill-conditioned contrast factor matrix the transformation from the refractive index to the concentration space leads to a deformation of a symmetric circle of uncertainty to a streched ellipse. This results in a rather high uncertainty of the Soret and thermodiffusion coefficient for two of the components but also in a significantly lower one for the thrid component.

Acknowledgements

We thank ESA and Roscosmos for providing the flight and operations opportunity in the framework of the DCMIX project (AO-2009-0858/1056).
The group in Bayreuth was supported by Deutsches Zentrum für Luft- und Raumfahrt (DLR) (50WM1544).
The Mondragon group acknowledges the support of the FETRAFLU (2018-CIEN-000101-01) from Gipuzkoa Program for Science, AT-NEMFLU (ESP2017-83544-C3-1-P) of the MINECO, and the Research Group Program (IT1009-16) from the Basque Government.

References

T. Triller, D. Sommermann, M. Schraml, F. Sommer, E. Lapeira, M.M. Bou-Ali, and W. Köhler, The Soret effect in ternary mixtures of water+ethanol+triethylene glycol of equal mass fractions: Ground and microgravity experiments, *Eur. Phys. J. E* (2019) 42: 27

Poster 017

The Electromagnetic Levitator (ISS-EML) on the International Space Station – Precise measurement of thermophysical properties of the titanium alloy Ti-Al6-V4 (Ti64)

M. Mohr[1], Y. Dong[1], R. K. Wunderlich[1], H.-J. Fecht[1]

[1]Institute of Functional Nanosystems, Ulm University, Ulm, Germany
markus.mohr@uni-ulm.de, yue.dong@uni-ulm.de, rainer.wunderlich@uni-ulm.de, hans.fecht@uni-ulm.de

Introduction

Titanium alloys generally exhibit high strength and toughness within a large temperature range. Combined with their high corrosion resistance and low density, titanium alloys are important in many fields of application. From applications in light-weight construction over high-temperature applications in turbine blades, to biomedical implants.

One of the most applied titanium alloys is the alpha-beta titanium alloy called Ti64 (Ti-6Al-4V), which has a good biocompatibility and good strength to weight ratio.

Fabrication of parts from Ti64 materials are typically performed by melting and casting, or by laser aided additive manufacturing methods. In both cases, the material is solidified from the liquid phase. Process optimizations rely on the simulation of the cooling and solidification process of the melt. Thermophysical properties, related to thermal and mass transport are necessary input parameters for such simulations. The measurement of Ti-alloys in the liquid phase is challenging or impossible. Classical thermoanalytical equipment, are container-based methods that suffer from the inevitable contact of the material with the container wall.

Containerless methods will enable the contact less measurement of thermophysical properties, which can efficiently prevent contaminations and parasitic container-wall reactions that could e.g. obscure measurements of the specific heat.

One approach is containerless processing during electromagnetic levitation of the sample. The method can principally be implemented on ground, however, the strong force necessary to lift the sample in 1g-conditions will lead to sample deformations and turbulent flows inside the droplet. Especially for samples with relatively low melting point, the eddy currents produced by the strong positioning field can already melt the sample which makes it impossible to reach the undercooled liquid range.

For most measurement methods it is important to have control over the fluid flow in the droplet and to be able to obtain a spherical sample. Hence the gravitational force has to be diminished.

Results and Discussion

We measured thermophysical properties of the Titanium alloy Ti64 (sample #12, Batch-1) on board the international space station (ISS) using the electromagnetic levitator (ISS-EML) in the European science module 'Columbus'.

We measured surface tension, viscosity, density, specific heat capacity and electrical resistivity of the sample as a function of temperature in the stable liquid phase and in the undercooled liquid phase (~200 K undercooling).

The surface tension and viscosity were measured using the oscillating drop method (Egry, Giffard, and Schneider 2005), specific heat capacity was obtained applying modulation calorimetry (Fecht and Johnson 1991; R K Wunderlich, Fecht, and Willnecker 1993; R. K. Wunderlich, Fecht, and Willnecker 1993) and the electrical resistivity was measured by the method described in Ref. (Lohöfer 2018).

The specific heat capacity will be compared with literature values from (Kaschnitz, Reiter, and McClure 2002).

Conclusions

We show the successful measurement of a number of thermophysical quantities of a Ti64 sample using the electromagnetic levitator ISS-EML.

Surface tension measurements are less prone to contaminations and the accuracy of the determined specific heat capacity can be higher than in container-based methods.

Acknowledgements

The authors acknowledge the access to the ISS-EML, which is a joint undertaking of the European Space Agency (ESA) and the DLR Space Administration. The reported work was conducted in the framework of the ESA MAP project ThermoProp (AO-099-022). We further acknowledge funding from the DLR Space Administration with funds provided by the Federal Ministry for Economic Affairs and Energy (BMWi) under Grant No. 50WM1759.

References

Egry, I., H. Giffard, and S. Schneider. 2005. "The Oscillating Drop Technique Revisited." *Measurement Science and Technology* 16:426–31.

Fecht, H. J. and W. L. Johnson. 1991. "A Conceptual Approach for Noncontact Calorimetry in Space." *Review of Scientific Instruments* 62(5):1299–1303.

Kaschnitz, E., P. Reiter, and J. L. McClure. 2002. "Thermophysical Properties of Solid and Liquid 90Ti-6Al-4V in the Temperature Range from 1400 to 2300 K Measured by Millisecond and Microsecond Pulse-Heating Techniques." *International Journal of Thermophysics* 23(1):267–75.

Lohöfer, Georg. 2018. "High-Resolution Inductive Measurement of Electrical Resistivity and Density of Electromagnetically Levitated Liquid Metal Droplets." *Review of Scientific Instruments* 89(12):124709.

Wunderlich, R. K., H.-J. Fecht, and R. Willnecker. 1993. "Power Modulation Technique for Noncontact High-temperature Calorimetry." *Applied Physics Letters* 62(24):3111–13.

Wunderlich, R K, H. J. Fecht, and R. Willnecker. 1993. "Power Modulation Technique for Noncontact High-Temperature Calorimetry." *Applied Physics Letters* 62(24):3111–13.

26th European Low Gravity Research Association Biennial Symposium and General Assembly
14th International Conference on "Two-Phase Systems for Space and Ground Applications"
European Space Agency Topical Teams meetings
Granada (Spain), September 24-27, 2019

Poster 028

Experimental Investigation of Boiling Phenomena on Microstructured Surfaces

Matthias Zimmermann[1], Axel Sielaff[1], Peter Stephan[1]
[1]Institute for Technical Thermodynamics, Technische Universität Darmstadt, Darmstadt, Germany
zimmermann@ttd.tu-darmstadt.de, sielaff@ttd.tu-darmstadt.de, pstephan@ttd.tu-darmstadt.de

Introduction

Surface modifications have been subject to extensive research in the boiling community in the last decades. Those modifications can lead to higher critical heat flux and heat transfer coefficients. The reasons for this increase are, however, still controversially discussed. Specific structure optimization or prediction of the boiling performance are not yet possible.

Experimental Setup

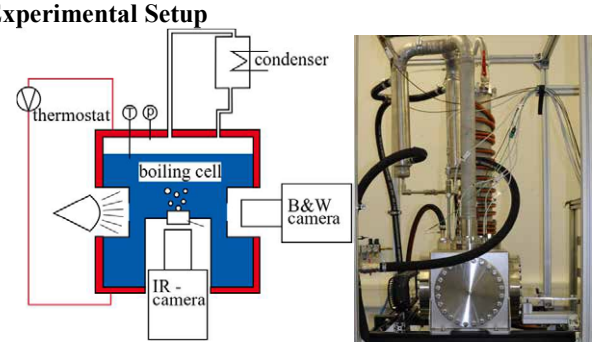

Figure 1: Schematic sketch and picture of the experimental setup.

The experimental setup (Figure 1) primarily consists of a stainless steel cube used as the boiling cell. The temperature of the cube is controlled by silicone oil flowing through the outer shell of the cube. A condenser is mounted on top of the cube. The temperature of the condenser is controlled by another silicone oil circuit. Windows inside the cube enable the observation of the boiling phenomena by a high speed B&W camera (*Mikrotron MotionBLITZ EoSens Cube 7*) and a reflex camera (*Nikon D90*). Additionally an infrared camera (FLIR X6901sc) is used to measure the local surface temperatures of the boiling surfaces. FC-72 is used as boiling fluid at various system pressures.

Microstructured surfaces

This study focuses on the boiling performance of surfaces, which are modified by copper needles. Therefore surfaces having copper needles with different length (7-20 µm) and diameters (1-2 µm) were manufactured. SEM images of one of the used surfaces are shown in Figure 2.

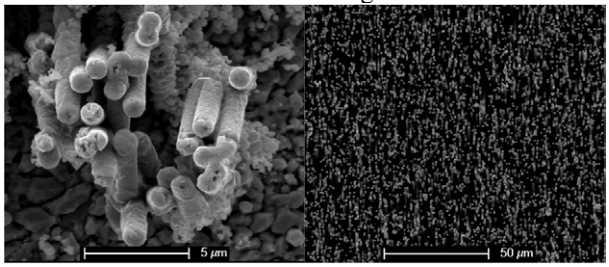

Figure 2: SEM images of a surface with copper needles.

Those surfaces were manufactured onto two different heater models. One heater consists of a copper cylinder with a PEEK insulation and a ceramic flat heater which is pressed against the bottom of the cylinder. This heater model is used to perform experiments up to critical heat flux. Furthermore the heated surface is 40 times the capillary length, therefore the boiling process is independent of the surface area and hence the boiling performance is transferable to industrial applications. [1]

The second heater model is an infrared-transparent crystal made of CaF_2. A chromium nitride and a chromium layer are sputtered on top of the crystal. A dielectric layer is applied onto the chromium layer and the copper needles are then manufactured on the dielectric layer. This heater model enables the measurement of local surface temperatures and heat fluxes. Therefore the influence of the surface structures on single and multiple bubbles is measurable.

Results and Conclusions

The results show a reduced critical heat flux at higher system pressures, compared to a smooth copper surface. The heat transfer coefficient, however, of the structured surfaces is increased. Furthermore the heat transfer coefficient of the microstructured surfaces show, contrary to the smooth surface no distinct pressure dependency, as seen in Figure 3.

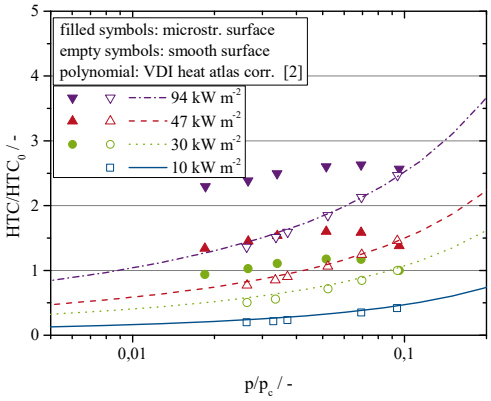

Figure 3: Comparison of the measurement results to a state of the art correlation [2].

Figure 3 shows the measured heat transfer coeffcients in relation to a reference heat transfer coefficient at $p/p_c = 0.1$ and a heat flux of 30 kWm^{-2}. The results for the smooth surface fit the correlation well. The heat transfer coefficients of the microstructured surface show a different behavior for various reduced pressures.

The used needle length does not have a significant influence on the heat transfer coefficient; however, the critical heat flux decreases with shorter neeldes. The enhanced heat transfer coefficient of the microstructured surfaces could be due to capillary flows into the needle array. The reason for the lower critical heat flux are probably vapour films, induced by the microneedles hindering the vapour bubbles from leaving the surface.

Acknowledgements
We kindly acknowledge the financial support by the German Research Foundation (DFG) within the Collaborative Research Centre 1194 "Interaction between Transport and Wetting Processes", Project C02

References

[1] R. Ray, J. Kim, Heater Size and Gravity Based Pool Boiling Regime Map: Transition Criteria Between Buoyancy and Surface Tension Dominated Boiling, *J. of Heat Transfer* 132 (2010) 091503
[2] VDI Heat Atlas, 2nd ed. Berlin, Heidelberg: Springer, 2010

26th European Low Gravity Research Association Biennial Symposium and General Assembly
14th International Conference on "Two-Phase Systems for Space and Ground Applications"
European Space Agency Topical Teams meetings
Granada (Spain), September 24-27, 2019

Poster 031

Measurements of diffusion coefficients of ethanol in supercritical carbon dioxide

Y. Gaponenko, J.C. Legros, V. Shevtsova

Microgravity Research Center, Université Libre de Bruxelles,Belgium;
ygaponen@ulb.ac.be, vshev@ulb.ac.be

Introduction

Carbon dioxide (CO2) is ubiquitous, inexpensive and less toxic than most other chemicals that are part of industrial processes. It can diffuse through some solids like a gas and dissolve some materials like a liquid. Its critical temperature Tc = 304.13 K is close to that of the ambient and its critical pressure pc = 7.38MPa is not too harsh so that its strongly varying density, together with other of its thermophysical properties, can often be conveniently tuned.

The use of supercritical carbon dioxide in extraction and fractionation processes is advantageous against traditional techniques. Because ethanol is used as a cosolvent with supercritical CO2 to obtain high content of extracted substance, the transport properties of CO2 + ethanol under high pressure are of particular interest for medical, food and other industries. However, especially the diffusion coefficients are among the least-well studied thermophysical properties of these systems.

We present results of experimental measurements of ethanol diffusion in CO2 in supercritical conditions where pressure and temperature of carbon dioxide are close to Widom line, where density changes rapidly with variation one of system parameters.

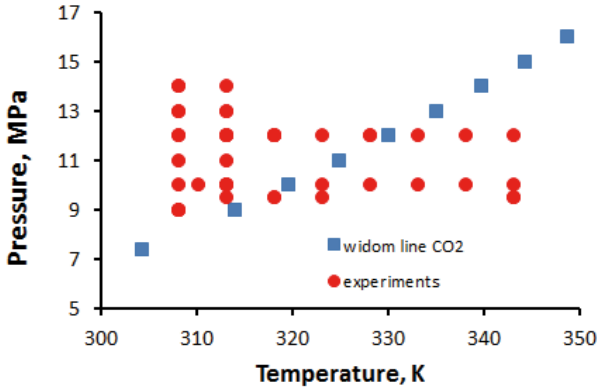

Figure 1: Experimental points and widom line of CO2.

Experimental methods

Taylor dispersion, also known as peak broadening technique, has been used for the measurement of diffusion coefficients. It builds on the diffusive spreading of a small volume of a solution injected into a laminar stream of a carrier fluid. Axial dispersion, mainly resulting from the parabolic flow profile, spreads out the solute pulse longitudinally, while radial diffusion confines the pulse. The combined effects of convective flow and molecular diffusion yield a Gaussian distribution once the mixture has flowed for a sufficient amount of time through a long capillary of uniform diameter. The shape of this distribution at the end of the capillary, known as Taylor peak, is monitored by a detector. Instead of the usual differential refractometer, a FT-IR spectrophotometer was employed in this work. This setup was designed and developed by Prof. Legros. The detail of experimental setup one may found in the papers by Ancherbak et al., 2016 and Guevara-Carrion et al., 2019.

Results

For the experiments a wide range of pressure and temperatures have been considered. Fig. 1 demonstrates p-T diagram with Widom line of CO2 together with the points where the experiments have been performed. A sample of the experimental results is shown in Fig.2 (top) as a signal of an FT-IR spectrophotometer (Jasco FT-IR 4100) where the absorbance changes with time. The diffusion coeffcients are obtained by fitting the response curve to the theoretical solution. Fig. 2 (bottom) presents a result of fitting processing.

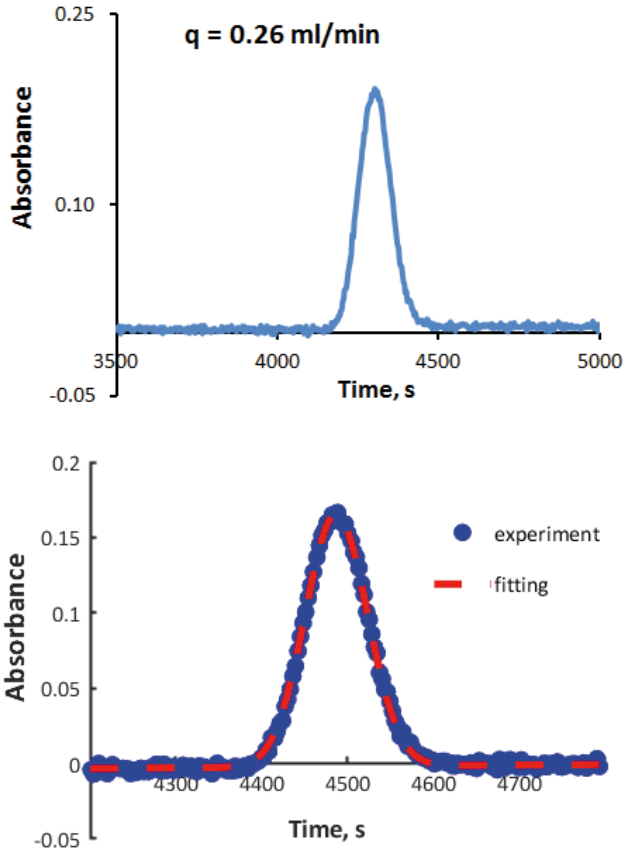

Figure 2: Experimental signal of absorbtion with time for p=12MPa and T = 318.15 K (top) and result of fitting processing (bottom).

Conclusions

We have performed an extensive experimental study of ethanol diffusion in carbon dioxide in supercritical conditions. The diffusion coefficients have been defined for different parameters near the Widom line of CO2. Two scenario of dependence the ethanol diffusion coefficients on density for liquid-like and gas like state of supercritical carbon dioxide was found.

Acknowledgements

This work is supported by the PRODEX programme of the Belgian Federal Science Policy Office, ESA.

References

S. Ancherbak, C. Santos, J.-C. Legros, A. Mialdun, and V. Shevtsova, Development of a high-pressure set-up for measurements of binary diffusion coefficients in supercritical carbon dioxide, Eur. Phys. J. E **39** (2016) 111

G. Guevara-Carrion, S. Ancherbak, A.Mialdun, J. Vrabec, V.Shevtsova, Diffusion of methane in supercritical carbon dioxide across the Widom line, submitted to Scientific Reports, 2019

26th European Low Gravity Research Association Biennial Symposium and General Assembly
14th International Conference on "Two-Phase Systems for Space and Ground Applications"
European Space Agency Topical Teams meetings
Granada (Spain), September 24-27, 2019

Poster 033

Influence of fluid flow on the evaporation of a sessile drop

Mebrouk Aitsaada[1a], Chafea Bouchenna[1b], Salah Chikh[1c], Lounès Tadrist[2d]

[1]USTHB, Faculty of Mechanical and Process Engineering, LTPMP, Alger 16111, Algeria
[2]Aix-Marseille Université, CNRS, Laboratoire IUSTI, UMR 7343, Marseille 13453, France
[a]m_aitsaada@yahoo.fr, [b]bouchennachafea@hotmail.fr, [c]salahchikh@yahoo.fr, [d]lounes.tadrist@univ-amu.fr

Introduction

Sessile drop evaporation is a process which has extensive applications such as spray cooling, thin film coating, inkjet printing, DNA stretching and deposition and surface patterning. It is a complex physical problem which involves fluid flow, heat and mass transfer as well as interactions between solid, liquid and gas phases (Bouchenna et al., 2017).

Sessile drop evaporation has been addressed for a long time by means of mass diffusion models generally valid in the case of evaporation at ambient temperature. However, it is shown theoretically that the evaporation flux is non-uniform along the liquid-gas interface when the contact line (CL) is pinned. This can induce radial outflow from the drop apex to the CL (Gelderblom et al., 2012). This liquid motion associated with evaporation–governs particle deposition at the periphery of colloidal drops usually called coffee-ring stain effect (Deegan et al., 2000). Furthermore, the non-uniform distribution of the evaporation flux on the drop surface generates a temperature gradient that can give rise to a thermo-capillary flow in the liquid. Ristenpart et al. (2007) showed analytically that the thermal conductivity ratio (substrate/droplet) controls the direction of the internal Marangoni flow. Temperature difference between the base and drop surface can in turn create buoyancy-induced flow (Barmi and Meinhart, 2014). Thermo-capillary effect may induce significant convective transport of heat and vapor in the gas phase near the drop, which can alter the evaporation flux distribution at liquid-gas interface (Yang et al., 2014).

In the present work, the convective flow inside and outside an evaporating water sessile drop is investigated using a comprehensive numerical model accounting for the effects of the strong evaporation near the contact line, the thermo-capillarity, the thermal buoyancy in the liquid phase and the thermo-solute buoyancy in the surrounding air. In addition to the governing equations in each phase, appropriate conservation of mass, momentum and energy are applied locally at the liquid-gas interface and accounting forb the dependence of the saturation concentration with temperature. Heat and mass transfer at the drop surface are analyzed during the lifetime of the drop whether the two fluid phases are in motion or not. Compared to the studies in the published literature, this more detailed analysis is based jointly on two main parameters: the wall temperature (T_w) and the thermal conductivity (k_s) of the substrate.

Numerical Model

We consider a small water drop which evaporates on a heated or unheated substrate, which may have a good thermal conductivity or not. The surrounding air is at ambient temperature T_∞= 25°C and relative humidity Ha = 40%. The lower face of the substrate is maintained at a temperature $T_w \geq T_\infty$. The drop evaporation is assumed to occur with pinned contact line**.** Buoyancy effect is included in the model with the Boussinesq approximation. Convective flow in both liquid and gas phases is governed by the equations of conservation of mass, momentum and energy coupled with the vapor transport equation in the surrounding air and heat conduction equation in the substrate. Mass conservation, momentum and energy balance at the liquid-gas interface are expressed in dimensionless forms as follows:

i) mass conservation,

$$\left(\vec{W}_\ell - \vec{W}_I\right)\cdot\vec{n} = R_\rho\left(\vec{W}_g - \vec{W}_I\right)\cdot\vec{n} = \frac{R_{\alpha_T}\left(\Delta C/\rho_\ell\right)}{Le\,Ma}\vec{J}^*\cdot\vec{n} \quad (1)$$

$\vec{n}$ is the outward normal unit vector, $\vec{W}_I$ is the velocity of the moving interface, $\vec{W}_{\ell,g}$ is the velocity of a liquid (gas) particle, $\vec{J}^*$ is the evaporation flux, ρ_ℓ is the liquid density and ΔC is equal to ($C_v(T_w)$ - Ha $C_v(T_\infty)$) where $C_v(T)$ is the saturated vapor concentration. Different dimensionless numbers appear in Eq. (1): Marangoni number (Ma), Lewis number (Le), ratio of gas/liquid density (R_ρ), ratio of gas/liquid thermal diffusivity (R_{α_T})**.**

ii) Shear-stress balance,

$$\left[\left(\vec{n}\,\bar{\bar{\tau}}_\ell\right) - \left(\vec{n}\,\bar{\bar{\tau}}_g\right)\right]\cdot\vec{t} = \vec{\nabla}T^*\cdot\vec{t} \quad (2)$$

$\vec{t}$ is the tangential unit vector and $\bar{\bar{\tau}}$ is the dimensionless stress tensor. The RHS in Eq. (2) represents the thermo-capillary effect.

iii) Energy balance,

$$\frac{Ja}{Le}\left(\frac{\Delta C}{\rho_\ell}\right)J^* + \left(R_k^g\nabla T_g^* - \nabla T_\ell^*\right)\cdot\vec{n} = 0 \quad (3)$$

$R_k^g = k_g/k_\ell$ is the ratio of gas/liquid thermal conductivity, $Ja = h_{\ell g}/(c_{P\ell}\Delta T)$ is the Jacob number, ΔT is equal to (T_w - T_∞), $h_{\ell g}$ is the latent heat of vaporization and $c_{P\ell}$ is the liquid specific heat.

The quasi-steady state and axisymmetric governing equations with the asssociated boundary conditions and interface conditions are solved numerically by a procedure based on finite volume method. The concentration and temperature gradients at the drop surface are then used to evaluate the heat exchanges and evaporation mass rate before deducing the drop lifetime.

Results and discussion

The numerical results are obtained for an evaporating water sessile drop of 10 mm^3 initial volume. Several models are implemented namely: thediffusion model, the model with internal flow, the comprehensive model with or without TSB (Thermo-Solutal Buoyancy). Figure 1 represents distributions of evaporation mass flux on the surface of the drop deposited on Aluminum (k_s = 237 W/m K) or PTFE (k_s = 0.25 W/m K) substrate. Decreasing the substrate thermal conductivity yields a local reduction of the evaporation. Convection due to thermo-capillarity and thermo-solute buoyancy in the surrounding air may induce important heat and mass transfer enhancement at the edge of the drop. Even with fluid flow, the cooling of the drop due to evaporation depends much more on the thermal compensation provided from the substrate.

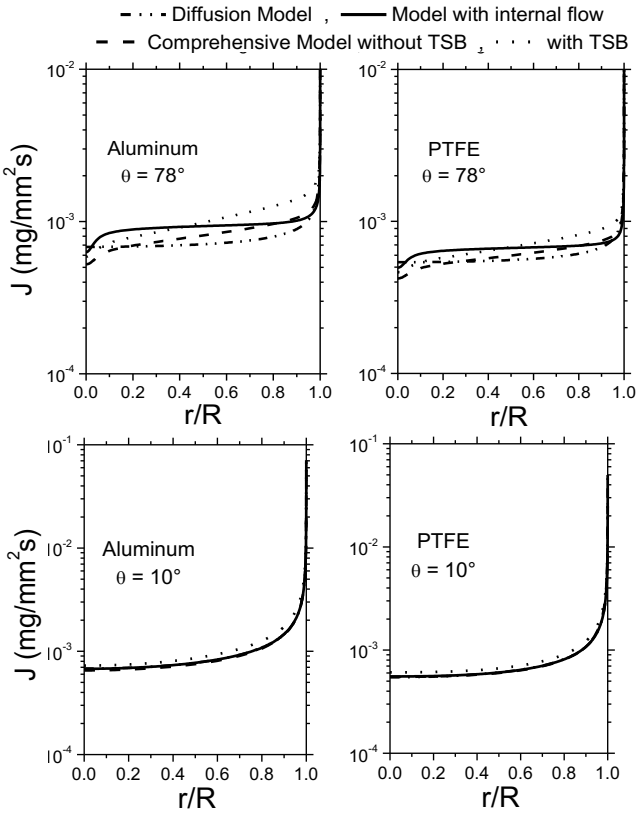

Figure 1: Distributions of evaporation mass flux on the surface of the drop deposited on Aluminum or PTFE substrate at contact angles of 78° and 10° (T_w= 50°C, TSB: Thermo-Solutal Buoyancy).

Figure 2 allows analyzing the evaporation kinetics by plotting the drop lifetime versus the substrate temperature. There is a strong decrease of the evaporation time t_0 as the wall temperatureincreases, whereas the thermal conductivity of the substrate seems to have less effect. With respect to the effect of fluid flow, it is evidenced that the comprehensive model that accounts for thermo-capillary internal convection as well as thermo-capillary and thermosolutal external convection ensures accurate estimation of the drop evaporation time. Otherwise, the use of the diffusion model or other convection models leads to overestimations of t_0 varying between 3.5% and 20%, when compared to comprehensive model in the range of wall temperature: 25-50°C and the range of substrate thermal conductivity: 0.0025-237 W/m K.

Conclusion

The evaporation rate is slightly increased by thermo-capillary convection in the liquid, whereas convection due to thermo-capillarity and thermo-solute buoyancy in the surrounding air may induce important heat and mass transfer enhancement at the drop edge. The comprehensive model of thermocapillary convection in liquid and thermocapillary-buoyancy convection in gas is the most suitable for accurate numerical simulations of the dynamic, thermal and solutal behavior of the sessile drop and its environment during evaporation under general conditions, but especially in heating conditions and on substrates of high thermal conductivities.

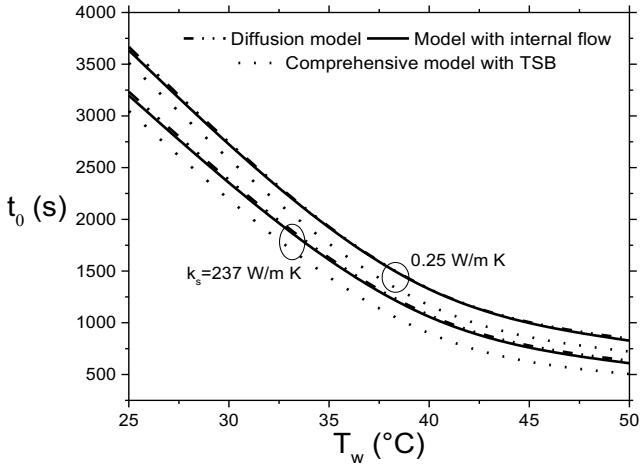

Figure 2: Drop lifetime (t_0) as a function of wall temperature for an Aluminum (k_s = 237 W/m K) or PTFE (k_s = 0.25 W/m K) substrate.

References

Bouchenna, C., Aitsaada, M. A., Chikh, S., Tadrist, L., Generalized formulation for evaporation rate and flow pattern prediction inside an evaporating pinned sessile drop. International Journal of Heat and Mass Transfer, 109, 482-500, 2017.

Gelderblom, H., Bloemen, O., and Snoeijer, J. H., Stokes flow near the contact line of an evaporating drop, *J. Fluid Mech.*, vol. 709, pp. 69–84, 2012.

Deegan,] R. D., Bakajin, O., Dupont, T. F., Huber, G., Nagel, S. R., and Witten, T. A, Contact line deposits in an evaporating drop, *Physical Review E*, 62(1):756–765, 2000.

Ristenpart, W. D., Kim, P. G., Domingues, C., Wan, J., and Stone, H. A., ''Influence of substrate conductivity on circulation reversal in evaporating drops'', *Phys. Rev. Lett.* 99 234502, (2007).

Barmi, M.R., Meinhart, C.D., Convective flows in evaporating sessile droplets, *J. Phys. Chem. B* 118 (9) 2414–2421, 2014.

Yang, K., Hong, F., Cheng, P., ''A fully coupled numerical simulation of sessile droplet evaporation using Arbitrary Lagrangian-Eulerian formulation'', *Int. J. Heat Mass Transfer* 70, 409-420, (2014)

26th European Low Gravity Research Association Biennial Symposium and General Assembly
14th International Conference on "Two-Phase Systems for Space and Ground Applications"
European Space Agency Topical Teams meetings
Granada (Spain), September 24-27, 2019

Poster 040

Effect of micro-gravity on boiling during the immersion of a water saturated porous matrix in hot oil

J. S. Lioumbas, Sotiris P. Evgenidis, Triantafyllos Tsilipiras, Margaritis Kostoglou, T. D. Karapantsios

Division of Chemical Technology, Department of Chemistry, Aristotle University of Thessaloniki, Thessaloniki, Greece;
lioumbas@gmail.com, sevgenid@chem.auth.gr, ttsilipi@auth.gr, kostoglu@chem.auth.gr, karapant@chem.auth.gr

Introduction

The effective enhancement in boiling heat transfer provided by porous-layer coatings is mainly attributed to combinations of an extended surface area effect, an increased nucleation site density effect and the bubble dynamics at the top of the layer adjacent to the liquid pool. However, up to now, no model has been proposed putting forward the above concepts in order to describe the heat transfer coefficient on such porous surfaces. In order to provide original experimental evidence to support such modeling efforts, an experiment is conceived, where a ceramic porous medium saturated with water is submerged in a hot immiscible liquid (i.e. oil) having only its top surface exposed to the oil. The hot liquid triggers boiling over and right below the surface of the porous medium. The employed heating approach circumvents the problem of non-uniform heating of the exposed porous surface which is a significant source of unsteadiness when heating porous substrates by electrical or radiation means from their bottom. As a result, the employed heating approach leads to smoother boiling operation.

The significant role of the buoyancy forces on the above phenomena has been recently reported (Lioumbas & Karapantsios, 2013; Lioumbas et al. 2014) after performing frying experiments at increased gravitational acceleration levels (i.e. from 1 to 9g). Experiments in the absence of gravitational acceleration further elucidate the role of inertia on bubble dynamics (growth, detachment, departure) during boiling in porous media.

For this reason, we designed and built a prototype carousel-type experimental apparatus (Figure 1). To simplify the geometry of the system, the porous matrix has only one surface exposed to hot oil, the others being thermally insulated. Therefore, the hot oil triggers boiling solely over the exposed porous surface. This particular experimental apparatus:

A. Allows the conduction of boiling experiments in the microgravity conditions provided during a Parabolic Flight Campaign. A flexible bellows system allows maintaining constant pressure inside the boiling chamber.
B. Permits the automated replacement of up to six different porous test specimens. A **fully automated system** (SCADA®) allows controlling the carousel type specimen disk.
C. Provides **temperature** measurements at three locations within a very distance below the porous surface (max. thickness: 1.5 mm) and **high speed video** recordings of the bubble dynamics above it.

Experiments are conducted at two different constant oil temperatures (i.e. 140 and 150 ºC). Continuous temperature measurements inside the oil and inside the porous matrix (at 0.5, 1.0 and 1.5mm below the surface), in conjunction with high speed imaging of emerging vapour bubbles over the porous surface (i.e. bubble growth rate, bubble detachment diameter, bubble detachment mode, bubble departure velocity, bubble population density), reveal the effect of gravity level on boiling phenomena over the porous matrix.

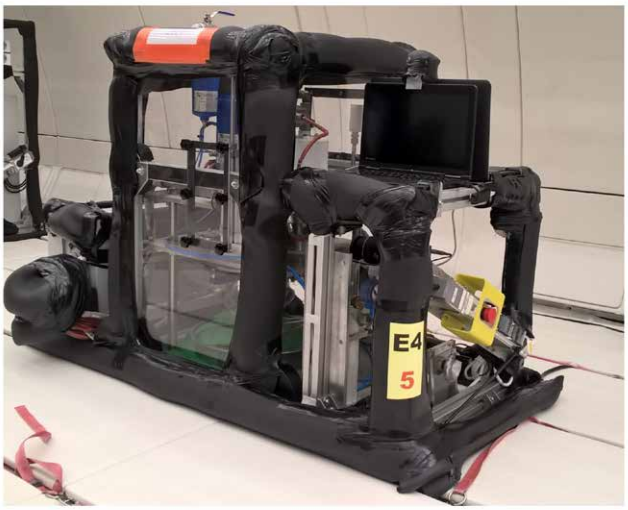

Figure 1: Device apparatus installed in plane during 66th PFC.

Results

In ***Figure 2***, images recorded during boiling over a ceramic porous material are presented for typical levels of gravitational acceleration (i.e. ~0.0, 1.0 and 1.8g/g_{earth}. From ***Figure 2*** it is apparent that:

- Bubbles are spherical for any gravitational acceleration level.
- Bubbles become smaller as the gravity level increases.
- Fewer pores are activated as the gravity level increases.
- Bubble generation and detachment continues even at microgravity conditions.

Figure 3 manifests how the frequency of bubble generation is associated with the produced total vapour volume for a wide range of gravitational accelation values (i.e. from 0.0 to 1.8 g/g_{earth}). Further analysis of the data is expected to allow the investigation on whether the theory (Di Marco, 2005) developed for vapor bubbles growth could be successfully applied in the particular case of boiling in porous media.

Conclusions

To our knowledge this is the first time that boiling in porous substrates is examined at microgravity conditions. The experimental data provide insight on the dominant physical mechanisms that control heat and mass transfer processes in boiling over porous materials. Specifically, for the first time it is seen that:

- Boiling continues regularly and systematically in porous

substrates even at microgravity conditions.
• The total volume of produced vapor is not seriously affected by gravity level.
• Bubble dynamics (size, population, generation frequency, growth) is affected by gravity level.

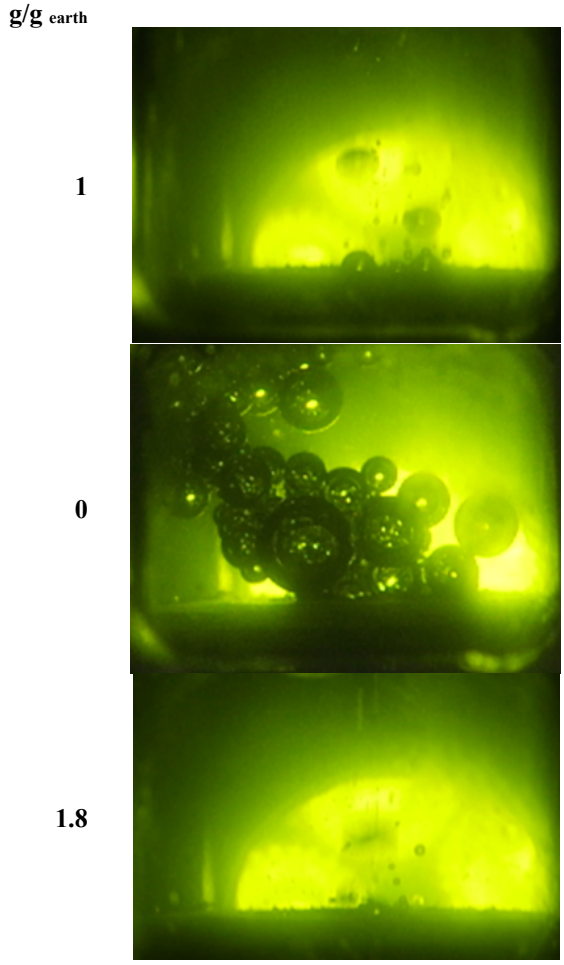

Figure 2: Typical bubble behaviour over a ceramic porous material for three different gravitational acceleration conditions.

The on-going development of predictive models and/or correlations that describe heat transfer over a broad range of gravity levels from hypergravity to microgravity conditions provide the link between the fundamental understanding of boiling, the importance of wettability and the elementary phenomena in porous media.

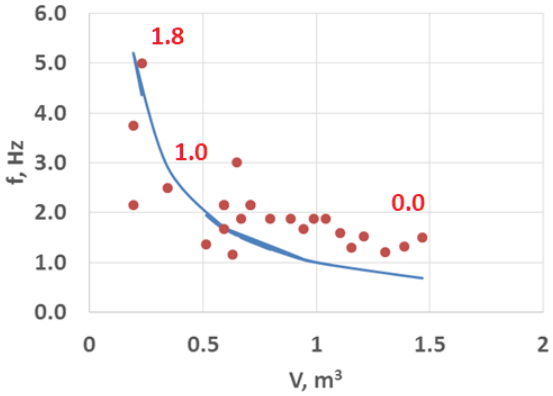

Figure 3: Bubbles frequency versus bubbles total volume for various g/g_{earth} levels (indicated with red letters on the plot, the continuous blue line represents a hyperbolic trendline).

Acknowledgements

The present activity was carried out with ESA funding (contracts: No.: 22470/09/NL/Cbi, CCN1 & BOILING: Multiscale Analysis of Boiling, No.: AO-2004-111) and under the umbrella of COST Action MP1106: 'Smart and green interfaces – from single bubbles and drops to industrial, environmental and biomedical application.

References

Di Marco, P., Birth, Life and death of gas bubbles rising in a stagnant liquid, Heat and Technology, 23, 2, 17-26 (2005).
Lioumbas, J.S., Karapantsios, T.D. Effect of increased gravitational acceleration in potato deep-fat frying. Food Research International, 55, pp. 110-118 (2014).
Lioumbas, J.S., Krause, J. & Karapantsios, T.D. "Hypergravity to explore the role of buoyancy in boiling in porous media", Microgravity Science and Technology, vol. 25, no. 1, pp. 17-25 (2013).

26th European Low Gravity Research Association Biennial Symposium and General Assembly
14th International Conference on "Two-Phase Systems for Space and Ground Applications"
European Space Agency Topical Teams meetings
Granada (Spain), September 24-27, 2019

Poster 041

Estimation of heat transfer coefficient during pre-boiling period in frying experiments at several sample orientations and gravity levels

J. S. Lioumbas[1], M. Kostoglou[1], T. D. Karapantsios[2]

[1]Division of Chemical Technology, Department of Chemistry, Aristotle University of Thessaloniki, Thessaloniki, Greece;
lioumbas@gmail.com, kostoglu@chem.auth.gr, karapant@chem.auth.gr

Introduction

The focus of this work is on the extraction of heat transfer coefficients from experimental data during the preboiling regime of potato frying by employing a specially designed device (***Figure 1***). Knowledge of these coefficients is necessary for the estimation of temperature spatial profiles at the inception of frying. In this way, not only understanding but also modelling of the frying process is facilitated. Heat transfer coefficients are estimated based on a one dimensional heat conduction model through matching theoretically predicted with experimentally measured temperature evolutions at three distinct distances below, but close to, the surface of the fried item. The tests cover a variety of experimental conditions regarding the initial oil temperature, fryer geometry, frying surface orientation, type of fried item, and level of gravitational acceleration. The dependence of heat transfer coefficients on the above experimental conditions is discussed.

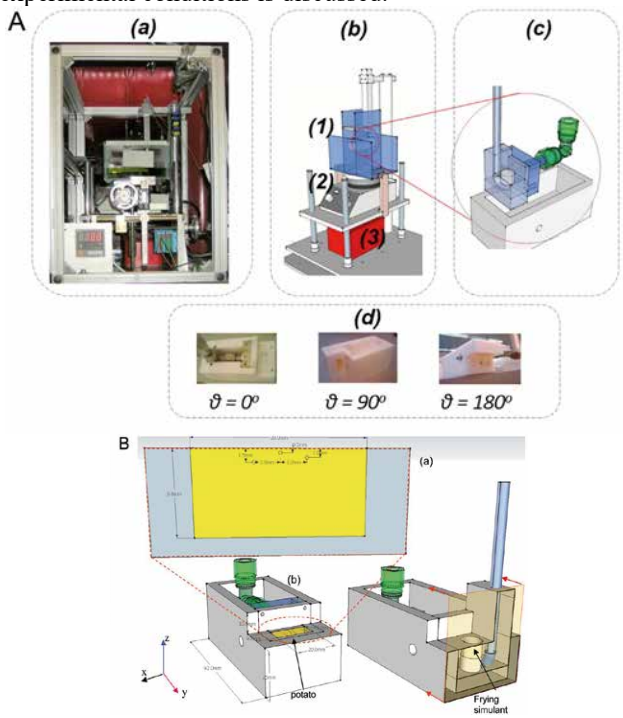

Figure 1: A. (a) Photographic description of the experimental apparatus as located inside the gondola of LDC; (b) Schematic description of the experimental apparatus basic parts: 1. Fryer, 2. Hot plate, 3. Hydraulic jack; (c) Schematic description of the frying simulant material and the insulating Teflon troughs; (d) Photographs of the double Teflon trough units at different exposed potato's surface orientation. B. (a) Thermocouples locations below exposed surface. (b) Double Teflon trough unit for a potato stick and an artificial porous sample (frying simulant). The transparent section cut allows the curved glass tube to be seen on the drawing.

Model description

Modeling of potato frying is a very demanding effort. Direct modelling based on a realistic pore morphology is out of the question. Even pore level modeling attempts are based on artificial geometrical constructions resembling the actual pore structure (Vauvre et al., 2015). The conventional approach is based on the homogenization procedure introducing a large number of effective parameters (Lioumbas and Karapantsios et al., 2012). The assessment of such a model against experiments performed under complex external heat transfer conditions is a difficult task since it requires estimation not only of frying parameters but also of parameters influenced by the external to the sample environment (e.g. oil bath).

The heat transfer coefficient, h, is calculated by Eq. (1):

$$k(T)\frac{\partial T}{\partial z} = h(T - T_{oil})$$

where T is the local temperature in the sample, T_{oil} refers to the oil temperature above the sample and k is the sample conductivity. It is noted that both h and T_{oil} are in general time depended. The initial condition for the above problem is that $T = T_0$ everywhere in the sample at $t = 0$ (T_0 is the initial sample temperature). The mathematical model quantities are related to the actual measured quantities (i.e. T and T_{oil}, temperature measurements are repeatable to a range within ±0.05°C). It is assumed that the oil experiences a high degree of mixing and so its temperatureis everywhere alike. So, T_{oil} in Eq. (1) is the experimentally measured oil temperature.

In case of a preheated sample (initial sample temperature close to the boiling one) the initial temperature profile in the potato at the inception of frying is known (e.g. Farid and Chen, 1998). However, this is not the case for in-process potato preheating where the temperature profile is developed by conduction heat transfer to the potato. The idea here is to decouple the pre-boiling conduction-dominated problem (dictated only by the external to the potato conditions) from the complex multi-parameter boiling (i.e, core frying) problem. This analysis leads to a temperature profile that can be used as initial condition for the subsequent boiling regime in a frying model. An inverse heat transfer problem (Ozisik and Orlande, 2000) is set for this purpose. The whole approach here is a typical example of the modern terminology of grey box modeling approach which is based on an appropriate combination of experimental data and theoretical analysis.

Influence of hypergravity on heat transfer coefficients

The effect of gravity level on heat transfer coefficient evolution is presented in Figure 2 for the horizontal facing up, horizontal facing down and vertical surface orientations,

respectively. In the case of the horizontal facing up orientation the variation of h versus time is qualitatively the same for all gravity levels. Nevertheless, the final steady values increase as gravity level increases but not in a linear fashion (Figure 2a). This is a confirmation of the hypothesis that heat is transferred by forced convection (at the sample level) which is induced by natural convective motion (at the oil bath level). In the case of the horizontal facing down orientation (Figure 2b), only a moderate effect is found when increasing the gravity level and this only for short times since at long times all values lie in proximity. This is compatible to the notion that at this orientation convection currents are suppressed at the bottom side of the specimen and so the global motion of oil in the bath governs chiefly heat transfer which means that only secondary convective currents and not the main rising currents in the bath affect the exposed surface. Finally, a quite different time profile of h appears in case of the vertical surface orientation (Figure 2c). Heat transfer coefficient initially increases with time and then decreases with the phenomenon being more intense as gravity level increases. The final h values are considerably larger than for other orientations and increase with gravity. Evidently, heat transfer is dominated by convection currents but the reason for the initial non-monotonic behavior is not clear and it might be attributed to the specific geometric features of the specific setup (since the same behavior is not seen in the different set-up used for terrestrial experiments).

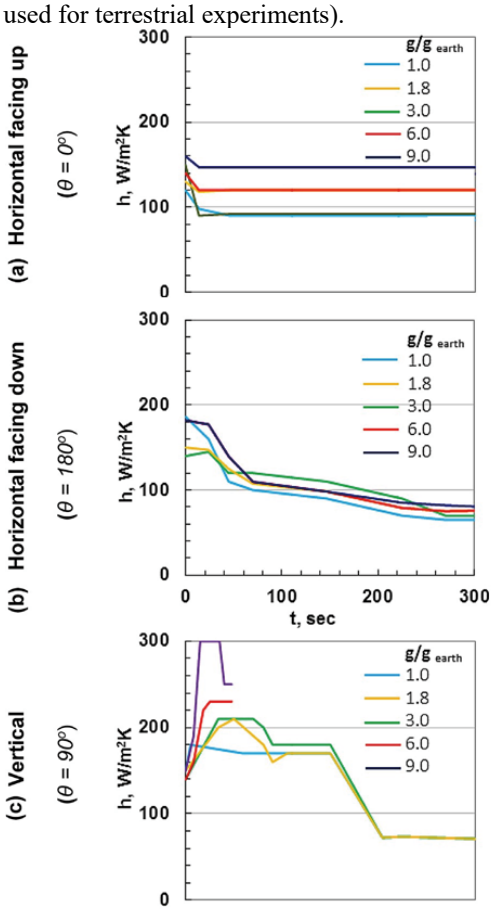

Figure 2: Dependence of the convection heat transfer coefficient, h, on various gravitational levels for all examined surface orientations: (a) horizontal facing up (θ = 0°), (b) horizontal facing down (θ = 180°); (c) vertical (θ = 90°). (Experimental conditions: T_{oil} = 150 °C; porous material = potato, oil bath = rectangular).

Conclusions

A conduction model has been employed to estimate the oil to sample heat transfer coefficients during the pre-boiling regime of frying under different experimental conditions. Among those conditions, special attention is paid to the role of the frying surface orientation and of the level of gravitational acceleration as these conditions are scarcely examined in literature despite their potential for industrial innovation. The inability to solve the oil bath heat transfer problem has led to the set up of an inverse heat transfer problem for the determination of an oil-to-sample heat transfer coefficient based on intra-sample temperature measurements. In case of a potato sample, the solution of the inverse problem allowed estimation of the heat transfer coefficient and of the intra-ample temperature profile that can be used as initial condition in the subsequent boiling regime in frying simulations. The relation of estimated heat transfer coefficients to the experimental conditions is discussed. In the case of a frying simulant material the experimental data are incompatible to the employed homogeneous conduction model suggesting that the assumption of thermal equilibrium between phases must be relaxed.

Acknowledgements

The present activity was under the umbrella of COST Actions MP1106 and CM1101 and the European Space Agency funded programs: "Influence of gravity conditions on mass and heat transfer in porous media" (Co. No. 22470/09/NL/CBi- Phase II), FASES (Fundamental and Applied Studies of Emulsion Stability) and PASTA (PArticle STAbilised Emulsions and Foams).

References

Farid, M.M., Chen, X.D., 1998. The analysis of heat and mass transfer during frying of food using a moving boundary solution procedure. Heat Mass Transfer/Waerme- und Stoffuebertragung 34 (1), 69–77.

Ozisik, M.N., Orlande, H.R.B., 2000. Inverse Heat Transfer: Fundamentals and Applications. Taylor and Francis, New York.

Lioumbas, J.S., Karapantsios, T., 2012. Effect of potato orientation on evaporation front propagation and crust thickness evolution during deep fat frying. J. Food Sci. 77 (1), E297–E305.

Vauvre, J.-, Patsioura, A., Olivier, V., Kesteloot, R., 2015. Multiscalemodeling of oil uptake in fried products. AIChE J. 61 (7), 2329–2353.

26th European Low Gravity Research Association Biennial Symposium and General Assembly
14th International Conference on "Two-Phase Systems for Space and Ground Applications"
European Space Agency Topical Teams meetings
Granada (Spain), September 24-27, 2019

Poster 045

Pharmacological approach to space related disorders: set-up of co-culture system for the study of wound healing in microgravity

L. Morbidelli1, S. Genah1, V. Ciccone1, F. Cialdai2, M. Monici2

[1]Department of Life Sciences, University of Siena, Via A. Moro 2, I-53100 Siena, Italy [2] ASAcampus Joint Laboratory, ASA Research Division, Dept. Experimental and Clinical Biomedical Sciences "Mario Serio", University of Florence, Viale G. Pieraccini 6, I-50139 Florence, Italy.
lucia.morbidelli@unisi.it

Introduction

Exposure to microgravity during space missions can induce many changes in living organisms. Astronauts during and after long-term space missions present different health problems, involving all functional systems and organs, potentially affecting mission performance. Bone loss, muscle atrophy, immune system dysregulation, cardiovascular deconditioning and changes in gastrointestinal and metabolic activities are among the most common space-related disorders (Strollo et al., 2018). These conditions can further have consequences on drug pharmacokinetics (PK) and pharmacodynamics (PD), thus making commonly used pharmacological therapies ineffective in space (Kast et al., 2017). Considering deep space exploration and missions of long duration, it is mandatory to prevent and adequately treat typical space-related disorders as sleep disturbances, allergies, space motion sickness, pain and sinus congestion, as other disorders or medical problems arising during time as traumatic injury.

The topic of our research is focused on how physio-pathological conditions related to long-term space missions influence drug bioavailability and therapeutic efficacy in astronauts.

In particular, the main goal of this study is to set-up and consolidate *in vitro* cell and tissue models to accurately mimic low gravity conditions for the analysis of pharmacological parameters as PK and drug efficacy and safety.

It is known that cells and tissues in the body are strongly influenced by microgravity in their architecture, intercellular communications, and overall functions (Maier et al., 2015, Cialdai et al., 2016). For *in vitro* cell culture models to accurately mimic low gravity conditions, the environment of the culture is a critical issue to be considered.

Materials and methods

The rotating wall vessel (RWV) bioreactor was designed by NASA to model microgravity. As the cells grow and develop in a low fluid-shear environment, cellular aggregates form on beads and can be sampled at different time points to monitor the response to various stimuli, both physical ones and drugs.

The first step of the project was to set-up modeled microgravity studies on cultured cells. Endothelial cells and fibroblasts were studied in order to evaluate the influence of microgravity on these cell types, fundamental for vascular function and angiogenesis, relevant for tissue healing. Thanks to RWV it is possible to assess the reciprocal molecular and functional interaction among different cell types and to study the effect of conventional or novel drugs (Cialdai et al., 2016).

Results

The results obtained document that the absence of gravity induces functional and moleulr changes in the single cell types. Concerning cell-cell interaction, while fibroblasts positively control endothelial cell migration and network formation in 3D-gels, their exposure to modeled microgravity in the RWV impairs the angiogenic phenotype of endothelial cells. The functional responses correlated with the differential release of angiogenic mediators.

Conclusions

In conclusion the RWV is a valid method to model microgravity and to study cellular functions and molecular features, allowing the monitoring of the interaction among different cell types

In perspective, fibroblast and endothelial pharmacological tuning appears a promising therapeutic approach to overcome problems related with tissue damage which can be worsened during life in space or in disease conditions very common on the Earth.

Acknowledgements

This research is funded by European Space Agency (ESA) and Italian Space Agecny (ASI).

References

F. Cialdai, L. Vignali, L Morbidelli, A. Colciago, F Celotti, A Santi, A Caselli, P Cirri, M. Monici, Modeled microgravity affects fibroblast functions related to wound healing, *Microgravity - Science and Technology* (2016) DOI 10.1007/s12217-016-9532-7

J. Kast, Y. Yu, C.V. Seubert, V.E. Wotring, H. Derendorf, Drugs in Space: pharmacokinetics and pharmacodynamics in astronauts, *Eur. J. Pharmaceutical Sci*. 109 (2017) S2-S8.

J.A. Maier, F. Cialdai, M. Monici, L. Morbidelli, The impact of microgravity and hypergravity on endothelial cells, *Biomed. Res. Int*. (2015) 434803. doi:10.1155/2015/434803.

F. Strollo, S. Gentile, G. Strollo, A. Mambro, J. Vernikos, Recent Progress in Space Physiology and Aging, *Front. Physiol*. 9 (2018) 1551. doi: 10.3389/fphys.2018.01551

Poster 051

Numerical simulation of long-term microgravity effects on the cardiovascular system. Validation and Results for Moon and Mars exploration scenarios.

A.Perez-Poch

UPC BarcelonaTech, Spain.
antoni.perez-poch@upc.edu

Introduction

We report on the results and validation of the model NELME (Numerical Emulation of Long-Term Microgravity Effect) across a wide variety of altered gravity scenarios. Computer simulations have become increasingly available tools for making predictions on the outcomes of complex physiological systems in extreme environments. However, technical limitations and difficulties of finding out opportunities to produce large series of experimental data to validate the models have made it difficult for these models to become available. In the recent years, this situation has changed as supercomputer facilities have increased their power; and more experimental data from parabolic flights and other altered gravity platforms are available to researchers as well. Results are provided about different simulations that have been conducted for short, medium-term and long exposures to microgravity; along with different events embedded. These simulations may include simulation of physical aerobic exercise during a mission, EVAs, thermal stress or human exposure to altered gravity scenarios (centrifuges, Martian or Lunar gravity, rocket launch, etc.). Risks for human health that may put in jeopardy a manned space mission in a variety of scenarios are evaluated and discussed.

1. Development and validation

Details on the development of NELME model are provided, a computer electrical-like physiological model which takes into account variables such as gender, weight, height and also environmental variables like temperature or exposure to gravity. From the model, we can retrieve output results related to the cardiovascular performance under stress and/or exposure to altered gravity. These measurements lead to an assessment of the deconditioning of the cardiovascular system in different scenarios. This is of interest, for example, in cases where it is unlikely that animal models or humans can be experimentally tested, such as long-term exposure to microgravity. The model has been validated through parabolic flights conducted at the Barcelona-Sabadell Airport using an aerobatic aircraft CAP10B. This aircraft is capable of providing parabolas of up to 8 seconds of microgravity preceded and followed by peaks of around 2 seconds of hypergravity (Perez-Poch et al. 2016). Experimental validation of the model in parabolic flight includes 5 different subject included in the sample. The model, once it has been validated, is intended to be applied to investigate on exposure of human exposure to different altered gravity scenarios.

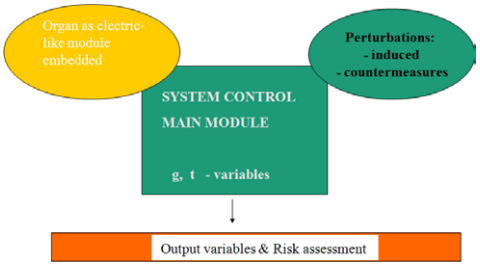

Figure 1: Modular concept of NELME software analyzer.

Initial validation was performed by applying the Runge-Kutta equations model on orthostatic intolerance by Heldt (Heldt et al. 2002) and comparing the results from this former model to that obtained in the electrical-like model simulation of our software. Results for the change in Arterial pressure (mmHg.), Mean heart rate (beats/min.) and Mean Stroke Volume are compatible with less than 10% error ($p<0,05$).

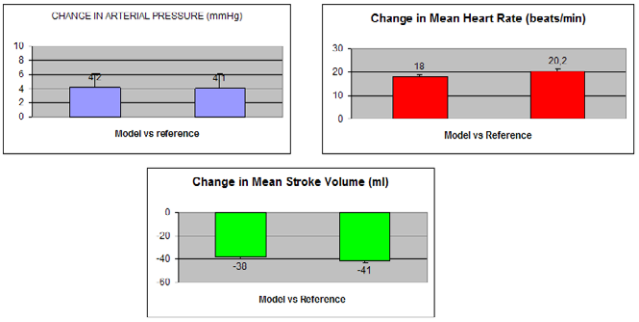

Figure 2: Initial validation of the NELME model implementation.

2. Simulation results

Results from the simulations account for a degree of impairment of human capabilities which may be of interest for designing future long-term human missions to Mars or other destinations. Interestingly, a long-time exposure to less than 0.35g seems to be as hazardous as a zero g for missions longer than three months, when we analyze the Vascular Resistance deconditioning (%, $p<0,05$) whereas aerobic exposure does not fully counteract the risks.

Aerobic exercise as countermeasure can also be studied in simulation, as we can model the induced physiological stress with an electrical-like analogy in the circuit model. Different patterns of exercise can be introduced in the former simulations, with different time and intensity protocolos. Then, risk reduction for the entire mission can be evaluated by using current standard

procedures (Stamelatos & Dezmull 2011).

Furthermore, it is well known that the most stressfull episodes in a manned space mission are the Extra Vehicular Activities (EVAs). We can also estimate the risk estimated with these demanding activities in terms of how they stress the cardiovascular system, taking into account both temperature increase, anaerobic and aerobic exercise.

We have then applied all these events into a full mission scenario to Mars and Moon, taking into account the different gravity loads involved in different parts of their mission, including a prolonged stay on the planets.

Some results from Moon missions risk estimation are shown in Figure 3.

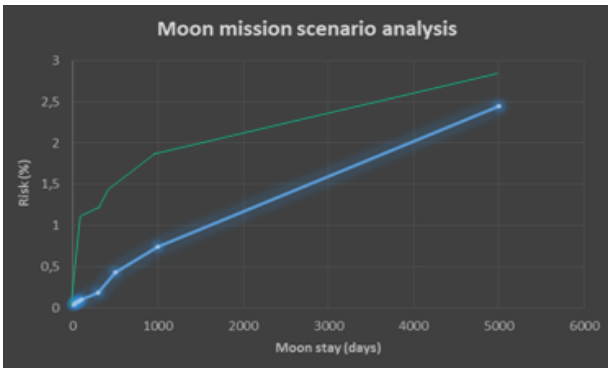

Figure 3: Moon mission scenario analysis risk estimation (green: with 1/week EVA)

A nearly linear increase appears between the associated risk with microgravity and lunar gravity exposure. However, the risks are within currently accepted limits of putting a mission into jeopardy. Aerobic exercise is fully accounted in this estimation, and, also in the line in green above, it can be seen the increase of the risk with a protocol of EVAs of no more than once per week.

We proceed in an analog way with Mars Mission scenarios, including a prolonged Mars stay on the planet, and a travel back to Earth (Figure 4).

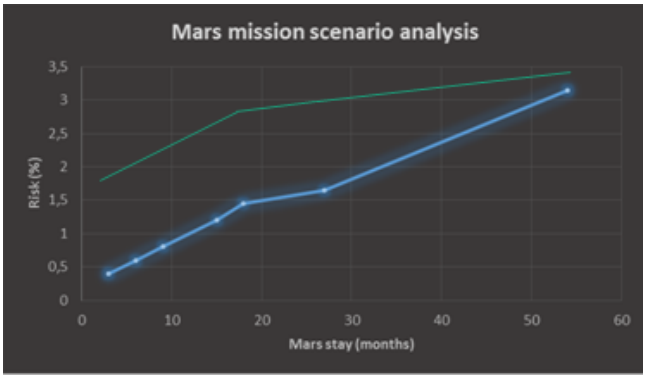

Figure 4: Mars mission scenario analysis risk estimation (green: with EVAs)

The final results are shown in blue line, and in green with the same protocol of 1 EVA per week. The associated risks are also within safe limits. However, it must be noted that we have not included radiation and possible accidents risks.

If those risks were added, and according to existing models, the risk associated to cardiovascular deconditiong should not exceed a 1-2% maximum risk. Furthermore, technological failures or solar events will certainly increase the total risk of the mission.

Conclusions

Numerical modelling has proven to be a valuable tool to predict possible risks of developing hazards in long-term mission scenarios. Our proposed electrical-like Model reproduces cardiovascular changes from previous modelling when returning to Earth, and has been validated from parabolic flight and comparison with former models of orthostatic intolerance.

Significant differences in heart rate output, mean arterial pressure and mean stroke volume appear in short-term scenarios. Also, long-term microgravity exposure simulations show a significant risk reduction, after aerobic exercise pattern applied, with gender differences, with women's more reduction than men's.

Microgravity exposure risks can be estimated for a variety of manned Moon and Mars scenarios, showing they are compatible with acceptable safety limits. EVAs are a significant added risk factor.

More studies are needed to fully understand the risks associated with the deconditioning of the cardiovascular system in long-term manned missions. These are the first steps of applying numerical multimodular models to the risk estimation of putting a manned space mission at risk.

References

Perez-Poch, A.; D. V. González, D. López, "Hypogravity research and educational parabolic flight activities conducted in Barcelona: a new hub of innovation in Europe." *Microgravity Science and Technology*, 28, **6** ,(2016), 603-609.

Heldt T. et al, "Computational modeling of cardiovascular response to orthostatic stress" *J. Appl Physiol* 92 (2002), 1239-1254.

Stamelatos M., Dezmull Hl, "Probability risk assessment for managers and practitioners". *NASA/SP-2011-3421* (2011).

Poster 053

PACKING GRAINS BY SHEARING

A.J. Batista-Leyva,,[1] Dariel Hernandez Delfn,[2] RC Hidalgo,[2] and Diego Maza[2,*]

[1] *Instituto Superior de Ciencia y Tecnologa Aplicadas (InSTEC)*
University of Havana, 10400 Havana, Cuba

[2] *Granular Media Lab*
Department of Physics and Applied Mathematics
Universidad de Navarra
Irunlarrea S/N, 31080, Pamplona, Navarra, Spain

In this work, we show experimental and numerical evidence about the possibility of inducing ordered collective motions in a granular sample subject to different wall vibrational conditions. Two different regimes are explored, a) geometrical non-symmetric boundary conditions and b) asymmetric temporal excitations. In the first case, we explore the different advective regimes induced by nonsymmetric containers when they are excited with harmonic perturbations. In the second situation, anharmonic temporal signals are applied to produce collective motions of the granular sample. The role of the gravity on the resulting dynamics is explored numerically.

* Corresponding author: dmaza@unav.es

26th European Low Gravity Research Association Biennial Symposium and General Assembly
14th International Conference on "Two-Phase Systems for Space and Ground Applications"
European Space Agency Topical Teams meetings
Granada (Spain), September 24-27, 2019

Poster 055

Non-Equilibrum fluctuations of concentrated polymer solutions

D. Zapf[1], W. Köhler[1]

[1] Physikalisches Institut, Universität Bayreuth, Bayreuth, Germany
werner.koehler@uni-bayreuth.de

Introduction

As part of the ESA project GIANT FLUCTUATIONS (NEUF-DIX) we are establishing, with support by DLR, a ground-based shadowgraph setup (Fig. 1) for the measurement of non-equilibrium fluctuations (NEFs). The signals ot these NEFs, such as the structure function S(q,Δt), are cut off by gravitational buoyancy effects. The full amplitude is reached only under microgravity conditions (Croccolo et al. 2006), for which the instrumentation is currently under development within the NEUF-DIX project. The aim of the here introduced setup is to conduct preparatory and accompanying ground based experiments under gravity conditions.

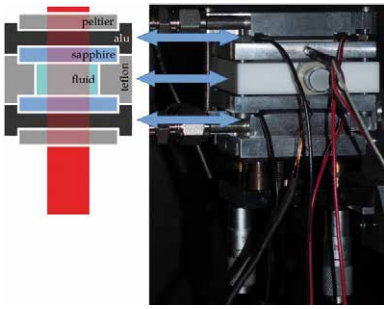

Figure 1: Sketch (left) and photographic image (right) of the temperature controlled fluid cell.

Objective

The big advantage of shadowgraphy is the possibility to observe fluctuations at extremely low q-vectors without the need to block the primary beam, as it is necessary in dynamic light scattering experiments. Additionally, shadowgraphy gives access to isothermal and non-isothermal transport coefficients, such as the thermal diffusivity $D_{th}=\kappa/\rho c_p$, the diffusion coefficient D and the Soret coefficient $S_T=D_T/D$ with D_T being the thermodiffusion coefficient.

A major problem for the investigation of the relaxation dynamics ($\sim\exp(-\Delta t/\tau)$) is that firstly the velocity fluctuations δv cannot be measured directly and secondly the temperature fluctuations δT relax very fast due to the high value of D_{th}. For our experiments on ternary systems we use polymer solutions with different concentrations. The solvent is a isomassic binary mixture of toluene and cyclohexane. Our aim is to investigate NEFs in dependence of the polymer concentration. From first measurements we can already deduce that higher polymer concentrations produce a stronger signal in a narrower q range.

One of our goals is the investigation of the relaxation behavior in the supercooled liquid on approach of the glass transition. Because of the high Tg-contrast between the polymer and the solvent, it is possible to approach the glass transition along the composition rather than the temperature axis (Rauch et al. 2002, 2003). Next to the glass transition, the relaxations are slowing down. The relaxation domains that are expected to govern our experiments are summarized in Fig. 2 and will be discussed in detail on our poster.

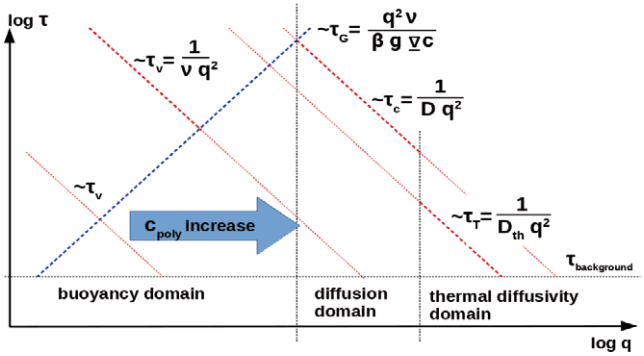

Figure 2: Sketched representation of the correlation times τ of the different relaxation processes. In bold lines the leading correlation property of the domain. Furthermore, the shift of the viscous relaxation, represented by the increase in the polymer concentration.

Conclusions

We have successfully established a new shadowgraphy setup. It will be used for ground based laboratory experiments that accompany and complement microgravity experiments in the framework of the NEUF-DIX project of ESA. The focus of the work performed in our group is on ternary mixtures which contain a polymer at higher concentration, leading to a slowing down of dynamics caused by the approach of the glass transition along the polymer concentration axis.

Acknowledgements

We thank ESA for support of the NEUF-DIX project. This work is supported by Deutsches Zentrum für Luft- und Raumfahrt (DLR) (Grant 50WM1850).

References

F. Croccolo, et al. , Effect of Gravity on the Dynamics of Nonequilibrium Fluctuations in a Free-Diffusion Experiment. *Annals of the New York Academy of Sciences* 1077.1 (2006) 365-379.

J. Rauch, W. Köhler, Diffusion and Thermal Diffusion of Semidilute to Concentrated Solutions of Polystyrene in Toluene in the Vicinity of the Glass Transition, *Phys. Rev. Lett.* 88 (2002) 185901

J. Rauch, W. Köhler, Collective and thermal diffusion in dilute, semidilute, and concentrated solutions of polystyrene in toluene, *J. Chem. Phys.* 119 (2003) 11977

Poster 061

Self-assembly by multi-drop evaporation of CNT-SiO_2 nanocomposites for applications in energy and medicine

H. Machrafi[1,2,3], C. Minetti[1], C.S. Iorio[1]

[1]Service Physical Chemistry, Université libre de Bruxelles, Brussels, Belgium, [2]GIGA-In Silico Medicine, Université de Liège, Liège, Belgium, [3]Thermodynamics of Irreversible Phenomena, Université de Liège, Liège, Belgium;
h.machrafi@ulb.ac.be, h.machrafi@uliege.be

Introduction

Water droplets containing carbon nanotubes (CNTs), SiO2 (silica) nanoparticles and mixtures of them, are deposited one drop after the other on a polycarbonate substrate. During evaporation of the droplets, the CNTs and silica nanoparticles go through a self-assembly process, forming a nanocomposite. A nanocomposite is prepared by depositing a pre-mixed CNT/silica droplet (Machrafi et al. 2018). This results into a homogeneous or layered nanocomposite of silica nanoparticles embedded in a porous CNT structure. The thickness, thermal and electrical conductivity (in both the perpendicular and parallel direction) of the composites are measured versus the number of depositions. The morphology of the nanomaterials is characterized by scanning electron microscopy (SEM).

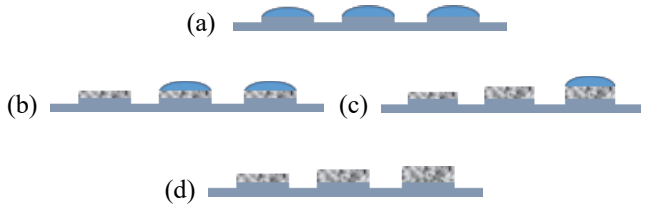

Figure 1: Schematic representation of the self-assembly process.

Schematically, the procedure is as follows. First, we deposit a certain number of droplets next to each other (a). Then, after evaporation, the nanotubes stick to the polycarbonate substrate. We add another droplet, except for the left spot (b). After evaporation, a thicker deposition is obtained on the second and third spot from the left (c). We add again another droplet, except for the first two spots. After evaporation, the third spot from the left shows an even thicker deposition (d). This can then be repeated as much as wanted.

Results

Figure 2 shows SEM images of the pre-mixed nanocomposite with a CNT network embedded with silica nanoparticles.

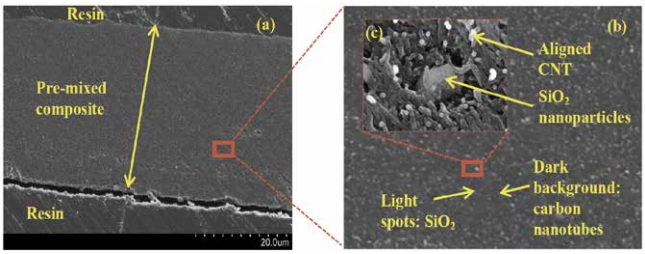

Figure 2: SEM images show a CNT alignment in a CNT-SiO_2 nanocomposite.

The one-dimensional confocal probe method is used to measure the thickness of the layers (see Figure 3). The pre-mixed composites showed an increase in the values in both the parallel and perpendicular directions of both the electrical and thermal conductivities, making them suitable for electrodes or battery-like applications. The values of the electrical and thermal conductivities in the perpendicular direction for the first composite decrease and increase, respectively, while for the parallel direction the values are significantly constant. As such, they would be useful as electrical insulators for optimal cooling. Thickness measurements showed that the pre-mixed composite is the denser one, due to a better alignment of the carbon nanotubes.

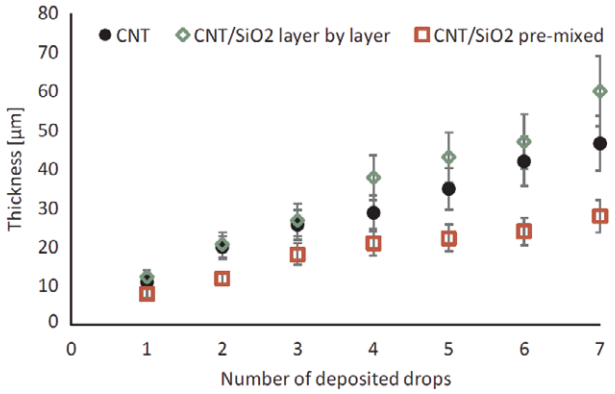

Figure 3: Thickness measurements indicate a better CNT alignment in a CNT-SiO_2 nanocomposite

Discussion

In this work, water droplets containing CNTs, SiO_2 nanoparticles and two types of composites are each evaporated on a polycarbonate substrate in order to form different self-assembled structures. The two types of composites considered in this work are as follows. The first is a composite prepared by depositing alternately a layer of CNTs and SiO_2 nanoparticles. The second is a composite prepared by depositing a premixed droplet containing CNTs and SiO2 nanoparticles. The morphology of the nanomaterials is characterized by scanning electron microscopy (SEM). The one-dimensional confocal probe method is used to measure the thickness of the layers. This has shown that the density of the created pre-mixed composites increases more than that of the CNT, while it increases less for the layer-by-layer one. The electrical and thermal conductivities have been measured both in the perpendicular and parallel direction with respect to the substrate. It is interesting to combine these results into the same discussion. We have observed that the number of CNT-laden deposited drops hardly affects the values of both the

electrical and thermal conductivity for both the perpendicular and parallel directions. As for the layer-by-layer composite, it appeared that the values in the parallel direction for both the electrical and thermal conductivities hardly changes. However, the values in the perpendicular direction showed opposite trends. For a higher number of deposited drops, it was shown that the perpendicular electrical conductivity decreases while that of the perpendicular thermal conductivity increases. This makes such a material interesting for electrical insulators, where one would like to dissipate generated heat rather quickly in order to keep the electrical device cool and electrically efficient at the same time. The pre-mixed composite showed an increase of the values in both the perpendicular and parallel directions for both the electrical and thermal conductivities. This could be of use for battery-like or electrode-like applications. Here one would obviously like to have a higher electrical conductivity, but also a higher thermal conductivity in order to avoid hot spots.
Finally, it should be noted that the wettability is also an important issue. Figure 4 shows the static, advancing and receding contact angles of

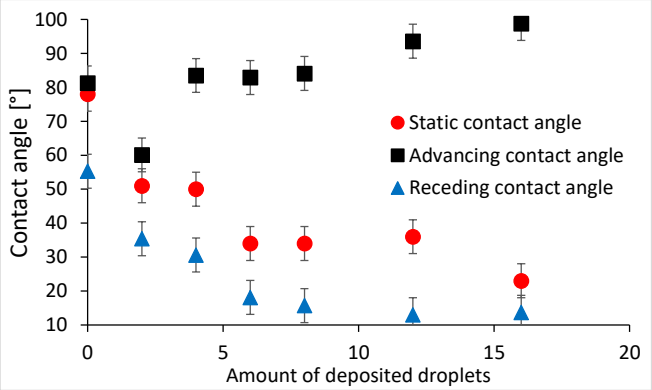

Figure 4: Receding and advancing contact angles of water on the coated substrates as a function of the amount of deposited droplets of CNTs.

Figure 4 shows that on increasing the amount of deposited droplets, the advancing contact angle increases slightly, while the receding contact angle decreases considerably. The contact angle hysteresis for water is greatly affected (increasing). It can be suggested that during an advancing contact angle, a higher coverage of nanoparticles on the substrate causes more pinning, so that the advancing contact angle increases. However, when the droplet is receding, the capillary forces that are higher with a higher coverage (due to a formed nanoporous structure) cause the receding contact angle to decrease.

Conclusions

The proposed method in this work is of little cost and hardly energyconsuming. With respect to the often-used dip-coating method, the procedure in this work contributes to a better control of depositing premixed solutions. This resulted into silica-induced CNT alignment with a higher density network, improving considerably the thermal and electrical properties in the aligned direction. This work shows that a simple and low-cost procedure is capable of preparing composites out of the same components, but with different properties.

Acknowledgements

The authors acknowledge financial support from the Prodex programme at BelSPo and the MAP Evaporation programme at ESA.

References

H. Machrafi, C. Minetti, V. Miskovic, P.C. Dauby, F. Dubois, C.S. Iorio, Self-assembly of carbon nanotube-based composites by means of evaporation-assisted depositions: Importance of drop-by-drop self-assembly on material properties, *Mat. Chem. Phys.*, 218 (2018) 1-9.

Poster 062

Granada (Spain), September 24-27, 2019

Reduced Glial Scarring Through Hypergravity Exposure

Yannick Lichterfeld, Timo Frett, Ruth Hemmersbach and Christian Liemersdorf
German Aerospace Center (DLR), Institute of Aerospace Medicine, Division of Gravitational Biology, Cologne, Germany
Yannick.Lichterfeld@dlr.de

roduction

ıral regeneration following injuries to the central nervous em (CNS) in mammals is inhibited by several factors. important mechanism preventing axon regrowth and the healing of a CNS injury is the formation of the glial . Key players in glial scar formation are reactive ocytes that migrate into the region of the injury and duce an inhibitory extracellular environment, rich in ndroitin sulfate proteoglycans (CSPGs) and other ıaling molecules. These, in turn, have an inhibiting effect axon growth and even actively induce axon dystrophy, ch has severe consequences for patients, e.g., loss of ronal signaling and in some cases permanent paralysis.
could show that exposure to altered gravity has a direct ct on primary astrocytes and that hypergravity in icular might be a viable tool to reduce glial scarring.

thods

cultivated primary murine cortical astrocytes *in vitro* er hypergravity conditions at constant 2g for several days to weeks by using the DLR Multi Sample Incubator trifuge (MuSIC, Fig. 1A) and compared key cellular racteristics with 1g controls. To investigate cellular amics and migration speed under hypergravity, we loyed our Hyperscope platform (Fig. 1B) at DLR, a y automated fluorescent live-cell imaging microscope alled on the :envihab human short-arm centrifuge HC). Additionally, using our group's expertise in the ınd-based simulation of microgravity by means of fast orotation (60 rpm) and also flight opportunities for eriments in real microgravity (DLR sounding rocket PHEUS8/ATEK) we were able to expose astrocytes to ce-like conditions and investigated their responses on a phological and protein-level.

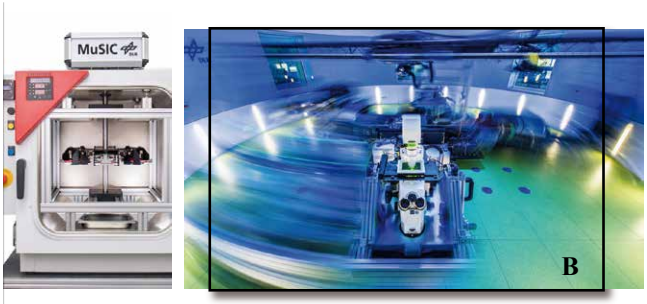

ıre 1: The Multi erscope on the :envihab centrifuge at DLR, Cologne, Germany

Results

On the one hand we could show that astrocyte spreading, a well-known effect of 2D cultures, is significantly reduced by about 20% due to hypergravity (2g) exposure, while on the other hand cell proliferation is unchanged. The diminished spreading of astrocytes in combination with morphological alterations indicates an impact of altered gravity conditions on the cytoskeleton. Since cellular migration depends on a fully functioning actin and tubulin cytoskeleton, we expected an impact of hypergravity on the migrational behavior of astrocytes. To test this hypothesis, we performed *in vitro* wound-healing assays (scratch-assays) on both the DLR incubator-centrifuge as well as the Hyperscope platform, enabling a live assessment of the migratory behavior of astrocytes during exposure to hypergravity. As a result, astrocyte migration was confirmed to be diminished by about 33% during an initial phase (Fig. 2) followed by cell adaptation with a less substantial but prolonged diminished migratory rate with about 10% reduction of cell velocity.

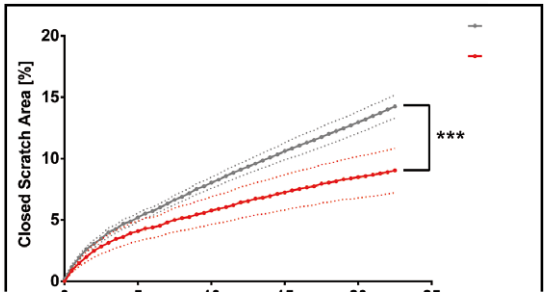

Figure 2: Live-cell analysis of the first 24 hours of an astrocyte scratch assay.

onclusions

ur results show that hypergravity represents a stimulus that hibits not only cell spreading but also astrocytic migration, hich in case of a CNS injury might reduce glial scarring d therefore increase the progression of neural generation.
ur further steps are the identification of the underlying echanisms, e.g., cytoskeletal alterations to generate an lvanced model of astrocyte responses to altered gravity. For this, the plan is to not only work with increased gravitational loading, but also mechanically unload the cells to see what cellular mechanisms respond to this kind of stimulus.

26th European Low Gravity Research Association Biennial Symposium and General Assembly
14th International Conference on "Two-Phase Systems for Space and Ground Applications"
European Space Agency Topical Teams meetings
Granada (Spain), September 24-27, 2019

Poster 063

The role of HSP90 chaperones in canalized and non-canalized growth responses of *Arabidopsis* seedlings to altered gravity

L. Kozeko

Institute of Botany of the National academy of sciences of Ukraine, Kyiv, Ukraine
liudmyla.kozeko@gmail.com

Introduction

Phenotypic plasticity is the ability of a genotype to produce different phenotypes in response to distinct environmental conditions (Piglucci 2001). Trajectories of plastic responses are canalized. A classic example of a canalized plastic response of a plant is the gravitropic reaction. Evolving under 1 *g* force, plants acquired the ability to respond to gravistimulation by producing a steady bend of the roots down. In contrast, weightlessness is unusual for the earth beings and results in the disorientation of plant growth (Kordym 2014).

The gravitropic response has been found to depend on the functioning of heat shock proteins HSP90 (Queitsch et al. 2002). This chaperone family is involved in many cellular processes through regulation of a diverse set of substrate proteins involved in hormonal signaling, cell cycle control, growth regulation etc. By assisting the functioning of the client proteins, HSP90s can support plastic reactions. However, their role in the plant growth under microgravity has not been clear.

Approaches

In this study, participation of two cytosolic HSP90s – stress-inducible AtHSP90-1 and constitutive AtHSP90-4 – in plastic responses of *Arabidopsis thaliana* to simulated microgravity and gravity stimulation has been assayed. Loss-of-function mutants *Athsp90-1* and *Athsp90-4* (NASC) were compared with Col-0 ecotype. Seedlings were grown in the dark: 1) at 1 *g* (control); 2) on a horizontal clinostat (2 rpm); 3) subjected to gravity stimulation (turning by 90°).

Results

In all cases, dark-grown seedlings had elongated hypocotyls and short roots. Both in stationary conditions and under rotation, knockout mutations of *AtHSP90-1* and *AtHSP90-4* caused an increase in heterogeneity of length of hypocotyls and roots, as well as their ratio that indicated the ability of HSP90s stabilize growth activity.

In addition, both mutant lines showed a decrease in hypocotyl length at 1 *g* when compared to Col-0. Under clinorotation, *Athsp90-1* seedlings had longer hypocotyls and shorter roots than Col-0. Moreover, growth of seedlings at the absence of a gravitational stimulus was characterized by a significant continual variability of the spatial arrangement of organs that is in accordance with literature data (Antonsen, Johnsson, 1998; Kordym, 2014). It led us to the conclusion that plant organisms do not have a canalized response to the unusual weightlessness / microgravity conditions.

Measurement of an angle of root bending at gravistimulation showed that deficiency of the HSP90s did not change the central tendency of the angle, but increased its variability. In particular, a few mutant seedlings had roots turned upward.

Conclusions

The obtained results demonstrated specific roles of inducible AtHSP90-1 and constitutive AtHSP90-4 in canalization / stabilization of the root gravitropic response (canalized plastic response), as well as in supporting / stabilization of the growth activity of seedling organs under clinorotaion (non-canalized plastic response).

References

M. Pigliucci Phenotypic plasticity. In: Fox C.W., Roff D.A., Fairbairn D.J. eds. *Evolutionary Ecology: Concepts and Case Studies*. NewYork, New York: Oxford University Press, 2001.

E.L. Kordyum Plant cell gravisensitivity and adaptation to microgravity. *Plant Biol*. 16, Suppl. 1 (2014) 79-90.

C. Queitsch, T.A. Sangster, S. Lindquist Hsp90 as a capacitor of phenotypic variation. *Nature* 417 (2002) 618-624.

F. Antonsen, A. Johnsson. Effects of microgravity on the growth of *Lepidium* roots. *J. Gravitational Physiol*. 5, 2 (1998) 13-21.

Poster 065

Microgravity experiments on thermo-electric flows

M. Meier[1], A. Meyer[1], Innocent Mutabazi[2], Christoph Egbers[1]
[1]Department of Aerodynamics and Fluid Mechanics, Brandenburg University of Technology Cottbus-Senftenberg, Siemens-Halske-Ring 14, 03046 Cottbus, Germany
[2]Normandie Université, UNIHAVRE, CNRS UMR 6294, Laboratoire "Ondes et milieux complexes", 53, rue de Prony, Le Havre 76058, France
m.meier@b-tu.de, innocent.mutabazi@univ-lehavre.fr

Introduction

Our experiments focus on the investigation of thermal convection in a dielectric liquid inside a vertical annular cavity under the influence of a radial electric force field. In most of our experiments we used a low viscous silicone oil as dielectric liquid. The inner and outer cylinders of radius R_1 and R_2, are maintained at temperatures T_1 and T_2 by heating and cooling fluid loops, respectively. In addition, an alternating electric potential is imposed to the inner cylinder while the outer one is grounded. A dielectrophoretic (DEP) force is induced in a dielectric fluid when an inhomogeneous electric field is applied to a dielectric fluid presenting an electric permittivity gradient. In our experiments, the temperature difference between the two cylinders ΔT induces the permittivity gradient, and the curvature of the cylindrical annulus provides the electric field inhomogeneity. The DEP force influences the flow of the fluid, and, hence, also affects the heat transfer at the cylindrical surfaces. This effect has been shown in experiments (e.g. Chandra and Smylie, 1972, Futterer et al., 2016). However, Earth's gravity inhibits a pure central force field in these experiments. Under Earth laboratory conditions, both forces are superimposed. Therefore, experiments has been performed under parabolic flight conditions which provide a low gravity phase of about 22s. In microgravity conditions we can pose the question, how efficiently "electric gravity" can replace the gravitational effect. After the execution of a series of parabolic flight experiment campaigns we are preparing now sounding rocket flight experiments within the TEXUS-program of the German Space Agency.

Experiments in weightlessness

Subsequently, since 2009, we performed 7 parabolic flight campaigns (PFCs) supported by the German Aerospace Center DLR and also three PFC supported by the Centre Nationale d'Études Spatiales (CNES) as a cooperative project with LOMC, Normandie University, Le Havre, France.

Generally, we could demonstrate (see A. Meyer et al. 2018 and M. Meier et al. 2018) that the dielectrophoretic force can induce a "electric buoyancy" in microgravity. This is visible through a rapid growth of a thermoelectric instability, analog to the classical Rayleigh-Bénard instability, during microgravity conditions. Beside heat transfer measurements over the gap, Particle Image Velocimetry (PIV), Synthetic Schlieren and Shadowgraph techniques have been the visualization methods in up-to-now 9 PFCs.

The application of the dielectrophoretic force under low-g and 1g conditions showed that the flow becomes unstable when the electric tension is sufficiently large. The shape of the unstable regimes depends on the aspect ratio of the cylindrical annulus, on the gravitational condition and on the set of control parameters. Under low-g conditions, the preferred critical mode is mainly helical, at least for low to moderate temperature differences between the two cylinders.

Both gravitational levels have been studied through a linear stability theory (Yoshikawa et al. 2013, Meyer et al. 2017) as well as through numerical simulations (Travnikov et al.) and exhibit a qualitatively good agreement with our experimental results. However, the threshold for the occurrence of instabilities is at larger electric potential in the experiments. The top and bottom boundaries stabilize the flow, and it is clear that for sufficiently large temperature differences, the Boussinesq approximation is no more valid.

Theoretical researches have considered microgravity conditions in order to focus on the DEP force, see e.g. Takashima 1979, but laboratory experiments have to involve the Earth's gravity effect, which is modifying the stability conditions of the system (see Seelig et al. 2019). Theoretical and numerical research presents an analogy between both convective modes (see Chandra and Smylie, 1972; Malik, et al., 2012; Yoshikawa et al., 2013 a); Yoshikawa et al., 2013 b)). Sitte and Rath (2003) verified the DEP-induced buoyancy effect by laboratory and parabolic flight experiments. 3-D numerical simulations have been performed by Travnikov et al. 2013, Kang and Mutabazi, 2019 and Gerstner (see Seelig et al., 2019).

Using PIV and Shadowgraph methods, it has been found that, under Earth's gravity condition, the first unstable regime takes the form of stationary columnar counter-rotating vortices. A stability diagram spanned by the thermal Rayleigh number and the dimensionless electric potential has been built experimentally and compared to results from a linear stability analysis (see Meyer et al., 2017).

For a set of given control parameters, the experimental measurements of velocity and temperature have been compared to numerical simulations and showed a good qualitative agreement. Indeed the columnar structure has been confirmed experimentally, numerically and theoretically and could be explained by simultaneous effect of the axial Earth gravity and the radial electric gravity.

Conclusions

pean Space Agency Topical Teams meetings

Granada (Spain), September 24-27, 2019

low gravity phase provided by the parabolic flights lasts ut 22s, which is too short to establish a fully developed moelectric instability in our experimental parameter ge. But, it has been possible to detect the growth of urbations which allowed us to build a stability diagram, haracterize the geometry of the flow, and to compare the wth rates of perturbations between Earth's gravity and ghtlessness environment.

sequently, we are now preparing a sounding rocket nt experiment - foreseen for the TEXUS 57 campaign. this experimental set-up, we developed a combination of dowgraph and PIV-techniques which we apply ultaneously for each experiment cell. Figure 1 gives an mple for the processed flow field images of the ndrical gap for natural and DEP-forced convection under h conditions. The combination of the two measurement niques allows the simultaneous visualization of the flow ern in vertical (integrated over the height) and idional direction.

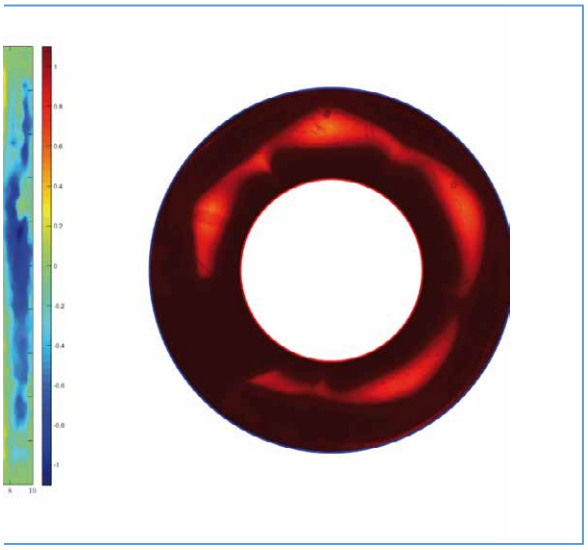

nside the
ıdrical gap. Experiment parameters: ΔT 2K, T0 25°C, 1g.
ıral convection with basic flow. Left picture from PIV-analysis;
t picture Shadowgraph image.

using the TEXUS-rocket with 6 minutes of microgravity e we will be able to determine the flow stability, the le shape and the corresponding heat transfer in our HD-experiments with much higher accuracy than in abolic flights.

knowledgements

project "Thermoelektrische Konvektion unter Schwerelosigkeit TEXUS)" is supported by the BMWi via the space administration of nan Aerospace Center DLR under grant no. 50WM1644. We also owledge the support of the Centre Nationale d'Études Spatiales ES), Novespace S.A. in Bordeaux, the TEXUS-group of Airbus Defence Space, Bremen and our technical staff at BTU.

erences

B. Chandra, D. E. Smylie, A laboratory model of thermal convection under a central force field. *Geophysical Fluid Dynamics,* 3 (1972) 211- 224.

B. Futterer, N. Dahley, C. Egbers, Thermal electro-hydrodynamic heat transfer augmentation in vertical annuli by the use of dielectrophoretic forces through a.c. electric field. *Int. J. Heat Mass Transfer* 93 (2016).

C. Kang, I. Mutabazi, Dielectrophoretic buoyancy and heat transfer in a dielectric liquid contained in a cylindrical annular cavity, *J. App. Phys.* 125 (2019), doi.10.1063/1.5086980.

S. Malik, H.N. Yoshikawa, O. Crumeyrolle, I. Mutabazi, Thermo-electro-hydrodynamic instabilities in a dielectric liquid under microgravity. *Acta Astronautica* 81 (2012) 563-569.

M. Meier, M. Jongmanns, A. Meyer, T. Seelig, C. Egbers, I. Mutabazi, Flow pattern and heat transfer in a cylindrical annulus under 1g and low-g conditions: Experiments, *Microgravity Sci. Technol.* 30 (2018) 699-712.

A. Meyer, M. Jongmanns, M. Meier, C. Egbers, I.Mutabazi, Thermal convection in a cylindrical annulus under a combined effect of the radial and vertical gravity, *C. R. Mecanique* 345 (2017) 11–20.

A. Meyer, Crumeyrolle, O., Mutabazi, I., Meier, M., Jongmanns, M., Renoult, M.-C., Seelig, T., Egbers, C.: Flow Patterns and Heat Transfer in a Cylindrical Annulus under 1g and low-g Conditions: Theory and Simulation, *Microgravity Sci. Technol. 30* (2018) 653–662.

T. Seelig, A. Meyer, P. Gerstner, M. Meier, M. Jongmanns, M. Baumann, V. Heuveline, C. Egbers, Dielectrophoretic force-driven convection in annular geometry under Earth's gravity, *International Journal of Heat and Mass Transfer* (accepted in April 2019)

B. Sitte, H. J. Rath, Influence of the dielectrophoretic force on thermal convection. *Exp. Fluids* (2003) vol. 34, pp. 24-27

V. Travnikov, O. Crumeyrolle, I. Mutabazi, Numerical investigation of the heat transfer in cylindrical annulus with a dielectric fluid under microgravity. *Phys. Fluids*, vol. 27 (2015) 054103.

M. Takashima, "Electrohydrodynamic instability in a dielectric fluid between two coaxial cylinders", *Mech.appl. Math.* 33 (1979) 93-103.

H.N. Yoshikawa, O. Crumeyrolle, I. Mutabazi, Dielectrophoretic force-driven thermal convection in annular geometry. *Phys. Fluids,* vol. 25 (2013) 024106

Poster 068

Sensitivity of plant plasma membrane to microgravity

Nedukha Olena M., Kordyum Elizabeth L., Vorobyova Tamara V.

Dep. Cell Biology and Anatomy, Institute of Botany of Nat. Acad. Sci. of Ukraine. Kiev, Ukraine. 01601, Kyiv, Tereschenkivska str., 2. E-mail: o.nedukha@hotmail.com

The sensitivity of the structure and function of the plasma membrane of pea seedlings to the effects of imitated microgravity (horizontal clinostation) is established. In these studies, the liquid chromatography method was used for the analysis of physico-chemical parameters of the plasma membrane fraction of epicotyles and plant roots, as well as the method of electron-cytochemical determination of the localization and activity of Ca^{2+}-ATP-ase in the studied samples of the pea. Imitation of microgravity provoked a strong decrease in the activity of Ca^{2+}-ATP-ase on the plasma membrane of cells and an increase in its activity on the endomembranes including of mitochondrial and nucleus envelope, endoplasmic reticulum, as well as on the membranes of dictyosomes of Golgi apparatus. Such changes were accompanied by changes in the content of glicerolipids, sphingolipids and sterols in the plasma membrane of roots and epicotyles of pea clinorotated seedlings in comparison with that in the control samples. The increase of content of LPS (lysophosphatidylcholine), PA (phosphatidic acid), PDME (phosphatidyldyl-dimethylethanolamine), PI (phosphatidylinositol) and PS (phosphatidylserine) was revealed in epicotyl's plasma membrane, whereas in root plasmalemma noted increase the content of LPS, LPE (lysopbosphatidylethanolamine), PC (phosphatidylcholine) and PG (phosphatidylglycerol), as well as reduction of phospholipids such as PS, RE and RA. The sterols content in epicotyle plasmalemma increased two times, in root - four times in imitated microgravity. As known, the sterols are important structural component of cell membranes, they take part in the transport of substances and also in the transmission of signals through the plasma membrane. It is possible, that the increasing sterols content has to lead to lowering membrane fluidity and increasing its rigidity. The obtained results suggest that the changes in the content of fatty acids and lipids of the plasma membrane, as well as the decrease in the activity of the Ca^{2+}-ATP-ase of the plasmalemma are interrelated and lead to changes in the regulatory properties of cells and the disruption of calcium transport and calcium balance in cells under the influence of imitated microgravity.

26th European Low Gravity Research Association Biennial Symposium and General Assembly
14th International Conference on "Two-Phase Systems for Space and Ground Applications"
European Space Agency Topical Teams meetings
Granada (Spain), September 24-27, 2019

Poster 072

Onset of thermoelectric convection in a vertical rectangular cavity with a horizontal temperature gradient and a high frequency voltage

E. B. Barry[1], C. Kang[1], H. N. Yoshikawa[2] & I. Mutabazi[1]

[1]Normandie Université, UNIHAVRE, Laboratoire Onde et Milieux Complexes, UMR 6294 CNRS
53 Rue de Prony – 76058 Le Havre cedex, France
[2]Intitut de Physique de Nice, UMR 7010 – Université Côte d'Azur,
1361 Route des Lucioles, 06560 Valbonne, France
elhadj-boubacar.barry@etu.univ-lehavre.fr, ckang44@uic.edu, harnurori.yoshikawa@unice.fr, mutabazi@univ-lehavre.fr

Introduction

The design of the heat echangers for microfluidic systems and for aeronautic and astronautic devices requires ore efficient sysems for energy saving.

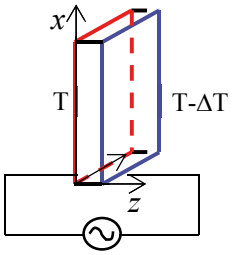

Figure 1: A heated vertical cavity with an electric voltage

Flow equations

A dielectric fluid of density ρ, viscosity ν, thermal expansion coefficient α, thermal diffusivity κ, and permittivity ε, is confined in a vertical rectangular cavity of width d subject to a horizontal temperature gradient $\Delta T/d$ and to an electric tension of frequency f and an effective voltage V_e. In Boussinesq approximation, the governing flow equations read (Mutabazi et al. 2016).

$$\nabla\cdot\mathbf{u} = 0 \qquad (1\text{-a})$$

$$\frac{\partial \mathbf{u}}{\partial t} + (\mathbf{u}\cdot\nabla)\mathbf{u} = -\nabla H + \nabla^2\mathbf{u} + \mathbf{B} \qquad (1\text{-b})$$

$$\frac{\partial \theta}{\partial t} + (\mathbf{u}\cdot\nabla)\theta = \frac{1}{Pr}\nabla^2\theta \qquad (1\text{-c})$$

$$\nabla\cdot\{(1-\gamma_e\theta)\mathbf{E}\} = 0, \quad \mathbf{E} = -\nabla\phi \qquad (1\text{-d})$$

where $\mathbf{u}$ is the velocity field, H is the generalized Bernoulli function, θ is the temperature field and $\mathbf{E}$ is the effective electric field and ϕ is the electric potential. The buoyancy term is given by

$$\mathbf{B} = \frac{1}{\mathrm{Pr}}\left(Ra\boldsymbol{e}_z - L\frac{\boldsymbol{g}_e}{\bar{g}_e}\right)\theta \qquad (2)$$

where $\boldsymbol{g}_e$ is the electric gravity and $\bar{g}_e$ represents the electric gravity in the centre of the cavity. The first term represent the Archimedean buoyancy while second term is the electric buoyancy. In case of long cavity (i.e. with a large aspect ratio Γ = L/d >> 1), the system of equations (1) has asolution which describes the conduction state and depends only on the z coordinate. It is given by

$$\theta(z) = -\beta z;\ \ W(z) = \frac{\gamma_a g}{6\nu}\frac{z}{d}\left(z^2 - \frac{d^2}{4}\right), E = -\frac{E_1}{1+\beta z} \qquad (3)$$

where

$$E_1 = \frac{\gamma_e V_e}{d}\left[ln\left(\frac{2-\gamma_e}{2+\gamma_e}\right)\right]^{-1} \text{ and } ,\gamma_a = \alpha\Delta T, \gamma_e = e\Delta T.$$

Linear stability results

Infinitesimal perturbations superimposed to the base state (3) are substituted into the equations (1) and then expanded into normal modes:

$$\left(\boldsymbol{u}', \boldsymbol{H}', \theta', \boldsymbol{\phi}'\right) = \left(\hat{\boldsymbol{u}}, \hat{\boldsymbol{H}}, \hat{\theta}, \hat{\boldsymbol{\phi}}\right) exp\left(st + ik_x x + ik_y y\right) \quad (4)$$

where s = σ-iω, k_x and $_{ky}$ are the wavnumbers, σ is the growth rate and ω is the perturbation of the perturbation.

The boundary conditions require that perturbations vanish at the boundaries. Solving the resulting eigenvalue problem is equivalent to finding the characteristic equation

$$F\left(Ra, L, Pr, \sigma, \omega, k_x, k_y\right) = 0 \qquad (5)$$

The linearized system of equations is solved with in-house code using discretization scheme and a Thebychev spectral collocation method [2]. Here are the main results:

1. For $L < L_c = 2128.7$, critical modes are stationary ($\omega = 0$) hydrodynamic modes for Pr < 12.45 and oscillatory thermal modes ($\omega \neq 0$) for Pr > 12.45. The hydrodynamic and thermal modes have periodicity in the x-diretion (i.e. $k_x \neq 0$) and are invariant in the y-direction ($k_y = 0$).
2. For $L \geq L_c$, critical modes are independent of Pr and occur in ofrm of stationary modes with a periodidity in the y direction (i.e.$k_y \neq 0$) and invariant in the x-direction (i.e. $k_x = 0$). These modes are represented by vertical vortices like columnar vortices obtained in cylindrical annulus under dielectrophoretic and Archimedean buoyancies (Kang et al. 2019).

Conclusions

Three convective (hydrodynamic, thermal and electric) modes are found in a heated vertical cavity with a high-frequency electric voltage.

Acknowledgements

This work was supported by the CNES and the Normandy Region.

References

I. Mutabazi, H. Yoshikawa, M.Tadie Fogaing, O. Crumeyrolle, V. Travnikov,O. Crumeyrolle, B. Futterer, C. Egbers, Thermo-electro-hydrodynamic convection under microgravity: a review, *Fluid Dyn. Res*. **48** (2016), 061413.

2. H. Yoshikawa, O. Crumeyrolle, I. Mutabazi, Dielectrophoretic force-driven thermal convection in annular geometry, *Phys. Fluids* **25** (2013), 024106.

3. C. Kang, I. Mutabazi, Dielectrophoretic buoyancyand heat transfer in a dielectric liquid contained in a cylindrical annular cavity, *J. Appl. Phys*. **125** (2019).

Poster 075

The Impact of Altered Gravity on Neuronal Activity

Kendrick Solano[1], Jens Hauslage, Ruth Hemmersbach, Christian Liemersdorf[1]

[1]German Aerospace Center (DLR), Institute of Aerospace Medicine, Department of Gravitational Biology, Cologne, Germany
kendrick.solano@dlr.de, christian.liemersdorf@dlr.de

Introduction

Learning and memory, cognitive processes and psychomotor functions are major key drivers to accomplish an optimal efficiency of human performance during manned spaceflight missions. Although astronauts are selected to be as the best candidates from a psychological point of view, it has been reported that spaceflight still has profound impacts on several aspects of human physiology. Especially the microgravity environment disturbs cognitive functions, such as spatial disorientation, disturbances of motor skills, visual illusions, impairments of concentration, and a general slowing-down of task performance (Manzey et al. 2008, Clément 2005). Furthermore, every aspect of human behavior, cognition and performance is based on the neuronal activity generated by billion of neurons, which is processed in the brain and transmitted via electrical activity through functional networks, where the neurons generate electro-chemical signals to relay information across synapses. Thus, altered synaptic neuronal transmission may lead to diminished human performance, while disruptions of neuronal transmissions are the main cause of a variety of mental disorders (Kandel et al. 2013).

Additionally, an excitatory input upon a neuron triggers an event called action potential (AP), which induces a rapid movement of ions across the cell membrane, creating an electrical signal which propagates down the axon causing neurotransmitter release at synaptic junctions (Kandel et al. 2013). Previous experiments with patch-clamping (isolated leech neuron) in the Drop Tower have shown that APs are gravity dependent; demonstrating a tendency to increase the frequency of spontaneous activity under microgravity conditions, due to a shorter latency of APs, thus increasing the excitability of the membranes, and lowering the AP threshold (Meissner et al. 2005). However such a technique is rather sensitive to external perturbances and does not reflect whether microgravity induce transient or long lasting changes. Therefore here we can ask ourselves: what is the impact of different gravity conditions on APs at a short- and long-term scale, and if excitability changes in neuronal networks show gravity dependence?

Outline

The current project aims at studying neuronal transmission changes induced by different gravity conditions, using *in vitro* primary murine neurons, cultured directly atop an electrophysiological system, which is embedded with biocompatible multielectrode arrays (MEA), capable of record and stimulate extracellular electrical signals from excitable cells. The use of neurons *in vitro,* in particular primary neurons from the hippocampus of embryonic E17.5 mice provides an ideal model to study neuronal activity under different gravity conditions. Primary neurons are being used for this project, as they show a very similar development as compared to the physiological development *in vivo* in the brain, forming mature networks including functional synapses.

Moreover, the focus of the project is on understanding the mechanistic contributions of the gravitational unloading on ion channels and synaptic signals to the control of neural networks *in vitro*. Therefore, we are interested in determining how microgravity influences astronaut performance at neuronal network level, as well as how hypergravity could be used as a countermeasure.

Objectives

The overall objective of this project is to develop a platform for the investigation of network behavior in primary neurons under altered gravity. To achieve this, the project aims to:

1. Devise a neuronal culture protocol for MEA chips for optimal cell growth, to increase the physiological maturity, based upon either the use of astrocyte-neuron co-culture with astrocytes plated over coverslips or astrocyte-conditioned medium with a peristaltic pump.
2. Integrate the MEA system to various gravity-research platforms, such as parabolic flights, sounding rockets, drop towers, and the DLR Short-Arm Human Centrifuge. This will enable us to better understand the influence of micro- and hypergravity on neuronal activity for the implications on brain plasticity adaptation and astronaut performance.
3. Develop a pipeline for the analysis offline of the electrophysiological data from the MEA experiments.
4. Study neuronal activity throughout developmental stages - from early stages of synaptogenesis to synaptic network formation onwards, under hypergravity conditions.
5. Study neuronal activity at mature networks under microgravity conditions as well as combining electrical and pharmacological stimulations.

References

G. Clément, Fundamentals of Space Medicine, *Springer* (2005).

E. Kandel, J. Schwartz, T. Jessell, S. Siegelbaum, A. Hudspeth, Principles of Neural Science, *McGraw Hill*, 5th Edition (2013)

D. Manzey, N. Kanas, Space Psychology and Psychiatry, *Springer* (2008).

K. Meissner, W. Hanke, Action potential properties are gravity dependent. *Microgravity Sci. Technol.* 17(2), 38–43 (2005).

26th European Low Gravity Research Association Biennial Symposium and General Assembly
14th International Conference on "Two-Phase Systems for Space and Ground Applications"
European Space Agency Topical Teams meetings
Granada (Spain), September 24-27, 2019

Poster 076

vgBoiling: Study on Gravity Scaling Law of Pool Boiling Phenomena Utilizing VGR of CSS

J. F. Zhao[1, 2], W. F. Du[1], X. Li[3], Z. H. Qiao[3], F. Ye[4], H. Guo[4], H. X. Li[5], J. J. Wei[5, 6]

[1] CAS Key Laboratory of Microgravity (National Microgravity Laboratory), Institute of Mechanics, Chinese Academy of Sciences, Beijing, China; [2] School of Engineering Science, University of Chinese Academy of Sciences, Beijing 100049, China; [3] Technology and Engineering Center for Space Utilization, Chinese Academy of Sciences, Beijing, China; [4] MOE Key Laboratory of Enhanced Heat Transfer and Energy Conservation and Beijing Key Laboratory of Heat Transfer and Energy Conversion, College of Environmental and Energy Engineering, Beijing University of Technology, Beijing, China; [5] State Key Laboratory of Multiphase Flow in Power Engineering, Xi'an Jiaotong University, Xi'an, China; [6] School of Chemical Engineering and Technology, Xi'an Jiaotong University, Xi'an, China
E-mails: jfzhao@imech.ac.cn; duwangfang@imech.ac.cn

Boiling heat transfer realizes the high-performance heat exchange due to latent heat transportation, resulting in its wide applications for high heat flux transfer both on the Earth and in space. It is also a complex and elusive process. Thus, a great amount of empirical correlations and semi-mechanistic models for engineering applications, which are mainly depended upon empirical data obtained from elaborately designed experiments, flood in the literature up to now. Although many empirical correlations and semi-mechanistic models include gravity as a parameter, they usually fail when extended beyond the range of gravity levels they were based on, namely 1g, high-g and low-g.

It is well known that gravity strongly affects boiling phenomenon by creating forces in the systems that drive motions, shape boundaries, and compress fluids. Furthermore, the presence of gravity can mask effects that ever present but comparatively small in normal gravity environment. Advances in the understanding of boiling phenomenon have been greatly hindered by masking effect of gravity.

Microgravity experiments offer a unique opportunity to study the complex interactions without gravity. On the progress in this field, many comprehensive reviews are available now. For example, Straub (2001), Di Marco (2003), Kim (2003, 2009), Ohta (2003), Zhao (2010), among many others, summarized the experimental and theoretical works all over the world.

There is, however, obvious incomparability between the results of different experiments on boiling phenomenon by different authors or even the same authors. This makes the boiling experiments in different gravity conditions often fail to reveal the gravity effect correctly. Raj et al. (2012a) presented a unified framework for scaling heat flux with gravity and heater size based on experimental results acquired for transition periods of approximately 3–5 s when the acceleration varied continuously from hypergravity to low-g and vice versa during parabolic flights. The gravity scaling parameter for heat flux was updated based on high quality microgravity data aboard ISS (Raj et al. 2012b), and its robustness in predicting low gravity heat transfer is further demonstrated by predicting many of the trends in the pool boiling literature that cannot be explained by any single model.

There are still several unsolved problems in the model of Raj et al. (2012a, b). The definition of the dimensionless temperature involves the temperatures of the boiling incipiency and of the critical heat flux (CHF), but the model didn't give a clear rule of their variations with gravity. It implicitly assumed unchangeable values for these two characteristic temperatures in different gravity conditions. There is no theoretical or empirical basis for this assumption. Moreover, recent numerical studies utilizing the lattice Boltzmann method showed that the temperature of CHF decreases with the gravity level (Ma et al. 2017; Feng et al. 2019). Thus, more theoretical and experimental studies are needed on this topic.

A new project, vgBoiling – gravity scaling law of pool boiling heat transfer and relevant bubble thermal dynamic behaviors, has been proposed and passed the relevant expert review. It will be conducted utilizing the Variable Gravity Rack (VGR) aboard the Chinese Space Station (CSS) in the near future.

Fig. 1 shows overview of the VGR (Wang et al. 2019). The VGR has two centrifuges with diameters of 900 mm and can provide the gravity range from 0.01 g_0 to 2 g_0, where g_0 denotes the gravity on Earth.

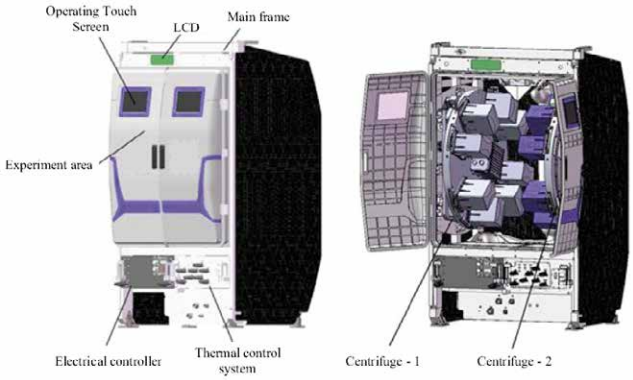

Figure 1: Overview of the VGR.

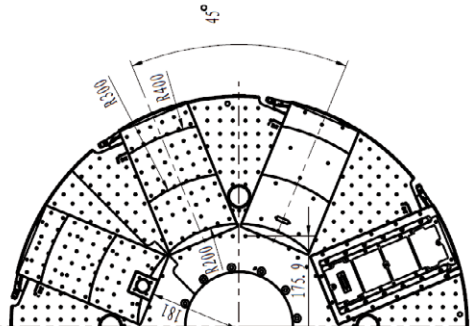

Figure 2: Topview of the centrifuge with standard experimental loads.

The centrifuge is the most important device of the VGR, which can rotate with a certain and varying speed to simulate a variable gravity level. Experiment loads will be locked on the top of the rotator (Fig. 2). A standard experiment load consists of a self-locking part, a container and several connecting rods that can realize the specific motion along radial and axial directions on the centrifuge.

There are two standard experiment loads, namely E-box and C-box, for vgBoiling (Fig. 3). Inside the E-box, there are a boiling chamber (Fig. 4) and a high-speed CCD. A pre-DAB with a novel integrated micro heater is fixed inside the boiling chamber. The integrated micro heater is fabricated by using MEMS technique. The substrate of the integrated micro heater is a $10 \times 10 \times 2$ mm^3 quartz glass wafer. On the back surface of the quartz glass wafer, a serpentine strip of platinum film acts simultaneously as the main heater to provide the input power for maintaining the boiling process and the temperature sensor to measure the average temperature on the back surface. 5 pulse bubble triggers for exciting bubble nuclei by using the method of local overheating are located on the top surface of the integrated micro heater. They can be activated independently and thus can realize different experimental modes including single-, double-, and multi-bubble boiling, as well as normal pool boiling in which no bubble trigger is activated. There are local temperature sensors on the top surface to measure the local temperature distribution underneath the growing bubble(s). Furthermore, inside the quartz glass wafer, there are also several local temperature sensors, which provide more detail information of three dimensional distribution of local temperature in the heating solid and then are more helpful to reveal the influence of the heater thermal parameters on pool boiling performance.

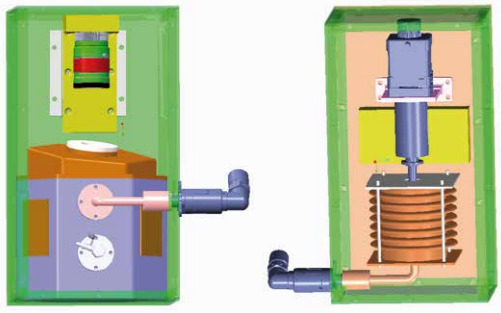

Figure 3: E-box (left) and C-box (right) for vgBoiling.

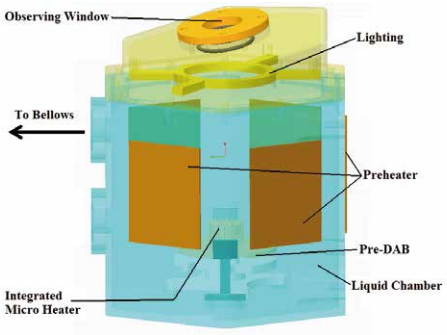

Figure 4: Boiling chamber.

A beryllium bronze bellows, which is fixed in the C-box and connected with the boiling chamber fixed in the E-box, acts as a pressure regulator to maintain the pressure inside the chamber approximately constant during the preheating and boiling processes with the help of constant background pressure environment inside the VGR.

The research contents of this project include: 1) Normal pool boiling in different gravity, focusing on the gravity scaling law of pool boiling heat transfer; 2) Single bubble boiling in different gravity, focusing on bubble dynamics and the influence of the heater thermal parameters on bubble growth and heat transfer performance; 3) Double bubble boiling in different gravity, focusing on bubble dynamics and the interaction mechanism between adjacent nucleation sites; 4) Multiple bubbles in different gravity, focusing on bubble dynamics and the effect of the number density of activated nucleation sites on boiling heat transfer.

The project of vgBoiling is presently in the phase of scheme demonstration. The device of vgBoiling will be installed on the VGR and launched with the CSS Experiment Capsule I "Wentian (WT)" in 2021. Further study is still ongoing.

Acknowledgements

The present study is supported financially by the National Natural Science Foundation of China (NSFC) under the grant of U1738105.

References

P. Di Marco, Review of reduced gravity boiling heat transfer: European research, *J. Jpn. Soc. Microgravity Appl.* 20(2003) 252–263.

Y. Feng, H. Li, K. Guo, X. Lei, J. Zhao, Numerical study on saturated pool boiling heat transfer in presence of a uniform electric field using lattice Boltzmann method, *Int. J. Heat Mass Transfer* 135(2019) 885–896.

J. Kim, Review of nucleate pool boiling bubble heat transfer mechanisms. *Int. J. Multiphase Flow* 35(2009) 1067-1076.

J. Kim, Review of reduced gravity boiling heat transfer: US research, *J. Jpn. Soc. Microgravity Appl.* 20(2003) 264–271.

X. Ma, P. Cheng, S. Gong, X. Quan, Mesoscale simulations of saturated pool boiling heat transfer under microgravity conditions, *Int. J. Heat Mass Transfer* 114(2017) 453–457.

H. Ohta, Review of reduced gravity boiling heat transfer: Japanese research. *J. Jpn. Soc. Microgravity Appl.* 20(2003), 272–285.

R. Raj, J. Kim, J. McQuillen, On the scaling of pool boiling heat flux with gravity and heater size, *J. Heat Transfer* 134(2012a) 011502.

R. Raj, J. Kim, J. McQuillen, Pool Boiling Heat Transfer on the International Space Station: Experimental Results and Model Verification, *J. Heat Transfer* 134(2012b) 011504.

J. Straub, Boiling heat transfer and bubble dynamics in microgravity. *Adv. Heat Transfer* 35(2001) 57–172.

S. K. Wang, K. Wang, Y. L. Zhou, B. Yan, X. Li, Y. Zhang, W. B. Wu, A. P. Wang, Development of the Varying Gravity Rack (VGR) for the Chinese Space Station, *Microgravity Sci. Technol.* 31(2019) 95-107.

J.F. Zhao, Two-phase flow and pool boiling heat transfer in microgravity. *Int. J. Multiphase Flow* 36(2010) 135-143.

26th European Low Gravity Research Association Biennial Symposium and General Assembly
14th International Conference on "Two-Phase Systems for Space and Ground Applications"
European Space Agency Topical Teams meetings
Granada (Spain), September 24-27, 2019

Poster 080

Statolith displacement in root statocytes in real and simulated microgravity

E. Kordyum, V. Brykov

Institute of Botany, National Academy of Sciences of Ukraine, Kyiv, Ukraine
cellbiol@ukr.net

Introduction

To simulate biological effects of microgravity in space flight, different ground-based facilities – slow and fast 2D clinostats, Random Positioning Machine, Free Fall Machine and magnetic levitation – are widely used (Beysens et al. 2011; Herranz et al. 2013) as experiments in "real *μg* are scarce, costly and time consuming" (Krause et al. 2018). Capacities and limitations of various devices to accurately and reliably simulate microgravity conditions, comparable to real microgravity in space, are constantly discussed (van Loon 2007; Herranz et al. 2013; Shinde et al. 2016). Recent comparative studies of the quality of microgravity simulation provided by different operational modes have shown the greatest suitability of fast 2D clinorotation for investigating the graviperception mechanism in *Chara* rhizoids in comparison with slower 2D and 3D clinorotation, and rotation of samples around two axes (Krause et al. 2018). In the given paper, we compare the position of amyloplasts–statoliths in root cap statocytes of higher plants under 1 g, slow and fast 2D clinorotation, real microgravity in space flight, vibration and acceleration in spacecraft launch mode using own and literary data.

1g conditions

Root cap statocytes in angiosperm plants are highly specialized graviperceptive cells and characterized by the structural polarity shown by the position of a blade-shape nucleus in the proximal part of the cell and the endoplasmic reticulum (ER) complex in its distal part, not all investigated species have a massive ER complex. Amyloplasts performing a statolithic function sediment in the distal part of the statocytes in the direction of the gravitational vector at some distance from the plasmalemma and thus not in contact with it (Volkman and Sievers 1979).

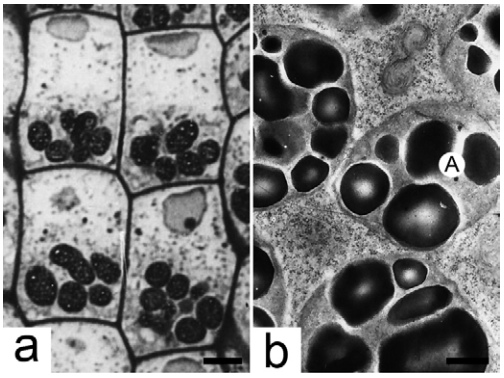

Fig. 1. *Beta vulgaris*. a – general view of statocytes, b – amyloplasts. Scale bar: a – 5 μm, b – 0.5 μm.

This polar arrangement of organelles is achieved and maintain by means of the cytoskeleton (Hensel 1984, 1988). Results of our investigations of *Beta vulgaris, Brassica rapa* and *Pisum sativum* correspond to literary data and show that amyloplasts are in close contact each other with the outgrowths of the outer membrane of the organelle envelope (Fig. 1, a, b).

Vibration and acceleration

To analyze the impact of vibration and acceleration in the space craft launch mode, *P. sativum* seedlings were placed on the installation modeling dynamic factors of space flight in the N.I. Vavilov Institute of General Genetics RAN within 8 min and fixed directly after exposure. Unlike control, mainly round amyloplasts distributed throughout the cytoplasm contacting with the plasmalemma, lomasomes, ER cisterns, and a nucleus.

μg conditions

Histogenesis and cell differentiation in the embryonal root cap of investigated plants occurred normally in real microgravity in space flight as in other species (Volkman et al. 1986; Kiss 2000; Kordyum and Chapman 2007; Perbal 2009; Kordyum 2014). A nucleus was situated in the proximal part of a cell. Amyloplasts, which did not sediment in the distal part of a statocytes in the absence of the gravitational vector, mainly concentrated in the center of a statocyte, organelles could contact in this case, and rarely in the other parts without contacting the plasmalemma (Fig. 2, a,b). There was an increase in vacuolization of the cytoplasm.

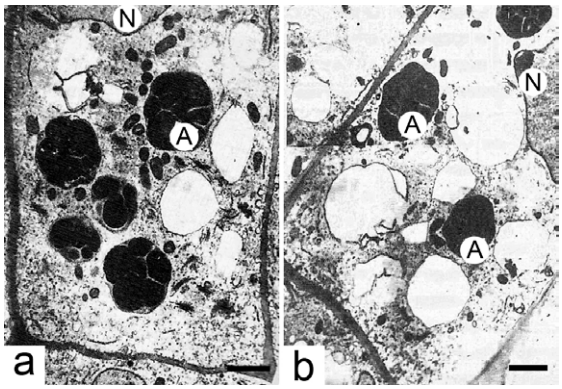

Fig. 2. Statocytes of *Brassica rapa*. a – amyloplasts occupy the cell center, b – scattered amyloplasts. Scale bar 2 μm.

Slow 2D clinorotation (2–5 rpm)

Amyloplasts singly or in groups were situated in different parts of a statocyte, particularly in the nucleus zone,

sometimes showed a tendency to concentrate in the cell center (Fig. 3,a,b). Organelles in groups could touch each other being at some distance from the plasmalemma. Progressive vacuolization of the cytoplasm also occurred.

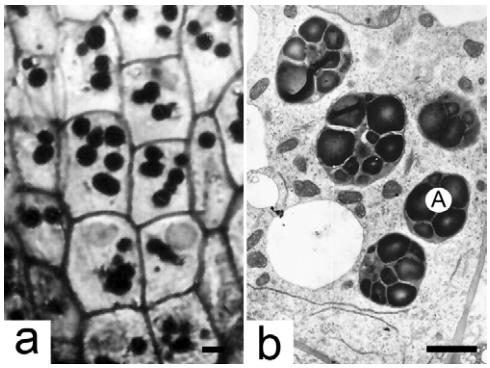

Fig 3. *Beta vulgaris*. a – general view of statocytes, b – amyloplasts. Scale bar: a – 10 µm, b – 5 µm.

Fast 2D clinorotation (50 rpm)

Distribution of amyloplasts throughout the cytoplasm of statocytes partly resembled this. under action of vibration and acceleration. Amyloplasts contacted directly with the plasmalemma or with lomasomes – more or less complex invaginations of the plasmalemma into the cytoplasm, also with a nucleus and ER cisterns, what was the distinguishing feature of amyloplast behavior under fast clinorotation. Most amyloplasts were oval in shape, often one end of organelles narrowed in various degrees, sometimes in the form of an elongated "spout", which contacted with the plasmalemma (Fig 4 a–d).

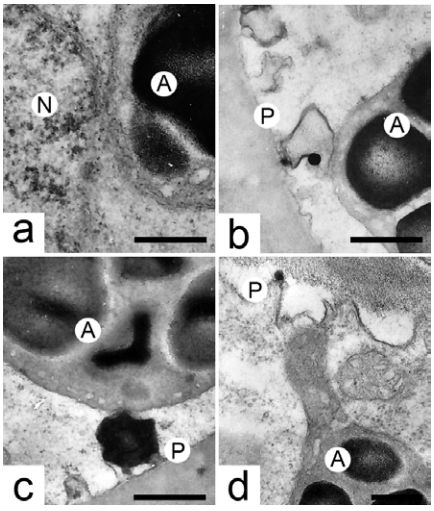

Fig. 4. *Pisum sativum*. Contacts of amyloplasts with the nucleus (a), lomasomes (b, c), plasmalemma (d). Scale bar 0.5 µm.

Conclusions

A comparison of the amyloplast behavior in root cap statocytes in real microgravity and under different speeds of horizontal clinorotation shows that slow 2D clinorotation is the most appropriate tool for its simulation in ground-based experiments. The differences in statolith responses to various modes of microgavity simulation in *Chara* rhizoids and roots of higher plants can be explained by 1) the nature of statoliths – compartments filled with crystallites of barium sulfate in *Chara* and cell organelles in roots of higher plants; 2) unequal sizes of rhizoids and roots, the last are larger and, although seedlings were located strictly on the axis of rotation, may deviate from the axis and perceive acceleration.

References

D. Beysens, L. Carotenuto, J. van Loon, M. Zell, Laboratory Science with Space Data (2011) Springer, Berlin.

W. Hensel, A role of microtubules in the polarity of statocytes from roots of *Lepidium sativum* L., *Planta* 162 (1984) 404-414.

W. Hensel, Demonstration by heavy meromyosin of actin microfilaments in extracted cress (*Lepidium sativum* L.) root statocytes, Planta 173 (1988) 142–143.

R. Herranz, R. Anken, J. Boonstra et al., Ground-based facilities for simulation of microgravity: organism-specific recommendations for their use, and recommended terminology, *Astrobiology*, 13 (2013),1–17.

J. Kiss, Mechanisms of the early stages of plant gravitropism, *Critical Rev. in Plant Sci.* 19 (2000) 551–573.

E. Kordyum, D. Chapman, Plants in Space (2007) Academperiodica Kyiv.

E. Kordyum, Plant cell gravisensitivity and adaptation to microgravity, *Plant Biol*. 16 suppl.1 (2014) 79–90.

L. Krause, M. Braun, J. Hauslage, R. Hemmersbach, Analysis of statolith displacement in *Chara* rhizoids for validating the microgravity-simulation quality of clinorotation modes, *Microgravity Sci. Techn.* 30 (2018) 229–236.

G. Perbal, From ROOTS to GRAVI-1: twenty five years for understanding how plants sense gravity, *Microgravity Sci. Techn*., 21 (2009) 3–10.

V. Shinde, S. Brungs, M. Henry et al., Simulated microgravity modulates differentiation processes of embryonic stem cells, *Cell Physiol*. *Biochem*. 38 (2016)1483-1499.

J. van Loon, Some history and use of the random positioning machine, RPM, in gravity related research, *Adv. Space Res.* 39 (2007) 1161–1165.

D. Volkman, H. Behrens, A. Sievers, Development and gravity sensing of cress roots under microgravity, *Naturwissenschaften* 73 (1986) 438–441.

D. Volkman, A. Sievers, Graviperception in multicellular organs, *Encycl. Plant Physiol*. New Ser. 7 (1979) 573–600.

S. Wuest, S. Richard, S. Kopp et al., Simulated microgravity: critical review on the use of random positioning machines for mammalian cell culture, *Biomed Res Int.* doi: 10.1155/2015/971474.

26th European Low Gravity Research Association Biennial Symposium and General Assembly
14th International Conference on "Two-Phase Systems for Space and Ground Applications"
European Space Agency Topical Teams meetings
Granada (Spain), September 24-27, 2019

Poster 084

Impact of clinorotation on microtubule regulation by tubulin-associated proteins in plants

G. Shevchenko

Institute of Botany, NAS Ukraine, Tereshchenkivska 2, 01004,

Kiev, Ukraine, e-mail: galli.shevchenko@gmail.com

Introduction

Plant cytoskeleton is highly dynamic structure responsible for cell division, growth and reaction to environmental stimuli. Dynamic nature of the cytoskeleton makes plants highly adaptive to changes. Functioning of two main cytoskeleton components (microtubules (MTs) and actin filaments (AFs) and their dynamic nature is facilitated by numerous associated proteins. Among them are MAP65-1, CLASP and Phospholipase D delta (PLD) known to bundle antiparallel MTs, regulate microtubule plus-end dynamics and stabilize cell wall-plasma membrane-cytoskeleton continuum. Evolutionally development of plant cell cytoskeleton took place under constant 1-g, and it is known that MTs tend to orient along mechanical tension promoting cell form, growth orientation and metabolic processes. However, clear picture of the cytoskeleton dynamics and its regulation is not totally defined. In order to clarify details of plant cytoskeleton regulation, we assume that remove of constant g-impact might decipher details of MT functioning. Therefore, we applied clinorotation and pharmacological approach (tubulin polymerization inhibitor oryzalin (OR)) and investigated *Arabidopsis thaliana* root growth and expression of *TUB6, ACT2, MAP65-1, CLASP* and *PLD delta* after 3 day treatment. Oryzalin was applied in order to enhance MT and AF disorganization which presumably occurred upon clinorotation (Shevchenko et al. 2007; 2009).

Materials and methods

A.thaliana seedling were germinated for 3 days on MS medium and then subsequently transferred on slow rotating (2rpm) 2D clinostats and treated by oryzalin (OR). There were 4 experimental sets: control, control + OR, clinostat and clinostat+OR. Seedlings were treated during 3 days and then proceeded for RNA extraction and qPCR reaction. In each set of experiment expression of *TUA6, ACT2, MAP65-1, CLASP* and *PLD delta* were analyzed both in plants on clinostats and after addition of oryzalin (10uM).

Results and discussion

Network of cortical microtubules (cMTs) undergoes reorganization upon various stresses and it still remains unclear how parallel orientation of MTs in cortical arrays is controlled and what determines whether an array will be oriented transverse or longitudinal relative to the cell axis. Fine network of AFs is co-localized with MTs and is also affected by external stimuli. Fine tuning of all cytoskeletal elements is aimed on plant adaptation to changed surroundings. Our experiments have shown that *A.thaliana* growth was impaired after both type of treatment, clinorotation and addition of oryzalin (Fig.1).

impact of either clinorotation or both factors on tubulin activity we have analysed expression profiles of *TUA6, ACT2, MAP65-1, CLASP* and *PLD delta*. Factorial analysis ANOVA has revealed that clinorotaton has not affected neither tubulin, not actin gene expression. Oryzalin treatment affected expression of *TUA6, MAP65-1* and *ACT2* evidencing MT disorganization and involvement of MAP65-1 and actin in this process, and therefore, revealing role of these proteins in MT stabilization in control. Thus, one could say that activity of MAP65-1 and actin depends upon the state of MTs (Shevchenko et al. 2008). It should be mentioned that in our previous investigations, application of actin disruptor cytochalasin D also affected both *TUA6* and *ACT2*. Above suggested interrelation between MTs and AFs in growth regulation (Shevchenko et al. 2008; 2009).

At the same time, interaction of both factors – clinorotation and OR does not impact *MAP65-1, CLASP* and *PLD delta* but affected *ACT2*. And this also proves mutual interrelationship between MTs and AFs. It is not excluded that such type of interrelation is regulated in a different way on clinostats.

Conclusions

Analysis of transcripts has shown that clinorotation does not affect expression of *TUA6, ACT2, MAP65-1, CLASP* and *PLDdelta.* At the same time, simultaneous application of both factors – clinorotation and oryzalin changed expression of *ACT2*. Above suggested mutually dependent functioning of cytoskeletal elements (MTs and AFs) and its different regulation upon influence of altered gravity. Our investigation contributes into understanding of plant cell growth regulation by mechanical stress and it helps to clarify cytoskeleton involvement in the mechanism of gravity signaling in plants.

References

G. Shevchenko, Ya.M. Kalinina, E.L.Kordyum, Interrelation between microtubules and microfilaments in the elongation zone of *Arabidopsis* root under clinorotation, Adv.Space Res. 39 (2007) 1171-1175.

G. Shevchenko, Ya.M. Kalinina, E.L.Kordyum, Tubulin cytoskeleton in *Arabidopsis thaliana* root cells under clinorotation, Microgravity Sci. and Technology 21 (2009) 187-190.

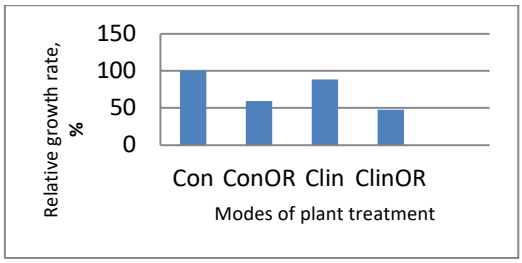

Figure1. Relative growth rate of *A.thaliana* seedlings on clinostats and addition of oryzalin

Common action of clinorotaton and OR affected root growth more severe. In order to decipher

26th European Low Gravity Research Association Biennial Symposium and General Assembly
14th International Conference on "Two-Phase Systems for Space and Ground Applications"
European Space Agency Topical Teams meetings
Granada (Spain), September 24-27, 2019

Poster 085

New results on the dynamic features of surfactant adsorption layers at water-oil interface from the FASTER experiment

Libero Liggieri[1], Francesca Ravera[1], Eva Santini[1], Giuseppe Loglio[1], Piero Pandolfini[1], Reinhard Miller[2], Jürgen Krägel[2], Alexander V. Makievski[3], Alexey G. Bykov[4], Boris A. Noskov[4] ,Volodimir I. Kovalchuk[5]

[1] CNR ICMATE, Genova, Italy; [2] MPI KGF, Golm, Germany; [3] Sinterface Technology, Berlin, Germany;
[4]St.Petersburg State University, Russia; [5] Institute of Biocolloid Chemistry, Kiev, Ukraine.
libero.liggieri@ge.icmate.cnr.it

The experiment FASTER, housed in the Columbus EDR and executed within the ESA MAP project "Fundamental and Applied Studies in Emulsion Dynamics – FASES", provided a huge set of data about the adsorption of surfactants at the water-oil interface. In fact, despite the experiments were concluded already in 2014, the elaboration/interpretation of all available data sets is yet not concluded. Based on Capillary Pressure tensiometry, adsorption kinetics and dilational viscoelasticity (the response of surface tension to extension/compressions of the interfacial area) of the adsorption layer were accurately measured, exploring the effects of the time-characteristics and intensities of the area perturbations, of the temperature and of the surfactant concentration. The experiments involved either single surfactants or mixtures of surfactants variably soluble in the aqueous and oil phases. Exploiting the purely diffusive mass transport conditions set by the microgravity environment, these data are useful to test and derive models for the interfacial features of adsorption layers which will find application in practical problems related to the utilization of surfacants, such as, for example the formulation of efficient additives for emulsions or foams stabilization or destabilization.
Here we recall the principles of the FASTER experiments and summarize new results obtained from the elaboration/interpretation of the data from the above experiments.

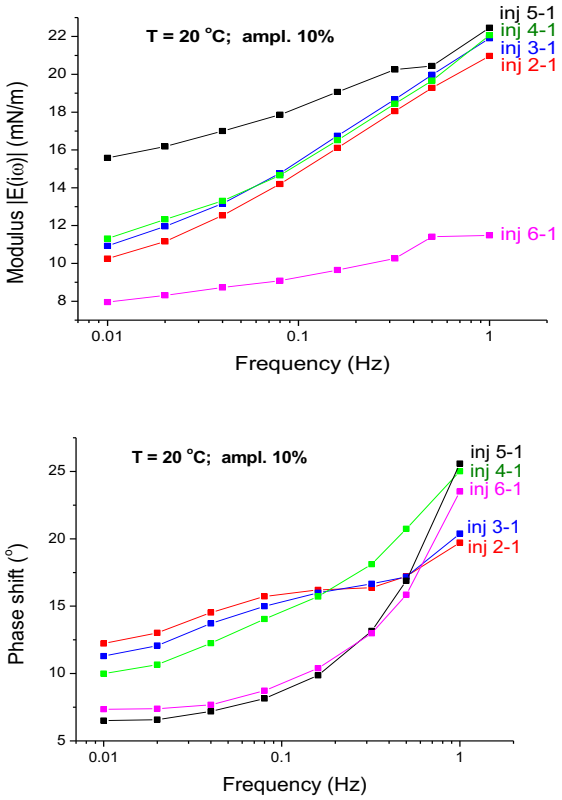

Figure 1: Measured modulus and phase of the dilational viscoelasticity, as a function of the frequency of the area perturbation, at the interface between hexane and aqueous solutions of mixtures of the non-ionic surfactant C13DMPO (variable concentrations, corresponding to the different plotted curves) and the cationic surfactant TTAB (fixed concentration).

Acknowledgements
ESA MAP Projects "Soft Matter Dynamics" and "Emulsion Dynamics and Droplet Interfaces -EDDI".
Contract no. 4770238802716000051O from the Russian Federation.

References:
G. Loglio et al., Dynamic Properties of Mixed Cationic/Nonionic Adsorbed Layers at the N-Hexane/Water Interface: Capillary Pressure Experiments Under Low Gravity Conditions. *Colloids Interfaces* 2 (2018) 53.

P. Pandolfini et al. Dynamic properties of Span-80 adsorbed layers at paraffin-oil/water interface: Capillary pressure experiments under low gravity conditions. *Colloids and Surfaces A: Physicochemical and Engineering Aspects* 532 (2017) 228-243.

Poster 087

Cell cycle's and growth's aspects for created of bioregenerative lifesupport systems.

Olga A. Artemenko
Institute of Botany NAS of Ukraine, Kyiv, Ukraine
oartemenko66@gmail.com

Introduction

The exploration of the influence of microgravity on living systems at cellular and molecular levels, as well genetic stability, growth, development, reproduction, aging, life span, behaviour and orientation of animals and plants is the basic of understanding of general biological problems of studing the role of gravity in biosphere functioning. In connection with planned future long-term manned missions to Moon (Moon base) and Mars, fundamental and applied questions about the abilities of plants to adapt in the first and next generations to the microgravity conditions in space flight assume ever-greater importance. It is generally accepted that plants are irreplaceable components of Bioregenerative Life-Support Systems, as far as they are sources of oxygen and food for crew, CO2 absorbers, regenerators of water through participation in recycling of organic wastes, and also green design for astronauts' psychological comfort (Kordyum et al. 2017).

As reduced gravity conditions for a long period are available only in an orbiting space vehicle, on Earth different facilities and space simulators are used, e.g. clinostats, random portioning devices, free-fall machines and others (Herranz et al. 2014). Despite some restrictions in simulating the effects of real microgravity of space flight on the ground, e.g. rotation devices in a gravitational field, ground-based facilities are widely used to investigate effects of altered gravity because they allow us to carry out experiments in the necessary time parameters and to use a greater number of analytical methods that are equivalent to the tasks of experiments in spaceflight conditions.

General growth events under altered gravity.

The discovery of plant cell gravisensitivity, which is one of the fundamental achievements of modern biology, is based on the metabolic and structural rearrangement of cells that are both specialised or not specialised for gravity perception in microgravity. It is useful to distinguish between cell graviperception and cell gravisensing: the first implies the active use of a gravitational stimulus by cells specialised for gravity perception, e.g. root and shoot statocytes; gravity perception results in the normal spatial orientation of plants, together with growth and vital activity (gravitropism, gravitaxis), while gravisensing applies to the structure and metabolic stability of cells in a gravitational field that are not specialized to graviperception and changes in microgravity [Kordyum 2014]. The most investigations aimed at solving the fundamental problems of cell biology and are in the knowledge of basic metabolic processes in the cell, growth, development and reproduction of plant organisms in microgravity.

As it is known, cell proliferation and growth are two essential cellular functions, which support plant growth and development and strictly coordinated under ground gravity conditions. In microgravity, cell proliferation appears to enhance, whereas cell growth becomes slower. This process is associated with an increase in the mitotic index (MI) and reducing the duration of the cell cycle with shortening of all interphase periods [Artemenko et al., 2005].

Analyzing the data of proliferative activity of root meristem cells in plants and cell cycle promotion in space flight and clinorotation we can do the following conclusions. The conflicting data about the increase or decrease of proliferative activity caused by the different timing of cell cycle research. During the first cell cycle is an increase the transcription of certain cell cycle genes and delay of transition from G1- phase to phase of DNA synthesis, which leads to a decrease of the proliferative pool. In all experiments we can see that in microgravity conditions and under clinorotation the duration of first cell cycle more than in control. This is due to prolongation of G1- or G2 (post synthetic) - phases in the cycle. However, in the later stages of growth the increase of proliferative activity might indicate the work of recovery and adaptation mechanisms of cell's life support. In addition, clinorotation just simulate some factors of space flight, whereas in a real space flight is added the action of cosmic radiation dose, reduced pressure, noise, vibration, acceleration and other. These differences in the conditions of the described experiments explain the variety of results on this issue, but they help to establish the integrity and completeness of the whole process of the cell cycle in terms of altered gravity and elucidate problems and questions that still need to explore (Artemenko 2017, 2019).

Some cell cycle regulation aspects. TF.

A comparison of the results of protein study and gene's transcription in plants showed a positive, some limited interaction between the regulation of protein synthesis and gene expression in general plant reactions under space flight conditions. The coordinated regulation of the interaction of plant cells is carried out by the synthesis of special hormones (cytokinin and auxin) which cause the signaling cascade in the cells (Herranz et al. 2014, Medvedev 2012, Tank et al. 2014). In the event that the signal leads to changes in the level of gene's expression, the transcript factor (TF) is often the end point of the cascade. TF - is one of the groups of proteins that provides for the reading and interpretation of genetic information. They bind DNA and promote the initiation of a program to increase or decrease transcription of the gene. Thus, they are need for the normal functioning of the body at all levels.

One of the most numerous types of TF plants is MYB-proteins (MYB-myeloblastosis). This family of TF contains proteins that controling such processes as root development, patterning of the leaf, formation of trichomes, cell cycle, circadian rhythms, transmission of a photochromic signal, etc (Ambawat et al. 2013). We analyzed the expression of TF MYB3R3 in *Arabidopsis thaliana* root cells in a stationary meristem of four-day seedlings and in the rudiments of the lateral roots. In conditions of clinorotation observed a loss of TF expression in comparison with control, which may be due to a decrease in the activity of the cell cycle and growth of the root. At the same time, in the rudiments of the lateral roots, when there is a peak of proliferative activity in the places of the formation of lateral roots, the expression of TF is also at a high level in both control and clinorotation. The difference in the size of the lateral roots of control and experiment is due to a later onset of growth of the lateral roots in the clinorotation conditions, which is confirmed by the earlier known data on the reduction of growth parameters in the conditions of the changed gravity (Artemenko 2019).

Conclusions

Results of the spaceflight experiments aboard space shuttles and orbital stations clearly show that although microgravity is an unusual factor for plants, they can grow and develop during space flight from seed-to-seed under more-or-less optimal conditions for plant growth, namely temperature, humidity, CO2, light intensity and direction, and substrate ventilation. In addition, seeds of high quality must be selected so as to achieve 100% germination in microgravity. The obtained data on the influence of clinorotation on the process and duration of the cell cycle phases, as well as subsequent changes in the growth and development of plants in these conditions, and are key in the development of onboard greenhouses and bioregenerative life support systems. Investigating the control of cell cycle events and the interaction between the molecular and cellular mechanisms of these processes is important for understanding undesirable changes in plant growth and development, since the quality and quantity of products that cosmonauts will use depend on it.

References

E.L. Kordyum, D.K. Chapman, Plants and microgravity: patterns of microgravity effects at the cellular and molecular levels, *Tsitol Genet*. 51(2) (2017) 47-58.

R. Herranz, F.J. Medina, Cell proliferation and plant development under novel altered gravity environments, *Plant Biol (Stuttg)* 16 (1) (2014) 23-30.

E.L. Kordyum, Plant cell gravisensitivity and adaptation to microgravity, J. *Plant Biology* 16 (1) (2014) 79-90.

O.A. Artemenko, Expression of δ1- and δ3-cyclins in root meristem cells of *Pisum sativum* L. by clinorotation, *Journal of Gravitational Physiology* 12 (1) (2005) 201-202.

O.A. Artemenko, The start of the cell cycle events in plants by the conditions of altered gravity, *Annals of the Romanian Society for Cell Biology* XXI (3) (2017) 36 – 42.

O. Artemenko, The definition of the cellular and molecular mechanisms of plants gravisensitive, *Front. Physiol. Conference Abstract: 39th ISGP Meeting & ESA Life Sciences Meeting* (2019). doi: 10.3389/conf.fphys.2018.26.00016

S. Medvedev, Physiology of Plants, *BHW-Petersburg* (2012) 512.

J.G. Tank, R. V. Pandya, V.S. Thaker, Phytohormones in regulation of the cell division and endoreduplication process in the plant cell cycle, *RSC Advances* 4 (24) (2014) 12605- 12613.

S. Ambawat, P. Sharma, N.R .Yadav et al., MYB transcription factor genes as regulators for plant responses: an overview, *Physiol Mol Biol Plants* 19 (2013) 307. https://doi.org/10.1007/s12298-013-0179-1

Poster 090

ACE2SPACE - Development of a low-gravity in-flight research environment

Arun Karwal[1], Marcel Verbeek[1], Hans Mulder[2] and Xander in't Veld[2]

[1]NLR Amsterdam, The Netherlands, [2] Delft University of Technology, The Netherlands;
arun.karwal@nlr.nl, marcel.verbeek@nlr.nl, t.j.mulder@tudelft.nl, a.c.intveld@tudelft.nl

Introduction

The Royal Netherlands Aerospace Centre NLR and Delft University of Technology (DUT), Faculty of Aerospace Engineering, together own and operate a modified Cessna Citation II research aircraft, registration PH-LAB. Missions for this aircraft are diverse and include a flying classroom environment, a testbed for new avionics, biofuel experiments and a platform for performing navaid calibration services, for industry and government customers.
Dedicated parabolic flight campaigns have been performed in the past, tailored for specific customers. It was decided to develop a more generic research facility to support low gravity flight testing demands, so that customization for future research campaigns is reduced, thus minimizing costs and maximizing flexibility. ACE2SPACE marks the joint effort of NLR and DUT in providing this upgraded in-flight low gravity facility for the research community.
The paper will discuss the development of this facility and will focus on the development of (a) pilot guidance to accurately fly zero-, Moon- and Mars gravity parabolas, (b) development of a generic cabin layout to accomodate the widest possible range of potential test equipment, and (c) the certification process for aircraft configuration and operational approval for flight tests.

Figure 1: PH-LAB parabolic flight.

Guidance

To fly a zero-g manoeuvre the pilot can use seat-of-the-pants cues or a small object free-floating in the cockpit, to fly the zero-g segment. Using this technique the pilot minimizes deviations from zero-g in the cockpit. Due to the physical dimensions of the aircraft the actual g-environment in the measurement section in the cabin differs a bit. To accurately fly a manoeuvre that minimizes deviations from the desired g-value at the measurement location in the cabin, the pilot will need flight guidance. This is true for zero-g flights, but becomes an absolute necessity for Moon- and Mars parabolas.

Based on earlier research simplified guidance was developed for the low-g portion of the parabola. The guidance is provided to the pilot on Augmented Reality (AR) glasses, and/or on regular pilot displays using an ARINC429 interface.

Cabin layout

The Citation cabin, although limited in size, provides options for a free-float environment for persons, but can also accomodate experiments, a zero-g flying classroom environment, or provide a glove box for fluid experiments. Several generic cabin layouts were identified, each addressing a specific research need.

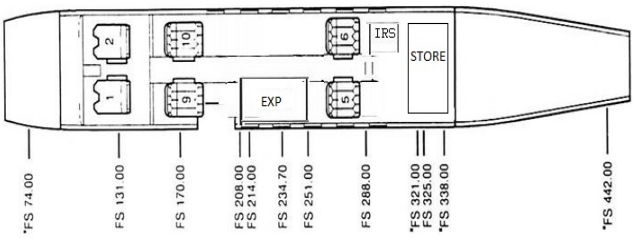

Figure 2: Cabin layout optimized for hosting external experiments

Certification issues

Aircraft configuration changes will always require an approval process through an organization with a Part-21 Design Organization Approval (DOA). NLR/TUDelft can rely on an in-house DOA for aircraft modifications. For the development of a parabolic research facility a blanket approval was sought (and obtained) for the most comprehensive configuration. This approval includes all other possible modifications considered. The aircraft operator now has a variety of options to provide a customized cabin layout to the customer, based on the generic design.
Performing a parabolic manoeuvre may in addition to aircraft certification, require operational approval from the designated CAA. For the development of a parabolic research facility, NLR/TUDelft Flight Operations have been granted a Permit To Fly (PTF) based on the results of a Safety Assessment and development of Instructions for Continued Airworthiness (ICA).

Conclusions

The development of a low-gravity in-flight research facility requires addressing issues in different domains. Pilot guidance development and display, cabin configuration management and certification, and applying for a PTF are addressed in this paper.

26th European Low Gravity Research Association Biennial Symposium and General Assembly
14th International Conference on "Two-Phase Systems for Space and Ground Applications"
European Space Agency Topical Teams meetings
Granada (Spain), September 24-27, 2019

Poster 095

Cytosolic calcium and Ca-ATPase of plant cells respond to simulated microgravity

Olena M. Nedukha 1[1], Elizabeth Kordyum 2[1]

[1] Institute of Botany, Nat. Acad. Sci. Ukraine;
email1: o.nedukha@hotmail.com; email2: cellbiol@ukr.net

Introduction

As the secondary messenger in a plant cell, cytosol calcium is known to respond to changes in vector and level of gravity (Perbal, Driss-Ecole, 2003, Toyota et al. 2008) by increasing the intracellular concentration of calcium ions, followed by activation of the Ca-depending enzymes, gene expression and protein modulation (Hausmann1 et al. 2014; Damm, Egli, 2014). We suggest that the change of calcium balance in plant cells under imitated microgravity is mediated by change of Ca^{2+}-ATPase activity. At the same time detailed studies concerning interconnection of Ca^{2+}-ATPase location and content of free calcium ions in cell roots exposed at imitated microgravity it is not enough studied. Therefore, the aim of our study was to study role of Ca^{2+}-ATPase and calcium ions in adaptation of plant seedlings to imitated microgravity (slow clinorotation). We used the model system - distal elongation roots zone (DEZ) to study the sensitivity of plant cells to horizontal clinorotation. The cells of this zone grow quickly stretching, the most sensitive and auxin, plays a major role in gravitropic reaction seedlings (Ishikawa, Evans, 1995).

1.Mateial and methods

6-day-old seedlings of *Pisum sativum* were grown in the Murasige and Scoog medium at darkness at 21°C, humidity of 70 % on the horizontal clinostat (2 rev/min) and in the stationary control near clinostats. Values for 50-55 seedlings were expressed including the standard error (± SE) for growth signs and cytochemical studies. The clinorotated and control root samples were loaded with a fluorescent calcium-specific dye Fluo-4M (10mM) for study of localization and relative content of calcium. Then the samples were carefully washed with buffer and were analyzed with a confocal microscope LSM 5 Pascal (Carl Zeiss, Germany) at the excision wavelength 488 nm and emission wavelength 516 nm. The cells of cortex first-third layers of DEZ roots were scanned. The "Pascal" program was used for relative quantitative evaluation of calcium ions in cytoplasm, organelles and cell walls. The values and distribution of a fluorescent intensity in the investigated cells were presented as a graph. The experimentation was completely repeatedly three times

Location of Ca^{2+}-ATPase activity in pea cortex root cells was achieved with the electron cytochemical method according to the standard Wachstein and Meisel protocol. The ultra-thin sections cut on an ultra-microtome, and observed using a JEM-1200EX electron microscope. The location of activity ATPase was judged by the presence of electron dense sediment, formed in places of activity of the enzyme. The density of electron cytochemical reaction product (lead phosphate precipitated granules) was determined using the program Image J. 25-30 cells of cortex from one root were used for the analysis. 4-5 roots were used for the morphometric study of the control samples and the appropriate number roots and cells of the clinorotated seedlings, accordingly.

2. Results

2.1. Laser scanning microscopic analysis of distribution and content of calcium in cells

Fluorescent analysis of distribution and content of calcium ions with the confocal microscopy in the presence of specific fluorescent indicator revealed certain changes in Ca relative content in pea root cells in response in altered gravity. In the control samples cells of root DEZ calcium ions in the presence of specific fluorescent indicator (Fluo-4) were brightly fluorescent in green color in cortex cells (Fig. 1a); DNA in nucleus fluoresced in blue color (staining with DAPI). In the cytoplasm of cortex cells the fluorescence intensity of calcium ions was 40 ± 0.37 relative units; in the cell walls and in periplasm space (near cell walls) - 75 ± 0.53 relative units. It was revealed that maximum frequency for fluorescence of calcium was 56977 (pixels, green graph) and the maximum frequency for fluorescence of DNA in nucleus was 182771 (pixels, blue graph) (Fig. 1c).

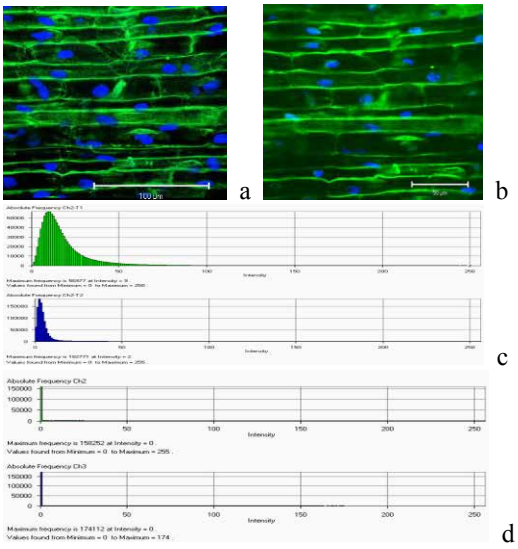

Figure 1. Fluorescence of calcium ions bound to specific indicator Fluo-4 in cortex DEZ cells of pea root visualized with confocal laser microscope in the control (**a)** and after clinorotation (**b**). On the figure **c** (control) and **d** (clinorotation) is shown absolute frequency of pixels for calcium (green graph) and DNA (blue graph).

Under cinorotation, the green fluorescence of free calcium ions and blue fluorescence of nucleus (DNA) was like to that in the control samples (Fig. 1b). However the fluorescence

intensity of complex calcium+Fluo-4 was changed. The level of calcium luminescence in cytoplasm was 67 ± 0.43 relative units and in cell wall and in periplasm space - 133 ± 1.53 relative units. The maximum frequency for calcium was three times more than that in the control samples and it was 158252 (pixels, green graph); the maximum frequency for fluorescence of DNA in nucleus was 174112 (pixels, blue graph) (Fig. 1d**).**

2.2. Electron cytochemical study of Ca^{2+} -ATPase

Electron cytochemical analysis localization Ca^{2+}-ATPase and its intensity in cortex cell of roots revealed significant changes in response of clinorotation. The study of the location of Ca-ATPase activities in the control samples showed that reaction exposed in plasma membrane (PM) and endomebranes: endoplasmic reticulum (ER) and envelope of organelles (Fig. 2a). The electron dense precipitate of the cytochemical reaction was presented by small electron dense granules lead phosphate of 10 nm and more or less. Tonoplast in most cells did not contain the reaction product, and the precipitate was rarely revealed in connection with tonoplast of solitary cells. The value of precipitate density on cellular structures is placed in the following order: PM > ER > tonoplast > vesicles > mitochondria and nucleus (Fig. 3).

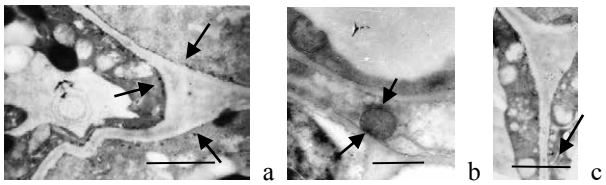

Figure 2. The fragments of pea DEZ root cortex cells in the stationary control (**a**) and clinorotation (**b, c**). Localization of Ca^{2+}-ATPase activity (arrows) in the cells. Bars = 1 μm.

Under clinorotation, the location of Ca^{2+}-ATPase activity in cortex cells was like to that in the control samples (Fig. 1b, c). However, the density of precipitate was significantly more on endomembranes, vesicles and mitochondria, but it was very reduction along of plasma membrane. Quantitative analysis of the density of the granules cytochemical reaction differs is presented on figure 3.

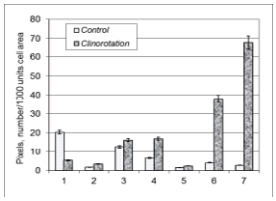

Figure 3. The density of precipitate of the cytochemical reaction (for Ca^{2+}-ATPase activity) in pea cortex DEZ roots grown in the control and under clinorotation. Legend: 1- plasma membrane, 2 – mitochondria, 3 – endoplasmic reticulum, 4 – tonoplast, 5 – nucleus, 6 – vesicles, 7 – membranes of in the zone contact of organelles.

Thus, the received results shown that short-term horizontal clinorotation influenced on calcium level in root cell and this phenomenon is accompanied by decrease activity ATPase on plasma membrane and enhance it activity on membranes of organelles envelope membranes. It is known that transient increases in cytosolic calcium are triggered by the opening of calcium channels (for passive ion influx), Ca^{2+}/H^{+} antiporter and Ca^{2+}-ATPases (for active transporters) (Sanders et al., 2002). Besides, early was established that the content of phospholipids and sterols of plasma membrane separated from pea root of 6-day-old clinorotated seedlings distinguish from that of PM samples of the stationary control (Nedukha et al., 2013) by increase of phytosterols and decrease of some phospholipids. Based on the results of our experimental investigations and the data mentioned above, the following suggests could be made:

1. Under clinorotation the structure and function of plasma membrane change;
2. The calcium channels of plasma membrane and also $Ca^{2+}/2H^{+}$ antiporter change speed (intensity) of one's functioning during imitated microgravity.

Conclusions

It is established the effect of short-term clinorotation on the increase content of calcium in cytoplasm of root cells and the decrease activity of Ca-ATPase on plasma membrane and increases its activity on endo membranes and organelles envelope. These results suggest that Ca^{2+}-ATPase redistribution on membranes it is necessary for the support of optimal calcium balance in cells under adaptation to clinorotation.

References

T.B. Damm, T.B. Egli, Calcium's role in mechano-transduction during muscle development, *Cellular Physiol* and Biochem 33 (2014) 249-271.

H. Ishikawa, M. Evans, Specialized zone of development of roots, *Plant Physiol* 109 (1995) 725-727.

N. Hausmann1, S. Fengler1, A. Hennig1, M. Franz-Wachtel, R. Hampp1, M. Neef, Cytosolic calcium, hydrogen peroxide and related gene expression and protein modulation in Arabidopsis cell cultures respond immediately to altered gravitation: parabolic flight data *Plant Biology* 16 (2014) 120–128.

Ishikawa H, Evans M. Specialized zone of development of roots. Plant Physiol. 1995, 109: 725-727.

T.B. Damm, M. Egli, Calcium's role in mechano-transduction during muscle development, *Cellular Physiology and Biochemistry* 33 (2014) 249-271.

O. Nedukha, E. Kordyum, V. Grakhov, T. Vorobjova, Effects of clinorotation on lipids and sterols content on pea plasmalemma. Abstracts of 13th Ukr Conf on Space Res. Yevpatoria, Crimea, Ukraine, 2-6 Sept. 2013, p 89.

G. Perbal, D. Driss-Ecole, Mechanotransduction in root gravity sensing cells, *Physiol Plantarum* 120 (2003) 303–311.

D. Sanders, J. Pelloux, C. Brownlee, J. Harper, Calcium at the cross roads of signaling, *Plant Cell,* 14 (2002) 401–417.

M. Toyota, T. Furuichi, H. Tatsumi, M. Sokabe, Cytoplasmic calcium increases in response to changes in the gravity vector in hypocotyls and petioles of Arabidopsis seedlings, *Plant Physiology*, 146 (2008) 505–514.

D. Volkmann, A. Sievers A. Graviperception in multicellular organs. In: *Encyclopedia of Plant Physiol*, Springer, Berlin. Eds. Haupt W, Feinleib M., 7 (1979) 573-600.

26th European Low Gravity Research Association Biennial Symposium and General Assembly
14th International Conference on "Two-Phase Systems for Space and Ground Applications"
European Space Agency Topical Teams meetings
Granada (Spain), September 24-27, 2019

Poster 096

About Heat Transfer Hosts

Daniele Mangini[1], Ana Frutos Pastor[2], Balázs Tóth[2], Hans Ranebo[2], Liesbeth De Smet[3] on behalf of ESA's Science, Payload Development and Operations Teams, Science Teams[5] and Space Industries[6]

[1] HE Space Operations BV for ESA, NL-2200AG Noordwijk, The Netherlands, E-mail: daniele.mangini@esa.int
[2] ESA-ESTEC, NL-2200AG Noordwijk, The Netherlands
[3] Space Applications Services for ESA, NL-2200AG Noordwijk, The Netherlands
[5] Science Teams: Aavid Thermalloy (IT), Aerospazio (IT), Air Liquide (FR), AIST (JP), ArianeGroup GmbH (DE), Argotec (IT), AUTh (GR), Beijing University of Aeronautics and Astronautics (CN), Beijing University of Technology (CN), CAS (CN), CCNY (US), CEA (FR), Chongqing University (CN), CSI (DE), Datec Coating (CA), Dream Coating S.A. (BE), Dublin City University (IE), ENEA (IT), ENSMA (FR), EPFL (CH), Eurapo (IT), Euro Heat Pipes (BE), Epsilon (FR), IITK (IN), IMFT (FR), Hexxcell Ltd. (UK), Hephaestus Boiler Makers and Engineering (GR), Interplanetary Expeditions (UK), INSA-LYON (FR), IUSTI (FR), In Quatro srl (IT), KTH (SE), Kutateladze IT (RU), LAPLACE (FR), Liebherr Aerospace (FR), M2P2 (FR), MADIREL (FR), MBSsrl (IT), Nanyang Technological University (CN), NLR (NL), North China Electric Power University (CN), Ònda (IT), Optec (BE), P' (FR), Politecnico di Milano (IT), Promete (IT), Selex ES (IT), Shanghai Jiao Tong University (CN), SIT (JP), SMU (US), Southeast University (CN), Sonaca Space GmbH (GE), Solar Tomorrow Inc. (CA), Sun Yat-sen University (CN), Techno System Developments (IT), Thalès Aliena Space (FR), Trinity College Dublin (IE), TU-Darmstadt (DE), UCLA (US), UFSC (BR), ULB-MRC (BE), ULB-TIPs (BE), UNIHEAT (IT), Vangeel Electrical (BE), Xi'an Jiaotong University (CN), York University (CA), ZARM (DE), Universities of Altai State (RU), Brighton (UK), Edinburgh (UK), Granada (ES), Hirosaki (JP), Illinois (US), Kyushu (JP), Liège (BE), Ljubliana (SI), Loughborough (UK), Maryland (US), Mons-Hainaut (BE), Naples (IT), Nottingham (UK), Ochanomizu (JP), Padova (IT), Pisa (IT), Purdue (US), Toronto (CA), Tyumen State (RU), Utsunomiya (JP)
[6] Space Industries: Airbus Defence and Space (Friedrichshafen, DE), Lambda-X (BE), QinetiQ Space NV (BE)

Introduction

Gas-liquid phase change processes have proved to be challenging to fully understand due, among others, to the intrinsic temporal and spatial scales as well as the masking effect of gravity in laboratory experiments. In coordination with the Two-phase Heat Transfer international topical team, the *European Space Agency* (ESA) established a research plan to tackle those fundamental questions, where reduced gravity experiments could contribute to a more complete scientific understanding of underlying processes. The implementation of the research roadmap is coordinated among space agencies world-wide. ESA's contribution of the coming years to this global effort lies on a series of experiments to be performed on-board the *International Space Station* (ISS), in a series of facilities, called *Heat Transfer Host*s, which are detailed in this publication.

Each of these facilities is designed around a given group of experiment candidates (called *insert*s) that require similar kinds of diagnostic capabilities, power, data management, etc. At the time of the workshop Heat Transfer Hosts 1 and 2 are expected to be in development and Heat Transfer Host 3 is actively prepared for its actual development.

Heat Transfer Host 1

Heat Transfer Host 1 is responsible for experiments in heat pipe like configuration, addressing the fundamentals of evaporation, dryout formation and the functioning of certain heat pipes. The insert candidates are:

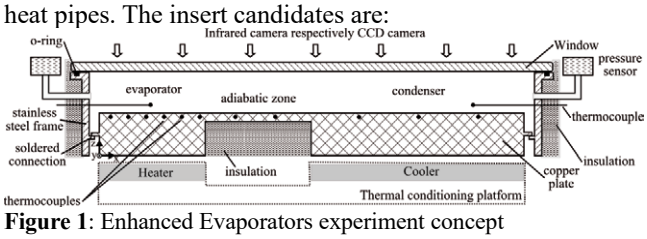

Figure 1: Enhanced Evaporators experiment concept

- *Enhanced Evaporators* (Figure 1) targets global heat transfer performance characterisation of multi-scale evaporator structures. Evaporation regimes, wetted area and consequently the three-phase contact line would be characterised together with the critical heat flux (boiling limit) in a capillary pumped loop.
- *Pulsating Heat Pipes* (Figure 2) aims at studying the thermal performance of such innovative devices in weightlessness, flow pattern analysis and local pressure fluctuation with various working fluids and geometries exploring also inertia dominated regimes in large hydraulic diameter tubes.

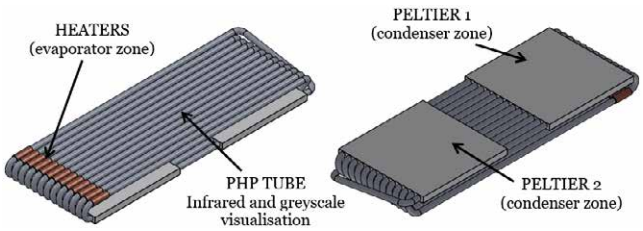

Figure 2: Pulsating Heat Pipes experiment concept

- *Self-rewetting Fluid* (Figure 3) targets the assessment of the heat transfer performances of self-rewetting liquid mixtures, with particular attention to the vapour-liquid interface temperature, the local liquid composition and liquid film thickness distributions as well as film stability and the dry patch formation. The effect of substrate characteristics and different mixtures will be tested in dedicated inserts.

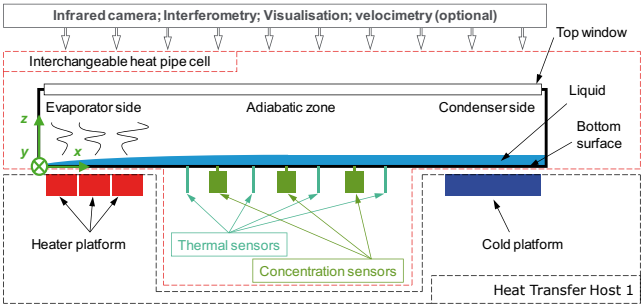

Figure 3: Self-rewetting Fluid experiment concept

Heat Transfer Host 2

Heat Transfer Host 2 is under development by a QinetiQ Space NV lead consortium under ESA contract. The insert candidates are:

- *Drop Evaporation* (Figure 4) will investigate thermocapillary convection and vapour diffusion processes as well as the effect of electric field on a series of evaporating sessile drops.

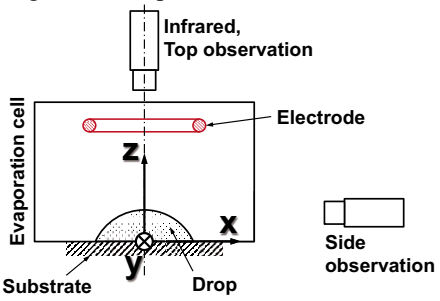

Figure 4: Drop Evaporation experiment concept

- *Condensation on Fins* (Figure 5) targets liquid film thickness distribution characterisation on a single axisymmetric condenser finger for average and local heat transfer coefficient assessment. Surface roughness and the test liquid are among the envisaged experiment parameters. The diagnostics capabilities highlighted in Figure 4 will be used.

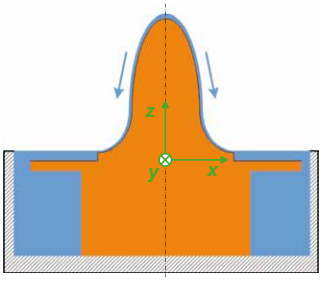

Figure 5: Condensation on Fins experiment concept

- *Marangoni in Films* (Figure 6) aims to better understand heat transport to an evaporating liquid film, through film thickness evolution and dynamics characterisation as well as the vapour concentration distribution. Surfactants are considered as a potential parameter.

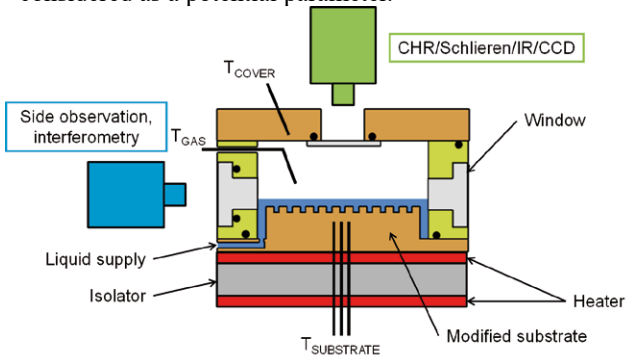

Figure 6: Marangoni in Films experiment concept

Heat Transfer Host 3

The feasibility of Heat Transfer Host 3 is matured by an Airbus Defence and Space lead consortium under ESA contract. The insert candidates, involving convective phase change processes are:

- *In-Tube Condensation* (Figure 7) targets void fraction, flow regime and stability characterisation as well as heat transfer coefficient (distribution) measurements and film thickness measurements for annular flow regime in various shapes of tube cross sections.

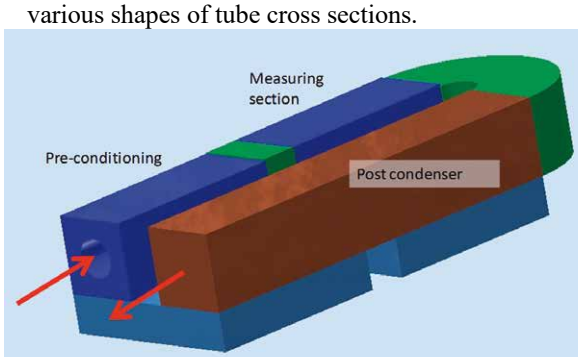

Figure 7: In-Tube Condensation experiment concept

- *Flow Boiling* aims at resolving the local heat transfer coefficient distribution in various flow regimes and correlate it with time resolved film thickness measurements and other flow characteristics (see test section in Figure 8).

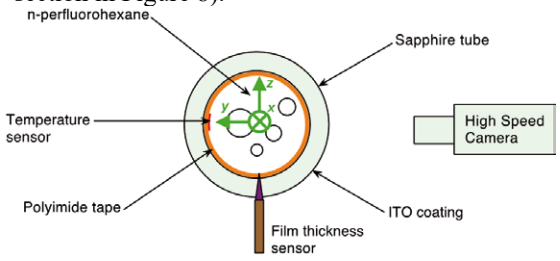

Figure 8: Flow Boiling test section concept

Candidates for future Heat Transfer Hosts

By the time of the preparation of the present abstract the following two experiment candidates have not been assigned to a specific Heat Transfer Host yet, pending programmatic decisions:

- *Boiling* would assess the effect of confinement, shear flow and electric field on a vapour bubble. Particular mixtures and the investigation of non-condensable gas impact are among the most significant objectives.
- *Shear Driven Film* focuses on determining the heat transfer coefficient, liquid dynamics, film thickness evolution, stability and eventual dry spot formation in liquid films under shear flow influence up-to critical heat flux.

It is important to stress that within the capabilities of the realised Heat Transfer Hosts further experiments might also be realised if experiments are proposed by the international topical team through a future ESA Announcement of Opportunity.

26th European Low Gravity Research Association Biennial Symposium and General Assembly
14th International Conference on "Two-Phase Systems for Space and Ground Applications"
European Space Agency Topical Teams meetings
Granada (Spain), September 24-27, 2019

Poster 098

Single bubble pool boiling within micro gravity conditions

Axel Sielaff[1], Matthias Zimmermann[1], Kai Schweikert[1], Philipp Hähnichen[1], Christian Wolf[1], Iman Nejati[1], Julian Krempel[1], Sebastian Kühnemund[1], Peter Stephan[1]
[1]Institute for Technical Thermodynamics, Technische Universität Darmstadt, Darmstadt, Germany
sielaff@ttd.tu-darmstadt.de

Introduction

Boiling is a process for highly efficient heat transfer, which is already used in many technical applications. However, the underlying physical processes are not yet sufficiently understood. Therefore, the design of new processes is subject to very high uncertainties. Furthermore, there are currently no sufficient design guidelines for non-terrestrial applications. For a better understanding of these fundamental physical phenomena, the multiscale boiling project will be carried out in weightlessness on the International Space Station (ISS) in the second half of 2019. In order to support this investigation, the authors are carrying out accompanying investigations as part of the ESA parabolic flight campaigns. This publication presents the results of the 70th and 71st parabolic flight campaigns. The influence of the waiting time between the beginning of the heating power and the nucleation of a single bubble on its growth process is presented, as well as the influence of the electric field and shear flow on the boiling of single bubbles in weightlessness. Further, the influence of the laser initiation on the first bubble is investigated.

Experimental Setup and Procedure

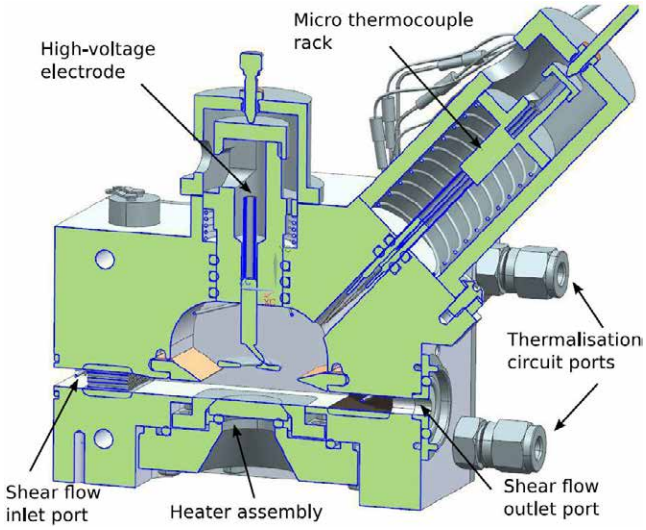

Figure 1: Schematic sketch and picture of the experimental setup.

The experimental setup basically corresponds to the structure of the multiscale boiling project on the ISS. For the execution of the experiments with changing gravity (0 - 1.8g) within parabolic flights, corresponding changes were made to the periphery. The inner part of the boiling cell (see Figure 1) is not modified.
The heater consists of a glass with a sputtered chrome heating layer and is inside the boiling cell. The boiling process is initiated by local overheating of an artificial cavity using a focused laser beam. The temperature distribution of the heater surface is measured by high-speed infrared (IR) thermography while the bubble shapes are observed with a high speed black and white camera. The liquid temperature is measured by standard temperature sensors (type K thermocouples) and a specially developed micro thermocouple rack. Two systems are used to exert forces on the vapor bubbles: an electric field applied by a disc-shaped electrode arranged above the substrate heater and a shear flow generated by a pump. As boiling fluid FC72 is used.
Using numerical simulation as well as the infrared data, high-resolution heat flows from the heater into the fluid are calculated locally and temporally.

Results and Conclusions

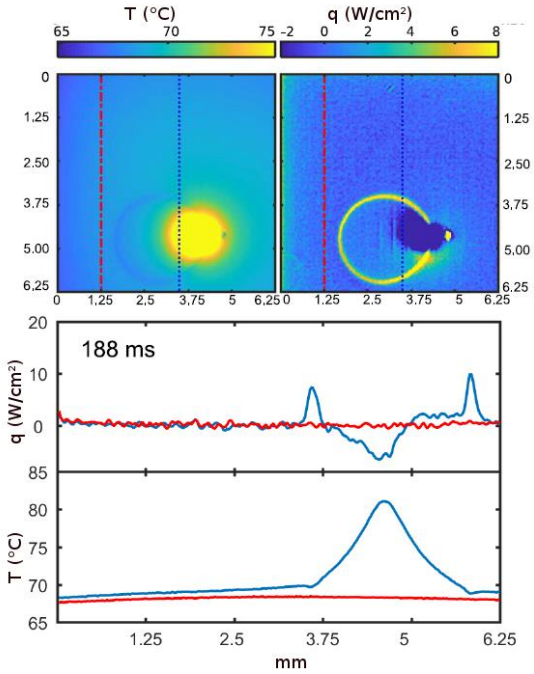

Figure 2: Temperature and heat flux profile for a single bubble. Preheating time = 30 s, laser power = 400 mW, heating power = 1.36 W/cm².

Figure 2 shows the temperature (top left) and heat flow profiles (top right) for the timestep 188 ms after nucleation. The lower part of the graph shows the temperature and heat flux curves for the intersection lines shown in red and blue in the pictures above. It can be seen that the laser leads to a local temperature increase. However, this does not lead to a significant increase in the heat flow into the bubble, since the thermal conductivity of the substrate heater is significantly higher than the vapor of the FC72 used. This can also be seen in Figure 3 in which the bubble diameters for different

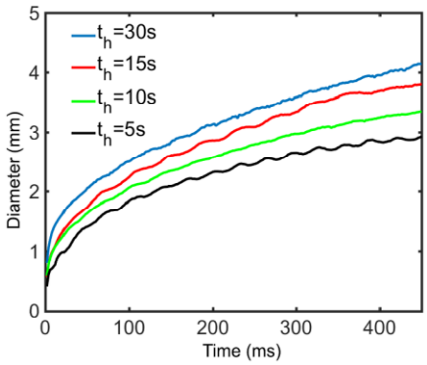

Figure 3: Bubble growth in weightlessness for different preheating times.

preheating times are shown. After switching off the laser (300 ms), no significant change in the bubble diameter can be detected. Numerical estimations show that a maximum of 4% of the power is fed into the bubble. Next to it, a significant influence of the heating time before nucleation on the bubble growth can be seen.

Acknowledgements

We kindly acknowledge the financial support by the German Aerospace Center (DLR) within the "Vapor-project" (50WM1654) and like to express our gratitude for the support of the European Space Agency (ESA) and Novespace. We further like to acknowledge the support by the German Research Foundation (DFG) within the Collaborative Research Centre 1194 "Interaction between Transport and Wetting Processes", in which the work is related to the Projects A01 and C02.

Poster 101

First tests of the capability of the Soft Matter Dynamics facility to produce and study emulsions

Fabrizia Salerni[1+], Angeliki Chondrou[2+], Robert Sütterlin[3], Davide Orsi[1], Eva Santini[4], Francesca Ravera[4], Margaritis Kostoglou[2], Thodoris Karapantsios[2], Libero Liggieri[4], Luigi Cristofolini[1,4*]

[1] –*University of Parma - Italy;* [2] –*Aristotle University Thessaloniki - Greece;*
[3]-*Airbus, Friedrichshafen– Germany;* [4] – *CNR ICMATE, Genova - Italy;*
+ those Authors contributed equally to the work

* - luigi.cristofolini@unipr.it

The study of the stability of emulsions is a subject of enormous technological relevance, with potential impact over various fields, from cosmetics, food and drug, to oil industry, just to mention a few. Emulsions are thermodynamically unstable, and different processes may lead to de-emulsification, the main of which are related to capillary and interfacial properties, such as A) drop coalescence and B) Ostwald Ripening. However, also gravity-related processes such as C) creaming and sedimentation affect emulsion stability, due to crowding of the drops and phase separation. Microgravity experiments may help elucidate the role of A) and B) by excluding C).

The project EDDI (Emulsion Dynamics and Droplet Interfaces), just approved by ESA, aims to a deeper understanding of the role of surfactants in emulsion production and stability, by systematic investigations of emulsions under aging in microgravity conditions. We shall employ the Soft Matter Dynamics facility (SMD, formerly known as FOAM-C) available onboard the International Space Station, whose main diagnostics is the noninvasive optical technique Diffusion Wave Spectroscopy (DWS). DWS is an optical correlation spectroscopy, based on the temporal analysis of the interference speckles of coherent light multiply scattered inside the sample. DWS allows to study both dynamical and structural features.

We report here on the results of preliminary tests performed in the framework of the activities of the EDDI research program. We characterized the performances of the "Elegant Breadboard" available at Airbus, Friedrichshafen, whose features are completely analogue to the Flying Model of the SMD. They have been extensively employed to study foams and granular material, and are now to be used on emulsions. We first demonstrate effective emulsification for a range of

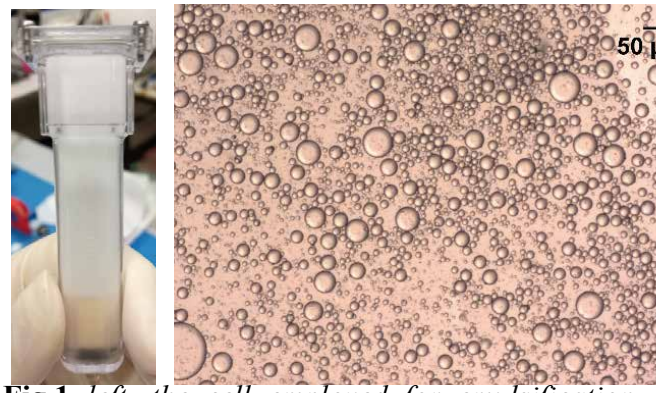

Fig.1 *left, the cell employed for emulsification, right , micrograph of the obtained emulsion*

food-grade oils and surfactants (Fig 1) by exploring different experimental parameters.

Next, we proceed to validate the optics, and the correlation schemes. Finally, we perform DWS experiments in different geometries, and validate the results against analogous experiments performed on the same and on similar emulsions in our standard laboratory setup for DWS experiments.

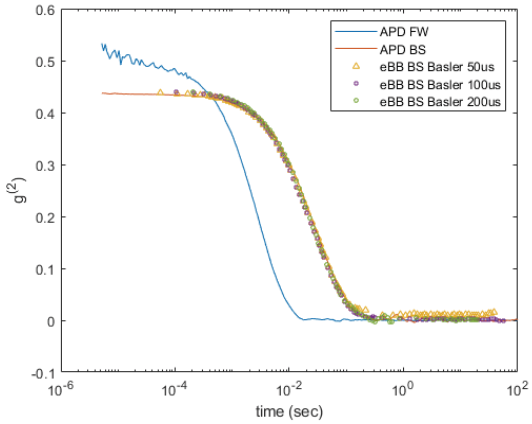

Fig.2: *Comparison of typical DWS correlation functions obtained on a reference sample with different detetcors and geometries (FW and BS). Note the nice overlap for all the BS correlation functions, irrespective of the different detectors and acquisistion parameters.*

Aknowledgements:
European Space Agency – Projects "Soft Matter Dynamics" and "Emulsion Dynamics and Droplet Interfaces".

Poster 104

Zebrafish in hypergravity: larval zebrafish experience changes in cartilage material properties after exposure to hypergravity

Aggleton, J. [1, 2], Lawrence, E.[1], Harniman, R.[3], van Loon, J.[4], Hammond, C. L.[1]

[1]School of Physiology, Pharmacology and Neuroscience, University of Bristol, Bristol, UK; [2] Department of Anthropology and Archaeology, University of Bristol, Bristol, UK; [3] School of Chemistry, University of Bristol, Bristol, UK; [4] Life & Physical Science, Instrumentation and Life Support Lab (TEC-MMG), ESA ESTEC, The Netherlands

jessye.aggleton@bristol.ac.uk, elizabeth.lawrence@bristol.ac.uk, rob.harniman@bristol.ac.uk, j.vanloon@vumc.nl, Chrissy.Hammond@bristol.ac.uk

Introduction

The relationship between genes, mechanical loading, and osteoarthritis is not fully understood. *col11a2* is a genetic mutation associated with Stickler syndrome and premature osteoarthritis (OA) in human patients and has been previously characterised in larval and adult zebrafish. As hypergravity can be used to simulate mechanical loading, we exposed wildtype and *col11a2* mutant larvae to high gravity conditions to examine the interplay between mechanical loading and genetic mutations.

Methods

Larval zebrafish with the *col11a2* mutation and wildtype zebrafish were exposed to continuous hypergravity for 48 hours from 3 days post fertilisation (dpf) to 5 dpf in the Large Diameter Centrifuge at ESA ESTEC, Noordwijk. Power calculations were used to determine sample size. The zebrafish were spun at 1 g, 3 g, and 6 g and a control group was kept in the lab at 1g with no spinning force. The zebrafish were fixed for analysis post-spin. Alcian blue alizarin red staining and immunostaining were used to identify changes to joint morphology, chondrocyte morphology, extracellular matrix (ECM) composition, mineralisation, and musculature in the zebrafish lower jaw following hypergravity exposure. Atomic force microscopy (AFM) was used to determine material properties and the resulting values were used to create finite element analyses (FEA) of the larval zebrafish lower jaws during jaw opening and closing.

Results

Analysis of zebrafish from different gravity levels reveals that lower jaw morphology, mineralization, and musculature were not affected. However, the material properties of the lower jaw cartilage were significantly altered in fish from higher gravity conditions, with zebrafish from the 6g condition showing stiffer cartilage. FEA showed that increased cartilage stiffness caused a reduction in overall strain and movement of the lower jaw, although the morphological pattern of strain remained similar.

Conclusions

Overall, this demonstrates that exposure to hypergravity affects cartilage material properties resulting in changes to jaw movement (predicted through modelling), but that this level and/or length of hypergravity exposure is not sufficient to cause gross changes to cartilage or muscle morphology in larval zebrafish.

Acknowledgements

This project was funded by the European Space Agency Academy, the Wellcome Trust and Versus Arthritis.

26th European Low Gravity Research Association Biennial Symposium and General Assembly
14th International Conference on "Two-Phase Systems for Space and Ground Applications"
European Space Agency Topical Teams meetings
Granada (Spain), September 24-27, 2019

Poster 119

Measurement of the diffusion coefficients of multicomponent systems by the open ended capillary and NMR

Q. Galand1[1], S. Van Vaerenbergh[1]

[1]Microgravity Research Center, Université libre de Bruxelles, Brussels, Belgium,
qgaland@ulb.ac.be

Introduction

The Open Ended Capillary (OEC) is a well kwown technique for the experimental determination of molecular diffusion coefficients. In an OEC run, solutions of different compositions are placed in contact as follows: at the beginning of the experiment, several "capillary" tubes, with an open end, are filled with a solution of composition $\boldsymbol{w_0}$ and are immersed in a bath maintained at constant composition $\boldsymbol{w_\infty}$, as shown at Fig. (1).

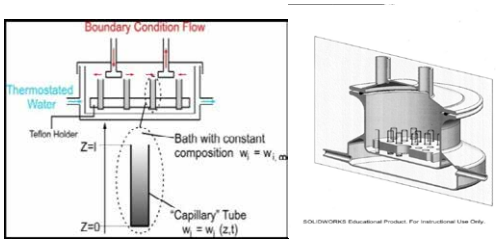

Figure 1: Schematic of our experimental set up for the OEC technique.

Inside the tubes, a diffusive profile of the chemical composition develops over time and results in an evolution of the average composition. Experimentally, capillaries are extracted from the bath and their composition is quantified. Provided a suitable concentration analysis technique is available, the OEC can be used to investigate multicomponent diffusion, as proposed in 2005 (Leahy-Dios et al, 2005). The entire matrix of diffusion coefficients is estimated by fitting the temporal evolution of the composition, as detailed in (Galand et al 2010). However, the complexity of the multicomponent mass transfers can limit the precision on the obtained coefficients. The experimental plan can be adapted and the use of several experimental runs with different initial conditions (Galand et al 2015) sometimes allows obtaining the cross diffusion coefficient with accuracy.

Results

In this presentation, we report experimental data obtained for several multicomponent systems composed of 1.,2.,3,4-Tetrahydronaphtalene, Isobultylbenzene, Dodecane, Toluene and C_{60} Fullerens.

We describe the experimental protocol developed for the accurate measurement of concentration through quantitative NMR experiments, and the experimental limitations in the use of the NMR for the determination of the concentration of C_{60} Fullerens in ternary systems.

On the other hand, we describe the experimental protocols implemented in the OEC experimental runs. From preliminary runs, we determine a set of initial and boundary conditions for the diffusion experiment, in order to optimize the accuracy on the determination of each of the Diffusion coefficient of the Fickian matrix.

Based on experimental data, with discuss the potential accuracy obtained by the our implementation of the Open Ended Capillary technique for the determination of the cross diffusion coefficients for DCMIX systems.

Conclusions

Isothermal Diffusion coefficients were measured by the Open Ended Capillary technique for several DCMIX system. The data analysis procedure is discussed in detail, with particular attention on the accuracy on the obtained cross diffusion coefficients.

Acknowledgements

This work was supported by the SODiUM and DCMIX Prodex Programs funded by the Belgian federal Science Policy Office (SSTC). We are very grateful to European Space Agency for its constant support through this program..

References

A. Leahy-Dios, M. M. Bou Ali, J. K. Platten, A. Firoozabadi, Measurement of molecular and thermal diffusion coefficients in ternary mixtures, *J. Chem. Phys*, 122, 234502 (2005).

Q. Galand, M. Luhmer, S. Van Vaerenbergh, Diffusion coefficients in multicomponent organic liquid mixture measured by the open ended capillary technique, *High Temperature High Pressure*, 38 (4), 329 (2010).

Q. Galand, S. Van Vaerenbergh, Contribution to the benchmark for ternary mixtures: measurement of diffusion and Soret coefficients of ternary system Tetrahydronaphtalene-Isobutylbenzene-n-Dodecane with mass fraction 80-10-10 at 25°C, *Eur. Phys. J. E.*, 38, 26 (2015).

Poster 122

Effect of Cell Configuration on the Soret Separation

T. Lyubimova[1,2], N. Zubova[1], A. Mialdun[3], V. Shevtsova[3]

[1]Institute of Continuous Media Mechanics UB RAS, Perm, Russia, [2]Perm State University, Perm, Russia,
[3]MRC - Microgravity Research Centre, Universit´e Libre de Bruxelles (ULB), Brussels, Belgium;
lyubimovat@mail.ru, yanca@yandex.ru, amialdun@ulb.ac.be, vshev@ulb.ac.be

Introduction

An experimental DCMIX cell consists of a transparent quartz rectangular frame sandwiched between two metal plates on top and bottom (Fig. 1a). Usually, in the numerical simulations of the mixture separation conducted as the part of the ground preparation of the experiment, a model cell having the shape of a rectangle or a rectangular parallelepiped is considered. The authors of the works (Mialdun et al. 2013, Lyubimova et al. 2018) performed the modelling of the real (non-ideal) cell configuration by modifying the thermal conditions at the lateral boundaries. The present paper directly takes into account the peculiarities of DCMIX cell geometry.

Problem configuration

We consider the separation of binary mixture in two-dimensional cells shown in Figs. 1b and 1c. The shape of computational domain described in Fig. 1c is very close to the real shape of DCMIX cell whereas in the domain described in Fig. 1b the compensation volume is absent. The effect of the cell geometry on the Soret coefficient value is studied.

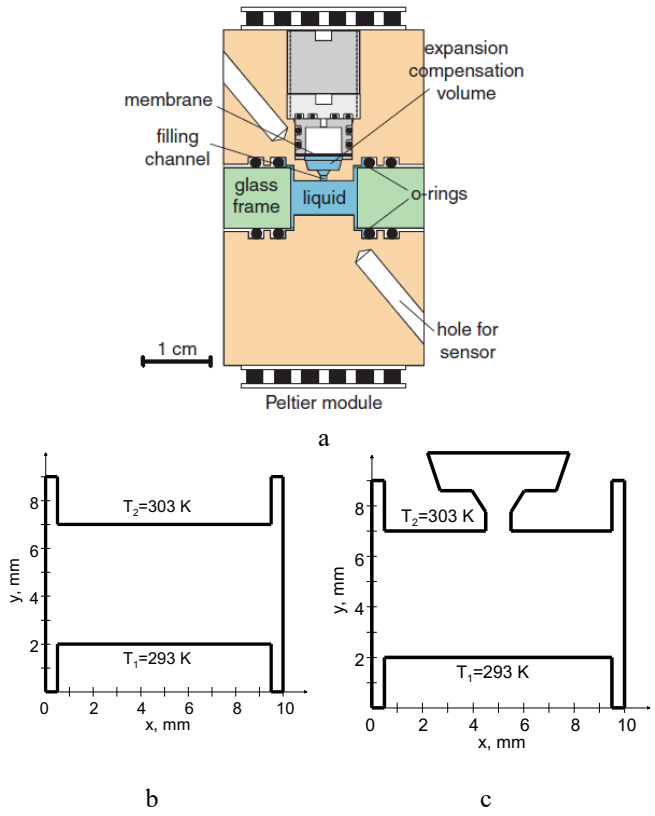

Figure 1: a – cross-section of the DCMIX cell, b, c – geometry of computational domain

Governing equations

Soret-induced convection of a binary mixture of tetralin and dodecane, taken in equal parts, is considered. This mixture was used in the space experiment DCMIX 1. The calculations were carried out in the framework of the Boussinesq approximation:

$$\partial_t \mathbf{V} + (\mathbf{V}\cdot\nabla)\mathbf{V} = -\rho_0^{-1}\nabla P + \nu\nabla^2\mathbf{V} + \\ +\left[1-\beta_T(T-T_0)-\beta_C(C-C_0)\right]\mathbf{g},$$

$$\partial_t T + \mathbf{V}\cdot\nabla T = \chi\nabla^2 T,$$

$$\partial_t C + \mathbf{V}\cdot\nabla C = D\left[\nabla^2 C + C_0(1-C_0)S_T\nabla^2 T\right],$$

$$\nabla\cdot\mathbf{V} = 0.$$

Here V is the velocity vector, P is the pressure, T is the temperature, C is the concentration of havier mixture component, β_T is the thermal expansion coefficient, β_C is coefficient of the solutal dependence of the density, ν is the viscosity of the mixture, $\mathbf{g}$ is the acceleration of gravity, χ is the thermal diffusivity, ρ_0, T_0 and C_0 are the reference density, temperature and concentration, D is the molecular diffusion coefficient and S_T is the Soret coefficient.

The boundaries of the cell are rigid and impermeable. The external vertical boundaries are thermally insulated and the constant different temperatures are maintained at the remaining boundaries.

In the absence of motion, the system tends to a stationary state, which is described by a zero diffusion flux: $\mathbf{J}_C = -\rho_0 D[\nabla C + S_T C_0(1-C_0)\nabla T] = 0$. In this case, we can calculate the Soret coefficient: $S_T = \nabla C/[C_0(1-C_0)\nabla T]$.

Numerical modelling was performed using the ANSYS Fluent software package with the mesh size $5\cdot10^{-5}$ m. At the initial time moment, the mixture was assumed to be homogeneous and the temperature linearly depending on the vertical coordinate. The calculations were performed for Earth gravity and zero gravity conditions.

Numerical results

In simple rectangular cell, at positive value of the Soret coefficient, no flow occurs and a purely diffusion process is observed. In this case, the concentration vertical profile becomes linear with time. The calculations carried out for the cells described in Figs. 1b and 1c have shown the occurrence of a weak flow in the terrestrial conditions. We will further denote the cell configurations in Fig. 1b and Fig. 1c as 1 and 2 respectively.

The temporal evolutions of the maximum value of the stream function in the cells 1 and 2 are presented in Fig. 2a. Accounting for the compensation volume results in a slight increase in the intensity of the flow in the cell. The values of the difference in concentrations at the points with coordinates (0.005 mm; 0.007 mm) and (0.005 mm; 0.002 mm) with and without compensation volume (Fig.2b) differ more substantially, ΔC has greater absolute value in the case of the cell 2. The structure of the steady-state flow has the form of four vortices arising at the corners of the cell (Fig. 3a), this flow strongly deforms concentration isolines near the side walls of the cell (Fig. 3b). In the central part of the cavity, when accounting for the compensation volume, a slight deformation of the isolines of concentration is observed.

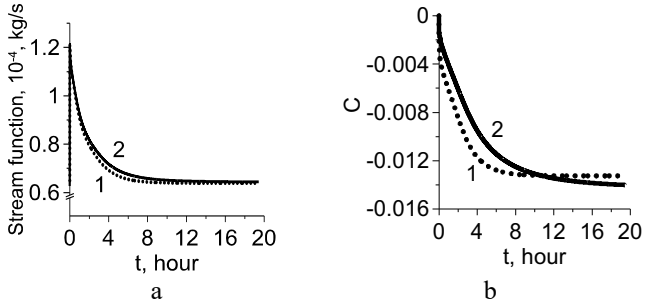

Figure 2: The time evolution of the maximum value of the stream function (a) and the concentration difference at the points with coordinates (0.005 mm; 0.007 mm) and (0.005 mm; 0.002 mm) (b) in the case of Earth gravity. Curve 1 – cell configuration 1, curve 2 – cell configuration 2.

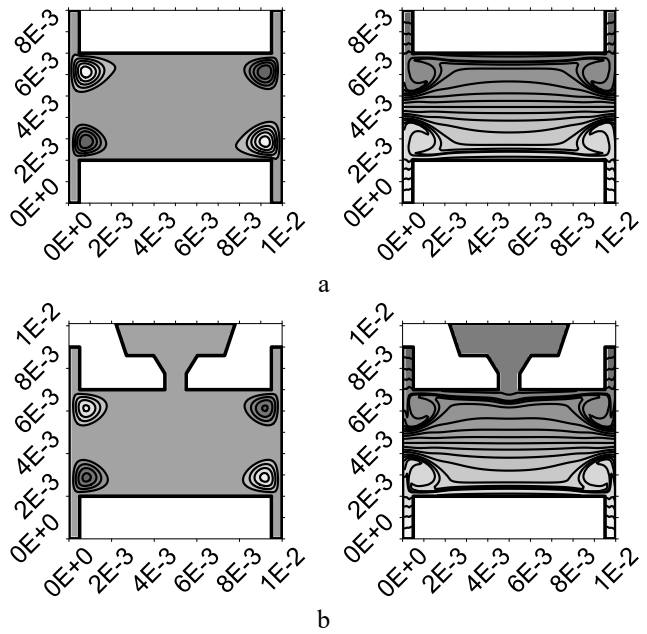

Figure 3: The steady-state fields of the stream function (left) and the concentration distribution (right) for the configuration of the cell 1 (a) and 2 (b). Earth gravity.

The concentration distributions established after about 20 hours of the process are shown in Figs 4a,b. It is seen that in zero gravity conditions, the isolines of concentration in the central part of the cavity are weakly deformed. There is a weak effect of the compensation volume on the concentration in the upper central part of the cell.

Using the maximum value of the separation of the mixture (the maximum value of the modulus) in the centers of the boundaries, it is possible to determine the value of the Soret coefficient. The calculations give the value of the Soret coefficient on Earth equal to $5.30 \cdot 10^{-3}$ 1/K for the cell 1 and $5.61 \cdot 10^{-3}$ 1/K for cell 2.

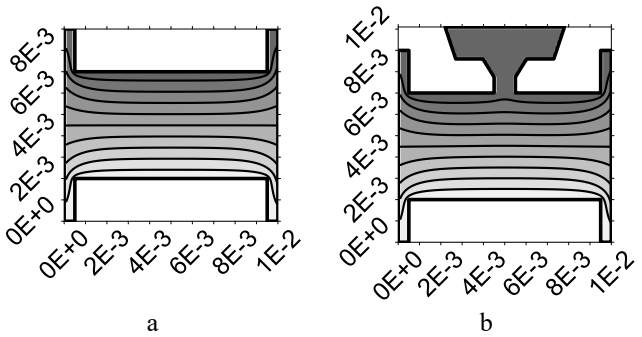

Figure 4: The steady-state concentration distributions for cell configuration 1 (a) and 2 (b). Zero gravity.

In the case of zero gravity conditions, the Soret coefficient values determined using the maximum difference in the centers of the boundaries of the cavity are equal to $9.10 \cdot 10^{-3}$ 1/K and $8.59 \cdot 10^{-3}$ 1/K for cells 1 and 2 respectively. The value known from the literature for this mixture is $9.2 \cdot 10^{-3}$ 1/K (see, for example, Mialdun et al. 2013).

Conclusions

Numerical simulation of the separation of binary mixture of tetralin and dodecane, taken in equal parts, in two-dimensional cells simulating a cell used for conducting a space experiment DCMIX under conditions of Earth gravity and zero gravity has been carried out. The imperfect cell shape, even in zero gravity conditions, causes deformation of the isolines of concentration, which affects the value of the Soret coefficient, calculated using the maximum value of the mixture separation.

Acknowledgements

This work was performed in the frame of DCMIX project (ESA-Roscosmos) and supported by FGUP TSNIIMASH. AM and VS acknowledge support of this work by the PRODEX program of the Belgian Federal Science Policy Office.

References

A. Mialdun, C. Minetti, Y. Gaponenko, V. Shevtsova, F. Dubois, Analysis of the Thermal Performance of SODI Instrument for DCMIX Configuration, *Microgravity. Sci. Technol.* 25 (2013) 83–94.

T. Lyubimova, N. Zubova, V. Shevtsova, Effects of Non-Uniform Temperature of the Walls on the Soret Experiment, *Microgravity. Sci. Technol.* 31 (2019) 1–11.

Poster 124

Drying of complex fluids ruled by collective diffusion of charged nanoparticles

M. Tirado-Miranda[1], C. Moraila-Martínez[2], M. Cabrerizo-Vílchez[1], M.A. Rodríguez-Valverde[1]

[1]Lab of Surface and Interface Physics, Applied Physics Department, University of Granada, Spain, [2] Facultad de Ciencias Físico-Matemáticas, Universidad Autónoma de Sinaloa, México;
mtirado@ugr.es, cmorailam@uas.edu.mx, mcabre@ugr.es, marodri@ugr.es

Introduction

Solidification and crystal growth can be enhanced in the microgravity environment of space, due to the cancellation of natural convection and buoyancy. When the local gradient of nanoparticle concentration increases during the evaporation of a drop/meniscus, the Fick's law establishes that an inward flow is created towards the bulk by particle cooperative diffusion. The surface concentration profile inside the drop is determined by the competition of the diffusive mass transfer, convective mass transfer and the particle deposition rate. Unlike self-diffusion coefficient (from the Stokes-Einstein equation), the cooperative diffusion coefficient of interacting particles becomes more pronounced in crowded environments (up to one order of magnitude higher).

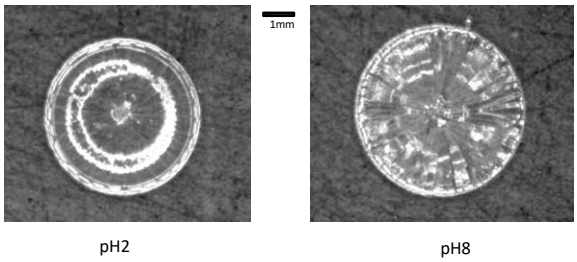

Figure 1: Top-view images of dried sessile drops of carboxylated-silica nanoparticles (12.5% v/v) at different electric charge states (pH solution) on PMMA surfaces.

In this work, we study the importance of the electrostatic inter-particle interactions for the relaxation of concentration gradients in the formation of nanoparticle deposits (Figure 1).

Materials and methods

We used commercial aqueous suspensions of carboxylated-silica nanoparticles (AttendBio Research, 50nm-diameter). We varied the particle electric charge through the medium pH (Figure 2) by using buffered solutions of low ionic strength (aprox 15 mM). We used a Zetasizer Nano device (Malvern, 4 mW He–Ne laser, 633 nm wavelength) to measure the electrophoretic mobility of the nanoparticles. We explored different particle concentrations. The maximum volume fraction of the suspension was 12.5% (w/w).

Sessile drops (100µl) of each nanoparticle suspension were placed onto smooth glass and PMMA substrates (with different wetting properties) and led to evaporate in still air (~RH 50%) and room temperature. The deposits were analyzed by using a white light confocal microscope (PLµ, Sensofar Tech S.L.) at 50× magnification (Nikon, 4-5mm×4-5mm). From the deposit profiles, we evaluated three linear dimensions: diameter (D), height (H) and width (W). An average value of each dimension was obtained from at least three profiles.

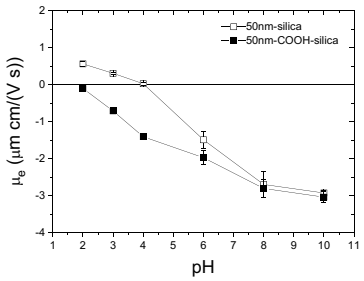

Figure 2: Electrophoretic mobility of (dilute) plain and carboxylated-silica nanoparticles in terms of the pH solution.

We characterized the "free" diffusion of the nanoparticles in suspension by using 3D-Dynamic Light Scattering (LS Instruments AG, 35mW He-Ne laser, 632.8 nm) to suppress multiple scattering contributions in concentrated systems. This technique conducts two simultaneous scattering experiments performed at different directions (cross-correlation). In this work, the intensity autocorrelation function for each suspension was measured at five different scattering angles (30º-60º-90º-120º-150º). The collective diffusion coefficient was determined by extrapolation to low-angle scattering ($q \rightarrow 0$).

Results

In Figure 3, we plot the collective diffusion of barely- and highly-charged nanoparticles. Above the fraction 0.050, the diffusion is favoured by electrostatic interactions, and the diffusion of uncharged nanoparticles scarcely increases as the concentration. We expect that the collective diffusion of charged particles is enhanced at high particle concentration, as happens for the drying.

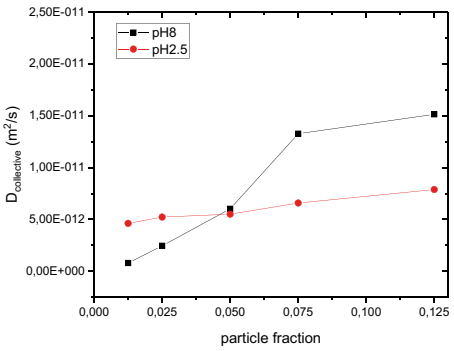

Figure 3: Collective diffusion coefficient of carboxylated-silica nanoparticles at different concentration and two electric states.

In Figure 4, the morphology of deposits on PMMA strongly depends on the particle concentration and electric state. In agreement with the collective diffusion results, the greater differences are found at low and high values of particle concentration. Precisely, there is a reverted behavior between

both electric states: from ring-like deposits with larger diameters towards smaller continuous deposits with central invagination, and viceversa. Lower diffusive flows lead to greater drop spreading. The width of the outer deposit of charged particles is maximum at lower concentration than the uncharged particles. It reflects a minimum diffusive flow and maximum convective flow. Diffusive flow of charged particles takes relevance at low particle concentration, when the gradient between the contact line and bulk is important. Otherwise, the height deposit does not reveal significant differences among barely- and highly charged particles because it mainly depends on the interfacial wedge (contact angle) formed by the drop. The receding contact angle of the substrate and the relative humidity dictate the strength of the convective velocity field.

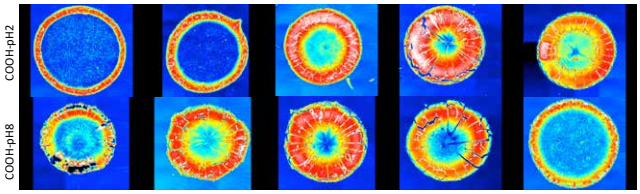

Figure 4: Topography images of dried sessile drops on PMMA surfaces of carboxylated-silica nanoparticles at different particle fraction (left-to-right: 0.0125, 0.025, 0.050, 0.075, 0.125) and two electric states.

Conclusions

We have found that ring-like deposits can be mitigated at low solid concentration if the long-range interparticle repulsion becomes important and the diffusion overcomes the particle transport by convection before reaching the triple line.

Acknowledgements

This research was financed by the State Research Agency (SRA) and European Regional Development Fund (ERDF) through the project MAT2017-82182-R.

References

Eur. Phys. J. E (2016) 39: 20

Droplets of colloids, Droplet Wetting and Evaporation, 2015, 279-294, Academic Press.

Langmuir 2010, 26(16), 13162–13167.

Langmuir 2017, 33, 5025−5036.

Physical Review Fluids 1, 084201 (2016).

J. Phys. Chem. C20111152813609-13616

Poster 125

Icephobic surfaces: an interplay between anti-icing and de-icing properties

M.A Fernandez, P. Ibañez-Ibañez, F.J. Montes Ruiz-Cabello, Miguel Cabrerizo-Vilchez. Miguel A. Rodríguez-Valverde

Lab of Surface and Interface Physics, Applied Physics Department, University of Granada, 18071 Granada, Spain
mafernandez@correo.ugr.es, fjmontes@ugr.es, mcabre@ugr.es, marodri@ugr.es

1. Introduction

Obtaining an ice-phobic surface or coating is a very difficult task with a wide variety of potential applications. It consists on the incorporation of anti-icing and de-icing properties simultaneously (Figure 1).

Anti-icing surfaces are able to prevent ice accretion or delay icing. These surfaces are in general very hydrophobic and able to delay water freezing. The required hydrophobicity must be understood in terms of high contact angles and low water adhesion. In this sense, it is well-accepted that superhydrophobic surfaces are the best candidates to be initially explored, because of their extreme water-repellency. However, the convenience of using superhydrophobic surfaces to delay water freezing is still a matter of controversy.

De-icing requires a very low adhesion to ice. In case icing is not avoidable, an easy release or ice detachment is also desired.

Figure 1: Icephobic surfaces: A combination of anti-icing and de-icing properties

In this work, we prepared a set of aluminium surfaces with different wettability properties: a smooth uncoated aluminium surface (control) a smooth hydrophobized surface and several superhydrophobic (rough+hydrophobic) to explore their performance as icephobic surfaces. The aim was to determine which factors influence the anti-icing and de-icing performance.

2. Materials and methods

Sample preparation

All the surfaces used in this study are aluminum surfaces. They were coated in pieces of roughly 10 cm^2. The smoothest surfaces were previously cleaned using detergent, flushed in water and sonicated in ethanol first, and in distillate water for 5 min each. An aluminum surfaces was hydrophobized by Dupont AF1600 deposition. The cleaned sample was sprayed with a solution of Dupont AF solved in a fluorocarbon solution of FC- 72 (3M). The superhydrophobic surfaces were roughened by acid etching in a 4M solution of HCl. After 15 min of etching, the surfaces were removed from the solution, washed in water and dried in the oven at 120ºC for 20 min. The dry surfaces were plasma-treated and later hydrophobized using several procedures (fluoropolymer-AF1600 deposition or silanization methods). All these surfaces were superhydrophobic as shown by their high drop mobility and high contact angles.

Anti-icing performance

We explored the ability of the surfaces to prevent icing by a combination of two independent studies: supercooled water shedding analysis and freezing delay experiments. For the first study we introduced our sample inside a freezing chamber at -20ºC. This surface was fixed on top of an inclined platform and it was continuously dripped with supercooled water droplets. The water was pumped from a container with ice-water at 0ºC located outside the chamber. This water was then circulated inside the chamber to ensure that water reaches its supercooled state before it comes into contact with the aluminum surface. We determined if icing occurs on the surface after few hours of dripping. For the water freezing delay we deposited an array of at least 50 drops on top of a 50 cm^2 sample produced in the same way as the smallest ones. This sample was introduced inside the freezing chamber and a cooling process was initiated. The temperature was monotonically decreased from room temperature down to less than -25ºC. The purpose of this study was to

analyze the percentage of drops which were frozen at each temperature. A comparison between different samples provided valuable information about the surface that delays freezing more efficiently.

De-icing performance

We measured the shear and tensile ice adhesion for each sample. A dynamometer was used for this purpose. We created cylindrical ice pieces with fixed volume on top of each surface using a hollow cylindrical mold which was firmly pressed against the surface (see Figure 2). A fixed amount of water (10mL) was deposited inside the mold and the sample was then introduced into the freezer. Once the ice was formed, the mold was pulled from the surface at constant rate and we measured the maximum force that was needed to detach the ice from the surface. This parameter is useful to estimate the ice adhesion. The shear adhesion was evaluated when the force was applied parallel to the surface while the tensile adhesion was measured when the force was applied perpendicular to it.

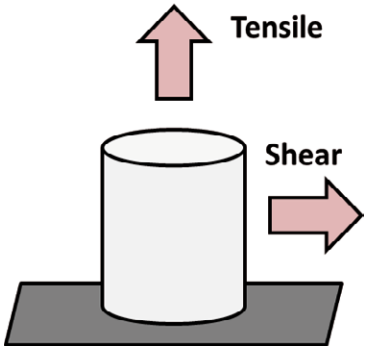

Figure 2: Tensile and Shear ice adhesion tests

3. Results

Our supercooled water dripping experiments revealed that all the superhydrophobic surfaces avoided icing after more than 12h of dripping. The uncoated aluminium surfaces showed the worse performance, because a small piece of ice remained attached to the substrate after few minutes of dripping. The results for hydrophobized aluminium surface were more satisfactory than those obtained for the uncoated sample because this sample was able to prevent icing for few hours. Freezing delay experiments showed an apparent contradiction between the surfaces features leading to freezing delay ability. We found that the relative humidity (RH) plays a key-role in the results. The trend that we observed was inverted when relative humidity changes from low to high values: at dry environment, the uncoated aluminium (the sample with lowest contact angle) showed the best performance among all the explored samples. In contrast, at humid environments, the surface with the best performance were the superhydrophobic samples (the samples with the highest contact angles).

The adhesion test experiments showed that superhydrophobic surfaces were the stickiest surfaces to ice. In contrast the coated aluminium smooth surface showed the best performance. These surprising results indicated that hydrophobicity, and in particular, superhydrophobicity is not linked to de-icing performance.

4. Conclusions

In this work, we found that ice-phobic properties cannot be attributed to superhydrophobicity. Several factors such as the roughness and the relative humidity affect negatively the ability of the superhydrophobic surfaces to prevent icing or mitigate the ice accretion. Smooth-hydrophobic surfaces showed a good balance between de-icing and anti-icing performance.

Acknowledgements

This research was supported by the project: MAT2017-82182-R funded by the State Research Agency (SRA) and European Regional Development Fund (ERDF).

References

Montes Ruiz-Cabello, F. J., Ibañez-Ibañez, P., Paz-Gomez, G., Cabrerizo-Vilchez, M., Rodriguez-Valverde, M. A. Fabrication of Superhydrophobic Metal Surfaces for Anti-Icing Applications. J. Vis. Exp. (138), e57635,.

Poster 136

Steady flows in axisymmetric channel of variable cross-section under periodic oscillation

A.Ivanova, V. Kozlov, I.Karpunin, O.Vlasova

PSHPU, Perm, Rusiia
a.ivanova@pspu.ru, kozlov@pspu.ru, karpunin_ie@pspu.ru, vlasova_o_a@mail.ru

Introduction

Oscillations of an incompressible viscous fluid near the solid boundaries lead to the generation of averaged flows. These flows known as "acoustic" ones are well studied in the limiting case of high frequencies when the characteristic sizes of a cavity (channel width or the cavity size) significantly exceed the thickness of the Stokes boundary layer $\delta \equiv \sqrt{2\nu/\Omega}$. Here Ω is the radian frequency of the fluid oscillation, ν – the coefficient of kinematic viscosity of the fluid. The averaged flows generated by the oscillations of fluid at moderate and low dimensionless frequencies is of particular interest. It was found that with decreasing the dimensionless frequency the averaged flows excited by oscillations in closed cavities rearrange, but do not disappear even at low dimensionless frequencies. The study of flows generated by fluid oscillations in channels of variable cross-section versus the dimensionless frequency is relevant from the technological point of view for controlling mass transfer in porous media.

Experimental setup & technique

The experimental setup is a closed hydraulic circuit, which includes a cavity *1* and a pump *2* (Fig. 1). The last one is moved by electrodymanic vibrator *3* and provides a harmonic change in the flow rate of the fluid pumped through the cuvette with linear oscillation frequency $f \equiv \Omega/2\pi = 1-11$ Hz. The oscillations of a plug *5* in tube *4* charactrise the volume of the pumped fluid, which varies in the range of $Q_0 = 0-60\,\text{cm}^3$. Two membranes *6* separate the working liquid and the fluid in the circuit.

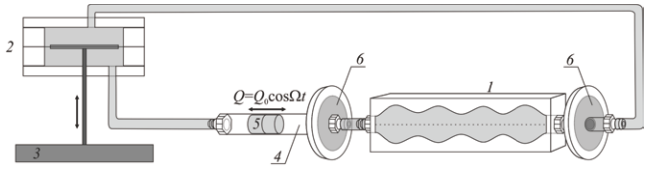

Figure 1: Scheme of experimental setup.

The experimental cavity is a transparent cavity in the form of a parallelepiped. The radii of the axisymmetric channel in the narrow and wide sections are $R_1 = 6.2$ mm and $R_2 = 15.0$ mm, the spatial period (the distance between the centers of the segments) is $\lambda = 42$ mm. Water glycerol mixture is used as the working fluid, the coefficient of kinematic viscosity of which varies in the range $\nu = 0.02-3.86$ St. The structure of the averaged flow in the axial section of the channel is investigated by the PIV method. Using the PIVLab program (Thielicke and Stamhuis 2014), pairs of frames are processed, the time interval between which is a multiple of the oscillation period of the fluid. Thus, the result of processing is the velocity field averaged over the period in the plane of the light knife (in the axial section of the channel).

Experimental results

Periodic variation of the flow rate of the fluid pumped through the channel leads to the generation of averaged flows in each of the channel cells. The averaged flow consists of a system of axisymmetric toroidal vortices that occupies the entire pore volume.

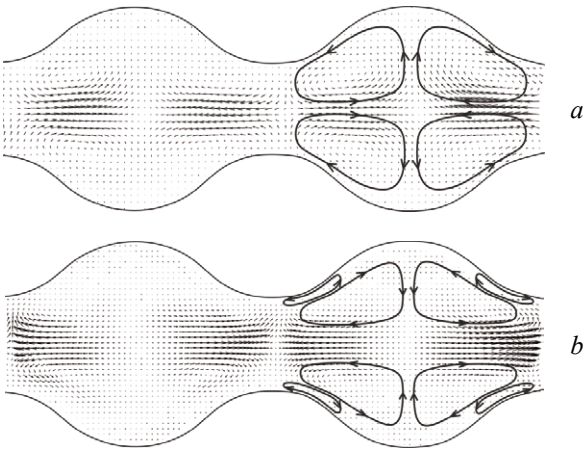

Figure 2: Transformation of the structure of the averaged flow in the channel with the dimensionless frequency of vibrations: $f = 2$ Hz, $b = 0.16$ mm, $\nu = 3.86$ St (*a*); 10 Hz, 0.09 mm, $\nu = 0.02$ St (*b*)

The parameter, which determines the structure of the averaged flows, is the dimensionless frequency $\omega \equiv \Omega R_1^2/\nu$. With an increase of ω (with a decrease in the viscosity of the fluid or an increase in the frequency of vibrations), the primary vortices are pressed against the sidewalls of the channel, their transverse size decreases. In the limiting case of high frequencies, they transform into relatively thin vortex structures localized in the Stokes boundary layers near the channel walls in the areas of its narrowing. These vortexes serve as generators of large-scale secondary

vortices. Figure 2 shows the velocity fields obtained by the PIV method in two cases: low (Fig. 2, *a*) and relatively high (Fig. 2, *b*) dimensionless frequencies. In the high-frequency case, the rotation of the fluid in the primary (near-wall) and secondary (out of boundary layer) vortices occurs in opposite directions (Fig. 2, *b*).

The averaged flows in the high-frequency region, $\omega \equiv \Omega R_1^2 / \nu >> 1$, when the transverse size of the channel significantly exceeds the thickness of the Stokes layer, are determined by pulsational Reynolds number $\mathrm{Re} \equiv b^2\Omega / \nu$. Here b is an amplitude of a piston oscillation of fluid in the narrow channel part. For given values of the oscillation frequency and the fluid viscosity, the dimensionless velocity of the averaged flow $V \equiv \upsilon R_1 / \nu$ increases with the Reynolds number according to a linear law V Re and depends on the dimensionless frequency. This allows introducing one dimensionless parameter $V/\mathrm{Re} \equiv \upsilon \mathrm{R}_1 / b^2\Omega$ to characterize the average flow velocity. Consider the dependence of this complex on the dimensionless frequency ω (Fig.3). The graph shows the mean values V/Re for each series of experiments at a fixed oscillation frequency of a fluid of definite viscosity. At moderate dimensionless frequencies, when the thickness of the boundary layer is comparable to R_1 and only the primary vortices are observed, the parameter does not change monotonically, a maximum is found at $\omega \approx 30$ (light points in Fig. 3).

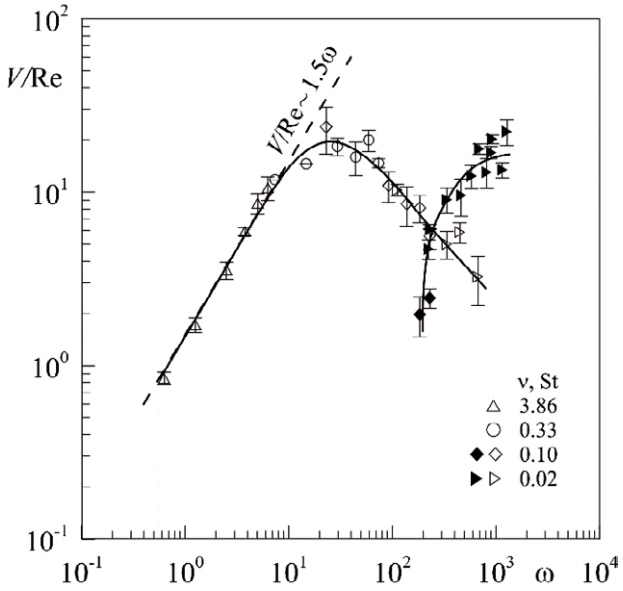

Figure 3: Dependency of intensity of primary vortexes (light marks) and secondary ones (filled marks) on dimensionless frequency

At low dimensional frequency, $\omega < 10$, the parameter V/Re grows with frequency proportionally. This is in agreement with results (Kozlov et al. 2017) in the of low frequency limit.

At $\omega > 30$ the velocity of the primary vortices decreases with a dimensionless frequency. With an increase in ω the thickness of the boundary layers, in which primary vortices are formed, decreases and, consequently, the transverse size of the vortices decreases, so the measurement of velocity primary vortexes at $\omega > 10^3$ becomes technically problematic.

Conclusions

An experimental study of averaged flows excited by fluid oscillations in an axisymmetric channel, the cross section of which varies periodically with the longitudinal coordinate, is performed. The research performed in a wide range of the dimensionless frequency variation showed that the harmonic oscillations of the fluid excite the averaged flow in the form of a system of toroidal vortex flows which structure and intensity are determined by the dimensionless frequency and by the pulsation Reynolds number in each of the channel segments. In the region of low dimensionless frequencies, when viscous forces determine the oscillating motion in the entire channel, the primary vortices occupy the entire volume of the channel. In this case, the direction of rotation of the vortices is opposite to the case of extremely high frequencies, when the entire volume of the channel is filled with the secondary vortices that develop outside the primary vortices localized in thin boundary layers. Based on the found transformation of structure and intensity of averaged flows with a dimensionless frequency, two dimensionless complexes could be introduced to characterize the intensity of the averaged flows in the entire range of dimensionless frequencies, from extremely low to extremely high.

Acknowledgements

The work was done in the frame of RFBR project № 17-41-590773 and partially supported by the Government of Perm Krai (research project C-26/174.9)
.

References

W.Thielicke, E.J. Stamhuis, PIVLAB-Towards user-friendly, affordable and accurate digital particle image velocimetry in MATLAB, *J. Open Res. Software* 2 (2014) e30.

V.G.Kozlov, N.V. Kozlov, V.D. Schipitsyn, Steady flows in an oscillating deformable container: Effect of the dimensionless frequency, *Phys. Rev. Fluids* 2 (2017) 094501.

Poster 137

Shadowgraph investigation of free-diffusion of glycerol and water under micro-gravity conditions using a cylindrical Flowing-Junction cell

P. Fruton[1], A.T. Ndjaka[1], L. García-Fernández[1,2], H. Bataller[1] and F. Croccolo[1]

[1]Laboratoire des Fluides Complexes et leurs Réservoirs – IPRA, UMR5150, E2S-Univ Pau & Pays Adour/CNRS/Total, 1 Allée du Parc Montaury, 64600 Anglet, France,
[2]Centre National d'Études Spatiales (CNES), 2 Place Maurice Quentin, 75001 Paris, France
paul.fruton@univ-pau.fr

Introduction

Diffusion is the physical phenomenon driven by the random walk of the fluid molecules in the presence of a concentration gradient. This process occurs at all scales from the microscopic to the mesoscopic and macroscopic ones. This is related to the fact that diffusion goes hand in hand with large amplitude and long wavelength fluctuations. We describe here an apparatus to create a step concentration gradient in a binary mixture of glycerol and water under the micro-gravity conditions available for a limited time during a parabolic flight.

Non-Equilibrium Fluctuation analysis in a free-diffusion experiment

Free-diffusion occurs whenever a concentration gradient is present in the bulk of an isothermal fluid mixture. During a free-diffusion process we investigate the non-equilibrium concentration fluctuations by means of dynamic shadowgraph. In such a way we have access to the fluctuations intermediate scattering functions that typically exhibit an exponential decay.

On ground, fluctuations are affected by diffusion and buoyancy forces depending on the wave number, i.e. the inverse of their size. As can be seen in Fig. 1, for large wave numbers (small fluctuations), diffusion overcomes gravity and the decay time is the typical diffusive one, proportional to $1/Dq^2$. For smaller wave numbers (large fluctuations), gravity dominates and the decay time is proportional to q^2 (Croccolo et al. 2006). Then, by fitting the decay times at large wave vectors, we obtain a precise measurement of the mass diffusion coefficient (Croccolo et al. 2012). However, the wave vector range is limited to large wave numbers due to the buoyancy forces.

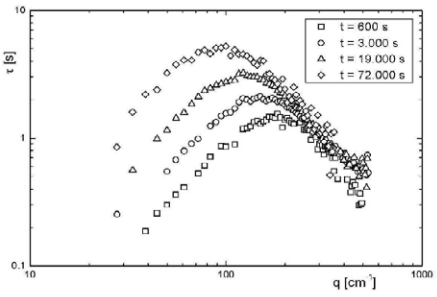

Figure 1: Decay time vs. wave number for a free-diffusion experiment of a glycerol solution in water (39% w/w) below a layer of pure water. For large q values the $1/Dq^2$ dependence can be observed, while for small q values a q^2 dependence appears. (Croccolo *PhD dissertation* 2006).

The glycerol-water mixture, previously characterised in normal gravity conditions (Croccolo et al. 2007), is planned to be studied for the first time in micro-gravity during a parabolic flight. Under these conditions, we could reduce the buoyancy forces and observe a full diffusive behaviour.

Experimental procedure: cylindrical Flowing-Junction Cell

In order to prepare the initial step concentration profile where a layer of water is superposed to a layer of a glycerol solution, we developed (Croccolo et al. 2019) a revised cylindrical Flowing-Junction Cell (c-FJC). In our device the two fluids are injected radially and symmetrically on the top and bottom of the cell. We flux out the mixture radially and symmetrically through a thin slit. Thus, a sharp interface between the two fluids is maintained both in stable (denser fluid at the bottom side of the cell) and in unstable conditions (denser fluid at the top side of the cell). This demonstrates that the device should work also in micro-gravity conditions. The fluids are continuously fluxed. When the flux is stopped the free-diffusion experiment starts.

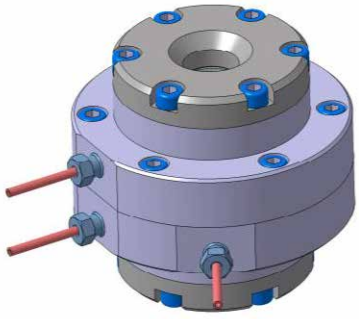

Figure 12: 3D drawing of the Flowing-Junction cell. The red tubes are the two inlets and the outlet used to flux. The cell is enclosed inside aluminium rings. It allows experiments at high pressure. Glass windows on top and bottom of the cell provide optical access for the Shadowgraph.

The future parabolic flight campaign is mainly intended to test the working principle of the FJC in micro-gravity conditions. The fluid behaviour will be monitored by Shadowgraph in order to understand if the interface can be kept flat and sharp also in the absence of the stabilizing effect of gravity. Several tests will be performed. Finally, if the interface will be considered of good quality, series of images will be recorded in order to investigate by Shadowgraphy the

concentration non-equilibrium fluctuations and to derive the mass diffusion coefficient of the investigated mixture under micro-gravity.

Conclusions

The benefits of the proposed experiment are twofold. First, we will validate the use of the Flowing-Junction Cell under micro-gravity conditions. We need to test if a sharp interface can be maintained. Both the different gravity levels (i.e. 1.8g, 1g and 0g) and the parabolic flight trajectory impact the interface. Second, once the interface stability is confirmed, we hope to be able to investigate the free-diffusion process over a large wave number range.

Acknowledgements

We acknowledge financial support from the Centre National d'Etudes Spatiales (CNES) and from the funding partners of the Industrial Chair CO2ES: E2S-UPPA, TOTAL, CNES and BRGM. L. García-Fernández gratefully acknowledges the CNES for the post-doctoral research grant.

References

F. Croccolo, D. Brogioli, A. Vailati, M. Giglio, D. S. Cannell, Effect of Gravity on the Dynamics of Nonequilibrium Fluctuations in a Free-Diffusion Experiment, *Ann. N.Y. Acad. Sci.* 1077 (2006) 365

F. Croccolo, *PhD dissertation*, Universit`a degli Studi di Milano, 2006.

F. Croccolo, D. Brogioli, A. Vailati, M. Giglio and D.S. Cannell, Non-diffusive decay of gradient driven fluctuations in a free-diffusion process, Physical Review E 76 (2007) 41112

F. Croccolo, H. Bataller, F. Scheffold, A light scattering study of non equilibrium fluctuations in liquid mixtures to measure the Soret and mass diffusion coefficient*, The Journal Of Chemical Physics* 137 (2012)

F. Croccolo, D. Brogioli, A. Vailati, Cylindrical flowing-junction cell for the investigation of fluctuations and pattern-formation in miscible fluids, *submitted* (2019)

Poster 140

Bottom-up assembly of a vascularized macrotissue using a microgravity bioreactor

Daniel T.O. Carvalho[1,2], Carlos de la Peña[1,2], Tália Figueiredo[1,2], Manuela Gomes[3,4], Cristina C. Barrias[1,2]

[1]i3S - Instituto de Investigação e Inovação em Saúde, Universidade do Porto, Portugal; [2]Biomaterials Group, INEB - Instituto de Engenharia Biomédica, Portugal; [3]3B's Research Group-Biomaterials, Biodegradables and Biomimetics, University of Minho, Headquarters of the European Institute of Excellence on Tissue Engineering and Regenerative Medicine, Guimarães, Portugal; [4]ICVS/3B's-PT Government Associate Laboratory, Braga/Guimarães, Portugal

Introduction

Exposure to near-weightlessness (i.e. microgravity) has been demonstrated to negatively affect the human body, both at cellular and systemic levels. Understanding the biological effects of microgravity exposure has thus become a priority to develop countermeasures and improve astronaut's health and performance in future human Space endeavors. Yet, advances in microgravity research has brought many other benefits to society on Earth, particularly on the biomedical field. A promising application is the use of microgravity technology in tissue engineering. Growing cells in microgravity, either in space or in bench-top bioreactors, has been shown to enable the formation of large tissue-like fragments, which are able to recapitulate the structure and function of their physiological counterparts (Unsworth et al. 1998). Different types of cells including osteoblasts, chondrocytes, mesenchymal stem/stromal cells (MSC) and hepatocytes have been reported to survive and assemble into physiologically relevant macrotissues, under microgravity conditions (Grimm et al. 2014).

Materials and Methods

In this study, we describe for the first time the culture and generation of a scaffold-free macrotissue using a high-aspect rotating vessel bioreactor (HARV, Synthecon Inc.). Multicellular spheroids composed of late endothelial progenitor cells, also called outgrowth endothelial cells (OEC) and MSC were used as building blocks and cultured in a HARV bioreactor at 10 rpm until static equilibrium was reached (Figure 1).

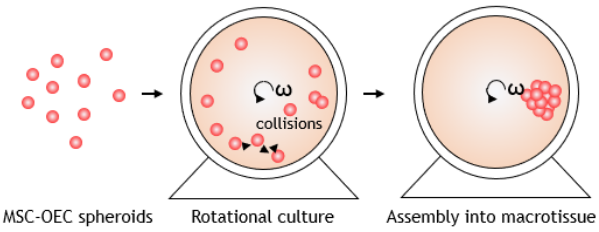

Figure 1: Schematic illustration of spontaneous spheroid aggregation and rotational motion (w, angular velocity) when cultured in a HARV bioreactor.

Immunohistochemistry was conducted to assess extracellular matrix (ECM) production and the degree of endothelial organization inside the macrotissue. To optimize the assembly process, the equations of motion for MSC-OEC spheroids were formulated and trajectories were optimized using COMSOL Multiphysics software.

Results

When cultured at a defined angular velocity, MSC-OEC spheroids described non-coincident rotational motions, which ultimately led to collision and tissue fusion. After 7 days in culture, one macrotissue with 2 mm in diameter was successfully obtained per reactor. Macrotissues showed a well-defined spherical morphology and an ECM enriched in fibronectin, collagen type I and collagen type IV. While collagen type I was ubiquitously expressed throughout the macrotissue, fibronectin predominantly accumulated in the periphery and collagen type IV in the innermost regions of the spheroids. Immunostaining against CD31 expresion revealed the formation of a primitive vascular-like network with OEC forming clusters and alignments surrounded by laminin (Figure 2).

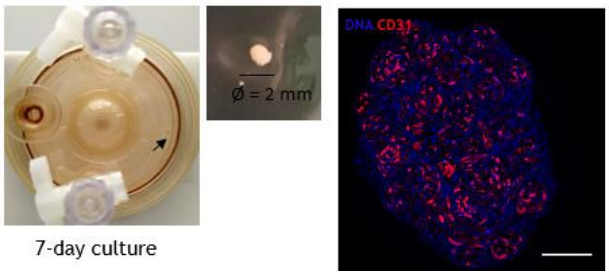

Figure 2: 7-day matured macrotissue in simulated microgravity (left, black arrow). Endothelial organization inside MSC-OEC macrotissues is highlighted by CD31 staining (right).

Conclusions

Our system offers unique opportunities for dynamic culture of multicellular spheroids and their assembly into macrotissue constructs, which could be exploited for therapeutic applications.

Acknowledgements

The present work was financially supported by FEDER - Fundo Europeu de Desenvolvimento Regional funds through the COMPETE 2020 Operacional Programme for Competitiveness and Internationalisation (POCI), Portugal 2020, and by Portuguese funds through FCT/MCTES in the framework of the project "Institute for Research and Innovation in Healt Sciences" (POCI-01-0145-FEDER-007274).

References

Grimm, D., Wehland, M., Pietsch, J., Aleshcheva, G., Wise, P., van Loon, J.,... & Bauer, J. (2014). Growing tissues in real and simulated microgravity: new methods for tissue engineering. Tissue Engineering Part B: Reviews, 20(6), 555-566.

Unsworth, B. R., & Lelkes, P. I. (1998). Growing tissues in microgravity. Nature medicine, 4(8), 901.

26th European Low Gravity Research Association Biennial Symposium and General Assembly
14th International Conference on "Two-Phase Systems for Space and Ground Applications"
European Space Agency Topical Teams meetings
Granada (Spain), September 24-27, 2019

Poster 142

GROWTH AND REGENERATION OF *XENOPUS LAEVIS* TADPOLES ON THE ISS: THE EDUCATIONAL EXPERIMENT XENOGRISS

AM. Rizzo[1], S. Zava[1], P.A. Corsetto[1], A. Norfini[2], M. Balsamo[2], A. Bardi[2], A. Farri[3], G. Giannini[3], A. Giovannoni[3], Y. Mini[3], L. Montemurro[3], A. Oleandro[3], L. Raugi[3], I. Tomberli[3], A. Zingoni[3], A. Fortuna[3], C. Meringolo[3], S. Cartocci[3], M. Monici[4]

[1]Department of Pharmacological and Biomolecular Sciences, Università degli Studi di Milano, Via D. Trentacoste 2 20134, Milan, Italy
[2]Kayser Italia, Livorno, Italy
[3] Istituto Tecnico Industriale Statale "A. Meucci", Florence, Italy;
[4]ASAcampus Joint Laboratory, ASA Res. Div.-Dept. of Experimental and Clinical Biomedical Sciences, University of Florence, Florence Italy;
*angelamaria.rizzo@unimi.it, monica.monici@unifi.it, stefano.cartocci@itismeucci.it

Introduction

Since life appeared on earth, the force of gravity has always been present and has made an important contribution to natural selection. The behavior and development of all organisms, animals and plants is influenced by this force. The role that gravity plays in biological processes can be revealed by studying these processes in conditions of microgravity, simulated or real, and making a comparison with what happens on Earth.

In the past, *Xenopus laevis* tadpoles have been used as a model system for many development and behavior studies both on ground and in the space environment. The data indicated effects of microgravity on some reflexes, on behavior and swimming pattern, and also showed effects on the development of the nervous system (1).

It is known that the processes of regeneration and growth share some basic mechanisms in common and the tadpoles of *Xenopus* represent an ideal model for studying the two processes simultaneously (2). We therefore hypothesized that the tadpole growth and regeneration of a part of the body, if amputated, are influenced by gravity.

The healing of a lesion is a complex process that requires the collaboration of different cell lines, whose functions are finely regulated during the entire evolution of the process from signals mediated by the extracellular matrix, biochemical and physical factors, of which gravity could represent an important aspect. When our protective barrier to the outside is interrupted, the damage must be repaired quickly and effectively. A temporary repair is obtained through the formation of a clot, which opens the way to the subsequent phases of the process. Then the immune cells come into play, which trigger the inflammatory response, then endothelial cells and fibroblasts invade the clot: the former are responsible for the neoangiogenesis, while the latter determine the contraction of the wound and the approximation of the margins. Meanwhile, keratinocytes migrate to reform the epithelium on the uncovered surface of the wound.

Most minor injuries heal quickly and efficiently within a week or two. However, the final product is not perfect, both from a functional and an aesthetic point of view: the damaged epidermal appendages (eg the hairs) are not regenerated and, when the wound heals, a scar connective tissue remains, characterized by a rich matrix of poorly organized collagen fibers, which form dense and parallel beams, very different from the collagen network typical of a mechanically efficient tissue (3).

The search for therapeutic strategies that could favor natural repair mechanisms and improve their efficiency must necessarily be based on a thorough knowledge of the basic biology of repair and regeneration processes (4). In recent years, our understanding of the mechanisms underlying the tissue repair process has progressed considerably, yet many questions remain unanswered. For example, because repair mechanisms are imperfect in adult mammals.

The Xenopus tadpole is a recognized and widely used model for developmental biology and regeneration biology studies (5). In fact, *Xenopus laevis* tadpole is able to regenerate the tail, including skin, muscles, notochord, spinal cord, neurons and blood vessels. This occurs through rapid tissue growth and a process of morphogenesis. Recent studies have shown that both during morphogenesis and in the early stages of tissue regeneration, a programmed cell death process is required, and apoptosis is indispensable for determining an adequate number of cells in regenerating tissues; in fact regeneration is inhibited when caspase 3 activity is inhibited (6). Furthermore, it has been observed that the Wnt and FGF signaling pathways are extremely important for a correct regeneration (7). One of the first evidences emerged from the research on tadpoles concerns the movement of keratinocytes during the re-epithelialization phase: in tadpoles the keratinocytes do not migrate by sliding through lamellipods, but are dragged forward by an actin "hollow" which acts as a "string" around the edge of the wound, narrowing it (8).

Biochemical factors are not the only factors that are relevant from a regulatory point of view. In fact, mechanical factors, such as stresses that deform the cell and the "tearing" of the plasma membrane at the time of injury, appear to be important activators of the damage response. The mechanical tensions at the wound site can also play a role in guiding collagen fibrillogenesis, because the altered tensions during wound closure influence the formation of the matrix, and therefore of the fibrotic scars (9).

Human and animal exposure to microgravity conditions induces alterations in the musculoskeletal system, immune function, endocrine system, embryonic development, growth. There are numerous parallels between the effects of microgravity on the human organism and some pathophysiological processes that occur on Earth. Microgravity, for example, induces changes in living organisms that are very similar to those that occur during aging (10). Furthermore, one of the systems to simulate

microgravity in the human organism consists in the prolonged lodging of the subject (Bed Rest, 11). On the ground both the aging conditions and the prolonged lodging have a negative impact on the regeneration of wounds, constituting an important socio-sanitary problem. Finally, the physical forces of surface tension and pressure greatly affect the regeneration of wounds, and their modification in space could constitute a further parameter to be considered in tissue regeneration in microgravity (12, 13).

For this reason we believe that the study of molecular mechanisms and the effects of microgravity conditions on tissue growth and regeneration is also relevant to fill this lack of knowledge in view of future space exploration missions, because tissue repair/regeneration is the process that makes organisms resilient to injury, allowing survival.

Microgravity significantly changes the physiology of our organism, inducing alterations similar to those indicated above, circulatory changes with reduced microcirculation, aging, hepatic metabolism, reduction of the apoptotic process, immune response, osteoporosis and loss of muscle mass (14). Therefore, the study of the influence of microgravity on the molecular mechanisms involved in regenerative processes appears to be particularly relevant in terms of application in future space travel missions because a detailed knowledge about the molecular mechanisms involved in tissue regeneration, improves the possibility to favour the capacity of organisms to repair lesions and, then, their resilience, increasing the chances of surviving in difficult environment.

Methods

The Italian Space Agency, within the frame of the mission "Beyond" has promoted the "YiSS - Youth ISS" competition. The objective of this educational initiative is to exploit the imaginative and inspirational potential of space to involve secondary school students in the process of conception and execution of a space experiments.

The XENOGRISS experiment was selected among others due to the active involvement of students, from the high school IT IS Meucci, into a multi-disciplinary project aimed at studying the effect of microgravity on growth and regeneration processes, using an animal model (tadpoles of *Xenopus laevis*) that allows observing both processes simultaneously. The project involves the preparation of a tadpole culture (4-6 animals) of *Xenopus laevis* within a Xenopus Experiment Unit (XEU, Kayser Italia). Half of the animals will undergo the amputation of a small tail segment, strictly following the procedures indicated by the ethics committee and the regulatory bodies on experimentation with animal models. The XEU will then be integrated in a powered Biokon and is planned to be launched with the SpaceX CRS-19 mission in Dicember 2019. The XEU will be activated by Captain Luca Parmitano, upon arrival on the ISS. The activation will ensure the feeding of the tadpoles, the exchange of water and the acquisition of images through a camera, to monitor the growth, regeneration and the swimming pattern.

The camera system and its electronic integration within the Biokon will be designed and realized by the students, under the supervision of Kayser, considering all the experiment and ISS requirements. The facility will be recovered with the same capsule after 30 days to allow the post flight analyses on the tadpoles and the retrieval of the experimental data for the correct replication in 1-*g* and simulated micro-*g* on ground using 3d clinostat.

Conclusions

The information acquired with this experiment will help to understand the mechanisms underlying the processes of growth, repair and regeneration of tissues and also the role of gravity and mechanical factors in these processes. A better understanding of the impact that unloading conditions may have in the aforementioned processes is important in defining protocols for the management of traumatic injuries, wounds and chronic ulcers both in space environment and on Earth.

Acknowledgements

This project is granted by Italian Space Agency Contract 2018-38-HH.0.
We would like to tank G. Galoforo, F. Ferranti, G. Valentini, R. Fortezza and P. Lepore from ASI, Telespazio, UTISS and Argotec for the support during the project and the Space mission.

References

1) Malacinski GM, Neff AW, *et al*. Developmental biology in outer space: spaceflight provides the opportunity for new studies. *Bioscience* 39 (1989) 314-320.
2) Beck CW, Izpisúa Belmonte JC, Christen B. Beyond early development: Xenopus as an emerging model for the study of regenerative mechanisms. *Dev Dyn.* 238 (2009) 1226-48.
3) Emin SA, Martin P, Tomic-Canic M. Wound repair and regeneration: Mechanisms, signaling, and translation. *Science Translational Medicine* 6 (2014) 265-266.
4) Martin P. Wound Healing: Aiming for Perfect Skin Regeneration, *Science* 276 (1997) 75-81.
5) Slack JM, Lin G, Chen Y. The Xenopus tadpole: a new model for regeneration research. *Cell Mol Life Sci*. 65 (2008) 54-63.
6) Tseng as, Adams DS, *et al.* Apoptosis is required during early stages of tail regeneration in Xenopus laevis. *Developmental Biology* 301 (2007) 62 69.
7) G. Lin, J.M.W. Slack. Requirement for Wnt and FGF signaling in Xenopus tadpole tail regeneration. *Developmental Biology* 316 (2008) 323 335.
8) Martin P1, Lewis J. Actin cables and epidermal movement in embryonic wound healing. *Nature 360* (1992) 179-83.
9) Monici M, Cialdai F, *et al.* An in vitro study on tissue repair: impact of unloading on cells involved in the modeling phase. *Microgravity Sci Tec* 23 (2011) 391-401.
10) Strollo F, Gentile S, et al. Recent Progress in Space Physiology and Aging. *Front Physiol.* 12 (2018) 9:1551.
11) Hargens AR, Vico L. Long-duration bed rest as an analog to microgravity. *J Appl Physiol* 120 (1985) 891-3.
12) Jiang M, Qiu J, *et al.* Changes in tension regulates proliferation and migration of fibroblasts by remodeling expression of ECM proteins. *Exp Ther Med.* 12 (2016) 1542-1550.
13) Monici M, Cialdai F. The Role of Physical Factors in Cell Differentiation, Tissue Repair and Regeneration. In book: Tissue Regeneration - From Basic Biology to Clinical Application (2012).
14) Pietsch J, Bauer J, *et al.* The effects of weightlessness on the human organism and mammalian cells. *Curr Mol Med.* (11) 2011 350-64.

26th European Low Gravity Research Association Biennial Symposium and General Assembly
14th International Conference on "Two-Phase Systems for Space and Ground Applications"
European Space Agency Topical Teams meetings
Granada (Spain), September 24-27, 2019

Poster 157

Lateral Sloshing of Magnetic Liquids in Microgravity

Á. Romero-Calvo[1,*], A.J. García Salcedo[1], F. Garrone[1], I. Rivoalen[1], G. Cano Gómez[2], E. Castro-Hernández[3], M. Á. Herrada Gutiérrez[3], F. Maggi[1]

[1] Department of Aerospace Science and Technology, Politecnico di Milano, Milan, Italy
[2] Departamento de Física Aplicada III, Universidad de Sevilla, Sevilla, Spain
[3] Área de Mecánica de Fluidos, Departamento de Ingeniería Aeroespacial y Mecánica de Fluidos, Universidad de Sevilla, Sevilla, Spain
* alvaro.romero.calvo@gmail.com

Introduction

The term sloshing refers to the forced movement of liquids in partially filled containers. In a low-gravity environment, the liquid mixes with pressurizing gas bubbles and adopts a random position inside the tank, resulting in unwanted perturbations and a complicated design (Dodge 2000). Liquid sloshing has consequently been a major concern for space engineers since the beginning of the space era.

The sloshing of magnetic liquids has distinctive characteristics that suggest an interesting approach to this problem. Magnetic fields can be used to shift the natural frequencies and damping ratios of an oscillating fluid (Kaneko et al. 2013). Due to the short range of the magnetic interaction, research has been historically focused on what is known as *magnetic liquid positioning* (Marchetta and Winter 2010). In the age of nanosatellites, however, propellant tanks are much smaller, and the whole fluid volume can be reached with small, low-cost magnets.

The implementation of magnetic sloshing dampers for spacecraft control requires an accurate understanding of basic physics and modelling capability of magnetic liquid dynamics. In this respect, the prediction of the forcing dynamics response of a ferrofluid pushed the authors to develop a dedicated theoretical framework and an equivalent mechanical model for microgravity conditions. High quality measurements of this unexplored phenomenon can only be obtained in microgravity, since the capillary regime, the study of lateral sloshing and the application of an inhomogeneous magnetic field are compelling characteristics for on-ground studies.

Following the experiment on axisymmetric magnetic liquid sloshing performed by the team *The Ferros* as part of ESA Drop Your Thesis! 2017 (Romero-Calvo et al., 2018), and in the framework of the UNOOSA DropTES Programme, StELIUM (Sloshing of magnetic LIqUids in Microgravity) will study the lateral sloshing of ferrofluids in microgravity. This new experiment will be launched four times at ZARM's Drop Tower in Bremen. The campaign, scheduled for November 2019, is expected to help validate the semi-analytical inviscid and CFD sloshing models developed by the authors.

Experimental Setup

The experimental setup of StELIUM, represented in Figure 1, has been designed to measure the lateral sloshing of a ferrofluid in microgravity. The fluid volume is excited by a single-period sinusoidal impulse with a given amplitude and frequency. Once the movement starts, the fluid is left oscillating under the influence of a static magnetic field.

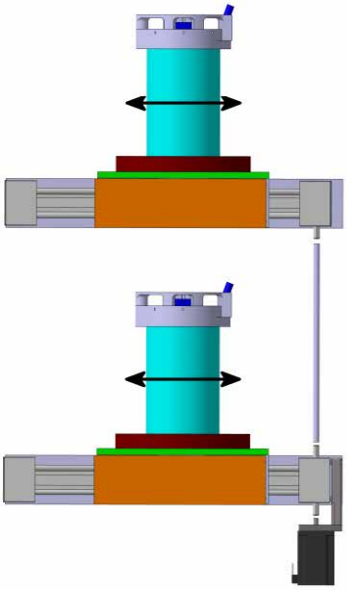

Figure 1: Experimental setup, composed by: ferrofluid vessels (clear blue), coils (brown), support platforms (green), detection system (light grey), sliding mechanism (dark grey), stepper engine (black), holders (orange). The black arrows represent the direction of the movement.

Two capsule platforms hold identical assemblies of the system. Each assembly is composed by a plexiglas container of 11 cm diameter and 20 cm height, filled up to 5 cm with a 1:10 volume solution of the Ferrotec EMG-700 water-based ferrofluid. The container is surrounded by a coil of 94.25 mm diameter with a width of 25 mm and 200 windings of a 1.8 mm copper wire. A PicoLAS LDP-CW 120-40 constant current power source feeds the coils with intensities ranging from 0 to 20 A. Both assemblies are simultaneously moved by a sliding mechanism, powered by a stepper engine and connected with an aluminium shaft.

A newly developed laser-based detection system measures the vertical displacement of 20 equally distributed points of the surface and the shape of the equilibrium meniscus. Redundant measurements are obtained with a laser time-of-flight sensor, a lateral camera and a pressure transducer.

The catapult mode of ZARM's drop tower offers 9.4 seconds of high-quality microgravity conditions. Due to the damping

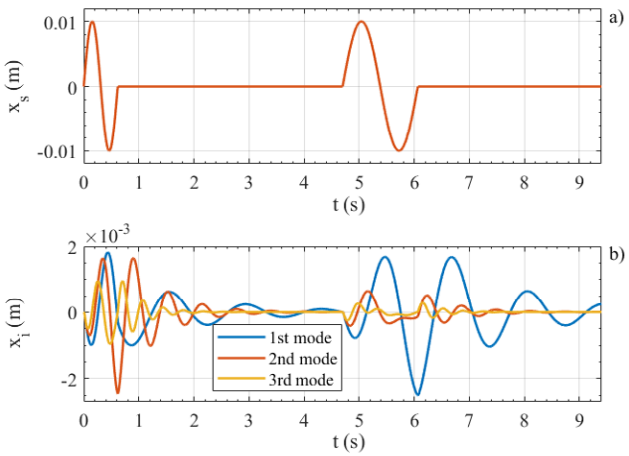

Figure 2: Example of the modal response of an equivalent mechanical sloshing model. (a) Lateral displacement imposed to the ferrofluid container, (b) Lateral displacement of the three spring-mass systems corresponding to the ferrofluid response.

of the oscillatory movement, two percussions can be applied with a separation of 4 seconds. The first is set at a frequency close to the second sloshing mode, while the second aims to excite the fundamental mode. This choice aims to produce two qualitatively different oscillations from which the natural frequencies can be easily extracted. Figure 2 represents the described excitation profile and the modal response of an equivalent sloshing mechanism composed by three spring-mass systems. The result is a maximized scientific output, with two symmetric oscillations at different frequencies for each launch.

Expected results

The measurements will be employed to (i) compute first two sloshing modes and frequencies of the system, (ii) extract damping ratios of each mode, (iii) compute the wall pressure distributions, and (iv) create a high-quality dataset for CFD validation.

The inviscid models developed by the authors point to significant increases of the natural sloshing frequencies due to the action of the magnetic field. These results, however, are highly dependent on the geometry of the system, the dynamics of the ferrofluid contact line or the effective contact angle at the wall, among others. The magnetic models that drive the dynamics of ferrofluids have also been a subject of discussion (Liu and Stierstadt 2009). Consequently, a strong scientific interest is placed on validating these models and clarifying the role of the different contributions.

Conclusions

As part of the UNOOSA DropTES Programme, the StELIUM student team aims to obtain unprecedented measurements of the lateral sloshing of ferrofluids in microgravity. These results will shed light on this relatively unexplored phenomenon and help validate the theoretical framework developed by the team. Significant contributions may be produced in fields like space propulsion or attitude dynamics and control. The experimental setup designed by the students will be catapulted at ZARM's drop tower in November 2019.

Acknowledgements

The authors thank the United Nations Office for Outer Space Affairs (UNOOSA) for its financial and administrative support in the framework of the UNOOSA DropTES Programme, the Deutsches Zentrum für Luft- und Raumfahrt e.V. (DLR) for its financial support, the Center of Applied Space Technology and Microgravity (ZARM) for its technical and financial support, and Politecnico di Milano, the University of Seville and the University of Colorado Boulder for ther contribution to the public outreach of the project.

References

F. T. Dodge, The New Dynamic Behavior of Liquids in Moving Containers, *Southwest Research Institute*, 2000.

S. Kaneko, T. Ishiyama y T. Sawada, Effect of an applied magnetic field on sloshing pressure in a magnetic fluid, *Journal of Physics: Conference Series*, vol. 412, p. 012018, 2013.

J. G. Marchetta y A. P. Winter, Simulation of magnetic positive positioning for space-based fluid management systems, *Mathematical and Computer Modelling*, vol. 51, pp. 1202-1212, 2010.

Á. Romero-Calvo, T. Hermans, G. Cano Gómez, L. Parrilla Benítez, M. A. Herrada Gutiérrez, and E. Castro-Hern ández, Ferrofluid dynamics in microgravity conditions, *Proceedings of the Second Symposium on Space Educational Activities,* 2018.

M. Liu and K. Stierstadt, Colloidal Magnetic Fluids, *Chap. Thermodynamics, Electrodynamics, and Ferrofluid Dynamics*, pp. 83–156, 2009

26th European Low Gravity Research Association Biennial Symposium and General Assembly
14th International Conference on "Two-Phase Systems for Space and Ground Applications"
European Space Agency Topical Teams meetings
Granada (Spain), September 24-27, 2019

Poster 170

INCIDENCE OF SPACE WEATHER ON IMMUNE SYSTEM AND DEVELOPPEMENT OF EPIDEMICS

Claude Gaudeau de Gerlicz, PhD (1), Andrey Ponomarenko, PhD (2), Lucas Yves, (1), Phillpe Bobola, PhD (1), Jean-Claude Borderon, MD (3), Xavier d'Hérouville, VMD (1) and Mathias Antoine, BTE (1)

(1) Bioespas International laboratory Tours, France: Bioespas.international@gmail.com

(2) Odessa National Medical University, Odessa, Ukraine: aponom@hotmail.com

(3) Asspic Santé : JC.Borderon@wanadoo.fr

ABSTRACT

Accumulated evidence suggests that the space weather could influence host-virus interactions and the immune response in animals, leading to epidemics of influenza. We proposed that the proteins of the Cryptochrome (CRY) family represent the part sensitive to the magnetic field of the epigenetic control mechanism. It is known that CRY are repressors of the CLOCK / BMAL1 circadian transcription complex activity. At the same time, the functional activity of CRY is very sensitive to weak MF due to pairs of radicals that occur periodically in the active site of CRY and mediate the mechanism of radical pairs of magnetoreception. The major circadian complex influences the expression of genes related to signaling pathways dependent on NF-κB and glucocorticoids.

Therefore MFs can alter the immune response and endocrine regulation that facilitate the endemic spread of viral diseases. CRY are sole proteins, which combines the MF-sensory and genome-regulatory functions.

The act as mediators between living beings and their electromagnetic environment thanks to the radical pair mechanism of magnetoreception. Biological reactions in living beings, including response to stress and infection depends on the function of the circadian transcriptional complex, which in turn may be regulated by magnetic fields, including the geomagnetic field. Space weather factors, (solar radiation, geomagnetic field fluctuations, etc...) are not an "electrical switch" which cause an immediate response, but rather a primer that which initiates hidden log-lasting process.

Evident results of such hidden activity can manifest months and years after the onset

of the causative cosmic/solar event. The geomagnetic surveillance and data analysis could improve epidemiological prognosis.

Conclusion

The model the epidemic-predisposing processes two expert systems have been elaborated: the Immune-Expert system and Biosphere-Expert system. Geomagnetic surveillance and data analysis could improve the epidemiological prognosis. To evaluate the health consequences of the weakened geomagnetic field (due to the causes described above), in terms of alterations in immunity and possible pathogen changes (on individual and population levels), we propose an experimental research scheme that could be conducted in parallel both on land and in the ISS. Finally, we propose to develop a modeling of all the predisposing factors of the epidemic process: two expert-systems were thus conceived.

REFERENCES

(1) Gaudeau C. et al, Immuno modelling, Scientific Data Management, Vol 3, n°4 1999

(2)Zaporozhan V., Ponomarenko A., Mecanisms of Geomagnetic Field Influence on gene expression using influenza as a Model System: basics of physical epidemiology, Int. J. Environ. Res. Public Health,7, 938-965, 2010

(3) Ponomarenko A. and Skripchenko G.. Some immunogenicity determinative factors (IDF) in influenza viruses Immunology Letters 56:305 (1997)

26th European Low Gravity Research Association Biennial Symposium and General Assembly
14th International Conference on "Two-Phase Systems for Space and Ground Applications"
European Space Agency Topical Teams meetings
Granada (Spain), September 24-27, 2019

Poster 175

Interaction between flow fields and evaporation of acoustically levitated droplet

Y. Sasaki[1], K. Kobayashi[1], A. Kaneko[1], K. Hasegawa[2], Y. Abe[1]

[1] Univ. of Tsukuba, Tsukuba, Japan, [2] Kogakuin Univ., Shinjuku, Japan;
S1820901@s.tsukuba.ac.jp

Introduction

In recent years, the container-less processing using levitation techniques has been attracted. This technique can solve problems such as heterogeneous nucleation and contamination due to container walls, thus it is expected to apply to material science, pharmatsutical science and analytical chemistry. Although an acoustic levitation is one of the promising levitation techniques, it is widely known that the characteristic internal and external flows of the levitated droplet occur due to nonlinear acoustic effects[1]. It has been pointed out that these flows influence on phase change of levitated droplets[2].

The purpose of this study is to elucidate relationships between these flows and phase change. In this paper, we focus on the visualization measurement of these flow structures. Water and ethanol were used and levitated as test fluids with different saturated vapor pressures. Internal and external flow structures of these test fluids were measured simultaneously by stereo PIV.

Internal and external flow structures were found to be transited depending on saturated vapor pressure. We also consider relationships between internal and external flows and phase change in the case of a droplet of 50wt% ethanol solution.

Results and discussion

¡Error! No se encuentra el origen de la referencia. shows transition of (A) internal and (B) external flow structures of 50wt% ethanol droplet. (A) Internal flow structure and (B) External flow structure were visualized by using stereo PIV and multiple exposure images, respectively.

Immediately after the stable levitation (t = 0 s), vertically symmetrical vortices were generated in the droplet, as shown in **¡Error! No se encuentra el origen de la referencia.**(A). As evaporation progresses, these vortices transitted (t = 30 s) and finally disappeared (t = 100 s). For external flow field, flow directions were toward the droplet itself as shown on the top and bottom of the droplet by pink arrows, immediately after the stable levitation (t = 0 s). Simultaneously, circular vortices which are shown as blue arrows were appeared at upper and lower edge of the droplet as shown in **¡Error! No se encuentra el origen de la referencia.**(B). With evaporation, these circular vortices expanded (t = 125 s), and direction of the external flow was transitioned (t = 250 s).

In order to quantify these flow transition with the evaporation of droplet, Fig. 2 shows that the thickness of the circular vortices increased as time passes. They were thickened

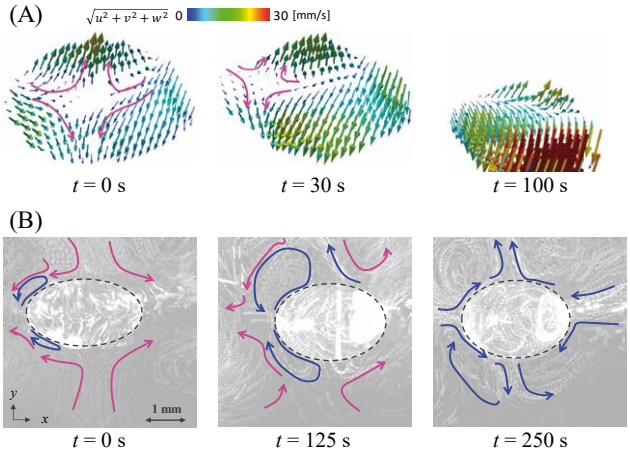

Fig. 1 Transition of (A) internal and (B) external flow structures of 50wt% Ethanol droplet

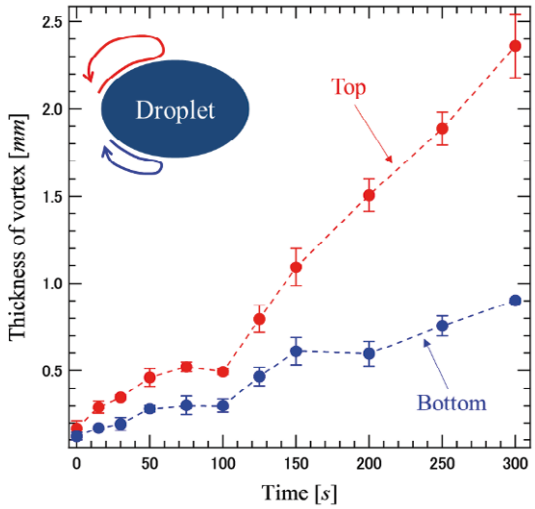

Fig. 2 Thickness of vortices around the droplet

slowly until t = 100 s and they expanded rapidly after t = 100 s. From these results, at first internal flow structure changes from vertically symmetrical vortices (t = 0 s) to rigid rotational motion (t = 100 s) and it decreases the amount of evaporation (less ethanol vapor around the droplet). Note that the change of the vapor concentration distribution around the droplet triggered the external flow structure transition.

Reference

1) Trinh, E. and Robey, J, Phy. Fluids, Vol. 6, 3567-3579(1994)

2) K. Kobayashi, A. Goda, K. Hasegawa, and Y. Abe, Phy. Fluids, **30**, 8, 082105, (2018)

Poster 182

Gravitational stress and multidrug resistance phenomena in human cancer cells

D. Przystupski[1], A. Górska[2], J. Kulbacka[3]

[1] Faculty of Medicine, Wroclaw Medical University, J. Mikulicza-Radeckiego 5, 50-345 Wroclaw, Poland; [2] Department of Biological Sciences, Institute of Experimental Biology, University of Wroclaw, Kanonia 6/8, 50-328 Wroclaw, Poland; [3] Department of Molecular and Cellular Biology, Wroclaw Medical University, Borowska 211A, 50-556, Wroclaw, Poland
dawid.przystupski@gmail.com

Introduction

Numerous studies have reported that gravity alteration has remarkable influence on growth and biological processes of tumorous cells. Therefore, gravity-related experiments have become an promising method to improve our knowledge in the field of cancer biology and may be useful to detect interesting implications for future cancer treatment. Most studies have tended to focus on the impact of altered gravity on the susceptibility to cytostatic drugs; however, issues linked to hypergravity have not been dealt with in depth. Our idea of biomedical research is supported by ESA and ESA Academy in Spin Your Thesis! 2019 competition which allowed us to use Large Diameter Centrifuge (LDC; Noordwijk, Netherlands) in order to evaluate the effect of simulated hypergravity on cancer cells. Taking this concept further an independent preliminary experiments were performed using Random Positioning Machine (RPM) to analyse the effect of simulated microgravity in controlled laboratory conditions.

Materials and methods

In an attempt to determine whether altered gravity might be one of the factors modulating multidrug resistance (MDR) in cancer cells we used well defined commercial human ovarian cancer cell line SKOV-3 resistant to cisplatin and doxorubicin. The cells were seeded on T25 cell culture flasks fully filled with growth medium (without the presence of air bubbles) and exposed to simulated microgravity for 1, 2, 4, 12, 24h in the presence of cisplatin as a model of cytostatic drug administered directly before the experiment. After centrifugation, the cells were detached and seeded on 6-well and 96-well plates for 24 and 72 hours to perform cytotoxicity, cell death and cell cycle analyses. Additionally, the cells were cultured on coverslips and fixed directly after the centrifugation to evaluate cell morphology using 3D Cell Explorer (Nanolive), confocal and scanning electron microscope.

Results

Our studies revealed that SKOV-3 cells are susceptible to simulated microgravity which affects cell morphology and drug efficiency. We observed altered cell shape, presence of membrane blebbing, lack of lamellipodia and intracellular rearrangement of cytoskeletal fibres (actin, β tubulin and zyxin) even when the cells were cultured on RPM for 2 hours (Fig. 1). Cytotoxicity, cell death and cell cycle assays showed increased percentage of apoptotic cells after centrifugation on RPM in the presence of cisplatin in comparison to control, not centrifuged cells.

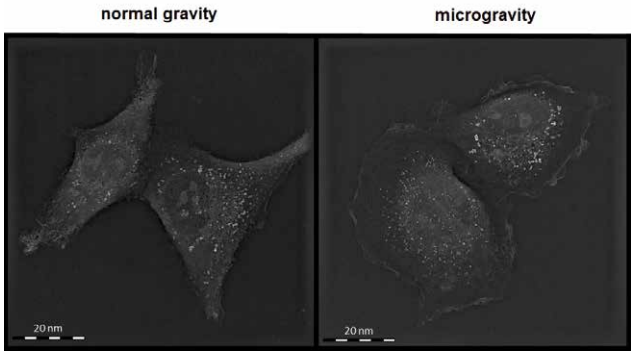

Figure 1: SKOV-3 cells morphology evaluated using 3D Cell Explorer after culturing for 2h on RPM.

Conclusions

We believe that gravitational stress may affect cell pathways involved in multidrug resistance phenomena, especially associated with cell membrane and cytosceleton, resulting in higher sensitivity of cancer cells to chemotherapeutics. The investigation and clarification of these phenomena may constitute initial step toward enhancing our understanding of the relationship between cellular resistance to chemotherapy and the response to various gravitational stimuli. In our view this experiment constitutes an excellent initial step toward enhancing our understanding of the relationship between cellular resistance to chemotherapy and the response to gravity alteration.

Acknowledgements

The work was created as part of the activity of the Student Research Group "Biology of Cancer Cell" at the Wroclaw Medical University (SKN No. K 148). The research was supported partially by the Statutory Funds of Wroclaw Medical University no. ST.E130.16.060 (manager prof. J. Zalewski), funds of Wroclaw University of Science and Technology and by "Najlepsi z Najlepszych 3.0" program no. POWER.Z600.18.002 founded by Polish Ministry of Science and Higher Education.

26th European Low Gravity Research Association Biennial Symposium and General Assembly
14th International Conference on "Two-Phase Systems for Space and Ground Applications"
European Space Agency Topical Teams meetings
Granada (Spain), September 24-27, 2019

Poster 184

The cytoprotective role of antioxidants in mammalian cells under rapidly varying UV conditions during stratospheric balloon campaign

A. Górska[1], D. Przystupski[2], , P. Wawryka[2], J. Kulbacka[3]

[1] Department of Biological Sciences, Institute of Experimental Biology, University of Wroclaw, Kanonia 6/8, 50-328 Wroclaw, Poland; [2] Faculty of Medicine, Wroclaw Medical University, J. Mikulicza-Radeckiego 5, 50-345 Wroclaw, Poland; [3] Department of Molecular and Cellular Biology, Wroclaw Medical University, Borowska 211A, 50-556, Wroclaw, Poland
agata_gorska@onet.eu

Introduction

The current age of dynamic development of the space industry brings the mankind closer to routine manned space flights and space tourism. This progress leads to a demand for intensive astrobiological research aimed at improving strategies of the pharmacological protection of the human cells against extreme conditions. Although routine research in space remains out of our reach, it is worth noticing that the unique severe environment of the Earth's stratosphere has been found to mimic subcosmic conditions, giving rise to the opportunity to use the stratospheric surface as a research model for the astrobiological studies. Our study included launching into the stratosphere a balloon containing mammalian normal and cancer cells treated with various compounds to examine whether these substances are capable of protecting the cells against stress caused by rapidly varying temperature, pressure and radiation, especially UV. Due to oxidative stress caused by irradiation and temperature shock, we used natural compounds which display antioxidant properties, namely - catechin isolated from green tea, honokiol derived from magnolia, curcumin from turmeric and cinnamon extract. "After-flight" laboratory tests have shown the most active antioxidants as potential agents which can minimize harmful impact of extreme conditions on human cells.

Materials and methods

Human ovarian cancer cells (SKOV-3; described as "cancer cells") and non-cancer Chinese hamster ovary cells (CHO-K1; described as "normal cells") after 24-hour incubation with various antioxidants were detached, suspended in freezing medium Bambanker™ and placed in microtubes 30 minutes before the balloon flight. Then, the samples were transported on ice to the starting point and placed in a radiation transmitting gondola, located on the environmental measurement unit with accelerometer and temperature, pressure and UV sensors. One half of the samples was covered with aluminum foil to protect the cells against irradiation – mostly UV (the samples described in the study as "protected against radiation"), another half was sent into the stratosphere without the protective layer (described as "not protected against radiation"). As a result, we were able to evaluate the effect of radiation on examined cells in the presence of various antioxidants. As a control we used the appropriate number of cells not treated with antioxidants and not sent into the stratosphere, which were incubated at 37°C in a humidified incubator with 5% CO2 during the flight. Directly after landing, the biological samples were transported on ice to the specialized laboratory, where after-flight tests were performed (membrane permeabilization assay, intracellular reactive oxygen species generation assay, mitochondrial activity in MTT assay, cell death assay, clonogenic assay, neutral comet assay and immunocytochemical staining). The scheme of the completed experiment is presented on Fig. 1.

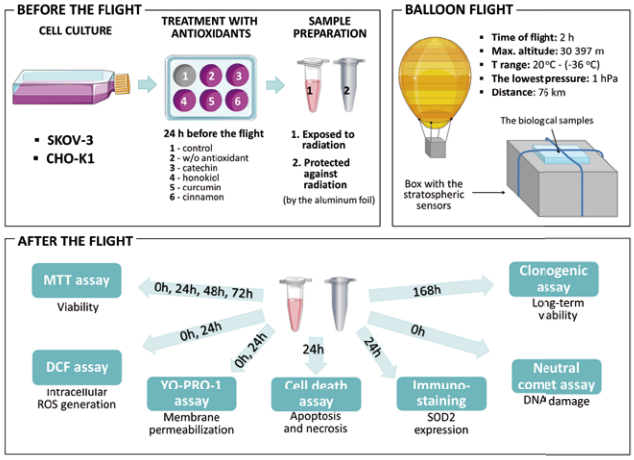

Figure 1: The schematic representation of the procedure of experiment and balloon flight.

Results and Conclusions

The biological samples were launched to the stratosphere on the 30th of April 2018, from Wrocław, Poland (51°06'23.6" N 17°03'32" E) at 11:30 AM. The balloon reached the stratosphere at maximal altitude of 30 298 m. The mission lasted about 2 hours: 90 min of ascent and 25 min of descent; ended at 1:25 PM. The biological samples were collected immediately after landing in Sulisław, Poland (52°23'49.9" N 18°45'52.8" E) and transported directly to the laboratory. During the first stage of ascending phase recorded ambient temperature dropped to -22°C. Subsequently, when the balloon reached the ozonosphere, the ambient temperature increased to -2°C. At the highest altitude, the temperature reached the lowest level of -35°C (Figure 2A) and the lowest pressure (1252 Pa) was measured (Figure 2B). Data provided by two UV sensors showed that top and side walls of the gondola were similarly exposed to the UV radiation during the balloon ascent. However, during the balloon descent there was a difference observed between the measured UV radiation on both sides of the gondola, caused by continuous rotations of the gondola in the last stage of the flight. (Figure 2C). Voltage level of 1170 mV correlates with the highest score (11) in the UV Index-exposition scale, which shows extreme exposure to the UV radiation causing immediate damage of unprotected human skin and eyes. On the right side of the chart there is a

clearly visible period measured by the 1st UV sensor when the parachute was opened, as a result, the gondola the gondola was stabilized. In the upper parts of the atmosphere, the UV dose was more than twofold the dose correlating with the maximum dose in the UV-Index scale (reaching nearly 2463 mV).

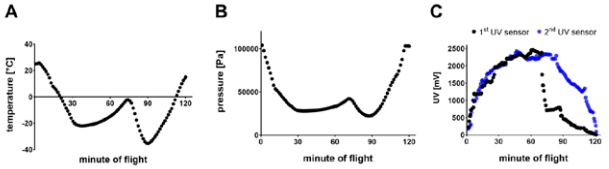

Figure 2: Temperature [°C], pressure [Pa] and UV radiation fluctuations [mV] during the balloon flight. The 1st UV sensor was located at the top wall of gondola, the 2nd UV sensor measured UV radiation at the side wall.

In our study, we analyzed changes in the functions of normal and cancer cells that occurred due to exposure to high radiation as well as low temperature and pressure during stratospheric flight. Our work has led us to a conclusion that the application of the carefully selected compounds enables us to manipulate cellular stress response depending on the type of cells. Final conclusions about the highest protective potential should be drawn based on the genotoxicity assays and cell death assays. Altogether, these findings suggest that honokiol and catechin have the best protective effect on the normal cells, whereas curcumin and cinnamon act as radio- and light-sensitizers increasing the percentage of apoptotic cancer cells and DNA damage.

The results constitute a significant step towards the investigation of possible strategies for the cell protection in space environment and provide new insights into the application of the examined compounds for the prevention and treatment of cancer. We believe that our research will remain valuable for resolving the difficulty of the human and biological material protection in space. Due to its relatively low costs, our approach remains the economic alternative for simulated subcosmic conditions conducted in the laboratory, which require far more expensive, specialized measurements.

Acknowledgements

The work was created as part of the activity of the Student Research Group "Biology of Cancer Cell" at the Wroclaw Medical University (SKN No. K 148). The research was supported partially by the Statutory Funds of Wroclaw Medical University no. ST.E130.16.060 (manager prof. J. Zalewski), funds of Wroclaw University of Science and Technology and by "Najlepsi z Najlepszych 3.0" program no. POWER.Z600.18.002 founded by Polish Ministry of Science and Higher Education.

26th European Low Gravity Research Association Biennial Symposium and General Assembly
14th International Conference on "Two-Phase Systems for Space and Ground Applications"
European Space Agency Topical Teams meetings
Granada (Spain), September 24-27, 2019

Poster 185

Heat Loss Analysis for Accurate Evaluation of Fluid Conditions at Test Section in Flow Boiling Experiments onboard International Space Station

Koichi Inoue[1], Haruhiko Ohta[2], Hitoshi Asano[3], Osamu Kawanami[4], Ryoji Imai[5], Koichi Suzuki[6], Yasuhisa Shinmoto[2], Yuuki Toyoshima[7], Satoshi Matsumoto[8]

[1]The University of Kitakyushu, Kitakyushu, Japan, [2]Kyushu University, Fukuoka, Japan, [3]Kobe University, Kobe, Japan, [4]University of Hyogo, Himeji, Japan, [5]Muroran Institute of Technology, Muroran, Japan, [6]Tokyo University of Science, Noda, Japan, [7]Japan Manned Space Systems Corporation, Tsukuba, Japan, [8]Japan Aerospace Exploration Agency, Tsukuba, Japan
inoue-k@kitakyu-u.ac.jp

Introduction

Boiling and two-phase flow thermal systems have a great potential for realizing high-efficiency heat exchange and heat transportation in future space systems. Boiling and two-phase flow phenomena can change with gravity level and therefore reliable fluid flow and heat transfer data under microgravity are essential for the thermal design of the space systems. Systematic flow boiling experiments have been carried out in the International Space Station (ISS) as a JAXA project named "TPF (Two-Phase Flow)" experiment. The detailed information on TPF experiment was reported by Ohta, et al. (2016).

For the precise analysis of the gravity effects, accurate evaluation of fluid conditions at the heating test section are quite important and the development of thermal models of heat loss from test fluid to the ambient is needed. In this paper, the heat loss characteristics of the TPF flight model (FM) in ISS are reported.

Experimental apparatus

A schematic diagram of test loop is shown in Fig. 1. The test loop consists of a circulating gear pump, a preheater, heating test sections, adiabatic observation sections, a condenser, accumulators, which are packed with auxiliary systems for power supply, data acquisition and image recording into the TPF FM with a size of 670mm × 810mm × 510mm. The TPF FM is mounted in the multi-purpose small payload rack (MSPR) in the Japanese experimental module "KIBO". Electric power, cooling water, avionics air, etc. are supplied from MSPR to TPF FM. Because the test loop is densely packed and avionics air passes through the inside of TPF FM for preventing local excessive temperature rise, the heat loss paths from the test loop to the ambient are very complicated and unknown.

The test fluid selected is perfluoro-hexane for the reduction of power supply and tube size. Subcooled test fluid is pumped into the preheater. The liquid subcooling or vapor quality at the inlet of the heating test sections is adjusted by the preheater. The system pressure is maintained at almost atmospheric pressure by the operation of mechanical accumulators.

The test loop has two heating test sections of a copper heating tube and a transparent glass heating tube. These two heating tubes are connected in parallel with valves and test fluid flows through either of heating tubes according to the experimental objects. In the present report, the heat loss from the test loop is analyzed for the copper heating tube. The copper heating tube has an inner diameter of 4.0mm and a heated length of 368mm. Electric heater and ten K-type thermocouples are attached to the copper heating tube. The copper heating tube is installed between stainless steel brackets and is covered by thermal insulation materials.

The preheater consists of a copper tube with outer diameter of 3/8inch, a thickness of 1mm and a length of approx. 1.6m. The preheater is operated by electric heaters and covered by thermal insulation materials.

Heat loss model development

For the accurate evaluation of fluid conditions at the test section of a copper heating tube, two heat loss models for $\dot{Q}_{loss,012}$, $\dot{Q}_{loss,345}$ are considered as shown in Fig. 2. To develop the heat loss models, preliminary experiments for single-phase liquid flow were performed. Test fluid was heated below the saturation temperature by the preheater and was introduced to the heating test section. When the test fluid is not heated at the copper heating tube, the heat loss $\dot{Q}_{loss,012}$, $\dot{Q}_{loss,345}$ can be calculated as

$$\dot{Q}_{loss,012} = \dot{Q}_{PH} - \dot{Q}_{f012} \quad (1)$$

$$\dot{Q}_{loss,345} = \dot{Q}_{f,345} \quad (2)$$

$$\dot{Q}_{f,012} = \dot{m}(h_2 - h_1) \quad (3)$$

$$\dot{Q}_{f,345} = \dot{m}(h_3 - h_2) \quad (4)$$

where $\dot{m}$ is mass flow rate of test fluid. $\dot{Q}_{PH}$ is power generation of the preheater. h_1, h_2, h_3 are liquid enthalpy estimated from T_1, T_2, T_3 as shown in Fig. 2.

$\dot{Q}_{loss,012}$ is well correlated by the temperature difference between the surface temperature of preheater $T_{PH,s}$ and avionics temperature T_{avio}, ($T_{PH,s}$ - T_{avio}), and is independent

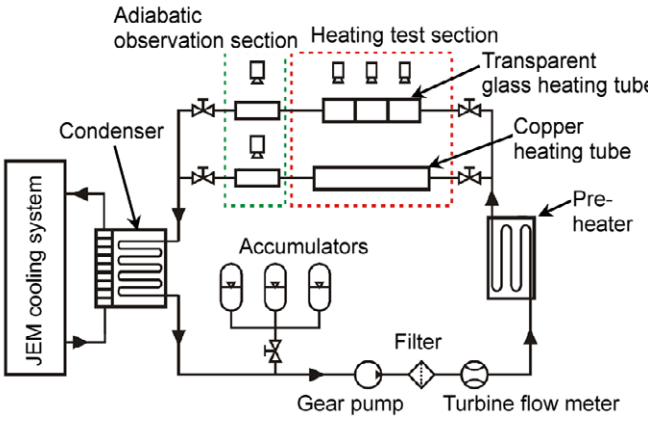

Figure 1: Flow boiling test loop for TPF experiment

of mass velocity G. Hence, it is conjectured that $\dot{Q}_{loss,012}$ can be estimated by Fig. 3 even for the case of liquid-vapor two-phase flow.

Figure 4 shows the relation between the heat loss $\dot{Q}_{loss,345}$ and the logarithmic mean temperature difference $\Delta T_{lm,345}$. $\Delta T_{lm,345}$ is calculated as

$$\Delta T_{lm,345} = \frac{T_2 - T_3}{ln\frac{T_2 - T_{avio}}{T_3 - T_{avio}}} \qquad (5)$$

$\dot{Q}_{loss,345}$ can be correlated by $\Delta T_{lm,345}$ and G. To develop the heat loss model for $\dot{Q}_{loss,345}$, four thermal resistance in series is considered.

$$R_{total} = R_1 + Y_1 + Y_2 + X \qquad (6)$$

where R is thermal resistance for convection heat transfer at the inner tube wall. Y_1 and Y_2 are thermal resistance for conduction in the copper tube wall and thermal insulation, respectively. X is surface radiation and convection resistance at the outer surface of thermal insulation. The value (X+Y_2) is influenced by the installation conditions in the rack to which the avionics air is introduced. Figure 5 shows the evaluation of (X+Y_2) by single-phase liquid flow experiments at higher mass velocity (G=300, 600 kg/m^{2}s). The value (X+Y_2) is regarded as almost constant.

Conclusions

Heat loss models of FM for ISS experiment have been developed to evaluate fluid condition at the copper heating test section. The improvement of the model at the heating test section will be performed to evaluate local heat transfer coefficients with high accuracy.

Acknowledgements

The authors would like to thank Mr. Ukena, Mr. Fujii, Ms. Semba, Mr. Miyawaki, Mr. Nakase, Mr. Inoue for their support in TPF experiment. The authors also thank JSF for the support of TPF project and IHI aerospace for the fabrication of the experimental apparatus.

References

H. Ohta, et al., Development of Boiling and Two-Phase Flow Experiments on Board ISS, Int. J. of Microgravity Science and Application, 33(1) (2016) paper No. 330102 to 330107.

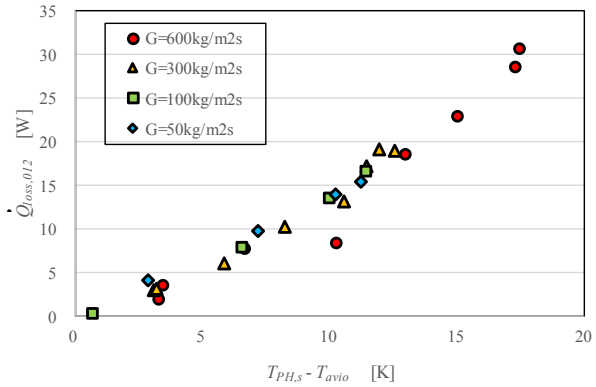

Figure 3: Heat loss $\dot{Q}_{loss,012}$

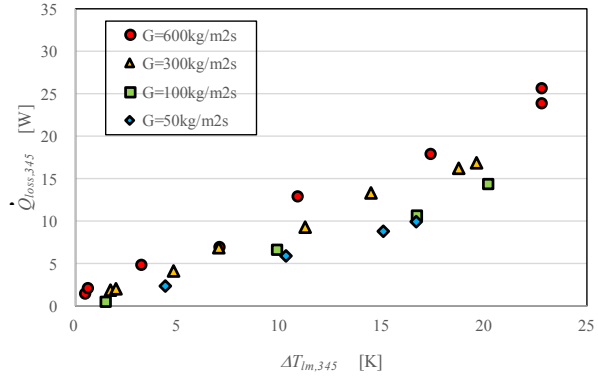

Figure 4: Heat loss $\dot{Q}_{loss,345}$

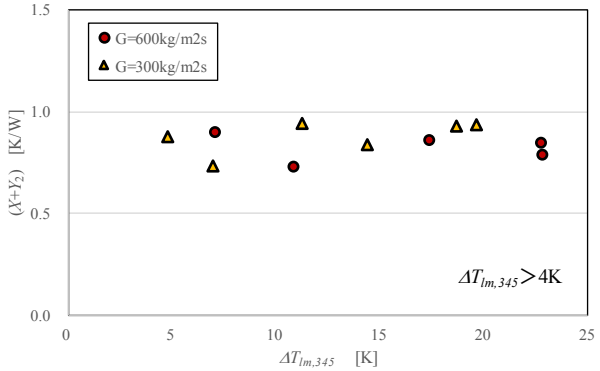

Figure 5: Thermal resistance of insulation materials for $\dot{Q}_{loss,345}$

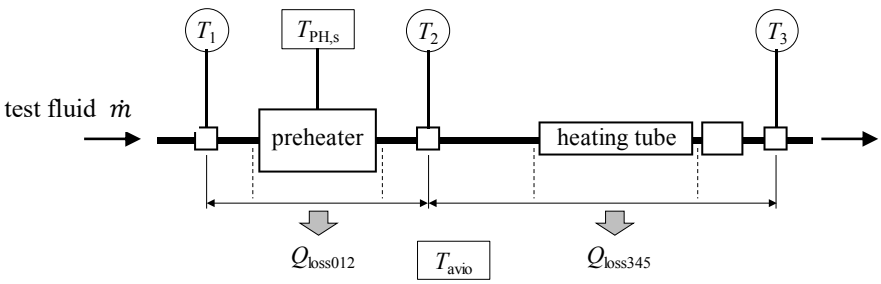

Figure 2: Heat loss models between preheater and copper heating test section

26th European Low Gravity Research Association Biennial Symposium and General Assembly
14th International Conference on "Two-Phase Systems for Space and Ground Applications"
European Space Agency Topical Teams meetings
Granada (Spain), September 24-27, 2019

Poster 190

Experimental Investigation of Gravitational Effects on Two-Phase Flow Behavior and Performance of Polymer Electrolyte Membrane Fuel Cells

Fang YE[1,*], Xuan LIU[1], Jian Fu ZHAO[2, 3], Hang GUO[1], Chong Fang MA[1]

1:MOE Key Laboratory of Enhanced Heat Transfer and Energy Conservation, and Beijing Key Laboratory of Heat Transfer and Energy Conversion, College of Environmental and Energy Engineering, Beijing University of Technology, Beijing 100124, China
2: Key Laboratory of Microgravity, Institute of Mechanics, Chinese Academy of Sciences, Beijing 100190, China
3: School of Engineering Science, University of Chinese Academy of Sciences, Beijing 100049, China
* Corresponding author, E-mail: yefang@bjut.edu.cn, Tel.: +86-10-67391985 ext. 8321

Introduction

Since the polymer electrolyte membrane fuel cell (PEMFC) was first applied in U.S. Gemini Space Program in the 1960s, the PEMFC as a prospective alternative power source has been researched extensively because of its high efficiency of energy conversion, environmental friendliness, high reliability and flexibility.

Owejan et al 2007, Li et al 2007. studied the influence of flow field channels and diffusion media properties on the water accumulation using the neutron radiography. Deevanhxay et al 2011. conducted the visualization of liquid water across the MEA of an operating PEMFCs using high-resolution soft X-ray radiography. Weng et al 2007 applied a PEMFC with transparent windows to observe the two-phase flow in the flow field, investigated the effect of the cathode water flooding on the cell stability and performance, and found that the water flooding became more severe as the cell operated at a low flow rate or low temperature. Liu et al (2006, 2007) self-designed a transparent PEMFC, and experimentally studied the liquid water accumulation and pressure drop both at the anode and cathode flow channels of an operating PEMFC. The results indicated that the liquid water at the cathode flow channels was much more than that of anode flow channels, the pressure drop at cathode side was higher than the anode side. Even though the PEMFC has received much attention in recent years, many researchers focus on the performance and two-phase flow behavior in the normal gravity. The performance and two-phase flow behavior experiment of the PEMFC at low temperature and short-term micro-gravitational environment had been conducted (Guo et al 2014, 2017). The performance and two-phase flow behavior at high temperature and low external circuit load were also completed (Guo et al 2016, 2014).

In this study, the performance and two-phase flow behavior at high temperature and high external circuit load at a 3.6 s short term micro-gravitational environment were investigated.

Experimental

The experimental PEMFC, a self-designed single cell (shown in Fig. 1), whose components were self-designed and self-manufactured except for the membrane electrode purchased by BCS fuel cell Inc.. A single serpentine flow channel with the width of 2 mm and the depth of 2 mm was applied in the PEMFC; the width of the rid was 2 mm. The PEMFC applied the up-entering and down-out design strategy to facilitate liquid water to remove. The MEA consisted of a polymer electrolyte membrane (Nafion 112) sandwiched by catalyst layers at the anode and cathode sides, and gas diffusion layers at the anode and cathode side. The active area supplied by the MEA was 25 cm^2 and the catalysts, Pt, loaded on the anode and cathode sides were both 1 mg/cm^2. The aluminum alloy was used as the material of the anode end plate to make the fuel cell lighter, the nonporous graphite was applied in cathode end plate to obtain the better performance and stability. The four sides of the square hole in the cathode end plate were modified at an angle (marked with blue circle), which broadened the accessible area of visible light.

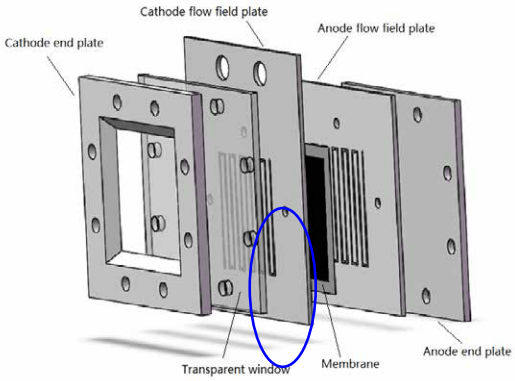

Fig.1 The diagram of experimental PEMFC

Results and discussion

Fig. 2 shows reproducibility of the experimental system, the performance curves of the PEMFC with vertical channels at oxygen flow rate of 60 ml/min.

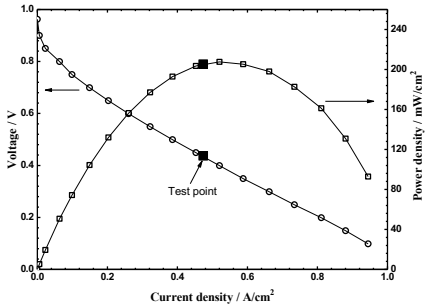

Fig. 2 Cell performance of the PEMFC with vertical flow channels in normal gravitational environment, O_2: 60 ml/min.

To manifest the reproducibility of the normal gravitational experiment, the cell performance was measured in the ground laboratory before half a month; the dates were shown as hollow symbols. After the ground experiment, the PEMFC operated for more than 1.5 h at the top of the drop tower in normal gravitational condition, and the dates at the external circuit resistance of 0.03 Ω were shown as solid

point. The test points were consistent with the performance curves at the ground laboratory, which indicated that the PEMFC achieved a stable operating state before the micro-gravitational experiment, and the experiment had a good reproducibility. Other group experiments followed the steps to be conducted, and obtained good reproducibility.

Two-phase flow behavior at the cathodic side of the PEMFC with vertical channels at oxygen flow rate of 60 ml/min is shown in Fig. 3. Before 0.000 s, the PEMFC ran at the top of the drop tower in the normal gravitational circumstance, at the time of 0.000 s, the drop capsule was released, and the PEMFC entered the 3.6 s micro-gravitational environment, at the time of 3.600 s, the drop capsule was recovered by the recovery string bag, the short-term micro-gravitational environment ended. Comparing images of gas-liquid two-phase flow behavior captured by the high speed video camera at different times, during the 3.6 s period, the liquid water aggregating at the bottom of flow channels is swept by the reactant gas, and evenly distributed to the gas diffusion layer, this phenomenon is marked with blue color. Compare the image of 0.000 s and the image of 2.000 s, the passive removal of liquid water can be clearly observed at the time of 2.000 s, the removal of liquid water increases the effective area of the electrochemical reaction and alleviates the water flooding to some degree, which causes the performance improvement of the PEMFC.

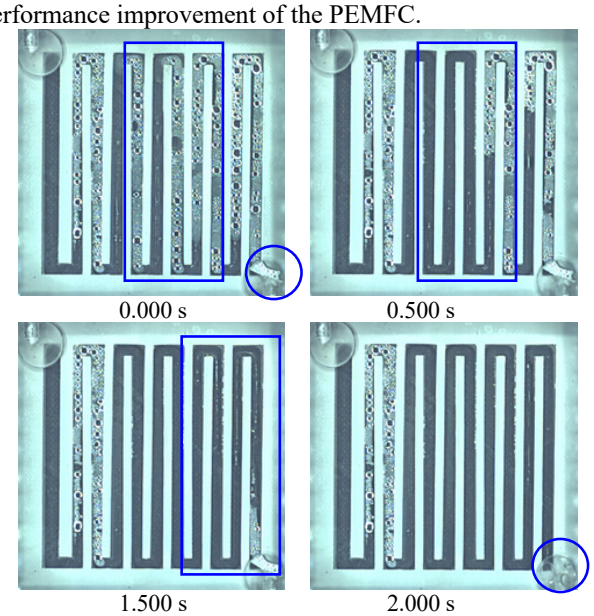

Fig. 3 Visualization of two-phase flow behavior at cathode flow field of the PEMFC with vertical channels at oxygen flow rate of 60 ml/min

Conclusions

In the paper, the performance and two-phase flow behavior of the PEMFC under the high external circuit load and at high temperature were investigated. Additionally, the gravitational effects on the performance and two-phase flow behavior were studied. The main results are as follows:

1. For the PEMFC with vertical channels in the normal gravity, the PEMFC with higher oxygen flow rate shows better performance at the high temperature and under the high external circuit load.
2. Through the comparison of two-phase behavior of the PEMFC with vertical channels and the PEMFC with horizontal channels, the same variation tendencies are presented; it is clearly observed that the liquid water aggregating in the flow channels decreases when oxygen flow rate increases.
3. When the PEMFC enters the micro-gravitational environment, the performance of the PEMFC at the high external circuit load and the high temperature has a slight change, except for the PEMFC with vertical channels at the flow rate of 60 ml/min. The liquid water aggregating in the flow field is little in other three cases of PEMFCs, therefore, the gravitational effects on the performance and two-phase flow behavior are slight.
4. Compared with previous published experimental dates, it is clearly found that the gravitational effect on the PEMFC with vertical channels is higher than that of horizontal channels, which has an important significance on the design of the PEMFC applied in the space missions.

Acknowledgements

The authors would like to appreciate the financial support from the National Natural Science Foundation of China (Grant No. 51476003). Additionally, thank Mr. Xiaohui Wu, Mr. Shixin Wan, and Mr. Minggang Wei for the kind help and discussion, and thank Ms. Junfen Li for the typesetting.

References

Owejan J P, Trabold T A, Jacobson D L, et al. Effects of flow field and diffusion layer properties on water accumulation in a PEM fuel cell[J]. *International Journal of Hydrogen Energy*, 2007, 32(17): 4489-4502.

Li X, Sabir I, Park J. A flow channel design procedure for PEM fuel cells with effective water removal [J]. *Journal of Power Sources*, 2007, 163(2): 933-942.

Deevanhxay P, Sasabe T, Tsushima S, et al. Investigation of water accumulation and discharge behaviors with variation of current density in PEMFC by high-resolution soft X-ray radiography [J]. *International journal of hydrogen energy*, 2011, 36(17): 10901-10907.

Weng F, Su A, Hsu C. The study of the effect of gas stoichiometric flow rate on the channel flooding and performance in a transparent fuel cell [J]. *International journal of hydrogen energy*, 2007, 32(6): 666-676.

Liu Xuan, Guo Hang, Ye Fang, et al. Water flooding and mass transfer enhancement in flow channels of PEMFCs [J]. *Journal of Engineering Thermophysics*, 2006: S2.

Liu X, Guo H, Ye F, et al. Water flooding and pressure drop characteristics in flow channels of proton exchange membrane fuel cells [J]. *Electrochimica Acta*, 2007, 52(11): 3607-3614.

Guo H, Liu X, Zhao J F, et al. Experimental study of two-phase flow in a proton exchange membrane fuel cell in short-term microgravity condition[J]. *Applied Energy*, 2014, 136: 509-518.

Guo H, Liu X, Zhao J F, et al. Gas-liquid two-phase flow behaviors and performance characteristics of proton exchange membrane fuel cells in a short-term microgravity environment[J]. *Journal of Power Sources*, 2017, 353: 1-10.

Guo H, Liu X, Zhao J F, et al. Effect of low gravity on water removal inside proton exchange membrane fuel cells (PEMFCs) with different flow channel configurations[J]. *Energy*, 2016, 112: 926-934.

26th European Low Gravity Research Association Biennial Symposium and General Assembly
14th International Conference on "Two-Phase Systems for Space and Ground Applications"
European Space Agency Topical Teams meetings
Granada (Spain), September 24-27, 2019

Poster 191

Effect of contact line on bubble growth and detachment in a micro-channel

L. BOUBENDIR[1], S. CHIKH[1], L. TADRIST[2]

[1] USTHB, Faculty of Mechanical and Process Engineering, LTPMP, Alger 16111, Algeria.
E-mail : bou_lynda4@yahoo.fr, salahchikh@yahoo.fr
[2] Aix Marseille Université, CNRS, Laboratoire IUSTI, UMR 7343, Marseille 13453, France.
E-mail : lounes.tadrist@univ-amu.fr

Introduction

Two-phase fluid flows inside mini/micro-channels are of practical importance in many miniaturized engineering systems. Two-phase systems still pose challenges for engineering design. The presence of gas–liquid interfaces, dominance of surface forces, moving contact lines, wettability, dynamic contact angle hysteresis and flow in confined geometries are some of the unique features of two-phase systems, which manifest into complex transport phenomena.

Most of the work done to date in this field did not bring any particular attention to the contact line (CL) that separates the three phases, solid, liquid and gas, at the injection orifice. For most theoretical, experimental or numerical works, the authors implicitly assumed that the CL is located and pinned at the inside diameter of the injection nozzle. To our knowledge only the experimental work of Vafaei and Wen 2010, Byakova et al. 2003, Wei Wang et al. 2006, Corchero et al. 2006 dealt with the motion of this CL during bubble growth.

A numerical approach is followed in this study to investigate effect of contact line on bubble growth and detachment on co-flowing air-water two-phase flow in a horizontal micro-channel. The continuous liquid phase is flowing in a tube of 500 µm inner diameter and the gas phase is axially injected through a nozzle of 110 µm inner diameter and 210 µm outer diameter. The two-phase flow is produced at the exit of the injection nozzle.

The model is based on a computational fluid dynamics (CFD) approach and is constructed with an open-source toolbox OpenFOAM (Open Field Operation and Manipulation), which utilizes a finite volume method to solve the Navier-Stokes equations along the volume of fluid (VOF) methodology to capture the liquid-gas interface. The volume of fluid method (VOF) is chosen because it does not impose any restrictions on the evolution of the interface shape.
The numerical predictions are illustrated by flow pattern visualizations and plots of geometrical variables like the contact line radius or the neck length. The numerical predictions obtained with this model are validated by experimental results (Vafaei et al. 2010, Zeguai et al. 2013, Quan and Hua 2008). The moving contact line is numerically visualized during bubble formation. The effect of contact line is analyzed and compared with constant contact line case.
The forces acting on the bubble during formation are analyzed for both cases: moving contact line and fixed contact line. A comparative study highlighted the differences between these two cases.

Figure 1 shows the formation of the bubble at the injection orifice of the gaseous phase in co-flowing water in a capillary tube. Since the wall of the injection nozzle has a given thickness, a detailed analysis allows depicting the contact line motion outward and inward along the wall thickness depending on the stresses applied at the interface. The visualization of a bubble being formed is shown by the phi color function (the phasic function) which shows two different colors, the red color represents the liquid phase and the blue color represents the gas phase. The outward movement of the contact line occurs during the first stage of bubble growth, then the contact line moves inward during the neck formation

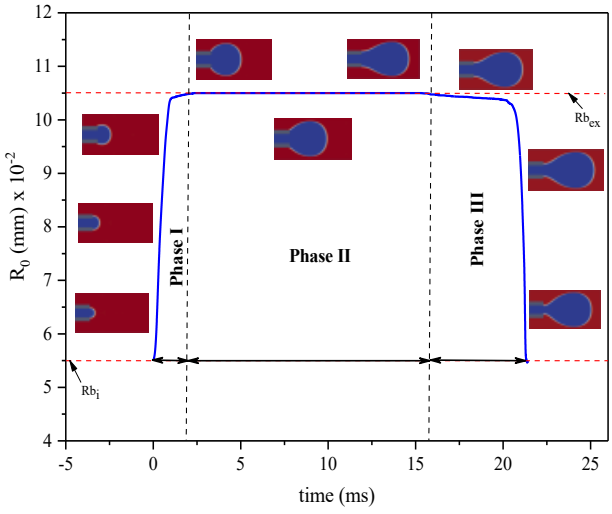

Figure 1: Variation of the radius of contact line versus time

(U_{GS}=0.014 m/s U_{LS}=0.076 m/s , d_b=0.11 mm, D=0.5 mm).

Figure 1 plots the evolution of the contact line radius (the continuous blue line). Three steps are exhibited during the bubble formation and correspond to a given behavior of the contact line.

It can be seen that the bubble formation goes through three phases, the first phase represents the expansion of the bubble where the radius of the contact line increases rapidly above the inner radius of the nozzle and reaches the outer radius in a few milliseconds. The second phase takes longer time and the contact line is pinned at the outer diameter of the wall of the injection nozzle, this phase represents the elongation of the bubble. The last phase represents the pinching and detachment of the bubble where the radius of the contact line decreases lasting for a very short period corresponds to the inward motion of the contact line untill it reaches the inner diameter of the nozzle, when the neck and the detachment occur.

This numerical analysis was completed with an analysis of the force balance to evaluate the main force forces acting on the bubble as a function of time.The investigations carried out allow to interpret the mechanics of detachment of bubbles in the absence of gravity and the movement of the contact line demonstrated experimentally.The effect of gravity is included and investigated for the vertical orientation of the capillary tube.

Conclusions

In-depth analysis of the nozzle wall describes the movement of the nip during the bubble growth process and its significant effect on its formation. We have shown that the size of the bubbles formed depends only on the contact line which is either fixed or mobile at the injection orifice of the gas phase. The comparative study of the forces applied on the forming bubble between the cases of a mobile and fixed contact line has made it possible to highlight the significant influence of the contact line. The detachment of the bubble is delayed with the movement of a contact line by comparing with that of a fixed contact line.

References

A. V. Byakova, S. V. Gnyloskurenko, T. Nakamura & O. I. Raychenko, Influence of wetting conditions on bubble formation at orifice in an inviscid liquid: Mechanism of bubble evolution. *Colloids and Surfaces A: Physicochemical and Engineering Aspects*, *229* (1–3) (2003) 19–32.

G. Corchero,A. Medina & F.J. Higuera, Effect of wetting conditions and flow rate on bubble formation at orifices submerged in water. *Colloids and Surfaces A: Physicochemical and Engineering Aspects*, *290* (1–3) (2006) 41–49.

S. Vafaei & D. Wen, Bubble formation on a submerged micronozzle. *Journal of Colloid and Interface Science*, *343* (1) (2010) 291–297.

W. Wang,K.H. Ngan,J. Gong & P. Angeli, Observations on single drop formation from a capillary tube at low flow rates. *Colloids and Surfaces A: Physicochemical and Engineering Aspects*, *334*(1–3) (2009) 197–202.

S. Quan & J. Hua, Numerical studies of bubble necking in viscous liquids. *Physical Review E - Statistical, Nonlinear, and Soft Matter Physics*, *77*(6) (2008) 1–11.

S. Zeguai, S. Chikh, L. Tadrist, Experimental study of two-phase flow pattern evolution in a horizontal circular tube of small diameter in laminar flow conditions, *International Journal of Multiphase Flow,* 55 (2013) 99–110.

26th European Low Gravity Research Association Biennial Symposium and General Assembly
14th International Conference on "Two-Phase Systems for Space and Ground Applications"
European Space Agency Topical Teams meetings
Granada (Spain), September 24-27, 2019

Poster 192

Experimental Investigation of Sessile Drop Evaporation on a Heated Inclined Substrate

Rafik Lankri [1a], Salah Chikh [2b], Lounès Tadrist [3c]

[1] Ecole Militaire Polytechnique, Laboratoire Turbomachines, Bordj El Bahri, Alger 16046, Algeria
[2] USTHB, Faculty of Mechanical and Process Engineering, LTPMP, Alger 16111, Algeria
[3] Aix-Marseille Université, CNRS, Laboratoire IUSTI, UMR 7343, Marseille 13453, France
[a] rafik_adz@yahoo.fr, [b] salahchikh@yahoo.fr, [c] lounes.tadrist@univ-amu.fr

roduction

lerstanding the process of the evaporation and the ciated heat and mass transfer in a sessile drop of liquid important for many industrial applications such as roelectronics, micro and nano-fabrication, inkjet printing, ibustion, etc. When a drop of liquid evaporates on a ace, the rate of heat and mass transfer as well as the es exerted on it depend on the geometry of the drop. stering the shape of a drop is a prerequisite for obtaining urately its volume and mass. Although the shape of small os of liquid deposited on horizontal surfaces can be ned by a simple spherical cap, the drops of greater size the vertical and inclined surfaces are more complex, ause the contact angles vary from a static advancing tact angle to a static receding contact angle.

hough a tremendous work on this topic has been carried during recent decades, research focusing on sessile drop poration on inclined surfaces remain limited. Kim et al. conducted a study on the evaporation process of a drop pure water on a flat surface whose inclination is trolled. Their results have shown that the evaporation e of an inclined drop becomes larger when increasing the ination angle and the gravity does not directly affect the poration dynamics. In another work, Yilbas et al. [2] estigated the dynamics of a water drop deposited on a rophobic substrate and looked at the influence of the p size and the inclination angle on the rolling or the ing of the drop during the inclination of the substrate. y obtained that increasing the drop size induces an ease in the adhesion forces, shear and drag on an ined wall. A good control of the operating conditions is datory for accurate measurements during experiments. vever, most of published works used room temperature hout any control, except Maurer et al. [3]. They used an conditioning system to control the working conditions.

aim of this study is to analyze the behavior and the poration kinetics of a sessile droplet of water deposited a substrate with varying inclination angle (φ = 0 °, 20 °, ° and 75 °) under controlled operating conditions bstrate temperature of 25°C and 40°C). The effect of the ity on the behavior of the drop during the evaporation cess is investigated by means of two experimental niques: the first is optical, it uses video recording and ge processing and the second is a thermal technique ed on heat flux measurements.

terials and Methods

experimental setup was mounted in order to follow in time the evolution of the evaporation dynamics of ile drops subject to their own weight or subject to the

encompasses several mechanical and electronic components. The test cell in which a heat flux sensor is placed and covered by a chosen substrate on which the drop is deposited, is instrumented to accurately control the temperature, the pressure and the relative humidity.

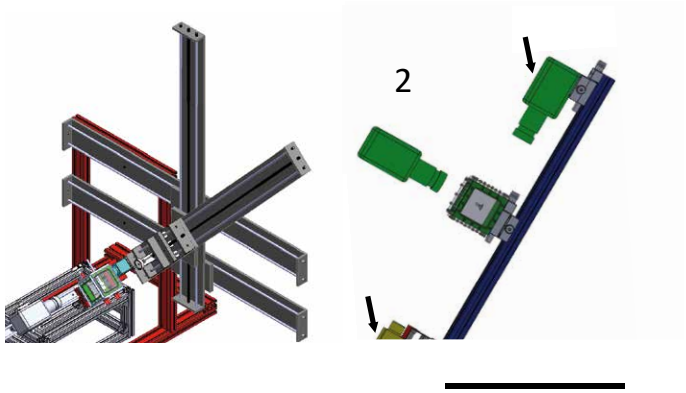

Figure 1: Schematic of the experimental setup
1. Side view camera, 2. Top view camera, 3. Light source

First the test cell is closed, then the operating conditions are set with programmable temperature controllers (PIDs), resistors, cooler and dehumidificator as well as the evaporator to regulate the inside conditions. After that, an injection system is used to deposit the drop with a micro-seringe with an uncertainty of 0.1 μL for the volume considered in this study (1 μL). Next, it is necessary to adjust the side view camera, the substrate and the light source on the same horizontal or inclined plane (figure 1). Optical settings are adjusted between the top view and the side view cameras for a good image quality. Finally, videos are recorded and an image processing tool (IC Measure) is used. Temperature, pressure, relative humidity and heat flux measurements are also logged and treated.

Results and discussion

Bi-distilled water is used as a working liquid. The operating conditions inside the enclosure were controlled and fixed for all the tests as follows: the relative humidity is set at 50% ± 5%, the pressure at 1 atm, the substrate temperature at 25 °C ± 0.5 °C and 40 °C ± 0.5 °C, the surrounding air temperature at 25 °C ± 0.5 °C. The inclination angles considered are φ = 0 °, 20 °, 45 ° and 75 °.

Two experimental techniques (optical and thermal) are used to deduce the different geometric properties of the drop as well as the heat flux exchanged between the drop and the surface of the substrate.

The evolution of the droplet volume for different substrate

in figure 2, it is shown that the trend follows a linear decay yielding a constant evaporation flux during the first part of the drop lifetime, then towards the end, it becomes non-linear with a slower kinetics. The effect of the inclination angle of the substrate is shown to slow down the evaporation kinetics as the angle increases.

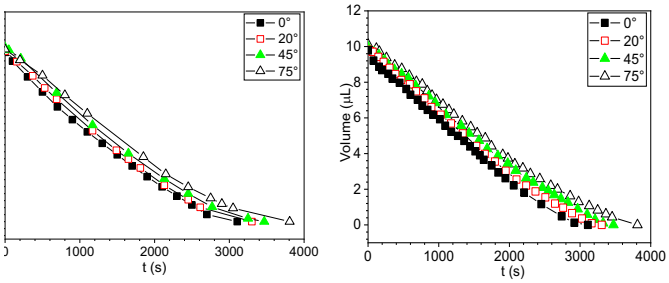

(a) (b)

Figure 2: Drop volume evolution during evaporation a) from visualization technique b) from thermal technique

Concerning the evolution of the geometrical parameters (table 1) a proportional relationship between the initial wetting radius and the inclination angle was found. Another proportional relationship between the initial advance angle, the initial hysteresis angle, the initial height, and the inclination of the plane has been recorded. An inverse proportionality variation between the initial receding angle and the angle of inclination is also observed.

Table 1: Geometrical parameters of the inclined drops

Inclination angle	**20°**		**45°**		**75°**	
Image						
Temperature (°C)	25	40	25	40	25	40
Initial height (mm)	1.68	1.65	1.64	1.62	1.62	1.60
Initial base radius (mm)	1.67	1.74	1.72	1.77	1.75	1.82
Initial receding angle (°)	80.1	79.2	65.6	67.8	62.6	64.7
Initial advancing angle (°)	95.7	94.1	98.2	98.7	103.4	103.2
Initial hysteresis angle (°)	15.6	14.9	32.5	30.9	40.7	38.5
Normalized onset time of depinning	0.69	0.42	0.52	0.31	0.24	0.15

It is noted that the heating temperature (25 °C and 40 °C) of the solid substrate does not affect much the initial hysteresis angle, as it is reported the drops deposited on substrate at 40 °C had a hysteresis angle slightly smaller than that deposited on a substrate maintained at 25 °C. The more the inclination angle increases, the more the initial hysteresis angle increases. This is due to the maximization of advancing contact angle and the minimization of the receding contact angle.

A linear relationship of proportionality was obtained between the inclined angle of the substrate and the droplet lifetime t_l (fig. 3). The results obtained revealed the onset time of depinning of the triple line is inversely proportional to the angle of inclination and the droplet lifetime t_l. This behavior can be explained by the fact that for more inclined substrate, the effect of the tangential component of gravity becomes bigger and takes over the forces of adhesion.

Figure 4, the average powers exchanged by the two techniques (optics and thermics) is plotted for a test cell temperature of 25°C. In terms of trend, one observes a linear dependence between the transmitted power and the angle of inclination of the substrate, the results obtained by the two techniques are in a very good agreement, such as the margin of error between the two methods is very weak.

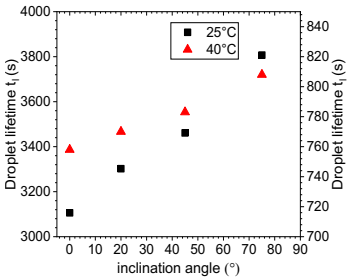

Figure 3: Droplet lifetime evolution. Left scale for 25°C and right scale for 40°C.

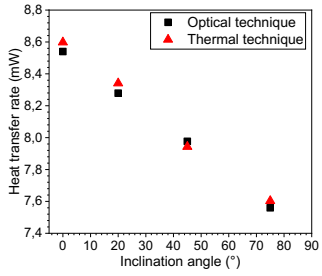

Figure 4: Heat transfer rate transmitted between the drop and the substrate, $T_{substrate}$ = 25°C.

Conclusions

The evaporation process of 10 µL of pure water deposited on an inclined aluminum substrate (φ=20°, 45° and 75°) and maintained at two temperatures of 25 and 40°C is experimentally studied with two measurement techniques.

The quantity of heat exchanged between the drop and the solid substrate shows a good agreement between the two techniques (optical and thermial), with a deviation of less than 5% on the recorded mean value. The deduction of the elementary variation of volume during the evaporation process by the thermal method is easier and more accurate than the optical method.

The obtained results revealed that the evaporation rate is inversely proportional to the angle of inclination. The more the substrate is tilted, the longer the droplet lifetime t_l is, while following a linear variation.

Additionally, the onset time of depinning is inversely proportional to the angle of inclination for the two temperatures with a faster depinning in the case of 40°C. This reduction in the onset time of depinning is explained by the increase in the tangential component of the weight, which induces a reduction in the force of adhesion. Thus causing the appearance of the depinning of contact line more prematurely.

References

[1] J.Y. Kim, I. G. Hwang and B.M. Weon," Evaporation of inclined water droplets," The Royal Society of Chemistry, 7 (2017) 48806–48818.

[2] B.S. Yilbas, A. Al-Sharafi, H. Alia and N. Al-Aqeeli, "Dynamics of a water droplet on a hydrophobic inclined surface: influence of droplet size and surface inclination angle on droplet rolling". RSC Adv. 7(2017) 48806-48818.

[3] T. Maurer, A. Mebus and U. Janoske, " Water Droplet Motion on an Inclining Surface", Proceedings of the 3rd International Conference on Fluid Flow, Heat and Mass Transfer, Paper No. 143.

26th European Low Gravity Research Association Biennial Symposium and General Assembly
14th International Conference on "Two-Phase Systems for Space and Ground Applications"
European Space Agency Topical Teams meetings
Granada (Spain), September 24-27, 2019

Poster 193

Transport Properties of Fluids for Exploration

R. Michael Banish

University of Alabama in Huntsville, Huntsville, Alabama, United States;
banishm@uah.edu

Introduction

The transfer, transport, of heat energy into or out of a fluid is governed by the thermal conductivity, or the thermal diffusivity. The thermal conductivity is the more widely used term, while the thermal diffusivity is the more physically descriptive term. Accurate values of the thermal diffusivity of fluids is important both for theoretical development as well as for industrial applications.

Convective Effects

Thermal transport of fluids on the Earth, under terrestrial gravity, occurs due to both conductive transport and convective transport. Convective heat transport dominates for most process or situations on earth. (Began et al. 1978 and 1980). Convection leads to more efficient heat transport, thus in a gravitational field heat energy is transferred at a higher rate than by conduction alone. In a terrestrial environment thermal diffusivity measurements are likely contaminated by convective contributions. In low-gravity environments, without convection, heat transfer will be lower, and heat transfer rates inferred from terrestrial measurements cannot be assumed to be valid in a low-gravity environment. Simple scaling illustrates the difficulty of obtaining purely diffusive transport in liquids. In a system of thermal diffusivity 10^{-1} to 10^{-3} cm^2/s and a typical diffusion distance of 1 cm, the characteristic diffusion velocity is of order 10^{-1} to 10^{-3} cm/s. Hence, if true diffusion is to be observed, convective flow velocities parallel to the concentration gradient must be of order 10^{-3} to 10^{-5} cm/s. In a system where a convective driving force is intentionally introduced, i.e., a temperature gradient, this condition is a priori not met. Thus, in liquids, the attainment of diffusion-dominated transport over macroscopic distances at normal gravity is obviously not a simple task. It is important, to confidently understand and model low-gravity process, to have accurate values of the thermal diffusivity of fluids common to low-gravity environments, or for materials that mimic fluids used in low-gravity environments. Low gravity measurements provide an opportunity to obtain accurate thermal diffusivity measurements. (Alexander et al 1977).

Project Goals and Materials

This project will determine the thermal diffusivity of liquid gallium samples on the suborbital Blue Origin New Shepard vehicle. The New Shepard vehicle transitions through about 150 seconds of low-gravity during flight. We will test the hardware by determining the thermal diffusivity of liquid gallium. Gallium represents an analog to possible heat transfer fluids, such a liquid ammonia, or other liquid metals. Gallium is non-toxic and non-reactive and represent good candidate materials for experiment validation before requesting additional flights with more complex systems; such as fluid pressurization, or more complex materials. The thermal diffusivity of liquid gallium has been measured in a range of gravity levels with widely varying results. The thermal diffusivity determination of the four samples will be separated by approximately 30 seconds during the 150 seconds of low-gravity. This will provide us with a range of outcomes to determine optimum gravitational conditions to achieve accurate values of the thermal diffusivity.

Methodology

We have developed, through NASA sponsorship on past projects, thermal diffusivity measurement methodologies that are particularly suited to experimental constraints in a low-gravity environment (Jalbert et al 1998, Jalbert et al. 1988, Pourpoint et al 2000, Banish et al 2014). These methodologies required only a (non-timed) heat pulse and subsequent temperature measurements in the heated fluid. For this proposal, we plan to test the operation of the hardware that has only been used in Earth gravity. This project will validate the applicability of the hardware to future low-gravity mission to support exploration initiatives, as well as providing values for theoretical validation.

Conclusions

We will determine the thermal diffusivity of four liquid gallium samples as the spacecraft transitions through a range of gravity levels. The results of these experiments will provide guidance as to what gravity levels is required to obtain convective contamination free thermal diffusivity values. These results may lead to sub-orbital vehicles being a primary method for thermal diffusivity determinations.

Acknowledgements

We wish to thank NASA for sponsorship of this project under grant 80NSSC18K1669 and Blue Origin for technical support.

References

A. Began, C.L. Tein, Fully developed natural counterflow in a long horizontal pipe with different end temperatures, Int. J. Heat and Mass Transfer, 21 (1978) 701-718,

A. Began, K Shigeo, Experimental study of natural convection in a horizontal cylinder with different end temperatures, Int. J. Heat and Mass Transfer, 23 (1980) 1117-26.

J.I.D. Alexander, J-F. Ramus, F. Rosenberger, Convective Contamination in Gravity Fields, Microgravity Science and Tech., 9 (1977) 510-516.

L.B. Jalbert, R.M. Banish, F. Rosenberger, *Real-time Diffusivity Measurements in Liquids at Several Temperatures with one Sample,* Phys. Rev. E57 (1998) 1727-35.

L.B. Jalbert, F. Rosenberger, R.M. Banish, *On the Insensitivity of Liquid Diffusivity Measurements to Deviations from 1-D Diffusion*, J. Phys.: Cond. Matter 10 (1998) 7113-18.

T. Pourpoint, R.M. Banish, F. Wessling, R.F. Sekerka, *A Real-time method for Thermal Diffusivity Determinations*, Rev. Sci. Instruments, 71 (2000) 4512-20.

R.M. Banish, J.I.D. Alexander, *Reduced Algorithms for Diffusivity Determinations*, in Transport Properties of Fluids, W.A. Wakeham, A. Nagashima, and M.J. Assael editors. IUPAC (2014).

26th European Low Gravity Research Association Biennial Symposium and General Assembly
14th International Conference on "Two-Phase Systems for Space and Ground Applications"
European Space Agency Topical Teams meetings
Granada (Spain), September 24-27, 2019

Poster 195

Performance assessment of ultrasonic waves for bubble control in LOX tanks

F. Suñol[1], D. A. Ochoa[2], M. Granados[3], J. E. García[4], and R. González-Cinca[5]

Department of Physics, UPC-BarcelonaTech, Barcelona, Spain;
[1]francesc.sunol@upc.edu, [2]diego.a.ochoa@upc.edu, [3]marta.granados.jimenez@estudiant.upc.edu, [4]jose.eduardo.garcia@upc.edu,
[5]ricard.gonzalez@upc.edu

Introduction

An efficient long-term storage of cryogenic propellants is a challenge for future space exploration missions. In long duration missions in low Earth orbit, issues associated to long-term storage, such as the cryogenic propellant loss due to boil-off, will require a proper management (Salerno 1999, Motil 2007). The vapour bubbles formed as a result of boil-off can generate foam structures, which could be hazardous in different operations in orbit. Since current heat insulation technologies are not able to provide a sufficient control of boil-off for long times, other techniques are required to minimize the effects of boiling in fuel tanks. An approach recently proposed by the UPC Laboratory of Microgravity consists in the use of acoustic fields for the control and elimination of bubbles. Bubble dynamics can be managed by the application of an acoustic field (Leighton 1974, Crum 1975). In the proposed technique, the force due to the acoustic wave generated by a piezoelectric transducer detaches the bubbles from the tank walls and moves them to the subcooled liquid where they collapse. This technique is currently under study in microgravity conditions at non-cryogenic temperatures. To be applicable in space, the technology has to be validated at cryogenic temperatures. However, numerous attempts to generate a valid acoustic signal at low temperatures have been performed without success. This is due to two facts: on one hand, piezoelectric materials are known to work lousy at the desired cryogenic conditions; on the other hand, the acoustic matching layer material loses its transmission properties at low temperatures, and consequently no acoustic signals can be transmitted into the fuel tank. However, recent studies have shown that epoxy resin-based acoustic matching layers can exhibit an increase in the transmission coefficient at cryogenic conditions, and experimental results show that the amplitude of the transmitted signal at low temperatures can increase by a factor of 1.5 the amplitude obtained at room temperature.

Experimental Setup

A transducer-rod system was built to test the possibility of using piezoelectric ceramics to generate ultrasonic pulses at cryogenic temperatures. This system consists in an aluminum rod 75 mm long and with a 12 mm x 12 mm square section. The shape of the rod ensures that one face of the rod is always in thermal contact with the platform connected to the cold finger, ensuring an optimal heat transfer from the cold finger of the cryogenic system to the transducer-rod system. Two lead zirconate titanate (PZT) based piezoelectric ceramics were attached mechanically at each end of the rod. The disc-shaped (1 mm thickness and 10 mm diameter) piezoelectric ceramics act as transducers that convert an electrical signal to an acoustic signal and vice-versa. One transducer acts as an emitter while the other one acts as a receiver. With the aim to ensure an optimal acoustic energy transfer to the aluminum rod, different materials were tested as acoustic matching layer. The best results were obtained using an epoxy resin, that increase linearly the acoustic impedance with a decrease of temperature.

Experimental measurements were obtained in a closed-loop cryogenic system. Liquid helium was recirculated through a cold finger using an ARS-4HW compressor and refrigerated by a Polyscience 6000 chiller. The transducer-rod system was placed inside a custom high-vacuum chamber with cylindrical shape, with a height of 20 cm and a diameter of 25 cm, built by Arscryo. Through thermal contact, the cold-finger is able to cool the cryogenic chamber to temperatures around 20 K. Temperature was reduced from 300 K to 87 K, while the pressure in the chamber ranged from 10^{-5} mbar to 10^{-7} mbar. Rectangular pulses with an amplitude of V_{pp} = 20 V and a width of 250 ns were generated at a frequency of 1 KHz using an Agilent 33220A generator, and sent to the emitter transducer. The electric pulse was converted to an acoustic signal that travels through the aluminum rod, and then converted back to an electric signal by the receiver transducer. The electric signal at the receiver was captured using an oscilloscope Keysight DSOX2004A. In order to reduce the inherent noise, the signal was averaged over 2048 samples.

Results and discussion

With the aim to study the feasibility of generating an ultrasonic signal at cryogenic conditions, a rectangular pulse is sent to the emitter transducer and converted to an acoustic signal. Part of the energy of the acoustic signal is reflected inside the piezoelectric ceramics and another part is transmitted into the aluminum rod. The acoustic matching layer determines the amount of energy transmitted into the rod. Previous measurements using cyanocrilate as acoustic matching layer showed that the amplitude of the received signal drops as the temperature approaches 130 K. Numerous attempts to generate an ultrasonic signal below 130 K were unsuccessful. However, using an epoxy resin-based matching layer, an ultrasonic signal with an increasing amplitude as the temperature decreases was obtained.

The transmitted acoustic signal travels at the speed of sound through the aluminum rod and after 12 μs, the signal is received in the receiver transducer and converted back to an electric signal. Fig. 1 shows an example of the shape of the received signal at different temperatures. 1. The peak-to-peak

amplitude of the received voltage increases as the temperature decreases.

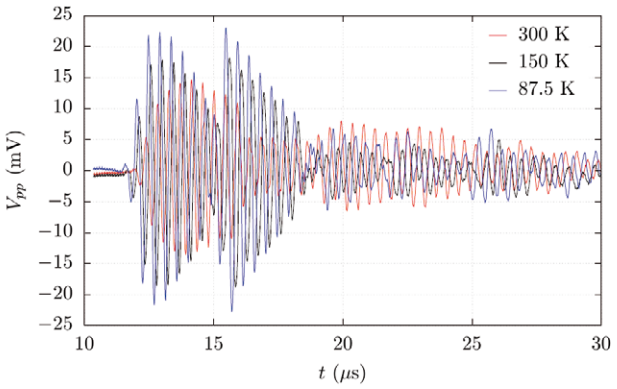

Figure 1: Shape of the received acoustic signal at different temperatures.

The peak-to-peak amplitude of the received signal was measured at different temperatures, from room temperature (300 K) to a temperature slightly below the boiling point of liquid oxygen (Fig.2). The peak-to-peak amplitude increases as temperature decreases, up to a factor of 1.5 compared with the one obtained at room temperature. This is due to an increase in the acoustic factor of 1.5 compared to the one obtained at room temperature, which is associated to an increase in the acoustic impedance of the epoxy-resin material as the temperature drops.

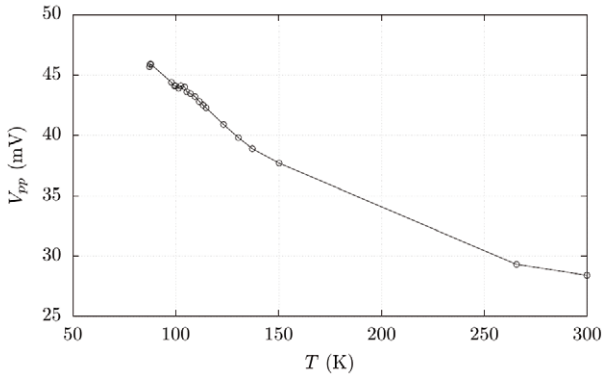

Figure 2: Peak-to-peak amplitude of the received acoustic signal as a function of the temperature.

Conclusions

Experimental measurements have been performed at cryogenic conditions to study the feasibility of generating ultrasonic signals at low temperatures. Experiments revealed that epoxy resin-based acoustic matching layers can exhibit an increase in the transmission coefficient at cryogenic conditions. The results obtained show that the amplitude of the transmitted signal at cryogenic temperatures can increase by a factor of 1.5 the value obtained at room temperature.

Acknowledgements

This research was supported by the Spanish Agencia Estatal de Investigación (project ESP2015-72277-EXP).

References

L.A. Crum, Bjerknes forces on bubbles in a stationary sound field, *J. Acoust. Soc. Am.* 57, 1363 (1975).

T.G. Leighton, The Acoustic Bubble, Academic Press, New York (1974).

S. M. Motil, M. L. Meyer, and S. P. Tucker, Cryogenic fluid management technologies for advanced green propulsion systems, Technical Report TM-2007-214810, NASA (2007).

L. J. Salerno and P. Kittel, Cryogenics and the human exploration of Mars, *Cryogenics*, 39:381-388, (1999).

26th European Low Gravity Research Association Biennial Symposium and General Assembly
14th International Conference on "Two-Phase Systems for Space and Ground Applications"
European Space Agency Topical Teams meetings
Granada (Spain), September 24-27, 2019

Poster 196

NewSpace: A New Era of Opportunities

Dr. Olympia.Kyriopoulos[1]

[1]OLYMPIASPACE, Darmstadt, Germany
olympia@olympiaspace.com

Introduction

OLYMPIASPACE was founded in the era of NewSpace, with the goal of easing access to space for everyone.
Historically, space was a paradigm dominated by government entities, almost intangible for society. Now we are witnessing a major shift from OldSpace to NewSpaee, a space era increasingly populated by entrepreneurs and visionaries.

Figure 1: Paradigm Shift OldSpace vs. NewSpace.

NewSpace market potential

At OLYMPIASPACE, we strongly believe that this revolutionary access to space, with its key point in the increased number of flights available at a relatively low-cost, is a concrete place of opportunities. Bank of America's Merrill Lynch (BoAML) sees the size of the space industry octuplicating in the next three decades, to at least $2.7 trillion.

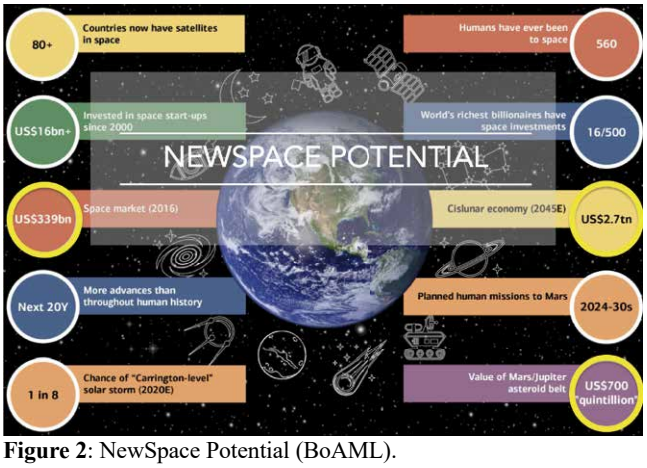

Figure 2: NewSpace Potential (BoAML).

Revolutionary access to space through sRLV

In the last decades, several solutions for suborbital reusable launch vehicles (sRLV) have been proposed and realized, ranging from rockets that vertically launch and land to winged spacecrafts that take-off and land horizontally. In both cases these reusable vehicles enable payloads to cross the threshold of space and to experience up to four minutes of microgravity.

The following table gives an overview of the currently existing platform for microgravity research and compares the classical opportunities with new, competitive sRLV ventures.

	Drop Tower	Parabolic Flights	TEXUS	sRLV
micro-g duration	9,3 s	20–25 s	360 s	180–240 s
micro-g quality	10^{-6} g	10^{-2}–10^{-4} g	10^{-4}–10^{-5} g	10^{-4}–10^{-5} g
max. acceleration	50g	2–4 g	20g	2–6 g
max. altitude	–	–	250 km	130 km
payload capacity	<1m^3, <265kg	variable	<1m^3, <400kg	<1m^3, <770kg
conduction of exp.	autonomous	hands-on	autonomous	hands-on / autonomous
preparation time	few weeks	few months	few years	few weeks
number of campaigns	3 × daily	2–3 per year	1–2 per year	4 × daily
total flight costs	5000–10k EUR	650k Euro	approx. 2M EUR	75k–600k EUR

Figure 3: Microgravity research flight opportunities.

In comparison to the existing microgravity platforms, they seek to offer a more flexible, efficient, inexpensive, frequent access to space for payloads and human-tended spaceflight. For biomedical research which is usually carried out in sequences of repeated series of consecutive experiments, these conditions are ideal. However, suborbital space flights could not only revolutionize biomedicine but also physical and life sciences.

Turnkey end-to-end solution

OLYMPIASPACE offers a full end-to-end service that includes all the legal and regulatory requirements in order to safely pick-up the payload, to perform the flight and return the payload, together with data analysis, to customers clients. These customers range from private companies and commercial entities, to research centres and educational institutions. The payload can be anything envisioned by the customer, from microgravity research experiments, to commercial products and not-for-profit ideas.

Conclusions

Space is no longer only a dream, but a viable path for future economic growth. Thanks to sRLV it will revolutionize the microgravity increasingly become a place where business and industry thrive.

References

M. Sheetz, The space industry will be worth nearly $3 trillion in 30 years, *Bank of America Merrill Lynch* (2017).

O. Kyriopoulos, Biomedizinische Forschung auf suborbitalen Flügen, Forschungsplattformen der Zukunft, *Flug- und Reisemedizin, 21 (4): 183–189* (2014).

Poster 197

A high precision experimental procedure to study capillary bridges.

Maxime Chinaud [1a], Loïc Tadrist [2b], Lounès Tadrist [1c]

[1]Aix-Marseille Université, CNRS, Laboratoire IUSTI, UMR 7343, Marseille 13453, France
[2] Microfluidics Lab, Mechanical and Aerospace Engineering Department, University of Liege, 4000 Liege, Belgium
[a] maxime.chinaud@univ-amu.fr, [b] loic.tadrist@uliege.be, [c] lounes.tadrist@univ-amu.fr

Introduction

Interfacial phenomena are encountered in many environment situations and involved in a huge number of industrial applications. In macrogravity, these effects may play a dominant role when two immiscible fluids are or are not in contact with a substrate. The heat and mass transfer across these interfaces are also governed by the shapes of these surfaces.

Plateau [1] and Rayleigh [2] were the first who investigated experimentally and theoretically the mechanics of interfaces. The Young-Laplace equation describes the shape of a surface between two fluids. However this equation is not easy to solve unless in some rare cases [XX]. The modelling of the adhesion force created by a capillary bridge is limited by this difficulty. Thus, we must rely on numerical computations to get insights on the effect of parameters on the capillary force.

The study of capillary bridges can also be done experimentally. However precise experimental data are difficult to obtain due to the small size of the experiment and the thermal and wetting conditions that may change the results. We consider for our experiment a drop of volatile liquid bridging two plates of the same solid. The capillary bridge is a standard configuration in which interfacial effects may be studied and characterized dynamically for several type of fluids [3].

In this extended abstract we present the design of an experimental procedure to observe capillary bridges and to measure the capillary forces with extreme precision and control on all external parameters. Some preliminary results are also presented as examples.

Materials and Methods

The experimental arrangement is sketched in Figure 1. A cylindrical plate of 2 cm in diameter is placed on a precision scale (*Mettle Toledo xs205* with precision of 1 µN). The tare is made to remove the effect of the weight of the plate.

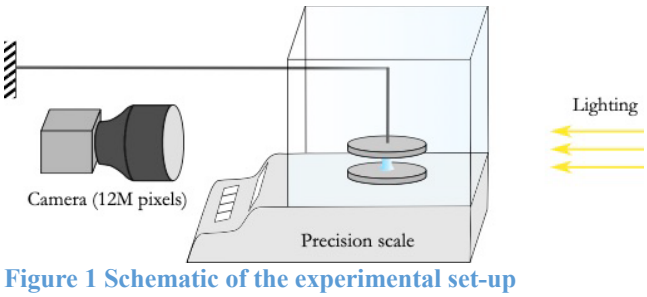

Figure 1 Schematic of the experimental set-up

A drop of volatile liquid (water or ethanol in our first experiments) is deposited on the bottom plate. The top plate is then approached until the liquid makes a bridge between the two solid plates. The height of the liquid bridge is then changed up to the desired height by moving upward or downward the top plate. At this step the position of the top plate is definitely fixed.

The shape of the bridge is recorded with a high resolution camera (*Basler ace - acA4024-8gm*, 4024x3036 pixels) at 0.03 Hz in the case of water and 0.1 Hz in the case of ethanol. The camera is fitted with a macro-objective (*Opto Engineering MC3-03X*). This configuration allows to zoom up to 0.8 micron per pixel which is close to the diffraction limit. The bridge is lighted by a LED light with a tracing paper diffusor to get a nice image. The light is filtered with an IR filter to avoid any unwanted warming up of the bridge. The solid plates are made of the same substrate (either PVC or aluminium of different roughness in our first experiments. The substrate nature can also be changed by gluing a small glass slide on the plate).

The liquid bridge is then let drying in controlled thermodynamic conditions (temperature 24ºC and humidity 65%). The bridge volume reduces until it breaks into two sessile drops. We stop the force and image recording at that point.

Controlability and precision

The study of a drying capillary bridge allows to study bridges of different volumes without external intervention. However, one has to notice that evaporation may cool down the capillary bridge creating temperature gradients at the liquid surface. Those gradients are known to trigger marangoni flows that may change the surface properties of the bridge both in terms of shape and force.

The geometry of our set-up, mainly the fact that the bridge is between two large plates, ensures that the evaporation is (i) driven by conduction (ii) almost 2D and (iii) as slow as necessary. By changing the plate sizes we can increase or decrease the evaporation debit. The evaporation has to be slow to allow the solid plates to warm up the bridge at the same rate as evaporation cools it down. When evaporation is slow enough, the temperature gradients are small enough not to create any Marangoni flow within the liquid. In this configuration, the thermal and mass transfer are safely disconnected from the capillary bridge mechanics.

The second major point for the reproducibility of a capillary experiment is the variation of the wetting angles. As the bridge dries, the wetting angles should quickly converge towards the value of the receiding angle. However, this is only true on extremely smooth surfaces. In the case of rough surface or surfaces contamined by dust, the contact line of the bridge may pin into the surface defect and (i) decrease the wetting angle and (ii) breaks the axi-symmetry of the bridge. To avoid the problem of dust, the plate is cleaned

before each experiment with ethanol. We also study the effect of roughness by varying the surface of the substrate using sand-papered aluminium plates with different grain sizes. The roughness of the aluminium plate are also measured after the sand-paper treatment.

Preliminary results

We give here the shape measurements made on a drying water droplet of height 1.5 mm bridging two PVC plates, in Figure 2. The bridge thins as the volume reduces. The bridge remains centered and the wetting angles does not vary proving that the roughness of the PVC plate does not affect the quasi-static shape of the capillary bridge. The simultaneous force acquisition is plotted in Figure 3. The force has a magnitude of some hundreds of micro-newtons at the begining of the experiment and decreases as the time increases (similarly as the volume decreases since volume decreases linearly in time). At approximately 2500s the bridge breaks which correspond to the vertical asymptote in Figure 3. The constant value of the force after break-up corresponds to the weight of the remainig droplet on the bottom plate.

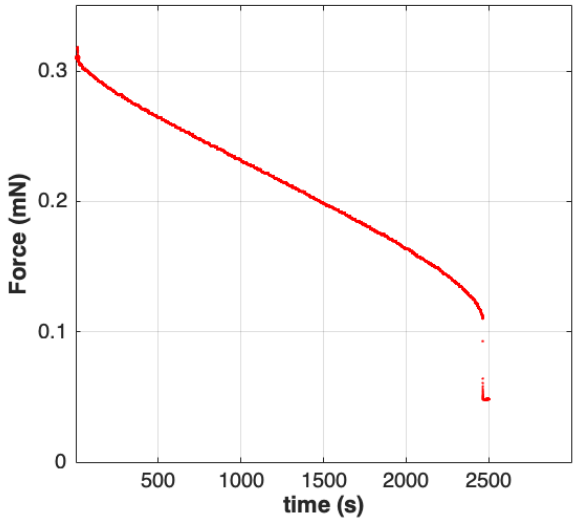

Fig.2: Capillay force variation versus time of a water capillary bridge on PVC substrates

The non-wetting case has also been investigated and brings insightful views on the force generated by a capillary bridge. We covered the PVC plate with hydrophobic teflon. A droplet of water was also deposited between the two plates and the top plate placed at the desired height. We observe in Figure 4 that the force generated by the capillary bridge is negative at the begining corresponding to a repulsive force. The bridge looks like a cushion with wetting angles larger than 90°. As the bridge dries, the wetting angles strongly decrease (which reveals some pining of the contact line) and the force goes from repulsion to attraction. The force then get to a maximum and then the bridge behaves as for the wetting case: it thins and the attractive force decreases until it breaks. The constant value of the force after break-up corresponds to the weight of the remainig droplet on the bottom plate.

Those preliminary results also show the importance of surface roughness in the pining of the triple line that may totally change the story about the force generated by a capillary bridge.

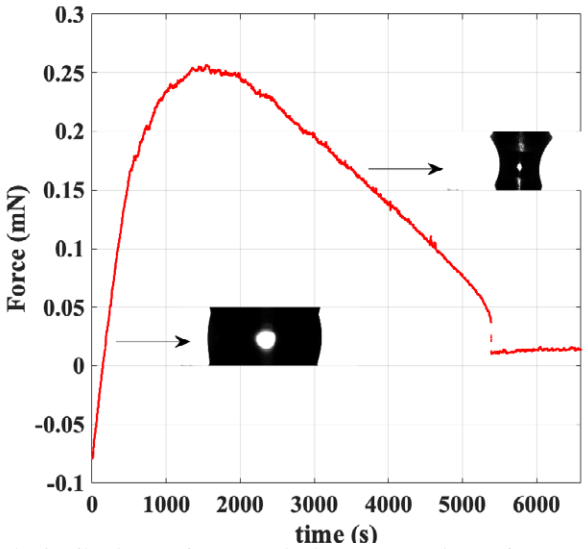

Fig.3: Capillary force variation versus time of an ethanol capillary bridge on teflon substrates

Futur works

We plan to use this well defined set-up of high precision to study the quasi-static behaviour of capillary bridges. Namely, we want to confront those experimental results to a new theory of capillary bridge break up as well as to a new approximate solution of the Young Laplace solution for an axi-symmetric bridge.

This precise set-up will also be used to measure some surface properties of complex fluids.

References

[1] Plateau, J. Statique expérimentale et théorique des liquides soumis aux seules forces moléculaires. Gauthier-Villars, 1873.
[2] Rayleigh, L. (1878). On the instability of jets. Proceedings of the London mathematical society, 1(1), 4-13.
[3] Tadrist, L., Motte, L., Rahli, O., Tadrist, L. Characterisation of interface propeies of fluids by evaporation of a capillary bridge. Royal Society Open Science (Under review)